Quantum Coherence and Covalency in Organometallic Lanthanide Complexes Investigated by Pulse EPR Techniques

A THESIS SUBMITTED TO THE UNIVERSITY OF MANCHESTER FOR THE DEGREE OF

Doctor of Philosophy

IN THE FACULTY OF SCIENCE AND ENGINNERING

2020

Lydia Nodaraki

Department of Chemistry

Contents

Contents 3

List of Figures 5

Abstract 7

Declaration 9

Copyright Statement 11

Acknowledgements 13

Chapter I. Introduction

- I.I Rationale for the alternative format 15
- I.II Organization of the thesis 15
- I.III Contributing authors 15

Chapter II. Introduction to electron paramagnetic resonance spectroscopy

- II.I Basic principles of EPR spectroscopy 18
- II.II Spin Hamiltonians 21
- II.III Introduction to pulsed EPR spectroscopy 26
  - II.III.I Relaxation times 28
  - II.III.II Hyperfine sublevel correlation (HYSCORE) spectroscopy 30
  - II.III.III Electron nuclear double resonance (ENDOR) spectroscopy 34

Chapter III. Review of the field

- III.I Application of pulse EPR to the study of molecular qubits 37
  - III.I.I Background 37
  - III.I.II Molecular spin systems as quantum bits 39
    - III.I.II.I Transition metal qubits 41
    - III.I.II.II Lanthanide metal qubits 43

- III.II Applications of HYSCORE to study the extend of covalency in f-element complexes

  - III.II.I Covalency of lanthanide and actinide elements 45
  - III.II.II Covalency studies via EPR spectroscopy 46

Chapter IV. Paper 1: Engineering electronic structure to prolong relaxation times in molecular qubits by minimizing orbital angular momentum 50

Chapter V. Manuscript draft 1: Low-valent Sc and Lu organometallic complexes as qudits with an increased Hilbert space 111

Chapter VI. Manuscript draft 2: Ligand effects on the spin relaxation dynamics and coherence manipulation of organometallic La^{II} potential qudits. 139

Chapter VII. Manuscript draft 3: An organometallic yttrium(II) spin qubit based on a rigid aryloxide ligand displaying enhanced coherence properties 182

Chapter VIII. Manuscript draft 4: Covalency in $LnCp^{tt}_3$ (Ln = Ce, Nd, Sm) evaluated via HYSCORE spectroscopy 211

Chapter V. Conclusions and future work 257

References 259

List of figures

Chapter II. Introduction to electron paramagnetic resonance spectroscopy

Figure 1. Electron Zeeman splitting for an unpaired electron, as a function of the strength of the magnetic field and the resonance condition.
Figure 2. Representation of continuous wave EPR spectra with (a) isotropic; (b), (c) axial; (d) rhombic symmetries. The upper curves represent the absorption spectra and lower curves the first derivative (CW spectra).
Figure 3. Energy levels of a system with an unpaired electron and a magnetic nucleus with nuclear spin of ½ as a function of the magnetic field. The vectors are noted the allowed EPR transitions ($\Delta m_S = \pm 1$ and $\Delta m_I = 0$) and at the lower part the splitting of the signal due to the hyperfine interactions is depicted.
Figure 4. The zero-field splitting diagram of the triplet state for (a) oblate and (b) prolate shaped spin density distribution.[12]
Figure 5. Schematic representation of the two-pulse primary echo sequence, with the magnetization vector on the top explaining how the echo is generated.
Figure 6. Schematic representation of the three-pulse ESEEM sequence for determining the spin lattice relaxation time.
Figure 7. Schematic representation of the two-pulse ESEEM sequence for determining the phase memory time.
Figure 8. Schematic representation of the inverted-echo four-pulse ESEEM sequence for determining the HYSCORE spectra.
Figure 9. Schematic representation of the Fourier transformation of the 2D time domain experimental data to a 2D frequency domain HYSCORE spectrum.
Figure 10. Theoretical HYSCORE powder patterns for an $S = 1/2$, $I = 1/2$ spin system with an axial hyperfine tensor (a) Strong-coupling case with $\nu_I = 3.5$ MHz, $a_{iso} = 18$ MHz, and $T = 6$ MHz; (b) Weak-coupling case with $\nu_I = 14$ MHz, $a_{iso} = 2.5$ MHz, and $T = 6$ MHz.[22]
Figure 11. X-Band (at 9.7 GHz) HYSCORE spectra of the ^{14}N region of CuNCTPP diluted in the Zn analogue powder sample, measured at g_z orientation ($\nu_{14N} = 0.9$ MHz) with $\tau = 100$ ns. [24]
Figure 12. Schematic representation of the Mims ENDOR sequence; the inter-pulse delays are fixed and the radiofrequency is varied.
Figure 13. Schematic representation of (a) the selective inversion of the electron spin population due to the π_{mw} pulse; (b) the selective inversion of the nuclear spin population due to the π_{rf} pulse; (c) the resulted electron spin saturation.
Figure 14. Schematic representation of the Davies ENDOR sequence; the inter-pulse delays are fixed and the radiofrequency is varied.

Figure 15. Schematic representation of the two states of (a) a classical bit; (b) a quantum bit $|\psi\rangle$ (Bloch sphere).
Figure 16. A schematic representation of the transient nutation pulse sequence, which implies a tipping pulse, prior of a standard Hahn echo sequence tilting the magnetisation through a tipping angle, $\theta = g\mu_B B_1 t_p/\hbar$, away from the alignment with the applied magnetic field.
Figure 17. Molecular structure of (a) a {Cr_7Ni} analogue; (b) the asymmetric two-{Cr_7Ni} linked by a Co(II) complex; (c) Schematic representation of the CNOT gate of the two-qubit assembly.[44]
Figure 18. (a) The Hahn echo decay curve at 10 K in CS_2 fitted by the biexponential equation, (inset) molecular structure of the $[V(C_8S_8)_3]^{2-}$; (b) Logarithmic temperature dependence of T_2 in different solvents.[45]
Figure 19. (a) Temperature dependence of T_1 and T_m relaxation times; (b) Rabi oscillations at 300 K for different microwave attenuations.[46]
Figure 20. (a) Hahn echo decay curves as a functions of the 2τ time at different temperatures; (b) Temperature dependence of the spin-lattice relaxation and phase memory time; (inset) Molecular structure of the $[Cu(mnt)_2]^{2-}$.[47]
Figure 21. (a) Zeeman diagram for the $m_J = \pm 4$, $I = 7/2$ ground state at g_z orientation; the grey lines correspond to the ideal D_{4d} symmetry, while the thick black ones assume the use of an extra 'axial + $B_4^4\hat{O}_4^4$' parameter (red lines indicate the location of CTs); (b) T_2 divergence at the CTs illustrated on the first four panels, while the rightmost panel shows T_2 values at various frequencies some of them well away from CTs.[48]
Figure 22. (a) Schematic representation of a molecular spin transistor based on a $TbPc_2$ molecule linked to source and drain gold electrodes; (b) Zeeman diagram exhibiting the energy of the two $J_z = \pm 6$ ground state split into four different sub-states due to the hyperfine interactions with the nuclear spin of $I = 3/2$.[50]
Figure 23. (a) Schematic of the structure of $[Th(Cp^{tt})_3]$ and $[U(Cp^{tt})_3]$; (b) Numbering scheme used for Cp^{tt} ligands and the molecular axis system; (c) Molecular structure of $[Th(Cp^{tt})_3]$ from single crystal X-ray diffraction.
Figure 24. X-Band continuous wave EPR spectra of polycrystalline samples of (a) $[Th(Cp^{tt})_3]$ at 100 K; (b) $[U(Cp^{tt})_3]$ at 5 K.
Figure 25. X-Band HYSCORE spectra (a) for complex $[Th(Cp^{tt})_3]$ at the ^{13}C region; (b) for complex $[U(Cp^{tt})_3]$ at the ^1H region (simulation with red).
Figure 26. (a) Molecular structure of $[Yp(Cp)_3]$; (b) FID-detected ERP spectrum (black) of YbCp3 and the corresponding first derivative (blue).
Figure 27. X-Band HYSCORE spectra at ^{13}C region and at 5.25 K (a) experiment; (b) simulation.

Abstract

Quantum coherence and covalency in organometallic lanthanide complexes investigated by pulse EPR techniques: a thesis submitted to the University of Manchester for the degree of Doctor of Philosophy in the Faculty of Science and Engineering.

The research presented in this thesis uses continuous-wave and pulsed electron paramagnetic resonance (EPR) techniques for the investigation of the electronic structure, relaxation and quantum coherence properties of a number of organometallic complexes of C_3 symmetry.

The compounds include either a di- or trivalent lanthanide or transition metal ions bound by three cyclopentadienyl ($Cp' = C_5H_4SiMe_3$, $Cp'' = C_5H_3(SiMe_3)_2$-1,3, $Cp^{tt} = C_5H_3(CMe_3)_2$-1,3), silyl-amide ($N'' = N(SiMe_3)_2$) or aryloxide ($OAr^{Ad,Ad,Me}$ = 2,6-Ad_2-4-Me-C_6H_2O) ligands, where Me and Ad refer to methyl and adamantane subsituents. Studies on $[Ln(Cp')_3]^-$ ($Ln^{II} = La^{II}$, Lu^{II} or Y^{II}), $[Sc\{N(SiMe_3)_2\}_3]^-$, $[La(Cp'')_3]^-$, $La(Cp^{tt})_3]^-$ and $[Y(OAr^{Ad,Ad,Me})_3]^-$ have revealed robust quantum coherence properties that could be monitored up to 120 K in frozen solutions and to 300 K in the solid-state single crystals. Nutation experiments enabled Rabi oscillations being observed for all possible electronuclear transitions, indicating the potential of the molecules as quantum bits despite their rich nuclear spin environment. Advanced pulse hyperfine EPR techniques, such as HYSCORE and ENDOR, are employed to characterize the environment of the metal ion in greater detail probing the electronic spin density trasfered to ligand nuclei.

Continuous wave and pulse EPR spectroscopy are also involved to study a family of Ln(III) complexes of formula $[Ln(Cp^{tt})_3]$ ($Ln^{III} = Ce^{III}$, Nd^{III}, Sm^{III}). Analysis of the results provided information on their electronic structure and relaxation times. These complexes do not display long coherence times due to the nature of their SOMO 4f-orbitals, leading to faster relaxation properties of the electrons. Hyperfine sublevel correlation (HYSCORE) spectroscopy is further used to study the weak interactions of the unpaired electron with the ligand ^1H and ^{13}C nuclei, probing that the metal ligand bonding is primarily ionic in these cyclopentadienyl trivalent lanthanide complexes.

Lydia Nodaraki
December 2020

Declaration

Title: Quantum coherence and covalency in organometallic lanthanide complexes investigated by pulse EPR techniques

Author: Lydia Nodaraki

I declare that no portion of the work referred to in this thesis has been submitted in support of an application for another degree or qualification of this or any other university or other institute of learning.

Signed:

Date: 14/12/2020

Copyright statement

The author of this thesis (including any appendices and/or schedules to the thesis) owns certain copyright or related right in it (the “Copyright”) and s/he has given The University of Manchester certain rights to use such Copyright, including for administrative purposes.

Copies of this thesis, either in full or in extracts and whether in hard or electronic copy, may be made **only** in accordance with the Copyright, Designs and Patents Act 1988 (as amended) and regulations issued under it or, where appropriate, in accordance with licensing agreements which the University has from time to time. This page must form part of any such copies made.

The ownership of certain Copyright, patents, designs, trademarks and other intellectual property (the “Intellectual Property”) and any reproductions of copyright works in the thesis, for example graphs and tables (“Reproductions”), which may be described in this thesis, may not be owned by the author and may be owned by third parties. Such Intellectual Property and Reproductions cannot and must not be made available for use without the prior written permission of the owner(s) of the relevant Intellectual Property and/or Reproductions.

Further information on this conditions under which disclosure, publication and commercialisation of this thesis, the Copyright and any Intellectual Property and/or Reproductions described in it may take place is available in the University IP Policy (see http://documents.manchester.ac.uk/DocuInfo.aspx?DocID=24420), in any relevant Thesis restriction declarations deposited in the University Library, The University Library’s regulations (see http://www.manchester.ac.uk/library/aboutus/regulations/) and in The University’s policy on Presentation of Theses.

Acknowledgements

First and foremost I would like to thank my supervisor Dr. Floriana Tuna for her invaluable supervision, continuous support and guidance during my PhD studies in Manchester. I am extremely grateful for her consistently encouragement, for her patience, motivation and plentiful experience in this field have made this an inspiring experience for me. My gratitude extends to my co-supervisor Prof. Eric McInnes; his immense knowledge and expertise was of vital importance in formulating the research questions and methodology. I would also like to thank Dr. David Mills for his valuable advice and knowledge in a "more synthetic" point of view.

My sincere gratitude also goes to Prof. Richard Winpenny and Prof. David Collison for their insightful comments and feedback during our meetings and conversation encouraging me to sharpen my thinking and my work to higher level. Many thanks also to Dr. Nicholas Chilton for his helpful advice on the theoretical approaches. I am grateful to Adam Brookfield for all the technical support, his kind patient and his tireless efforts to help.

I am greatly indebted to Prof. William Evans, Dr. David Woen and Dr. David Huh from the University of California, as well as the members of the Mills group from the University of Manchester and especially Dr. Jingjing Liu and Dr. Fabrizio Ortu for allowing me to work so extensively on their fascinating molecular systems and giving me the opportunity to study these molecules from an EPR perspective.

A special thanks to a number of people, past and current members of the magnets and EPR group in Manchester: Ana-Maria, Valentina, Andreas, Marcus, Guillem, Edmund, Daniel S., Marie-Emmanuelle, Alena, Ivana, Luisa, Jonatan, Amal, Oka, Ali, Daniel T., Diana and Dalal for cherished time spent together in the lab and the office, for all the help and support. I am particularly grateful to Dr. Ana-Maria Ariciu, Dr. Valentina Lukinovic, Dr. Marcus Giansiracusa, Dr. Andreas Kostopoulos, Dr. Guillem Brandariz de Pedro and Dr. Marie-Emmanuelle Boulon for welcoming me in Manchester, for supporting my "EPR baby steps" and for making each day more enjoyable.

I am also thankful to the EPSRC for the financial support during my studies, as well as the UK National EPR Research Facility and Service at the University of Manchester and all the members for their valuable support.

Enormous thank you to Ana-Maria for being my friend, my tutor and my support. I am honestly grateful for the uncountable memories, the endless discussions and the infinite laughter and tears. Finally, I would like to express my gratitude to my parents Manolis and Georgia and my brother Michalis for all the love, the unconditional support and the continuous encouragement. Thank you for always being there for me!

Chapter I. Introduction

I.I Rationale for the alternative format

This thesis is presented in a journal format and each of the Chapters is written in a suitable style for journal publication. An alternative format thesis exhibits a number of benefits compared to a standard format thesis such as i) minimizing the conflict of repetition of a previously published work; reducing the risk of self-plagiarism ii) promoting the publication of the results obtained during the PhD project and iii) ensuring that each draft is presented as a well structure body of work, including sufficient and completed information and results for publication. In addition each of the Chapters includes introduction and background on the current topic, in order to maintain the coherence and unity of the manuscript.

I.II Organization of the thesis

Chapter I presents a preface of the thesis, including the contributions of the author to the draft manuscripts and published material. *Chapter II* provides a general introduction to electron paramagnetic resonance (EPR) spectroscopy, with an emphasis on advanced pulse EPR techniques. *Chapter III* introduces applications of pulse EPR spectroscopy for the investigation of molecular spin quantum bits and metal to ligand covalency. *Chapter IV* involves a peer-reviewed publication reporting electronic structure engineering to enhance relaxation times in lanthanide qubits. *Chapter V* contains a manuscript in preparation probing divalent Lu and Sc complexes as molecular qudits. *Chapter VI* comprises a manuscript in preparation describing the effect of the ligand on the coherence properties of a series of La^{II} complexes. *Chapter VII* consists of a manuscript in preparation, which presents a rigid Y^{II} organometallic complex with enhanced qubit properties. *Chapter VIII* contains a manuscript in preparation focusing on the applications of pulse EPR spectroscopy to quantify the covalency of lanthanide organometallic complexes. Finally, *Chapter IX* outlines a summary of the work undertaken.

I.III Contributing authors

Paper, Chapter IV, "Engineering electronic structure to prolong relaxation times in molecular qubits by minimizing orbital angular momentum". Ana-Maria Ariciu, Lydia Nodaraki and Floriana Tuna collected and interpreted the EPR spectroscopy data, with support from Andreas K. Kostopoulos and Eric J. L. McInnes. David H. Woen and Daniel N. Huh synthesized and characterized the compounds under the supervision of William J. Evans.

Conrad A. P. Goodwin made the EPR samples. Nicholas F. Chilton performed and interpreted the DFT and CASSCF calculations. William J. Evans and Richard E. P. Winpenny proposed the initial concept. Floriana Tuna designed the work and supervised Ana-Maria Ariciu and Lydia Nodaraki. Richard E. P. Winpenny, Floriana Tuna, Ana-Maria Ariciu, Nicholas F. Chilton and Eric J. L. McInnes wrote the manuscript, with contributions from all the authors.

Draft manuscript, Chapter V, "Low-valent Sc and Lu organometallic complexes as qudits with an increased Hilbert space". The experiemental EPR data included in this research communication were collected, analyzed and interpreted by Lydia Nodaraki and Ana-Maria Ariciu under the supervision of Floriana Tuna, Eric J. L. McInnes and Richard E. P. Winpenny. David H. Woen and Daniel N. Huh synthesized the compounds under the supervision of William J. Evans, and Fabrizio Ortu prepared the EPR samples. This work was designed and supervised by Floriana Tuna. Lydia Nodaraki and Ana-Maria Ariciu wrote the manuscript with support from Floriana Tuna.

Draft manuscript, Chapter VI, "Ligand effects on the spin relaxation dynamics and coherence manipulation of organometallic La^{II} *potential qudits".* EPR studies and analysis were performed by the author of the thesis, under the guidance of Floriana Tuna, Eric J. L. McInnes and Richard E. P. Winpenny. David H. Woen and Jingjing Liu synthesized the compounds under the supervision of William J. Evans and David P. Mills respectively. Fabrizio Ortu and Jingjing Liu prepared the samples for the EPR measurements. The initial concept was proposed and designed by Floriana Tuna, Eric J. L. McInnes and Richard E. P. Winpenny. The manuscript was written by Lydia Nodaraki under the guidance of Floriana Tuna.

Draft manuscript, Chapter VII, "*An organometallic Y(II) spin qubit based on a rigid aryloxide ligand displaying enhanced coherence properties*". EPR data were collected, analysed and interpreted by Lydia Nodaraki with support from Floriana Tuna. David H. Woen has synthesized the compound under the supervision William J. Evans, and Fabrizio Ortu prepared the samples for the EPR measurements. Floriana Tuna designed the EPR work, and supeprvised Lydia Nodaraki. The manuscript was written by Lydia Nodaraki under the guidance of Floriana Tuna.

Draft manuscript, Chapter VIII, "*Covalency in* $LnCp^{tt}_3$ *(Ln = Ce, Nd, Sm) evaluated via HYSCORE spectroscopy*". EPR measurements and analysis were carried out by Lydia

Nodaraki with support from Floriana Tuna, Ana-Maria Ariciu and Eric J. L. McInnes. Jingjing Liu synthesized and characterized the compounds, mounted the samples for EPR study under the supervision of David P. Mills and Fabrizio Ortu, and wrote a summary on introduction and description of the new compounds. The initial concept was proposed and designed by Floriana Tuna, Eric J. L. McInnes and David P. Mills. Letitia Birnoschi performed CASSCF calculations under the supervision of Nicholas Chilton. Lydia Nodaraki wrote the manuscript under the main guidance of Floriana Tuna, with contribution from all coauthors.

Chapter II. Introduction to Electron Paramagnetic Resonance Spectroscopy

Electron Paramagnetic Resonance (EPR) or Electron Spin Resonance (ESR) spectroscopy is a sensitive and accurate technique to characterise paramagnetic species, which relies on the absorption of electromagnetic radiation by a paramagnetic sample placed in an external magnetic field.[1] At the early stage, this technique was applied to biological paramagnetic molecules, while later a range of transition metal complexes, organic radicals and defects in materials were probed.

EPR spectroscopy concerns the investigation of the electron spin interactions with the external applied magnetic field, the interactions between electron and nuclear spins (m_I) and the electron spin - electron spin interactions.[2] Therefore the interpretation of an EPR spectrum can provide unique information on the electronic and geometric structures; such as g-values, hyperfine couplings and zero-field splitting parameters which are directly related to the environment of the unpaired electrons.

There are two main types of EPR spectroscopic techniques: continuous-wave (CW) EPR and pulsed EPR. Continuous wave EPR spectra are recorded using a microwave radiation of a constant frequency; the external magnetic field is swept slowly until the resonance condition is fulfilled. The features appearing in a CW spectrum correspond to transitions between the quantized states of the electron spins. On the other hand, pulsed EPR experiments are based on the manipulation of spins with sequences of microwave pulses; exciting the spins and leading to microwave emitted signals created by the sample magnetisation. In pulse EPR spectroscopy the signal depends on the dynamic properties of the spin systems, leading to spectra with spectral and spin relaxation information.

Pulsed EPR spectroscopy exhibits important advantages over the CW techniques, such as higher spectral resolution, direct measure of relaxation times and detection of long distances between paramagnetic species. However, they are complementary techniques with the CW methods being more suitable for identifying electron spin state transitions, while pulse EPR techniques are powerful by means of detecting transitions of electron nuclear interactions within electron spin states.

II.I Basic principles of EPR spectroscopy

The principle behind the Electron Paramagnetic Resonance spectroscopy is the interaction between the unpaired electron spin with an external magnetic field (Zeeman effect). Thus, EPR spectroscopy focuses on the electrons, which show an intrinsic spin angular momentum,

S. An electron spin has a quantum number of $S = \frac{1}{2}$, which has two possible spin states: a spin-up state with $m_s = +\frac{1}{2}$ and a spin-down state with $m_s = -\frac{1}{2}$. In the absence of an external magnetic field the electron spin is randomly orientated and the two m_s states are degenerate.[3] However, once an external magnetic field is applied the magnetic moment of the electron aligns parallel or anti-parallel with the direction of the applied field which results a splitting of the electron spin energy levels with different m_s values, and thus in the lifting of the degeneracy. The splitting of the m_s levels is proportional to the strength of the magnetic field, while the energy of the states is given by the equation[4]:

$$E(m_s) = m_s g_e \mu_B B \quad (1)$$

where the free electron g value is g_e = 2.0023, μ_B denotes the Bohr magneton and B the applied magnetic field in Tesla.

The energy difference between the two Zeeman states is given by:

$$\Delta \mathrm{E} = E\left(m_s = +\frac{1}{2}\right) - E\left(m_s = -\frac{1}{2}\right) = g_e \mu_B B \quad (2)$$

Therefore, in EPR spectroscopy the electromagnetic irradiation of the sample can typically be used to induce transition between the energy levels, leading to the EPR resonance condition when the energy difference between the energy levels with $|\Delta m_s| = 1$ matches the available microwave energy (hv). Thus, the equation that describes the absorption or emission of microwave radiation between the two m_s states is[5]:

$$\Delta \mathrm{E} = hv = g_e \mu_B B \quad (3)$$

where h is the Planck constant an v the microwave frequency.

During a continuous wave EPR experiment the electromagnetic radiation frequency remains constant and the magnetic field is scanned. When the resonance condition is fulfilled, the energy of the irradiation field matches the energy gap ΔE. A transition between the two spin states is induced by absorption or emission of microwave radiation that flips the spin. The EPR transitions can be observed as an absorption spectrum but usually in a CW EPR spectroscopy the first derivative of the absorption spectrum is detected, enhancing the resolution by emphasizing on the rapidly changing features of the spectrum.

The g-factor or Landé factor is a unique “fingerprint” for each system determined by the local environment of the paramagnetic centers. Equation (3) in the resonance field can be expressed as:

$$g = \frac{hv}{\mu_B B} \quad (4)$$

and the g value can be calculated from the frequency (v) and field (B) values using:

$$g = 0.714484 \frac{v(MHz)}{B(Gauss)} \quad (5)$$

($h = 6.626 \cdot 10^{-34}$ J · s and $\mu_B = 9.274 \cdot 10^{-28}$ J · G^{-1})

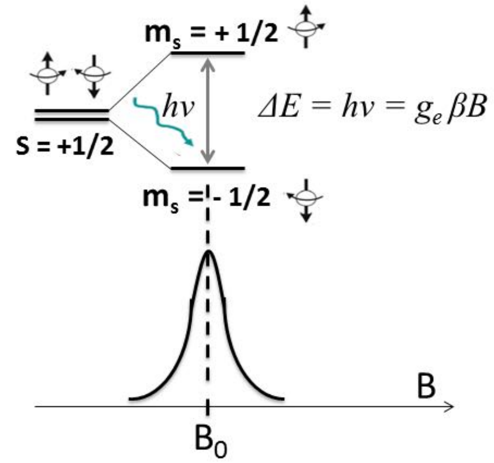

Figure 4. Electron Zeeman splitting for an unpaired electron, as a function of the strength of the magnetic field and the resonance condition.

The field at which the resonance signal is observed determines the g-factor of an EPR signal. The free electron g-value is g_e = 2.0023. In real systems a deviation from the free electron g value can be observed, particularly when spin-orbit coupling interactions between electronic ground and excited states occurs. In that case the electron spin and the orbital angular momentum are coupled giving $g \neq g_e$.[6] The system is no longer isotropic due to spin orbit interaction, with the Zeeman splitting term depending on the crystal field symmetry and orientation of the system in the external magnetic field. However, in liquid solution samples the rotational and translational motion of the molecules compensate the anisotropy of the g-factor, giving an isotropic feature $g_{iso} = \frac{g_x + g_y + g_z}{3}$. On the other hand, the EPR spectrum of a single crystal often depends on the relative orientation of the crystal axis towards the external magnetic field vector. However, in the case of a polycrystalline sample the spectrum occurs as a superposition of randomly oriented crystals. The g-factor is then described as anisotropic and it needs to be treated as a g-tensor in order to represent the orientation dependence. The anisotropic g-tensor in a general coordinate system is represented as a 3×3 symmetric matrix $\begin{pmatrix} g_{xx} & g_{xy} & g_{xz} \\ g_{xy} & g_{yy} & g_{yz} \\ g_{xz} & g_{yz} & g_{zz} \end{pmatrix}$, which depends on the orientation of B with respect to g_{ij} in an arbitrary orientation. Nevertheless, in the orthogonal coordinate axis (x, y, z) of the g tensor, the off-diagonal elements are zero and thus the diagonal tensor can be describes as $\begin{pmatrix} g_{xx} & 0 & 0 \\ 0 & g_{yy} & 0 \\ 0 & 0 & g_{zz} \end{pmatrix}$.

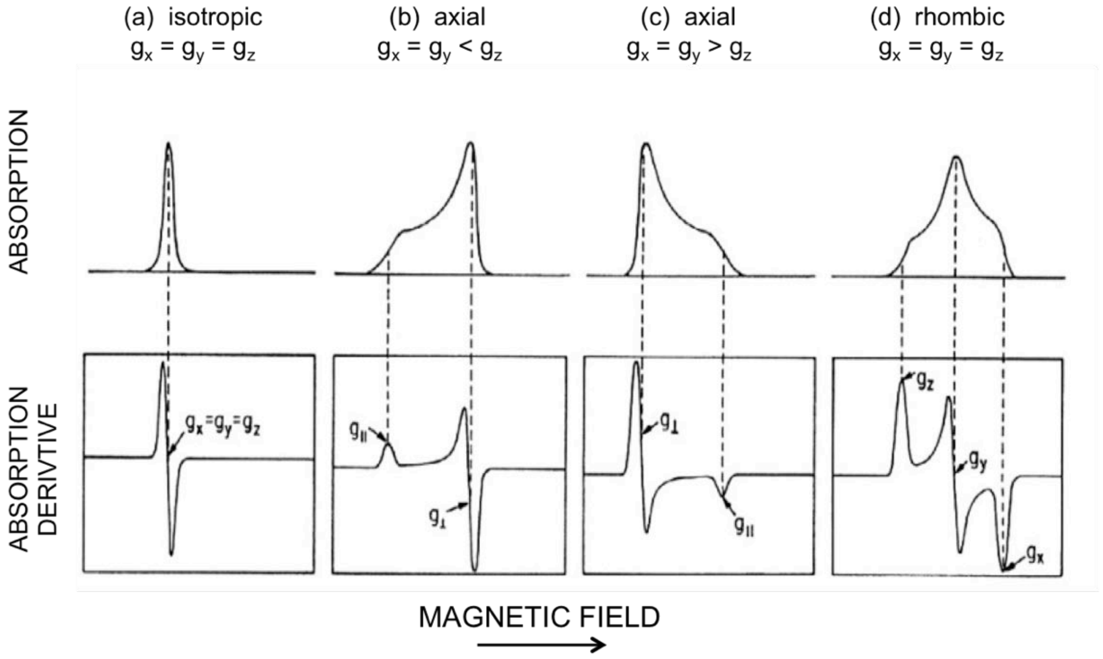

Figure 5. Representation of continuous wave EPR spectra with (a) isotropic; (b), (c) axial; (d) rhombic symmetries. The upper curves represent the absorption spectra and lower curves the first derivative (CW spectra).

The anisotropy of the g-tensor can be classified as isotropic, axial or rhombic.[7] In the isotropic case, no orientation dependence is observed; this usually occurs in high symmetric systems ($g_x = g_y = g_z$). In systems with axial symmetry, two of the g-tensor components are identical ($g_{\perp}$) and the one will deviate ($g_{//}$), corresponding to one unique axis of the orientation ($g_x = g_y \neq g_z$). Finally, in the rhombic symmetric systems all three axes will differ leading to three different g values ($g_x \neq g_y \neq g_z$).

EPR experiments can be performed at different microwave frequencies, and the resonance condition will be fulfilled at different strengths of the applied magnetic field. X-band (ca. 9.4 GHz) is the most commonly used microwave frequency, while other frequencies include: L-band (1 GHz), S-band (3.8 GHz), K-band (24 GHz), Q-band (34 GHz) and W-band (94 GHz).

II.II Spin Hamiltonians

A system of an unpaired electron in a magnetic field is characterized by the interaction of the magnetic moment with the external magnetic field. The addition of further electron or nuclear spins requires the introduction of the effective spin, which is determined by the interactions of the electron spin with other electron or nuclear spins. Therefore, the spin Hamiltonian of the effective spin can be described as:[8]

$$\widehat{\mathcal{H}_0} = \widehat{\mathcal{H}_{EZ}} + \widehat{\mathcal{H}_{NZ}} + \widehat{\mathcal{H}_{HF}} + \widehat{\mathcal{H}_{ZFS}} + \widehat{\mathcal{H}_{NQ}}$$

$$\widehat{\mathcal{H}_0} = \frac{\mu_B}{\hbar} B g \hat{S} - \mu_N \sum_{k=1}^{N} \frac{g_{n,k}}{\hbar} B \widehat{I_k} + \sum_{k=1}^{N} \hat{S} A_k \widehat{I_k} + \hat{S} D \hat{S} + \hat{I} P \hat{I} \quad (6)$$

where $\widehat{\mathcal{H}_{EZ}}$ is the Electron Zeeman interaction

$\widehat{\mathcal{H}_{NZ}}$ is the Nuclear Zeeman interaction

$\widehat{\mathcal{H}_{HF}}$ is the Hyperfine interaction

$\widehat{\mathcal{H}_{ZFS}}$ is the Zero-field splitting interaction

$\widehat{\mathcal{H}_{NQ}}$ is the Nuclear Quadrupole interaction

Electron Zeeman interaction

As it has been described above, the Zeeman interaction occurs between the electron spin moment and the external magnetic field, which can be written as

$$\widehat{\mathcal{H}_{EZ}} = \frac{\mu_B}{\hbar} B g \hat{S} \quad (7)$$

Nuclear Zeeman interaction

The interaction of the nuclear spin with the external applied magnetic field is described by the nuclear Zeeman splitting and it is analogous to the electron Zeeman interaction. The Hamiltonian for that is given by:

$$\widehat{\mathcal{H}_{NZ}} = -\frac{g_N \mu_N}{\hbar} B \hat{I} \quad (8)$$

where the g_N and I are related to the type of the nucleus. The nuclear Zeeman interaction is much smaller than the electron Zeeman interaction, because the electron Bohr magneton is three orders of magnitude larger than the nuclear Bohr magneton. Therefore, the nuclear Zeeman interaction does not have much contribution to the EPR spectrum, and it might become important only in the case where it will be in the same order of magnitude as the hyperfine interaction.

Hyperfine interaction

The hyperfine interactions arise from the magnetic interactions of the electron spin coupled with the nearby nuclei having non-zero nuclear spin. Two mechanisms contribute to the coupling of the electron and nuclear spins; the first one is the Fermi-contact interaction arising from finite electron spin density on the nucleus and the second one is the anisotropic dipolar contribution resulting from the dipole-dipole interaction between the magnetic moments of the electron and the nuclear spins.[9] In principle the hyperfine interactions are anisotropic because of the dipolar component, but in some systems such as in liquid solution samples the anisotropic part is averaged out. The Hamiltonian can be described as:

$$\widehat{\mathcal{H}_{HF}} = \hat{S}A\hat{I} = a_{iso}\hat{S}\hat{I} + \hat{S}T\hat{I} \quad (9)$$

The Fermi contact interaction is isotropic and a consequence finite electron spin density at the nucleus, $|\Psi(0)|^2$. The isotropic hyperfine interaction arises solely for an electron resides (spin density) on the *s*-orbitals (or orbitals with partial *s*-character)[10] due to the non-zero density at the nuclear center, which allows the direct contact of the electron with the nucleus. Hence, the energy of this interaction is defined as:[10]

$$a_{iso} = \frac{2}{3}\frac{\mu_0}{\hbar} g_e\beta_e g_n\beta_n |\Psi_0(0)|^2\, \hat{S}\hat{I} \quad (10)$$

On the other hand, the dipolar hyperfine coupling can be described by the classical dipole-dipole interaction as presented in the following equation:

$$\widehat{\mathcal{H}_{d\imath p}} = \frac{\mu_0}{4\pi\hbar}\cdot\frac{1}{r^3} g_e\beta_e g_n\beta_n \left[SI - \frac{3(Sr)(Ir)}{r^2}\right] \quad (11)$$

where μ_0 is the permeability of the vacuum and r is the distance between the two spins connected by the vector r and T is the symmetric and traceless dipolar hyperfine coupling tensor. The dipole-dipole interaction depends on the relative orientation of the magnetic moments and thus is anisotropic when the electron resides in a non-spherical orbital. Purely dipolar interaction is expected when the electron spin is located in a molecular orbital with a nodal point at the nucleus (*p*-, *d*- or *f*-orbitals)[11] and when the symmetry of the system is lower than cubic.

Hyperfine interactions are extremely useful in EPR spectroscopy as they provide information of the direct environment of the electron spin. In EPR spectroscopy there are two different types of hyperfine interactions, both occur between unpaired electron and a magnetic nucleus. Nuclear hyperfine interactions or just hyperfine interactions are caused by the interactions of electron spins with nuclear magnetic momenta, while superhyperfine interactions originate from the interaction of electron spins with the non-zero nuclear spin of neighboring nuclei. Thus, further splitting of the hyperfine structure may occur due to the superhyperfine interactions, which are extremely small but useful as they provide a direct evidence of covalency in coordination compounds.

The effect of the hyperfine interaction occurs as a perturbation on the nuclear Zeeman energy levels leading to an increase or reduction of the energy levels, depending on the magnitude of the hyperfine interaction, α. The hyperfine interactions cause the splitting of the EPR lines, which depends on the number and the type of coupled nuclei. Thus, the EPR lines are split into $2nI + 1$ (n = number of nuclei and I = nuclear spin). So, in the case of hydrogen atom which has an electron spin of $\frac{1}{2}$ and a nuclear spin of $\frac{1}{2}$, the energy level diagram showing the electron Zeeman and nuclear Zeeman levels, and the perturbation of hyperfine interactions is depicted in Figure 3.

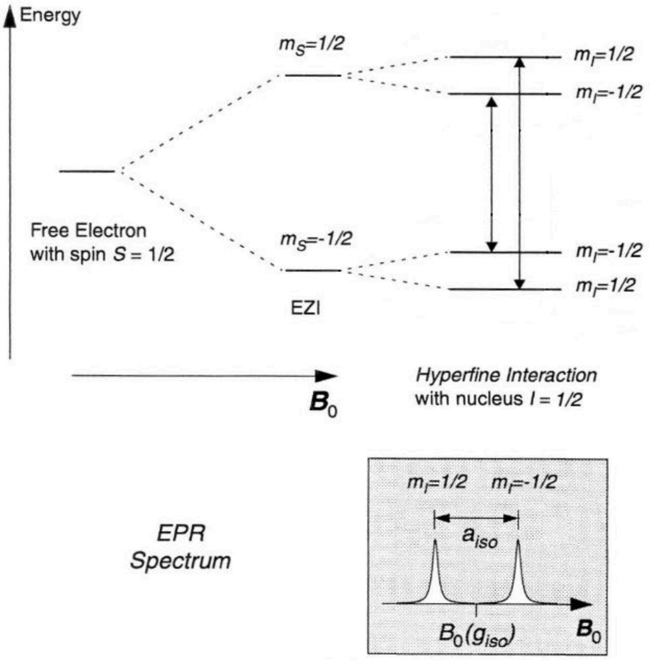

Figure 6. Energy levels of a system with an unpaired electron and a magnetic nucleus with nuclear spin of ½ as a function of the magnetic field. The vectors are noted the allowed EPR transitions ($\Delta m_S = \pm1$ and $\Delta m_I = 0$) and at the lower part the splitting of the signal due to the hyperfine interactions is depicted.

Zero-field splitting interaction

The zero-field splitting (ZFS) phenomenon arises in paramagnetic systems with multiple unpaired electrons (i.e. $S > \frac{1}{2}$), due to spin-spin coupling (SSC), which is the dipolar interaction among pairs of unpaired electrons and spin-orbit coupling (SOC) the interaction of electron spin angular momentum with its electron orbital angular momentum. In a single ion case the ZFS interaction could only occur from the SOC, as the SSC needs at least two unpaired electrons, in this case SOC interaction is only leading to g anisotropy. Zero-field splitting interaction refers to the magnetic sublevel fine structure of unpaired electrons in such molecular orbitals in the absence of an external magnetic field, resulting in the lifting of the degeneracy of the m_S states. The ZFS interaction can be expressed as the following Hamiltonian:

$$\widehat{\mathcal{H}_{ZFS}} = \hat{S}D\hat{S} \quad (12)$$

where D is termed as the dipolar or ZFS interaction tensor and is traceless and symmetric.

The diagonalization of the ZFS tensor produce two independent parameters D and E, which are defined from the principal values of the D tensor and characterized by the dipole-dipole interaction:

$$D = \frac{3}{2}D_z \quad (13) \text{ and } E = \frac{1}{2}\left(D_x - D_y\right) \quad (14)$$

The principal axes of the ZFS have to fulfill the two following conditions $/D/ > /3E/$ and $/D_z/ < /D_x/, /D_y/$. The D value is determined by the average distances between the two spins, and the E value corresponds to the rhombicity of the D tensor. It is noteworthy that the D and E values are affected by the chosen z-axis, which has to be the axis, which maximizes the dipolar coupling. Both D and E parameters can be positive or negative, the sign of the D value is determined by the spin density distribution ($D>0$ for oblate shaped spin density ions, $D<0$ for prolate shaped spin density ions), while the sign of the E is related with the direction of the x and y ZFS axis, without a physical meaning.[12] The z-axis of the ZFS also depends on the shape of the spin distribution, for prolate shaped ions it comes along the principal symmetry axis, while for oblate spin distribution it is pointed perpendicular to the xy-plane axis.

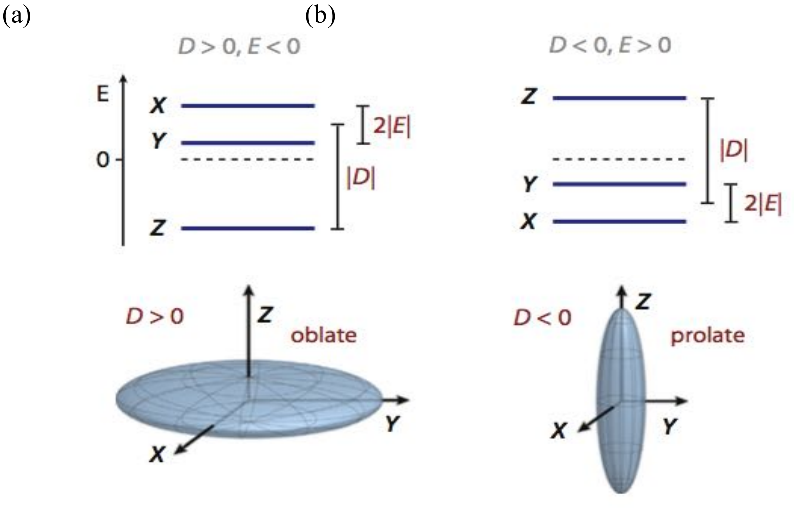

Figure 4. The zero-field splitting diagram of the triplet state for (a) oblate and (b) prolate shaped spin density distribution.[12]

For instance, in the case of a compound with $S = 1$, the dipole-dipole interaction contribute to the splitting of the triplet state into three different levels with the m_S states of -1, 0, +1 values. The D value is assigned as the energy difference between the lowest and the highest energy states in the case of an axially symmetric system and/or between the lowest energy state and the middle of the two higher energy states. Moreover, the E parameter exists only in orthorhombic systems and corresponds to the x and y energy separation.

Nuclear Quadrupole interaction

Nuclei with nuclear spin, I, larger than $\frac{1}{2}$ exhibit a non-spherical charge distribution causing a nuclear electric quadrupole moment, Q (e.g. Q = 0.0204 b for ^{14}N),[13] which interact with the electric-field gradient (EFG) generated by the nuclei and the electron distribution in the nearest environment of the nucleus. The coupling of the charge distribution with the electric-field gradient is called quadrupole interaction (NQ) and the quadrupole energy is given by the following Hamiltonian:

$$\widehat{\mathcal{H}_{NQ}} = \hat{I}P\hat{I} \quad (15)$$

where P is the nuclear quadrupole tensor, a 3×3 symmetric and traceless matrix.

In principal axes system the nuclear quadrupole spin Hamiltonian can be expressed as:

$$\widehat{\mathcal{H}_{NQ}} = \frac{e^2qQ}{4I(2I-1)\hbar}\left[\left(3\widehat{I_z^2} - \widehat{I^2}\right) + \eta\left(\widehat{I_x^2} - \widehat{I_y^2}\right)\right] \quad (16)$$

where $e^2qQ\hbar^{-1}$ is the nuclear quadrupole coupling constant and $\eta = \left(P_x - P_y\right)P_z^{-1}$ is the asymmetric parameter, which are the only two parameters, apart from its orientation, determining the quadrupole tensor P.

The nuclear quadrupole interaction usually is not observed directly in continuous wave EPR spectra ($\Delta m_s = \pm 1$, $\Delta m_I = 0$), acting as a small second-order perturbations to the electron spin energy levels, but it becomes important in more advanced hyperfine EPR techniques such as ESEEM and ENDOR experiments ($\Delta m_s = 0$, $\Delta m_I = \pm 1$).

II.III Introduction to pulsed EPR spectroscopy

Continuous wave EPR provide us a great deal of information related to the identity and oxidation state of the metal center and/or the local environment around the unpaired electron. However, if the magnitude of the couplings is small these interactions will not be resolved by the conventional CW methods. Pulsed EPR spectroscopy has been developed in order to the limitations of the CW experiments in spectral and time resolution. As a means of isolating weakly coupled spins, not observable by CW EPR, a number of advanced pulsed EPR techniques have been developed. In pulsed EPR experiments the manipulation of spins is achieved by the application of short high-power microwave pulses, in the order of ten to hundreds of nanoseconds.

Pulsed EPR techniques can be classified into two main categories; the electron nuclear double resonance (ENDOR) and the electron spin echo envelope modulation (ESEEM) techniques. In the former technique the signal occurs after the excitation of nuclear spin transitions by microwave and radiofrequency radiation, while in the latter method nuclear transition frequencies are measured by the application of microwave pulses, which leads to the detection of electron or nuclear coherences.

When an electron spin magnetic moment is placed in an external magnetic field, B, coming along the z-axis, the magnetic moment feels a torque inducing the precession of the magnetization along the axis of the magnetic field at a Larmor frequency, $\nu_L = /\gamma/B$,[14] where γ is the gyromagnetic ratio. At thermal equilibrium, the magnetic moment of the sample is aligned parallel to the magnetic field, B, and remains constant in time. However, during a pulse EPR experiment the application of microwave pulses, perpendicular to the magnetic moment, tilts the magnetization away from the z-axis causing a precessing motion around this axis. The net magnetization is then rotated and the magnetization in the x, M_x and y, M_y direction become non-zero, thus the relaxation of the magnetization towards M_z corresponds to the exponential function of T_1 (longitudinal or spin lattice) relaxation time and the loss of the coherence in the xy-plane is described as T_2 (transverse or spin spin relaxation time).

In the majority of the pulsed EPR experiments, the investigation of the spin systems is happening by the detection of an echo after the application of a microwave pulse sequence. The primary echo is one of the most fundamental sequences using a two-pulse echo experiment ($\pi/2$ - τ - π - τ - *echo*) to excite the spins. The first pulse is a $\frac{\pi}{2}$ pulse which flips the magnetisation vector in the xy-plane where the spin packets will dephase, during the free evolution time, with some of them moving faster and some slower due to the different Larmor frequencies. Then, after a delay time, τ, a second π pulse is applied leading to 180 degrees inversion of the magnetization vectors, while the spins packet will still rotate with the same speed in the same direction. However, because of the inversion π pulse the spin packets will now refocus and after a time τ all spin packets will catch up producing an emission signal, which is termed as the primary or Hahn echo.[15] The Hahn echo sequence is used to perform the simplest pulse EPR experiment; the echo-detected field swept (EDFS) experiment. The Hahn echo sequence is applied at each different static magnetic field position and the intensity of the echo is monitored. The EDFS spectra correspond to the absorption analog of the CW EPR spectra, however anisotropic relaxation effects usually affect it. The EDFS signal can also provide spectrally resolved ESEEM information due to the interaction with the surrounding nuclear spins.

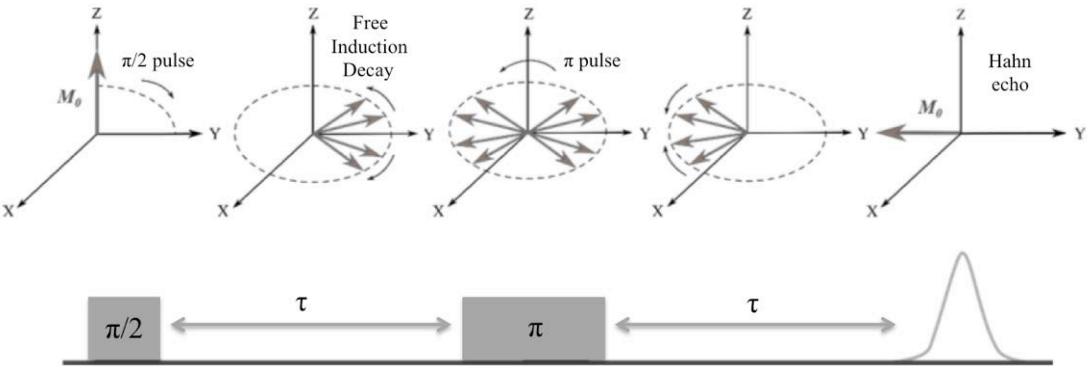

Figure 5. Schematic representation of the two-pulse primary echo sequence, with the magnetization vector on the top explaining how the echo is generated.

II.III.I Relaxation times

During a pulsed EPR experiment, the equilibrium of the spin system is perturbed by the microwave pulses, which excite the spins. The excited spins relax back to the thermal equilibrium state by different relaxation processes; the fundamental relaxation processes are the longitudinal and the transverse relaxation time, which are characterised by the T_1 and T_m relaxation times, respectively.[16]

Longitudinal T_1 relaxation time

The longitudinal or spin lattice relaxation describes the relaxation of the magnetization vector of the system back to the equilibrium along the z axis. The mechanism of this relaxation involves an exchange of energy between the spin system and the surrounding lattice through dynamic interactions (molecular rotations and vibrations), leading to changes of the population of the electron spin states. The spin-lattice relaxation, T_1, can be measured using a three pulses sequence, called 'inversion recovery' experiment. In practice the experiment is based on the inversion of the magnetization to the $-z$ orientation by a π pulse, followed by the signal detection via a Hahn echo sequence (π - τ - $\pi/2$ - τ - π - τ - *echo*).[17] During the measurement the time, T, between the first π pulse and the detection sequence is incremented and thus the recovery of the magnetization is monitored until saturation is achieved. The process is modelled as a bi-exponential equation:

$$Y(t) = Y(0) + Y_1 e^{(-t/T_1)} + Y_{SD} e^{(-t/T_{SD})} \quad (17)$$

where Y_1 and Y_{SD} are the amplitudes and T_{SD} is the spectral diffusion time constant.

During the free evolution the resonance frequency of a spin can shift due to relaxation driven flips of coupled nuclear or electron spin in the vicinity. This process is called spectral diffusion, which in the case of precessing spins decreases the echo intensity due to the complete rephrase of the spin ensemble. Hence, the spectral diffusion process reduces the inversion recovery and phase memory time.

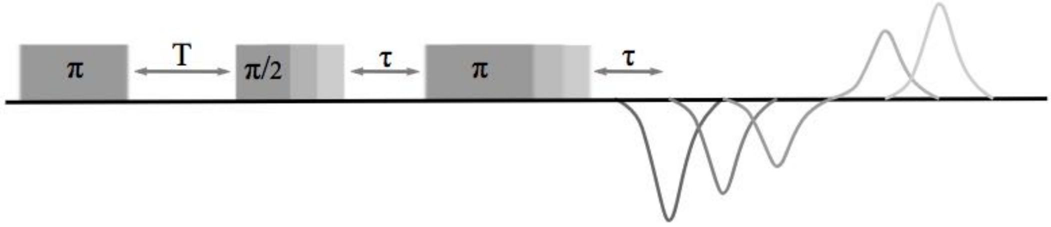

Figure 6. Schematic representation of the three-pulse ESEEM sequence for determining the spin lattice relaxation time.

Transverse T_2 relaxation time

The transverse or spin-spin relaxation time describes the loss of the phase coherence of the spin packets in the *xy*-plane. The most common experiment to measure spin-spin relaxation time two-pulses separated by time τ identical the primary echo sequence, except that the separation between the pulses is incremented gradually. This causes the shifting of the echo in time scale and thus decay is observed. The echo decay constant T_m, is termed phase memory time constant and includes the relaxation time of any processes that cause loss of electron spin phase coherence. The phase memory time contains T_2 processes, but also additional effects of spectral and instantaneous diffusion.[18] Therefore, T_m is always shorter than T_2, because of other contributing relaxation processes. The echo decays as a function of τ, typically in an exponential or stretch-exponential manner described below:

$$Y(2\tau) = Y(0)e^{(-2\tau/T_m)S} \quad (18)$$

where S is the stretching parameter.

During a two-pulse relaxation experiment the intensity of the electron spin echo is measured as a function of τ, resulting not only in the decay of the spin echo signal but the signal will also be modulated, due to nuclear modulation effects (ESEEM), with the nuclear frequencies of magnetic nuclei coupled to the electron spin. For strongly modulated systems, the following equation is used to extract a precise value for the phase memory time:

$$Y(2\tau) = Y(0)e^{(-2\tau/T_m)S}(1 + k\sin(\omega t + \Phi)) \quad (19)$$

where k is the modulation depth, ω is the Larmor angular frequency of a nucleus I coupled to the electron spin and ϕ is the phase correction.

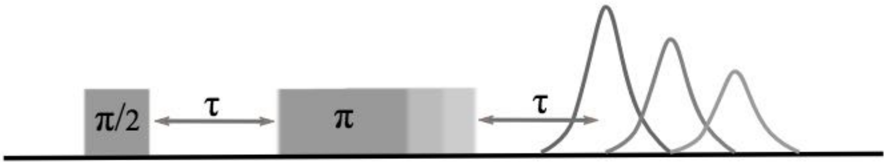

Figure 7. Schematic representation of the two-pulse ESEEM sequence for determining the phase memory time.

II.III.II Hyperfine sublevel correlation (HYSCORE) spectroscopy

HYperfine Sublevel CORrElation (HYSCORE) spectroscopy is an important technique, which offers increased resolution for measuring weak hyperfine couplings between electron spins and nuclear spins in the vicinity.[19] The analysis of HYSCORE data gives important information about electron spin density distributions, distances and bond angles. HYSCORE is essentially a two-dimensional ESEEM experiment[20] which uses a four-pulse microwave sequence, $\pi/2$ - τ - $\pi/2$ - t_1 - π - t_2 - $\pi/2$ - τ - *echo*; the first two $\frac{\pi}{2}$ pulses that are separated by a time τ create the nuclear coherence, which evolves during the t_1 time in the α spin manifold. More specifically, the first $\frac{\pi}{2}$ pulse produces electronic coherence by the excitation of an allowed or forbidden transition. After time τ, the second $\frac{\pi}{2}$ pulse will excite the same EPR transition; leading either to the return of the electron on its original state with the same orientation of the nuclear spin state (when both of these two transitions are allowed or forbidden), or it will return but with an inverted nuclear spin state (when one of the $\frac{\pi}{2}$ pulse excites an allowed and the other one a forbidden transition). Then, a mixing π pulse is applied in order to associate the nuclear coherence states and transfer the nuclear coherence in the second β spin manifold, which evolves during t_2 time with a different frequency. The final $\frac{\pi}{2}$ pulse converts the nuclear coherence into detectable electron coherence, which is then monitored as an electron spin echo modulated by the nuclear frequencies.

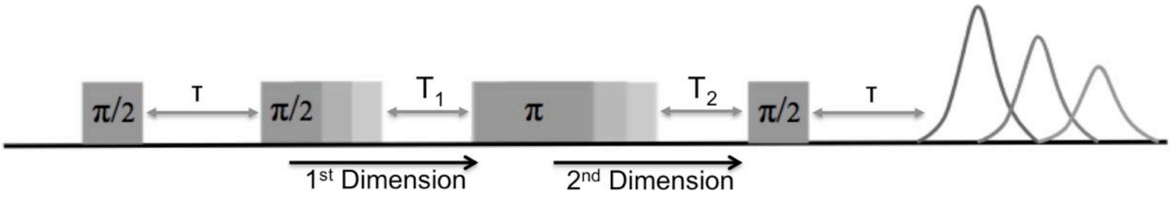

Figure 8. Schematic representation of the inverted-echo four-pulse ESEEM sequence for determining the HYSCORE spectra.

In more details, for a system with S = ½ and I = ½, the echo modulation formula of the HYSCORE experiment can be written as:[21]

$$V_{4p}(\tau, t_1, t_2) = 1 - \frac{k}{4}(V_I + V_{IIa} + V_{IIb} + V_{IIIa} + V_{IIIb}) \quad (20)$$

where k is the modulation depth.

The different modulation contributions stemming from the different coherence transfer pathways are:

$$V_I = 3 - \cos(\omega_\beta \tau) - \cos(\omega_\alpha \tau) - sin^2\eta cos(\omega_+\tau) - cos^2\eta \cos(\omega_-\tau) \quad (21)$$

$$V_{IIa} = C_\alpha(\tau)\cos\left(\omega_\alpha\left(t_2 + {}^{\tau}/_{2}\right)\right) + C_\beta(\tau)\cos\left(\omega_\beta\left(t_2 + {}^{\tau}/_{2}\right)\right) \quad (22)$$

$$V_{IIb} = C_\alpha(\tau)\cos\left(\omega_\alpha\left(t_1 + {}^{\tau}/_{2}\right)\right) + C_\beta(\tau)\cos\left(\omega_\beta\left(t_1 + {}^{\tau}/_{2}\right)\right) \quad (23)$$

$$V_{IIIa} = C_c(\tau)cos^2\eta\left[\cos\left(\omega_\alpha t_1 + \omega_\beta t_2 + \omega_+ {}^{\tau}/_{2}\right) + \cos\left(\omega_\beta t_1 + \omega_\alpha t_2 + \omega_+ {}^{\tau}/_{2}\right)\right] \quad (24)$$

$$V_{IIIb} = -C_c(\tau)sin^2\eta\left[\cos\left(\omega_\alpha t_1 - \omega_\beta t_2 + \omega_- {}^{\tau}/_{2}\right) + \cos\left(\omega_\beta t_1 - \omega_\alpha t_2 - \omega_- {}^{\tau}/_{2}\right)\right] \quad (25)$$

where ω_α and ω_β are the nuclear frequencies of the α and β manifolds

The three different coefficients of the above equations C_α, C_β, C_γ are τ-dependent terms that introduce blind spots similar to the tree-pulse ESEEM case. The different terms in the equations (20) are used to describe the nuclear spins precession with the frequencies of the α/β manifold during t_1 and of the α/β manifold during t_2. The V_I component doesn't involve any coherence evolution since the polarization remain constant during the delay time t_1 and t_2, thus it doesn't contribute to the HYSCORE modulation. The V_{IIa} term corresponds to the case where nuclear polarization (NP) created during t_1 is transferred to nuclear coherence (NC) by the application of the mixing π pulse, which then evolves during t_2 time leading to a modulation term depending on the τ and t_2 times. The reverse pathway is applied for the V_{IIb} term; the NC, which is created by the preparation pulse, is transformed to NP via the π pulse. V_{IIIa} and V_{IIIb} are the most important terms for the HYSCORE experiment, as they are the two main contributions giving oscillations in the time domain spectrum. V_{IIIa} and V_{IIIb} describe the evolution of the NC during t_1, which is then transferred to another m_s manifold by the π pulse, and finally evolves with a different frequency during the delay time t_2.

The two-dimensional HYSCORE spectrum is recorded as a time domain signal by the independent variation of the t_1 and t_2 delay times, while after Fourier transformation a 2D frequency-domain spectrum with ω_1 and ω_2 axes is generated. The 2D frequency domain spectrum is featuring cross peaks linking the nuclear frequencies of the different m_s manifolds. The V_{IIa} and V_{IIb} terms lead to axial peaks $(0,\omega_\alpha)(0,\omega_\beta)$ and $(0,\omega_\beta)(0,\omega_\alpha)$, which are not useful for the interpretation of the data and usually are removed by the baseline correction. The terms V_{IIIa} and V_{IIIb} of the equation (20) give rise to cross peaks at $(\omega_\alpha,\omega_\beta)(\omega_\beta,\omega_\alpha)$ and at $(\omega_\alpha,-\omega_\beta)(\omega_\beta,-\omega_\alpha)$.

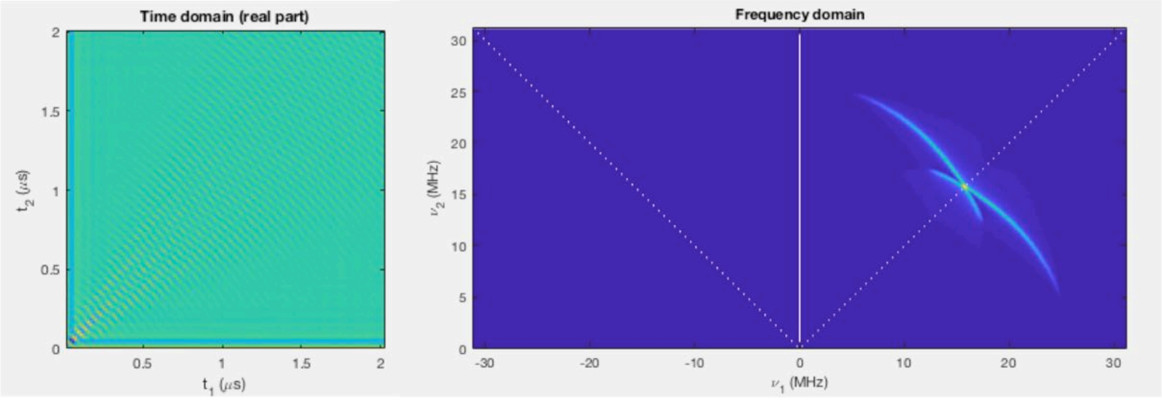

Figure 9. Schematic representation of the Fourier transformation of the 2D time domain experimental data to a 2D frequency domain HYSCORE spectrum.

A HYSCORE spectrum consists of four quadrants, which are characterised by different combinations of the signs of the nuclear frequencies. The peaks occurring in the upper right (+,+) and lower left (−,−) quadrants are generated by weakly-coupled nuclei, $|a_{\mathrm{iso}}| < 2|\nu_L|$, while the peaks which appear in the upper left (+,−) and lower right (−,+) quadrants correspond to strongly-coupled nuclei, $|a_{\mathrm{iso}}| > 2|\nu_L|$. In addition, V_{IIIa} is dominant in the weakly coupled cases; when η is close to 0, while the HYSCORE spectra is dominated by the V_{IIIb} in the strongly coupled cases; when η is approaching $\frac{\pi}{2}$.

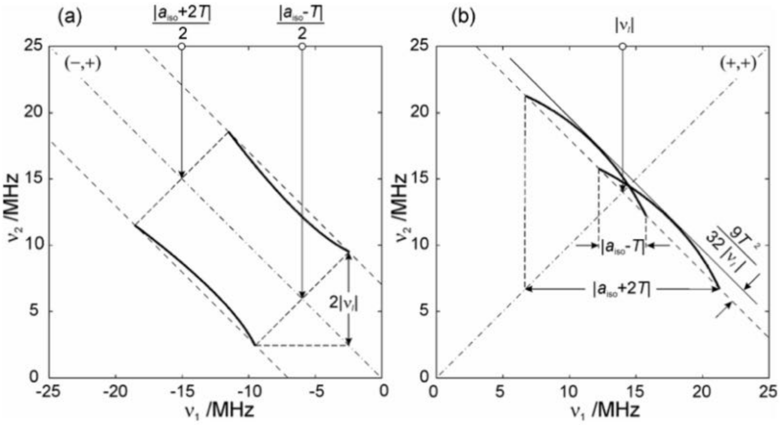

Figure 10. Theoretical HYSCORE powder patterns for an $S = 1/2$, $I = 1/2$ spin system with an axial hyperfine tensor (a) Strong-coupling case with $\nu_1 = 3.5$ MHz, $a_{\mathrm{iso}} = 18$ MHz, and $T = 6$ MHz; (b) Weak-coupling case with $\nu_1 = 14$ MHz, $a_{\mathrm{iso}} = 2.5$ MHz, and $T = 6$ MHz.[22]

In Figure 10 typical HYSCORE spectra for $S = ½$ and $I = ½$ for the strongly and weakly coupled region are depicted. In the strong-coupling case, where $|a_{\mathrm{iso}}| > 2|\nu_I|$, the two ridges are oriented parallel to the diagonal and they are separated by $|2\nu_I|$. In the weakly-coupling case, where $|a_{\mathrm{iso}}| < 2|\nu_I|$, the two arcs deviate from the anti-diagonal at $|\nu_I|$, while the maximum curvature of the ridges at $\boldsymbol{\nu}_{\mathbf{max}} = \frac{9T^2}{32|\nu_I|}$ (26) can determine the anisotropy of the hyperfine interactions.[23]

However, in the case when the electron spin interacts with high-spin nuclei ($I \geq 1$) the number of the possible cross peaks in the HYSCORE spectra increases and the analysis of the spectra is more complicated. For instance, if the unpaired electron is coupled to a ^{14}N we expect two single-quantum ($|\Delta m_I| = 1$) nuclear transitions and one double-quantum ($|\Delta m_I| = 2$) nuclear transitions for each of the spin manifolds, due to quadrupole interaction of the ^{14}N nucleus. The single-quantum (SQ) nuclear transitions frequencies show a first order dependence on the nuclear quadrupole tensor, which leads to the broadening of the signal. By contrast, the quadrupole tensors contribute in second order to the double-quantum (DQ) transitions, leading to more intense and less broad ridges. The DQ nuclear frequencies can be estimated by the following equation:[21]

$$V^{DQ}_{\alpha,\beta} = 2\sqrt{\left(\nu_I \pm \frac{\alpha/2\pi}{2}\right)^2 \left(\frac{e^2qQ}{4h}\right)^2 (3+\eta^2)} \qquad (27)$$

where α is the hyperfine coupling, Q is the electric quadrupole moment and η is the quadrupole asymmetry parameter.

However, when the nuclear Zeeman and hyperfine interactions are much stronger than the nuclear quadrupole interaction, the probability of the DQ transitions is very small and the SQ signals dominate the HYSCORE spectra.

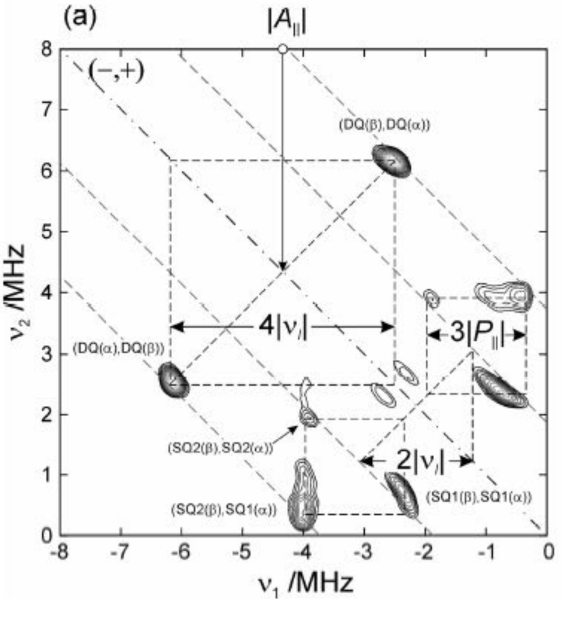

Figure 11. X-Band (at 9.7 GHz) HYSCORE spectra of the ^{14}N region of CuNCTPP (NC-TPP = 5,10,15,20-tetraphenyl-2-aza-21-carbaporphyrina) diluted in the Zn analogue powder sample, measured at g_z orientation (ν_{14N} = 0.9 MHz) with τ = 100 ns.[24]

In the X-Band HYSCORE spectra of a Cu(II) N-confused tetraphenylporphyrin complex the DQ and SQ cross peak signals are observed in the strongly coupled quadrant.[24] The DQ transitions lie parallel to the antidiagonal centred on the hyperfine coupling and separated by $4|\nu_I|$. The SQ transitions are also centred on the hyperfine splitting value but this time they are spaced by $2|\nu_I|$. Furthermore, cross peaks which correlate the single- and double- quantum frequencies are detected close to the antidiagonal, while the single quantum transitions are further split due to the quadrupole coupling P, which results in the detection of extra cross peaks on the spectrum.

II.III.III Electron nuclear double resonance (ENDOR) spectroscopy

Electron Nuclear Double Resonance (ENDOR) spectroscopy is one of the main hyperfine techniques for measuring nuclear transition frequencies of paramagnetic systems. ENDOR methods are based on the transfer of polarization between electron and nuclear transitions. During and ENDOR experiment both microwave (MW) and radio frequency irradiation (RF) are involved for the excitation of the electron transition and nuclear transition, respectively. The nuclear polarization is created by a single MW pulse is changed by a selective RF pulse, which is then transferred to electron coherence over the detection period and observed via an electron spin echo. Two different types of pulse ENDOR techniques have been developed by Mims in 1964 and Davies in 1974. Mims ENDOR method exhibits high sensitivity but it undergoes from blind spots observed in the EPR spectra, while Davies ENDOR experiment the blind spots have been eliminated by the use of longer selective pulses, which unfortunately results in lower sensitivity of the signal.

Mims ENDOR

The Mims ENDOR method operates with a stimulated echo sequence of three non-selective $\frac{\pi}{2}$ pulses ($\pi/2_{MW}$ - τ - $\pi/2_{MW}$ - π_{RF} - $\pi/2_{MW}$ - τ - *echo*),[25] which creates the polarization pattern, while a long radio frequency (RF) pulse is applied to excite the nuclear transitions. The preparation sequence ($\pi/2$ - τ - $\pi/2$) generates a gated polarization pattern in the EPR line; the first $\frac{\pi}{2}$ pulse causes rotation of the magnetisation to the *-y* orientation, which is under free evolution for time τ; then the second $\frac{\pi}{2}$ pulse moves the magnetisation back to the *z*-orientation by converting it to longitudinal magnetisation. During the mixing time *T*, a selective RF pulse is applied to change the polarization of the EPR transition; when the applied RF pulse is on resonance with the nuclear transition, the EPR frequency is shifted by a value depending on the hyperfine coupling (a quarter of this pattern is shifted by $+a_{\text{iso}}$ and another quarter by -a_{iso}). The last $\frac{\pi}{2}$ pulse transfers the magnetisation back in the *xy*-plane where the spins are refocused and then defocused leading to a stimulated echo at τ time after the last pulse.

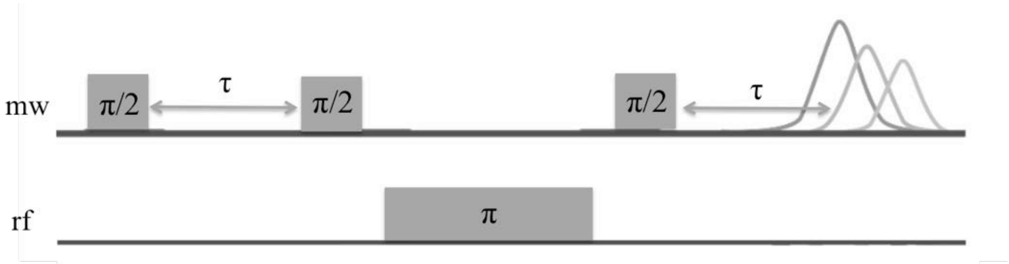

Figure 12. Schematic representation of the Mims ENDOR sequence; the inter-pulse delays are fixed and the radiofrequency is varied.

The ENDOR efficiency in a Mims experiment shows a cosine dependency of the ENDOR intensity as a function of the observed hyperfine coupling, α_{iso},

$$F_{ENDOR} = \frac{1}{4}(1 - cos(\alpha_{iso}\tau)) \qquad (28)$$

According to this formula, for $\alpha_{iso}\tau = 2k\pi$, with k = 0, 1, 2…, the stimulated echo is cancelled out due to absolute destructive interference of the polarized pattern. Hence, for a certain combinations of the α_{iso} and τ the Mims ENDOR signal reduces to zero; referred as blind spot behaviour and can result in misinterpretation of the ENDOR spectra. In order to avoid the loss of spectral information, Mims ENDOR spectra may have to be recorded with several different τ values to ensure that peaks are not missing from the detected ENDOR spectrum.

Davies ENDOR

Davies ENDOR technique is a population-transfer experiment, which relies on the selective excitation of only one of the allowed EPR transitions. Thus, this method is suitable for systems with larger hyperfine couplings compared to Mims ENDOR. The sequence of this experiment; π_{MW} - π_{RF} - $\pi/2_{MW}$ - τ - π_{MW} - τ - *echo*,[25] starts with a selective π microwave pulse that inverts the electron spin populations of the E1 and E3 manifolds.

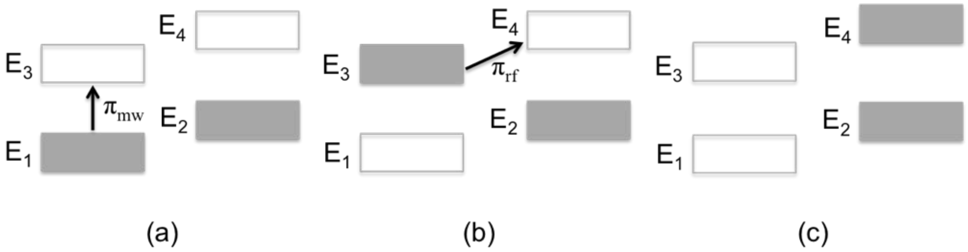

Figure 13. Schematic representation of (a) the selective inversion of the electron spin population due to the π_{mw} pulse; (b) the selective inversion of the nuclear spin population due to the π_{rf} pulse; (c) the resulted electron spin saturation.

During the mixing period a selective π_{RF} pulse at varying radiofrequencies is applied. If this pulse is on resonance with one of the nuclear frequencies, this leads to the reverse of the nuclear spin polarization and the reduction of the population difference for this particular EPR transition. The difference of the population is then recorded by the detection sequence ($\pi/2$ - τ - π - τ - *echo*), by monitoring the primary echo intensity as a function of the radio frequency, which is incremented stepwise.

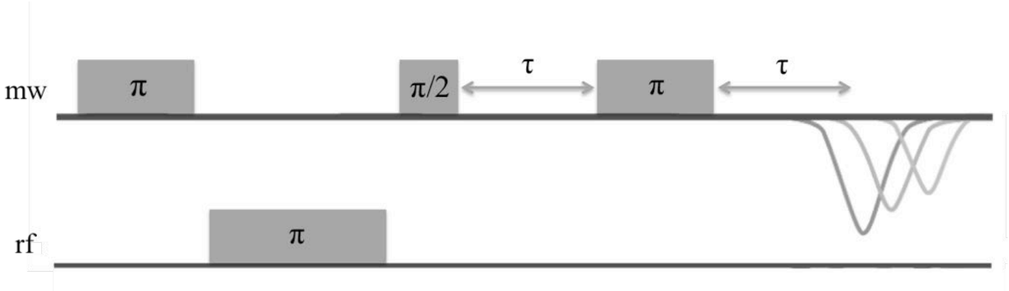

Figure 14. Schematic representation of the Davies ENDOR sequence; the inter-pulse delays are fixed and the radiofrequency is varied.

The absolute ENDOR intensity as a function of the selectivity of the inversion π pulse is described by

$$V(\eta_S) = V_{max}\frac{\sqrt{2}\eta_S}{(\eta_S^2 + {}^1\!/_2)} \quad (29) \quad with \quad \eta_S = \frac{t_\pi a_{iso}}{2\pi} \qquad (29)$$

where $V_{\max}$ is the higher ENDOR intensity, t_π is the length of the preparation MW π pulse and a_{iso} the observed hyperfine coupling.

The inversion pulse acts as a filter for weaker hyperfine couplings because of the very long length of the π pulse, the number of spins that contribute to the experiment reduces and the sensitivity is decreased for small couplings. Additionally in the Davies ENDOR spectroscopy blind spots are not observed due to the higher HF coupling of the systems.

Chapter III. Review of the Field

III.I Applications of pulsed EPR to the study of molecular spin qubits

III.I.I Background

The field of quantum technologies has the potential to advance a wide range of scientific areas, including simulation of quantum systems, metrology and cryptography.[26] Significant progress has been made through the understanding of the elementary unit of quantum information processing (QIP), the quantum bit. Quantum bits or qubits are the fundamental unit of information in a quantum computer, and the quantum analogues of the classical bits.[27] In contrast to the classical bit which takes one of the well-defined 'up' or 'down' electronic states, qubits are quantum mechanical two level systems which simultaneously exist in any linear combination of the 'up' (or 0) or 'down' (or 1) microstates. The state of the qubit can be written as:

$$|\psi\rangle = \alpha\,|0\rangle + \beta\,|1\rangle \qquad (30)$$

where α and β are complex numbers, with $|\alpha|^2$ and $|\beta|^2$ representing the probabilities of measuring at $|0\rangle$ and $|1\rangle$ state, respectively. Thus, these numbers need to satisfy the normalisation condition $|\alpha|^2 + |\beta|^2 = 1$. The state of a qubit can be described more generally as:

$$|\psi\rangle = \cos(\vartheta/_2)\,|0\rangle + e^{i\varphi}\sin(\vartheta/_2)\,|1\rangle \qquad (31)$$

where θ and φ are the polar and azimuthal angles, respectively. Based on the equation (31), θ indicates how close is the state of the qubit to either the 1 or 0 states, while the angle φ is termed as the qubit phase. All the superposition states of a qubit can be visualized as points on a sphere surface known as the Bloch sphere (Figure 15), while the state of a qubit can be represented by the Bloch vector laying on the surface of the sphere. This unique ability of qubits to exist in a coherent superposition of both $|0\rangle$ and $|1\rangle$ states,[28] allows inherent parallel computational operation taking place, which lead simultaneously to multiple solutions and much faster calculation.

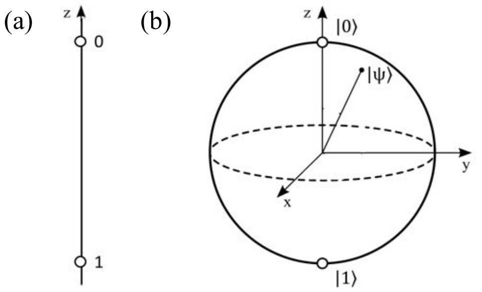

Figure 15. Schematic representation of the two states of (a) a classical bit; (b) a quantum bit $|\psi\rangle$ (Bloch sphere).

Electronic spin (S = ½) is the simplest two-level quantum system and a promising qubit candidate, demonstrating long coherence time and highly modulating properties. The dipole moment of an electron is by definition a two-level system with the two different orientations of the spin; 'spin-up' or m_s = + ½ and 'spin-down' or m_s = - ½, corresponding to the $|0\rangle$ and $|1\rangle$ states. During the last decades, various materials have been proposed as quantum bits ranging from vacancies or impurities in solids,[29] quantum dots,[30] and superconductive systems,[31] to trapped ions[32] and polarized photons.[33] In 2000, a specific set of criteria was formalized by David DiVincenzo establishing the quantum bit requirements.[34] According to them a qubit should be or display: (a) a well-defined and scalable quantum two-level system, (b) the ability to initialize the state of the qubits to a simple basic state; as each algorithm requires a well-known state to start the computation, while it is also necessary for the error correction procedure, (c) a long relevant coherence time - the lifetime of the superposition state, much longer than the gate operation time during which quantum information should be preserved, (d) the ability to devise a universal set of quantum gates built from a set of deterministic unitary instructions, and (e) a qubit-specific measurement capability; allowing the extraction of information after the completion of the quantum computation. The above principles need to be simultaneously met by a material, so it can be considered as a possible quantum bit.

The current state-of-the-art in molecular electron spin qubits is mainly focused on the quantum coherence - decoherence - mechanisms. Coherence usually describes the formation of an entagled state, whereas the term decoherence denotes the decay of or loss of the quantum phase information. The loss of the information contained in a qubit is principally due to its interaction with the surrounding environment. Two different mechanisms are involved in the decoherence process: (a) interaction with phonons and vibrations within the material[35] (b) through space interaction with neighbouring electronic and nuclear spins.[36] The first mechanism is related to the spin-lattice relaxation (T_1) which involves direct flips of the qubits due to the interactions of the inverted spins with thermal vibration (phonons) of the surrounding lattice. Spin-lattice relaxation is dominated by modulation of the spin-orbit coupling (SOC) via local and extended vibrational modes. The mixing of the spin and orbital angular momentum caused by the SOC, allows the exchange of energy between the system and the thermal lattice. T_1 dominates the relaxation pathway at higher temperature and defines the upper limit for coherence times. As such, it is crucially important to control spin-lattice relaxation, which ultimately enables lengthening of the coherence time (or phase memory time). The second mechanism describes the coherence time (T_2), which measures the lifetime of the coherent superposition state, illustrating the time that the quantum information is preserved. Spin decoherence is mainly induced by spin-spin (electron-electron, electron-nuclear and nuclear-nuclear) interactions. Hence, interaction of the electron qubit with its environment can cause the rapid collapse of the fragile electron spin superposition state due to spin decoherence. Long enough quantum coherence time is required for the successful application of the qubits in the field of quantum technologies. The main target for any possible qubit candidate is a phase memory time 10^4 times longer than the quantum operation or quantum gate time.[34] A typical length of a gate time is in the range of 10 ns which necessitates approximately 100 μs for the coherence time in order to be able to perform logic functions.

A crucial property of the quantum bits is their ability to access any arbitrary coherent superposition states. This essential ability of the qubits is demonstrated by transient nutation experiments. Variable power nutation experiments are performed to demonstrate coherent spin manipulation of the spin qubits. During the nutation studies an external oscillatory magnetic field adjusts the energy of a qubit manipulation with a resonant microwave pulse, leading to one of the superposition states. The applied nutation or tipping pulse (t_p) creates different superposition states by varying the length and the power of the microwave radiation (Figure 16). Thus, the revealed oscillatory behaviour between coherent back-and-forth quantum transitions of the ground and the excited spin state is called Rabi oscillations.[37] The Rabi frequency, Ω_R, is the angular frequency of these oscillations and describes the coupling strength of the spin with the applied microwave field. A useful 'figure of merit' for the evaluation of a quantum bit, Q_M,[38] is the number of coherent single-qubit operations in the time length of a T_2 and is quantified as $2\Omega_R T_2$, where Ω_R is the Rabi frequency; the angular frequency of the Rabi oscillations.

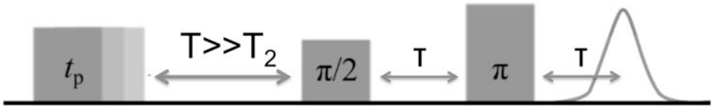

Figure 16. A schematic representation of the transient nutation pulse sequence, which implies a tipping pulse, prior of a standard Hahn echo sequence tilting the magnetisation through a tipping angle, $\theta = g\mu_B B_1 t_p/\hbar$, away from the alignment with the applied magnetic field.

III.I.II Molecular spin systems as quantum bits

In the field of quantum technologies, a major focus of research has been on the design of molecular spin qubits with long quantum coherence times and on the extension of these molecular designs to multiple qubit architectures for the implementation of quantum operations. Designing materials that fulfil the DiVincenzo criteria - which guarantees their viability as spin qubits - is a major goal. However, these superposition states are very fragile and could easily be wiped out by interactions of the electron spin with its environment. Spin decoherence induced by lattice vibrations, electric and magnetic noise, is a crucial obstacle for the development of solid-state quantum computers.

Several types of materials are currently investigated as potential quantum bits including superconductive circuits, ion traps, polarized photons, semiconductor quantum dots along with both nuclear[39] and electronic spins.[40] Each of these qubit platforms exhibits advantages and disadvantages. For instance, superconducting circuits offer an interesting commercial platform for quantum computation; but also pose difficulties in assembling multiple qubits due to the nearest-neighbor couplings. Atom and ion traps have been successfully scaled up to multiple qubit architectures, with great potential for quantum simulator purposes, although they suffer from slow switching speeds compared to solid-state devices.[41]

Electronic and nuclear spin qubits are under significant research efforts towards exploiting them as the elementary unit of information in quantum devices. Nuclear spin qubits exhibit remarkable long coherence time, with a record of 39 minutes at room temperature,[42] because of their inherent shielding from the surrounding environment. Despite this, nuclear spins are not the most promising qubit candidates due to their low magnetic moment and very weak interactions, the manipulation and incorporation to circuits is challenging. In contrast, electronic spins are notably well suited to serve as molecular spin qubits; displaying an important advantage of high chemical tunability. The versatile nature of the molecular systems is a key tool for the development of solid-state molecular spin qubits through bottom-up chemistry approaches. Coordination chemistry offers a wide range of options for the rational design of the spin environments, reduction of magnetic noise, and scalability by replication and organisation using supramolecular chemistry principles. The latter is important for the successful coupling of the spin qubits as a means of implementing quantum algorithms, facilitating the idea of constructing quantum devices based on molecular spin qubits.

Numerous transition metal and lanthanide complexes have been investigated for the purpose of quantum information processing. Quantum computation requires qubits with long coherence times. Several synthetic strategies have been employed targeting molecules with enhanced phase memory time. The most commonly used is the elimination of decoherence sources; including the use of nuclear spin-free ligands, the use of deuterated ligands and solvents and the magnetic dilution in solid state systems.

III.I.II.I Transition metal qubits

Initial investigations on a molecular system of heterometallic wheels {Cr_7Ni} (Figure 17a), with an $S = ½$ spin ground state, highlighted its long coherence times and thus its potential as spin qubit. Significant enhancement of the T_m time was observed after deuteration of the pivalate ligands, from 0.55 μs for the $Cr_7NiF_8(piv)_{16}$ to 3.8 μs for the $Cr_7NiF_8(piv\text{-}d_8)_{16}$ at 1.8 K.[43] The weakly coupling of multiple spin systems lies behind the idea of creating quantum logic gates, assembling {Cr_7Ni} rings into more complicated molecular architectures was one of the first examples in the trail of functional quantum gates. In Figure 17b the two Cr_7Ni rings[44] are oriented in different directions leading to distinct spatial orientation of the anisotropy, which enables their independent manipulation. In addition, the use of a cobalt (II) complex as a linker, allows reversible switch off of the magnetic interaction via oxidation and reduction of the Co ion.

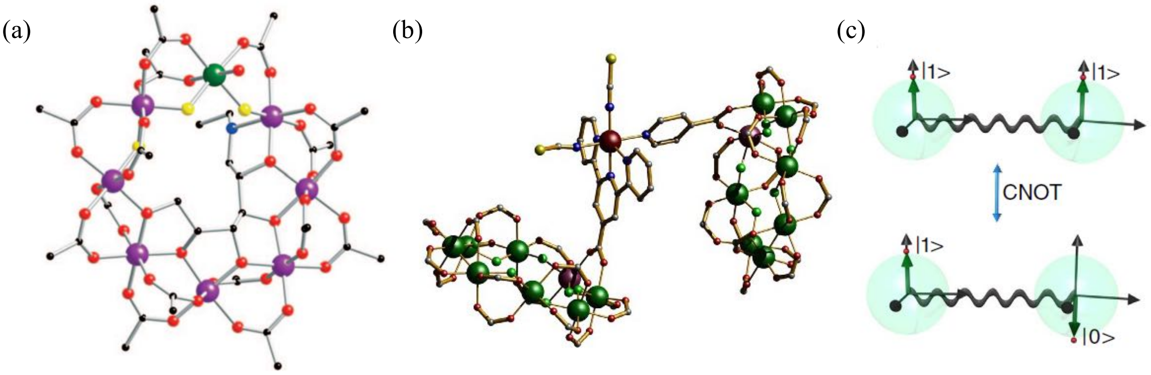

Figure 17. Molecular structure of (a) a {Cr_7Ni} analogue; (b) the asymmetric two-{Cr_7Ni} linked by a Co(II) complex; (c) Schematic representation of the CNOT gate of the two-qubit assembly.[44]

In the quest towards microsecond relaxation times, the most exceptional optimisation was observed for a vanadium (IV) complex, $[V(C_8S_8)_3]^{2-}$,[45] which is based on a nuclear spin-free ligand. The relaxation studies were carried out in nuclear spin-free solvent CS_2 showing a record T_m value of 0.7 ms at 10 K under optimised conditions of high dilution. (Figure 18a) It is noteworthy that similar measurements were performed after dissolution of $[V(C_8S_8)_3]^{2-}$ in d_7-DMF/d_8-toluene, a nuclear spin active solvent, leading to phase memory time two orders lower than the one measured in carbon disulphide.[45] Comparison of the T_m data below 60 K shows a significant increase of T_m for the sample measured in CS_2, indicative that decoherence originating from the nuclear spins dominates the low temperature regime. Above 60 K, the T_m time approaches 1 μs in all solvents (Figure 18b), suggesting that thermal vibrations and spin-lattice relaxation are the main source of decoherence.

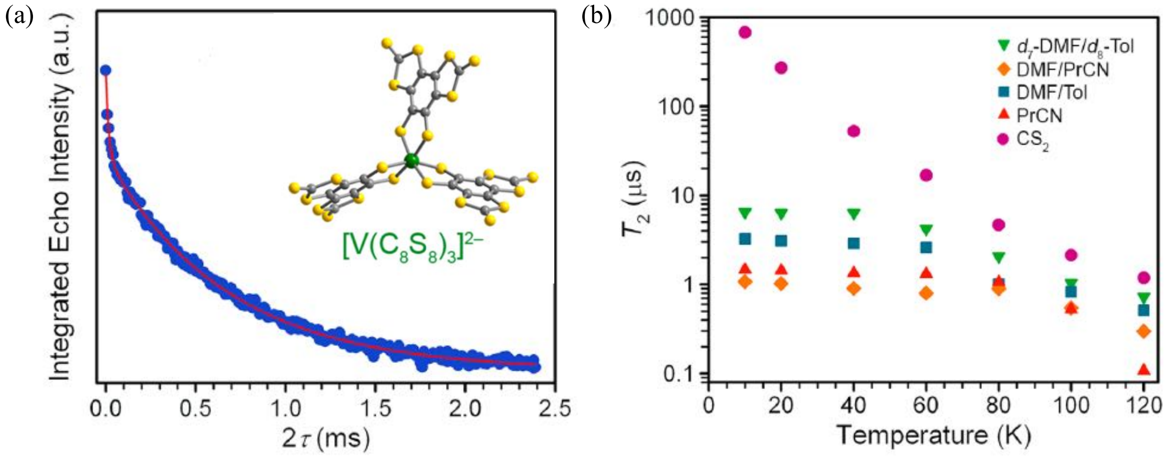

Figure 18. (a) The Hahn echo decay curve at 10 K in CS_2 fitted by the biexponential equation; (inset) molecular structure of the $[V(C_8S_8)_3]^{2-}$; (b) Logarithmic temperature dependence of T_2 in different solvents.[45]

One step closer to the desired solid-state materials with long coherence times at relatively high temperatures was the investigation of the coherence time of a vanadyl phthalocyanine complex, VOPc,[46] a S = ½ system based on a V(IV) ion. A single crystal sample of the VOPc complex diluted in the isostructural diamagnetic TiOPc host was studied, displaying a phase memory time of 1 μs (Figure 19a), as well as occurrence of quantum Rabi oscillations at room temperature (Figure 19b). Importantly, this complex shows robust qubit behaviour despite the presence of spin-active nuclei (^{1}H and ^{14}N nuclei) in the molecular environment of the electronic spin.

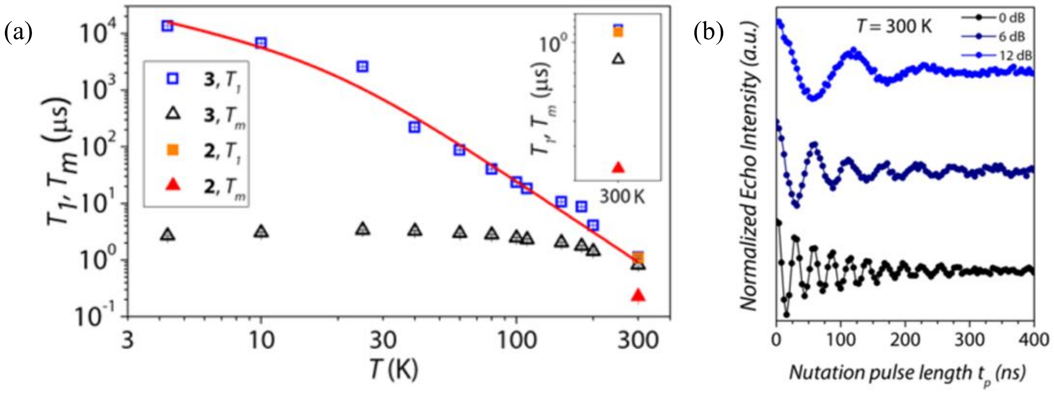

Figure 19. (a) Temperature dependence of T_1 and T_m relaxation times; (b) Rabi oscillations at 300 K for different microwave attenuations.[46]

Another successful approach for lengthening T_m was demonstrated with a Cu^{II} complex, $[Cu(mnt)_2]^{2-}$ (mnt = maleonitriledithiolate),[47] where the organic ligands were selected to carry a limited number of spin-active nuclei and methyl groups. Solid-state measurements were performed on a magnetically diluted sample in the diamagnetic Ni^{II} analogue, exhibiting remarkable coherence time of 68 μs at 7 K and 0.6 μs at room temperature (Figure 20).

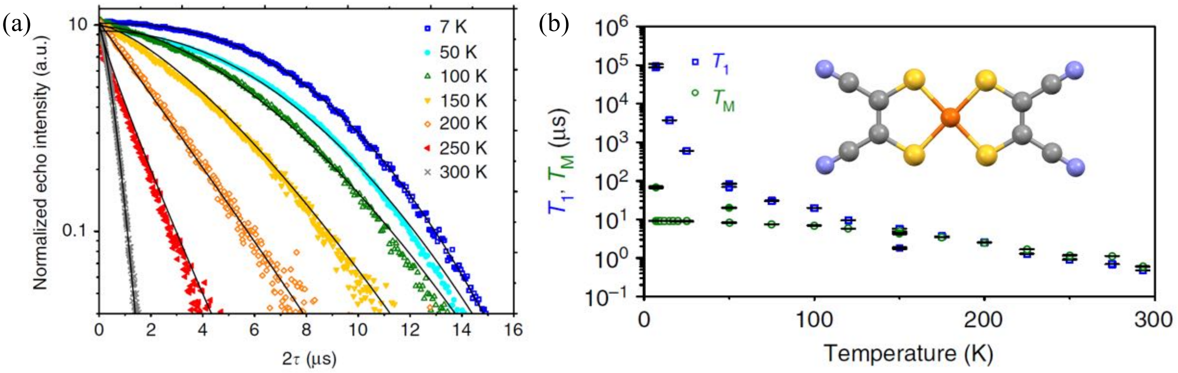

Figure 20. (a) Hahn echo decay curves as a functions of the 2τ time at different temperatures; (b) Temperature dependence of the spin-lattice relaxation and phase memory time; (inset) Molecular structure of the $[Cu(mnt)_2]^{2-}$.[47]

III.I.II.II Lanthanide metal qubits

Considering that the interaction of the electronic spin with its environment is a major source of decoherence, an interesting proposal is to engineer the energy-level structure of the molecule, generating molecular spin qubits that are insensitive to the magnetic noise. This strategy can be accomplished by mixing of the qubit coherent states, as a means of introducing an avoided level crossing (or tunnelling gap) between the two states, resulted in ideal conditions (atomic clock transitions, CTs) for the quantum coherent studies. At this preferably operating point the fluctuation of the applied magnetic field has no impact on the spin qubit dynamics, which is protected against decoherence originating from dipolar interactions. This approach was followed for a lanthanide polyoxometalate (POM) complex, based on a Ho^{III} ion encapsulated in between two molecular tungsten oxide moieties, $[Ho(W_5O_{18})_2]^{9-}$.[48] Long quantum coherence was detected at the applied magnetic fields corresponding to the clock transitions, with the phase memory time approaching 8.4 μs at 5 K (Figure 21b). The protected nature of the spin qubit, due to the avoided level crossings (Figure 21a), with respect to the local magnetic noise results in relatively long quantum coherence times without considering any optimisation of the sample conditions such as dilution or deuteration aimed to minimise the dipolar interactions.

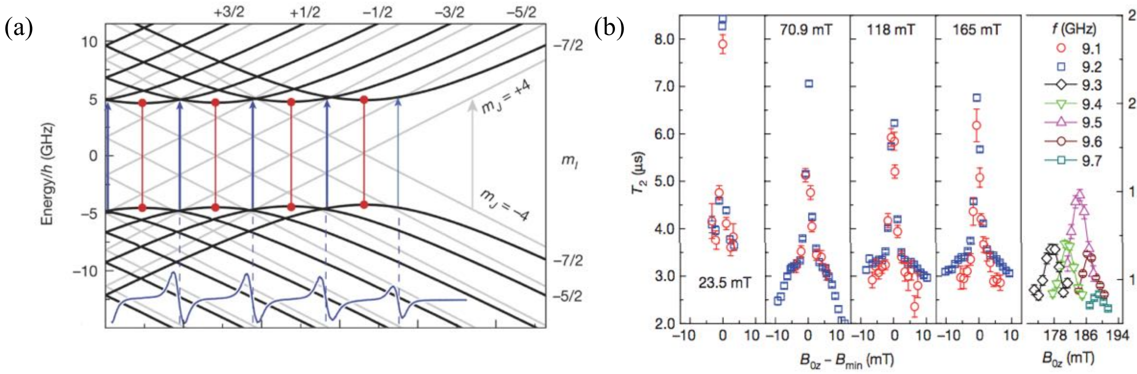

Figure 21. (a) Zeeman diagram for the $m_J = \pm 4$, $I = 7/2$ ground state at g_z orientation; the grey lines correspond to the ideal D_{4d} symmetry, while the thick black ones assume the use of an extra 'axial + $B_4^4\hat{O}_4^4$' parameter (red lines indicate the location of CTs); (b) T_2 divergence at the CTs illustrated on the first four panels, while the rightmost panel shows T_2 values at various frequencies some of them well away from CTs.[48]

Following a similar idea of protecting the electronic spin from the interaction with the environment, the encapsulation of the spin qubit in a sheltered cage can eliminate the interferences with the neighbouring spins. The versatile nature of the fullerenes supports the strategy when employing them as hosts for a variety of spin qubits. A fascinating example is that of the metallofullerenes of Y, Sc and La@C82,[49] found to have T_m relaxation times longer than 200 μs (225, 245 and 204 μs for Y@C82, Sc@C82 and La@C82, respectively) below 10 K, for all the three encapsulated ions.

Recent studies shows that there is possible to scale up quantum resources by exploiting the multiple magnetic states of the same molecule. This is possible when employing systems with a larger multiplet ground state, the qudits (d states). An example of a d = 4 qudit is the bis-phthalocyanine Tb^{III} complex TbPc$_2$ ($m_J = \pm 6$), due to the nuclear spin quadraplet $I = 3/2$ of Tb^{III} (Figure 22b) with unevenly spaced levels arising for the combination of hyperfine and nuclear quadrupole interactions.[50] Coherent nuclear spin manipulation has be achieved by using microwave pulses leading to much longer relaxation times, but also lower Rabi frequencies because of the weaker nuclear magnetic moment compared to the electronic ones. Remarkably, further studies on this molecule exhibit a great achievement for QIP in a single molecule; enabling the first implementation of a quantum algorithm (Grover's search algorithm).[51]

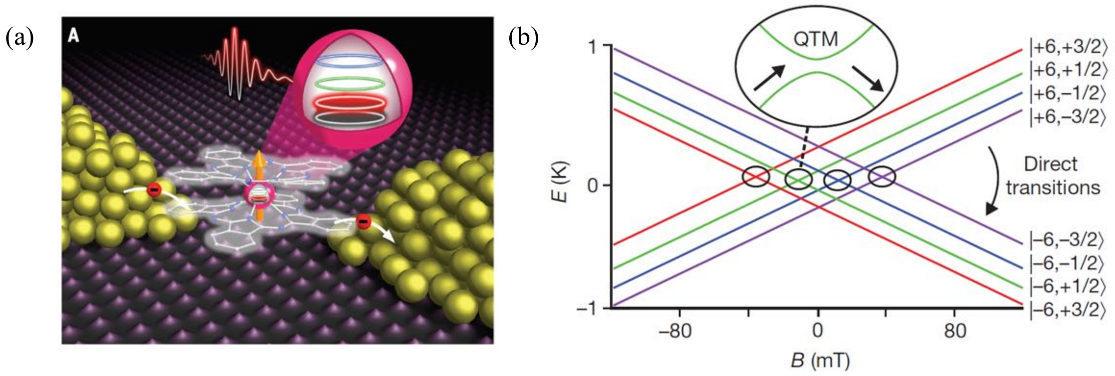

Figure 22. (a) Schematic representation of a molecular spin transistor based on a $TbPc_2$ molecule linked to source and drain gold electrodes; (b) Zeeman diagram exhibiting the energy of the two $J_z = \pm 6$ ground state split into four different sub-states due to the hyperfine interactions with the nuclear spin of $I = 3/2$. The field-induced avoid level crossings (black circles) around zero field, allowing for tunnelling (QTM) of the electron spin.[50]

III.II Applications of HYSCORE to study the extent of covalency in f-element complexes.

III.II.I Covalency of lanthanide and actinide elements

The electronic structures of the f-element compounds have been a source of intensive research, because of the combination of strong electron correlation, the weak ligand field of the metal centres and the relativistic effects, which is found only in the f-elements. Moreover, the electronic properties of the f-element compounds have an essential role for furthering our understanding of f-orbital bonding, since the f-orbitals possess limited radial extension not allowing significant perturbation by the ligand field.[52]

In general, the f-elements are referred as chemically hard Lewis acids, thus their bonding assumed to be strongly ionic.[52] The ionic bonding of the lanthanides is also related to the nature of the 4f-orbitals. The highly contracted nature of the rare earth ions leads to strongly localized 4f-orbitals, which make them unavailable for bonding, and thus the interactions between lanthanide ions and organic ligands considered as mostly ionic.[53]

On the other hand, the properties of the actinide ions lie in between the d-elements and the lanthanide ions, due to the greater radial extension of the 5f orbitals. The lighter actinides (Ac to Am) display more common features with the transition metal centres; wide range of oxidation states and more covalent bonds. Along the actinides series, occupation of the 5f-orbitals become more favourable than the 6d and 7s-orbitals resulting in a more lanthanide-like behaviour. The heavier member of actinides, usually are found in the trivalent oxidation state and they also show a more ionic bonding.

The similar chemical behaviour of the lanthanides and the late actinides makes their chemical separation difficult, which is important for the recycle of the nuclear waste. The successful separation of the trivalent actinide elements from the trivalent lanthanides, which are produced during the fission of nuclear fuels, are of tremendous technological interest. Current methods for this kind of separation are based on the slightly preference of the minor actinides on soft-donor ligands[54] in contrast to the trivalent lanthanides. The selectivity of the minor actinides is often thought to originate from a stronger interaction of An(III) with relatively softer donor ligands (mainly N) and an increase in covalency of the An-L bonding compared to Ln-L bonds.

The covalency of the metal ligand bond is difficult to quantify experimentally,[55] even thought, a variety of spectroscopic methods have been applied in order to study the covalency, which consists of electron paramagnetic resonance (EPR),[56] ligand K-edge X-ray absorption (XANES),[57] Mössbauer[58] and photoelectron spectroscopy.[59] In addition, nuclear magnetic resonance spectroscopy (NMR)[60] can be applied for measuring the covalency, but is restricted to diamagnetic systems.

III.II.II Covalency studies via EPR spectroscopy

Electron paramagnetic resonance spectroscopy is a promising technique for measuring the covalency of actinide and lanthanide elements. The interpretation of the EPR spectra gives information about the g-factor, the hyperfine coupling and the ligand hyperfine coupling called ‘superhyperfine’. Therefore, the covalency can be measured via the ‘superhyperfine’ coupling arising from the interaction of the electron spin of the metal with paramagnetic nuclei on the ligands. HYSCORE technique can be used to quantify the electron spin density on the ligand nuclei with non-zero nuclear spin, allowing an estimation of the degree of covalency in metal-ligand bonds.

Experimental studies of halide complexes of the f-elements have been previously reported.[61] The doped CaF_2, SrF_2 and BaF_2 (just for U^{III}) single crystal with U^{III} and Nd^{III} were used, in order to measure the superhyperfine interaction of the fluorine ligand with the metal-based unpaired electrons. For the U^{III} doped crystal an even number of transitions is observed which is attributed to the interactions of odd number of fluorine nuclei. While for the Nd^{III} doped single crystal, no ligand hyperfine was obtained, confirming that the electrons in the 4f-orbitals do not have a significant contribution to the chemical bonding.

More detailed covalency measurements are based on pulsed EPR spectroscopy, which allows the detection of weaker interactions and provides information on spin dynamics. Covalency studies in actinides complexes via pulsed EPR techniques have been previously reported by our group,[62] in which two mononuclear actinide complexes, $[An(Cp^{tt})_3]$ (An^{III} =

Th or U and Cp^{tt} = $C_5H_3{}^tBu_2$-1,3) based on a substituted cyclopentadienyl derivative were studied.

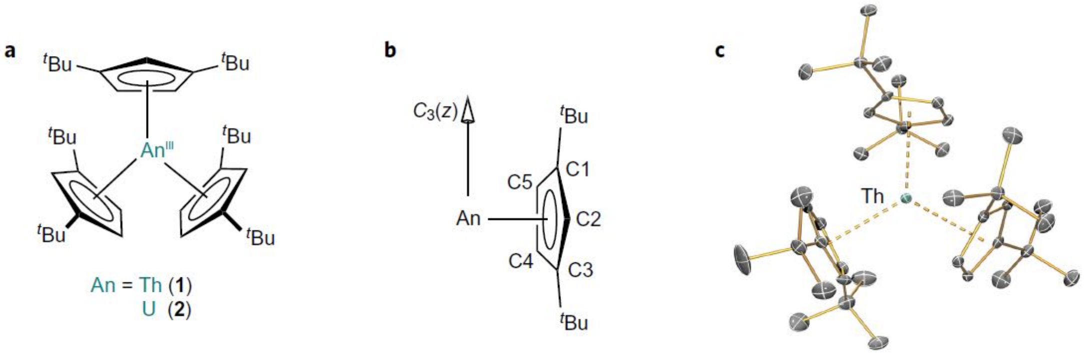

Figure 23. (a) Schematic of the structure of [Th(Cp^{tt})$_3$] and [U(Cp^{tt})$_3$]; (b) Numbering scheme used for Cp^{tt} ligands and the molecular axis system; (c) Molecular structure of [Th(Cp^{tt})$_3$] from single crystal X-ray diffraction.[62]

Continuous wave measurements were performed for both complexes, with an axial symmetry to be observed for the Th^{III} complex (at 100 K) with the following electronic *g*-values of $g_\perp = 1.880$ and $g_\parallel = 1.974$. In contrast, the U^{III} complex exhibits a less symmetric EPR spectrum with rhombic features below 5 K and the effective *g*-values of $g_x = 3.05$, $g_y = 1.65$ and $g_z < 0.5$. It is noteworthy that for the Th^{III} derivative DFT studies indicates a 6d^{1}5f^0 configuration, which is consistent with the experimental *g* values and the appearance of the EPR signal at high temperature; thus the Th^{III} acts like a d-block element. However, the U^{III} analogue has a 5f^3 configuration and the EPR signal was observed up to ~40 K, indicating a more lanthanide-like behaviour for the U^{III} complex.

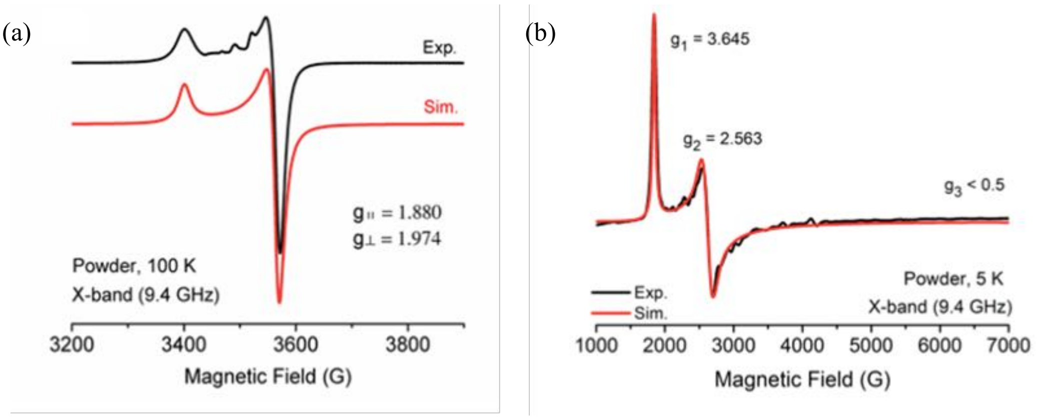

Figure 24. X-Band continuous wave EPR spectra of polycrystalline samples of (a) [Th(Cp^{tt})$_3$] at 100 K; (b) [U(Cp^{tt})$_3$] at 5 K.[62]

HYSCORE measurements were obtained in order to quantify the hyperfine interactions with the ^{1}H and ^{13}C nuclei on the ligands, and thus the covalency of the actinide ions. For [Th(Cp^{tt})$_3$] both ^{1}H and ^{13}C region were reported, with the interpretation of the data suggesting dipolar (A^{dip}) and spin density contributions (A^{Cn}) of a total of ~6% spin population on the three Cp^{tt} ligands. In the case of the U^{III} complex, in the HYSCORE spectra only the interaction with the ^{1}H was performed due to the detection of a very weak signal in the ^{13}C region. The analysis of the data in the case of U^{III} complex also determined the presence of dipolar and spin density contribution, with a ~1.9% of the carbon 2p$_{\pi}$-spin population at each H on the rings which leads to a total of ~ 17% spin population over all three Cp^{tt} ligands.

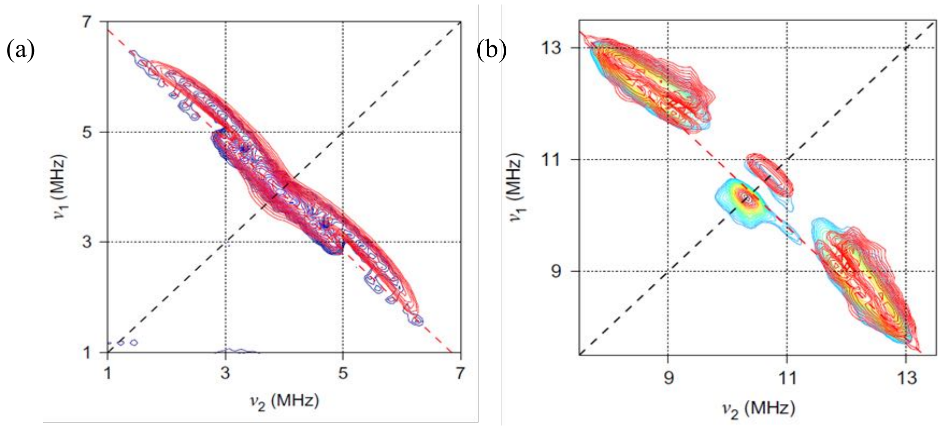

Figure 25. X-Band HYSCORE spectra (a) for complex [Th(Cp^{tt})$_3$] at the ^{13}C region; (b) for complex [U(Cp^{tt})$_3$] at the ^{1}H region (simulation with red).[62]

Similar studies for the covalency of a late lanthanide ion have been previously reported for a mononuclear tris-cyclopentadienyl ytterbium complex, [Yb(Cp)$_3$].[63] The molecular symmetry of the complex is close to C_{3h} with the plane of the Cp rings being almost exactly parallel to the pseudo-3-fold axis. The X-Band CW and FID EPR spectra of the YbCp$_3$ complex were simulated by the following spin Hamiltonian parameters, $g_{\perp}$ = 6.0659 and $g_{||}$ = 1.9245. Moreover, small satelites are observed due to hyperfine interactions with ^{171}Yb (I = 1/2, 14.4 %) and ^{173}Yb (I = 5/2, 16.2 %), giving A$_{\perp}$ = 1287 MHz; A$_{||}$ = -4805 MHz and A$_{\perp}$ = 354 MHz; A$_{||}$ = 1322 MHz, respectively.

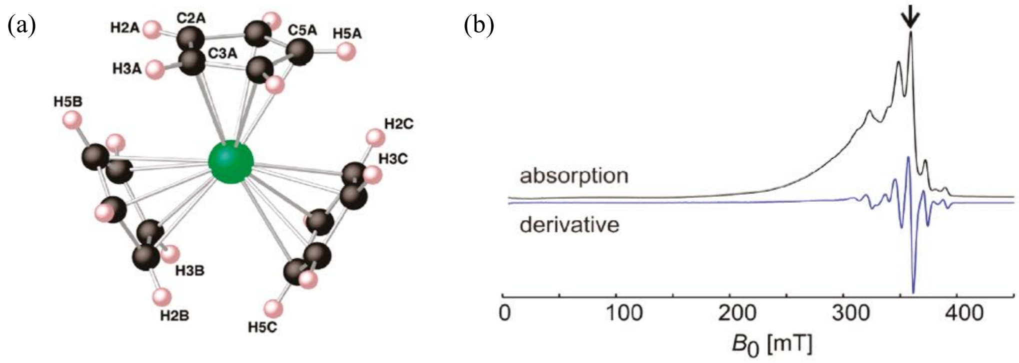

Figure 26. (a) Molecular structure of [Yp(Cp)$_3$]; (b) FID-detected ERP spectrum (black) of YbCp$_3$ and the corresponding first derivative (blue).[63]

The ^{13}C HYSCORE spectra measured on the perpendicular component were modelled with an isotropic contribution occurring from the spin density on the *s*-orbital and an axial contribution by cause of the spin density on the $2p_{\pi}$-orbitals. The best simulation of these data was obtained using an isotropic contribution to the hyperfine of $A_s = 0.4 \pm 0.1$ MHz and a point dipole contribution of $A_p = 1.6 \pm 0.1$ MHz. The analysis of the data shows an evidence of significant covalency on the Yb^{III}-orbitals, and the accumulation of the spin-density on the ^{13}C of the ligands was calculated as 12.6 % in total for all the Cp rings.

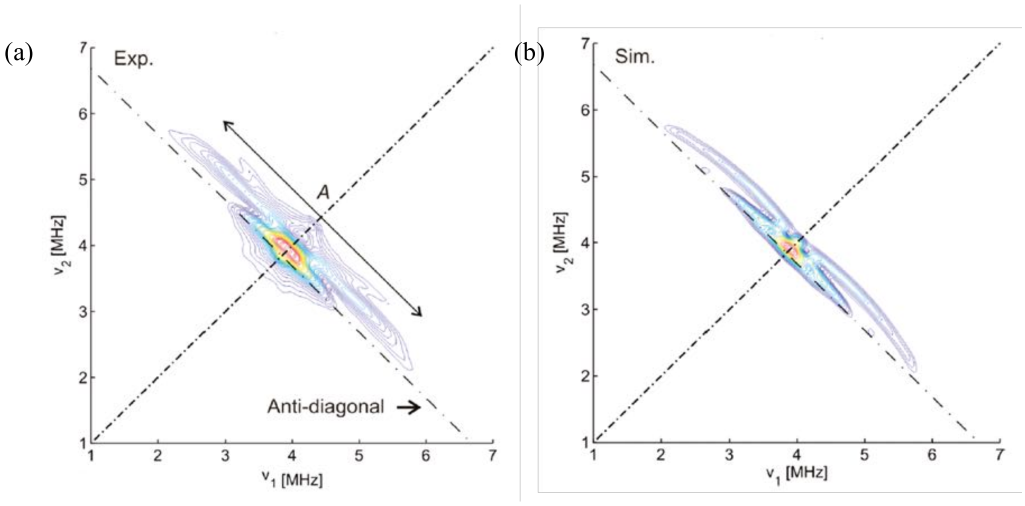

Figure 27. X-Band HYSCORE spectra at ^{13}C region and at 5.25 K (a) experiment; (b) simulation.[63]

The previously reported studies of covalency on the actinide complexes via HYSCORE spectroscopy show significantly greater total spin density on the ligands for the U^{III} than Th^{III} complex. In addition, comparison of the HYSCORE spectra of the Yb^{III} with the Th^{III} complex displays apparent similarities, which indicates covalency akin to the late lanthanides and the light actinides despite the 4f versus 5f/6d valence orbitals. Having in mind all the above, in order to extent our knowledge of inner transition metals covalency to the early lanthanide ions, we choose a mononuclear family of the following lanthanide complexes; $[Ln(Cp^{tt})_3]$ with Ln = La, Ce, Nd, Sm. The above compounds are isostructural with the previously reported Th^{III} and U^{III} complexes, as a means of more appropriate comparison.

Chapter IV. Paper 1

“Engineering electronic structure to prolong relaxation times in molecular qubits by minimising orbital angular momentum”

A.-M. Ariciu, D. H. Woen, D. N. Huh, L. E. Nodaraki, A. K. Kostopoulos, C. A. P. Goodwin, N. F. Chilton, E. J. L. McInnes, R. E. P. Winpenny, W. J. Evans and F. Tuna.

nature COMMUNICATIONS

ARTICLE

https://doi.org/10.1038/s41467-019-11309-3 OPEN

Engineering electronic structure to prolong relaxation times in molecular qubits by minimising orbital angular momentum

Ana-Maria Ariciu[1,2,4], David H. Woen[3,4], Daniel N. Huh[3], Lydia E. Nodaraki[1], Andreas K. Kostopoulos[1], Conrad A.P. Goodwin[1], Nicholas F. Chilton[1], Eric J.L. McInnes[1,2], Richard E.P. Winpenny[1], William J. Evans[3] & Floriana Tuna[1,2]

The proposal that paramagnetic transition metal complexes could be used as qubits for quantum information processing (QIP) requires that the molecules retain the spin information for a sufficient length of time to allow computation and error correction. Therefore, understanding how the electron spin-lattice relaxation time (T_1) and phase memory time (T_m) relate to structure is important. Previous studies have focused on the ligand shell surrounding the paramagnetic centre, seeking to increase rigidity or remove elements with nuclear spins or both. Here we have studied a family of early 3d or 4f metals in the +2 oxidation states where the ground state is effectively a ^2S state. This leads to a highly isotropic spin and hence makes the putative qubit insensitive to its environment. We have studied how this influences T_1 and T_m and show unusually long relaxation times given that the ligand shell is rich in nuclear spins and non-rigid.

---

[1] School of Chemistry, The University of Manchester, Oxford Road, Manchester M13 9PL, UK. [2] Photon Science Institute, The University of Manchester, Oxford Road, Manchester M13 9PL, UK. [3] Department of Chemistry, University of California, Irvine, CA 92697-2025, USA. [4]These authors contributed equally: Ana-Maria Ariciu, David H. Woen. Correspondence and requests for materials should be addressed to R.E.P.W. (email: richard.winpenny@manchester.ac.uk) or to W.J.E. (email: wevans@uci.edu) or to F.T. (email: floriana.tuna@manchester.ac.uk)

euenberger and Loss first proposed using electron spins within molecules for quantum information processing (QIP) [1] by showing how the Grover algorithm could be mapped onto a Mn_{12} cage[2]. Since then several groups have examined two-level ($S = 1/2$) molecular spin systems as possible qubits[3–12] and the Grover algorithm has been implemented in a four-level molecular qudit[13]. Molecular electron spin qubits have an obvious disadvantage: as they are molecules, the magnetic moments of nuclear spins and molecular vibrations will produce noise that could cause electron spin relaxation and therefore loss of phase information within the qubit before computations can be performed. Studies to address this disadvantage include use of advanced microwave pulse sequences[3] to repair the damage done by noise and hence increase phase memory times (T_m). A second approach uses spin transitions that do not vary with magnetic field at first order[12], often called clock transitions; the lack of dependence on local field renders the qubit insensitive to its environment and hence lengthens T_m.

The magnetic noise in molecules is dominated at low temperatures by nearby nuclear spins undergoing flip-flop processes causing an oscillating magnetic field: reducing this source of noise has been widely studied to engineer better qubits[7–11]. Removal of nuclear spins from the qubit and/or embedding the molecule in a nuclear-spin-free lattice has led to phase memory times (T_m) long enough to permit coherent spin manipulation via Rabi oscillations[9–11], sometimes even at room temperature[11]. However, even in the absence of nuclear spins, T_m becomes limited by spin-lattice relaxation (T_1) that is strongly temperature dependent. T_1 is dominated by modulation of spin-orbit coupling via molecular vibrations. It is the spin-orbit coupling that mixes spin and orbital angular momentum, hence enabling exchange of energy between the spin system and the lattice when the electronic energy levels are modulated. Reducing the impact of molecular vibrations is a challenge. The intuitive approach is to reduce the influence of molecular vibrations by making a more rigid molecule or lattice, which does lead to longer phase memory times by lengthening T_1[11].

We noted a study where Zn^+ ions, encapsulated in a metal-organic framework, show phase memory times of 2 µs at room temperature[14]. This is ascribed to the unpaired electron being in a ^2S state and hence with minimal anisotropy. Therefore, we sought a molecular species that would mimic the highly isotropic nature of these embedded Zn^+ ions. All molecular qubits proposed thus far have the unpaired electron spin in a p-, d- or f-orbital and have little s-character. Our target was a molecule with a ^2S ground state.

We identified a family of molecules that might exemplify this strategy. The compounds are three-coordinate with local pseudo-C_3 symmetry at the metal ion. In this point group, the lowest energy d-orbital is $d_z{}^2$ and it has the same irreducible representation as an s-orbital; therefore, the s- and $d_z{}^2$ orbitals will mix and regardless of the relative admixture of the two atomic orbitals, an S-like state will result as both orbitals have $m_l = 0$. The compounds contain early d-block or 4f-block metals in the +2 oxidation state, which is very unusual for the metals involved. The four compounds are: $[K(2.2.2\text{-cryptand})][Y(Cp')_3]$ **1** ($Cp' = C_5H_4SiMe_3$)[15,16] (Supplementary Fig. 1); $[K(2.2.2\text{-cryptand})][Lu(Cp')_3]$ **2**; $[K(2.2.2\text{-cryptand})][La(Cp')_3]$ **3**; and $[K(2.2.2\text{-cryptand})][Sc\{(N(SiMe_3)_2\}_3]$ **4**. These complexes flout the established criteria[17] for long T_1 or T_m in molecular qubits, as they are far from rigid and contain numerous hydrogen atoms and multiple methyl groups, whose rotation is a known decoherence mechanism[18]. Yet here we report coherent spin manipulations on **1** at room temperature. We achieve this by engineering the electronic configuration of the metal centre, an approach that could be combined with the beautiful engineering of the ligand shell demonstrated by other groups[7–11].

Results

Electron paramagnetic resonance spectroscopy. In compounds **1**–**4** the metal centre in the anion is three-coordinate with a pseudo-C_3 axis passing through the metal, perpendicular to the plane defined by the Cp′ centroids in **1**–**3** and the N atoms in **4** (Fig. 1a). In all cases the continuous-wave EPR (CW-EPR) spectroscopy of a fluid solution of these compounds shows a multiplet due to hyperfine coupling (A) of the single unpaired electron to the metal nucleus (Supplementary Fig. 2; Table 1). On freezing the solutions, a small axial g-anisotropy is observed in all cases; where z is coincident with the *pseudo*-C_3 axis), with a near isotropic hyperfine coupling (Fig. 2a; Table 1). The highly isotropic hyperfine coupling and minimal g-anisotropy suggests that the electron is in an S-like state.

We focus here on **1** as it has an isostructural diamagnetic analogue $[K(2.2.2\text{-cryptand})][Yb(Cp')_3]$ **5**, and therefore it can be doped into **5** to yield a paramagnetically dilute crystalline sample. The studies described below were performed on both frozen solutions of **1** and on single crystals of **1@5** at a doping level of approximately 2%. Probing the spin dynamics of **1** with pulsed EPR methods, echo-detected field-swept EPR (EDFS; see Fig. 2a and Supplementary Fig. 2) spectra[19] of **1** in THF are entirely consistent with CW-EPR; these spectra persist up to temperatures limited only by thawing of the solvent. In order to investigate the spin dynamics of **1** at higher temperatures, we studied a single crystal of **1@5** which gives identical g and A^Y parameters to the frozen THF solution of **1**, and confirms the assignment of the principal directions of g_z and $g_{x,y}$ with respect to the molecular structure (Fig. 2b, Supplementary Figs. 3 and 4). For a single crystal of **1@5**, we find spin echoes between 5 and 300 K.

Relaxation measurements (Supplementary Figs. 5–9) show that T_1 is ~10–20 ms below 10 K, but remains as long as 2 µs at 300 K, while T_m varies between 2 and 0.4 µs in the same temperature range (Fig. 2e; Supplementary Tables 1-4). T_1 and T_m are very similar between frozen solution and single crystal measurements, showing that the spin dynamics of **1** are independent of the phase of the sample; this is also remarkable because the THF (C_4H_8O) solvent is rich with ^1H nuclear spins. Furthermore, T_1 and T_m are also largely independent of molecular orientation or which nuclear spin m_I transition is monitored (see different observer positions in Fig. 2). T_1 has a Raman-like dependence on temperature above 20 K ($T_1 = C^{-1}T^{-n}$; $C = 1.3(3) \times 10^{-8}\ \mu s^{-1}\ K^{-n}$, $n = 3.16(5)$), and only a very weak temperature dependence below 20 K. T_m has a much weaker temperature dependence than T_1, and, due to the coincidence of the data for frozen solution and single crystal phase, we suspect that T_m is limited by nuclear spin diffusion given the ^1H-rich environment of the molecule. (There is a minimum in T_m around 80 K due to methyl-group rotations.) Importantly, at room temperature T_m is smaller than T_1 by a factor of 4–5 and hence T_1 has not limited T_m and spin echoes are still observable.

Given the long T_m times, we are able to perform coherent spin manipulations as demonstrated by observation of Rabi oscillations[20] even at room temperature for **1@5** in transient nutation experiments (Fig. 2c and Supplementary Figs. 11–22). These periodic oscillations in echo intensity as a function of the duration of a preceding nutation pulse correspond to cyclical generation of $|\pm m_S\rangle$ superposition states. All oscillations show the characteristic linear dependence of Rabi frequency (Ω_R) on nutation pulse attenuation (Fig. 2d and Supplementary Figs. 11–23). Ω_R is independent of temperature and the m_I transition being monitored (Supplementary Figs. 16 and 23), and is very similar between **1@5** and a frozen THF solution of **1** (Supplementary Figs. 11–23).

The robustness of spin coherence in **1** prompted us to investigate the spin distribution by CW and pulsed EPR methods.

euenberger and Loss first proposed using electron spins within molecules for quantum information processing (QIP) [1] by showing how the Grover algorithm could be mapped onto a Mn_{12} cage[2]. Since then several groups have examined two-level ($S = 1/2$) molecular spin systems as possible qubits[3–12] and the Grover algorithm has been implemented in a four-level molecular qudit[13]. Molecular electron spin qubits have an obvious disadvantage: as they are molecules, the magnetic moments of nuclear spins and molecular vibrations will produce noise that could cause electron spin relaxation and therefore loss of phase information within the qubit before computations can be performed. Studies to address this disadvantage include use of advanced microwave pulse sequences[3] to repair the damage done by noise and hence increase phase memory times (T_m). A second approach uses spin transitions that do not vary with magnetic field at first order[12], often called clock transitions; the lack of dependence on local field renders the qubit insensitive to its environment and hence lengthens T_m.

The magnetic noise in molecules is dominated at low temperatures by nearby nuclear spins undergoing flip-flop processes causing an oscillating magnetic field: reducing this source of noise has been widely studied to engineer better qubits[7–11]. Removal of nuclear spins from the qubit and/or embedding the molecule in a nuclear-spin-free lattice has led to phase memory times (T_m) long enough to permit coherent spin manipulation via Rabi oscillations[9–11], sometimes even at room temperature[11]. However, even in the absence of nuclear spins, T_m becomes limited by spin-lattice relaxation (T_1) that is strongly temperature dependent. T_1 is dominated by modulation of spin-orbit coupling via molecular vibrations. It is the spin-orbit coupling that mixes spin and orbital angular momentum, hence enabling exchange of energy between the spin system and the lattice when the electronic energy levels are modulated. Reducing the impact of molecular vibrations is a challenge. The intuitive approach is to reduce the influence of molecular vibrations by making a more rigid molecule or lattice, which does lead to longer phase memory times by lengthening T_1[11].

We noted a study where Zn^+ ions, encapsulated in a metal-organic framework, show phase memory times of 2 µs at room temperature[14]. This is ascribed to the unpaired electron being in a ^2S state and hence with minimal anisotropy. Therefore, we sought a molecular species that would mimic the highly isotropic nature of these embedded Zn^+ ions. All molecular qubits proposed thus far have the unpaired electron spin in a p-, d- or f-orbital and have little s-character. Our target was a molecule with a ^2S ground state.

We identified a family of molecules that might exemplify this strategy. The compounds are three-coordinate with local pseudo-C_3 symmetry at the metal ion. In this point group, the lowest energy d-orbital is $d_z{}^2$ and it has the same irreducible representation as an s-orbital; therefore, the s- and $d_z{}^2$ orbitals will mix and regardless of the relative admixture of the two atomic orbitals, an S-like state will result as both orbitals have $m_l = 0$. The compounds contain early d-block or 4f-block metals in the +2 oxidation state, which is very unusual for the metals involved. The four compounds are: [K(2.2.2-cryptand)][Y(Cp′)$_3$] **1** (Cp′ = $C_5H_4SiMe_3$)[15,16] (Supplementary Fig. 1); [K(2.2.2-cryptand)][Lu(Cp′)$_3$] **2**; [K(2.2.2-cryptand)][La(Cp′)$_3$] **3**; and [K(2.2.2-cryptand)][Sc{(N(SiMe$_3$)$_2$}$_3$] **4**. These complexes flout the established criteria[17] for long T_1 or T_m in molecular qubits, as they are far from rigid and contain numerous hydrogen atoms and multiple methyl groups, whose rotation is a known decoherence mechanism[18]. Yet here we report coherent spin manipulations on **1** at room temperature. We achieve this by engineering the electronic configuration of the metal centre, an approach that could be combined with the beautiful engineering of the ligand shell demonstrated by other groups[7–11].

Results

Electron paramagnetic resonance spectroscopy. In compounds **1**–**4** the metal centre in the anion is three-coordinate with a pseudo-C_3 axis passing through the metal, perpendicular to the plane defined by the Cp′ centroids in **1**–**3** and the N atoms in **4** (Fig. 1a). In all cases the continuous-wave EPR (CW-EPR) spectroscopy of a fluid solution of these compounds shows a multiplet due to hyperfine coupling (A) of the single unpaired electron to the metal nucleus (Supplementary Fig. 2; Table 1). On freezing the solutions, a small axial g-anisotropy is observed in all cases; where z is coincident with the *pseudo*-C_3 axis), with a near isotropic hyperfine coupling (Fig. 2a; Table 1). The highly isotropic hyperfine coupling and minimal g-anisotropy suggests that the electron is in an S-like state.

We focus here on **1** as it has an isostructural diamagnetic analogue [K(2.2.2-cryptand)][Yb(Cp′)$_3$] **5**, and therefore it can be doped into **5** to yield a paramagnetically dilute crystalline sample. The studies described below were performed on both frozen solutions of **1** and on single crystals of **1@5** at a doping level of approximately 2%. Probing the spin dynamics of **1** with pulsed EPR methods, echo-detected field-swept EPR (EDFS; see Fig. 2a and Supplementary Fig. 2) spectra[19] of **1** in THF are entirely consistent with CW-EPR; these spectra persist up to temperatures limited only by thawing of the solvent. In order to investigate the spin dynamics of **1** at higher temperatures, we studied a single crystal of **1@5** which gives identical g and A^Y parameters to the frozen THF solution of **1**, and confirms the assignment of the principal directions of g_z and $g_{x,y}$ with respect to the molecular structure (Fig. 2b, Supplementary Figs. 3 and 4). For a single crystal of **1@5**, we find spin echoes between 5 and 300 K.

Relaxation measurements (Supplementary Figs. 5–9) show that T_1 is ~10–20 ms below 10 K, but remains as long as 2 µs at 300 K, while T_m varies between 2 and 0.4 µs in the same temperature range (Fig. 2e; Supplementary Tables 1-4). T_1 and T_m are very similar between frozen solution and single crystal measurements, showing that the spin dynamics of **1** are independent of the phase of the sample; this is also remarkable because the THF (C_4H_8O) solvent is rich with ^1H nuclear spins. Furthermore, T_1 and T_m are also largely independent of molecular orientation or which nuclear spin m_I transition is monitored (see different observer positions in Fig. 2). T_1 has a Raman-like dependence on temperature above 20 K ($T_1 = C^{-1}T^{-n}$; $C = 1.3(3) \times 10^{-8}\ \mu s^{-1}\ K^{-n}$, $n = 3.16(5)$), and only a very weak temperature dependence below 20 K. T_m has a much weaker temperature dependence than T_1, and, due to the coincidence of the data for frozen solution and single crystal phase, we suspect that T_m is limited by nuclear spin diffusion given the ^1H-rich environment of the molecule. (There is a minimum in T_m around 80 K due to methyl-group rotations.) Importantly, at room temperature T_m is smaller than T_1 by a factor of 4–5 and hence T_1 has not limited T_m and spin echoes are still observable.

Given the long T_m times, we are able to perform coherent spin manipulations as demonstrated by observation of Rabi oscillations[20] even at room temperature for **1@5** in transient nutation experiments (Fig. 2c and Supplementary Figs. 11–22). These periodic oscillations in echo intensity as a function of the duration of a preceding nutation pulse correspond to cyclical generation of $|\pm m_S\rangle$ superposition states. All oscillations show the characteristic linear dependence of Rabi frequency (Ω_R) on nutation pulse attenuation (Fig. 2d and Supplementary Figs. 11–23). Ω_R is independent of temperature and the m_I transition being monitored (Supplementary Figs. 16 and 23), and is very similar between **1@5** and a frozen THF solution of **1** (Supplementary Figs. 11–23).

The robustness of spin coherence in **1** prompted us to investigate the spin distribution by CW and pulsed EPR methods.

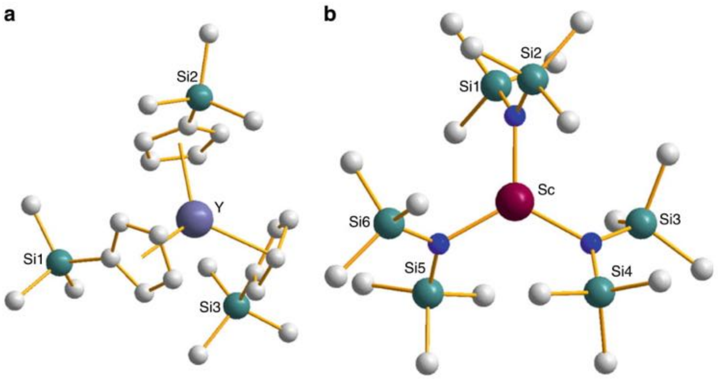

Fig. 1 Molecular structures in the crystal. **a** The $[Y(Cp')_3]^-$ anion in **1**. **b** The $[Sc\{(N(SiMe_3)_2\}_3]^-$ anion in **4**. Grey unlabelled atoms are carbon; blue unlabelled atoms are nitrogen. H-atoms omitted for clarity

Table 1 Observed *g*-values and hyperfine coupling constants for 1–4 in frozen solution at X-band (*ca.* 9.5 GHz)

Compound	*I*	Abundance (%)	*g*	|*A*| (MHz)
1	1/2	99.9	$g_z = 2.001$, $g_{x,y} = 1.986$	$A_z = 98.6$, $A_{x,y} = 100.8$
2	7/2	97.0	$g_z = 1.975$, $g_{x,y} = 1.945$	$A_z = 1070$, $A_{x,y} = 1121$
3	7/2	99.9	$g_z = 1.978$, $g_{x,y} = 1.935$	$A_z = 400$, $A_{x,y} = 420$
4	7/2	100.0	$g_z = 1.997$, $g_{x,y} = 1.964$	$A_z = 640$, $A_{x,y} = 620$

We have quantified the electron spin density on the ligands with hyperfine sub-level correlation and electron nuclear double resonance (HYSCORE and ENDOR respectively;[19] see Fig. 3) measurements on **1** in THF solution. Weak hyperfine couplings to ^{1}H and ^{13}C nuclei are observed (Fig. 3, Supplementary Figs. 25–29; Table 2; the orientation of the Cp′ ring with respect to the molecular C_3 axis is shown in Supplementary Fig. 24), and are on the order of 1–2 MHz for the Cp′ ligands. We can be confident that we are not missing any large ligand hyperfine interactions (i.e. >4 MHz) because there is no resolution of ^{1}H hyperfine in the CW EPR (which has narrow linewidths).

Pulsed EPR studies of **2**–**4** confirm this is a general phenomenon; as there was not an easily available diamagnetic host for these complexes we have had to restrict our measurements to the melting point of the THF solvent (90 K). In this temperature range the behaviour for T_1 for **1**–**4** is very similar. T_m for **1**–**3** are almost identical in this range; compound **4** shows a fall in T_m at the highest temperature measured compared with the other compounds.

Electronic structure calculations. Density functional theory (DFT) calculations[21] on the crystal structure of the anion in **1** give excellent agreement with experiment and are independent of the functional and basis set chosen (Table 2 and Supplementary Tables 10–13). The calculated ^{89}Y hyperfine is dominated by the Fermi-contact term (i.e. electron density at the ^{89}Y nucleus) and the spin-dipolar contribution is almost insignificant (hence the vanishing anisotropy) (Supplementary Table 14). The Fermi-contact term is dominated by the singly-occupied molecular orbital (SOMO) in which the unpaired electron resides (Fig. 4a), with small contributions from polarisation of core s-states. Löd-win analysis suggests 62% of the total spin density is metal-based, with the other 38% delocalised across the ligand atoms: the metal contribution breaks down as 7.5% s-based, 1.8% p-based and 52% d-based. Despite the significant d-orbital contribution to the spin density, the hyperfine interactions are much more isotropic than predicted based on atomic wavefunctions[22], which would suggest $|A_z^Y - A_{x,y}^Y| \sim 29$ MHz, compared to the ca. 5 MHz calculated and 2 MHz observed here. The same conclusions can be drawn for an optimised structure of the anion in **1** or when the electrostatic potential of the crystalline environment is included (see Supplementary Fig. 30), indicating this is not a quirk of the crystalline geometry nor gas-phase calculations.

In order to understand the minimal *g*-anisotropy of **1**, we have conducted complete active space self-consistent field (CASSCF) calculations[23] using the RAS-probing technique[24] (see Supplementary Methods, Supplementary Figs. 31–33, Supplementary Tables 15–26) on the crystal structure of the anion in **1**. After including spin-orbit coupling, the *g*-values of the ground $S = 1/2$ state are $g_{x,y} = 1.989(1)$ and $g_z = 2.002$, in excellent agreement with the experimental data and DFT results (Table 1). The ground state SOMO is only 58% derived from Y-based functions suggesting that it is substantially delocalised (Supplementary Table 17). This Y contribution is dominated by the $4d_z{}^2$ function (Fig. 4b and Supplementary Fig. 34), in good agreement with the spin density determined from DFT (Fig. 4a). Despite this however, the extensive delocalisation onto the ligands and significant Y s-orbital contribution dominate the spin Hamiltonian, giving an essentially isotropic hyperfine interaction. The result is that the anisotropic component accounts for only $(A_z - A_x)/A_{\mathrm{iso}} \approx 2\%$ of the total hyperfine coupling.

Our CASSCF calculations show that the first excited state is only *ca.* 9000 cm^{-1} above the ground state where the unpaired electron occupies a diffuse ligand orbital (largest *Y* contribution is 3% 4d, with 89% deriving from ligand functions; Supplementary Fig. 35 and Supplementary Table 18); calculations where the electrostatic potential of the crystalline environment is included show similar results, indicating that this is not the result of an

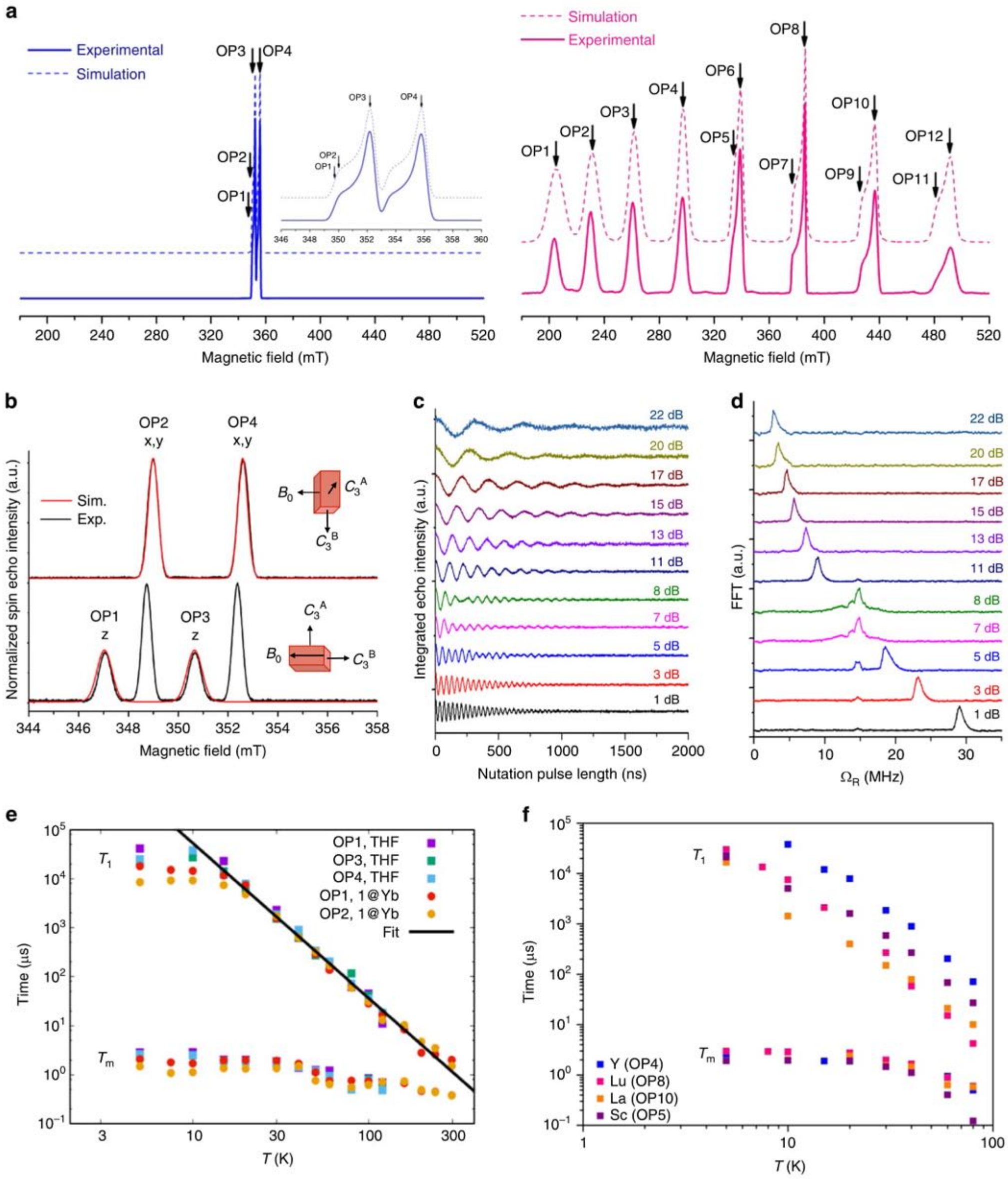

Fig. 2 Echo-detected field-swept EPR spectra. Experimental (full) and simulated (dashed) EDFS spectra at 50 K and X-band (9.85 GHz) for a 10 mM THF solution of compounds **1** (blue) and **2** (pink), with the parameters in Table 1. **b** Experimental (black) and calculated (red) EDFS spectra at 200 K and X-band (9.75 GHz) for a single crystal of **1@5** at two selected orientations (Supplementary Figs. 3 and 4). Simulations are only for molecule **B**, such that only the resonances along the z-axis for molecule **B** are simulated in the lower figure (see Supplementary Methods for definition of molecule **B**). **c**, Rabi oscillations for **1@5** at 298 K and $B_0 = 347$ mT (OP1), acquired with different microwave attenuations (Supplementary Tables 5–9); **d** Fourier transforms of nutation data in **c**, giving the Rabi frequency (the 15 MHz signal is due to ^{1}H ESEEM). **e** Relaxation times measured by pulsed EPR methods for **1** in two phases (frozen THF solution and single crystal **1@5**); black line is a simultaneous fit of all the T_1 data above 20K with $T_1 = C^{-1}T^{-n}$ where $C = 1.3(3) \times 10^{-8}$ µs^{-1} K^{-n} and $n = 3.16(5)$ (Supplementary Tables 1–4). **f** T_1 and T_m dependence to 100 K for a single representative orientation of **1**, **2**, **3** and **4**. Observer positions OP1-OP12 mark the magnetic fields where time-dependent pulsed EPR experiments were performed

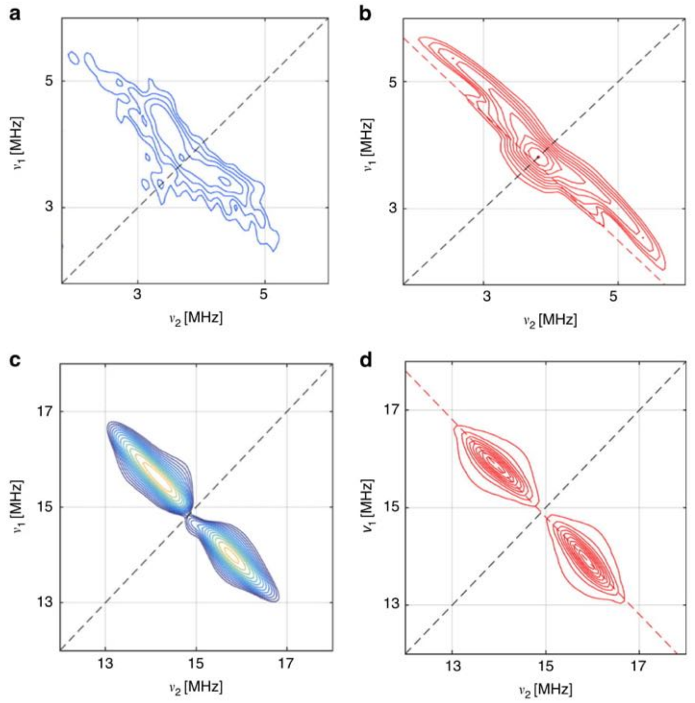

Fig. 3 Pulsed EPR studies of a frozen solution of **1** (10 mM, THF). **a** ^{13}C HYSCORE spectrum at 50 K and $B_0 = 352$ mT (OP3). **b** Simulation of the data in (**a**). **c** ^{1}H HYSCORE spectrum at 50K and OP3. **d** Simulation of the data in (**c**). Simulations used EasySpin[32]

Table 2 Experimental and calculated spin Hamiltonian parameters for 1

Compound	*T* (K)	*g*	|*A*| (MHz)
1 (10 mM, THF)	295	$g_{iso} = 1.991$	$\|A_{iso}{}^{Y}\| = 102$
1 (10 mM, THF)	50	$g_z = 2.001$, $g_{x,y} = 1.986$	$A_z{}^{Y} = 98.6$, $A_{x,y}{}^{Y} = 100.8$ $A_{\|\|}{}^{C2/5} = 2.8$,[a] $A_{\perp}{}^{C2/5} = 0.4$ $A_{\|\|}{}^{C3/4} = 0.83$,[a] $A_{\perp}{}^{C3/4} = 0.3$
~2% **1@5**	200	$g_z = 1.999$, $g_{x,y} = 1.986$	$\|A_z{}^{Y}\| = 99.5$, $\|A_{x,y}{}^{Y}\| = 101.3$
DFT (gas-phase)	-	$g_z = 2.003$, $g_{x,y} = 1.990(1)$	$A_z{}^{Y} = -93.86$, $A_{x,y}{}^{Y} = -88.7$[4] $\|A_{iso}{}^{C1-5}\| = 1.1$[8] $\|A_{iso}{}^{H2-5}\| = 2$[1]
CASSCF (gas-phase)	-	$g_z = 2.002$, $g_{x,y} = 1.989(1)$	-

[a] For the parallel and perpendicular ^{13}C hyperfines, the labels refer to the local principal axes, with the unique axis defined by the Cp′ π-system, i.e., orthogonal to the molecular *z* axis

unbound electron in the gas-phase (Supplementary Figs. 44–55 and Supplementary Tables 16 and 27–37). There are seven excited states less than 20,000 cm^{-1} above the ground state, all having the unpaired electron in very diffuse ligand-based orbitals (Supplementary Figs. 35 to 41 and Supplementary Tables 18–24). This indicates that the electron is easily delocalised across the molecule, and explains why the ground state SOMO cannot be simply described as either a 4d$_{z}{}^{2}$ or 5s function on Y. Indeed, it is not until the ninth and tenth excited states (at ca. 34,000 cm^{-1}) that we find other metal-dominated MOs, which correspond mainly to the Y-based 4d$_{xz}$ and 4d$_{yz}$ functions (Supplementary Figs. 42 and 43, Supplementary Tables 25 and 26). The large energy gap to the 4d excited orbitals quenches the orbital angular momentum and this leads to the small *g*-anisotropy of the ground state.

Discussion

The experimental data and computational results demonstrate without question that complex **1** has a very isotropic $S = 1/2$ ground state with weak spin orbit coupling (small *g*-shift and *g*-anisotropy) and s-orbital-dominated hyperfine interaction. The isotropic nature of the spin Hamiltonian is consistent with the observation that there is no significant variation in relaxation dynamics for different orientations, despite the 4d$_{z}{}^{2}$ admixture to the SOMO. We believe this is key to the unexpected relaxation properties of **1**.

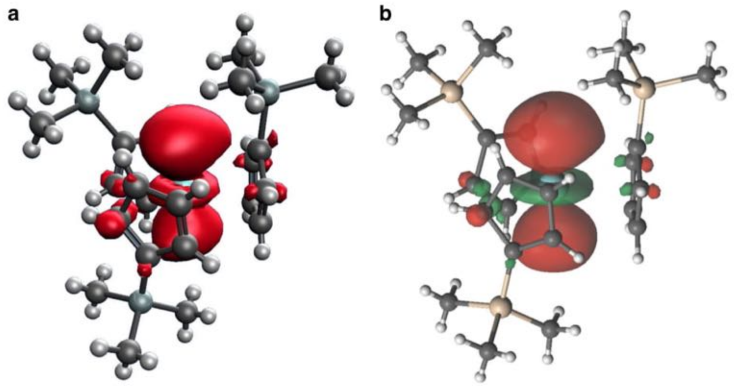

Fig. 4 The calculated electronic structure of the anion in **1**. This shows: **a** spin density from DFT; **b** the SOMO (natural orbital for the ground $S = 1/2$ state) from CASSCF

The room temperature T_1 and T_m of 2 and 0.4 μs, respectively, for **1** can be compared to the few other transition metal complexes that exhibit room temperature coherence (Fig. 5): [VO(Pc)] (Pc = phthalocyanine; 0.001% dilution) has T_1 and T_m of 1 and 0.8 μs, respectively;[25,26] [VO(dmit)$_2$] (dmit = 1,3-dithiole-2-thione-4,5-dithiolate; 5% dilution) has T_1 and T_m of 3 and 1 μs, respectively;[11] [Cu(mnt)$_2$] (mnt^{2-} = maleonitriledithiolate; 0.001% dilution) has T_1 and $T_m \approx 0.6$ μs[8]. The latter two examples exploit nuclear-spin-free ligands, while the first example has a highly rigid phthalocyanine ligand framework. Neither of these features is present in **1**, nor have we optimised the magnetic dilution.

A consequence of the small anisotropy and SOC in **1** is a longer than expected T_1, brought about by reducing the effect of molecular vibrations in this non-rigid molecule. This becomes more important at higher temperatures where T_m does not become limited by T_1 up to 300 K. The delocalised nature of the SOMO may also contribute to lengthening T_1. In the few literature examples where coherence is observed at room temperature, both [VO(Pc)] and [Cu(mnt)$_2$] reach the $T_m = T_1$ limit (Supplementary Fig. 10).

This still does not explain the surprisingly long T_m values given the nuclear spin-rich, methyl group rich and flexible coordination geometry of **1**. It is possible that the ligand nuclei are close enough to the paramagnetic metal ion such that their participation in nuclear spin diffusion is limited: the diffusion-barrier radius has been estimated at ca. 6 Å in studies of nitroxyl and trityl radicals:[18] the Y-H(Cp) distances are 3.1–3.3 Å in **1**, and the Y-H(Me) distances lie in the range 3.8–6.4 Å. In addition, even when nuclear spin diffusion dominates decoherence, it can be enhanced by small amplitude librations that result in significant changes in the resonance frequency[18]. This effect is minimised near principal axes where the resonance frequency is least sensitive to orientation: the resonance condition for the essentially isotropic **1** is necessarily flat with respect to molecular orientations, hence this mechanism will be largely quenched. This will be true of any T_m mechanism that works by dynamic averaging of g and A anisotropy.

We conclude that the robust relaxation behaviour of **1** is intrinsically associated with the isotropic electronic structure, which is due to quenching of the orbital angular momentum in the ground state. The near isotropic magnetic properties mean that **1** is behaving spectroscopically like an atomic ^{2}S-state. Preliminary solution phase studies (Fig. 2f) and calculations (Supplementary Table 14) of **2**–**4** show this is a general phenomenon; **4** contains amide ligands, not Cp ligands, and hence the phenomenon is due to engineering the electronic structure of the metal and not due to a specific ligand.

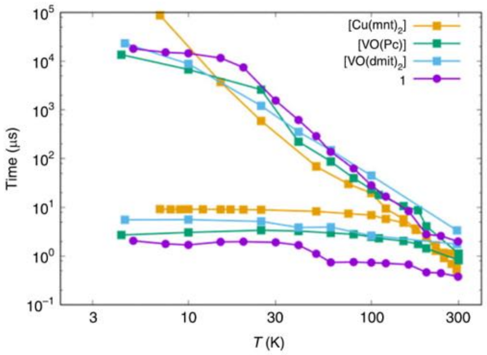

Fig. 5 Spin-lattice and phase memory times for molecular spin qubits. Comparison of T_1 (upper) and T_m (lower) as a function of temperature for [Cu(mnt)$_2$] (0.001% solid-state dilution), [VO(Pc)] (0.001% solid-state dilution), [VO(dmit)$_2$] (5% solid-state dilution), and ~2% **1@5**

There are variations between the behaviour of **1**–**4**; the g-values are most isotropic and nearest the free electron g-value for **1** (Table 1). This also correlates with T_1 being longest for **1** at any temperature measured. Compounds **2** and **3** are very similar to each other, and it could be assumed that in both cases the spin-orbit coupling would be larger than in **1** due to the higher atomic number (Lu and La vs. Y); we suspect this is the origin of the larger g-shift and shorter T_1 in both compounds. Compound **4** falls outside this trend, as Sc is lighter than Y and yet has a larger g-shift and shorter T_1 than **1**, and this could be connected with some influence of the different ligand. A future synthetic target is a *tris*-cyclopentadienyl scandium(II) compound to make the direct comparison.

The utility of a $^2S_{1/2}$-like electronic ground state has long been exploited in trapped atom/ion qubits studied at milli-Kelvin temperatures[27–29]. Studies on alkali metal atoms[30] and silver atoms[31] by pulsed or CW EPR methods give similar T_1 values to those found here in a molecular anion, however such studies are limited to the melting point of the matrices used, which is always well below room temperature. It is a challenge to produce a pure ^{2}S state within a molecule and the next target to increase coherence times must be to engineer both the electronic structure of the metal ion and the vibrational modes of the ligand.

Methods

Continuous-wave EPR measurements. Continuous-wave (CW) electron paramagnetic resonance (EPR) spectra of solution samples of **1** (Fig. 2a) were recorded on either a Bruker EMX 300 or a Bruker ElexSys E580 EPR spectrometer operating at X-band (ca. 9.4–9.8 GHz) and variable temperatures. CW EPR spectra of oriented single crystals of **~2% 1@5** (Fig. S3) were collected with a Bruker ElexSys E580 instrument operating at ca. 9.7 GHz and varied temperatures and equipped with a goniometer that allowed controlled crystal rotation. An identical setup was used to measure the same crystal by echo-detected pulsed-EPR methods. Crystals were indexed by X-ray crystallography to determine the precise orientation of the crystallographic axes.

Pulsed EPR measurements. Pulsed EPR spectra were recorded with a Bruker ElexSys E580 instrument equipped with either a MD5 or a MD4 resonator and operating at *ca*. 9.7 GHz and various temperatures. Solution samples of different concentrations (2, 5 and 10 mM in THF) were investigated to check reproducibility and to achieve an acceptable signal-to-noise response in HYSCORE and ENDOR experiments.

DFT and CASSCF calculations. All DFT calculations were performed using ORCA 4.0.0.2[21] with the unrestricted Kohn-Sham formalism on the $S = 1/2$ ground state of the anions in **1**–**4**. For geometry optimisations we started with the crystal structures. State-averaged CASSCF calculations for the anion in **1** were performed with MOLCAS 8.0[23].

Data availability

Supplementary information is available in the online version of the paper. Reprints and permissions information are available online at www.nature.com/reprints. Publisher's note: Springer Nature remains neutral with regard to jurisdictional claims in published maps and institutional affiliations.

Received: 29 April 2019 Accepted: 26 June 2019
Published online: 26 July 2019

References

1. Leuenberger, M. & Loss, D. Quantum computing in molecular magnets. *Nature* **410**, 789–793 (2001).
2. Grover, L. K. Quantum computers can search arbitrarily large databases by a single query. *Phys. Rev. Lett.* **79**, 4709–4712 (1997).
3. Morton, J. J. L. et al. Bang-band control of fullerene qubits using ultrafast gates. *Nat. Phys.* **2**, 40–43 (2006).
4. Lehmann, J., Gaita-Ariño, A., Coronado, E. & Loss, D. Spin qubits with electrically gated polyoxometalate molecules. *Nat. Nanotechnol.* **2**, 312–317 (2007).
5. Nakazawa, S. et al. Synthetic two-spin quantum bit: g-engineered exchange-coupled biradical designed for controlled-NOT gate operations. *Angew. Chem. Int. Ed.* **51**, 9860–9864 (2012).
6. Aromí, G., Aguilà, D., Gamez, P., Luis, F. & Roubeau, O. Design of magnetic coordination complexes for quantum computing. *Chem. Soc. Rev.* **41**, 537–546 (2012).
7. Wedge, C. J. et al. Chemical engineering of molecular qubits. *Phys. Rev. Lett.* **108**, 107204 (2012).
8. Bader, K. et al. Room temperature quantum coherence in a potential molecular qubit. *Nat. Commun.* **5**, 6304- (2014).
9. Zadrozny, J. M., Niklas, J., Poluektov, O. G. & Freedman, D. E. Millisecond coherence time in a tunable molecular electronic spin qubit. *ACS Cent. Sci.* **1**, 488–492 (2015).
10. Pedersen, K. S. et al. Toward molecular 4f single-ion magnet qubits. *J. Am. Chem. Soc.* **138**, 5801–5804 (2016).
11. Atzori, M. et al. Quantum coherence times enhancement in vanadium(IV)-based potential molecular qubits: the key role of the vanadyl moiety. *J. Am. Chem. Soc.* **138**, 11234–11244 (2016).
12. Shiddiq, M. et al. Enhancing coherence in molecular spin qubits via atomic clock transitions. *Nature* **531**, 348–351 (2016).
13. Godfrin, C. et al. Operating quantum states in single magnetic molecules: implementation of Grover's quantum algorithm. *Phys. Rev. Lett.* **119**, 187702 (2017).
14. Morra, E. et al. Electronic and geometrical structure of Zn+ions stabilized in the porous structure of Zn-loaded zeolite H-ZSM-5: a multifrequency CW and pulse EPR study. *J. Phys. Chem. C* **121**, 14238–14245 (2017).
15. MacDonald, M. R., Bates, J. E., Ziller, J. W., Furche, F. & Evans, W. J. Completing the series of +2 ions for the lanthanide elements: synthesis of molecular complexes of Pr^{2+}, Gd^{2+}, Tb^{2+} and Lu^{2+}. *J. Am. Chem. Soc.* **135**, 9857–9868 (2013).
16. Woen, D. H. et al. Solution synthesis, structure, and CO2 reduction reactivity of a Sc2+ Complex, $\{Sc[N(SiMe_3)_2]_3\}^{1-}$ *Angew. Chem., Int. Ed.* **56**, 2050-2053 (2017).
17. Ardavan, A. et al. Will Spin-relaxation times in molecular magnets permit quantum information processing? *Phys. Rev. Lett.* **98**, 057201 (2007).
18. Eaton, S. S. & Eaton, G. R. Relaxation times of organic radicals and transition metal ions. *Biol. Magn. Reson.* **19**, 29–154 (2000).
19. Schweiger, A. & Jeschke, J. *Principles of Pulse Electron Paramagnetic Resonance*, (Oxford University Press, Oxford, 2001).
20. Rabi, I. I. Space quantisation in a gyrating magnetic field. *Phys. Rev.* **51**, 652–654 (1937).
21. Neese, F. The ORCA program system. *Wiley Interdiscip. Rev.: Comput. Mol. Sci.* **2**, 73–78 (2012).
22. Morton, J. R. & Preston, K. F. Atomic parameters for paramagnetic resonance data. *J. Magn. Reson.* **30**, 577–582 (1978).
23. Aquilante, F. et al. Molcas 8: new capabilities for multi-configurational quantum chemical calculations across the periodic table. *J. Comp. Chem.* **37**, 506–541 (2016).
24. Veryazov, V., Malmqvist, P. Å. & Roos, B. O. How to select active space for multiconfigurational quantum chemistry? *Int. J. Quant. Chem.* **111**, 3329–3338 (2011).
25. Atzori, M. et al. Room-temperature quantum coherence and Rabi oscillations in vanadyl phthalocyanine: toward multifunctional molecular spin qubits. *J. Am. Chem. Soc.* **138**, 2154–2157 (2016).
26. Bader, K., Winkler, M. & van Slageren, J. Tuning of molecular qubits: very long coherence and spin lattice relaxation times. *Chem. Commun.* **52**, 3623–3626 (2016).
27. Kielplinski, D. et al. A decoherence-free quantum memory using trapped ions. *Science* **291**, 1013–1015 (2001).
28. Monroe, C. Quantum information processing with atoms and photons. *Nature* **416**, 238–246 (2002).
29. Blatt, R. & Wineland, D. Entangled states of trapped atomic ions. *Nature* **453**, 1008–1015 (2008).
30. Jones, R., Howard, J. A., Joly, H. A., Edwards, P. P. & Singer, R. J. EPR study of alkali metal atoms in hydrocarbon matrices. *Magn. Res. Chem.* **33**, S98–S106 (1995).
31. Michalik, J. & Kevan, L. Temperature dependence of electron spin-lattice relaxation of radiation-produced silver atoms in polycrystalline aqueous and glassy organic matrices. Importance of relaxation by tunnelling modes in disordered matrices. *J. Magn. Reson.* **31**, 259–270 (1978).
32. Stoll, S. & Schweiger, A. EasySpin, a comprehensive software package for spectral simulation and analysis in EPR. *J. Magn. Reson.* **178**, 42–55 (2006).

Acknowledgements

This work was supported by the European Union, via a doctoral scholarship to A.-M.A. (FP7-PEOPLE-2013-ITN MAGIC Initial Training Network; grant agreement no. 606831), and MOLSPIN COST Action CA15128; the U.S. National Science Foundation (CHE-1565776); the Ramsay Memorial Trust (fellowship to N.F.C.), the Leverhulme Trust (fellowship to F.T. reference RF-2018-545/4); the Engineering and Physical Sciences Research Council (DTG doctoral scholarships to L.N. and A.K.K.), The University of Manchester, The University of California, Irvine, and the UK National EPR Facility and Service. We thank Dr Joe McDouall for insightful conversations, and Profs. Joris van Slageren and Roberta Sessoli for providing experimental data for the $[Cu(mnt)_2]$, [VO (Pc)] and $[VO(dmit)_2]$ complexes.

Author contributions

A.-M.A. and L.N. and F.T. collected and interpreted the EPR spectroscopy data, with support from A.K.K. and E.J.L.M. D.H.W. and D. N. H. synthesised and characterised the compounds under the supervision of W.J.E. C.A.P.G. made the EPR samples. N.F.C. performed and interpreted the DFT and CASSCF calculations. W.J.E. and R.E.P.W. proposed the initial concept. F.T. designed the work and supervised A.-M.A. R.E.P.W., F.T., A.-M.A., N.F.C. and E.J.L.M. wrote the manuscript, with contributions from all co-authors.

Additional information

Supplementary Information accompanies this paper at https://doi.org/10.1038/s41467-019-11309-3.

Competing interests: The authors declare no competing interests.

Reprints and permission information is available online at http://npg.nature.com/reprintsandpermissions/

Peer review information: *Nature Communications* thanks the anonymous reviewer for their contribution to the peer review of this work. Peer reviewer reports are available.

Publisher's note: Springer Nature remains neutral with regard to jurisdictional claims in published maps and institutional affiliations.

Methods

Continuous-wave EPR measurements. Continuous-wave (CW) electron paramagnetic resonance (EPR) spectra of solution samples of **1** (Fig. 2a) were recorded on either a Bruker EMX 300 or a Bruker ElexSys E580 EPR spectrometer operating at X-band (ca. 9.4–9.8 GHz) and variable temperatures. CW EPR spectra of oriented single crystals of **~2% 1@5** (Fig. S3) were collected with a Bruker ElexSys E580 instrument operating at ca. 9.7 GHz and varied temperatures and equipped with a goniometer that allowed controlled crystal rotation. An identical setup was used to measure the same crystal by echo-detected pulsed-EPR methods. Crystals were indexed by X-ray crystallography to determine the precise orientation of the crystallographic axes.

Pulsed EPR measurements. Pulsed EPR spectra were recorded with a Bruker ElexSys E580 instrument equipped with either a MD5 or a MD4 resonator and operating at *ca*. 9.7 GHz and various temperatures. Solution samples of different concentrations (2, 5 and 10 mM in THF) were investigated to check reproducibility and to achieve an acceptable signal-to-noise response in HYSCORE and ENDOR experiments.

DFT and CASSCF calculations. All DFT calculations were performed using ORCA 4.0.0.2[21] with the unrestricted Kohn-Sham formalism on the $S = 1/2$ ground state of the anions in **1**–**4**. For geometry optimisations we started with the crystal structures. State-averaged CASSCF calculations for the anion in **1** were performed with MOLCAS 8.0[23].

Data availability

Supplementary information is available in the online version of the paper. Reprints and permissions information are available online at www.nature.com/reprints. Publisher's note: Springer Nature remains neutral with regard to jurisdictional claims in published maps and institutional affiliations.

Received: 29 April 2019 Accepted: 26 June 2019
Published online: 26 July 2019

References

1. Leuenberger, M. & Loss, D. Quantum computing in molecular magnets. *Nature* **410**, 789–793 (2001).
2. Grover, L. K. Quantum computers can search arbitrarily large databases by a single query. *Phys. Rev. Lett.* **79**, 4709–4712 (1997).
3. Morton, J. J. L. et al. Bang-band control of fullerene qubits using ultrafast gates. *Nat. Phys.* **2**, 40–43 (2006).
4. Lehmann, J., Gaita-Ariño, A., Coronado, E. & Loss, D. Spin qubits with electrically gated polyoxometalate molecules. *Nat. Nanotechnol.* **2**, 312–317 (2007).
5. Nakazawa, S. et al. Synthetic two-spin quantum bit: g-engineered exchange-coupled biradical designed for controlled-NOT gate operations. *Angew. Chem. Int. Ed.* **51**, 9860–9864 (2012).
6. Aromí, G., Aguilà, D., Gamez, P., Luis, F. & Roubeau, O. Design of magnetic coordination complexes for quantum computing. *Chem. Soc. Rev.* **41**, 537–546 (2012).
7. Wedge, C. J. et al. Chemical engineering of molecular qubits. *Phys. Rev. Lett.* **108**, 107204 (2012).
8. Bader, K. et al. Room temperature quantum coherence in a potential molecular qubit. *Nat. Commun.* **5**, 6304- (2014).
9. Zadrozny, J. M., Niklas, J., Poluektov, O. G. & Freedman, D. E. Millisecond coherence time in a tunable molecular electronic spin qubit. *ACS Cent. Sci.* **1**, 488–492 (2015).
10. Pedersen, K. S. et al. Toward molecular 4f single-ion magnet qubits. *J. Am. Chem. Soc.* **138**, 5801–5804 (2016).
11. Atzori, M. et al. Quantum coherence times enhancement in vanadium(IV)-based potential molecular qubits: the key role of the vanadyl moiety. *J. Am. Chem. Soc.* **138**, 11234–11244 (2016).
12. Shiddiq, M. et al. Enhancing coherence in molecular spin qubits via atomic clock transitions. *Nature* **531**, 348–351 (2016).
13. Godfrin, C. et al. Operating quantum states in single magnetic molecules: implementation of Grover's quantum algorithm. *Phys. Rev. Lett.* **119**, 187702 (2017).
14. Morra, E. et al. Electronic and geometrical structure of Zn+ions stabilized in the porous structure of Zn-loaded zeolite H-ZSM-5: a multifrequency CW and pulse EPR study. *J. Phys. Chem. C* **121**, 14238–14245 (2017).
15. MacDonald, M. R., Bates, J. E., Ziller, J. W., Furche, F. & Evans, W. J. Completing the series of +2 ions for the lanthanide elements: synthesis of molecular complexes of Pr^{2+}, Gd^{2+}, Tb^{2+} and Lu^{2+}. *J. Am. Chem. Soc.* **135**, 9857–9868 (2013).
16. Woen, D. H. et al. Solution synthesis, structure, and CO2 reduction reactivity of a Sc2+ Complex, $\{Sc[N(SiMe_3)_2]_3\}^{1-}$ *Angew. Chem., Int. Ed.* **56**, 2050-2053 (2017).
17. Ardavan, A. et al. Will Spin-relaxation times in molecular magnets permit quantum information processing? *Phys. Rev. Lett.* **98**, 057201 (2007).
18. Eaton, S. S. & Eaton, G. R. Relaxation times of organic radicals and transition metal ions. *Biol. Magn. Reson.* **19**, 29–154 (2000).
19. Schweiger, A. & Jeschke, J. *Principles of Pulse Electron Paramagnetic Resonance*, (Oxford University Press, Oxford, 2001).
20. Rabi, I. I. Space quantisation in a gyrating magnetic field. *Phys. Rev.* **51**, 652–654 (1937).
21. Neese, F. The ORCA program system. *Wiley Interdiscip. Rev.: Comput. Mol. Sci.* **2**, 73–78 (2012).
22. Morton, J. R. & Preston, K. F. Atomic parameters for paramagnetic resonance data. *J. Magn. Reson.* **30**, 577–582 (1978).
23. Aquilante, F. et al. Molcas 8: new capabilities for multi-configurational quantum chemical calculations across the periodic table. *J. Comp. Chem.* **37**, 506–541 (2016).
24. Veryazov, V., Malmqvist, P. Å. & Roos, B. O. How to select active space for multiconfigurational quantum chemistry? *Int. J. Quant. Chem.* **111**, 3329–3338 (2011).
25. Atzori, M. et al. Room-temperature quantum coherence and Rabi oscillations in vanadyl phthalocyanine: toward multifunctional molecular spin qubits. *J. Am. Chem. Soc.* **138**, 2154–2157 (2016).
26. Bader, K., Winkler, M. & van Slageren, J. Tuning of molecular qubits: very long coherence and spin lattice relaxation times. *Chem. Commun.* **52**, 3623–3626 (2016).
27. Kielplinski, D. et al. A decoherence-free quantum memory using trapped ions. *Science* **291**, 1013–1015 (2001).
28. Monroe, C. Quantum information processing with atoms and photons. *Nature* **416**, 238–246 (2002).
29. Blatt, R. & Wineland, D. Entangled states of trapped atomic ions. *Nature* **453**, 1008–1015 (2008).
30. Jones, R., Howard, J. A., Joly, H. A., Edwards, P. P. & Singer, R. J. EPR study of alkali metal atoms in hydrocarbon matrices. *Magn. Res. Chem.* **33**, S98–S106 (1995).
31. Michalik, J. & Kevan, L. Temperature dependence of electron spin-lattice relaxation of radiation-produced silver atoms in polycrystalline aqueous and glassy organic matrices. Importance of relaxation by tunnelling modes in disordered matrices. *J. Magn. Reson.* **31**, 259–270 (1978).
32. Stoll, S. & Schweiger, A. EasySpin, a comprehensive software package for spectral simulation and analysis in EPR. *J. Magn. Reson.* **178**, 42–55 (2006).

Acknowledgements

This work was supported by the European Union, via a doctoral scholarship to A.-M.A. (FP7-PEOPLE-2013-ITN MAGIC Initial Training Network; grant agreement no. 606831), and MOLSPIN COST Action CA15128; the U.S. National Science Foundation (CHE-1565776); the Ramsay Memorial Trust (fellowship to N.F.C.), the Leverhulme Trust (fellowship to F.T. reference RF-2018-545/4); the Engineering and Physical Sciences Research Council (DTG doctoral scholarships to L.N. and A.K.K.), The University of Manchester, The University of California, Irvine, and the UK National EPR Facility and Service. We thank Dr Joe McDouall for insightful conversations, and Profs. Joris van Slageren and Roberta Sessoli for providing experimental data for the $[Cu(mnt)_2]$, [VO (Pc)] and $[VO(dmit)_2]$ complexes.

Author contributions

A.-M.A. and L.N. and F.T. collected and interpreted the EPR spectroscopy data, with support from A.K.K. and E.J.L.M. D.H.W. and D. N. H. synthesised and characterised the compounds under the supervision of W.J.E. C.A.P.G. made the EPR samples. N.F.C. performed and interpreted the DFT and CASSCF calculations. W.J.E. and R.E.P.W. proposed the initial concept. F.T. designed the work and supervised A.-M.A. R.E.P.W., F.T., A.-M.A., N.F.C. and E.J.L.M. wrote the manuscript, with contributions from all co-authors.

Additional information

Supplementary Information accompanies this paper at https://doi.org/10.1038/s41467-019-11309-3.

Competing interests: The authors declare no competing interests.

Reprints and permission information is available online at http://npg.nature.com/reprintsandpermissions/

Peer review information: *Nature Communications* thanks the anonymous reviewer for their contribution to the peer review of this work. Peer reviewer reports are available.

Publisher's note: Springer Nature remains neutral with regard to jurisdictional claims in published maps and institutional affiliations.

Open Access This article is licensed under a Creative Commons Attribution 4.0 International License, which permits use, sharing, adaptation, distribution and reproduction in any medium or format, as long as you give appropriate credit to the original author(s) and the source, provide a link to the Creative Commons license, and indicate if changes were made. The images or other third party material in this article are included in the article's Creative Commons license, unless indicated otherwise in a credit line to the material. If material is not included in the article's Creative Commons license and your intended use is not permitted by statutory regulation or exceeds the permitted use, you will need to obtain permission directly from the copyright holder. To view a copy of this license, visit http://creativecommons.org/licenses/by/4.0/.

© The Author(s) 2019

Electronic Supplementary Information

Engineering electronic structure to prolong relaxation times in molecular qubits by minimising orbital angular momentum

Ana-Maria Ariciu,[a,b,§] David H. Woen,[c,§] Daniel N. Huh,[c] Lydia Nodarki,[a] Andreas K. Kostopoulos,[a] Conrad A. P. Goodwin,[a] Nicholas F. Chilton,[a] Eric J. L. McInnes,[a,b] Richard E. P. Winpenny,[a,]* William J. Evans,[c,]* and Floriana Tuna[a,b,]*

[a]*School of Chemistry, The University of Manchester, Oxford Road, Manchester, M13 9PL, UK.*

[b]*Photon Science Institute, The University of Manchester, Oxford Road, Manchester, M13 9PL, UK.*

[c]*Department of Chemistry, University of California, Irvine, California, 92697-2025, United States.*

§ These authors contributed equally.

Supplementary Figures

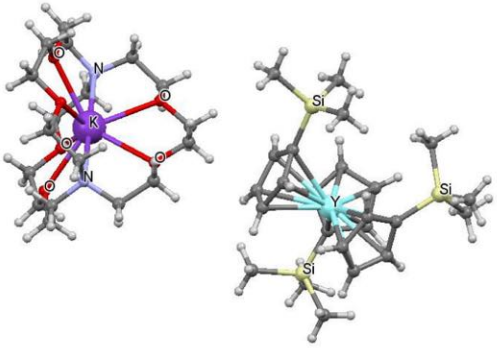

Supplementary Figure 1. Molecular structure of **1**: light blue, Y; yellow, Si; purple, K; light purple, N; red, O; grey, C; light grey, H.[2]

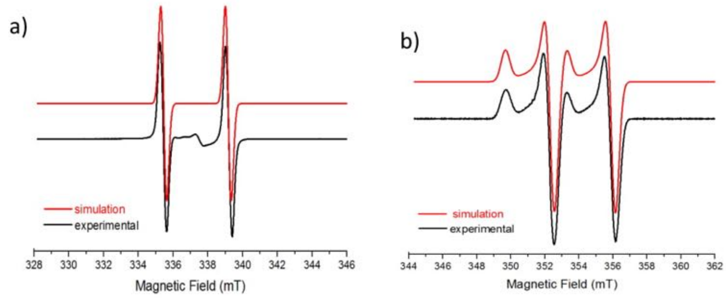

Supplementary Figure 2. Experimental (black) and simulated (red) X-band CW-EPR spectra for **1** (10 mM in THF). Simulation parameters: g_{iso} = 1.991; $A_{iso}(^{89}Y)$ = 102 MHz: a) 295 K fluid solution at 9.40 GHz; b) 50 K frozen solution at 9.85 GHz.

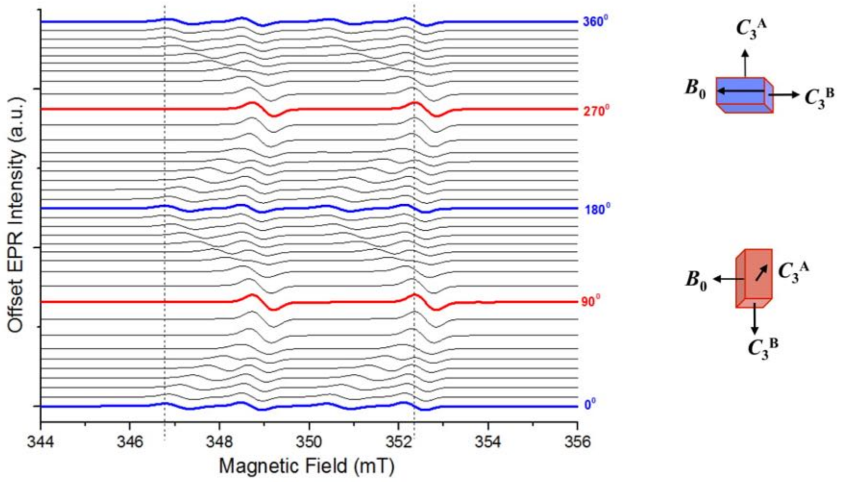

Supplementary Figure 3. X-band CW EPR road-map for a single crystal of **~2% 1@5** at 200 K and 9.755 GHz, following stepwise rotation around C_3 of molecules **A** (see above). At positions highlighted in blue, B_0 is along the C_3 axis of molecules **B**, and nearly perpendicular to C_3 of molecules **A**. At positions highlighted in red, B_0 is perpendicular to C_3 of both **A** and **B**, and thus the measured signal allows determination of $g_{x,y}$. The effective g-values are: g_z = 1.999 and $g_{x,y}$ = 1.986.

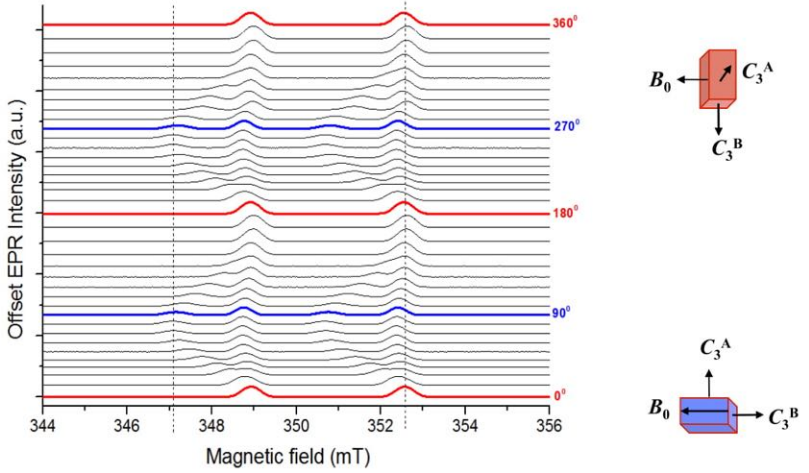

Supplementary Figure 4. EDFS road-map (angular dependence profile) for single crystal **~2% 1@5** following stepwise rotation **(**10 deg. increments) around C_3 of molecules **A,** recorded at 200 K and 9.755 GHz (X-band). At positions highlighted in red, B_0 is perpendicular to C_3 of molecules **A** and **B;** the observed double resonance EPR signal is simulated with $g_{x,y}$ = 1.986, and $A_{x,y}$ (^{89}Y) = 101.3 MHz. At positions highlighted in blue, B_0 is along the C_3 axis of molecules **B**, and nearly perpendicular to C_3 of molecules **A**. Simulation of the data provides g_z = 1.999, $g_{x,y}$ = 1.986, A_z = 99.5 and $A_{x,y}$ = 101.3 MHz (see Fig. 2b and Table 2 in the main text).

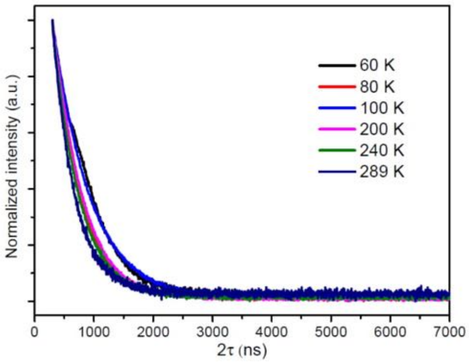

Supplementary Figure 5. Normalized Hahn echo signal intensities as a function of the inter-pulse delay 2τ, for **~2% 1@5** (single crystal) at B_0 = 349 mT (**OP2** in Fig. 2b; $B_0 \perp C_3$) and selected temperatures.

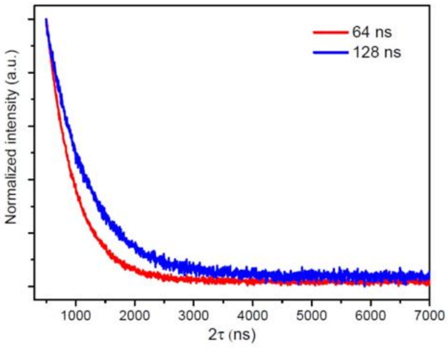

Supplementary Figure 6. Normalized Hahn echo signal intensities as a function of the inter-pulse delay 2τ for **~2% 1@5** (single crystal) at B_0 = 352.6 mT (**OP4** in Figure 2b; $B_0 \perp C_3$) and 100 K. The rate of relaxation varies with the pulse length, with more selective (longer) pulses being more effective in suppressing proton modulations.

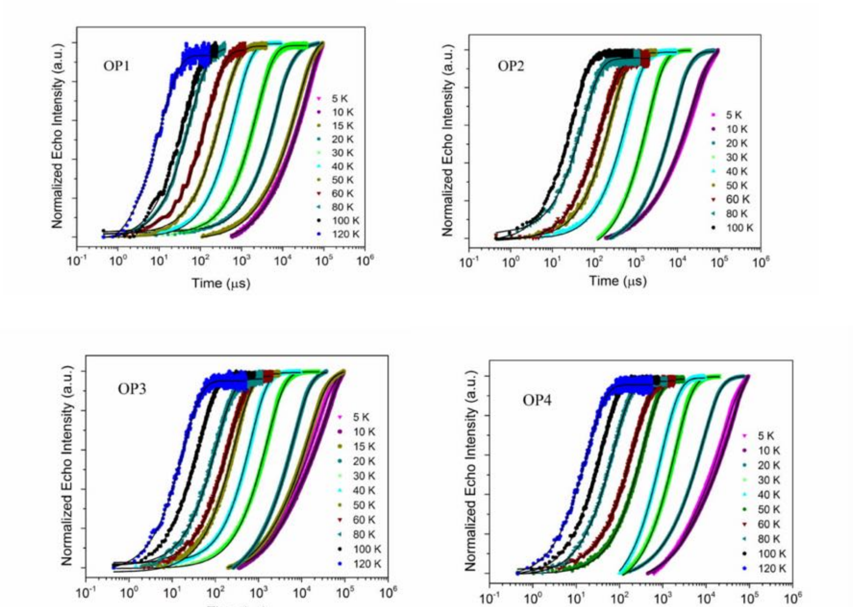

Supplementary Figure 7. Inversion recovery data for **1** (10 mM; THF) at selected temperatures between 5 and 120 K, and at B_0 of 349.8 mT (**OP1**), 350.3 mT (**OP2**), 352.2 mT (**OP3**), and 355.9 mT (**OP4**). The red lines are best fits to the biexponential model (Eq. 3), giving the parameters in Supplementary Table 3. The observer positions OP1-OP4 are indicated in Fig. 2a (main text).

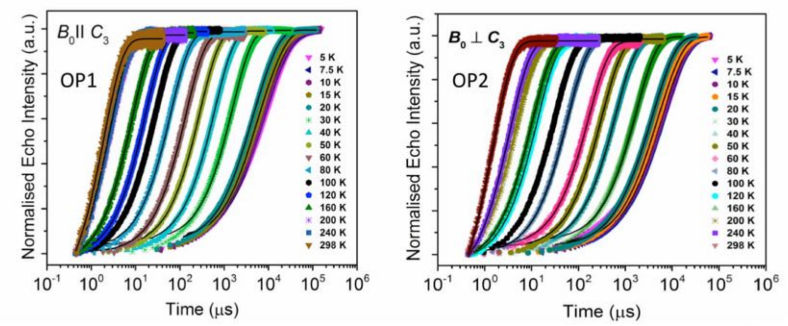

Supplementary Figure 8. Inversion recovery data for **~2% 1@5** (single crystal) at different temperatures between 5 and 298 K, and at B_0 of 347 mT (**OP1**), or 349 mT (**OP2**). The solid lines are best fits to the biexponential model (Eq. 3), giving the parameters in Supplementary Table 4. The observer positions OP1-OP4 are indicated in Fig. 2b (main text).

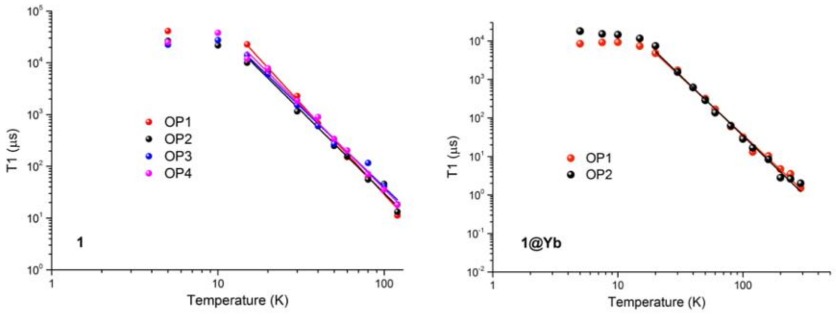

Supplementary Figure 9. Temperature dependence of T_1 for (**left**) **1** (THF) and (**right**) **~2% 1@5** (single crystal), at X-band and different observable positions, indicated in Figs. 2a and 2b. The solid lines represent the best fits to equation $T_1^{-1} = CT^n$ with n = 3 - 3.5.

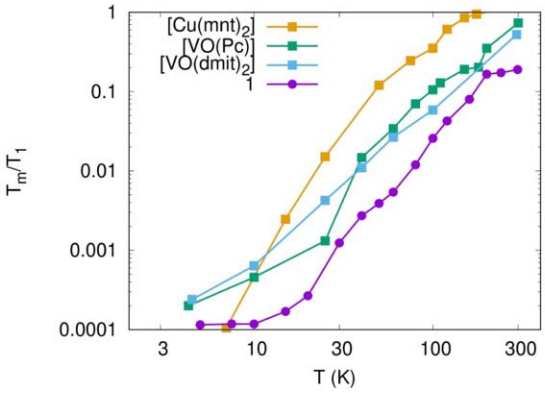

Supplementary Figure 10. T_m/T_1 as a function of temperature for: ~2% **1@5**; [Cu(mnt)$_2$] (0.001% solid-state dilution) (8), [VO(Pc)] (0.001% solid-state dilution) (26); [VO(dmit)$_2$] (5% solid-state dilution) (11).

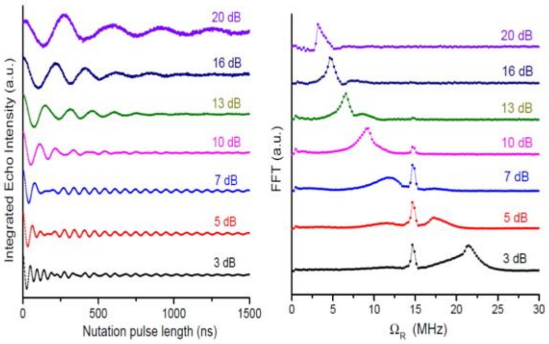

Supplementary Figure 11. (Left) Rabi oscillation for **1** (THF) at 120 K and B_0 = 349.8 mT (**OP1**; Fig. 2a), acquired with different microwave attenuations; (Right) corresponding Fourier transforms.

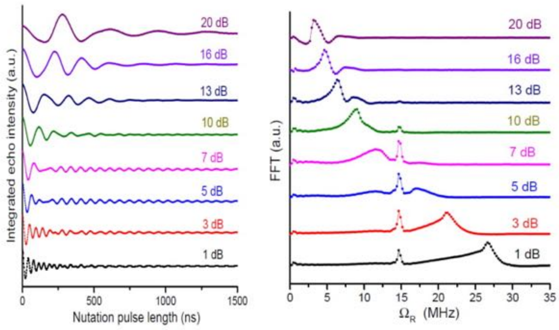

Supplementary Figure 12. (Left) Rabi oscillations for **1** (THF) at 40 K and B_0 = 349.8 mT (**OP1**; Fig. 2a), acquired with different microwave attenuations; (Right) corresponding Fourier transforms.

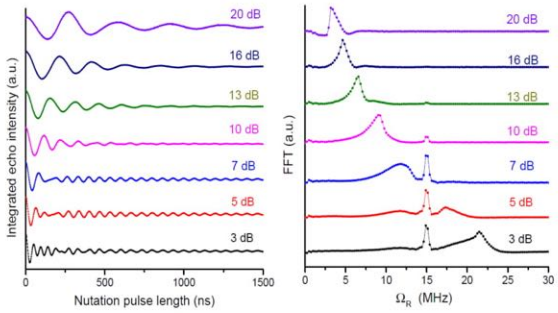

Supplementary Figure 13. (Left) Rabi oscillation for **1** (THF) at 120 K and B_0 = 355.9 mT (**OP4**; Fig. 2a), acquired with different microwave attenuations; (Right) corresponding Fourier transforms.

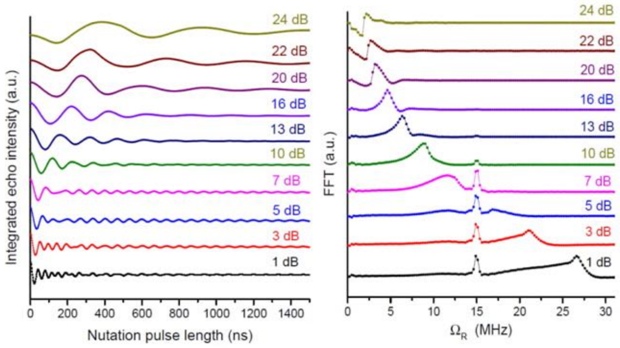

Supplementary Figure 14. (Left) Rabi oscillation for **1** (THF) at 40 K and B_0 = 355.9 mT (**OP4**; Fig. 2a), acquired with different microwave attenuations; (Right) corresponding Fourier transforms.

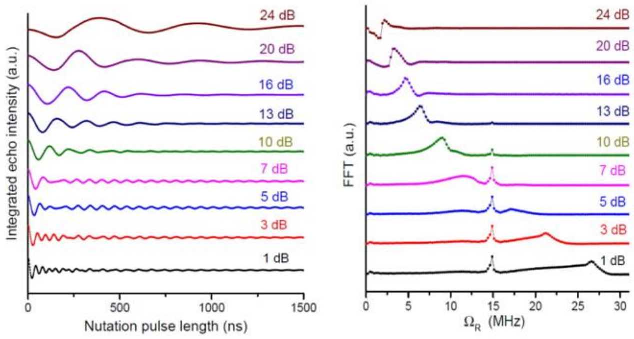

Supplementary Figure 15. (Left) Rabi oscillation for **1** (THF) at 40 K and B_0 = 352.2 mT (**OP3**; Fig. 2a), acquired with different microwave attenuations; (Right) corresponding Fourier transforms.

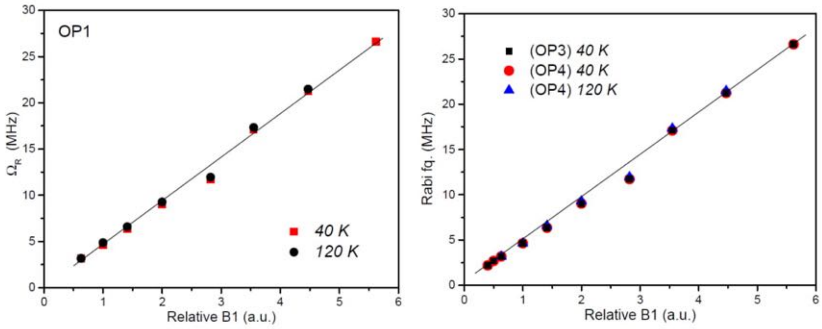

Supplementary Figure 16. B_1 dependence of the Rabi frequency (Ω_R) for **1** (THF) measured at 40 and 120 K, for different observable positions (Fig. 2a). The solid line is a guide for the eye emphasizing the linear behaviour ($B_1 \propto \sqrt{P}$, where P is the microwave power).

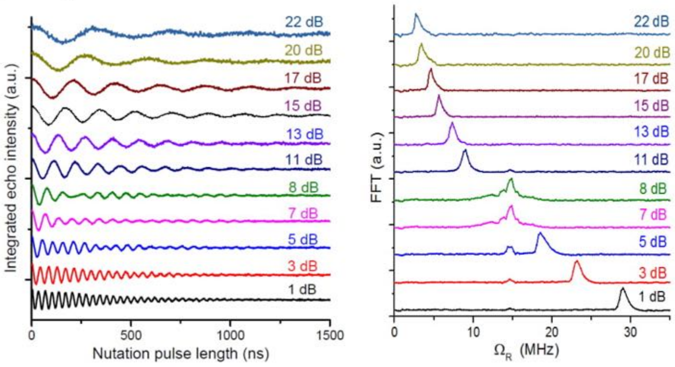

Supplementary Figure 17. (Left) Rabi oscillation for **~2% 1@5** (single crystal) at 298 K and B_0 **=** 347 mT (**OP1**; Fig. 2b; $B_0||C_3$), acquired with different microwave attenuations; (Right) corresponding Fourier transforms.

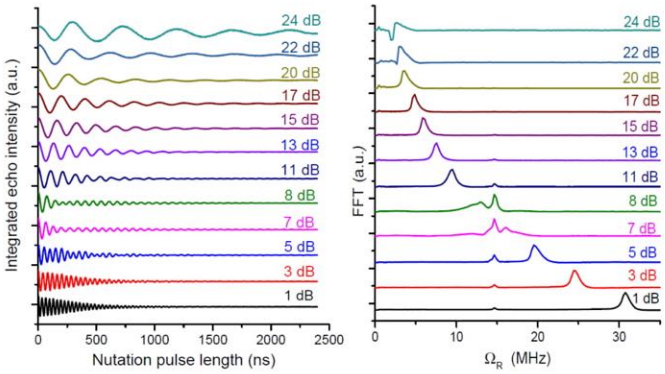

Supplementary Figure 18. (Left) Rabi oscillation for **~2% 1@5** (single crystal) at 120 K and B_0 = 347 mT (**OP1;** Fig 2b; B_0 || C_3), acquired with different microwave attenuations; (Right) corresponding Fourier transforms.

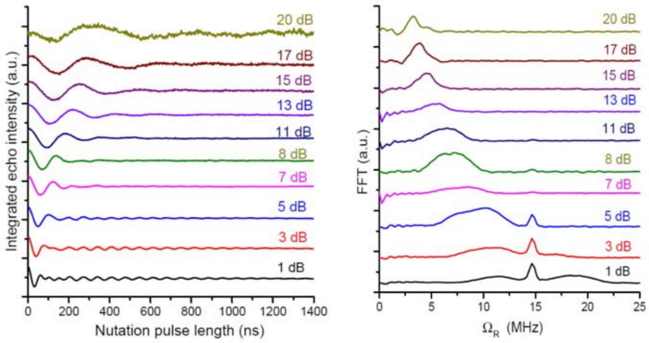

Supplementary Figure 19. (Left) Rabi oscillation for **~2% 1@5** (single crystal) at 298 K and B_0 = 349 mT (**OP2;** Fig. 2b; $B_0 \perp C_3$)**,** acquired with different microwave attenuations; (Right) corresponding Fourier transforms.

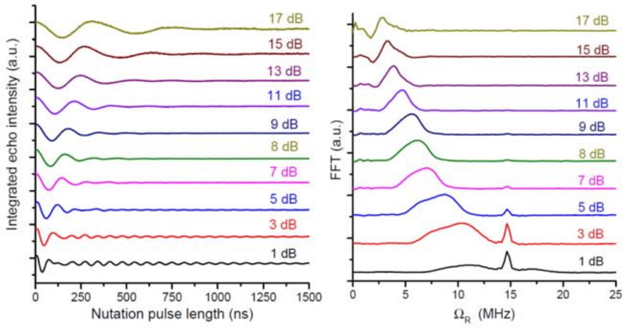

Supplementary Figure 20. (Left) Rabi oscillation for **~2% 1@5** (single crystal) at 120 K and B_0 = 349 mT (**OP2;** Fig. 2b; $B_0 \perp C_3$) acquired with different microwave attenuations; (Right) corresponding Fourier transforms.

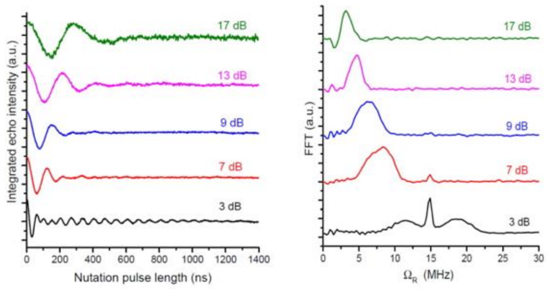

Supplementary Figure 21. (Left) Rabi oscillation for **~2% 1@5** (single crystal) at 298 K and B_0 = 352.7 mT (**OP4;** Fig. 2b; $B_0 \perp C_3$), acquired with different microwave attenuations; (Right) corresponding Fourier transforms.

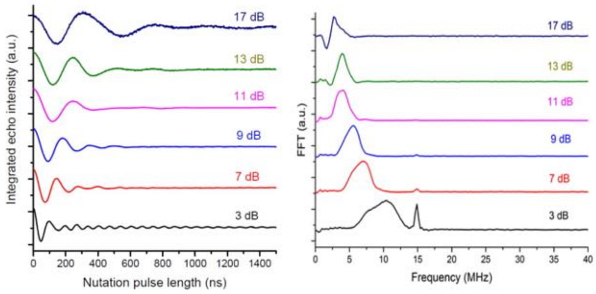

Supplementary Figure 22. (Left) Rabi oscillation for **~2% 1@5** (single crystal) at 120 K and 352.7 mT (**OP4;** Fig. 2b; $B_0 \perp C_3$), acquired with different microwave attenuations; (Right) corresponding Fourier transforms.

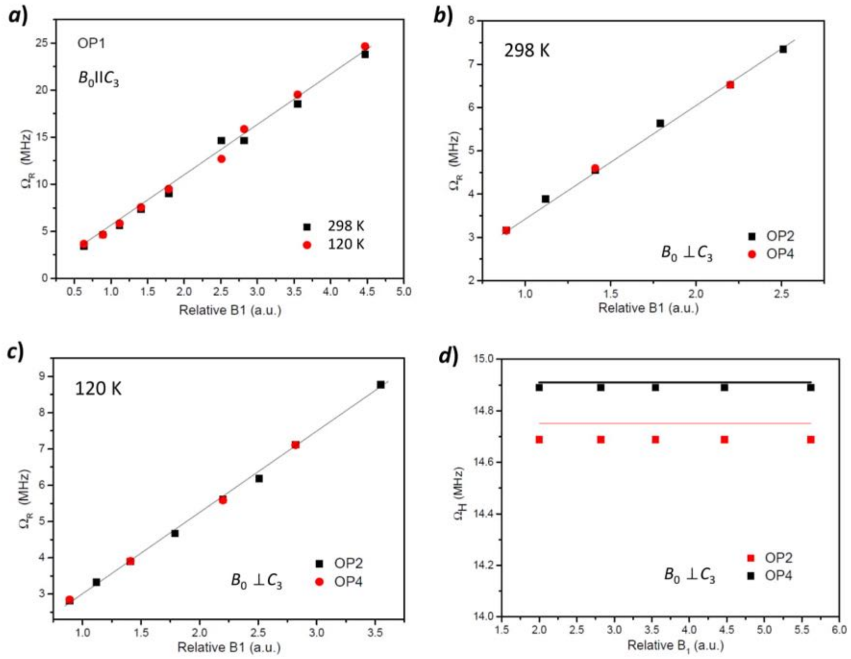

Supplementary Figure 23. B_1 dependence of the (**a-c**) Rabi frequency (Ω_R), and (**d**) ^{1}H nuclear frequency (Ω_H), for **~2% 1@5** (single crystal), measured at different observable positions (Fig. 2b), and temperatures of 120 and 298 K. The solid line is a guide for the eye emphasizing the linear behaviour ($B_1 \propto \sqrt{P}$, where P is the microwave power).

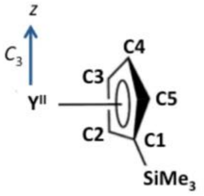

Supplementary Figure 24. Schematic representation for the binding of a Cp' ring in **1,** and the direction of the molecular C_3 axis.

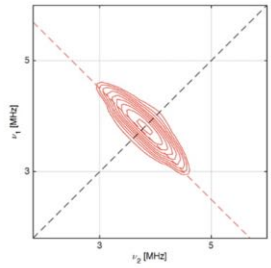

Supplementary Figure 25. Calculation of the ^{13}C HYSCORE spectrum of **1** based on the dipole model only (see text). The dashed-red antidiagonal lines mark the ^{13}C Larmor frequency.

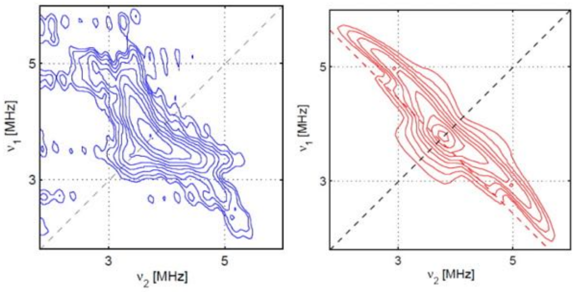

Supplementary Figure 26. (Left) ^{13}C HYSCORE spectrum for **1** (THF) at B_0 = 349.7 mT (**OP1**; Fig. 2a), T = 50 K and X-band (9.848 GHz) (Right) Calculation taking into account the point-dipole interactions and the associated spin densities at $C^{2,5}$ and $C^{3,4}$, yielding: $A_{\parallel}^{C2,5}$ = 2.8 MHz; $A_{\perp}^{C2,5}$ **=** 0.4 MHz, and $A_{\parallel}^{C3,4}$ = 0.825 MHz; and $A_{\perp}^{C3,4}$ **=** 0.3 MHz. The dashed-red antidiagonal line marks the ^{13}C Larmor frequency.

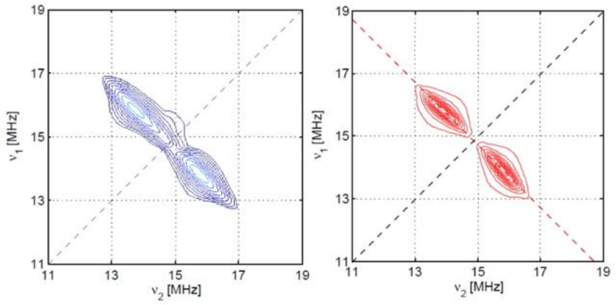

Supplementary Figure 27. (Left) ^{1}H HYSCORE spectrum for **1** (THF) at B_0 = 349.7 mT (**OP1**; Fig. 2a), T = 50 K, and X-band (9.848 GHz). (Right) Calculation based on the model described in the text, with a_{iso} =-0.7 MHz. The dashed-red antidiagonal line marks the ^{1}H Larmor frequency.

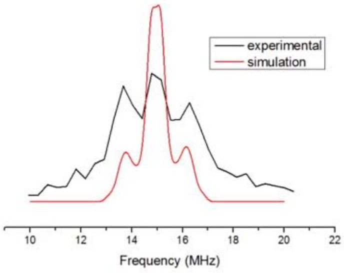

Supplementary Figure 28. ^{1}H Davies-ENDOR spectrum of **1** (THF) at $B_0 = 352.6$ mT (**OP3**; Fig. 1b) and $T = 50$ K (black), and its calculation based on the model described in the text (red).

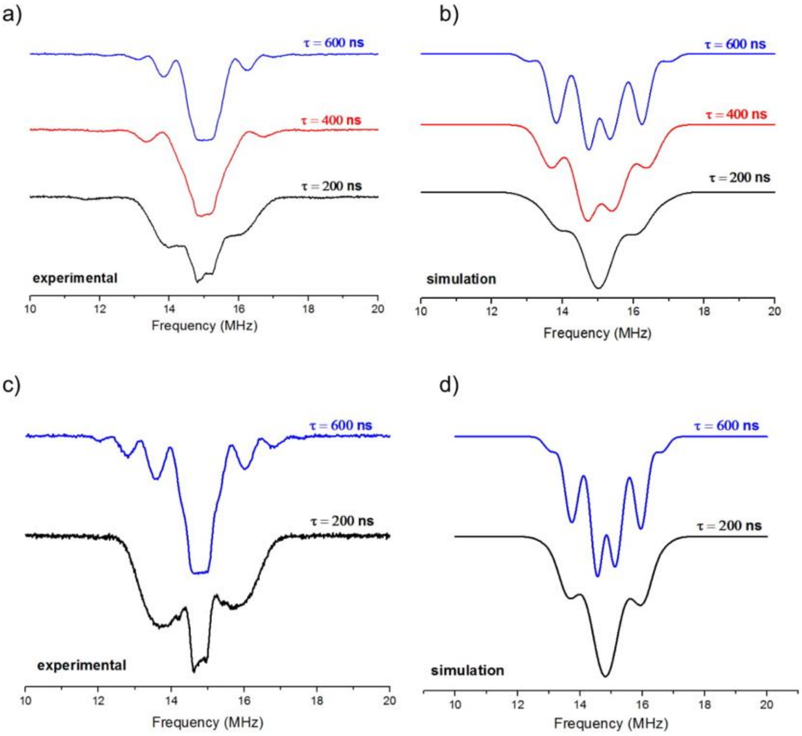

Supplementary Figure 29. ENDOR spectroscopy of **1**. a) ^{1}H Mims-ENDOR spectra of **1 (THF)** at $B_0 = 352.6$ mT (**OP3**; Fig. 1b), $T = 10$ K and different τ values; b) Correspondent calculations based on the model described in the text; c) ^{1}H Mims-ENDOR spectra at 10 K and $B_0 = 349$ mT (**OP1**; Fig. 2a); d) Simulation of the data in Supplementary Figure 29c. Simulations used EasySpin.

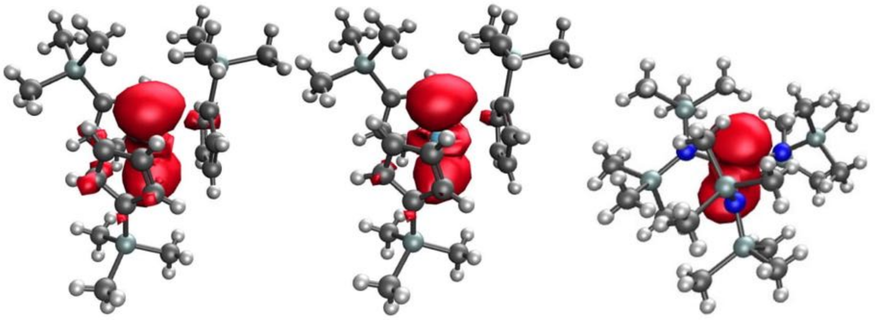

Supplementary Figure 30. A rendering of the spin density from DFT for the crystal structure anions in **2-4** (left to right, respectively).

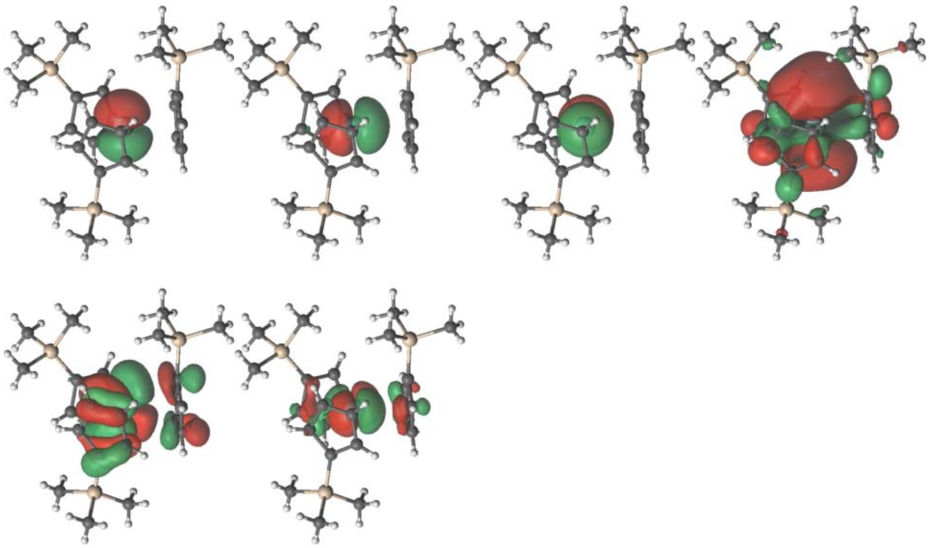

Supplementary Figure 31. Orbitals 130 – 135 in the active space in the CASSCF calculations for the crystalline geometry of **1** (isovalue = 0.02).

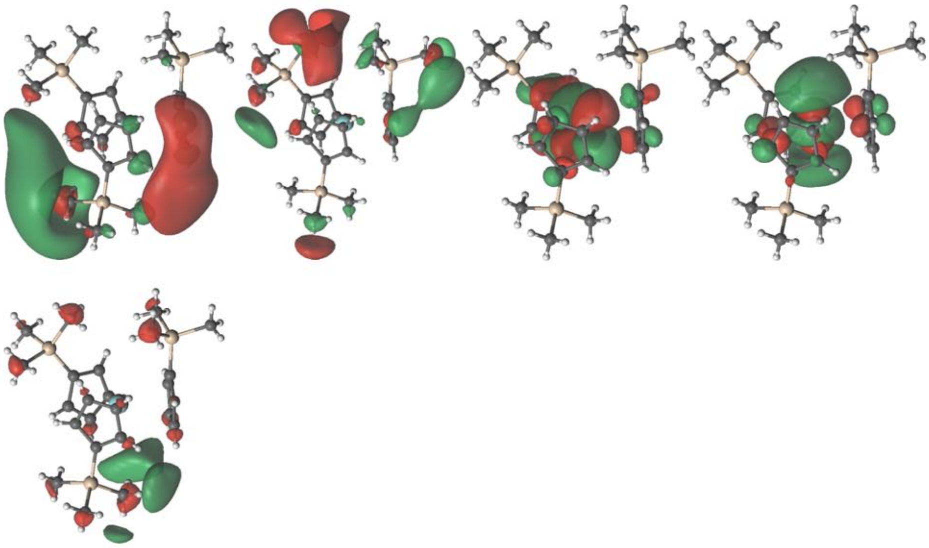

Supplementary Figure 32. Orbitals 136 – 140 in the active space in the CASSCF calculations for the crystalline geometry of **1** (isovalue = 0.02).

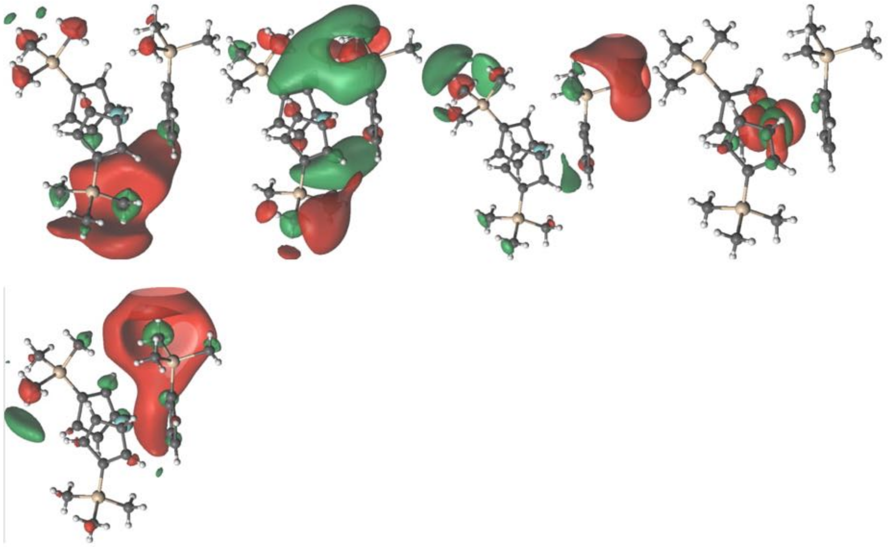

Supplementary Figure 33. Orbitals 141 – 145 in the active space in the CASSCF calculations for the crystalline geometry of **1** (isovalue = 0.02).

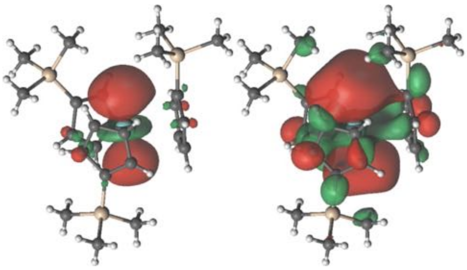

Supplementary Figure 34. Natural SOMO for state 1 in the CASSCF calculations for the crystalline geometry of **1**. Isovalue = 0.04 (left) and 0.02 (right).

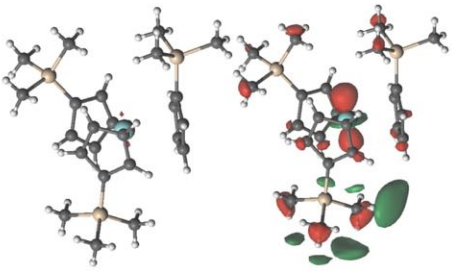

Supplementary Figure 35. Natural SOMO for state 2 in the CASSCF calculations for the crystalline geometry of **1**. Isovalue = 0.04 (left) and 0.02 (right).

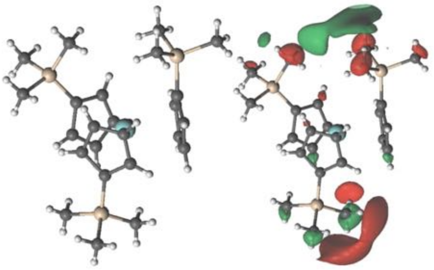

Supplementary Figure 36. Natural SOMO for state 3 in the CASSCF calculations for the crystalline geometry of **1**. Isovalue = 0.04 (left) and 0.02 (right).

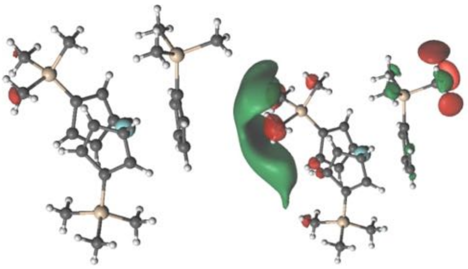

Supplementary Figure 37. Natural SOMO for state 4 in the CASSCF calculations for the crystalline geometry of **1**. Isovalue = 0.04 (left) and 0.02 (right).

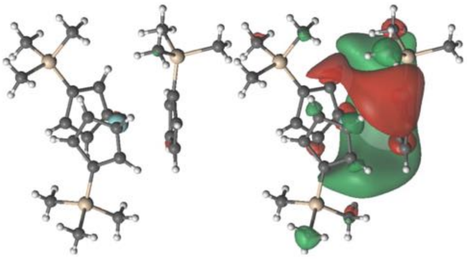

Supplementary Figure 38. Natural SOMO for state 5 in the CASSCF calculations for the crystalline geometry of **1**. Isovalue = 0.04 (left) and 0.02 (right).

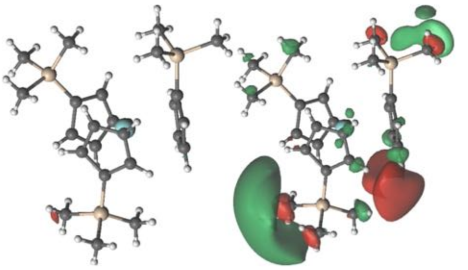

Supplementary Figure 39. Natural SOMO for state 6 in the CASSCF calculations for the crystalline geometry of **1**. Isovalue = 0.04 (left) and 0.02 (right).

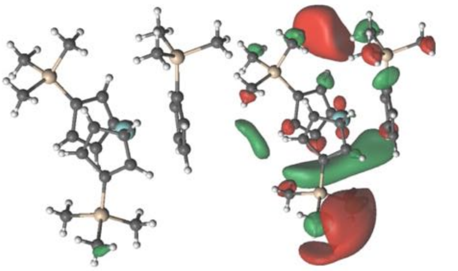

Supplementary Figure 40. Natural SOMO for state 7 in the CASSCF calculations for the crystalline geometry of **1**. Isovalue = 0.04 (left) and 0.02 (right).

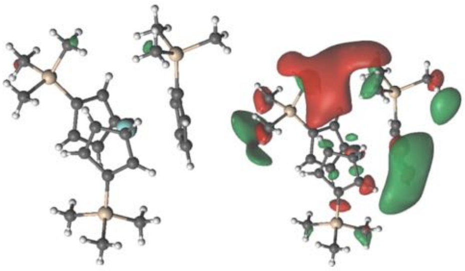

Supplementary Figure 41. Natural SOMO for state 8 in the CASSCF calculations for the crystalline geometry of **1**. Isovalue = 0.04 (left) and 0.02 (right).

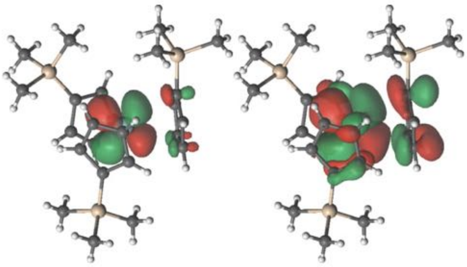

Supplementary Figure 42. Natural SOMO for state 9 in the CASSCF calculations for the crystalline geometry of **1**. Isovalue = 0.04 (left) and 0.02 (right).

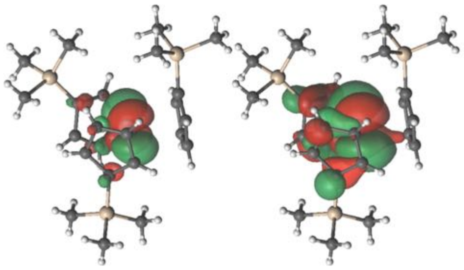

Supplementary Figure 43. Natural SOMO for state 10 in the CASSCF calculations for the crystalline geometry of **1**. Isovalue = 0.04 (left) and 0.02 (right).

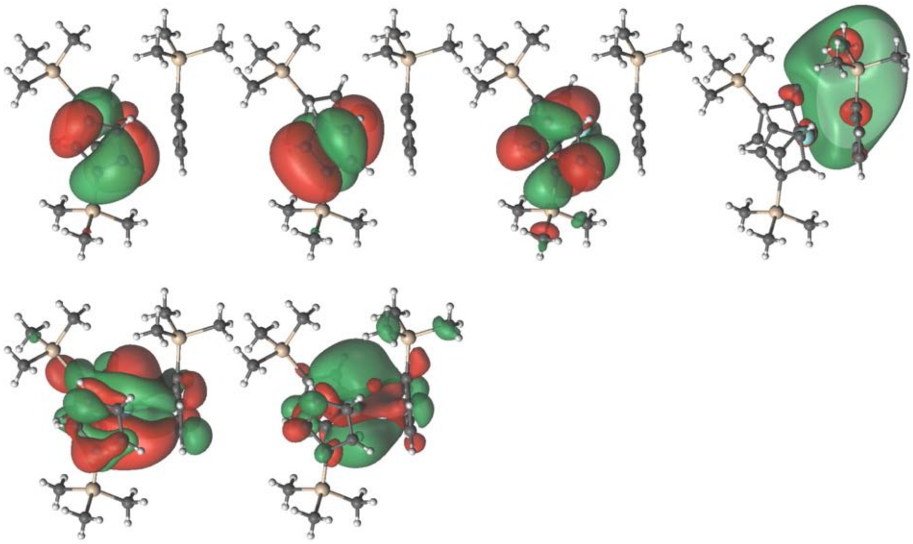

Supplementary Figure 44. Orbitals 131 – 136 in the active space in the CASSCF calculations for the crystalline geometry of **1** with a sphere of point charges (isovalue = 0.02).

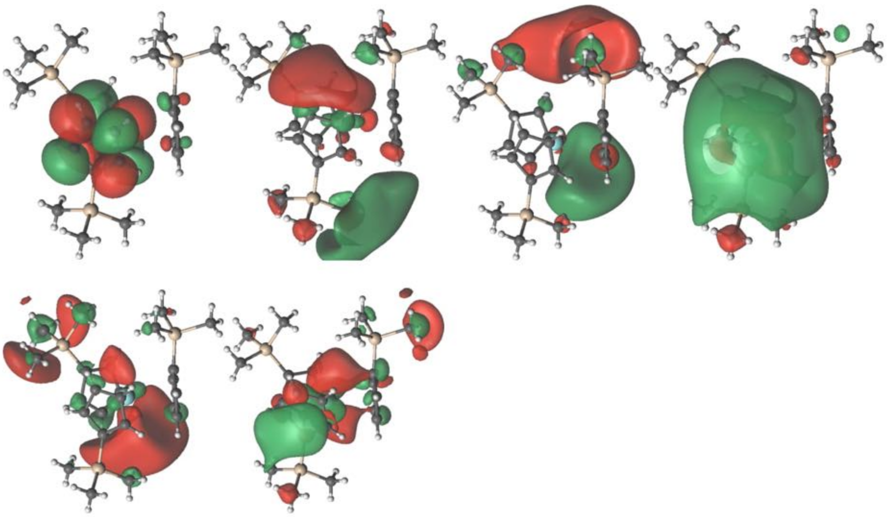

Supplementary Figure 45. Orbitals 137 – 142 in the active space in the CASSCF calculations for the crystalline geometry of **1** with a sphere of point charges (isovalue = 0.02).

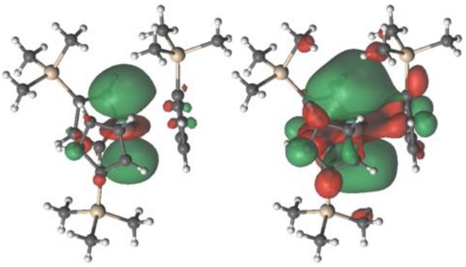

Supplementary Figure 46. Natural SOMO for state 1 in the CASSCF calculations for the crystalline geometry of **1** with a sphere of point charges. Isovalue = 0.04 (left) and 0.02 (right).

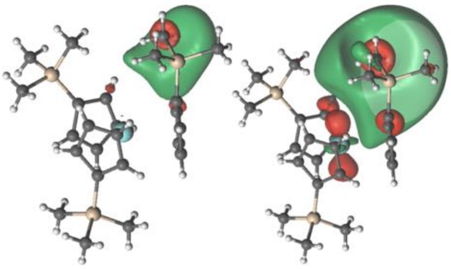

Supplementary Figure 47. Natural SOMO for state 2 in the CASSCF calculations for the crystalline geometry of **1** with a sphere of point charges. Isovalue = 0.04 (left) and 0.02 (right).

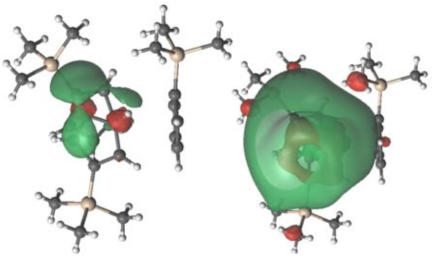

Supplementary Figure 48. Natural SOMO for state 3 in the CASSCF calculations for the crystalline geometry of **1** with a sphere of point charges. Isovalue = 0.04 (left) and 0.02 (right).

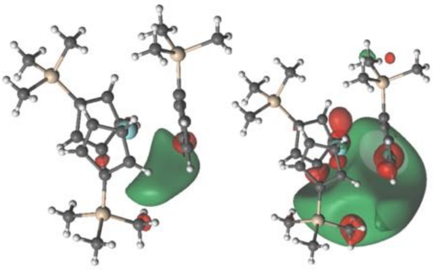

Supplementary Figure 49. Natural SOMO for state 4 in the CASSCF calculations for the crystalline geometry of **1** with a sphere of point charges. Isovalue = 0.04 (left) and 0.02 (right).

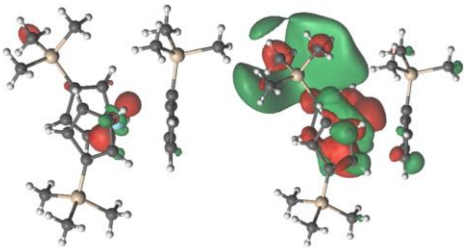

Supplementary Figure 50. Natural SOMO for state 5 in the CASSCF calculations for the crystalline geometry of **1** with a sphere of point charges. Isovalue = 0.04 (left) and 0.02 (right).

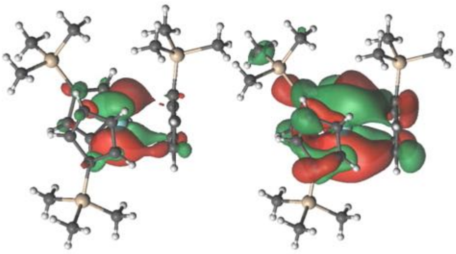

Supplementary Figure 51. Natural SOMO for state 6 in the CASSCF calculations for the crystalline geometry of **1** with a sphere of point charges. Isovalue = 0.04 (left) and 0.02 (right).

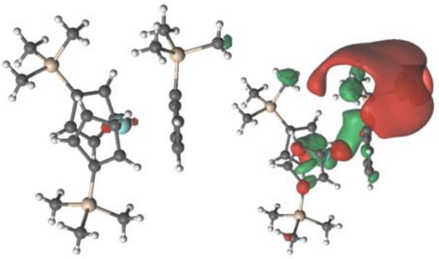

Supplementary Figure 52. Natural SOMO for state 7 in the CASSCF calculations for the crystalline geometry of **1** with a sphere of point charges. Isovalue = 0.04 (left) and 0.02 (right).

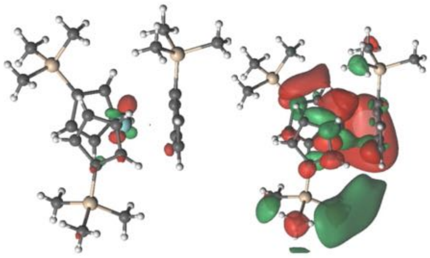

Supplementary Figure 53. Natural SOMO for state 8 in the CASSCF calculations for the crystalline geometry of **1** with a sphere of point charges. Isovalue = 0.04 (left) and 0.02 (right).

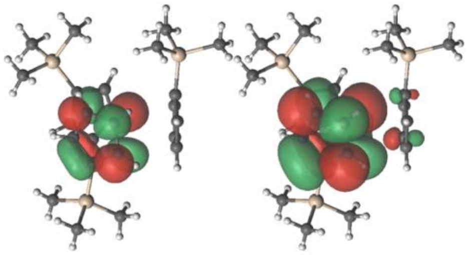

Supplementary Figure 54. Natural SOMO for state 9 in the CASSCF calculations for the crystalline geometry of **1** with a sphere of point charges. Isovalue = 0.04 (left) and 0.02 (right).

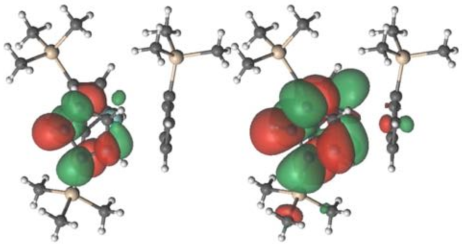

Supplementary Figure 55. Natural SOMO for state 10 in the CASSCF calculations for the crystalline geometry of **1** with a sphere of point charges. Isovalue = 0.04 (left) and 0.02 (right).

Supplementary Tables

Supplementary Table 1. Extracted phase memory time constants for **1** (THF), at X-band (**OP1-OP4**; Fig. 2a).

T (K)	**OP1** T_m (ns)	**x**	**OP2** T_m (ns)	**x**	**OP3** T_m (ns)	**x**	**OP4** T_m (ns)	**x**	$t(\pi/2)$ (ns)
5	2851.9	1.55	1971.5	1.55	2380.8	1.75	2606.3	1.86	256
10	2886.2	1.51	1924.9	1.47	2493.8	1.80	2481.2	1.91	256
15	2012.9	1.53	1998.0	1.50	1911.0	1.50	1894.5	1.50	256
20	2010.9	1.52	1961.5	1.54	1888.7	1.44	1875.2	1.50	256
30	1872.0	1.51	1861.0	1.53	1745.6	1.46	1725.8	1.45	256
40	1388.8	1.28	1497.6	1.36	1468.3	1.35	1445.0	1.35	256
50	1243.8	1.27	1142.8	1.20	1189.4	1.26	1190.8	1.27	256
60	1211.0	1.03	1116.3	1.17	939.9	1.10	937.5	1.15	64
80	507.2	1.00	467.1	1.00	510.9	1.00	497.7	1.00	64
100	844.7	1.00	515.2	1.00	810.0	1.00	755.6	1.00	64
120	693.2	1.00	580.3	1.00	560.9	1.00	484.2	1.00	64

Supplementary Table 2. Extracted phase memory time constants for single crystal **~2% 1@5** (**OP1-OP2**; Fig. 2b)

T (K)	OP1 (z) T_m (ns)	**x**	$t(\pi/2)$ (ns)	OP2 (x,y) T_m (ns)	**x**	$t(\pi/2)$ (ns)
5	2067.9	1.70	256	1480.5	1.50	128
7.5	1783.5	1.65	256	1082.6	1.40	128
10	1701.0	1.60	256	1121.5	1.43	128
15	1963.0	1.60	256	1359.2	1.42	128
20	1983.5	1.58	256	1330.9	1.30	128
30	1921.4	1.62	256	1355.3	1.28	128
40	1684.4	1.67	256	1483.4	1.27	128
50	1119.7	1.62	256	752.0	1.30	128
60	741.6	1.50	128	634.8	1.41	64
80	756.1	1.40	64	545.0	1.40	64
100	734.8	1.20	64	620.7	1.30	64
120	712.9	1.00	64	707.1	1.10	64
160	672.6	1.00	64	733.0	1.00	64
200	464.7	1.00	64	487.9	1.00	64
240	449.7	1.00	64	440.0	1.00	64
298	378.5	1.00	64	375.2	1.00	64

Supplementary Table 3. Extracted spin lattice relaxation time constants for **1** (THF) (**OP1-OP4**; Fig. 2a)

	OP1		**OP2**		**OP3**		**OP4**	
T (K)	T_1 (μs)	T_{SD} (μs)	T_1 (μs)	T_{SD} (μs)	T_1 (μs)	T_{SD} (μs)	T_1 (μs)	T_{SD} (μs)
5	41273.6	2598.7	26637.5	1994.6	22367	2201.2	24954	2314.6
10	38009.7	3100.4	21672.3	1770.9	27449.6		37952	3199.2
15	22780	1761.6	10083.6	293.4	14115.2		12002.8	1090.1
20	7056	41.1	7605.7		5988		7855.8	
30	2290		1155.6		1527.2		1852.8	
40	667.3		602.9		614.6		897	
50	327.2		249.2		272.9		338	
60	150.8		156.5		202.4		203	
80	61.5		55.6		115.7		71.2	
100	45.1		45.5		41.2		35.6	
120	11.2		13.2		18.3		18	

Supplementary Table 4. Extracted spin lattice relaxation time constants for **~2% 1@5** (**OP1-OP2**; Fig. 2b)

	OP1 ($B_0 \parallel C_3$)		**OP2** ($B_0 \perp C_3$)	
T (K)	T_1 (μs)	T_{SD} (μs)	T_1 (μs)	T_{SD} (μs)
5	17951.8	4588.3	8465	540.5
7.5	15109.6	3750.3	9159.5	2677.6
10	14444.8	3750.3	9199.1	2965.7
15	11582.8	3200.7	7357.7	2085.2
20	7423.5	2159.3	4771.6	2346.8
30	1548		1716.6	1193.6
40	616.5		626.5	
50	287.2		320	
60	137.1		167.8	
80	63.2		59.7	
100	28.5		31.5	
120	16.7		13.1	
160	8.4		10.3	
200	2.8		4.7	
240	2.6		3.5	
298	2		1.5	

Supplementary Table 5. Rabi frequencies for **1** (THF) at B_0 = 349.8 mT (**OP1**; Fig. 2c)

Attenuation (dB)	Relative B_1 (a.u.)	Ω_R (MHz) at 40 K	Ω_R (MHz) at 120 K
1	5.62	26.69	-
3	4.47	21.19	21.46
5	3.55	17.01	17.23
7	2.82	11.90	11.97
10	2	9.05	9.15
13	1.41	6.53	6.61
16	1	4.74	4.83
20	0.63	3.23	3.22

Supplementary Table 6. Rabi frequencies for **1** (THF**)** at B_0 = 355.9 mT (**OP4**; Fig. 2c)

Attenuation (dB)	Relative B_1 (a.u.)	Ω_R (MHz) at 40 K	Ω_R (MHz) at 120 K
1	5.62	26.64	-
3	4.47	21.07	21.46
5	3.55	16.64	17.37
7	2.82	12.05	12.01
10	2	8.94	9.19
13	1.41	6.39	6.59
16	1	4.67	4.65
20	0.63	3.28	3.24
22	0.5	2.69	
24	0.4	2.21	

Supplementary Table 7. Rabi frequencies for **1** (THF) at B_0 = 352.2 mT (**OP3;** Fig. 2c)

Attenuation (dB)	Relative B_1 (a.u.)	Ω_R (MHz) at 40 K
1	5.62	26.60
3	4.47	21.17
5	3.55	17.10
7	2.82	11.90
10	2	8.98
13	1.41	6.47
16	1	4.74
20	0.63	3.36
24	0.4	2.17

Supplementary Table 8. Rabi frequencies for **~2% 1@5** (single crystal) at 347 mT (**OP1;** Fig. 2c; $B_0||C_3$).

Attenuation (dB)	Relative B_1 (a.u.)	Ω_R (MHz) at 120 K	Ω_R (MHz) at 298 K
1	5.62	30.74	29.04
3	4.47	24.65	23.8
5	3.55	19.52	18.54
7	2.82	15.86	14.64
8	2.51	12.69	14.64
11	1.79	9.51	9.02
13	1.41	7.56	7.32
15	1.12	5.85	5.61
17	0.89	4.63	4.64
20	0.63	3.66	3.41
22	0.5	2.92	2.68
24	0.4	2.19	

Supplementary Table 9. Rabi frequencies for **~2% 1@5** (single crystal) at B_0 = 349 and 352.7 mT (**OP2** and **OP4**; Fig. 2c; $B_0 \perp C_3$).

Att. (dB)	Rel. B_1 (a.u.)	Ω_R (MHz) at 120 K **OP2**	Ω_R (MHz) at 120 K **OP4**	Ω_R (MHz) at 298 K **OP2**	Ω_R (MHz) at 298 K **OP4**
3	4.47	10.23	10.25		
5	3.55	8.78		9.26	
7	2.82	7.12	7.11	8.51	8.51
8	2.51	6.18		7.35	
9	2.2	5.6	5.58	6.52	6.53
11	1.79	4.67		5.64	
13	1.41	3.9	3.91	4.56	4.59
15	1.12	3.23		3.89	
17	0.89	2.81	2.84	3.17	3.16

Supplementary Table 10. Basis sets used for geometry optimisations (20).

Compound	**Metal atom**	**Non-metal atoms**
1	old-DKH-TZVP	DKH-def2-TZVP
2	SARC-DKH-TZVP	DKH-def2-TZVP
3	SARC-ZORA-TZVP	ZORA-def2-TZVP
4	old-DKH-TZVP	DKH-def2-TZVP

Supplementary Table 11. Summary of DFT results for the crystal structure of **1**. Basis sets on all other atoms were DKH-def2-TZVP.

		A^{Y} (MHz)				Lödwin fractional spin density				*g*-values		
Functional	**Y basis set**	A_x	A_y	A_z	A_{iso}	**Y**	**Y(s)**	**Y(d)**	**Y(p)**	g_x	g_y	g_z
PBE	old-DKH-SVP	-90.4244	-90.9842	-95.0167	-92.1418	0.6165	0.0786	0.5203	0.0175	1.9909	1.9922	2.0026
	old-DKH-TZVP	-88.3904	-89.0201	-93.8617	-90.4241	0.6167	0.0751	0.5237	0.0180	1.9892	1.9907	2.0026
	old-DKH-TZVPP	-88.8710	-89.5021	-93.7129	-90.6953	0.6102	0.0757	0.5214	0.0139	1.9893	1.9908	2.0026
	ANO-RCC-DZP	-87.9309	-88.5608	-91.5312	-89.3409	0.5809	0.0716	0.4945	0.0146	1.9895	1.9910	2.0026
	Sapporo-DKH3-TZP-2012	-90.1572	-90.7353	-94.6198	-91.8374	0.6346	0.0758	0.5467	0.0117	1.9902	1.9916	2.0026
	Sapporo-DKH3-QZP-2012	-91.4170	-91.9986	-95.6088	-93.0081	0.6271	0.0762	0.5389	0.0113	1.9900	1.9914	2.0026
BP86	old-DKH-TZVP	-92.2487	-92.8690	-97.7665	-94.2948	0.6269	0.0719	0.5351	0.0199	1.9888	1.9903	2.0026
	Sapporo-DKH3-TZP-2012	-93.7947	-94.3650	-97.9639	-95.3745	0.6435	0.0722	0.5584	0.0130	1.9899	1.9913	2.0026
B3LYP	old-DKH-TZVP	-95.3484	-96.0436	-100.8021	-97.3980	0.6357	0.0730	0.5468	0.0159	1.9864	1.9881	2.0026
	Sapporo-DKH3-TZP-2012	-95.1732	-95.8114	-99.2390	-96.7412	0.6519	0.0741	0.5680	0.0105	1.9879	1.9894	2.0027
TPSSh	old-DKH-TZVP	-88.9258	-89.5573	-92.6207	-90.3679	0.6404	0.0748	0.5446	0.0210	1.9890	1.9904	2.0026
	Sapporo-DKH3-TZP-2012	-85.8018	-86.3833	-87.4726	-86.5525	0.6560	0.0746	0.5687	0.0140	1.9900	1.9912	2.0026
M06	old-DKH-TZVP	-95.2193	-95.9954	-103.7934	-98.3360	0.6527	0.0905	0.5344	0.0279	1.9869	1.9890	2.0027
	Sapporo-DKH3-TZP-2012	-83.1192	-83.9206	-90.9025	-85.9808	0.6868	0.0906	0.5755	0.0280	1.9879	1.9900	2.0026
PBE0	old-DKH-TZVP	-92.2376	-92.8894	-94.7304	-93.2858	0.6479	0.0748	0.5524	0.0207	1.9881	1.9895	2.0023
	Sapporo-DKH3-TZP-2012	-92.6475	-93.2515	-94.1271	-93.3420	0.6639	0.0746	0.5763	0.0140	1.9892	1.9905	2.0024
Average	-	-91(3)		-95(4)	-92(4)	0.64(2)	0.077(6)	0.54(2)	0.017(5)	1.990(1)		2.0026(1)

Supplementary Table 12. DFT results using ZORA relativistic Hamiltonian for the crystal structure of **1**. Basis sets on all other atoms were ZORA-def2-TZVP.

Functional	**Y basis set**	A_x	A_y	A_z	A_{iso}	g_x	g_y	g_z
PBE	old-ZORA-SVP	-102.4753	-103.5730	-105.1821	-103.7435	1.9912	1.9925	2.0026
	old-ZORA-TZVPP	-97.3283	-98.3425	-100.1217	-98.5975	1.9911	1.9925	2.0026

Supplementary Table 13. DFT results for the crystal structure of **1** with point charges at the Y and K lattice sites.

Functional	**Y basis set**	A_x	A_y	A_z	A_{iso}	g_x	g_y	g_z
PBE	old-DKH-TZVP	-98.4899	-99.3885	-103.2942	-100.3909	1.9874	1.9893	2.0023

Supplementary Table 14. Hyperfine coupling parameters from DFT for **1-4**, calculated with PBE, DKH and the appropriate def2-TZVP basis set.

Compound/Structure	**Metal basis set**	A^Y **(MHz)**				**Lödwin fractional spin density**				***g*-values**		
		A_x	A_y	A_z	A_{iso}	**Metal**	**Metal(s)**	**Metal(d)**	**Metal(p)**	g_x	g_y	g_z
1 (crystalline)	old-DKH-TZVPP	-88.3904	-89.0201	-93.8617	-90.4241	0.6167	0.0751	0.5237	0.0180	1.9892	1.9907	2.0026
1 (optimised)	old-DKH-TZVPP	-70.1384	-71.2243	-75.6440	-72.3355	0.5716	0.0630	0.4929	0.0157	1.9900	1.9946	2.0025
2 (crystalline)	SARC-DKH-TZVP	989.4181	991.8951	1004.8720	995.3951	0.6237	0.1040	0.5062	0.0165	1.9664	1.9716	2.0021
2 (optimised)	SARC-DKH-TZVP	917.3997	920.1777	933.4989	923.6921	0.5977	0.0921	0.4921	0.0159	1.9684	1.9734	2.0023
3 (crystalline)	SARC-DKH-TZVP	311.2075	312.8486	324.9602	316.3388	0.6780	0.0871	0.5792	0.0072	1.9664	1.9683	2.0021
3 (optimised)	SARC-DKH-TZVP	336.9145	338.6541	350.3511	341.9732	0.6801	0.0881	0.5805	0.0071	1.9644	1.9662	2.0019
4 (crystalline)	old-DKH-TZVP	552.1476	556.8163	589.1498	566.0379	0.7978	0.1292	0.6581	0.0104	1.9833	1.9845	2.0017
4 (optimised)	old-DKH-TZVP	537.0734	541.3868	572.7468	550.4023	0.7684	0.1237	0.6338	0.0109	1.9845	1.9856	2.0017

Supplementary Table 15. Occupation numbers in the state averaged CASSCF calculation for the crystalline geometry of **1**.

Orbital	130	131	132	133	134	135	136	137	138	139	140	141	142	143	144	145
Occupation	1.98	1.98	1.98	0.10	0.11	0.01	0.10	0.10	0.11	0.01	0.10	0.10	0.10	0.10	0.01	0.10

Supplementary Table 16. Relative energies of the 10 lowest states for CASSCF calculations of **1**.

State	**Energy (cm^{-1})**	
	Crystalline	**Crystalline (point charges)**
1	0	0
2	9242	4698
3	9860	10301
4	12246	14930
5	13559	18401
6	16158	19634
7	16909	20896
8	18814	26665
9	33572	28531
10	34142	31136

Supplementary Table 17. Contributions > 3% to the natural SOMO for state 1 in **1** (total for atomic angular momenta).

AO	**Contribution (%)**
Y(4d)	50.1
Y(5s)	5.3
Total	
Y	57.7
Ligand	42.3

Supplementary Table 18. Contributions > 3% to the natural SOMO for state 2 in **1** (total for atomic angular momenta).

AO	**Contribution (%)**
H38(2s)	5.2
H32(2s)	4.0
H36(2s)	3.7
Y(4d)	3.4
H39(2s)	3.3
Y(6s)	3.2
H35(2s)	3.2
Total	
Y	10.6
Ligand	89.4

Supplementary Table 19. Contributions > 3% to the natural SOMO for state 3 in **1** (total for atomic angular momenta).

AO	**Contribution (%)**
H38(2s)	6.3
H19(2s)	5.1
H21(2s)	4.2
H8(2s)	4.0
H39(2s)	3.9
H36(2s)	3.7
H9(2s)	3.3
H16(2s)	3.3
H18(2s)	3.2
H37(2s)	3.1
Total	
Y	2.8
Ligand	97.2

Supplementary Table 20. Contributions > 3% to the natural SOMO for state 4 in **1** (total for atomic angular momenta).

AO	**Contribution (%)**
H6(2s)	6.7
H5(2s)	5.9
H1(2s)	5.3
H16(2s)	5.2
H2(2s)	4.7
H15(2s)	4.7
H14(2s)	4.5
Total	
Y	3.9
Ligand	96.1

Supplementary Table 21. Contributions > 3% to the natural SOMO for state 5 in **1** (total for atomic angular momenta).

AO	**Contribution (%)**
Y(6p)	7.7
H25(2s)	7.7
H11(2s)	5.2
Y(7p)	4.7
H22(2s)	4.1
H28(2s)	3.8
H10(2s)	3.5
H26(2s)	3.1
H35(2s)	3.0
Total	
Y	15.8
Ligand	84.2

Supplementary Table 22. Contributions > 3% to the natural SOMO for state 6 in **1** (total for atomic angular momenta).

AO	**Contribution (%)**
H31(2s)	7.9
H32(2s)	7.8
H14(2s)	4.2
H12(2s)	3.7
H16(2s)	3.6
H18(2s)	3.4
Total	
Y	6.9
Ligand	93.1

Supplementary Table 23. Contributions > 3% to the natural SOMO for state 7 in **1** (total for atomic angular momenta).

AO	**Contribution (%)**
H35(2s)	8.4
H36(2s)	4.3
H24(2s)	3.9
H22(2s)	3.4
H9(2s)	3.2
Total	
Y	5.9
Ligand	94.1

Supplementary Table 24. Contributions > 3% to the natural SOMO for state 8 in **1** (total for atomic angular momenta).

AO	**Contribution (%)**
H2(2s)	5.5
H21(2s)	4.7
H13(2s)	4.4
H15(2s)	4.1
H27(2s)	3.7
H5(2s)	3.4
H7(2s)	3.3
Y(6d)	3.3
H8(2s)	3.3
H14(2s)	3.1
H20(2s)	3.1
Total	
Y	7.4
Ligand	92.6

Supplementary Table 25. Contributions > 3% to the natural SOMO for state 9 in **1** (total for atomic angular momenta).

AO	**Contribution (%)**
Y(4d)	59.5
Y(5d)	20.3
Total	
Y	82.6
Ligand	17.4

Supplementary Table 26. Contributions > 3% to the natural SOMO for state 10 in **1** (total for atomic angular momenta).

AO	**Contribution (%)**
Y(4d)	58.2
Y(5d)	21.2
Total	
Y	82.7
Ligand	17.3

Supplementary Table 27. Occupation numbers in the state averaged CASSCF calculation for the crystalline geometry of **1** with a sphere of point charges.

Orbital	131	132	133	134	135	136	137	138	139	140	141	142
Occupation	1.95	1.95	0.15	0.10	0.11	0.10	0.14	0.10	0.10	0.10	0.10	0.10

Supplementary Table 28. Contributions > 3% to the natural SOMO for state 11 in **1** with a sphere of point charges (total for atomic angular momenta).

AO	**Contribution (%)**
Y(4d)	48.5
Y(5s)	5.6
Total	
Y	56.5
Ligand	43.5

Supplementary Table 29. Contributions > 3% to the natural SOMO for state 2 in **1** with a sphere of point charges (total for atomic angular momenta).

AO	**Contribution (%)**
H18(2s)	25.9
H10(2s)	10.2
H26(2s)	6.3
H17(2s)	5.7
H19(2s)	5.2
H18(1s)	4.5
C7(2s)	4.0
Y(4d)	3.9
H25(2s)	3.0
Total	
Y	10.7
Ligand	89.3

Supplementary Table 30. Contributions > 3% to the natural SOMO for state 3 in **1** with a sphere of point charges (total for atomic angular momenta).

AO	**Contribution (%)**
H29(2s)	14.3
H28(2s)	12.5
Y(6p)	5.6
Y(5p)	4.0
Y(4d)	3.8
Y(7p)	3.6
H27(2s)	3.2
H34(2s)	3.0
Total	
Y	19.9
Ligand	80.1

Supplementary Table 31. Contributions > 3% to the natural SOMO for state 4 in **1** with a sphere of point charges (total for atomic angular momenta).

AO	**Contribution (%)**
H11(2s)	12.6
H25(2s)	8.1
H24(2s)	7.4
H37(2s)	6.7
Y(6p)	5.2
H38(2s)	4.3
H39(2s)	3.3
Y(6s)	3.2
Total	
Y	19.5
Ligand	80.5

Supplementary Table 32. Contributions > 3% to the natural SOMO for state 5 in **1** with a sphere of point charges (total for atomic angular momenta).

AO	**Contribution (%)**
Y(4d)	8.5
H3(2s)	8.2
H2(2s)	6.8
H1(2s)	5.1
Total	
Y	14.9
Ligand	85.1

Supplementary Table 33. Contributions > 3% to the natural SOMO for state 6 in **1** with a sphere of point charges (total for atomic angular momenta).

AO	**Contribution (%)**
Y(4d)	32.9
H3(2s)	3.2
Total	
Y	40.2
Ligand	59.8

Supplementary Table 34. Contributions > 3% to the natural SOMO for state 7 in **1** with a sphere of point charges (total for atomic angular momenta).

AO	**Contribution (%)**
H16(2s)	8.2
H15(2s)	7.7
H21(2s)	6.0
H14(2s)	5.0
H22(2s)	3.3
H8(2s)	3.2
Y(4d)	3.2
Total	
Y	7.5
Ligand	92.5

Supplementary Table 35. Contributions > 3% to the natural SOMO for state 8 in **1** with a sphere of point charges (total for atomic angular momenta).

AO	**Contribution (%)**
H25(2s)	6.4
H35(2s)	5.2
H36(2s)	4.3
Y(4d)	4.1
H34(2s)	3.8
H39(2s)	3.5
H38(2s)	3.4
Y(6d)	3.2
Total	
Y	12.0
Ligand	88.0

Supplementary Table 36. Contributions > 3% to the natural SOMO for state 9 in **1** with a sphere of point charges (total for atomic angular momenta).

AO	**Contribution (%)**
C17(2p)	23.2
C18(2p)	21.5
C19(2p)	9.6
Y(4d)	5.2
C21(3d)	4.4
C18(3d)	4.3
C17(3d)	4.0
C19(3d)	3.7
Y(5f)	3.7
C20(3d)	3.2
Total	
Y	11.9
Ligand	88.1

Supplementary Table 37. Contributions > 3% to the natural SOMO for state 10 in **1** with a sphere of point charges (total for atomic angular momenta).

AO	**Contribution (%)**
C20(2p)	26.6
C21(2p)	22.2
C19(2p)	7.3
C17(2p)	4.8
C20(3d)	3.7
C19(3d)	3.6
C21(3d)	3.6
C17(3d)	3.3
Total	
Y	7.9
Ligand	92.1

Supplementary Methods

All manipulations and syntheses were conducted with rigorous exclusion of air and water using standard Schlenk line and glovebox techniques under an argon or dinitrogen atmosphere. Solvents were sparged with UHP argon and dried by passage through columns containing Q-5 and molecular sieves prior to use. 2.2.2-Cryptand (4,7,13,16,21,24-hexaoxa-1,10-diazabicyclo[8.8.8]hexacosane, Aldrich) was placed under vacuum (10^{-3} Torr) for 12 h before use. Anhydrous $LnCl_3$ (Ln = Y, Yb),[1] $KC_5H_4SiMe_3$,[2] $(C_5H_4SiMe_3)_3Ln$ (Ln = Y,[3] Yb[4]), potassium graphite,[5] and $[K(2.2.2\text{-cryptand})][(C_5H_4SiMe_3)_3Ln]$ (Ln = Y (**1**),[6] Yb[4]) were prepared according to literature procedures. Magnetically dilute complex **~2% 1@5** was obtained by recrystallization from a solution mixture that contained the appropriate amounts of isostructural $[K(2.2.2\text{-cryptand})][(C_5H_4SiMe_3)_3Y]$ (**1**) and $[K(2.2.2\text{-cryptand})][(C_5H_4SiMe_3)_3Yb]$ compounds, the latter acting as the diamagnetic matrix. The molecular structure of compound **1** is presented in Supplementary Figure 1.

Synthesis of single crystals of ~2% 1@5 (2% doping level): In an argon atmosphere glovebox, [K(2.2.2-cryptand)][($C_5H_4SiMe_3$)$_3$Y] (2 mg, 0.002 mmol) and [K(2.2.2-cryptand)][($C_5H_4SiMe_3$)$_3$Yb] (100 mg, 0.09 mmol) were dissolved in 1 mL of THF to afford a dark green solution. Dark green single crystals of **~2% 1@5** were grown over two days at −35 °C from slow vapor diffusion of Et_2O into the THF solution.

Continuous-wave EPR Measurements. Continuous-wave (CW) electron paramagnetic resonance (EPR) spectra of solution samples of **1** (Figs. 2a) were recorded on either a Bruker EMX 300 or a Bruker ElexSys E580 EPR spectrometer operating at X-band (*ca.* 9.4-9.8 GHz) and variable temperatures. CW EPR spectra of oriented single crystals of **~2% 1@5** (Supplementary Figure 3) were collected with a Bruker ElexSys E580 instrument operating at *ca.* 9.7 GHz and varied temperatures, and equipped with a goniometer that allowed controlled crystal rotation. An identical setup was used to measure the same crystal by echo-detected pulsed-EPR methods (see below). Crystals were indexed by X-ray crystallography to determine the precise orientation of the crystallographic axes. Similarly to **1** and its Yb analogue, compound **~2% 1@5** crystallises in a Monoclinic ($P2_{1/C}$) space group. Its single crystal unit cell parameters: a = 16.22 Å, b = 24.79 Å, c = 14.04 Å, α = 90°, β = 90.57°, γ = 90°, and V = 5344, are similar to those of **1** (a = 15.8992(9) Å, b = 24.2949(14) Å, c = 13.7571(8) Å, α = 90°, β = 91.0257(8)°, γ = 90°, V = 5313.1(5) Å^3),[6] and diamagnetic host [K(2.2.2-cryptand)][($C_5H_4SiMe_3$)$_3$Yb] (a = 15.9471(5) Å, b = 24.2284(8) Å, c = 13.8243(5) Å, α = 90°, β = 91.1563(4)°, γ = 90°, and V = 5340.2(3) Å^3).[4] We note that molecules pack in the crystal in different ways, being classified in two groups: **A** and **B**, whose C_3 axes (that is the axis perpendicular to the plane made by the centroids of the three Cp' ligands bound to Y^{2+}) are orthogonal. As such, we have chosen to rotate the crystal around the C_3 axis of one of such molecules, in order to access such an orientation that molecules **B** would have their C_3 axis parallel to the static B_0 field (Supplementary Figure 3), while molecules **A** remained aligned with C_3 perpendicular to B_0. This allowed determination of both g_z and $g_{x,y}$ components at the same time (Table 2, main text). Spectra were simulated using the EasySpin software.[7]

Pulsed EPR Measurements. Pulsed EPR spectra were recorded with a Bruker ElexSysE580 instrument equipped with either a MD5 or a MD4 resonator, and operating at *ca*. 9.7 GHz and various temperatures. Solution samples of different concentrations (2, 5 and 10 mM in THF) were investigated to check reproducibility and to achieve an acceptable signal-to-noise response in HYSCORE and ENDOR experiments. Single crystal measurements I involved an identical instrumental set-up as described above.

Echo-detected EPR. The echo-detected field–swept (EDFS) spectra (Figs. 2a, 2b and Supplementary Figure 4) were recorded with a two-pulse primary Hahn-echo sequence ($\pi/2$ - τ - π - τ - *echo*),[8] with microwave pulse lengths of 16 and 32 ns, respectively, a fixed delay time τ = 300 ns, and with the variation of the static B_0 magnetic field.

Phase Memory Time (T_m). Electron spin echo envelope modulation (ESEEM) measurements involved monitoring the echo intensity generated with a primary Hahn-echo sequence as a function of τ. A similar pulse sequence was used to measure the phase memory time, T_m, with the difference that longer pulse durations (up to 512 nm) were necessary to suppress possible ^{1}H nuclear modulation effects in the echo decays (Supplementary Figure 5). T_m was determined by least squares fitting of the experimental echo decay data using a stretched exponential function with a solver based on the Levenberg-Marquardt algorithm.

The fitting function used was:

$Y(2\tau) = Y(0)e^{(-2\tau/T_m)X}$ (Equation 1)

or, for strongly modulated data,

$Y(2\tau) = Y(0)e^{(-2\tau/T_m)X}(1 + k\sin(\omega t + \Phi))$ (Equation 2)

where k is the modulation depth, ω is the Larmor angular frequency of a nucleus I coupled to the electron spin, ϕ is the phase correction, X is the stretching parameter, $Y(2\tau)$ is the echo integral for a pulse separation τ, and $Y(0)$ is the echo intensity extrapolated to $\tau = 0$.[9-12]

The extracted T_m times for **1** and **~2% 1@5** are given in Supplementary Tables 1 and 2. Owing to the 2p-ESE decays being dependent on experimental conditions, with longer (more selective) pulses resulting in longer relaxation decays (Supplementary Figure 6), comparison between the extracted T_m values at those temperatures must be regarded with caution.

Spin–lattice Relaxation Time (T_1). Spin-lattice relaxation time data (Supplementary Figures 7 and 8) were acquired with a standard magnetisation inversion recovery sequence, π–t–$\pi/2$–τ–π–τ–*echo*,[8] with t_π = 32 ns, τ = 320 ns, and variable t. The spin-lattice relaxation time constant, T_1, was determined by fitting the experimental data to the following biexponential decay function:

$Y(t) = Y(0) + Y_1e^{(-t/T_1)} + Y_{SD}e^{(-t/T_{SD})}$ (Equation 3)

where Y_1 and Y_{SD} are the amplitudes, and T_{SD} is the spectral diffusion time constant,[11] giving the results presented in Figs. 2e, 2f and S9, and Supplementary Tables 3 and 4. The presence of two decays is commonly attributed to the occurrence of both spectral diffusion and spin-lattice relaxation of which the latter is usually assigned as being the slower process.[12] We notice that the magnetization recovery curves do not reach full saturation below 15 K, indicating that the T_1 spin-lattice relaxation time is very long. Fitting such curves to an exponential model is likely to introduce some inaccuracy in the determination of the T_1 values at these temperatures.

Transient Nutation Experiments (Rabi oscillations). The transient nutation data (Figs. 2c and 2d, and Supplementary Figures 11 to 22) were acquired with a three-pulse nutation sequence, t_p–t_w–π/2–τ–π–τ–*echo*.[8,13] The length of the tipping pulse, t_p, pulse was varied in 2 ns increments, whilst those of the pulses π/2 and π were kept fixed at the optimal values needed to generate a maximum echo intensity, for $t_p = 0$. The t_w and τ delays were kept constant at 6 μs (chosen to be much longer than T_m) and 200 ns, respectively. The Rabi frequency, Ω_R, was determined by zero-filling the Rabi oscillation curves, followed by Fast Fourier Transform (FFT). Ω_R is expected to vary linearly with B_1, as opposed to nuclear modulations that are insensitive to the strength of B_1 (Supplementary Figures 16 and 23) (11).

HYSCORE (Hyperfine sub–level correlation) Measurements. The HYSCORE spectra were recorded with a four–pulse sequence, π/2–τ–π/2–t_1–π–t_2–π/2–*echo*,[8] with pulses π/2 and π of 16 and 32 ns, respectively, and fixed τ (130, 200 or 400 ns). Times t_1 and t_2 were varied from 100 to 5200 ns in increments of 20 ns. 256 data points were collected in both dimensions. A four-step phase-cycle procedure was used to eliminate unwanted echo contributions. Fourier transformation of the data in both directions yielded 2D (υ_1,υ_2) spectra (Figure 3a,c and Supplementary Figures 26 and 27) in which the nuclear cross-peaks (i.e. peaks that correlate nuclear frequencies from opposite spin-manifolds) of the ^{1}H and ^{13}C nuclei appeared in the (+,+) quadrant of the (υ_1,υ_2) map, at separations equivalent with the corresponding hyperfine coupling frequencies (weak coupling regime: $2|\upsilon_n|>|A|$).[8] The contour lineshape of the cross peaks, and their displacement from the anti-diagonal about the nuclear Larmor frequency (υ_n), relate to the magnitude and anisotropy of the hyperfine couplings, and thus analysis of the HYSCORE spectra allows to determine such parameters. Spectra modelling with EasySpin[7] has assumed that the total hyperfine coupling matrix (**A**) for a given ^{13}C nucleus *n* is determined by the spin density at nucleus *n* ($\mathbf{A}^{Cn}$), and the point dipole (through space) interactions with spin density at other atoms k ($\mathbf{A}^{dip}$), according to the equation: $\mathbf{A} = \mathbf{A}^{Cn} + \mathbf{A}^{dip}$.[10] $\mathbf{A}^{Cn}$ relates directly to the covalency. A^{dip} is given by Equation (4):

$$A^{\mathrm{dip}} = \frac{\mu_0}{4\pi h}\beta_e\beta_n \sum_k \rho_k \frac{3(\mathbf{g}.\mathbf{n_k})(\tilde{\mathbf{n}}_\mathbf{k}.g_n\mathbf{1}) - \mathbf{g}.g_n\mathbf{1}}{r_k^3} \qquad \text{(Equation 4)}$$

where **g** and $g_n\mathbf{1}$ are the electron and nuclear **g** (3x3) matrices (g_n is a scalar; **1** is the unit matrix), β_e and β_n are the electron and nuclear magnetons, ρ_k is the electron spin population at atom k ($0 \leq \rho_k \leq 1$), r_k is $n\ldots k$ distance, $\mathbf{n}_k$ and $\tilde{\mathbf{n}}_k$ are the $n\ldots k$ unit vector expressed in the molecular frame (a column vector) and its transpose, h is the Plank's constant, and μ_0 is the vacuum permittivity. It is also assumed that g_z lies along the C_3 unique axis (Supplementary Figure 24), and the dominant spin density is located at the yttrium ion (ρ_Y = 1). $\boldsymbol{A}^{\mathrm{dip}}$ is then calculated for each unique carbon position in the Cp' ligands, using the crystallographic coordinates of the atoms. Simulations considering only $\mathbf{A}^{\mathrm{dip}}$ do not produce satisfactory results (Supplementary Figure 25). By contrary, addition of $\mathbf{A}^{\mathrm{Cn}}$ to $\mathbf{A}^{\mathrm{dip}}$ allows to reproduce the experimental data (Figs. 3a,b and Supplementary Figure 26). As the non-metal frontier orbitals of $[Y(Cp')_3]^-$ comprise the π-systems of the Cp' rings, the bulk of any spin density transferred from the metal ion will be in these C 2pπ - orbitals.[10,15] Thus, for each matrix $\boldsymbol{A}^{\mathrm{Cn}}$ (assumed to be axial) we fix the unique axis to be oriented along the 2pπ direction (*i.e.* in the molecular xy plane), which allows to determine A_z and $A_{x,y}$ per each C site (Table 2, main text). The $2p_\pi$ spin population (ρ_p) at the individual carbon positions can be derived from Equation (5):[10]

$$A_{\parallel} - A_{\perp} = 6/5\rho_p P_p \qquad \text{(Equation 5)}$$

where P_p is the electron nuclear dipolar coupling parameter for unit population (ρ_p = 1) of a ^{13}C 2p orbital. Using the theoretical value of P_p = 268 MHz[15], we derive C $2p_\pi$ spin populations of ρ_p = 0.008 and 0.002, i.e. 0.8% at C2 and C5, and 0.2%, at C3 and C4.

Modelling of ^{1}H HYSCORE region for **1** involved a similar approach. We initially calculated the point dipolar ^{1}H hyperfine constants for all protons of the cyclopentadienyl rings, and all protons of the methyl groups supposed to be close to the Y(II) ion. This calculation failed to reproduce the experimental data. We then added a contribution from the C $2p_\pi$ spin density on the Cp' ligands, which can occur via spin polarisation of the C-H bond.[10,16] Generally, the hyperfine coupling of an α-proton in a π radical has its principal values oriented with the smallest component along the C-H vector, one along the $2p_\pi$ direction, and the largest component orthogonal to the $2p_\pi$ and C-H directions.[17] As the C-H bonds of the Cp' rings are in the molecular xy plane, we expect the largest component to be oriented along the molecular z-axis (C_3 axis). The hyperfine matrix takes the form $[a_H/2, a_H, 3a_H/2]$, where a_H is the isotropic component, expected to have a negative sign. Best simulation of the ^{1}H HYSCORE data was achieved with a_{iso} = -0.7 MHz (Figs. 3c,d and Supplementary Figure 27). The isotropic hyperfine constant a_H at the α-proton relates to the spin density in the asociated C $2p_\pi$ orbital by the simple McConnell relationship: $a_{iso} = Q_{CH}*\rho_{p,}$, where Q_{CH} is the ^{1}H hyperfine coupling expected to be observed for $\rho_p = 1$. With Q_{CH} = - 84 MHz (determined from studies of Cp radicals)[17] and a_{iso} = -0.7 MHz, we get ρ_p = 0.00833 (**0.83 %**) for $C^{2,5}$ in excellent agreement with ρ_p = 0.008 from analysis of the ^{13}C data. This gives a total of ~ 6 % spin population on the three Cp' rings.

ENDOR (Electron nuclear double resonance) Measurements. Davies-ENDOR data (Supplementary Figure 28) were acquired with the standard pulse sequence, π–πRF–π/2–τ–π–τ–*inverted echo,*[19] with microwave pulses π/2 and π of 128 and 256 ns, respectively. Mims-ENDOR data (Supplementary Figure 29) were recorded by using a stimulated-echo sequence, π/2–τ–π/2–πRF–π/2–τ–*stimulated echo,*[19] based on three non-selective π/2 pulses (16 ns). In both cases, a radiofrequency pulse πRF of 12 μs was used. In order to correct the effect of potential blind spots, Mims-ENDOR spectra were collected at different inter-pulse delays, τ (200-600 ns). Spectra were simulated using Stoll's Easy Spin software,[26] yielding a_{iso} = -0.7 MHz for $H^{2/5}$ and a_{iso} = -0.27 MHz for $H^{3/4}$, which are in good agreement with the HYSCORE data.

DFT calculations. All DFT calculations were performed using ORCA 4.0.0.2 (18) with the unrestricted Kohn-Sham formalism on the *S* = 1/2 ground state of the anions in **1-4**. For geometry optimisations we started with the crystal structures, employed the PBE functional with the second order DKH transformation for the relativistic Hamiltonian, used the RI approximation for both the Coulomb and exchange integrals (using the SARC/J auxiliary basis) and Grimme's D3BJ dispersion corrections (19), along with tight SCF convergence criteria (TIGHTSCF, Grid3, FinalGrid5); basis sets are given in Supplementary Table 10. Only for **3** ($[La(Cp')_3]^-$) did we have problems with such an optimisation strategy, which could be resolved using the ZORA relativistic Hamiltonian.

To calculate the hyperfine coupling, most calculations employed the second order DKH transformation for the relativistic Hamiltonian, however we also checked that our results were consistent when employing the ZORA Hamiltonian; in both cases picture change effects were accounted for by setting the "picturechange" flag to "true". In all cases the non-metal atoms were described with the appropriate def2-TZVP basis set (either DKH-def2-TZVP or ZORA-def2-TZVP) (20). All calculations employed the RI approximation for both the Coulomb and exchange integrals where appropriate, employing the SARC/J auxiliary basis sets. To explore the metal atom basis set and exchange-functional dependence of these calculations, we performed hyperfine calculations for the crystal structure of **1** (Supplementary Table 11), finding an isotropic Y hyperfine coupling of *ca.* -100 MHz in all cases. We also found no significant changes using the ZORA Hamiltonian (Supplementary Table 12), nor when accounting for the electrostatic potential of the crystalline environment by using a sphere of 30 Å radius of point charges located at the K and Y lattice sites, with charges of +1 and -1, respectively (Supplementary Table 13).

As there was no significant effect on the obtained hyperfine parameters for the anion in **1** upon change of metal basis set, functional, relativistic Hamiltonian or inclusion of the crystalline electrostatic potential, we subsequently calculated the hyperfine parameters for both crystalline and optimised structures for the anions of **1-4** in the gas phase using the PBE functional, the appropriate def2-TZVP basis set, and the DKH Hamiltonian (Supplementary Table 14). Overall we find excellent agreement with the experimental data (Table 1 in main text), where all metal hyperfine coupling parameters and the *g*-values are nearly isotropic.

The orbital breakdown of the spin densities for **2-4** are remarkably similar to that described in the main text for **1**; only 50 – 80% of the spin density is located on the metal atom, in predominantly s and d functions (Supplementary Table 14). Despite the significant d-component and "d_{z^2}" appearance of the spin density (Figure S30), the anisotropies of the calculated metal hyperfines ($|A_z^Y - A_{x,y}^Y|/|A_{iso}^Y|$) are only on the order of 1 – 7% (Supplementary Table 14).

CASSCF calculations. State-averaged CASSCF calculations for the anion in **1** were performed with MOLCAS 8.0 (21). We used basis sets from the ANO-RCC library (22,23) with VTZP quality for the Y ion, VDZP quality for the Cp ring carbon atoms, and VDZ quality for all other atoms. The two electron integrals were Cholesky decomposed with a threshold of 10^{-8}. We employed an active space of 7 electrons in 16 orbitals (Supplementary Figures 31 to 33 and Supplementary Table 15), which was optimised for the 10 lowest-lying states (Supplementary Table 16). The natural orbitals (SOMOs) for each root were obtained by diagonalising the state-specific first-order density matrix (Supplementary Figures 34 to 43 and Supplementary Tables 17 to 26). Our calculations with a sphere with radius 30 Å of point charges at the K and Y lattice sites with +1 and -1 charges, respectively, yielded the appropriate active space as 5 electrons in 12 orbitals (Supplementary Figures 44 and 45 and Supplementary Table 27). The corresponding natural orbitals (SOMOs) for the ground state are practically identical to the gas-phase result (Supplementary Figure 46 and Supplementary Table 28), and states 2 – 5 are also diffuse ligand-based functions

(Supplementary Figures 47 to 50 and Supplementary Tables 29 to 32). However, state 6 at 19,634 cm^{-1} has significant Y 4d character (Supplementary Figure 51 and Supplementary Table 33), which is quite different to the gas-phase calculation, and thus the electrostatic crystalline potential has lowered the first 4d function by *ca.* 10,000 cm^{-1}. States 7 and 8 are diffuse ligand functions like for the gas-phase results (Supplementary Figures 52 and 53 and Supplementary Tables 34 and 35), however now states 9 and 10 are π* orbitals on the Cp' ring that is proximate to the K$^+$ counter ion (Supplementary Figures 54 and 55 and Supplementary Tables 36 and 37); these charge transfer states are now much lower in energy due to the stabilisation from the positive charge of the K$^+$ cation. Despite these differences in the higher energy states, the ground state SOMO and the diffuse character of the low-lying ligand-based excited states remains, and appears to be an intrinsic feature of this molecule.

Supplementary References

1. Taylor, M. D. *Chem. Rev.* **1962**, *62*, 503-511.
2. Peterson, J. K.; MacDonald, M. R.; Ziller, J. W.; Evans, W.J. *Organometallics* **2013**, *32*, 2625-2631.
3. MacDonald, M. R.; Ziller, J. W.; Evans, W. J. *J. Am. Chem. Soc.* **2011**, *133*, 15914-15917.
4. Fieser, M. E.; MacDonald, M. R.; Krull, B. T.; Bates, J. E.; Ziller, J. W.; Furche, F.; Evans, W. J. *J. Am. Chem. Soc.* **2015**, *137*, 369-382.
5. Bergbreiter, D. E; Killough, J. M. *J. Am. Chem. Soc.* **1978**, *100*, 2126-2134.
6. MacDonald, M. R.; Bates, J. E.; Ziller, J. W.; Furche, F.; Evans, W. J. *J. Am. Chem. Soc.* **2013**, *135*, 9857-9868.
7. S. Stoll, R. D. Britt, *Phys. Chem. Chem. Phys.*, **2009**, *11*, 6614-6625.
8. A. Schweiger, J. Jeschke, Principles of Pulse Electron Paramagnetic Resonance, Oxford University Press (2001).

9. C. J. Wedge, G. A. Timco, E. T. Spielberg, R. E. George, F. Tuna, S. Rigby, E. J. L. McInnes, R. E. P. Winpenny, S. J. Blundell, and A. Ardavan, *Phys. Rev. Lett.* **2012**, *108*, 107204/1-107204/5.

10. A. Formanuik, A.-M. Ariciu, F. Ortu, R. Beekmeyer, A. Kerridge, F. Tuna, E. J. L. McInnes, D. Mills, *Nature Chem.* **2017**, *9*, 578-583.

11. K. S. Pedersen, A.-M. Ariciu, A. McAdams, H. Weihe, J. Bendix, F. Tuna, S. Piligkos, *J. Am. Chem. Soc.* **2016**, *138*, 5801-5804.

12. K. Bader, M. Winkler, J. van Slageren, *Chem. Commun.* **2016**, *52*, 3623-3626.

13. J. Yang, Y. Wang, Z. Wang, X. Rong, C. K. Duan, J. H. Su, J. Du, *J. Phys. Rev. Lett.*, **2012**, *108*, 230501.

14. M. J. Graham, J. M. Zadrozny, M. Shiddiq, J. S. Anderson, M. S. Fataftah, S. Hill, D. E. Freedman, *J. Am. Chem. Soc.* **2014**, *136*, 7623.

15. J. R. Morton, K. F. Preston, *J. Magn. Reson.*, **1978**, *30*, 577-582.

16. N. M. Atherton. Principles of electron spin resonance, Ellis Horwood Ltd (1993).

17. F. Gerson, W. Huber, Electron spin resonance spectroscopy of organic radicals. Wiley-VCH (2003).

18. Neese, F. The ORCA program system. *WIREs Comput. Mol. Sci.* **2**, 73–78 (2012).

19. S. Grimme, J. Antony, S. Ehrlich, H. Krieg, *J. Chem. Phys.* **132**, 154104 (2010).

20. Weigend, F. & Ahlrichs, R. Balanced basis sets of split valence, triple zeta valence and quadruple zeta valence quality for H to Rn: Design and assessment of accuracy. *Phys. Chem. Chem. Phys.* **7**, 3297–3305 (2005).

21. Aquilante, F. *et al.* Molcas 8: New capabilities for multiconfigurational quantum chemical calculations across the periodic table. *J. Comput. Chem.* **37**, 506–541 (2016).

22. Roos, B. O., Lindh, R., Malmqvist, P.-Å., Veryazov, V. & Widmark, P.-O. Main Group Atoms and Dimers Studied with a New Relativistic ANO Basis Set. *J. Phys. Chem. A* **108**, 2851–2858 (2004).

23. Roos, B. O., Lindh, R., Malmqvist, P.-Å., Veryazov, V. & Widmark, P.-O. New Relativistic ANO Basis Sets for Transition Metal Atoms. *J. Phys. Chem. A* **109**, 6575–6579 (2005).

Chapter V - Manuscript draft 1

Low-valent Sc and Lu Organometallic Complexes as Qudits with an Increased Hilbert Space

Lydia E. Nodaraki,[1,2] Ana-Maria Ariciu,[1,2] Daniel N. Huh,[3] Richard E.P. Winpenny,[1] Eric J. L. McInnes,[1,2] William J. Evans[3] and Floriana Tuna[1,2]

[1]School of Chemistry, The University of Manchester, Oxford Road, Manchester M13 9PL, UK
[2]Photon Science Institute, The University of Manchester, Oxford Road, Manchester M13 9PL, UK
[3]Department of Chemistry, University of California, Irvine, CA 92697-2025

Abstract: The design of molecular spin systems for quantum information technologies demands the engineering of their electronic structures and ligand environments in order to reduce spin decoherence. Herein we investigate the spin dynamics and coherence properties of two divalent lanthanide organometallic complexes [K(2.2.2-cryptand)][Lu(Cp′)$_3$] (**1**) (Cp′ = $C_5H_4SiMe_3$) and [K(2.2.2-cryptand)][Sc{N(SiMe$_3$)$_2$}$_3$] (**2**) which demonstrated potential as electronic spin-based qubits. Long spin lattice (T_1) relaxation and phase coherence (T_2) times were measured by pulse EPR spectroscopy, with the latter reaching 3 μs and 2 μs, respectively; the long coherence times allow coherent spin manipulation of each electronuclear transition at relatively high temperatures (80 K for **1** and 60 K for **2**). HYSCORE spectroscopy was also involved to study the influence of the metal-ligand covalency on coherence properties, demonstrating significantly greater total spin density of 21% on the ligands of **1** compared to the previously reported of 6% of the [Y(Cp′)$_3$]$^-$ analogue.[1]

INTRODUCTION

There is a significant current interest in the development of molecular magnetic systems with ability to fulfill the so-called DiVincenzo criteria[2] for the implementation of quantum computing. According to these criteria a quantum bit (or qubit) must be a well-defined and scalable multi-level quantum system that displays a sufficiently long coherence time (i.e. the lifetime of the superposition state), is capable to be initialized into a specific introductory state,[3] is individually measurable, and is able to form universal quantum gates. Various systems have been proposed as qubit candidates such as nitrogen-vacancy pairs in diamonds,[4] electronic defects on silicon,[5] trapped ions[6] and superconductive circuits.[7] Among them electronic[8] and nuclear[9] spins exhibit major advantages as potential spin qubits due to their chemical tenability that enables the development of qubits with long coherence times as well as engineering the interactions between them in order to build scalable qubit architectures for executing quantum algorithms. One serious drawback for utilising molecular spin systems as qubits is the high fragility of the quantum superposition states that can lead to loss of information under strong quantum decoherence conditions.[10] Major decoherence sources for molecular qubits include the magnetic noise originating from dipolar or electro-nuclei hyperfine interactions,[11] and the molecular thermal vibrations (phonons).[12] Several strategies to reduce quantum decoherence have been proposed, including the removal of the nuclear spins from the immediate surroundings of the electron spins, e.g. using nuclear-spin free ligands or solvents,[13] use of increased magnetic dilutions,[14] and use of highly rigid ligands.[15]

In a recent study we have demonstrated that a divalent Y complex[1] with a ^2S configuration exhibits robust quantum coherence due to its highly isotropic spin state, which makes the putative qubit insensitive to its environment. Following this study, we now report the investigation of the electronic and coherent properties of other two complexes, [K(2.2.2-cryptand)][Lu(Cp′)$_3$] **1** (Cp′ = $C_5H_4SiMe_3$) and [K(2.2.2-cryptand)][Sc{N(SiMe$_3$)$_2$}$_3$] **2**. Herein we targeted metals with higher nuclear spins, i.e. $I = 7/2$ for both Sc and Lu ions, in order to exploit the electronuclear interactions that yields a molecule of four qubit-systems or a qudit with d=8, and exponentially increasing the Hilbert space available for quantum information processing. In both complexes, the metal ion adopts the unusual +2 oxidation state with the unpaired electron residing either in a *d* or *s* orbital. In addition, as a means of probing the influence of the local environment, complex **1** is based on a similar cyclopentadienyl ligand as used in the Y^{II} example, while **2** includes three silyl-amide moieties. Both compounds are 3-coordinate and exhibit a local pseudo-C_3 symmetry, which is important to lower the energy of the d_{z2} orbital of the metal ion. This gives opportunity of orbital admixture between d_{z2} and *s* (4*s* for Sc; 6*s* for Lu) resulting in an *S*-like ground state for the complexes.

RESULTS AND DISCUSSION

Synthesis and characterization

Compound **1** and **2** were synthesized using a previously reported procedure that implies reducing trivalent [Lu(Cp′)$_3$][16] or [Sc{N(SiMe$_3$)$_2$}$_3$][17] with potassium graphite, KC_8, in the presence of [2.2.2]-cryptand. The molecular symmetry of the complexes is *pseudo*-C_{3h}, with the 3-fold unique axis perpendicular to the plane formed by the centroids of the Cp′ ligands in **1** and nitrogen atoms in **2**. The binding of the three ligands to the central metal ion leads in each case to an almost planar trigonal arrangement, with one of the angles formed in each case being slightly higher than the ideal arrangement of 120° degrees (123.26°, 118.51° and 118.20° for **1**; and 119.06°, 122.40° and 118.53° for **2**). Based on the crystal structures of the complexes, the geometric parameters of the $[Lu(Cp')_3]^-$ and $[Sc\{N(SiMe_3)_2\}_3]^-$ (Figure 1) show small differences in the metal to ligand distances leading to average separations of 2.6779 Å for Lu-C and 2.1292 Å for Sc-N. The average Lu…Si distance in **1** is 4.031 Å, while in **2** the structure is formed via a Sc-N direct bond which brings the Si ion closer to the metal at an average bond distance of 3.303 Å. However, the metal to hydrogen atoms distances do not show significant differences between the two complexes, with the closest H atoms found at 3.131 Å for **1** and 3.096 Å for **2**. Furthermore, **1** crystalizes in the monoclinic $P2_1/c$ space group, while **2** in the triclinic space group $P\bar{1}$.

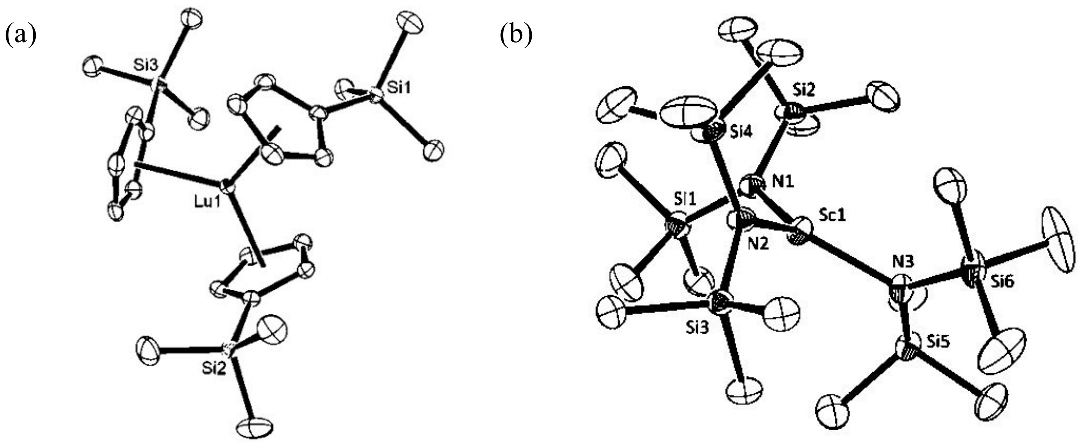

Figure 1. Molecular structure of (a) $[Lu(Cp')_3]^-$ (**1**) and (b) $[Sc\{N(SiMe_3)_2\}_3]^-$ (**2**) anions. Counterions and hydrogen atoms are omitted for clarity.

Electron Paramagnetic Resonance

Frozen solution echo-detected field-swept (EDFS) EPR spectra[18] of complexes **1** and **2** (Figure 2) display an axial 8-line pattern caused by hyperfine interactions of the unpaired electron with the nuclear spins of ^{175}Lu (97.4%, I = 7/2) and ^{45}Sc (100%, I = 7/2), respectively. Simulation of the spectra has provided g- and A-tensor values as follows: $g_{\|}$= 1.975, $g_{\perp}$= 1.945, $A_{\|}$ = 1070 MHz and $A_{\perp}$ = 1121 MHz for **1**, and $g_{\|}$= 1.997, $g_{\perp}$= 1.964, $A_{\|}$ = 640 MHz and $A_{\perp}$ = 620 MHz for **2**. This nearly isotropic feature of the hyperfine tensors would be unusual for a system considered to have an unpaired electron residing in a d_{z2} orbital. It would rather support our assumption that the electron resides in a more isotropic environment of an *s*-orbital.[15]

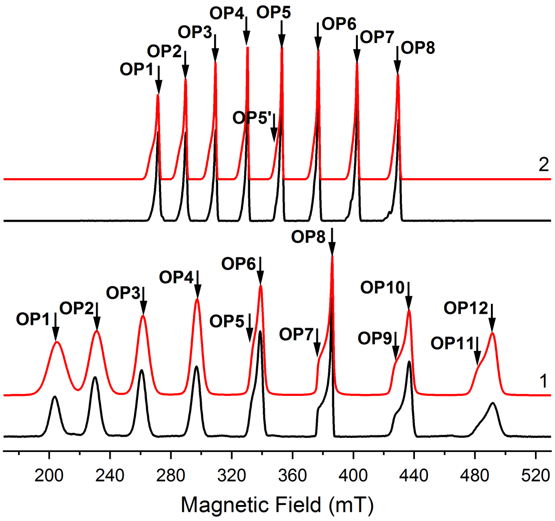

Figure 2. Experimental (black) and simulated (red) X-band (9.71 GHz) EDFS spectra for **1** and **2**, recorded in THF (10 mM) at 5 and 40 K, respectively; simulation parameters are given in Table 1. Observer positions **OP1-OP12** mark the magnetic fields at which time-dependent pulsed EPR data were collected.

Table 1. Extracted EPR parameters for **1** and **2** (10 mM; THF).

	g value	A (MHz)	A (Gauss)
RT	$g_{iso} = 1.974$	$A_{iso} = 1184$	$A_{iso} = 428$ [16]
5 K	$g_{\parallel} = 1.975$; $g_{\perp} = 1.945$	$A_{\parallel}$ (^{175}Lu) = 1070 $A_{\perp}$(^{175}Lu) = 1121	$A_{\parallel}$ (^{175}Lu) = 387 $A_{\perp}$ (^{175}Lu) = 412
RT	$g_{iso} = 1.977$	$A_{iso} = 592$	$A_{iso} = 214$ [17]
40 K	$g_{\parallel} = 1.997$; $g_{\perp} = 1.964$	$A_{\parallel}$ (^{45}Sc) = 640 $A_{\perp}$(^{45}Sc) = 620	$A_{\parallel}$ (^{45}Sc) = 229 $A_{\perp}$(^{45}Sc) = 225

Measurements of the spin lattice relaxation (T_1) and phase memory (T_m) times were performed at several **OP** observer positions as indicated in Figure 2. The spin-lattice relaxation times were obtained by fitting the echo traces (Figures S5 and S6) generated with a standard magnetisation inversion recovery pulse sequence[18] to a bi-exponential function (see the supporting information eqn. 2). T_1 displays both field and temperature dependency and varies from *ca.* 4 μs at 80 K to 29 ms at 5 K (**OP1**; Table S5) for **1**, and from *ca.* 3 μs at 80 K to 33 ms at 5 K (**OP4**; Table S6) for **2**. Phase memory times were estimated by fitting the time decay traces (Figures S3 and S4) of the electron spin echo[18] using a stretch mono-exponential relation[19] (see the supporting information eqn. 1). At lower temperatures, longer length microwave pulses were used to measure T_m as a means to restrict proton modulations that would otherwise impact the 2p-ESE decay. The phase memory times are slightly temperature (but not field) dependent with a higher value of 3 μs for **1** (**OP8**; Table S3) and 2 μs for **2** (**OP5**; Table S4) observed at 5 K. As seen in Figs *S*5 and *S*6, the magnetization recovery curves of **1** and **2** do not reach full saturation at temperatures below 15 K, indicating that T_1 is very long at these temperatures. Fitting such curves to an exponential model is likely to introduce some inaccuracy in the determination of the T_1 values at these temperatures. Moreover, the T_1 relaxation times were fitted using the Raman process described by the $T_1 = C^{-1}T^{-n}$ equation,[20] with the following parameters occurring from the fit: C = 1.14(6) x 10^{-7} μs^{-1}K^{-n} and n = 3.14(6) for **1**; and C = 1.36(7) x 10^{-7} μs^{-1}K^{-n} and n = 2.75(9) for **2**.

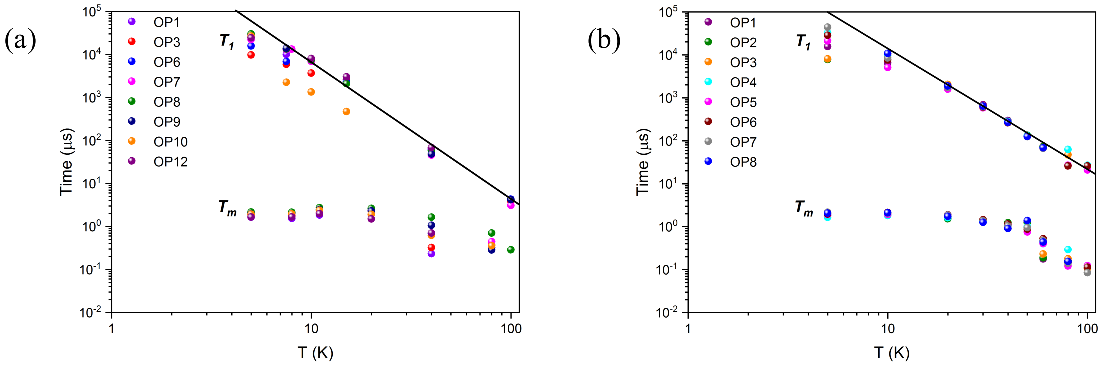

Figure 3. Temperature dependence of T_1 and T_m for a frozen solution (10 mM, THF) of (a) **1** and (b) **2**, measured at X-band and different observer positions, as indicated in Figure 2. The black line in both graphs shows the fitting of the T_1 data above 10 K with the Raman equation, $T_1 = C^{-1}T^{-n}$.

In order to probe that the observed long relaxation times in such highly concentrated sample enable coherent manipulation of the electron-spin, as required for qubits, transient nutation experiments were performed.[21] Thus, insertion of a tipping angle, $\theta = g\mu_B B_1 t_p/\hbar$ in the front of a standard Hahn-echo sequence generates a smooth oscillation on the detected signal, due to the cycling of the electronic spin through all the arbitrary superposition states of its ± M_S sub-states. The resulted oscillations termed as Rabi oscillations[22] are shown in Figure 4, confirming the ability of the system to have eight ^{175}Lu or ^{45}Sc electronuclear states accessible for selective coherent spin manipulations.[23] The Fourier transform analysis shows that the Rabi frequency, Ω_R, is linearly field dependent on the microwave field strength, B_1, as opposed to nuclear modulations that are insensitive to variations in B_1 (Figures 5, S7 and S14).

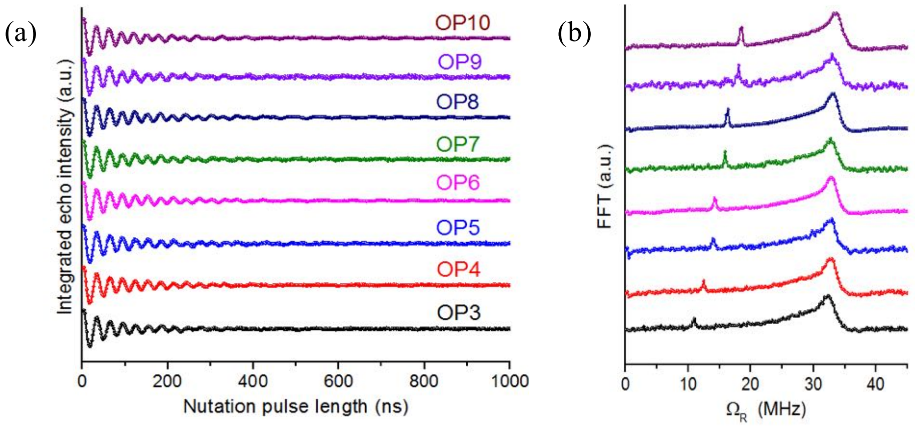

Figure 4. (a) Rabi oscillations for **1** (THF) at 80 K and different field positions (**OP3–OP10**; Figure 2), acquired at 0 dB; (b) corresponding Fourier transforms of the data in (a).

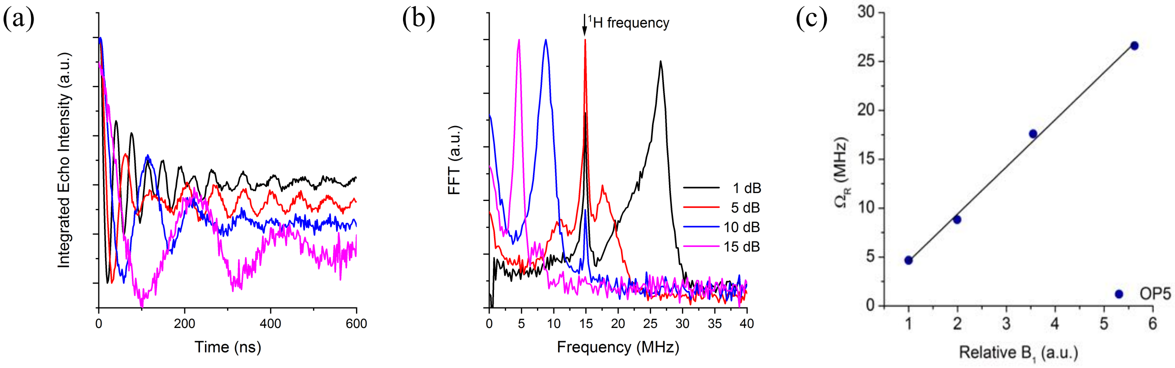

Figure 5. (a) Rabi oscillations for **2** (THF) at 60 K acquired at **OP5** with different applied power (from 1 dB up to 15 dB), (b) corresponding Fourier transforms of data in (a); and (c) B_1 dependence of the Rabi frequency (Ω_R) for **2** with the solid line being the linear fitting of the data.

Closer inspection of the EDFS data for **1** and **2** show a negligible axial anisotropy for both g and A tensors (Table 1) suggesting that the unpaired electron in both systems may not solely reside in a pure d_{z2} orbital. To gain more the understanding of the environment of the metal ions further studies such as two-dimensional hyperfine sublevel correlation (HYSCORE) spectroscopy[18] were performed. HYSCORE was involved with the aim of quantifying the weak hyperfine interactions of the primarily metal-based unpaired electron with the ^{13}C and ^{1}H nuclei of the Cp′ ligands for **1** and ^{14}N and ^{1}H of the amide ligands for **2**, relying on the assumption that some electron spin density from the metal can be transferred towards the ligands.

The HYSCORE data of **1** and **2** (Figures 7-10) were modelled using a previously reported theoretical model,[24] based on the presumption that the total hyperfine coupling matrix (**A**) for a given ^{13}C nucleus n is determined by contribution of the spin density at nucleus n ($\mathbf{A}^{\mathrm{Cn}}$), and the point dipole interactions with spin density at other atoms k ($\mathbf{A}^{\mathrm{dip}}$), according to:

$$\mathbf{A} = \mathbf{A}^{\mathrm{Cn}} + \mathbf{A}^{\mathrm{dip}} \quad \text{(Equation 1)}$$

$\mathbf{A}^{\mathrm{Cn}}$ describes a direct relation to the covalency of the bond, while $\mathbf{A}^{\mathrm{dip}}$ is calculated using the following Equation 2:

$$A^{\mathrm{dip}} = \frac{\mu_0}{4\pi h}\beta_e\beta_n\sum_k \rho_k \frac{3(\mathbf{g}.\mathbf{n_k})(\tilde{\mathbf{n}}_\mathbf{k}.g_n\mathbf{1})-\mathbf{g}.g_n\mathbf{1}}{r_k^3} \quad \text{(Equation 2)}$$

where $\mathbf{g}$ and $g_n\mathbf{1}$ are the electron and nuclear $\mathbf{g}$ (3x3) matrices (g_n is a scalar; 1 is the unit matrix), β_e and β_n are the electron and nuclear magnetons ($\beta_e = 9.27\cdot10^{-24}$ $\mathrm{J\cdot T^{-1}}$; $\beta_n = 5.05\cdot10^{-27}$ $\mathrm{J\cdot T^{-1}}$), ρ_k is the electron spin population at atom k ($0 \le \rho_k \le 1$), r_k is $n\ldots k$ distance (in m), $\mathbf{n}_k$ and $\tilde{\mathbf{n}}_k$ are the $n\ldots k$ unit vector expressed in the molecular frame (a column vector) and its transpose, h is the Plank's constant ($6.63\cdot10^{-34}$ J·s) and μ_0 is the vacuum permittivity ($1.26\cdot10^{-6}$ $\mathrm{T^2\cdot J^{-1}\cdot m^3}$). The nuclear g-values for ^{1}H and ^{13}C are: $g_\mathrm{H} = 5.586$ and $g_\mathrm{C} = 1.405$. For further calculations, it is assumed that only centres that carry significant spin population make significant contribution to **A**.

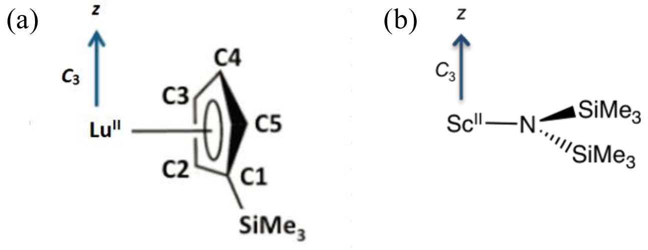

Figure 6. Schematic representation for the binding of (a) $C_5H_4SiMe_3$ (Cp′) ligands in **1,** and (b) $N(SiMe_3)_2$ ligands in **2**, and the direction of the molecular C_3 axis.

Simulation of the experimental ^{13}C HYSCORE data for **1** required calculation of the $\mathrm{A^{dip}}$ for each unique carbon position in the Cp′ ligands using the crystal structure parameters. The three Cp′ ligands bind to metal so that the $\mathrm{Lu^{II}}$ ion lies in the plane defined by the centroids of the three Cp′ rings. Subsequently, we assumed that g_z is along the C_3 unique axis (Figure 6), with the three Cp′ centroids being in the molecular xy plane (idealized C_{3h} point group). Thus, the g-tensor is used to define the molecular axis system. Moreover, as the dominant spin density is located at the lutetium(II) site, $\rho_{\mathrm{Lu}} = 1$ was assumed in all calculations. Simulation of ^{13}C HYSCORE for **OP3** using the dipolar parameters produced unsatisfactory results (Figure 7c), indicating that an only spin-dipole contribution is insufficient.[25] Indeed, addition of $\mathrm{A^{Cn}}$ to $\mathrm{A^{dip}}$ reproduced nicely the experimental data (Figure 7a–b). Each matrix $\mathrm{A^{Cn}}$ assumed to be axial with the unique axis to be oriented along the $2p_\pi$ direction (i.e. in the molecular xy plane). Since the non-metal frontier orbitals of $[\mathrm{Lu(Cp')_3}]^-$ involve the π-systems of the Cp′ rings, any spin density donated from the metal ion to the ligand will be transferred in the $2p_\pi$ orbitals of the carbon atoms.[26] Therefore for the simulation of the carbon region we will use only two free variables per each C site, the $A_{\parallel}^{Cn}$ and $A_{\perp}^{Cn}$. Due to the symmetry of the Cp′ ligand (i.e. the *xy* mirror plane), two different sets of hyperfines will be used as the C_2 and C_5, and C_3 and C_4 are equivalent. After trial-and-error modelling, excellent reproduction of the experimental ^{13}C HYSCORE data for **OP3** was obtained with $A_{\parallel}^{C2,5}$ = 10.26 MHz; $A_{\perp}^{C2,5}$ = 1.14 MHz, and $A_{\parallel}^{C3,4}$ = 2.2 MHz; and $A_{\perp}^{C3,4}$ = 0.6 MHz, where the labels refer to the principal axes of A^{Cn}. Hence, the $2p_{\pi}$ spin population (ρ_p) at the individual carbon positions can be derived from:

$$A_{\parallel} - A_{\perp} = 6/5\rho_p P_p \quad \text{(Equation 3)}$$

where P_p is the electron nuclear dipolar coupling parameter for unit population (ρ_p = 1) of a ^{13}C 2*p* orbital. Using the theoretical value of P_p = 268 MHz[27] it is derived the C $2p_{\pi}$ spin populations of ρ_p = 0.0283 and 0.005, i.e. 2.83% and 0.5%, for $C^{2,5}$ and $C^{3,4}$, respectively.

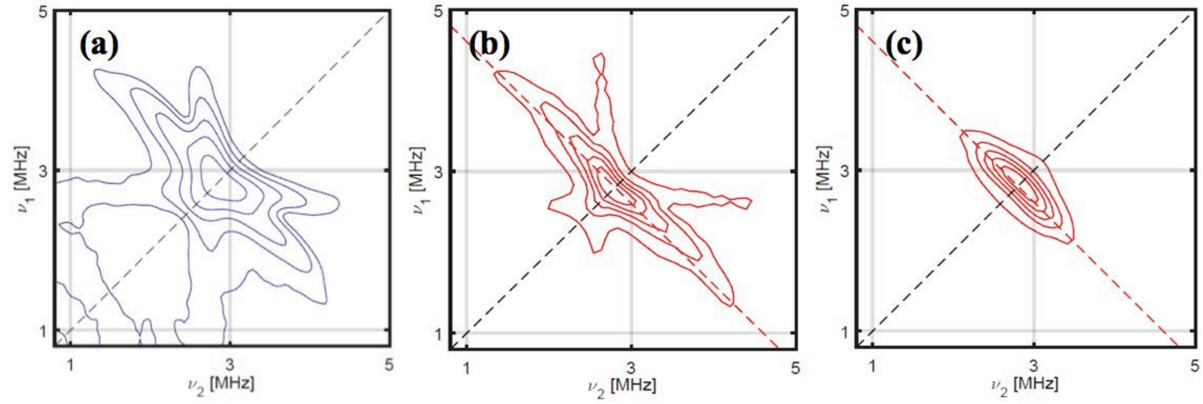

Figure 7. (a) ^{13}C HYSCORE spectrum for **1** (THF) at B_0 = 260.6 mT (OP**3**; Figure 3), T = 15 K, and X-band (9.7098 GHz); (b) Calculation based on the model described in the main text, which includes a dipolar component, and spin densities at $C^{2,5}$ and $C^{3,4}$; (c) Calculation based on the dipole model only. The dashed-red antidiagonal lines mark the ^{13}C Larmor frequency.

Modelling of ^{1}H HYSCORE region for **1** involved a similar approach. At first the point dipolar ^{1}H hyperfine constants for all protons of the cyclopentadienyl rings were calculated, as well as all protons of the methyl groups that were close to the Lu(II) ion, however the dipole only calculation didn’t reproduce the experimental data. For the successful simulation of the experiment an additional to the dipolar contribution should be taken into account; this contribution of the C $2p_{\pi}$ spin density on the Cp′ ligands arise via spin polarisation of the C-H bond.[27] Typically, the principal values of a hyperfine matrix of an α-proton in a π radical are oriented with largest component orthogonal to the $2p_{\pi}$ and C-H directions, with the smallest component along the C-H vector and the third one along the $2p_{\pi}$ direction.[28] In this molecule because of the C2-H2 bond lying in the molecular *xy* plane, the largest component is expected to be oriented along the molecular z-axis (C_3 axis). The hyperfine matrix takes the following form [$\alpha_{H/2}$, α_H, $3\alpha_{H/2}$], where α_H is the isotropic component and is expected to display a negative sign. Best simulation of the ^{1}H HYSCORE data was obtained with $\alpha_{iso} = -2.38$ MHz (Figure 8). McConnell model[29] relates the isotropic hyperfine constant α_H of an α-proton to the spin density of the pertinent C $2p_\pi$ orbital by the following relationship: $\alpha_{iso} = Q_{CH} \cdot \rho_p$, where Q_{CH} is the ^{1}H hyperfine coupling expected to be observed for $\rho_p = 1$. With $Q_{CH} = -84$ MHz (determined from studies of Cp radicals)[28] and $\alpha_{iso} = -2.38$ MHz, we obtain $\rho_p = 0.0283$ (2.83 %) for $C^{2,5}$ in excellent agreement with $\rho_p = 0.0283$ from analysis of the ^{13}C data. This gives a total of ~ 6.66 % spin population on the Cp′ ring.

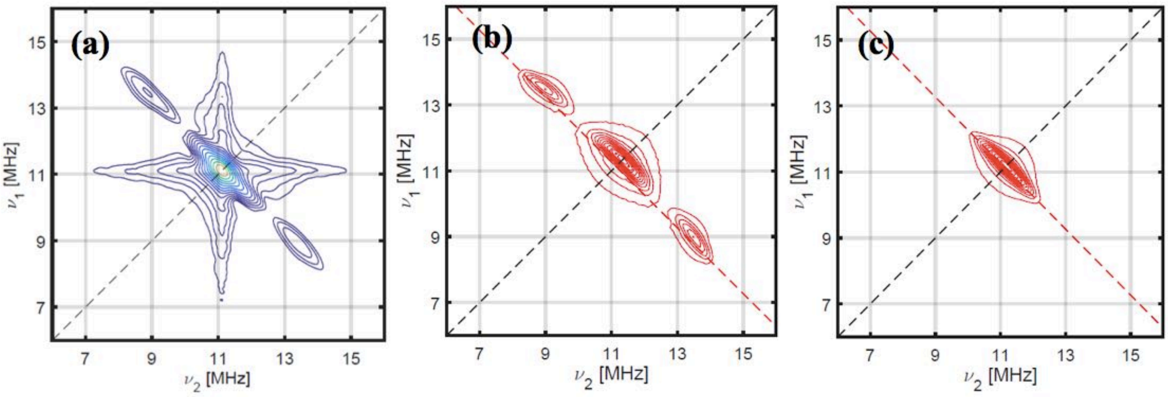

Figure 8. (a) ^{1}H HYSCORE spectrum for **1** (THF) at $B_0 = 260.6$ mT (**OP3**; Figure 3), T = 15 K, and X-band (9.7098 GHz); (b) Calculation based on the model described in the text; (c) Calculation based on the dipole model only. The dashed-red antidiagonal line marks the ^{1}H Larmor frequency.

For complex **2**, HYSCORE signals were only detected in the ^{1}H and ^{14}N region, while in the case of ^{13}C the signal-to-noise ratio is limited by the low natural ratio of ^{13}C as well as the poor electronic density transferred from the ^{45}Sc to the carbon atoms. Hence, the same theoretical point dipole model mentioned above was used for the calculation of the dipolar constants between the electron and the nuclear spins of the ^{1}H and ^{14}N nuclei. Nevertheless, due to the difference in the coordination system of the two compounds the simulation approach is slightly different. Modelling of the ^{14}N ($I = 1$) should consider the quadrupole interaction, while in our case second quantum transitions or any combination of a double quantum, DQ, and a single quantum, SQ, is not observed.[30] Thus, quadrupole parameters were not taken into account for the simulation. Initially, the point dipolar ^{14}N hyperfine constants for the three coordinated nitrogen atoms were calculated, but this model proved to be insufficient for the simulation of the spectra Figure 9a); thus, an additional contribution of spin density on the amide ligands was considered. The simulation of the ^{14}N HYSCORE spectra for **OP5** was performed by assuming equivalent contribution of the three nitrogen atoms (N_1-N_3) on the ligands, as M-N distances do not differ significantly. Adding of a term accounting for the spin polarisation on the nitrogen atom generated ridges that match the spectral features recorded in the strongly coupled quadrant of the HYSCORE spectrum, but the weak coupling region (the right quadrant of the HYSCORE spectrum) was not reproduced (see the supporting information, Figure S20). Adding the contribution of nitrogen atoms of 2.2.2-cryptand, which is present in the structure, enabled a nice modelling of the spectra. The two nitrogen atoms (N_4 and N_5) of the cryptand are considered to be spectroscopically equivalent due to their similar distance from the metal ion. Best simulation of the ^{14}N HYSCORE data was achieved with the following set of hyperfine interactions: N_{amide} = [12.6, -1, -1] and $N_{cryptand}$ = [4.2, -2.5, -2.5] (Figure 9b).

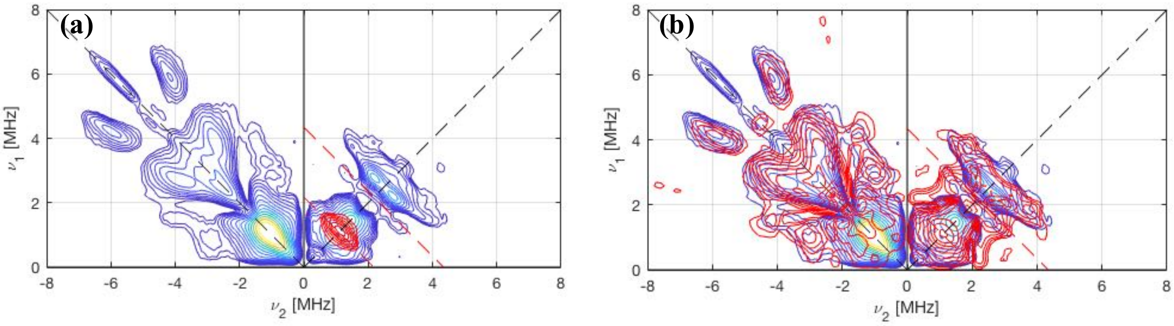

Figure 9. (a) ^{14}N HYSCORE spectrum for **2** (THF) at B_0 = 353.7 mT (**OP5**; Figure 2), T = 40 K, and X-band (9.7356 GHz) with the calculation (red) based on the dipole model only; (b) Calculation based on the model described in the text; The dashed-red antidiagonal line marks the ^{14}N Larmor frequency.

For modelling the ^{1}H HYSCORE region of **2** we initially used a point dipole model on the assumption that the dipolar contributions would be dominant in this complex, given its structure. However, this model did not reproduce the experimental ^{1}H HYSCORE data of **2**, even when dipolar constants of all hydrogen atoms in the structure were considered (Figure 10a). As in the case of complex **1**, we needed to include an additional spin-density to our model. Since both carbon and silicon of the amide ligand are *sp^3*-hybridized atoms; a π-radical is not possible to be formed precluding the transfer of spin density via spin polarization of the C-H bond. Thus, a different mechanism of spin transfer arises possibly as spin delocalization of the electronic density. As the dipolar constant calculations are based on the crystal structure the freely rotation of the methyl groups of the amide ligand in the solution conditions are not considered. Furthermore, this rotation assures that the atomic orbitals has an equal share in the spin delocalization generating a more isotropic environment, which is in accordance with the weak degree of polarization that could lead to a negligible anisotropy. Indeed, excellent simulation of the ^{1}H HYSCORE data was achieved using an isotropic hyperfine coupling of $\alpha_{iso} = 1.2$ MHz (Figure 10b). Besides, a second approach was also applied considering additional contribution transferred via spin polarization from the C-H bond of the methyl groups. Thus, the hyperfine tensors adopt the following form [$\alpha_{H/2}$, α_H, $3\alpha_{H/2}$], where α_H is the isotropic component and it is expected to be negative. This approach led to $\alpha_{iso} = -1.2$ MHz (see supporting information Figure S21), with the agreement between the simulation and the experiment to be reasonable. Nevertheless, the first approach is more rational as it does not examine contributions from the C $2p_\pi$ spin density on the Cp′ ligands.

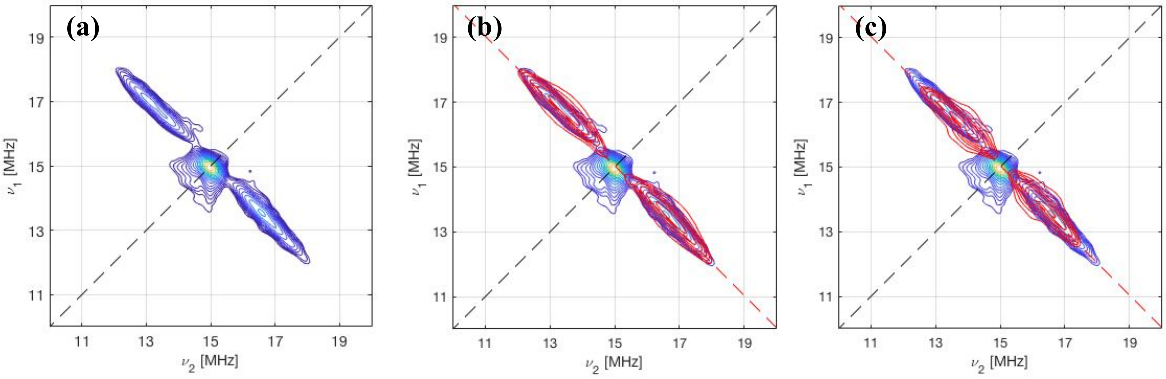

Figure 10. (a) ^{1}H HYSCORE spectrum for **1** (THF) at $B_0 = 353.7$ mT (**OP5**; Figure 2), T = 40 K, and X-band (9.7356 GHz); (b) Calculation based on the model described in the text; (c) Calculation based on the dipole model only. The dashed-red antidiagonal line marks the ^{1}H Larmor frequency.

CONCLUSIONS

In summary, we report continuous wave and pulsed EPR studies of two organometallic complexes, a lutetium (II) complex [K(2.2.2-cryptand)][Lu(Cp′)$_3$] (**1**) and a scandium (II) complex [K(2.2.2-cryptand)][Sc(N(SiMe$_3$)$_2$)$_3$] (**2**). Continuous-wave and echo-detected field-swept (EDFS) spectra display nearly isotropic *g* and *A* tensors for both ^{175}Lu and ^{45}Sc ions, confirming a configuration that approaches that of an atomic ^{2}S state due to admixing between the low energy d_{z^2} and *s* orbitals. Various pulsed EPR techniques, such as ESSEM, ENDOR and HYSCORE, have been involved to characterize the spin state of this compound, and to study the hyperfine interactions and coherence properties. Analysis of the HYSCORE spectra shows that 21% of total electron spin density is delocalized on the Cp′ ligands of **1**, while in the case of the previously reported Y(II) example this percentage fall to 6% of total spin density on the cyclopentadienyl rings. Despite the very rich nuclear spin environment (^{1}H, ^{13}C, ^{14}N, ^{29}Si), both compounds display long lived quantum coherence, as well as nuclear Rabi modulations, at relatively high temperatures, probing their potential as molecular spin quantum bits. We also proved that all electronuclear transitions in **1** and **2**, occurring from the interaction of the unpaired electron of ^{175}Lu and ^{45}Sc with the nuclear spin

($I = 7/2$), are accessible for quantum information processing. Our results suggest that a new approach to design robust qubits is the use of molecular systems with near isotropic nature, such as molecules with unpaired electron residing in an *s*-like orbital. Thus, the negligible orbital angular momentum of the ground state generates a system less sensitive to the magnetic noise that is responsible for the quantum decoherence.

REFERENCES

1. A.-M. Ariciu, D. H. Woen, D. N. Huh, L. E. Nodaraki, A. K. Kostopoulos, C. A. P. Goodwin, N. F. Chilton, E. J. L. McInnes, R. E. P. Winpenny, W. J. Evans and F. Tuna. Engineering electronic structure to prolong relaxation times in molecular qubits by minimising orbital angular momentum. *Nat. Commun.*, **2019**, *10*, 3330.
2. D. P. DiVincenzo. The physical implementation of quantum computation. *Fortschr. Phys.*, **2000**, *48*, 771-783.
3. J. Tuorila, M. Partanen, T. Ala-Nissila and M. Mottonen. Efficient protocol for qubit initialization with a tunable environment. *npj Quantum Inf*, **2017**, *3*, 27.
4. M. W. Dohertya, N. B. Manson, P. Delaney, F. Jelezko, J. Wrachtrup and L. C. L. Hollenberg. The nitrogen-vacancy colour centre in diamond. *Physics Reports*, **2013**, *528*, 1-45.
5. W. F. Koehl, B. B. Buckley, F. J. Heremans, G. Calusine and D. D. Awschalom. Room temperature coherent control of defect spin qubits in silicon carbide. *Nature*, **2011**, *479*, 84-87.
6. R. Blatt and D. Wineland. Entangled states of trapped atomic ions. *Nature*, **2008**, *453*, 1008-1015.
7. J. Clarke and F. Wilhelm. Superconducting quantum bits. *Nature*, **2008**, *453*, 1031-1042.
8. M. Leuenberger and D. Loss. Quantum computing in molecular magnets. *Nature*, **2001**, *410*, 789-793.
9. A. Dréau, P. Spinicelli, J. R. Maze, J.-F. Roch and V. Jacques. Single-Shot Readout of Multiple Nuclear Spin Qubits in Diamond under Ambient Conditions. *Phys. Rev. Lett.*, **2013**, *110*, 060502.
10. W. H. Zurek. Decoherence, einselection, and the quantum origins of the classical. *Rev. Mod. Phys.*, **2003**, *75*, 715.
11. A. Morello, P. C. E. Stamp and I. S. Tupitsyn. Pairwise Decoherence in Coupled Spin Qubit Networks. *Phys. Rev. Lett.*, **2006**, *97*, 207206.
12. S. Ballmann, R. Härtle, P. B. Coto, M. Elbing, M. Mayor, M. R. Bryce, M. Thoss and H. B. Weber. Experimental Evidence for Quantum Interference and Vibrationally Induced Decoherence in Single-Molecule Junctions. *Phys. Rev. Lett.*, **2012**, *109*, 056801.
13. C. J. Wedge, G. A. Timco, E. T. Spielberg, R. E. George, F. Tuna, S. Rigby, E. J. L. McInnes, R. E. P. Winpenny, S. J. Blundell and A. Ardavan. Chemical Engineering of Molecular Qubits. *Phys. Rev. Lett.*, **2012**, *108*, 107204.
14. K. Bader, D. Dengler, S. Lenz, B. Endeward, S.-D. Jiang, P. Neugebauer and J. van Slageren. Room temperature quantum coherence in a potential molecular qubit. *Nat. Commun.*, **2014**, *5*, 5304.
15. M. Atzori, L. Tesi, E. Morra, M. Chiesa, L. Sorace and R. Sessoli. Room-Temperature Quantum Coherence and Rabi Oscillations in Vanadyl Phthalocyanine: Toward Multifunctional Molecular Spin Qubits. *J. Am. Chem. Soc.*, **2016**, *138*, 2154-2157.
16. M. R. MacDonald, J. E. Bates, J. W. Ziller, F. Furche and W. J. Evans. Completing the Series of +2 Ions for the Lanthanide Elements: Synthesis of Molecular Complexes of Pr^{2+}, Gd^{2+}, Tb^{2+}, and Lu^{2+}. *J. Am. Chem. Soc.*, **2013**, *135*, 9857-9868.
17. D. H. Woen, G. P. Chen, J. W. Ziller, T. J. Boyle, F. Furche and W. J. Evans. Solution Synthesis, Structure, and CO2 Reduction Reactivity of a Scandium(II) Complex, $\{Sc[N(SiMe_3)_2]_3\}$. *Angew. Chem. Int. Ed.*, **2017**, *56*, 2050-2053.

18. A. Schweiger and J. Jeschke. Principles of Pulse Electron Paramagnetic Resonance. Oxford University Press, Oxford, **2001**.
19. A. Lunghi and S. Sanvito. Electronic spin-spin decoherence contribution in molecular qubits by quantum unitary spin dynamics. *J. Magn. Magn. Mater.*, **2019**, *487*, 165325.
20. S. S. Eaton, G. R. Eaton, Distance Measurements in Biological Systems by EPR. In biological magnetic resonance; Lawrence J. Berliner Sandra S. Eaton Gareth R. Eaton Eds.; Klewer Academic/Plenum Publishers: New York , **2000**.
21. K. S. Pedersen, A.-M. Ariciu, S. McAdams, H. Weihe, J. Bendix, F. Tuna and S. Piligkos. Toward Molecular 4f Single-Ion Magnet Qubits. J. Am. Chem. Soc., **2016**, *138*, 5801-5804.
22. I. I. Rabi. Space quantisation in a gyrating magnetic field. *Phys. Rev.*, **1937**, *51*, 652-654.
23. M. J. Graham, J. M. Zadrozny, M. Shiddiq, J. S. Anderson, M. S. Fataftah, S. Hill and D. E. Freedman. Influence of electronic spin and spin-orbit coupling on decoherence in mononuclear transition metal complexes. *J. Am. Chem. Soc.*, **2014**, *136*, 7623-7626.
24. A. Formanuik, A.-M. Ariciu, F. Ortu, R. Beekmeyer, A. Kerridge, F. Tuna, E. J. L. McInnes and D. Mills. Actinide covalency measured by pulsed electron paramagnetic resonance spectroscopy. *Nat. Chem.*, **2017**, *9*, 578-583.
25. S. Stoll and R. D. Britt. General and efficient simulation of pulse EPR spectra. *Phys. Chem. Chem. Phys.*, **2009**, *11*, 6614-6625.
26. N. M. Atherton. Principles of electron spin resonance, Ellis Horwood Ltd, **1993**.
27. J. R. Morton and K. F. Preston. Atomic parameters for paramagnetic resonance data. *J. Magn. Reson.*, **1978**, *30*, 577-582.
28. F. Gerson, W. Huber. Electron Spin Resonance Spectroscopy of Organic Radicals. Wiley-VCH, **2003**.
29. H. M. McConnell and D. B. Chesnut. Comments on “Theory of isotropic hyperfine interactions in π-electron radicals”. *J. Chem. Phys.*, **1958**, *28*, 107.
30. J. Harmer, G. Mitrikas and A. Schweiger. Advance pulse EPR methods for the characterization of metalloproteins. Part of Biological Magnetic Resonance, **2009**.

ACKNOWLEDGEMENTS

This work was supported by the Engineering and Physical Sciences Research Council via a DTG doctoral scholarship to L.N., the European Union via a doctoral scholarship to A.-M.A. (FP7-PEOPLE-2013-ITN “MAGIC” Initial Training Network; grant agreement no. 606831), the Leverhulme Trust - fellowship to F.T. (reference RF-2018-545/4), The University of Manchester, The University of California and the UK National EPR Facility and Service.

Electronic Supplementary Information

Low-Valent Sc and Lu Organometallic Complexes as Qudits with an Increased Hilbert Space

Lydia E. Nodaraki,[1,2] Ana-Maria Ariciu,[1,2] Daniel N. Huh,[3] ~~[1]~~-Richard E.P. Winpenny,[1] Eric J. L. McInnes,[1,2] William J. Evans[3] and Floriana Tuna[1,2]

[1]School of Chemistry, The University of Manchester, Oxford Road, Manchester M13 9PL, UK
[2]Photon Science Institute, The University of Manchester, Oxford Road, Manchester M13 9PL, UK
[3]Department of Chemistry, University of California, Irvine, CA 92697-2025

Contents

Supplementary EPR Information for complex **1** and **2**

1. Additional continuous wave (CW) and echo-detected field-swept (EDFS) spectra
2. Relaxation studies
    2.1 Phase memory time measurements
    2.2. Spin-lattice relaxation time measurements
3. Transient nutation data
    3.1 Nutation experiments of **1**
    3.2 Nutation experiments of **2**
4. Hyperfine sublevel correlation (HYSCORE) spectroscopy
    4.1 HYSCORE experiments of **1**
    4.2 HYSCORE experiments of **2**

Supplementary EPR Information for complex 1 and 2

1. Continuous wave and echo-detected field-swept

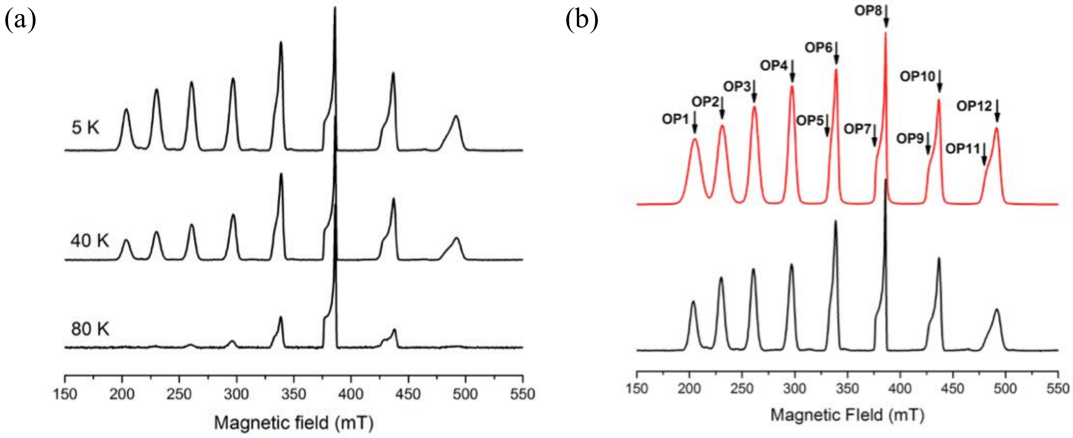

Figure S1. (a) X-Band EDFS EPR spectra of a frozen solution (10 mM in THF) of **1** measured at 5, 40 and 80 K and (b) Experimental (black) and simulated (red) EDFS spectra for **1** at 40 K; simulation parameters are given in Table 1. Observer positions **OP1-OP12** mark the magnetic fields at which time-dependent pulsed EPR data were collected.

Table S1. Summary of observal field positions **OP1–OP12** of **1** (Figure S1b).

Magnetic Field		Magnetic Field	
203.7 mT	OP1	376.7 mT	OP7
230.3 mT	OP2	385.9 mT	OP8
260.6 mT	OP3	427.4 mT	OP9
296.8 mT	OP4	436.7 mT	OP10
332.8 mT	OP5	482.8 mT	OP11

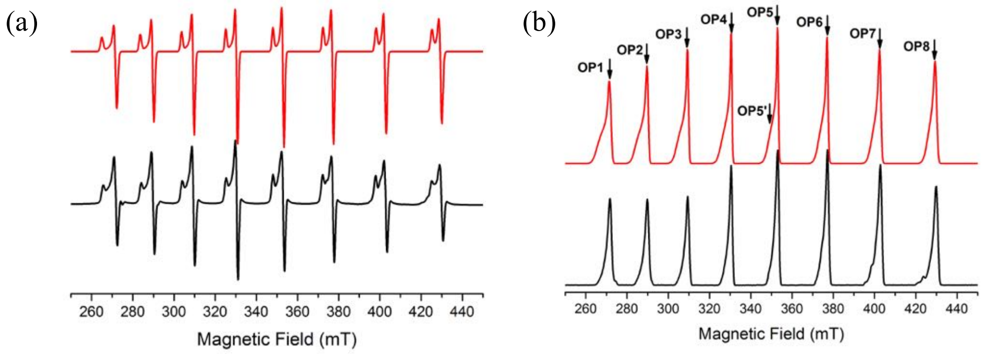

Figure S2. (a) X-Band continuous wave EPR spectrum at 40 K of complex **2** simulated with $g_\perp$ = 1.964 and $g_\parallel$ = 1.997 ($A_\perp$ = 620 MHz and $A_\parallel$ = 640 MHz), (b) EDFS EPR spectrum at 40 K (X-band) measured with 16 ns and 32 ns π/2 and π microwave pulses, respectively simulated with the same parameters as the CW spectrum.

Table S2. Summary of observal field positions **OP1–OP8** of **1** (Figure S2b)

Magnetic Field		Magnetic Field	
272.0 mT	OP1	353.7 mT	OP5
290.2 mT	OP2	377.7 mT	OP6
309.8 mT	OP3	403.7 mT	OP7
331.1 mT	OP4	430.8 mT	OP8
349.5 mT	OP5´		

2. Relaxation Studies

2.1 Phase memory time measurements

The Phase Memory time, T_m, measurements were carried out using a Hahn echo sequence (*π/2–τ–π–τ–echo*) with gradually increasing the inter-pulse delay, τ. Using microwave pulse length of 32 ns or 128 ns for π pulse, strong proton-electron spin modulation was observed. In order to suppress the ^{1}H modulation in the echo decays, longer microwave pulses of length π = 256 ns or π = 1000 ns were used. The fitting functions used for the echo decays were

$$Y(2\tau) = Y_0 e^{(-2\tau/T_m)^k} + c \quad (1)$$

where Y_0 is the amplitude and k is the stretch factor.

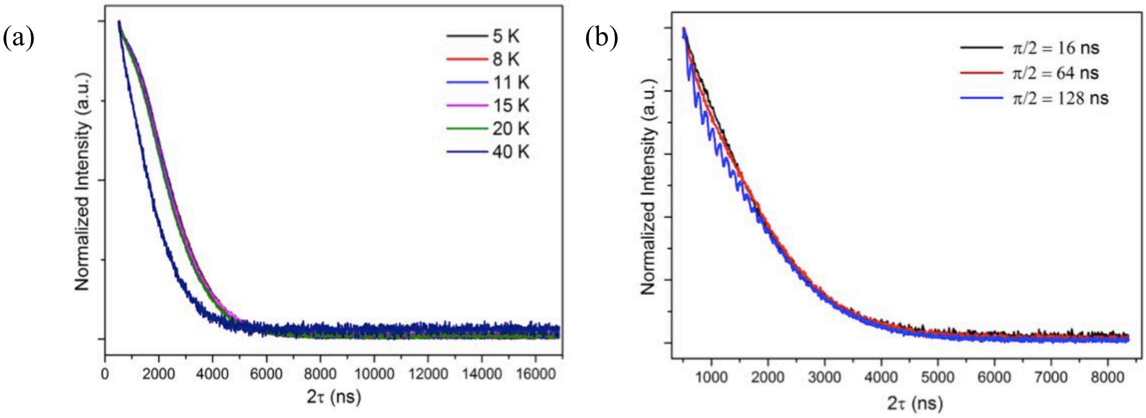

Figure S3. (a) Normalized Hahn-echo signal intensities as a function of the inter-pulse delay 2*τ*, for **1** at B_0 = 385.9 mT (**OP8**) and selected temperatures (5–40 K); (b) Normalized Hahn-echo signal intensities as a function of the inter-pulse delay 2*τ* for **1** at B_0 = 385.9 mT (**OP8**) and 40 K.

Table S3. Extracted phase memory time constants for **1** (THF), at X-band (**OP1**–**OP12**).

T (K)	**OP1** T_m (ns)	**OP3** T_m (ns)	**OP6** T_m (ns)	**OP7** T_m (ns)	**OP8** T_m (ns)	**OP9** T_m (ns)	**OP10** T_m (ns)	**OP12** T_m (ns)	$t(\pi/2)$ (ns)
5					2976.8				64
	2264.1	2524.6	2716.5	2834.4	2780.6	2666.3	2596.3	2332.7	128
	1648.2	1904.1	2055.1	2164.4	2158.9	1953.2	1934.1	1656.9	256
8	2098.1	2375.8	2643.2	2878.2	2780.3	2604.7	2519.9	2197.5	128
	1546.8	1825.2	2044.4	2149.7	2137.9	1953.2	1946.4	1661.6	256
11		2222.5			2917.2		2492.8		64
	1844.8	2131.8			2747	2455.8	2383.3	1977.5	128
15	1464.7	1748.9	2331.9		2845.8	2616.4	2180	2034.2	64
		1502		2449.2	2681.3	2261.5			128
20	1230.9	1280.1			2743.3			1100.7	64
				2397	2631.9	2292.2	1907.9	1500.9	128
40		472.9							16
	233.2	324.8	693.6		1642.8	1070.8	623.4	705.7	64
				1899.4	1777.8				128
80		370.2	325.6		700.9	284.1	355.2		16
				443.6					64
100					287.7				16

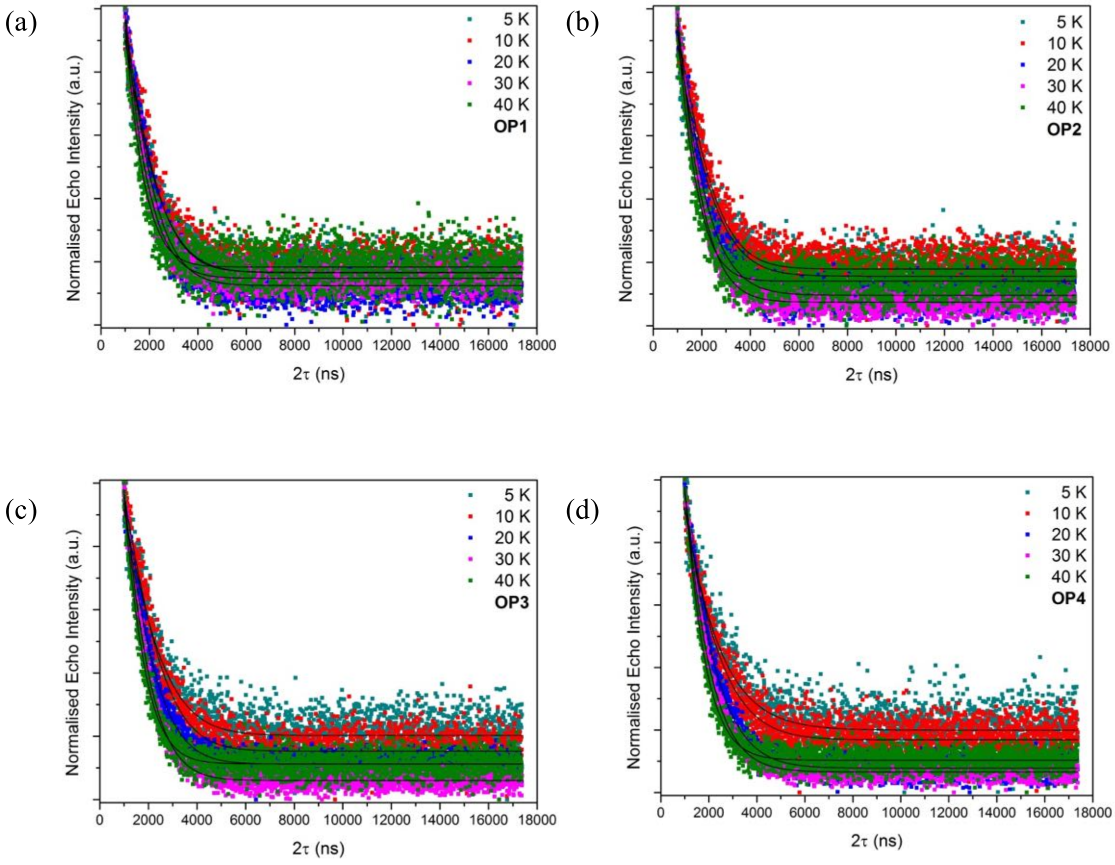

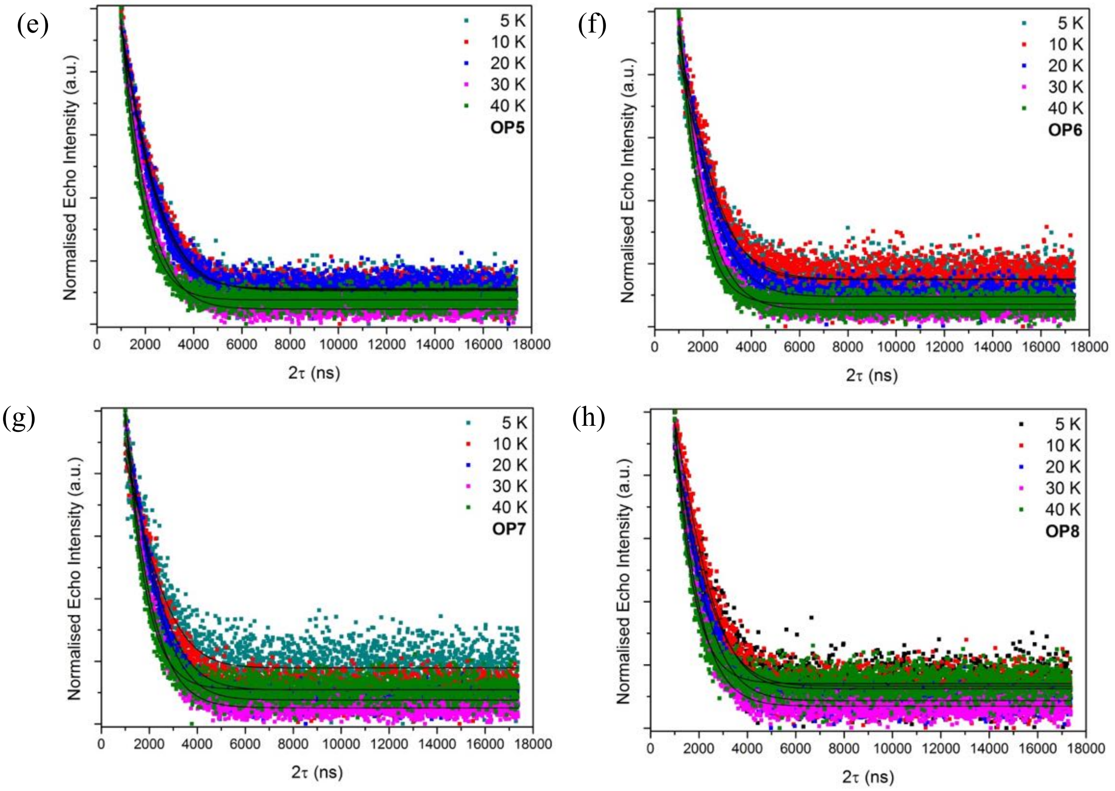

Figure S4. Normalised Hanh-echo signal intensities of **2** as a function of the inter-pulse delay 2τ at different **OP** field positions (**OP1-OP8**) and at selected temperatures (5 K-40 K).

Table S4. Extracted phase memory time constants for **2** (THF), at X-band (**OP1–OP8**).

T (K)	**OP1** T_m (μs)	**OP2** T_m (μs)	**OP3** T_m (μs)	**OP4** T_m (μs)	**OP5** T_m (μs)	**OP6** T_m (μs)	**OP7** T_m (μs)	**OP8** T_m (μs)
5	1.795	1.875	1.893	1.638	1.907	1.96	2.17	2.064
10	1.826	1.907	1.963	1.812	1.939	2.143	2.072	2.102
20	1.57	1.521	1.713	1.611	1.901	1.876	1.86	1.745
30	1.318	1.353	1.371	1.304	1.46	1.461	1.361	1.259
40	1.085	1.243	1.153	1.049	1.105	1.149	1.035	0.907
50	1.341	1.242	0.886	1.019	0.755	0.873	0.95	1.386
60	0.178	0.188	0.23	0.398	0.404	0.524	0.474	0.441
80	0.143	0.162	0.179	0.293	0.122	0.145	0.141	0.156
100			0.106	0.12	0.124	0.114	0.085	

2.2 Spin-lattice relaxation time measurements

For the spin–lattice relaxation time, T_1, measurements were carried out by using a standard magnetization inversion recovery pulse sequence (*π–t–π/2–τ–π–τ–echo*) with 16 and 32 ns π/2 and π pulse lengths, respectively, using a fixed τ and variable t. The T_1 was calculated by fitting the experimental data according to the following equation:

$$Y(t) = Y_1 e^{(-t/T_1)} + Y_{SD}^{(-t/T_{SD})} \quad (2)$$

where Y_1 and Y_{SD} are the amplitudes and T_{SD} is the spectral diffusion time constant.

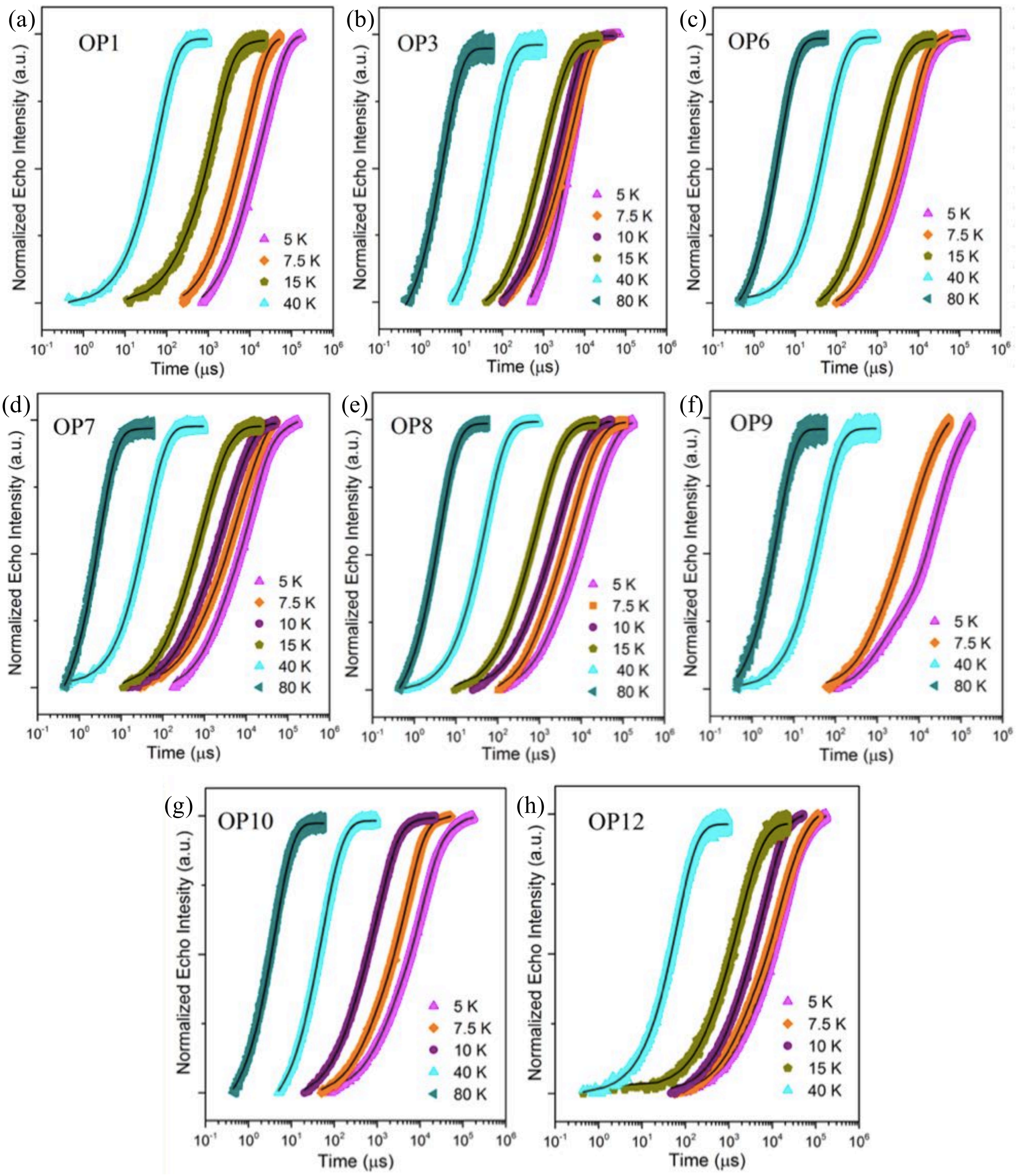

Figure S5. Inversion recovery data for **1** (10 mM; THF) at selected temperatures between 5 and 80 K, and at B_0 of 203.7 mT (**OP1**), 260.6 mT (**OP3**), 338.7 mT (**OP6**), 376.7 mT (**OP7**), 385.9 mT (**OP8**), 427.4 mT (**OP9**), 436.7 mT (**OP10**), and 491.9 mT (**OP12**). The black lines are best fits to the biexponential model (Equation S3), giving the parameters in Table S3.

Table S5. Extracted spin lattice relaxation time constants for **1** (THF) at X-band (**OP1–OP12**).

T (K)	**OP1**		**OP3**		**OP6**		**OP7**	
	T_1 (μs)	T_{SD} (μs)	T_1 (μs)	T_{SD} (μs)	T_1 (μs)	T_{SD} (μs)	T_1 (μs)	T_{SD} (μs)
5	29122.1	4032.4	9729	272.6	15757.6	4987.6	22199	4145.4
7.5	10029	1342.7	5918.3	659.3	6873.9	892.9	12942	1805.6
8							13343	2020.7
10			3676.9				6912.5	1101.8
15	2554.5		2624.6		2324.4	542.4	2086.9	446.8
40	65.7		57.8		62.5		45.6	
80	3.9		3.9		4.3		3.1	

T (K)	**OP8**		**OP9**		**OP10**		**OP12**	
	T_1 (μs)	T_{SD} (μs)	T_1 (μs)	T_{SD} (μs)	T_1 (μs)	T_{SD} (μs)	T_1 (μs)	T_{SD} (μs)
5	29945	4852.2			26862	4886	24372	3763.8
7.5	13381	2265.1	13988	2052.2	2265.1	1805.6		
8								
10	7504.5	1343.7			1343.7	1101.8	8063.1	1134.5
15	2100.2	472.7			472.7	446.8	3030.6	753.4
40	58.2		48.3				68.9	
80	4.2		4.2					

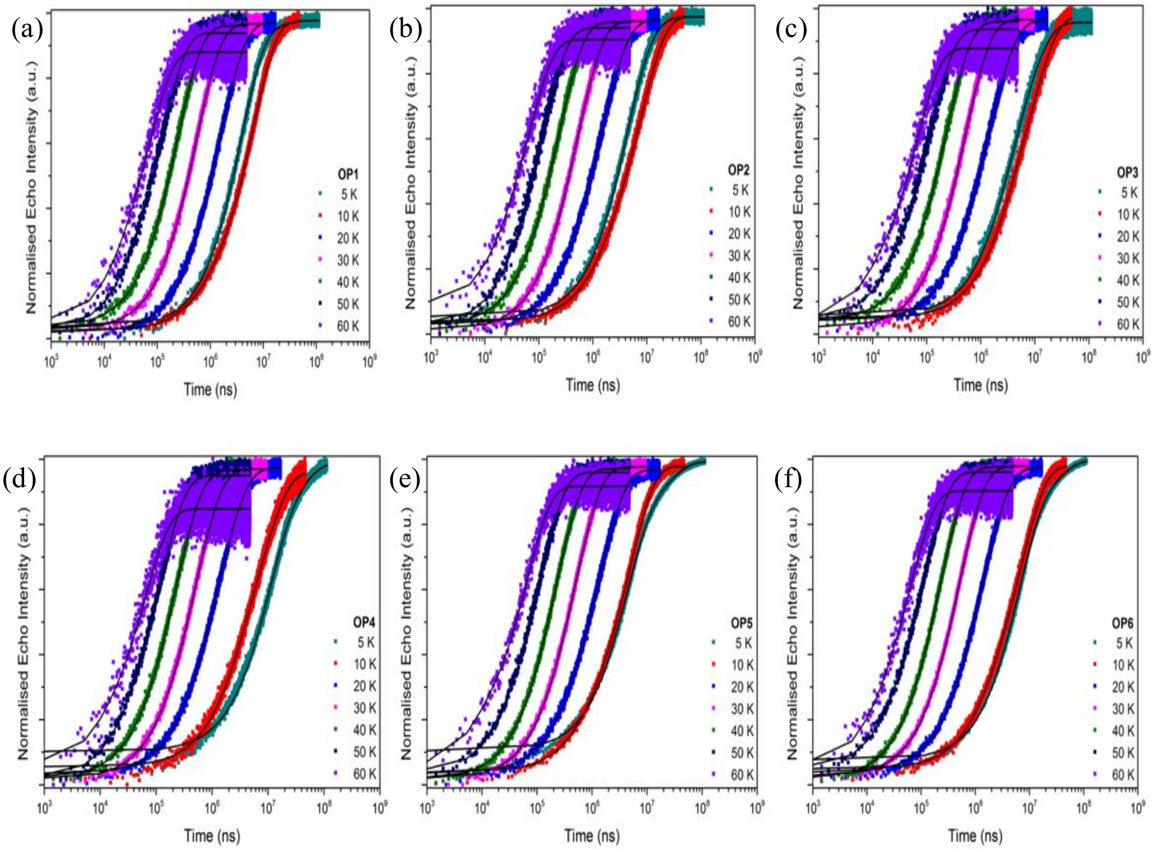

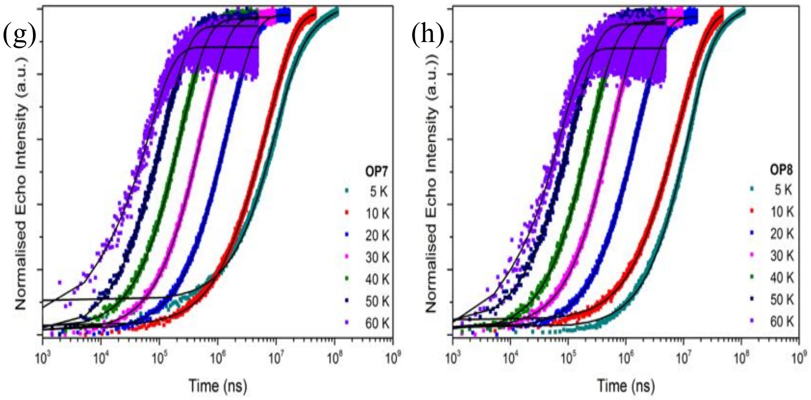

Figure S6. Normalised echo intensities of 2 as a function of time, t, in a standard inversion recovery sequence at variable temperatures (5 K-60 K) and at different OP positions (OP1-OP8). The black lines are fits to the biexponential model.

Table S6. Extracted spin lattice relaxation time constants for **2** (THF), at X-band (**OP1–OP8**).

T (K)	**OP1** T_1 (μs)	**OP2** T_1 (μs)	**OP3** T_1 (μs)	**OP4** T_1 (μs)	**OP5** T_1 (μs)	**OP6** T_1 (μs)	**OP7** T_1 (μs)	**OP8** T_1 (μs)
5	15548	7790	8103	32601	21116	28466	44147	149795
10	6492	8423	10375	9437	5060	7639	8453	10827
20	1928	2009	2054	1770	1595	1888	1728	1892
30	691	635	656	639	588	609	618	642
40	298	268	272	282	268	263	272	270
50	133	134	127	132	125	127	124	126
60	74	73	68	67	68	68	67	69
80			47	63	27	26		
100			21	27	21	26		

3. Transient Nutation data

3.1 Nutation experiments of **1**

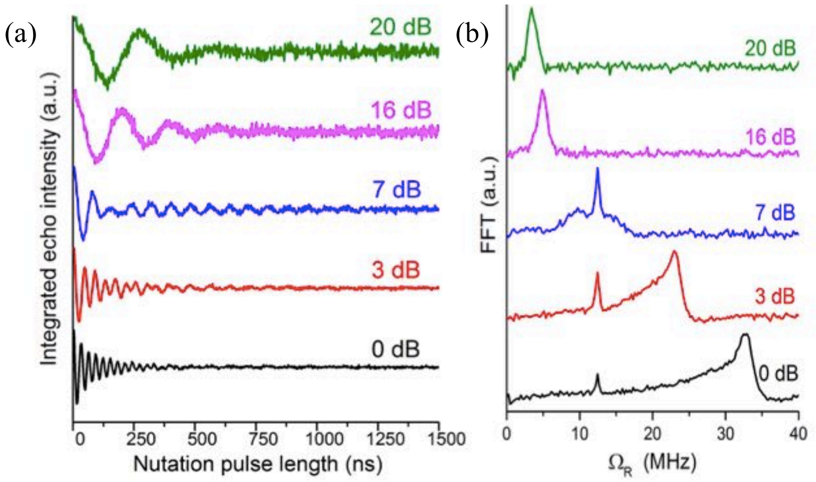

Figure S7. (a) Rabi oscillation for **1** (THF) at 80 K and B_0 = 296.8 mT (**OP4**), acquired with different microwave attenuations; (b) corresponding Fourier transforms.

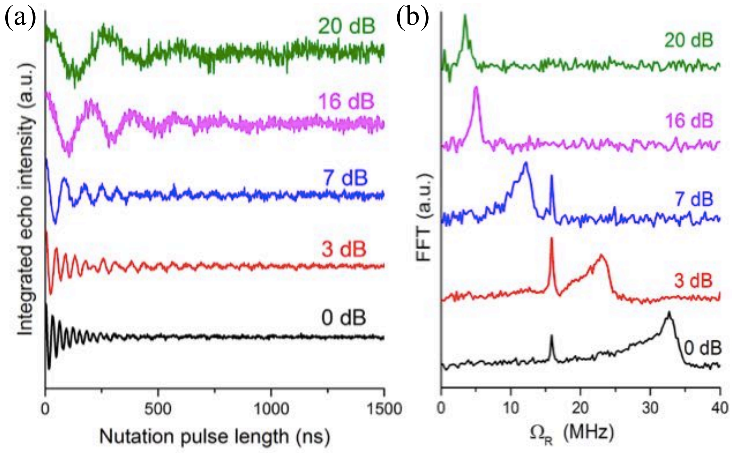

Figure S8. (a) Rabi oscillation for **1** (THF) at 80 K and B_0 = 377.1 mT (**OP7**), acquired with different microwave attenuations; (b) corresponding Fourier transforms.

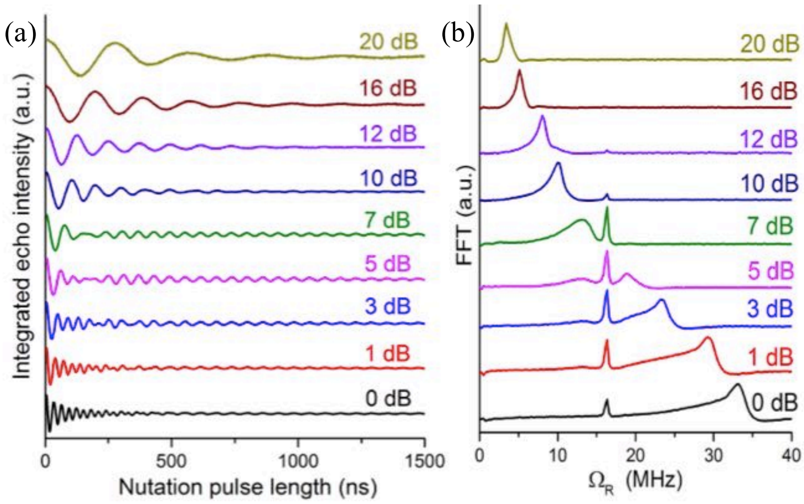

Figure S9. (a) Rabi oscillation for **1** (THF) at 80 K and B_0 = 385.9 mT (**OP8**), acquired with different microwave attenuations; (b) corresponding Fourier transforms.

Table S7. Rabi frequencies for **1** (THF) at B_0 = 296.3 mT, B_0 = 377.1 mT and B_0 = 386.9 mT (**OP4**, **OP7** and **OP8**) at 80 K.

Attenuation (dB)	Relative B_1 (a.u.)	Ω_R (MHz) **OP4**	Ω_R (MHz) **OP7**	Ω_R (MHz) **OP8**
0	6.31	32.94	32.69	33.1
1	5.62	–	–	29.28
3	4.47	22.96	22.96	23.12
5	3.55	–	–	18.79
7	2.82	12.45	12.2	13.17
10	2	–	–	10
12	1.59	–	–	8.05
16	1	4.88	4.88	4.88
20	0.63	3.41	3.41	3.41

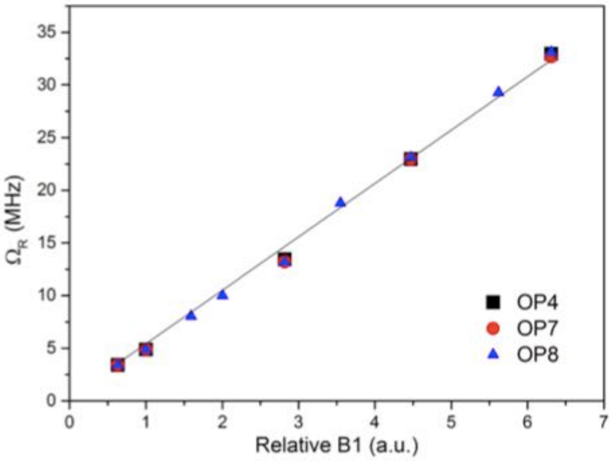

Figure S10. B_1 dependence of the Rabi frequency (Ω_R) for **1** measured at 80 K and different observable positions. The solid line is a guide for the eye emphasizing the linear behaviour ($B_1 \propto \sqrt{P}$, where P is the microwave power).

3.2 Nutation experiments of **2**

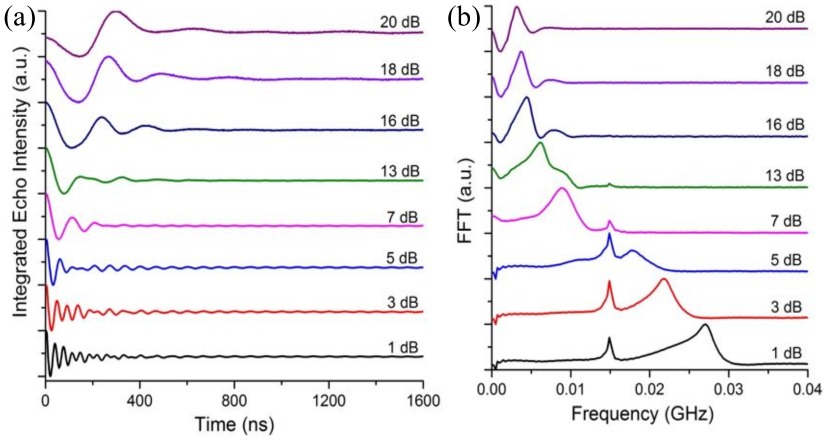

Figure S11. (a) Rabi oscillation for **2** (THF) at 24 K and B_0 = 353.7 mT (**OP5**), acquired with different microwave attenuations; (b) corresponding Fourier transforms.

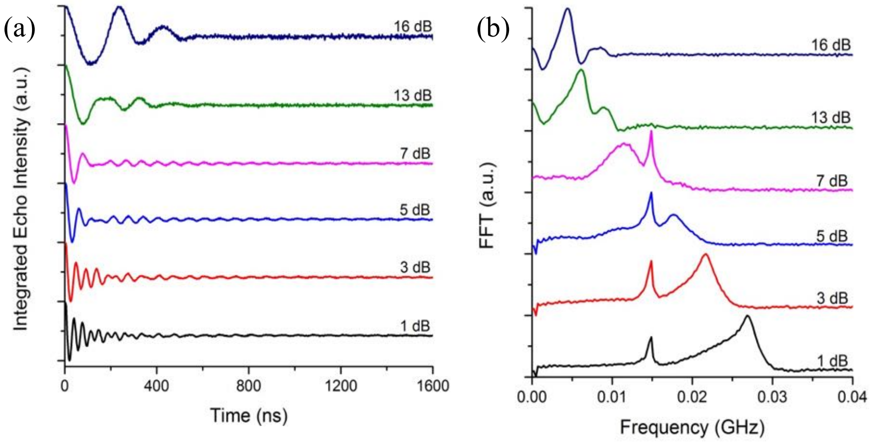

Figure S12. (a) Rabi oscillation for **2** (THF) at 24 K and B_0 = 349.5 mT (**OP5´**), acquired with different microwave attenuations; (b) corresponding Fourier transforms.

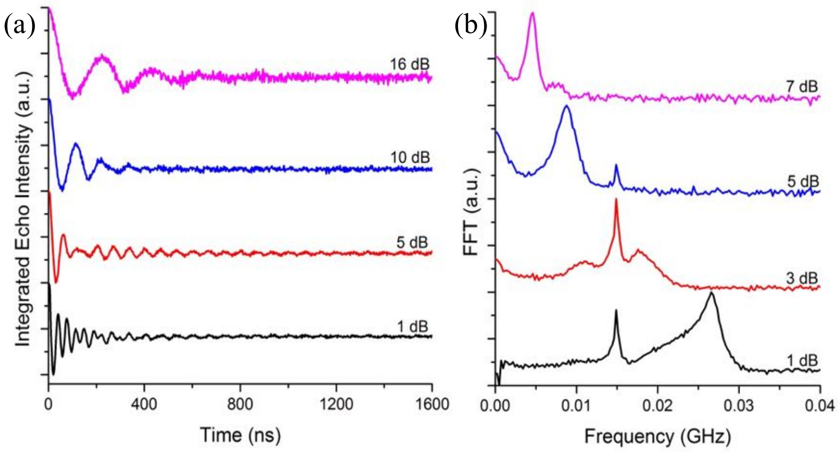

Figure S13. (a) Rabi oscillation for **2** (THF) at 60 K and B_0 = 353.7 mT (**OP5**), acquired with different microwave attenuations; (b) corresponding Fourier transforms.

Table S8. Rabi frequencies for **2** (THF) at B_0 = 349.5 mT (**OP5′**), and B_0 = 353.7 mT (**OP5**) at 24 and 60 K.

Attenuation (dB)	Relative B_1 (a.u.)	Ω_R (MHz) **OP5′ - 24 K**	Ω_R (MHz) **OP5 – 24 K**	Ω_R (MHz) **OP5 – 60 K**
1	5.62	26.89	27.02	26.61
3	4.47	21.69	21.76	-
5	3.55	17.68	17.72	17.60
7	2.82	11.55	8.95	-
10	1.99	-	-	8.81
13	1.41	6.11	6.18	-
16	1	4.45	4.38	4.66
18	0.79	-	3.68	-
20	0.71	-	3.13	-

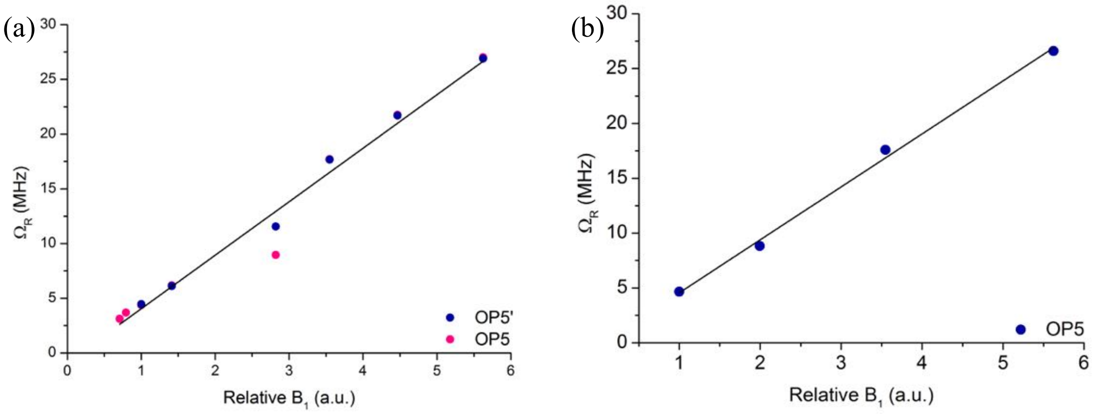

Figure S14. $B1$ dependence of the Rabi frequency (Ω_R), measured at different observable positions (**OP5′** and **OP5**) and at (a) 24 K and (b) 60 K. The solid line is a linear fitting of the traces ($B1 \propto \sqrt{P}$, where P is the microwave power).

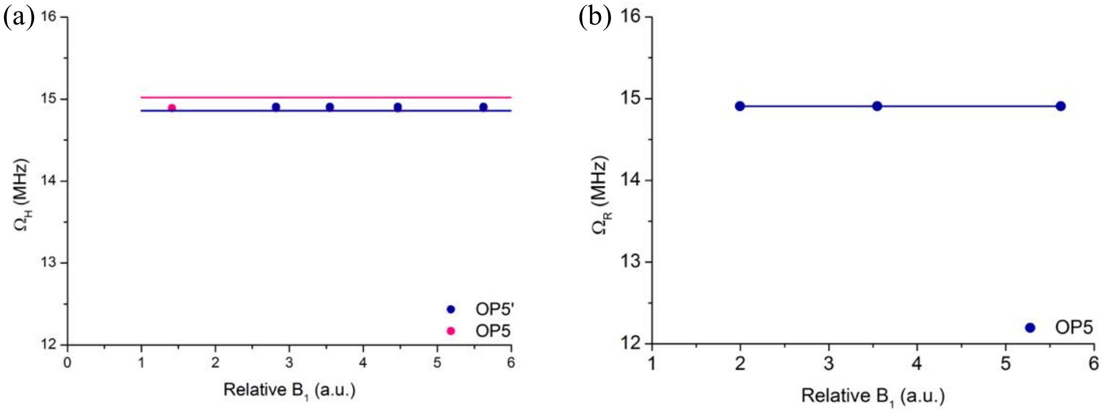

Figure S15. $B1$ dependence of the ^{1}H nuclear frequency (Ω_H) measured at different observable positions (**OP5′** and **OP5**) and at (a) 24 K and (b) 60 K. The solid line represents that theoretical Ω_H value.

4. Hyperfine sublevel correlation (HYSCORE) spectroscopy

For HYSCORE experiments, a four-pulse spin echo envelope modulation sequence, $\pi/2$ - τ - $\pi/2$ - t_1 - π - t_2 - $\pi/2$ - *echo*, with t_1 and t_2 independently varied was used. In HYSCORE experiment the first two $\pi/2$ pulses generate nuclear coherence, which is then transferred by the mixing π pulse from one electron spin manifold to another. Fourier transformation leading to a frequency domain spectrum, in which for weakly-coupled nuclei ($2|v_n|>|A|$) cross-peaks will appear about at the Larmor frequencies (v_n). The ridges of the spectra are due to the anisotropic hyperfine couplings; moreover, their length and the shift from the anti-diagonal about the nuclear Larmor frequency, v_n, depend on the anisotropy and the magnitude of the hyperfine couplings.

4.1 HYSCORE experiments of **1**

Same model was used for the simulation of the ^{1}H and ^{13}C HYSCORE data for **1** at other operational fields, including both *xy* and *z* orientations. Best simulation of the experimental ^{13}C HYSCORE spectra recorded at the observer position **OP7** (Figure S16) was obtained with $A_{\parallel}^{C2,5} = 10.26$ MHz; $A_{\perp}^{C2,5} = 0.57$ MHz, and $A_{\parallel}^{C3,4} = 3.84$ MHz; and $A_{\perp}^{C3,4} = 1.28$ MHz. Thus, using the McConnell model we extract C $2p_{\pi}$ spin populations of $\rho_p = 0.0296$ and 0.0077, i.e. 2.96% and 0.77%, for $C^{2,5}$ and $C^{3,4}$, respectively. Modelling of ^{1}H HYSCORE region for **1** at **OP7** (Figure S17) involved a similar approach, with the dipole only model not reproducing the experimental data. However, considering the effect of spin polarisation and thus the contribution of the spin density at C $2p_{\pi}$ on the Cp′ ligands, lead to a nice simulation of the ^{1}H HYSCORE spectra with $\alpha_{iso} = -2.48$ MHz (Figure S17). Analysis of the α_{iso} value yield to $\rho_p = 0.0296$ (2.96 %) for $C^{2,5}$, which is in excellent agreement with $\rho_p = 0.0296$ derived from the analysis of the ^{13}C data. Bringing a sum of 7.46 % spin population on each Cp′ ring, and a total of 22.38% on the three Cp′ ligands present in the molecular structure of **1**.

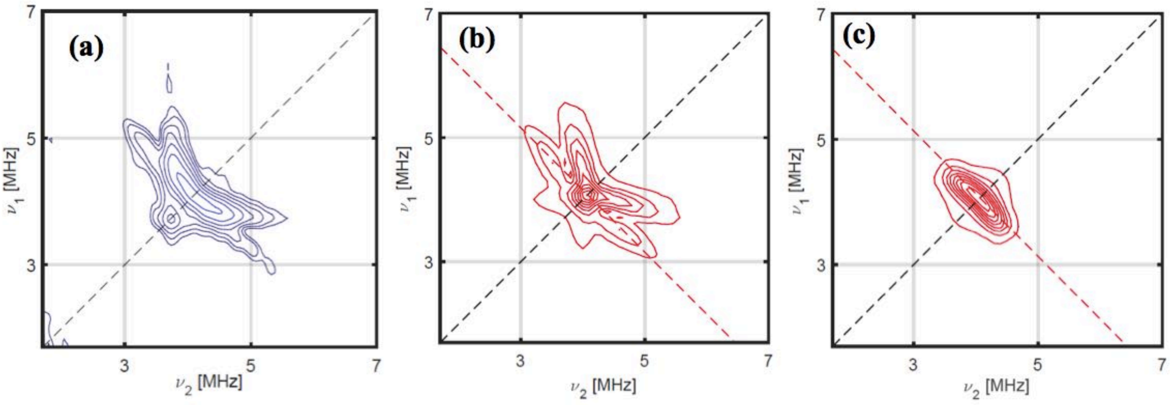

Figure S16. (a) ^{13}C HYSCORE spectrum for **1** (THF) at $B_0 = 376.7$ mT (**OP7**; Figure 2, $T = 15$ K, and X-band (9.7098 GHz); (b) Calculation based on the model described in the main text, which includes a dipolar component, and spin densities at $C^{2,5}$ and $C^{3,4}$. (c) Calculation based on the dipole model only. The dashed-red antidiagonal lines mark the ^{13}C Larmor frequency.

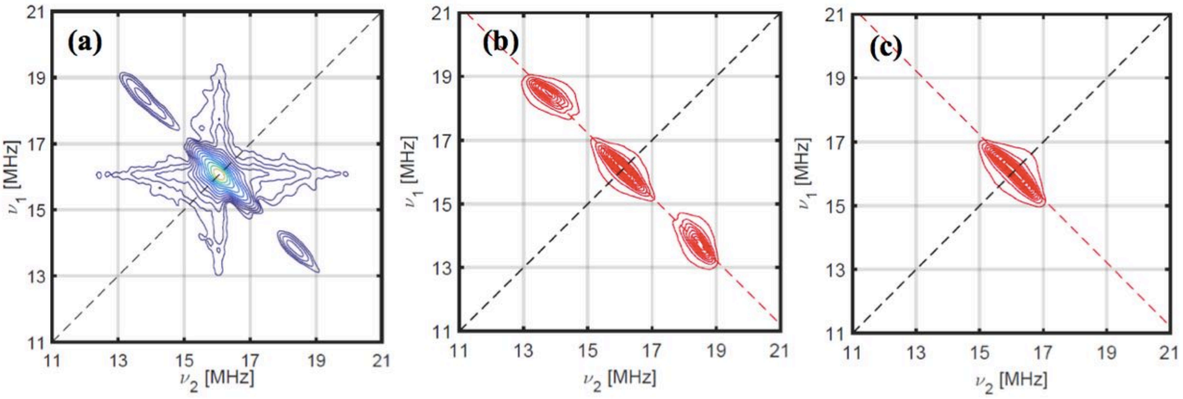

Figure S17. (a) ^1H HYSCORE spectrum for **1** (THF) at $B_0 = 376.7$ mT (**OP7**; Figure 2), $T = 15$ K, and X-band (9.7098 GHz); (b) Calculation based on the model described in the text; (c) Calculation based on the dipole model only. The dashed-red antidiagonal line marks the ^1H Larmor frequency.

Similarly, from the successful simulation of the experimental ^{13}C HYSCORE data for **OP8** (Figure S18) the following sets of hyperfine parameters were obtained: $A_{\parallel}^{C2,5} = 9$ MHz; $A_{\perp}^{C2,5} = 0.5$ MHz, and $A_{\parallel}^{C3,4} = 3.36$ MHz; and $A_{\perp}^{C3,4} = 1.12$ MHz. Applying the McConnell relation, which translates them to C $2p_{\pi}$ spin populations of $\rho_p = 0.0264$ and 0.0069, i.e. 2.64% and 0.69%, for $C^{2,5}$ and $C^{3,4}$, respectively. Moreover, for the ^1H HYSCORE region of **1** for **OP8** (Figure S19), an excellent simulation of the experimental spectra was achieved with $\alpha_{\mathrm{iso}} = -2.22$ MHz. This leads to $\rho_p = 0.0264$ (2.64 %) for C^{2,5}, which is in great agreement with $\rho_p = 0.0264$ derived from analysis of the ^{13}C data. Resulting a sum of ~ 6.66 % spin population on the Cp′ ring and a total of ~ 20.78 % spin population on all three Cp′ rings.

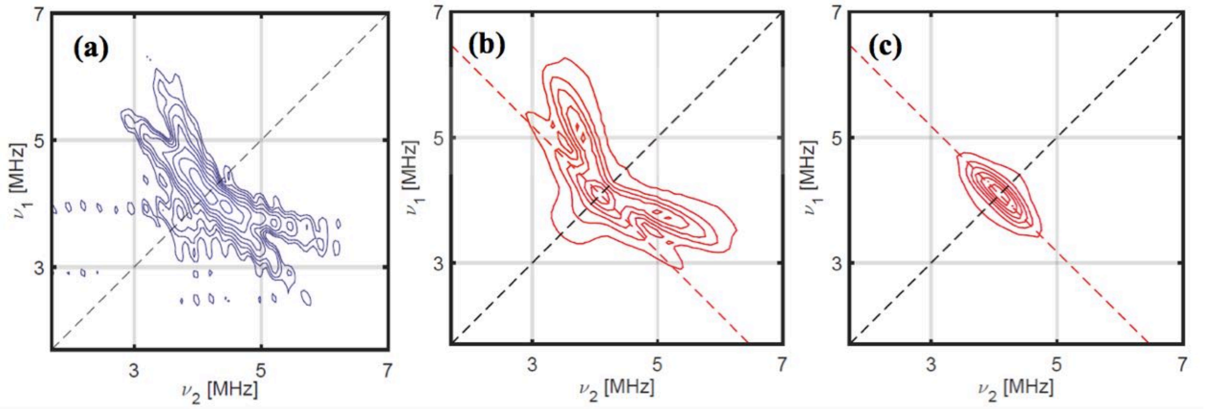

Figure S18. (a) ^{13}C HYSCORE spectrum for **1** (THF) at B_0 = 385.8 mT (**OP8;** Figure 3), T = 15 K, and X-band (9.7098 GHz); (b) Calculation based on the model described in the main text, which includes a dipolar component, and spin densities at C^{2,5} and C^{3,4}; (c) Calculation based on the dipole model only. The dashed-red antidiagonal lines mark the ^{13}C Larmor frequency.

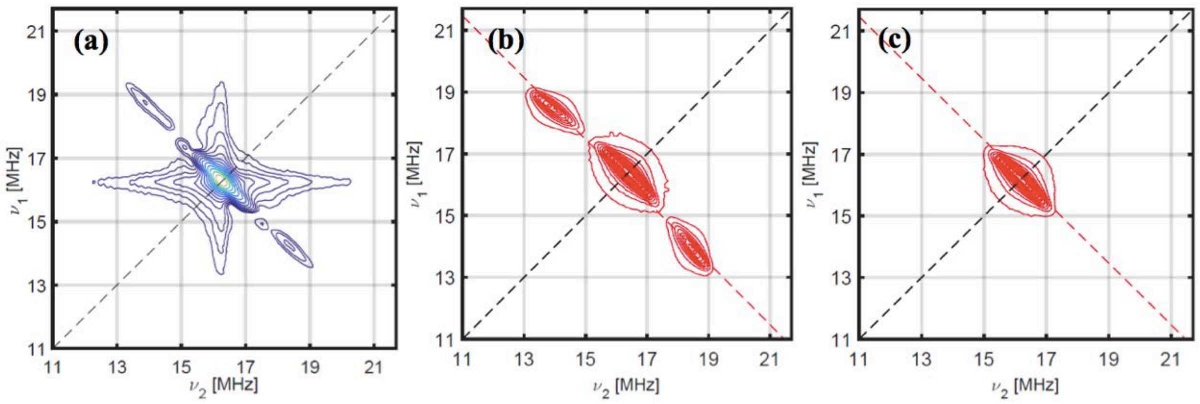

Figure S19. (a) ^{1}H HYSCORE spectrum for **1** (THF) at B_0 = 358.8 mT (**OP8**; Figure 2), T = 15 K, and X-band (9.7098 GHz). (b) Calculation based on the model described in the text; (c) Calculation based on the dipole model only. The dashed-red antidiagonal line marks the ^{1}H Larmor frequency.

4.2 HYSCORE experiments of **2**

Simulation trial for the ^{14}N HYSCORE region of complex **2** using only the nitrogen atoms (N_1-N_3) of the silyl-amide ligands coordinated to the Sc^{II} ion.

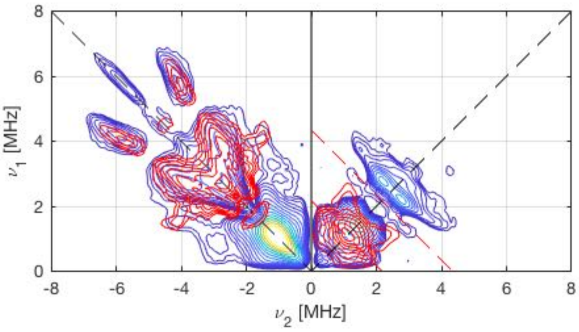

Figure S20. X-band (9.7356 GHz) ^{14}N HYSCORE spectrum for **2** (THF) at B_0 = 353.7 mT (**OP5**; Figure 2), and at T = 40 K with the calculation (red) based on the model described in the text only for the N atoms of the silyl-amide ligands (dipolar and spin-polarization contribution); The dashed-red antidiagonal line marks the ^{14}N Larmor frequency.

For the simulation of the ^{1}H HYSCORE region of **2** a second approach was adopted with the assumption that the additional to the dipolar contribution arise from spin polarization of the C-H bond of the methyl groups. Thus, the contribution from the C 2p_π spin density on the Cp′ ligands is included, with the typical hyperfine coupling of an α-proton in a π radical taking the following form [$\alpha_{H/2}$, α_H, 3$\alpha_{H/2}$], where α_H is the isotropic component. The best simulation using this model was developed with α_{iso} = –2.38 MHz (Figure S21).

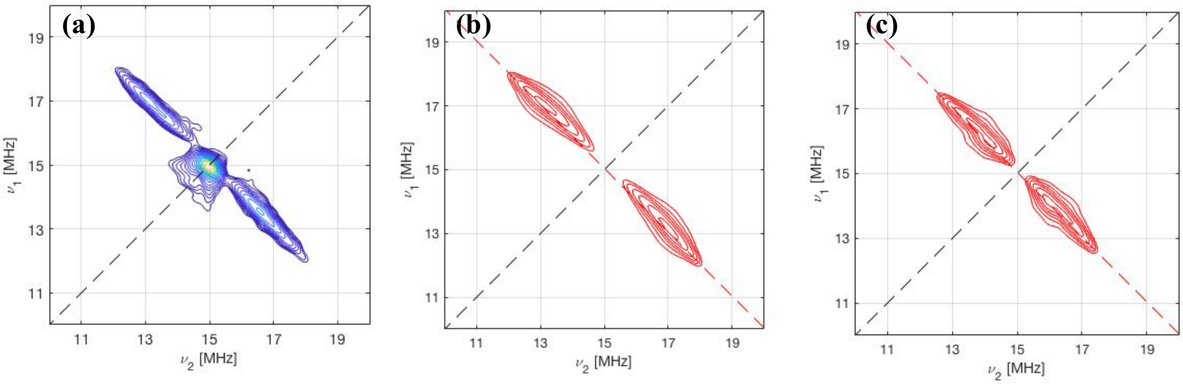

Figure S21. (a) ^{1}H HYSCORE spectrum for **2** (THF) at B_0 = 353.7 mT (**OP5**; Figure 2), T = 40 K, and X-band (9.7356 GHz); (b) Calculation based on the model described in the text; (c) Calculation based on the dipole model only. The dashed-red antidiagonal line marks the ^{1}H Larmor frequenc

Chapter VI. Manuscript draft 2:

Ligand Effects on the Spin Relaxation Dynamics and Coherence Manipulation of Organometallic La^{II} Potential Qudits

Lydia E. Nodaraki,[1,2] Ana-Maria Ariciu,[1,2] Daniel N. Huh,[3] Jingjing Liu,[1] Fabrizio Ortu,[1] Richard E.P. Winpenny,[1] Eric J. L. McInnes,[1,2] David P. Mills,[1] William J. Evans[3] and Floriana Tuna[1,2]

[1]School of Chemistry, The University of Manchester, Oxford Road, Manchester M13 9PL, UK
[2]Photon Science Institute, The University of Manchester, Oxford Road, Manchester M13 9PL, UK
[3]Department of Chemistry, University of California, Irvine, CA 92697-2025

ABSTRACT: Quantum information processing (QIP) offers opportunity to utilize the electronic states of molecules for data processing. This allows speeding up of computation through the encoding of the vast Hilbert space of a general quantum state, and use of quantum mechanics to implement the calculation algorithms. A major challenge is to be able to handle a large number of qubits while preserving their quantum properties. Use of qudits (multilevel quantum systems featuring d quantum states; d > 2) enables to expand the amount of information that could be encoded and processed with the same number of quantum objects. Here we present the first pulsed EPR studies on La(II) complexes that permit a eight dimensions Hilbert space, opening up the possibility of performing quantum operations within a single molecule. The three complexes investigated, [K(2.2.2-cryptand)][La(Cp')$_3$] (**1**), [K(2.2.2-cryptand)][La(Cp'')$_3$] (**2**) and [K(2.2.2-cryptand)][La(Cp^{tt})$_3$] (**3**), feature cyclopentadienyl derivatives (Cp' = $C_6H_5SiMe_3$; Cp'' = $C_6H_4(SiMe_3)_2$; Cp^{tt} = $C_6H_4(CMe_3)_2$) as ligands and display a C_3 symmetry. Pulse electron paramagnetic resonance (EPR) studies have revealed long spin-lattice relaxation, T_1, and phase memory, T_m, times for all three compounds. Only a small variation in T_1 across the series was observed, while T_2 remains largely unchanged (2.0 (**1**), 2.2 (**2**) and 2.4 μs (**3**)). Coherence spin manipulation is performed by the observation of Rabi quantum oscillations up to 80 K in this nuclear spin-rich environment (^{1}H, ^{13}C and ^{29}Si), suggesting remarkable robustness of the coherence properties in this series of complexes. We demonstrate that all eight electronuclear transitions resulted from the interaction of the electron with the nuclear spin (I = 7/2) of ^{139}La can be coherently manipulated using microwave pulses. Application of HYSCORE techniques allow us to quantify the electron spin density at ligand nuclei for the first time showing a total spin population on the three ligands of 27%, 7.8% and 24.4% for **1**, **2** and **3**, respectively.

The chemistry of lanthanide (Ln) ions is largely dominated by the trivalent oxidation state regardless of the number of the 4f valence electrons.[1] One possible explanation for the prevalence of the Ln trivalent oxidation state is the balance between lattice and ionization enthalpies. However, recent advances in organometallic chemistry have made it possible to stabilize the divalent oxidation state for almost all elements of the 4f series.[2] One critical factor for accessing the uncommon +2 oxidation state is the choice of the ligand. Cyclopentadienyl ligands have been previously employed for the stabilization of Ln^{2+} ions (for all the lanthanide ions except Pm), demonstrating that the tris-Cp ligand environment is significantly important for the reduction of the lanthanide metals (4f^n Ln^{3+} to 4f^{n-1} Ln^{2+}).[3] Structural, spectroscopic and density functional theory (DFT) studies have indicated that the trigonal environment assured by three cyclopentadienyl ligands significantly stabilizes the (n+1) d_z^2 orbital, suggesting a 4f^{n}5d^1 ground state configuration for the reduced Ln^{2+} ion,[4] and 4d^1 for Y^{2+}.[5] We are particularly intrigued about the possibility to stabilize electronic configurations with unpaired electrons residing in a d orbital rather than f. In spite of significant advances made in the synthesis of divalent organometallic lanthanide complexes, there is little known about their electronic structures and chemical bonding.[6] A proper engineering of their electronic structures could be advantageous, giving opportunity to exploit their multi-level structure for quantum information processing with the possibility of encoding information in their electronuclear states, thus forming multi-state qudits (d is the dimension of the Hilbert space). Some Ln elements possess large nuclear spins, hence we can expect several electronuclear transitions to be accessible for coherent spin manipulations via microwave pulses. We recently reported remarkable quantum properties in a tris-cyclopentadinyl yttrium(II) complex, demonstrating its potential as a four-level quantum system.[7] The *pseudo*-C_3 symmetry plays a central role as it leads to the admixture of the *s*- and d_z^2 atomic orbitals, contributing to a highly isotropic S = ½ ground state. This demonstrates the importance of the ligand environment in the design of a robust quantum bit (qubit),[8] which is relatively insensitive to the environmental noise. Here we demonstrate that the nuclear Hilbert space can be expanded through the interaction of the electron with the nuclear spin of

^{139}La(II) isotope (I = 7/2; 99.95 natural abundance), thus leading to qu*d*its with d = 8. This can be regarded as an alternative route for the realization of multi-level systems that enable larger and more complex calculation algorithms within a single molecular unit. We report the occurrence of robust quantum coherence and coherent spin manipulations in a family of lanthanum(II) tris-cyclopentadienyl complexes, [K(2.2.2-cryptand)]-[La(Cp')$_3$] (**1**), [K(2.2.2-cryptand)][La(Cp'')$_3$] (**2**) and [K(2.2.2-cryptand)][La(Cp^{tt})$_3$] (**3**) (Figure 1) that contain one unpaired electron primarily residing in a low-energy d$_{z2}$ orbital, and three Cp ligands featuring one or two RMe$_3$ (R = Si or C) functional groups (Cp' = $C_6H_5SiMe_3$; Cp'' = $C_6H_4(SiMe_3)_2$; Cp^{tt} = $C_6H_4(CMe_3)_2$). The structural similitude of the complexes enables to assess the impact of different substituents attached to the Cp ring on the quantum coherence properties of the complexes, and to gain better understanding of the decoherence processes.

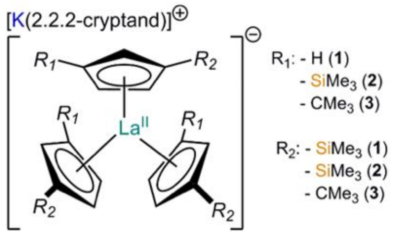

Figure 1. Schematic representation of the structures of **1**, **2** and **3**.

The synthesis and structural characterization of **1**[9], **2**[10] and **3**[11] have been previously reported. In these compounds the La(II) ion is located in the middle of the plane formed by the centroids of the three Cp ligands leading to a nearly planar trigonal arrangement. The three-coordinated compounds display a local *pseudo*-C$_3$ symmetry at the metal center, with the C$_3$ axis passing through the metal, and perpendicular to the plane made by the centroids of the three Cp rings bound to metal. The geometric parameters of the anions are very similar for the three different complexes, while the average La-C(Cp) distances are 2.853 Å, 2.884 Å and 2.901 Å for **1**, **2** and **3**, respectively. At the same time, the average of the La-centroid lengths are 2.586 Å (**1**) 2.620 Å (**2**) and 2.638 Å (**3**), showing that the most bulky Cp substituents lead to longer distances.

Echo-detected field-swept (EDFS) pulse EPR spectra for complexes **1**-**3**, measured on THF solution (Figure 2) display a 8-line pattern due to the hyperfine interaction of the unpaired electron with the nuclear spin of ^{139}La^{II} ion (I = 7/2, with 99.95 % natural abundance). The analysis of the data was carried out with EasySpin[12] using the axial Hamiltonian $\hat{H} = g\mu_B BS + IAS$, where g is the axial g-tensor and A the axial hyperfine coupling tensor. Excellent reproductions of the EDFS experimental spectra of **1**, **2**, and **3** were obtained with the set of parameters given in Table 1 (Figure 2). Simulation of the EDFS spectra of **2** is further improved by the addition of a small portion of an unknown species (Figure S7). This is not unexpected, as previous reports have shown existence of both [K(dme)$_x$][La(Cp'')$_3$] and [La(Cp'')$_2$(dme)$_y$] in thermal equilibrium in the EPR spectra of THF solutions of [La(Cp'')$_3$] undergoing reduction in the presence of K.[13] All parameters resulted from simulation (Table 1) are in line with the values reported in the literature for La(II) complexes.[14]

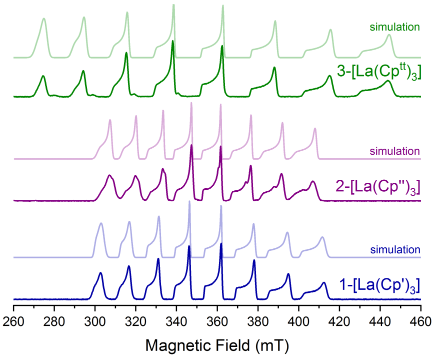

Figure 2. Echo-detected field-swept spectra of **1** (blue), **2** (purple) and **3** (green) recorded at X-band (9.67GHz) on frozen THF solutions (see Table 1 for simulation parameters).

Hyperfine interactions can involve two different mechanisms: the Fermi-contact (through bond) interaction and the anisotropic dipolar (though space) coupling.[15] The isotropic Fermi contact interaction arises from the finite electron spin density at the nucleus and can be related to the partial 6s-orbital character of the SOMO orbital (which is predominantly d$_{z^2}$).[16] The insignificant difference of the A_{iso} values (426.7 MHz (**1**) and 391.7 MHz (**2**)), for complexes **1** and **2**, containing SiMe$_3$ substituents, might suggest a comparable s-character of the SOMO orbital. However, complex **3** shows a much larger A_{iso} (636.7 MHz) indicating increased s-orbital character of the formal 5d$_{z^2}$ orbital relative to that of **1** and **2**. The non-equidistant peak-to-peak separation as the strength of applied magnetic field increases, in both CW (Figure S5-S8) and EDFS spectra (Figure 2), is ascribed to the second order contributions to the A_{iso} coupling constants. Moreover, the sharp linewidth of the peaks suggest that La(II) experiences long electron spin relaxation.

Table 1. Extracted EPR parameters for **1**, **2** and **3** (10 mM; THF).

	T (K)	g	A (MHz)	A (G)
1	80	$g_{\parallel}$ = 1.999 $g_{\perp}$ = 1.956	$A_{\parallel}$ = 420 $A_{\perp}$ = 430	$A_{\parallel}$ = 150 $A_{\perp}$ = 157
	295	g = 1.994	A = 430	A = 154[14]
2	80	$g_{\parallel}$ = 2.001 $g_{\perp}$ = 1.950	$A_{\parallel}$ = 392 $A_{\perp}$ = 385	$A_{\parallel}$ = 140 $A_{\perp}$ = 141
	295	g = 1.990	A = 372	A = 133.5[10]
3	40	$g_{\parallel}$ = 1.998 $g_{\perp}$ = 1.934	$A_{\parallel}$ = 650 $A_{\perp}$ = 630	$A_{\parallel}$ = 232 $A_{\perp}$ = 233

The relaxation times of all complexes were measured using adequate pulse EPR sequences (see SI). The spin-lattice relaxation times (T_1) at different temperatures were obtained by fitting the data collected with a magnetization inversion recovery sequence (*π - t - π/2 - τ - π - τ - echo*, with variable *t*)[17] to a bi-exponential function (Figures S9-S17; Tables S1-S3). At high temperatures, T_1 shows field and temperature dependence, while below 10 K it is not determined by the field and reaches the values of ~19 ms for **1**, ~8 ms for **2**, and ~53 ms for **3**. Significantly longer relaxation times were found for the *z*-orientation ($B_0 \parallel C_3$) for all three complexes. However, for both orientations a Raman-like dependence of T_1 with the temperature can be assumed; fitting of the data by the Raman mechanism equation, CT^n,[18] provided the following Raman parameters $C_1 = 1.07(4) \cdot 10^{-6}$ μs^{-1}, $n_1 = 2.58(5)$ for **1**, $C_2 = 8.73(2) \cdot 10^{-7}$ μs^{-1}, $n_2 = 2.71(2)$ for **2** and $C_3 = 1.23(7) \cdot 10^{-7}$ μs^{-1}, $n_3 = 3.22(7)$ for **3**. In contrast, the spin-spin relaxation times (T_m) exhibit temperature - but not field - dependence, and reach values as high as 2 μs for **1**, 2.2 μs for **2**, and 2.4 μs for **3** at 5 K. Surprisingly, long coherent times are observed notwithstanding that each of the complex contains a plethora of ^{1}H nuclei, and no attempt was done to dilute or deuterate the compounds.

Due to the sufficiently long relaxation times, we were able to perform further pulsed EPR experiments to probe the coherent manipulation of the electron-spin. Transient nutation experiments were carried out at variable microwave powers by placing a tipping pulse, t_p, in front of a standard Hahn echo sequence, which tilts the magnetization through an angle, $\theta = g\mu_B B1 t_p/\hbar$.[19] The applied magnetic field quantizes the alignment of the spin into two well discrete states $m_S = \pm \frac{1}{2}$, and any deviation from the alignment of the spin with one of these two states constitutes a superposition of the two states. During the nutation measurement the magnetization is tilted away from alignment with the applied magnetic field by the microwave pulse applied, whose length is varied to enable cycling of the spin through all arbitrary superposition states. If the system is a qubit, a smooth oscillation in the detected signal is observed, known as Rabi oscillation.[20]

As observed in Figure 3a (and Figures S31-S40, S43-S51 and S54-S57) Rabi oscillations are detected for all eight electronuclear transitions of the three complexes, indicating that this system can function as a qu*d*it with d=8. Fourier transform analysis of these oscillations (Figure 3b and S31-S40, S43-S51 and S54-S57) reveals a clear linear dependence of the Rabi frequency, Ω_R, (most prominent peak) with the microwave field strength, B_1 (Figure 3c and S41, S52 and S58). Note that nuclear spins and cavity background effects could also generate oscillations on the intensity of the spin echo, leads to the necessity to record the nutation data at multiple pulse powers. Indeed, a sharp peak, which is B_1-independent and corresponds to the Larmor frequency of ^{1}H nuclei[21] is observed, indicating that some interaction between electron and ^{1}H nuclei on ligands and/or solvent does occur. Such interactions are disadvantageous for QIP as they cause quantum coherence and thus shortenings of the lifetime of qubit or qudit. More importantly, the nutation data provide information on the properties of the qubit. The time period between a maximum and the adjacent minimum of the oscillation corresponds to the flipping time of the spin, meaning the time required for executing a logical operation.[22] Crucially, the operation time parameter needs to be notably shorter than the lifetime of the qubit in order the qubit to be functional. This time was calculated to be 78, 115 and 105 ns for complex **1**, **2** and **3**, respectively, using the experimental nutation data recorded under 16 dB applied mw power for the $|S, m_s\rangle$ transition $|-1/2, +1/2\rangle \rightarrow |+1/2, +1/2\rangle$. Nevertheless, this time span reduces significantly when pulses with higher power are applied leading to faster flipping of the spins. The qubit figure of merit, Q_M, is defined as $2\Omega_R T_2$ and represents the number of coherent single–qubit NOT computational operations.[23] For complexes **1**, **2** and **3** the Q_M value is 156, 128 and 130, respectively, which are in agreement with reported Q_M values for molecular complexes.[24]

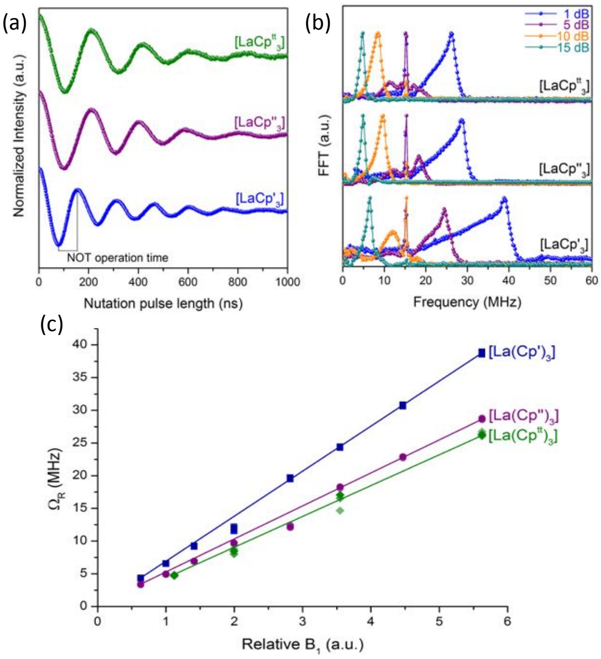

Figure 3. (a) Nutation (Rabi oscillations) data for **1** (**OP10**), **2** (**OP5**) and **3** (**OP3**) measured at 16 dB for the $|-1/2, +1/2\rangle \rightarrow |+1/2, +1/2\rangle$ transition measured at 20 K; (b) Fourier transforms of the nutation data at different microwave powers; and (c) B_1 dependence of the Rabi frequency (Ω_R); the solid line is a guide of the eye emphasizing the linear behaviour.

As noted previously, stabilization of the divalent oxidation state of the lanthanum ion implies an electronic configuration change from $4f^05d^0$ to $4f^05d^1$ upon reduction of La^{3+} to La^{2+}.[10,25] However, the assumption that the unpaired electron of La purely resides in the lowest energy $5d_{z2}$ orbital is in discordance with the too small anisotropy of the *g*- and hyperfine (A)- tensors, based on CW and EDFS data. Hence, a more detailed characterization of the lanthanum environment in **1**, **2** and **3** was necessary and was attempted by using the two-dimensional hyperfine sublevel correlation (HYSCORE) technique.[26] This hyperfine method allows to quantify small hyperfine interactions of the unpaired electron of La^{II} with the ^{1}H and ^{13}C nuclei of the different cyclopentadienyl ligands. Following the assumption that the unpaired electron do not purely reside on the 5d orbital, HYSCORE spectroscopy will report on the electron spin density transferred to the proton and carbon atoms of the ligands via the weak hyperfine interactions.

HYSCORE spectroscopy uses a four-pulse electron spin-echo sequence, *π/2 - τ - π/2 - t1 - π - t2 - π/2 - τ - echo*, which generates correlations between the nuclear frequencies in the *α* and *β* electron spin manifolds. To quantify the interactions of the electron with the proton and carbon on the Cp ligands, a theoretical model[27] was used to simulate the HYSCORE data. This model is based on the assumption that the total hyperfine coupling matrix (A) for a given ^{13}C nucleus is determined by the contribution of the spin density at the carbon nucleus n (A^{Cn}) plus the point dipole (through space) interactions with spin density at other atoms (A^{dip}), $A = A^{Cn} + A^{dip}$. The following equation was used to calculate the dipolar interaction constants based on the crystal structure of each of the complexes:

$$A^{dip} = \frac{\mu_0}{4\pi h}\beta_e\beta_n \sum\nolimits_k \rho_k \frac{3(g\cdot n_k)(\tilde{n}_k \cdot g_n 1) - g\cdot g_n 1}{r_k^3}$$

where g and g_n1 are the electronic and nuclear g matrices (g_n is the nuclear g-values; 1 is the unit matrix), β_e and β_n are the electron and nuclear magnetons, ρ_k is the spin population at the k atom, n_k and $\tilde{n}_k$ are the n…k unit vectors (expressed in the molecular frame), h is the Plank's constant and μ_0 the vacuum permittivity. Assuming predominant spin density on the La ions ($\rho_{La} = 1$), the point dipolar (A^{dip}) interactions of each carbon position in the Cp ring were calculated based on the crystallographic coordinates. Hence, the molecular axis system was defined in reference to the *g*-tensor, with the g_z component lying along the C_3 unique axis. Initially, we focused on the simulation of the ^{13}C carbon region, which allows a more direct account of the spin density in the $2p_\pi$ orbitals of the carbon atoms of the cyclopentadienyl ligands. These non-metal frontier orbitals are involved in covalent, metal-ligand interaction, and therefore the bulk of any spin density transferred from the metal to the Cp ligands will be in these C $2p_\pi$ orbitals. All simulations were performed under the assumption that the each A^{Cn} matrix is axial, and the unique axis is aligned with the $2p_\pi$ direction (ie. in the molecular *xy* plane), enabling to resolve A_z and A_{xy} for each C atom. First attempts were performed based only on the point dipole interactions, with the calculated spectra not matching with the experimental ones (Figures 4b, 5b and 6b). Therefore we added covalent spin density contribution to the dipolar hyperfine components.

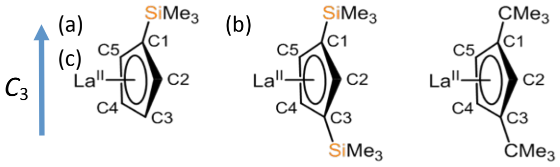

Figure 4. Schematic representation of the (a) La-Cp', (b) La-Cp'' and (c) La-Cp^{tt} along with the labels used for the HYSCORE simulations and the orientation of the C_3 axis.

For **1**, we obtained excellent simulations with $A^{C2,5}_{z,xy}$ = 13.4, 3.4 MHz and $A^{C3,4}_{z,xy}$ = 5.3, 0.9 MHz (Figure 4a), detecting large coupling with $C^{2,5}$, smaller interaction with $C^{3,4}$, while C^{1} shows negligible contribution to the ^{13}C couplings. For complex **2**, the best simulation of the experimental ^{13}C HYSCORE spectra was achieved with $A^{C2}_{z,xy}$ = 7.3, 0.8 MHz and $A^{C1,3}_{z,xy}$ = 2.0, 0.8 MHz (Figure 5a), while negligible densities was considered for C^{4} and C^{5}. Finally, for complex **3**, simulation based on the following ^{13}C hyperfine values; $A^{C2,}_{z,xy}$ = 13.4, 1.8 MHz, $A^{C1,3}_{z,xy}$ = 5.6, 0.6 MHz and $A^{C4,5}_{z,xy}$ = 0.8, 0.6 MHz, gave us great agreement between experimental and calculated data (Figure 6a). Hence, in this case the contribution from the $2p_\pi$-spin density of all C atoms on the Cp^{tt} ligand was observed, while the dominant one was again obtained for C^{2}. Unfortunately we were not able to resolve the g_z orientation for any of the three complexes due to a very weak signal (signal-to-noise ratio is limited by the fast relaxation and low natural abundancy of the ^{13}C). In addition, the $2p_\pi$ spin polarization (ρ_p) for each carbon atom on the ring can be estimated by using the following equation: $A_\parallel - A_\perp = {}^{6}/_{5}\,\rho_P P_P$, where P_p is the electron nuclear dipolar coupling parameter for unit population ($\rho_p = 1$) of a ^{13}C 2p orbital. Applying the theoretical value of P_p = 268 MHz,[28] the $2p_\pi$ spin polarization was calculated for each carbon and the values are listed in Table 2.

Table 2. Calculated spin Hamiltonian parameters via HYSCORE experiments for **1**, **2** and **3** (10 mM; THF).

	1-La	2-La	3-La
C^1	-	$A_\parallel = 2.0$ $A_\perp = 0.8$ $\rho_P = 0.003$	$A_\parallel = 5.6$ $A_\perp = 0.6$ $\rho_P = 0.015$
C^2	$A_\parallel = 13.4$ $A_\perp = 3.4$ $\rho_P = 0.031$ $\alpha_{iso} = -2.612(H^2)$	$A_\parallel = 7.3$ $A_\perp = 0.8$ $\rho_P = 0.020$ $\alpha_{iso} = -1.698(H^2)$	$A_\parallel = 13.4$ $A_\perp = 1.8$ $\rho_P = 0.050$ $\alpha_{iso} = -3.030(H^2)$
C^3	$A_\parallel = 5.3$ $A_\perp = 0.9$ $\rho_P = 0.014,$ $\alpha_{iso} = -1.149(H^3)$	$A_\parallel = 2.0$ $A_\perp = 0.8$ $\rho_P = 0.003$	$A_\parallel = 5.6$ $A_\perp = 0.6$ $\rho_P = 0.015$

C^4	$A_\parallel = 5.3$ $A_\perp = 0.9$ $\rho_P = 0.014$ $\alpha_{iso} = -1.149(H^4)$	-	$A_\parallel = 0.8$ $A_\perp = 0.6$ $\rho_P = 0.0006$ $\alpha_{iso} = -0.052(H^4)$
C^5	$A_\parallel = 13.4$ $A_\perp = 3.4$ $\rho_P = 0.031$ $\alpha_{iso} = -2.612(H^5)$	-	$A_\parallel = 0.8$ $A_\perp = 0.6$ $\rho_P = 0.0006$ $\alpha_{iso} = -0.052(H^5)$

A similar approach was followed for the modelling the ^{1}H HYSCORE spectra. The point dipole-only model again failed to reproduce the experimental data, even though dipolar interactions are expected to dominate the calculations because of the large magnetic moment of the ^{1}H. Thus, in order to reproduce the spectra we needed to add a contribution that takes into account the spin density transferred from the carbons of the Cp rings to the protons bounded to them, via spin polarization of the C-H. The hyperfine matrix to an α proton in π radicals typically takes the form [$\alpha_{iso}/2$, α_{iso}, $3\alpha_{iso}/2$], where the smallest component is oriented along the C-H bond, the middle one, α_{iso}, follows the $2p_\pi$ direction, while the largest hyperfine occurs as the cross-product of the $2p_\pi$ and C-H orientation. Excellent simulations of the spectra were obtained (Figures 4-6). For **1**, we found $\alpha_{iso} = -2.612$ MHz for $H^{2,5}$ and $\alpha_{iso} = -1.149$ MHz for $H^{3,4}$, for both g_{xy} and g_z orientations (Figure 4c,d). For complex **2**, data were satisfactory simulated with $\alpha_{iso} = -1.698$ MHz for H^2, while contributions from the protons attached to C^4 and C^5 are negligible due to the negligible densities at these carbons (Figure 5c,d). Finally, for complex **3** addition of spin polarization contribution for the proton attached to C^2 (no protons are attached to $C^{1,3}$, and the amount of spin density at $C^{4,5}$ is insignificant) models nicely the experimental data providing $\alpha_{iso} = -3.030$ MHz for H^2 (Figure 6c,d). The isotropic hyperfine constant α_{iso} at the α-proton is linked to the spin density at the associated C $2p_\pi$ orbital by the simple McConnell relationship, $\alpha_{iso} = Q_{CH} \cdot \rho_P$,[29] where Q_{CH} is the ^{1}H hyperfine coupling that would be observed for $\rho_P = 1$. With $Q_{CH} = -84$ MHz from studies od Cp radicals,[30] we obtained spin densities at C for **1** of 3.1% for $C^{2,5}$ and 1.5% for $C^{3,4}$, for **2** of 2.0% for C^2 and 0.3% for $C^{1,3}$ and finally, for **3** of 5.0% for C^2, 1.5% for $C^{1,3}$ and negligible spin density of 0.06% for $C^{4,5}$.

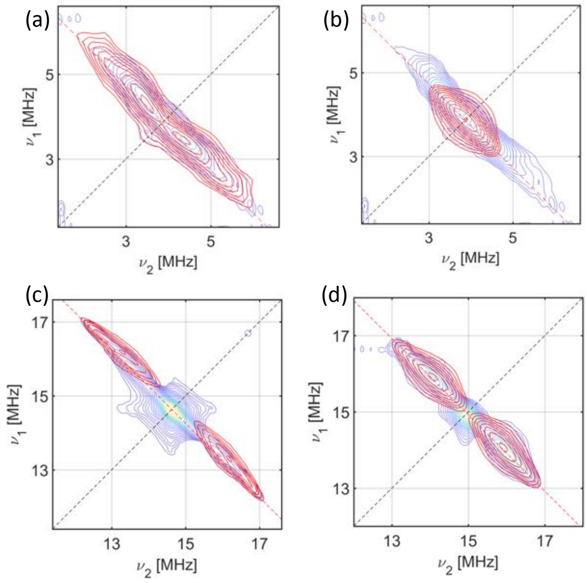

Figure 4. X-band HYSCORE spectra for **1** (a) ^{13}C region at a static field of $B_0 = 360.8$ mT (at g_{xy}) with calculation in red based only on the point dipole model including C^1-C^5; (b) same as for (a) but the simulation (red) includes spin density contribution on the ^{13}C hyperfine interactions; (c) ^{1}H region at a static field of $B_0 = 345.3$ mT (at g_{xy}) with calculation in red based on the La-H point dipole model summed with the spin polarization contribution to the hyperfine at H^2-H^5 resulting from $2p_\pi$-spin density from the corresponding carbon atoms; (d) ^{1}H region at a static field of $B_0 = 353.8$ mT (at g_z) with the simulation based on the same model as for (c).

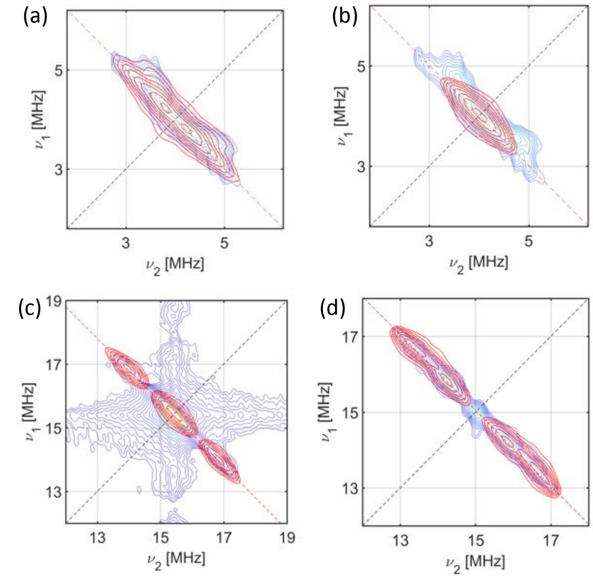

Figure 5. X-band HYSCORE spectra for **2** (a) ^{13}C region at a static field of $B_0 = 373.8$ mT (at g_{xy}) with calculation in red based only on the point dipole model including C^1-C^5; (b) same as for (a) but the simulation (red) includes spin density contribution on the ^{13}C hyperfine interactions; (c) ^{1}H region at a static field of $B_0 = 361.7$ mT (at g_{xy}) with calculation in red based on the La-H point dipole model that includes H^2, H^4 and H^5 summed with the spin polarization contribution to the hyperfine only at H^2 resulting from $2p_\pi$-spin density from C^2; (d) ^{1}H region at a static field of $B_0 = 352.8$ mT (at g_z) with the simulation based on the same model as for (c).

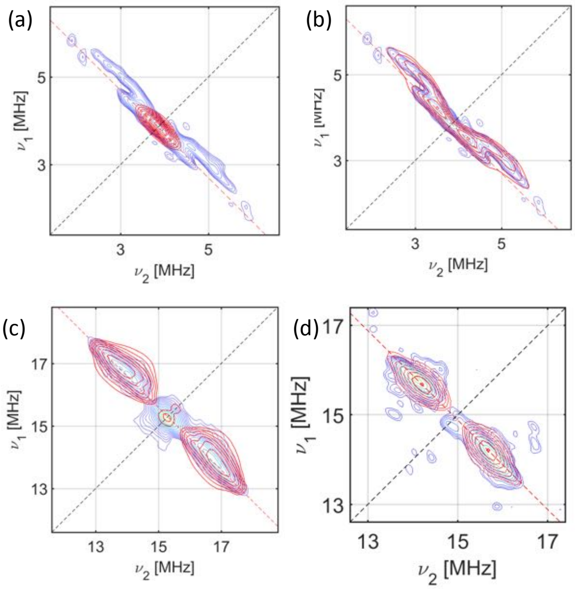

Figure 6. X-band HYSCORE spectra for **3** (a) ^{13}C region at a static field of B_0 = 362.2 mT (at g_{xy}) with calculation in red based only on the point dipole model including C^1-C^5; (b) same as for (a) but the simulation (red) includes spin density contribution on the ^{13}C hyperfine interactions; (c) ^{1}H region at a static field of B_0 = 362.2 mT (at g_{xy}) with calculation in red based on the La-H point dipole model summed with the spin polarization contribution to the hyperfine at all H atoms on the Cp^{tt} ring (H^2, H^4 and H^5) resulting from 2p$_\pi$-spin density from the corresponding carbon atoms; (d) ^{1}H region at a static field of B_0 = 352.4 mT (at g_z) with the simulation based on the same model as for (c).

In conclusion, pulse electron paramagnetic resonance (EPR) studies of three new organometallic La^{II} complexes based on -Cp' (**1**), -Cp'' (**2**) and -Cp^{tt} (**3**) were reported. By modifying the chemical structure of the molecules we investigated the effect of various substituents on the spin dynamics of the electronic spin qubits. Phase memory values display inconsequential difference between the three complexes, while T_1 times show an important prolongation from 8 ms (**2**) to 19 ms (**1**) and more importantly 53 ms for **3**. Combination of the relaxation times measurements with the metal-ligand covalency data, collected via HYSCORE spectroscopy, demonstrates that spin-lattice relaxation time is influenced by the spin-delocalization onto the ligands.[31] Longer spin-lattice and phase memory relaxation times obtained for **3** are in accord with the greater spin density on the -Cp^{tt} rings, and the increased energy of the vibrational modes judged by the higher rigidity of the ligand. All electronuclear transitions were accessed and Rabi oscillations were observed up to 80 K. Additionally similar NOT operation times and Q$_M$ values were recorded for all complexes, with **1** implementing a faster inversion of the qubit phase and thus, allowing higher number of single–qubit NOT computational operations in a given time.

References

1. R. E. Connick. Oxidation states of the rare-earth and actinide elements. *J. Chem. Soc.*, **1949**, S235-S241.

2. (a) T. F. Jenkins, D. H. Woen, L. N. Mohanam, J. W. Ziller, F. Furche and W. J. Evans. Tetramethylcyclopentadienyl ligands allow isolation of Ln(II) ions across the lanthanide series in [K(2.2.2-cryptand)][(C$_5$Me$_4$H)$_3$)Ln] complexes. *Organometallics*, **2018**, 37, 3863-3873. (b) D. Turcitu, F. Nief and L. Ricard. Structure and reactivity of homoleptic samarium(II) and thulium(II) phosphonyl complexes. *Chem.-Eur. J.*, **2003**, 9, 4916-4923. (c) Z. Xie, S. Wang, Q. Yang and T. C. W. Mark. Application of new versatile ligand to lanthanide(II) chemistry: Synthesis, reactivity, and structure of a new class of organolanthanide complexes. *Organometallics*, **1999**, 18, 2420-2427.

3. (a) M. P. Coles, P. B. Hitchcock, M. F. Lappert and A. Protchenko. Syntheses and structures of the crystalline, highly, crowded 1,3-bis(trimethylsilyl)cyclopentadienyls [MCp″$_3$] (M = Y, Er, Yb), [PbCp″$_2$], [{YCp″$_2$(μ-OH)}$_2$], [(ScCp″$_2$)$_2$](μ-η^2:η^2-C$_2$H$_4$)], [YbCp″$_2$Cl(μ-Cl)K(18-crown-6)], and [{K Cp″}]∞. *Organometallics*, **2012**, 31, 2682-2690. (b) W. J. Evans. Tutorial on the role of cyclopentadienyl ligands in the discovery of molecular complexes of the rare-earth and actinide metals in new oxidation states. *Organometallics*, **2016**, 35, 3088-3100. (c) M. R. MacDonald, J. E. Bates, J. W. Ziller, F. Furche and W. J. Evans. Completing the series of 2+ ions for the lanthanide elements: Synthesis of molecular complexes of Pr^{2+}, Gd^{2+}, Tb^{2+}, and Lu^{2+}. *J. Am. Chem. Soc.*, **2013**, 135, 9857-9868.

4. M. R. MacDonald, J. E. Bates, M. E. Fieser, J. W. Ziller, F. Furche and W. J. Evans. Expanding rare-earth oxidation state chemistry to molecular complexes of holmium(II) and erbium(II). *J. Am. Chem. Soc.*, **2012**, 134, 8420-8423.

5. M. R. MacDonald, J. W. Ziller and W. J. Evans. Synthesis of a crystalline molecular complex of Y^{2+}, [(18-crown-6)K][(C$_5$H$_4$SiMe$_3$)$_3$Y]. *J. Am. Chem. Soc.*, **2011**, 133, 15914-15917.

6. S. Labouille, C. Clavaguéra and F. Nief. Theoretical insights into the nature of divalent lanthanide-ligand interactions. *Organometallics*, **2013**, 32, 1265-1271.

7. A.-M. Ariciu, D. H. Woen, D. N. Huh, L. E. Nodaraki, A. K. Kostopoulos, C. A. P. Goodwin, N. F. Chilton, E. J. L. McInnes, R. E. P. Winpenny, W. J. Evans and F. Tuna. Engineering electronic structure to prolong relaxation times in molecular qubits by minimising orbital angular momentum. *Nat. Commun.*, **2019**, 10, 3330.

8. M. Atzori, L. Tesi, E. Morra, M. Chiesa, L. Sorace and R. Sessoli. Room-Temperature Quantum Coherence and Rabi Oscillations in Vanadyl Phthalocyanine: Toward Multifunctional Molecular Spin Qubits. *J. Am. Chem. Soc.*, **2016**, 138, 7, 2154-2157.

9. M. E. Fieser, M. R. MacDonald, B. T. Krull, J. E. Bates, J. W. Ziller, F. Furche, W. J. Evans. Structural, Spectroscopic, and Theoretical Comparison of Traditional vs Recently Discovered Ln^{2+} Ions in the [K(2.2.2-

cryptand)][($C_5H_4SiMe_3$)$_3$Ln] Complexes: The Variable Nature of Dy^{2+} and Nd^{2+}. *J. Am. Chem. Soc.*, **2015**, 137, 369-382.

10. P. B. Hitchcock, M. F. Lappert, L. Maron and A. V. Protchenko. Lanthanum Does Form Stable Molecular Compounds in the +2 Oxidation State. *Angew. Chem. Int. Ed.*, **2008**, 47, 1488-1491.

11. J. Liu, PhD thesis, University of Manchester, 2019.

12. S. Stoll and A. Schweiger. Easyspin, a comprehensive software package for spectral simulation and analysis in EPR. *J. Magn. Reson.*, **2006**, 178, 42-55.

13. M. C. Cassani, M. F. Lappert and F. Laschi. First identification by EPR spectra of lanthanum(II) organometallic intermediates (and $E_{\frac{1}{2}}$ for $La^{3+} \rightarrow La^{2+}$) in the C–O bond activation of dimethoxyethane. *Chem. Commun.*, **1997**, 1563-1564.

14. D. H. Woen, D. N. Huh, J. W. Ziller and W. J. Evans. Reactivity of Ln(II) complexes supported by $(C_5H_4Me)^{1-}$ ligands with THF and $PhSiH_3$: Isolation of ring-opened, bridging alkoxyalkyl, hydride, and silyl products. *Organometallics*, **2018**, 37, 3055-3063.

15. C. Karunakaran and M. Balamurugan. Spin resonance spectroscopy: Principles and applications, Chapter 4: Electron paramagnetic resonance spectroscopy, *Elsevier*, **2018**.

16. T. F. Hunter and M. C. R. Symons, Spin polarization in atoms and π-radicals, *Nature*, **1967**, 213, 1121-1122.

17. A. Schweiger and J. Jeschke. Principles of Pulse Electron Paramagnetic Resonance. *Oxford University Press*, Oxford, **2001**.

18. S. S. Eaton, G. R. Eaton, Distance Measurements in Biological Systems by EPR. In biological magnetic resonance; Lawrence J. Berliner Sandra S. Eaton Gareth R. Eaton Eds.; Klewer Academic/Plenum Publishers: New York, **2000**; vol 19, pp 29-154

19. G. Wolfowicz and J. J. L. Morton. Pulse techniques for quantum information processing, *eMagRes*, **2016**, Vol 5: 1515-1528.

20. I. I. Rabi. Space quantisation in a gyrating magnetic field. *Phys. Rev.*, **1937**, 51, 652-654.

21. J. M. Zadrozny, J. Niklas, O. G. Poluektov and D. Freedman. Millisecond coherence time in a tunable molecular electronic spin qubit. *ACS Cent. Sci.*, **2015**, 1, 488-492.

22. E. Coronado. Molecular magnetism: from chemical design to spin control in molecules, materials and devices. *Nat. Rev. Mater.*, **2019**, 5, 87-104.

23. G. Aromi and O. Roubeau. Handbook on the physics and chemistry of rare earths, Vol. 56, Chapter 3: Lanthanide molecules for spin-based quantum technologies, *Elsevier*, **2019**.

24. M. J. Martínez-Pérez, S. Cardona-Serra, C. Schlegel, F. Moro, P. J. Alonso, H. Prima-García, J. M. Clemente-Juan, M. Evangelisti, A. Gaita-Ariño, J. Sesé, J. van Slageren, E. Coronado and F. Luis. Gd-based single-ion magnets with tunable magnetic anisotropy: Molecular design of spin qubits. *Phys. Rev. Lett.*, **2012**, 108, 247213.

25. C. Cassani, Y. K. Gun’ko, P. B. Hitchcock, A. G. Hulkes, A. V. Khvostov, M. F. Lappert and A. V. Protchenko. Aspects of non-classical organolanthanide chemistry. *J. Organomet. Chem.*, **2002**, 647, 71-83.

26. S. Van Doorslaer, Hyperfine Spectroscopy: ESSEM, *eMagRes*, **2017**, Vol 6: 51-70.

27. A. Formanuik, A.-M. Ariciu, F. Ortu, R. Beekmeyer, A. Kerridge, F. Tuna, E. J. L. McInnes and D. Mills. Actinide covalency measured by pulsed electron paramagnetic resonance spectroscopy. *Nat. Chem.*, **2017**, 9, 578-583.

28. J. R. Morton and K. F. Preston. Atomic parameters for paramagnetic resonance data. *J. Magn. Reson.*, **1978**, 30, 577-582.

29. H. M. McConnell and D. B. Chesnut. Comments on “Theory of isotropic hyperfine interactions in π-electron radicals”. *J. Chem. Phys.*, **1958**, 28, 107.

30. F. Gerson, W. Huber. Electron Spin Resonance Spectroscopy of Organic Radicals. *Wiley-VCH*, **2003**.

31. M. S. Fataftah, M. D. Krzyaniak, B. Vlaisavljevich, M. R. Wasielewski, J. M. Zadrozny and D. E. Freedman. Metal-ligand covalency enables room temperature molecular qubit candidates. *Chem. Sci.*, **2019**, 10, 6707-6714.

Electronic Supplementary Information

Ligand Effects on the Spin Relaxation Dynamics and Coherence Manipulation of Organometallic La^{II} Potential Qudits

Lydia E. Nodaraki,[1,2] Ana-Maria Ariciu,[1,2] Daniel N. Huh,[3] Jingjing Liu,[1] Fabrizio Ortu,[1] Richard E.P. Winpenny,[1] Eric J. L. McInnes,[1,2] David P. Mills,[1] William J. Evans[3] and Floriana Tuna[1,2]

[1]School of Chemistry, The University of Manchester, Oxford Road, Manchester M13 9PL, UK
[2]Photon Science Institute, The University of Manchester, Oxford Road, Manchester M13 9PL, UK
[3]Department of Chemistry, University of California, Irvine, CA 92697-2025

Table of Contents

1. General Experimental Considerations
2. Molecular structures of complexes **1**, **2** and **3**
3. Additional EPR Spectra for complexes **1**, **2** and **3**
    - 3.1 CW and EDFS EPR spectra
    - 3.2 Spin-Lattice Relaxation Measurements
    - 3.3 Phase Memory Time Measurements
    - 3.4 Transient Nutation Experiments
    - 3.5 HYSCORE Spectra

1. General Experimental Considerations

All manipulations and syntheses were conducted with rigorous exclusion of air and water using standard Schlenk line and glovebox techniques under an argon or dinitrogen atmosphere. Preparation and characterisation of the complexes followed previously reported methods.[1] All EPR samples were prepared under strict anaerobic conditions and measured in flame-sealed quartz EPR tubes to avoid oxidation of La^{2+} to La^{3+}. For EPR studies in solution, two procedures were followed. For complexes **1** and **2,** a solution of the respective complex of concentration 10 mM (in THF) was transferred to the EPR quartz tube within an Ar glove box, and subsequently the tube was taken out to be flame sealed under vacuum once being kept frozen using liquid nitrogen. For **3**, a 10 mM solution of $[La^{III}(Cp^{tt})_3]$ was treated with KC_8 *in-situ*, to reduce La^{3+} to La^{2+}, and the EPR tube was then flame sealed and immediately frozen under nitrogen to enable safe EPR investigation.

Continuous-wave (CW) EPR spectra were performed on polycrystalline and THF solution samples using a Bruker EMX 300 EPR spectrometer operating at X-band frequency (ca. 9.4 GHz) and equipped with a liquid He cryostat for cooling to low temperatures. Field corrections were applied using Bruker strong pitch ($g = 2.0028$) as a reference, and spectra were baselined before simulation. The CW EPR spectra were simulated with the EasySpin[2] toolbox within Matlab. Pulsed EPR measurements were conducted on frozen solution samples with a Bruker ElexSys 580 spectrometer operating at X-band frequency (ca. 9.7 GHz) and equipped with a MD5 resonator and a liquid He cryostat. Simulation of the spectra were performed using EasySpin.[3]

2. Molecular structures of complexes 1, 2 and 3.

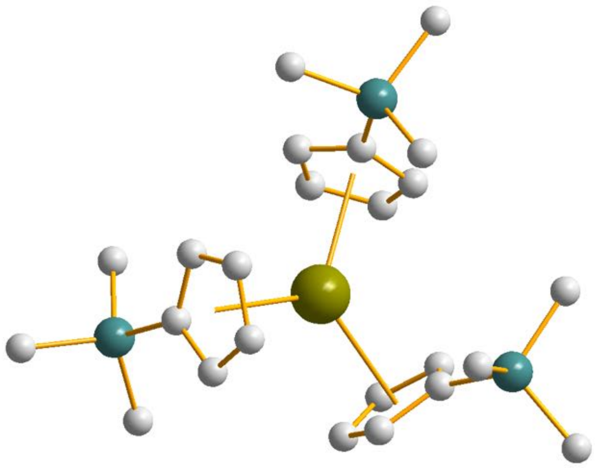

Figure S1. Molecular structure of $[La(Cp')_3]^-$ (**1**).[4] Colour code: La-gold, C-grey, Si-dark cyan. Counterions and hydrogen atoms are omitted for clarity.

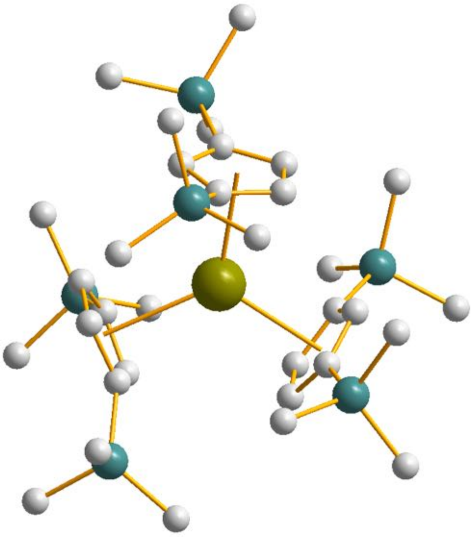

Figure S2. Molecular structure of [La(Cp'')$_3$]$^-$ (**2**).[5] Colour code: La-gold, C-grey, Si-dark cyan. Counterions and hydrogen atoms are omitted for clarity.

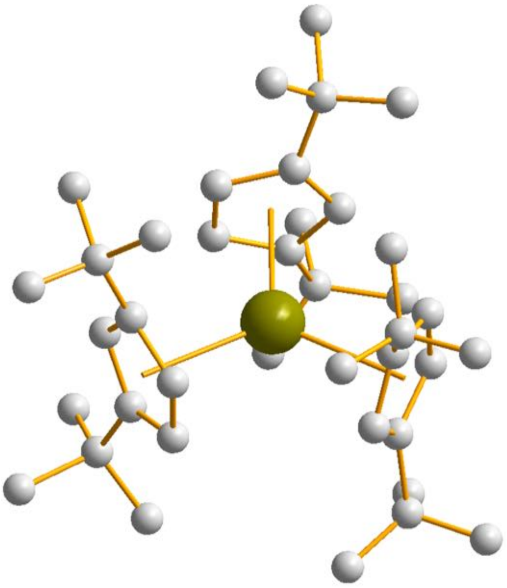

Figure S3. Molecular structure of [La(Cp^{tt})$_3$]$^-$ (**3**).[6] Colour code: La-–gold, C-grey. Counterions and hydrogen atoms are omitted for clarity.

3. Additional EPR spectra for complexes 1, 2 and 3

The pulse sequence used to record the echo-detected field-swept (EDFS) spectra was a Hahn-echo sequence *($\pi/2$ - τ - π - τ - echo)*, with $\pi/2$ and π pulse lengths of 16 ns and 32 ns, respectively, and a fixed delay time of τ = 180 ns.

3.1 CW and EDFS EPR spectra

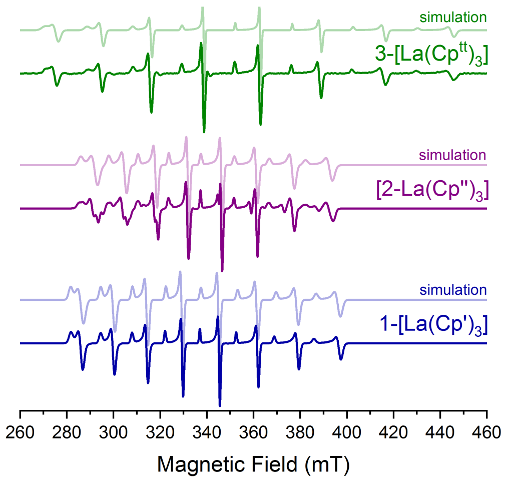

Figure S4. X-band CW EPR spectra of complexes **1**-blue, **2**-purple and **3**-green complexes measured at 40 K in frozen solutions 10 mM THF samples. Experimental spectra are shown with a bold line and the simulation is represented with the transparent line (simulation parameters Table 1).

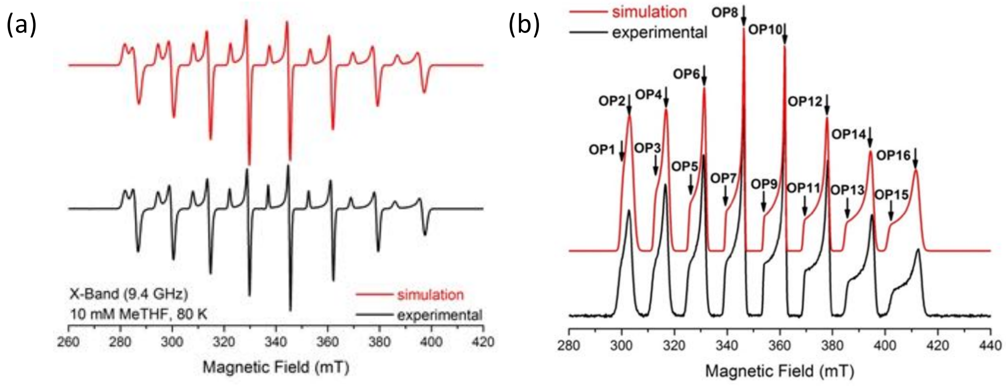

Figure S5. (a) Continuous wave and (b) echo detected field swept EPR spectra of **1** measured at 40 K in a 10 mM THF frozen solution and at X-band frequency. In both cases, experimental spectra are shown with black line and the simulated spectra are displayed in red (simulation parameters Table 1). Observer positions OP1-OP16 mark the magnetic field at which further pulse EPR experiments were performed.

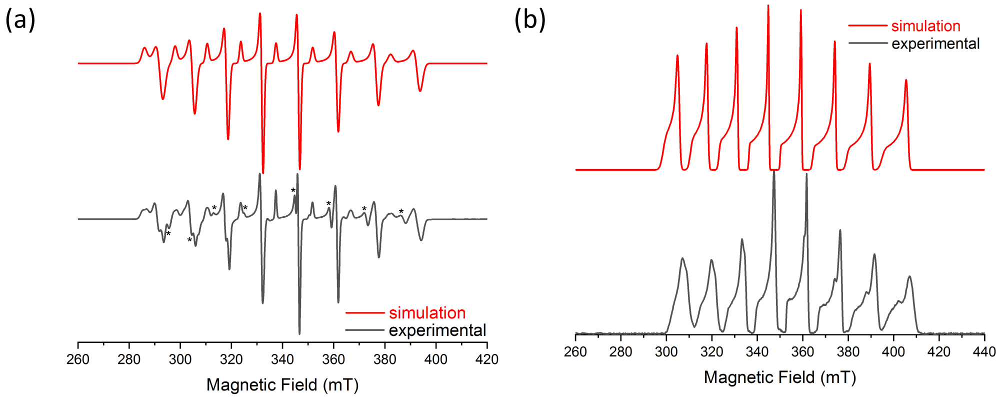

Figure S6. (a) Continuous wave and (b) echo detected field swept EPR spectra of **2** measured at 40 K in a 10 mM THF frozen solution and at X-band frequency. In both cases, experimental spectra are shown in black line and the simulated spectra are displayed in red (simulation parameters Table 1).

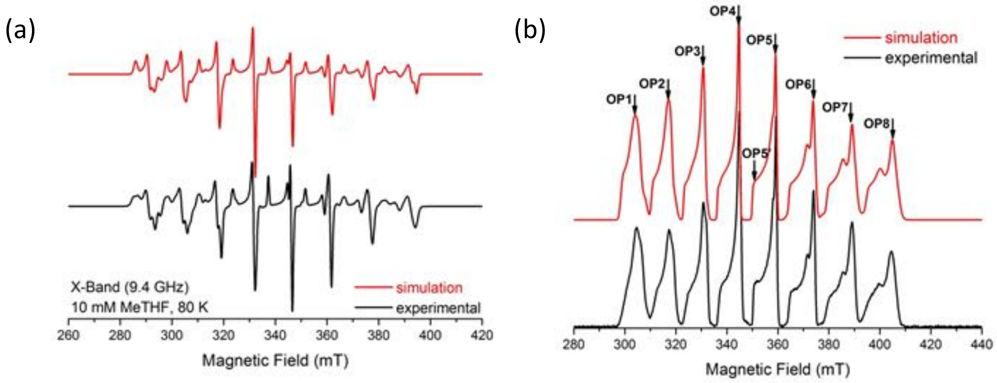

Figure S7. (a) Continuous wave and (b) echo detected field swept EPR spectra of **2** measured at 40 K in a 10 mM THF frozen solution and at X-band frequency. In both cases, experimental spectra are shown with black line and the simulated spectra are displayed in red. Simulation include secondary species modelled by the following parameters $g_{\parallel}$ = 2.001 and $g_{\perp}$ = 1.958, $A_{\parallel}$ = 352 MHz and $A_{\perp}$ = 362 MHz. Observer positions OP1-OP8 mark the magnetic field at which further pulse EPR experiments were performed.

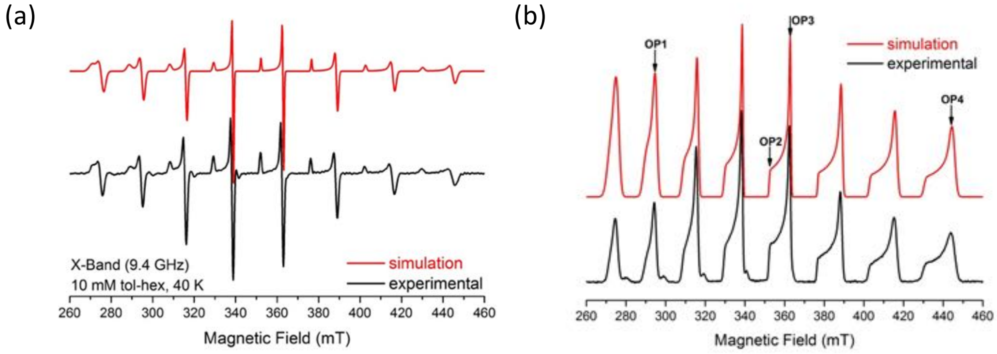

Figure S8. (a) Continuous wave and (b) echo detected field swept EPR spectra of **3** measured at 40 K in a 10 mM THF frozen solution and at X-band frequency. In both cases, experimental spectra are shown with black line and the simulated spectra are displayed in red (simulation parameters Table 1). Observer positions OP1-OP4 mark the magnetic field at which further pulse EPR experiments were performed.

3.2 Spin-Lattice Relaxation Measurements

Measurements of the spin–lattice relaxation time, T_1, measurements were carried out by using a standard magnetization inversion recovery pulse sequence (*π - t - π/2 - τ - π - τ - echo*) with 16 and 32 ns π/2 and π pulse lengths, respectively, with a fixed *τ* and variable *t*. The time constant T_1 was extracted by fitting the experimental data according to the following equation:[7]

$$Y(t) = Y(0) + Y_1 \mathrm{e}^{(-t/\mathrm{T}_1)} + Y_{\mathrm{SD}} \mathrm{e}^{(-t/T_{\mathrm{SD}})} \quad (1)$$

where Y_1 and Y_{SD} are the amplitudes and T_{SD} is the spectral diffusion time constant.

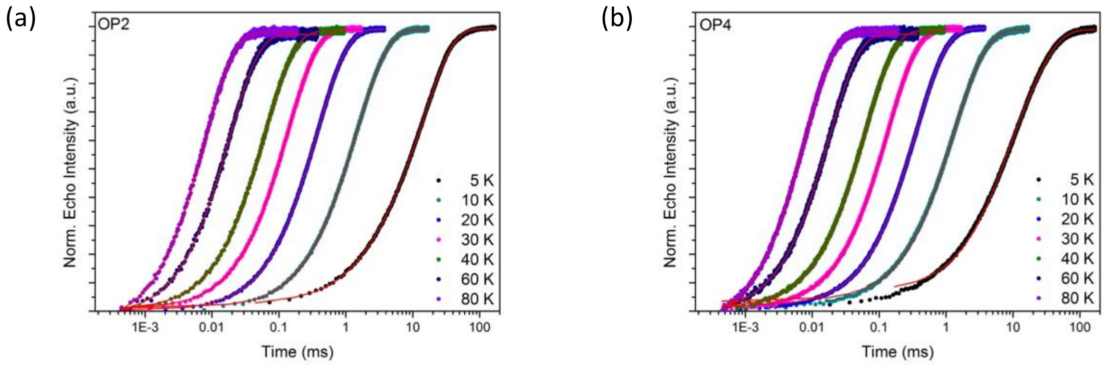

Figure S9. Normalized echo integral as a function of time, t, in a standard inversion recovery sequence for **1** at OP2 (a) and OP4 (b) at selected temperatures. The red line represents the best fitting of the data to the biexponential model, with parameters in Table S1.

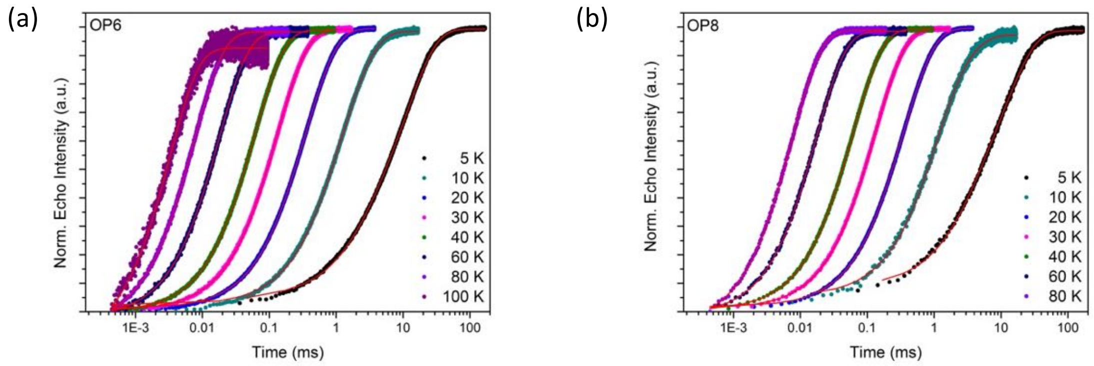

Figure S10. Normalized echo integral as a function of time, t, in a standard inversion recovery sequence for **1** at OP6 (a) and OP8 (b) at selected temperatures. The red line represents the best fitting of the data to the biexponential model, with parameters in Table S1.

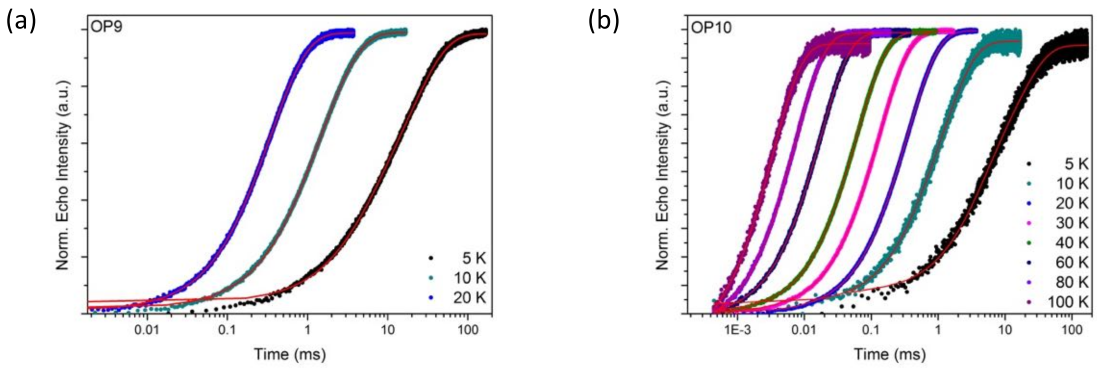

Figure S11. Normalized echo integral as a function of time, t, in a standard inversion recovery sequence for **1** at OP9 (a) and OP10 (b) at selected temperatures. The red line represents the best fitting of the data to the biexponential model, with parameters in Table S1.

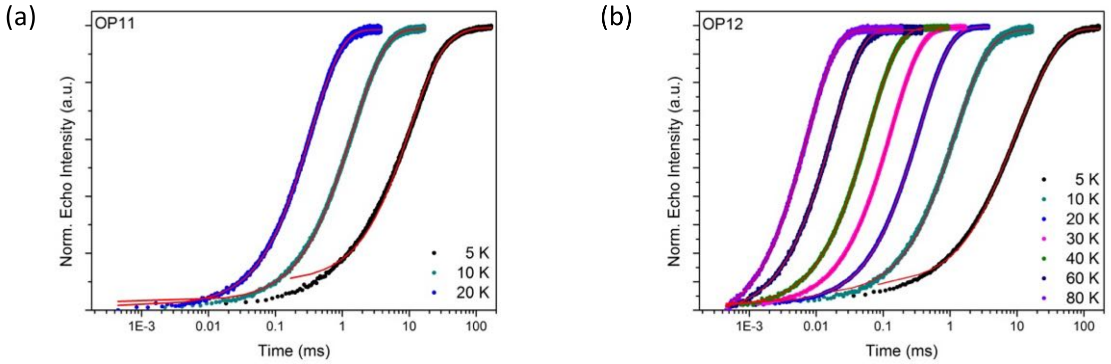

Figure S12. Normalized echo integral as a function of time, t, in a standard inversion recovery sequence for **1** at OP11 (a) and OP12 (b) at selected temperatures. The red line represents the best fitting of the data to the biexponential model, with parameters in Table S1.

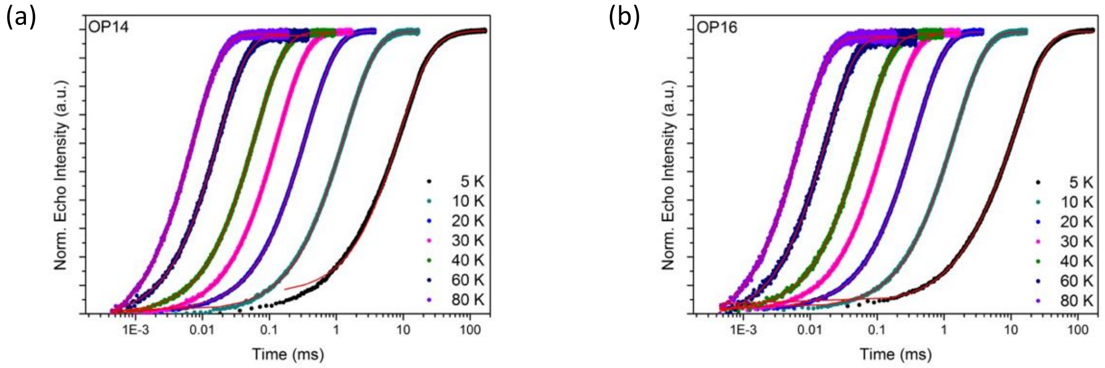

Figure S13. Normalized echo integral as a function of time, t, in a standard inversion recovery sequence for **1** at OP14 (a) and OP16 (b) at selected temperatures. The red line represents the best fitting of the data to the biexponential model, with parameters in Table S1.

Table S1. Extracted spin-lattice relaxation time constants (T_1) for **1** in μs (10 mM THF) at X-band, based on Figures S9 –S13.

T(K)	OP1		OP2		OP3		OP4	
	T_1 (μs)	T_{SD} (μs)	T_1 (μs)	T_{SD} (μs)	T_1 (μs)	T_{SD} (μs)	T_1 (μs)	T_{SD} (μs)
5	24781	5006	14982	1963	17419	2387	19396	5237
10	1888	743	1699	627	1891	773	1855	857
20	416	234	408	161	389	147	420	219
30			146	62			149	79
40			68	38			67	43
60			20	10			20	12
80			9	6			8	6

T(K)	OP5		OP6		OP7		OP8	
	T_1 (μs)	T_{SD} (μs)	T_1 (μs)	T_{SD} (μs)	T_1 (μs)	T_{SD} (μs)	T_1 (μs)	T_{SD} (μs)
5	28448	2845	11860	1930	26998	6482	12616	2724
10	1848	712	1730	743	1900	777	2360	912
20	390	167	409	190	392	174	406	184
30			149	84	133	13	145	73
40			67	40	52	3	64	20
60			24	16	20	15	60	12
80			8	6	5	2	8	6

T(K)	OP9		OP10		OP11		OP12	
	T_1 (μs)	T_{SD} (μs)	T_1 (μs)	T_{SD} (μs)	T_1 (μs)	T_{SD} (μs)	T_1 (μs)	T_{SD} (μs)
5	21008	4251	16654	3400	22785	8514	19017	4529
10	1879	747	1429	411	1879	725	2403	965
20	393	183	399	180	394	183	401	187
30	124	41	149	87			147	79
40	53	36	79	54			65	35
60	18	4	21	15			16	11
80	5	1	10	7			8	6

T(K)	OP13		OP14		OP15		OP16	
	T_1 (μs)	T_{SD} (μs)	T_1 (μs)	T_{SD} (μs)	T_1 (μs)	T_{SD} (μs)	T_1 (μs)	T_{SD} (μs)
5	16390	2807	24863	8217	18885	2400	13143	1768
10	1916	793	1667	664	2114	1056	1656	600
20	392	168	413	209	401	185	409	187
30			145	74			148	74
40			65	33			66	31
60			19	14			18	4
80			7	4			8	5

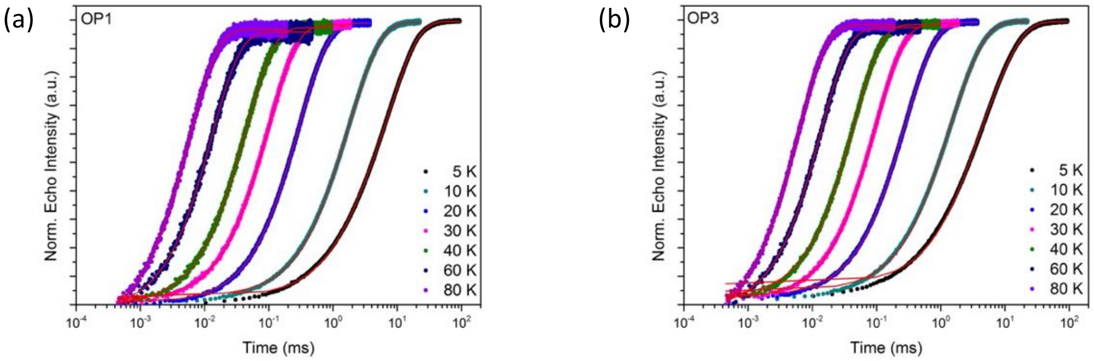

Figure S14. Normalized echo integral as a function of time, t, in a standard inversion recovery sequence for **2** at OP1 (a) and OP3 (b) at selected temperatures. The red line represents the best fitting of the data to the biexponential model, with parameters in Table S2.

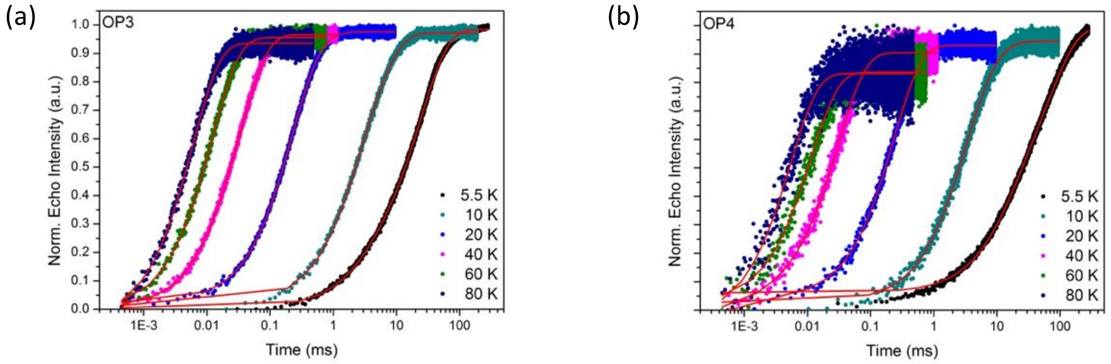

Figure S15. Normalized echo integral as a function of time, t, in a standard inversion recovery sequence for **2** at OP5’ (a) and OP7 (b) at selected temperatures. The red line represents the best fitting of the data to the biexponential model, with parameters in Table S2.

Table S2. Extracted spin-lattice relaxation time constants (T_1) for **2** in µs (10 mM THF) at X-band (9.7GHz), based on Figures S14–S15.

T(K)	OP1		OP2		OP3		OP4		OP5	
	T_1 (μs)	T_{SD} (μs)	T_1 (μs)	T_{SD} (μs)	T_1 (μs)	T_{SD} (μs)	T_1 (μs)	T_{SD}(μs)	T_1 (μs)	T_{SD}(μs)
5	8062	1407	8005	2127	11211	2764	7295	1953	8878	2474
10	2297	860	2169	758	2501	854	1968	677	2156	780
20	344	186	341	163	333	148	-	-	332	143
30	121	81	129	82	88	46	117	74	120	76
40	46	17	44		34	9	65	41	48	17
60	27	12	39	13	9	*	15	10	15	9
80	7	5	8	5	4	*	8	6	7	4

*mono-exponential equation was used

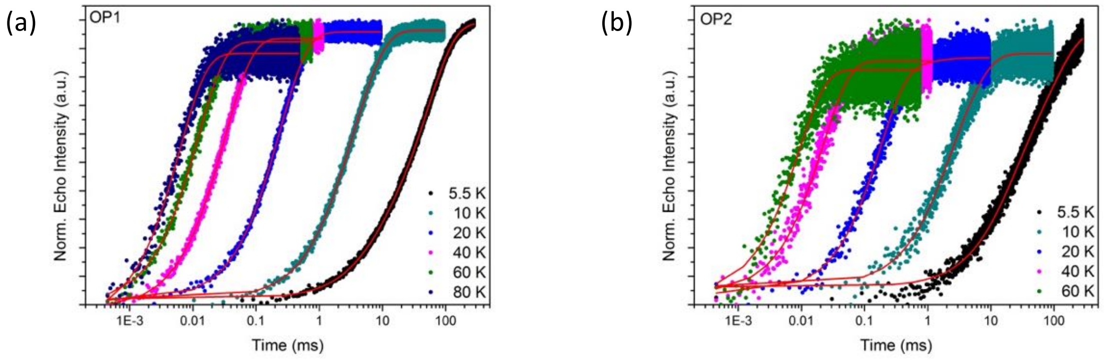

Figure S16. Normalized echo integral as a function of time, t, in a standard inversion recovery sequence for **3** at OP1 (a) and OP2 (b) at selected temperatures. The red line represents the best fitting of the data to the biexponential model, with parameters in Table S3.

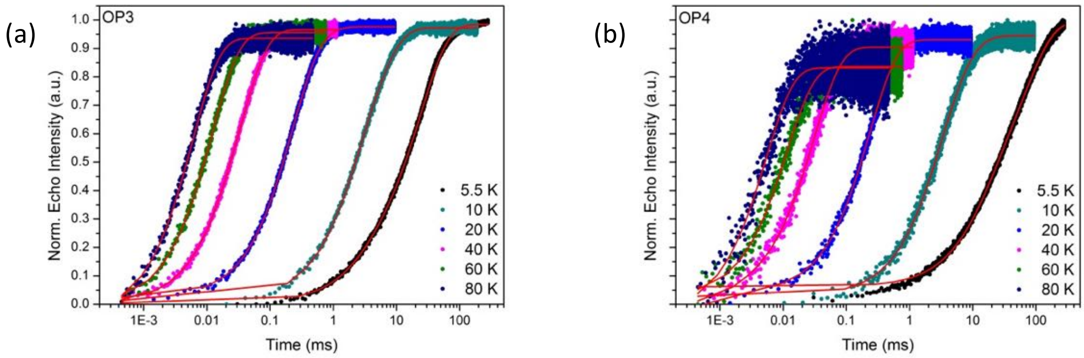

Figure S17. Normalized echo integral as a function of time, t, in a standard inversion recovery sequence for **3** at OP3 (a) and OP4 (b) at selected temperatures. The red line represents the best fitting of the data to the biexponential model, with parameters in Table S3.

Table S3. Extracted spin-lattice relaxation time constants for **3** in μs (10 mM THF) at X-band (9.7GHz), based on Figures S16–S17.

T (K)	OP1		OP2		OP3		OP4	
	T_1 (μs)	T_{SD} (μs)	T_1 (μs)	T_{SD} (μs)	T_1 (μs)	T_{SD} (μs)	T_1 (μs)	T_{SD} (μs)
5.5	52891	6244	97780	16458	24463	2683	71807	13205
10	4478	1650	4199	1416	4752	1725	5688	2603
20	357	224	1047	173	429	212	234	2
40	33	7	22	*	34	12	31	2
60	12	*	9	*	12	*	11	*
80	6	*			6	*	5	*

*mono-exponential equation was used

3.3 Phase Memory Time Measurements

Measurements of the phase memory time, T_m, measurements were carried out using a Hahn echo sequence (*π/2 - τ - π - τ - echo*)[7] with gradually increasing the inter-pulse delay, *τ*. Using microwave pulse length of 32 ns or 128 ns for *τ* pulse, strong proton-electron spin modulation was observed. In order to suppress the ^{1}H modulation in the echo decays, longer microwave pulses of length *τ* = 256 ns or *π* = 1000 ns were used. The fitting function used for the echo decays is the following:

$$\mathrm{Y}(2\tau) = \mathrm{Y}(0)\mathrm{e}^{(-2\tau/T_{\mathrm{m}})^{S}} \quad (2)$$

where S is the stretch factor.

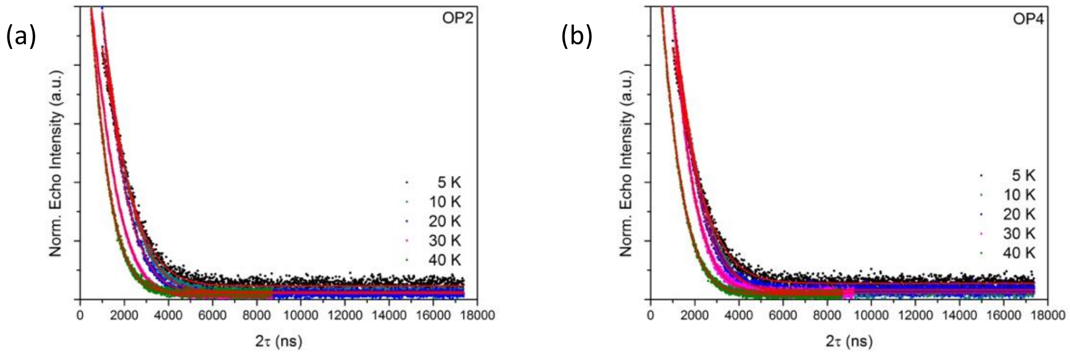

Figure S18. Normalized echo integral of **1** as a function of 2τ measured at (a) OP2 and (b) OP4 and at variable temperatures. The red lines correspond to the best fit using the mono-exponential decay, with parameters in Table S4.

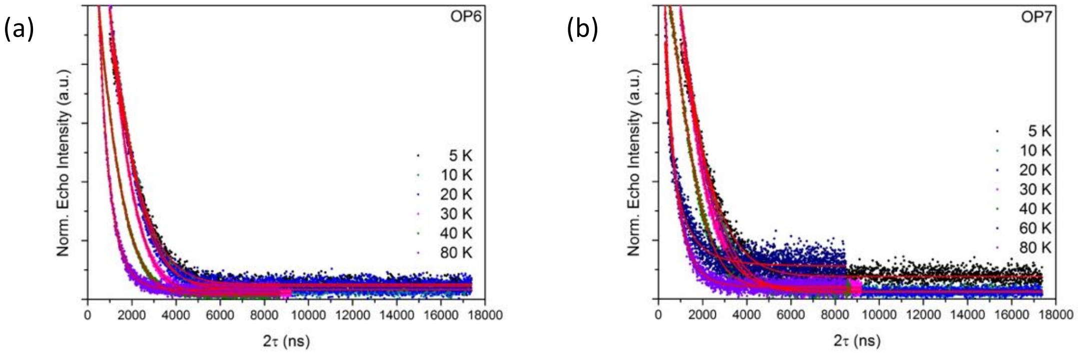

Figure S19. Normalized echo integral of **1** as a function of 2τ measured at (a) OP6 and (b) OP7 and at variable temperatures. The red lines correspond to the best fit using the mono-exponential decay, with parameters in Table S4.

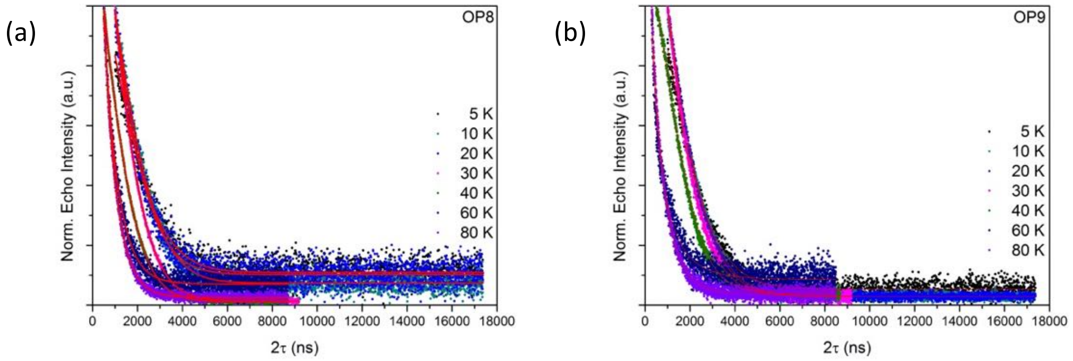

Figure S20. Normalized echo integral of **1** as a function of 2τ measured at (a) OP8 and (b) OP9 and at variable temperatures. The red lines correspond to the best fit using the mono-exponential decay, with parameters in Table S4.

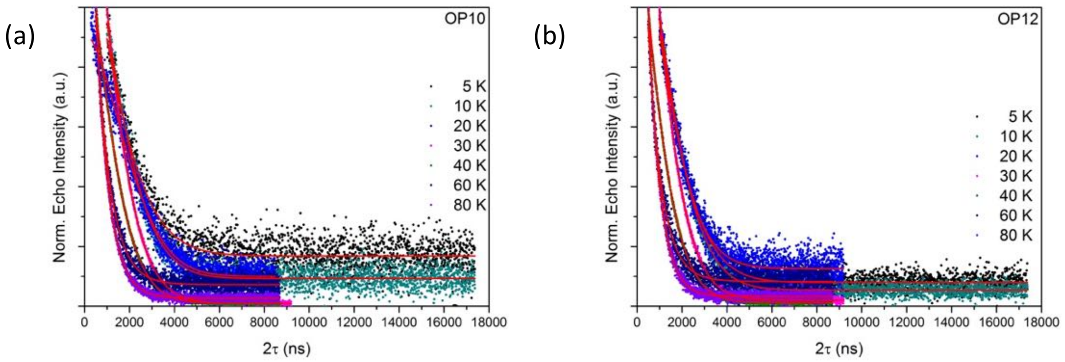

Figure S21. Normalized echo integral of **1** as a function of 2τ measured at (a) OP10 and (b) OP12 and at variable temperatures. The red lines correspond to the best fit using the mono-exponential decay, with parameters in Table S4.

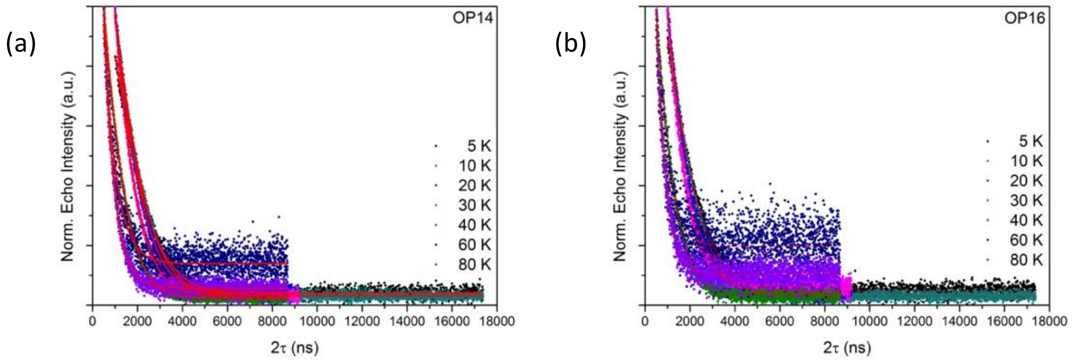

Figure S22. Normalized echo integral of **1** as a function of 2τ measured at (a) OP14 and (b) OP16 and at variable temperatures. The red lines correspond to the best fit using the mono-exponential decay, with parameters in Table S4.

Table S4. Extracted phase memory time (T_m) for **1** in μs (10 mM THF) at X-band, based on Figures S18–S22.

T (K)	**OP1**	**OP2**	**OP3**	**0P4**	**OP5**	**OP6**	**OP7**	**OP8**
5	1.839	1.903	1.883	1.886	1.944	1.979	2.012	2.016
10	1.703	1.715	1.757	1.789	1.85	1.879	1.953	1.964
20	1.497	1.482	1.537	1.573	1.664	1.706	1.794	1.743
30		1.176		1.283		1.429	1.483	1.529
40		1.013		1.108		1.248	1.537	1.407
60		0.484		0.474		0.569	0.481	0.628
80		0.393		0.436		0.463	0.4	0.54
T (K)	**OP9**	**OP10**	**OP11**	**OP12**	**OP13**	**OP14**	**OP15**	**OP16**
5	2.041	1.899	2.01	1.93	1.912	1.905	1.807	1.822
10	2	1.999	1.962	1.906	1.808	1.778	1.754	1.683
20	1.884	2.38	1.793	1.72	1.624	1.555	1.457	1.394
30	1.645	1.558		1.411		1.236		1.119
40	1.71	1.45		1.292		1.113		0.951
60	0.43	0.629		0.552		0.572		0.388
80	0.477	0.576		0.513		0.447		0.359

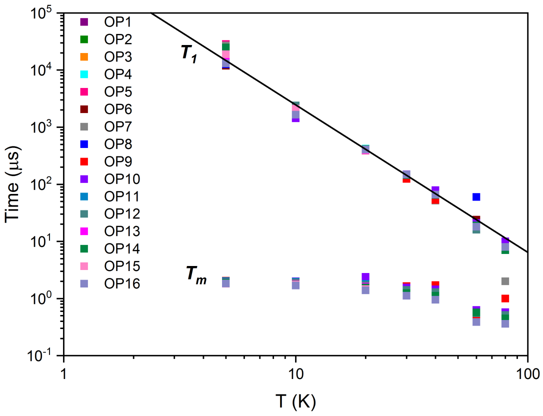

Figure S23. Temperature dependence of T_1 and T_m for **1** at X-band (9.7 GHz) and at different observer positions, as indicated in the Figure S2. The solid line corresponds to the best fit of the T_1 data with the following equation $T_1^{-1} = CT^n$ with the Raman parameters of C_1 = 1.07(4) × 10^{-6} μs^{-1} and n_1 = 2.58(5).

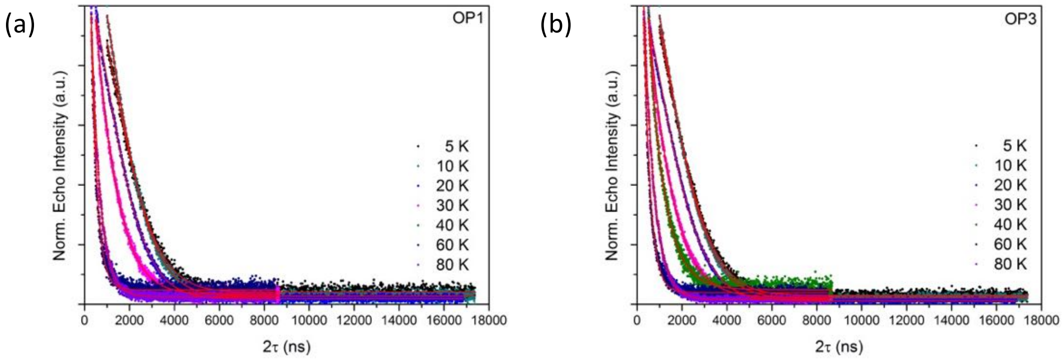

Figure S24. Normalized echo integral of **2** as a function of 2τ measured at (a) OP1 and (b) OP3 and at variable temperatures. The red lines correspond to the best fit using the mono-exponential decay, with parameters in Table S5.

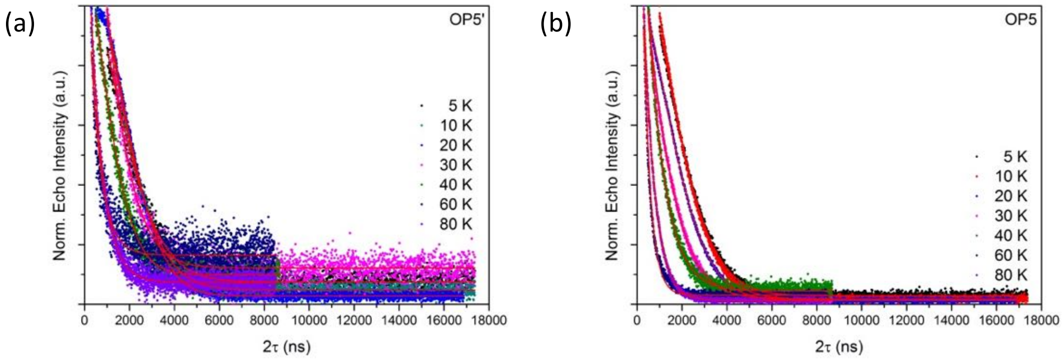

Figure S25. Normalized echo integral of **2** as a function of 2τ measured at (a) OP5’ and (b) OP5 and at variable temperatures. The red lines correspond to the best fit using the mono-exponential decay, with parameters in Table S5.

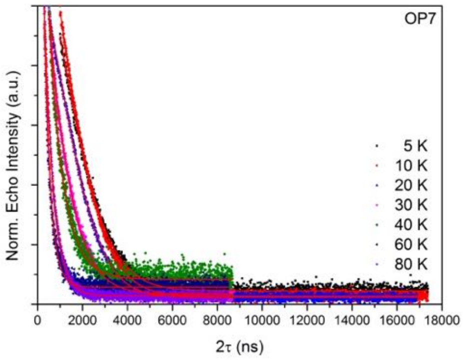

Figure S26. Normalized echo integral of **2** as a function of 2τ measured at OP7 at variable temperatures. The red lines correspond to the best fit using the mono-exponential decay, with parameters in Table S5.

Table S5. Extracted phase memory time constants (T_m) for **2** in μs (10 mM THF) at X-band (9.7GHz), based on Figures S24–S26.

T (K)	OP1	OP2	OP3	OP4	OP5
5	2.144	2.255	2.218	2.243	2.100
10	2.021	2.136	2.145	2.131	1.998
20	1.854	2.003	2.361	2.099	1.947
30	1.104	1.201	1.381	1.375	1.156
40	0.623	0.659	1.429	0.811	0.594
60	0.269	0.293	0.492	0.316	0.284
80	0.374	0.468	0.555	0.519	0.407

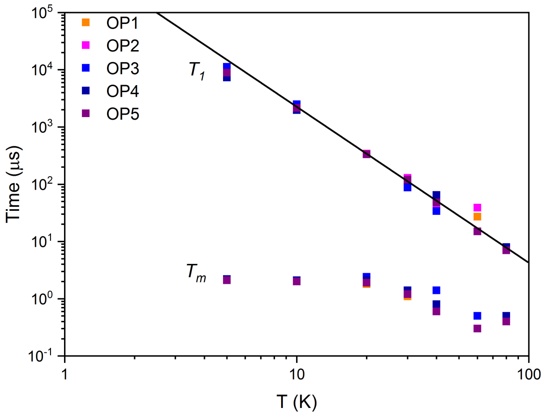

Figure S27. Temperature dependence of T_1 and T_m for **2** at X-band (9.7 GHz) and at different observer positions, as indicated in the Figure S3. The solid line corresponds to the best fit of the T_1 data with the following equation $T_1^{-1} = CT^n$ with the Raman parameters of C_2 = 8.73(2) × 10^{-7} μs^{-1} and n_2 = 2.71(2).

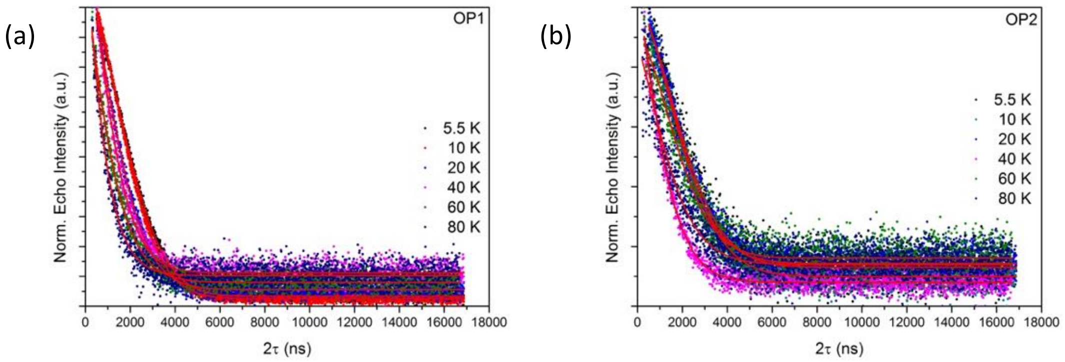

Figure S28. Normalized echo integral of **3** as a function of 2*τ* measured at (a) OP1 and (b) OP2 and at variable temperatures. The red lines correspond to the best fit using the mono-exponential decay, with parameters in Table S6.

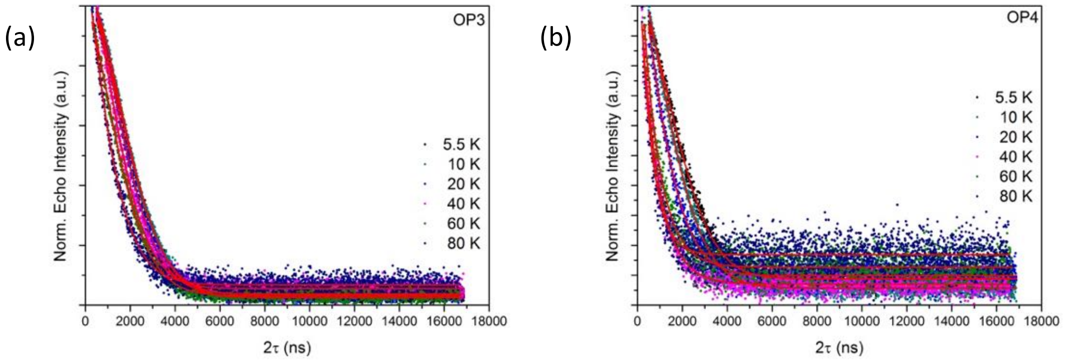

Figure S29. Normalized echo integral of **3** as a function of 2*τ* measured at (a) OP3 and (b) OP4 and at variable temperatures. The red lines correspond to the best fit using the mono-exponential decay, with parameters in Table S6.

Table S6. Extracted phase memory time constants (T_m) for **3** in μs (10 mM THF) at X-band (9.7 GHz), based on Figures S28–S29.

T (K)	OP1	OP2	OP3	0P4
5.5	2.377	-	2.439	2.295
10	2.217	2.476	-	1.985
20	1.793	2.313	2.135	1.441
40	1.334	2.218	1.842	0.799
60	1.25	2.229	1.87	0.78
80	0.888	1.697	1.307	0.57

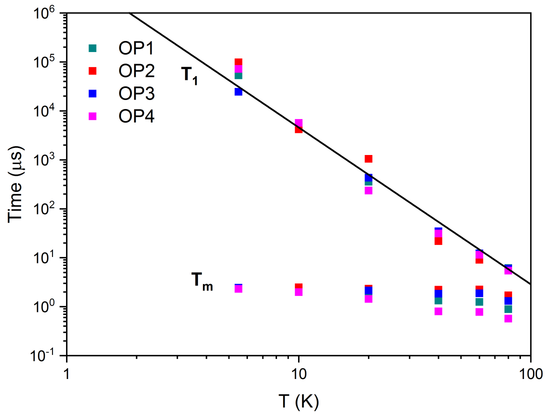

Figure S30. Temperature dependence of T_1 and T_m for **3** at X-band (9.7 GHz) and at different observer positions, as indicated in the Figure S4. The solid line corresponds to the best fit of the T_1 data with the following equation $T_1^{-1} = CT^n$ with the Raman parameters of C_3 = 1.23(7) × 10^{-7} μs^{-1} and n_3 = 3.22(7).

3.4 Transient Nutation Experiments

In the transient nutation experiments, a nutation pulse, t_p, rotated the magnetization through an angle $\theta = \mu_B B_1 t_p/\hbar$, followed by a two-pulse Hahn-echo detection sequence t_p - t_w - $\pi/2$ - τ - π - τ - *echo*, with fixed τ = 200 ns and t_w = 6000 ns that is chosen to be much longer than T_m time. The Rabi frequency, Ω_R, was determined by zero-filling the Rabi oscillation curves followed by a fast Fourier transform (FFT).

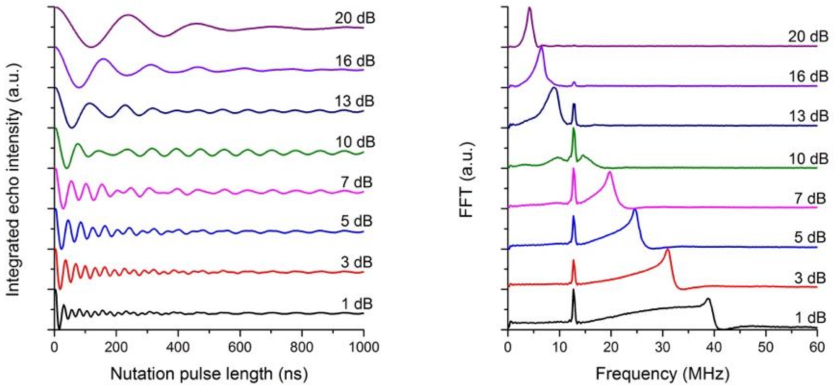

Figure S31. (left) Rabi oscillations for **1** at OP2 and at 20 K, acquired at different microwave attenuations, and (right) the corresponding Fourier transforms.

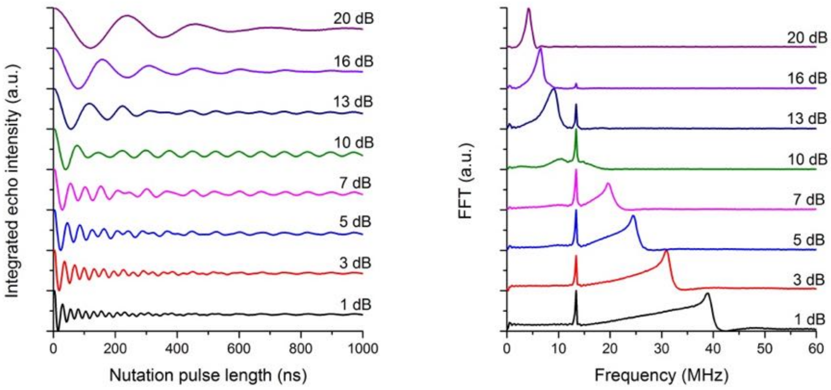

Figure S32. (left) Rabi oscillations for **1** at OP4 and at 20 K, acquired at different microwave attenuations, and (right) the corresponding Fourier transforms.

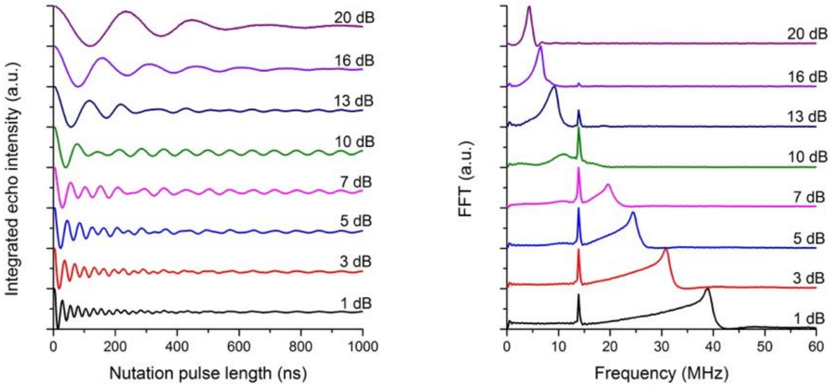

Figure S33. (left) Rabi oscillations for **1** at OP6 and at 20 K, acquired at different microwave attenuations, and (right) the corresponding Fourier transforms.

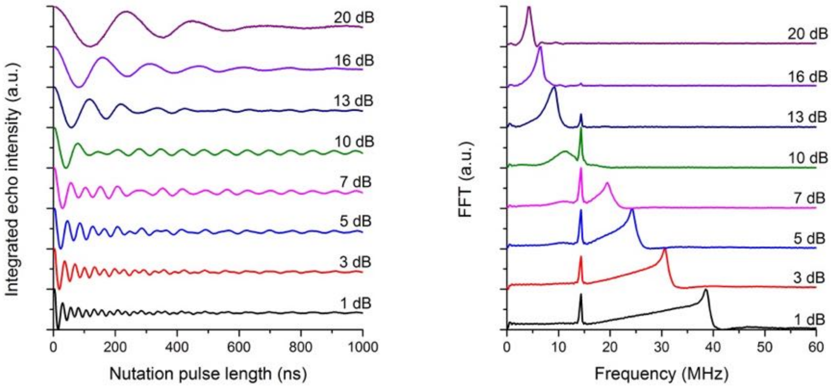

Figure S34. (left) Rabi oscillations for **1** at OP7 and at 20 K, acquired at different microwave attenuations, and (right) the corresponding Fourier transforms.

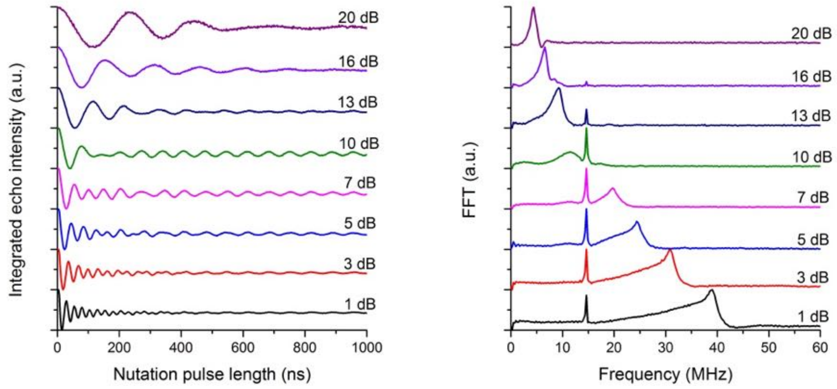

Figure S35. (left) Rabi oscillations for **1** at OP8 and at 20 K, acquired at different microwave attenuations, and (right) the corresponding Fourier transforms.

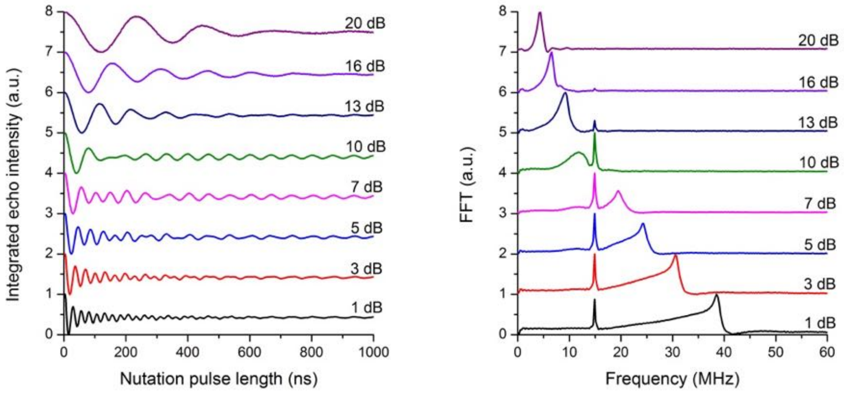

Figure S36. (left) Rabi oscillations for **1** at OP9 and at 20 K, acquired at different microwave attenuations, and (right) the corresponding Fourier transforms.

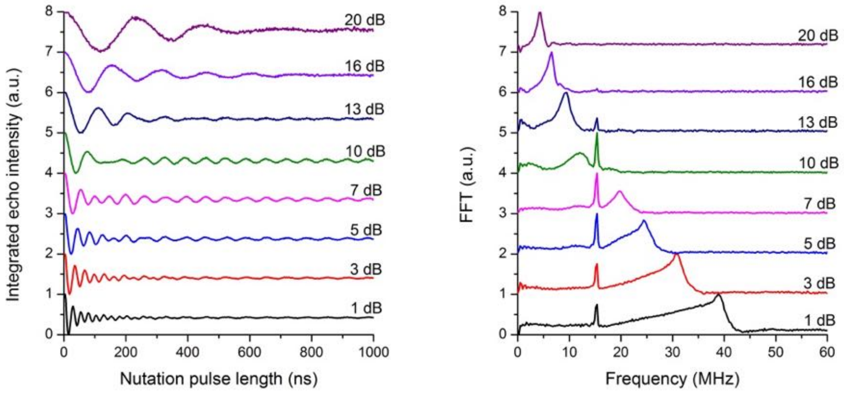

Figure S37. (left) Rabi oscillations for **1** at OP10 and at 20 K, acquired at different microwave attenuations, and (right) the corresponding Fourier transforms

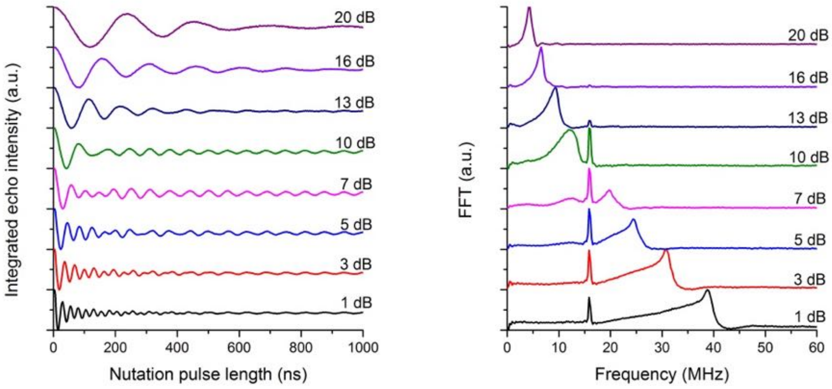

Figure S38. (left) Rabi oscillations for **1** at OP12 and at 20 K, acquired at different microwave attenuations, and (right) the corresponding Fourier transforms.

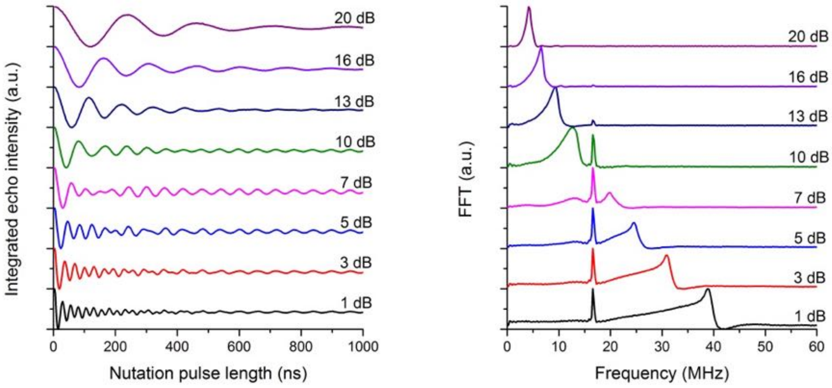

Figure S39. (left) Rabi oscillations for **1** at OP14 and at 20 K, acquired at different microwave attenuations, and (right) the corresponding Fourier transforms.

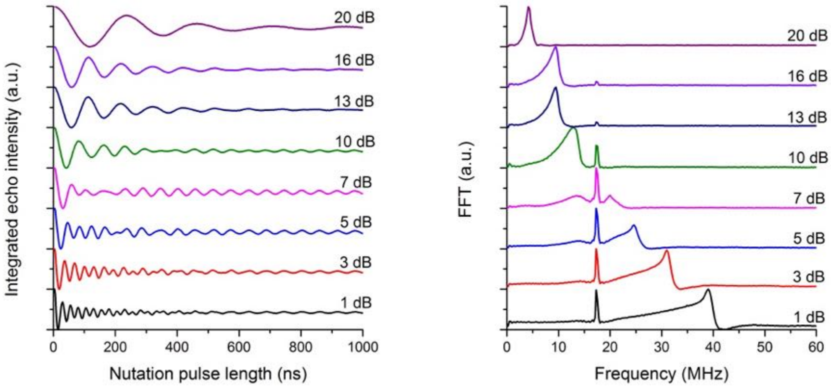

Figure S40. (left) Rabi oscillations for **1** at OP16 and at 20 K, acquired at different microwave attenuations, and (right) the corresponding Fourier transforms.

Table S7. Rabi frequencies for **1** in a 10 mM THF at 20 K.

Attenuation (dB)	Relative B_1 (a.u.)	OP2	OP4	OP6	OP7	OP8	OP9	OP10	OP12	OP14	OP16
1	5.62	38.87	38.87	38.92	38.59	38.95	38.54	38.88	38.81	38.91	39.03
3	4.47	30.99	30.93	30.77	30.61	30.87	30.59	30.75	30.77	30.91	31
5	3.55	24.64	24.51	24.48	24.28	24.46	24.29	24.48	24.45	24.52	24.59
7	2.82	19.75	19.67	19.62	19.48	19.76	19.46	19.78	19.83	19.88	19.97
10	1.99	14.55	10.56	11.23	11.53	11.86	12.04	12.29	12.08	12.65	12.9
13	1.41	9.02	9.09	9.12	9.15	9.29	9.21	9.33	9.34	9.28	9.49
16	1	6.48	6.52	6.54	6.49	6.6	6.57	6.52	6.56	6.56	9.38
20	0.63	4.23	4.21	4.33	4.28	4.38	4.29	4.29	4.26	4.21	4.26

Table S8. Rabi frequencies for **1** in a 10 mM THF at 80 K.

Attenuation (dB)	Relative B1 (a.u.)	OP2	OP8	OP10	OP14
3	4.47	30.28	30.16	30.07	30.24
7	2.82	19.27	19.27	19.23	19.45
13	1.41	8.89	9.09	9.05	9.28

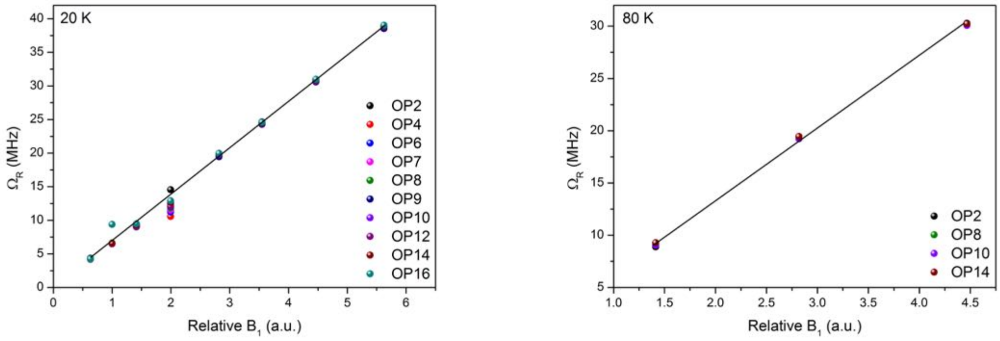

Figure S41. B_1 dependence of the Rabi frequency (Ω_R) of **1** at different observable positions (OP) and at (left) 20 K and (right) 80 K. The solid line is a guide for the eye emphasizing on the linear behaviour.

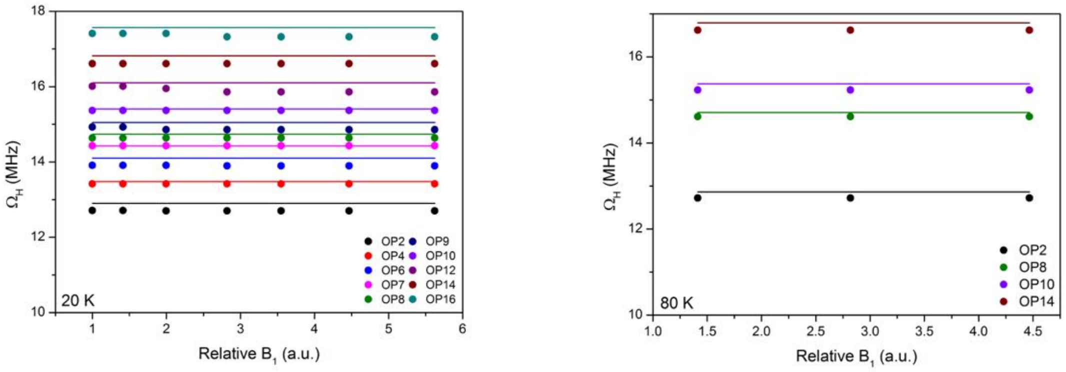

Figure S42. B_1 dependence of the ^{1}H nuclear frequency (Ω_H) of **1** at different observable positions (OP) and at (left) 20 K and (right) 80 K. The solid line shows the theoretical ^{1}H nuclear frequency (Ω_H) for each OP.

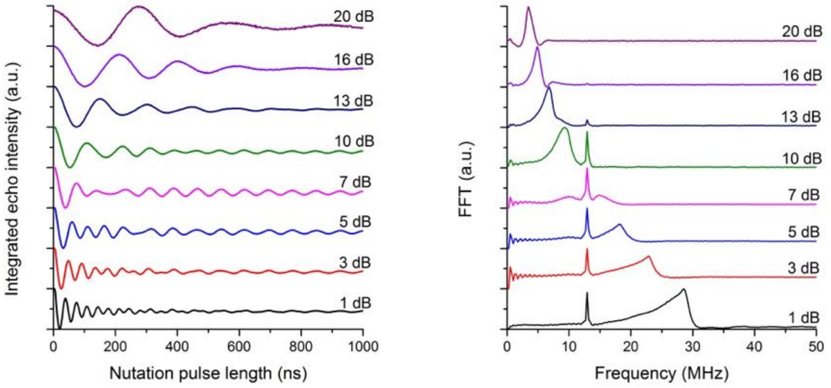

Figure S43. (left) Rabi oscillations for **2** at OP1 and at 20 K, acquired at different microwave attenuations, (right) corresponding Fourier transforms.

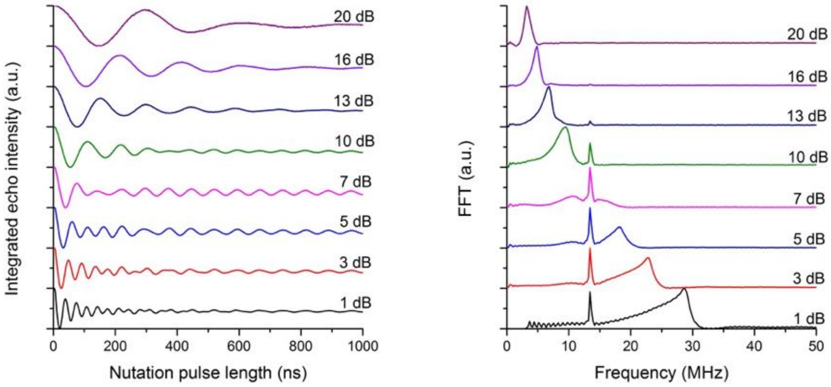

Figure S44. (left) Rabi oscillations for **2** at OP2 and at 20 K, acquired at different microwave attenuations, and (right) the corresponding Fourier transforms.

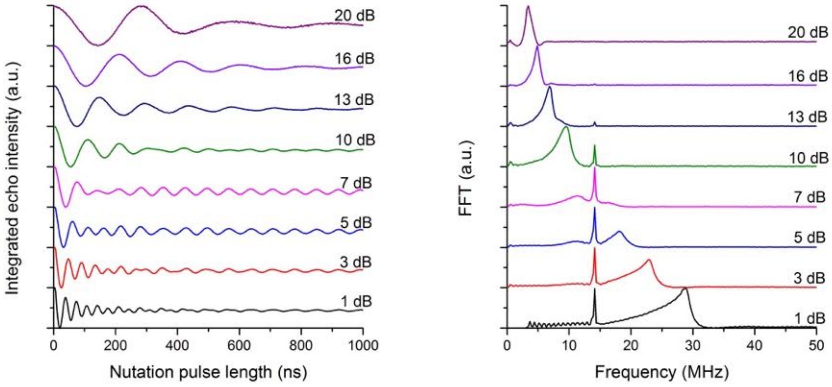

Figure S45. (left) Rabi oscillations for **2** at OP3 and at 20 K, acquired at different microwave attenuations, and (right) the corresponding Fourier transforms.

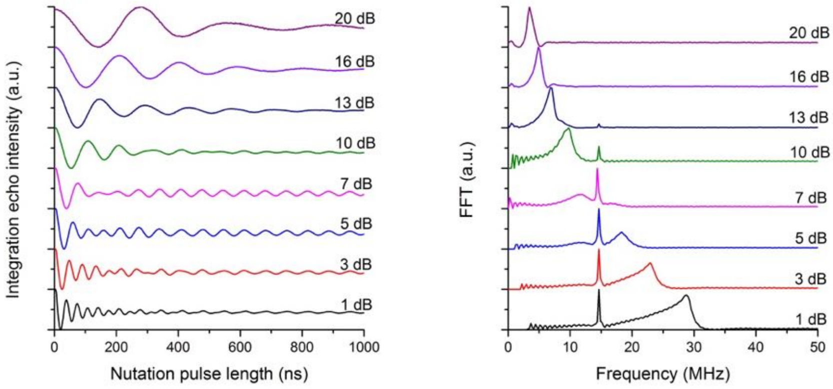

Figure S46. (left) Rabi oscillations for **2** at OP4 and at 20 K, acquired at different microwave attenuations, and (right) the corresponding Fourier transforms.

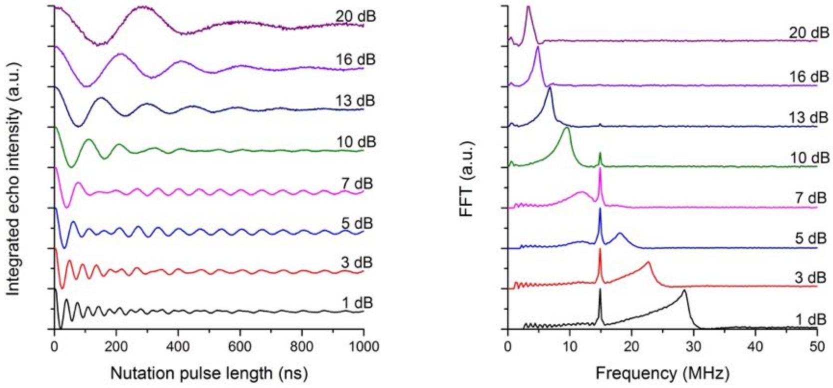

Figure S47. (left) Rabi oscillations for **2** at OP5’ and at 20 K, acquired at different microwave attenuations, and (right) the corresponding Fourier transforms.

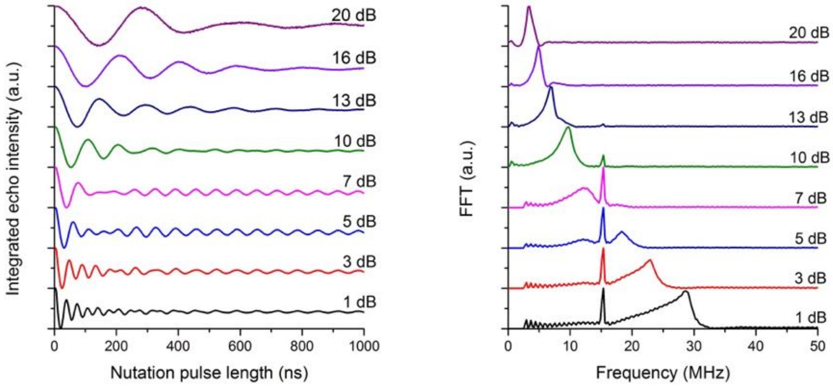

Figure S48. (left) Rabi oscillations for **2** at OP5 and at 20 K, acquired at different microwave attenuations, and (right) the corresponding Fourier transforms.

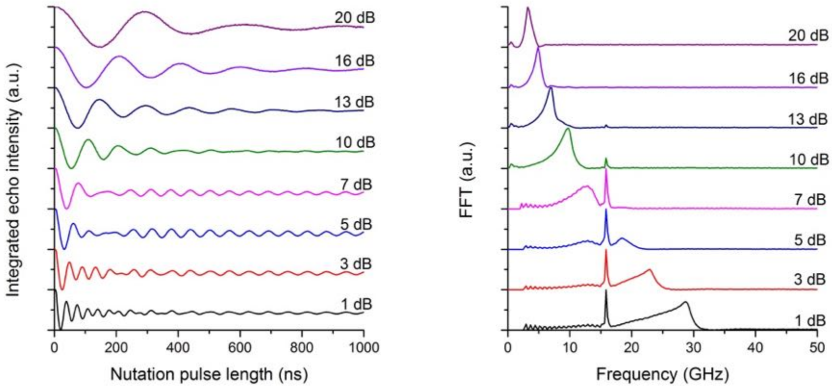

Figure S49. (left) Rabi oscillations for **2** at OP6 and at 20 K, acquired at different microwave attenuations, and (right) the corresponding Fourier transforms.

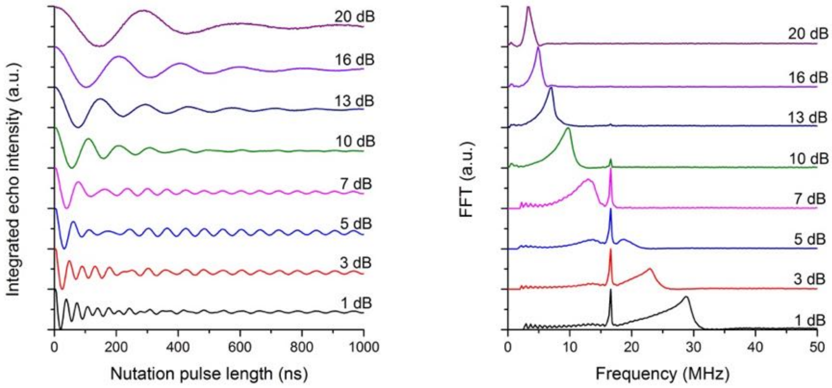

Figure S50. (left) Rabi oscillations for **2** at OP7 and at 20 K, acquired at different microwave attenuations, (right) corresponding Fourier transforms.

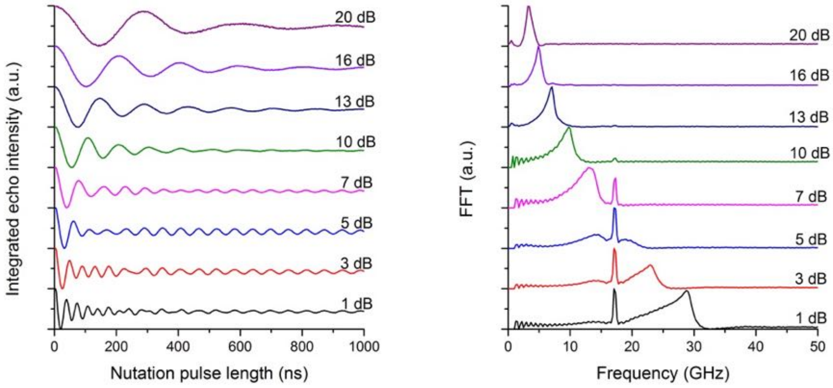

Figure S51. (left) Rabi oscillations for **2** at OP8 and at 20 K, acquired at different microwave attenuations, and (right) the corresponding Fourier transforms.

Table S9. Rabi frequencies for **2** in a 10 mM THF at 20 K.

Attenuation (dB)	Relative B1 (a.u.)	OP1	0P2	OP3	OP4	OP5’	OP5	OP6	OP7	OP8
1	5.62	28.56	28.65	28.73	28.8	28.54	28.61	28.71	28.81	28.82
3	4.47	22.9	22.78	22.93	22.93	22.69	22.89	22.89	22.96	22.95
5	3.55	18.18	18.17	18.18	18.31	18.08	18.31	18.42	18.65	18.93
7	2.82	15.09	10.9	11.17	12.05	12.34	12.45	12.86	12.99	13.2
10	1.99	9.34	9.45	9.51	9.75	9.56	9.69	9.67	9.74	9.77
13	1.41	6.84	6.76	6.83	6.96	6.83	6.96	6.95	6.95	6.95
16	1	4.89	4.84	4.83	5	4.86	4.88	4.87	4.92	4.9
20	0.63	3.44	3.19	3.34	3.42	3.3	3.32	3.24	3.3	3.28

Table S10. Rabi frequencies for **2** in a 10 mM THF at 60 K.

Attenuation (dB)	Relative B_1 (a.u.)	OP1	OP3	OP5	OP7
3	4.47	23.09	23.09	23.09	23.18
7	2.82	15.05	11.34	12.25	13.06
13	1.41	6.88	6.88	6.88	7.02

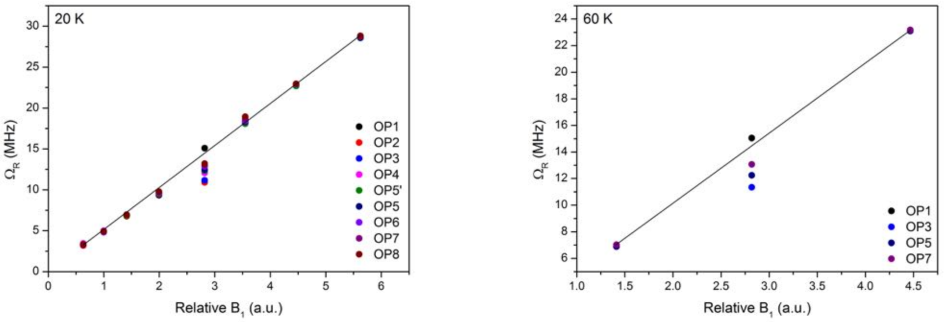

Figure S52. B_1 dependence of the Rabi frequency (Ω_R) of **2** at different observable positions (OP) and at (left) 20 K and (right) 60 K. The solid line is a guide for the eye emphasizing on the linear behaviour.

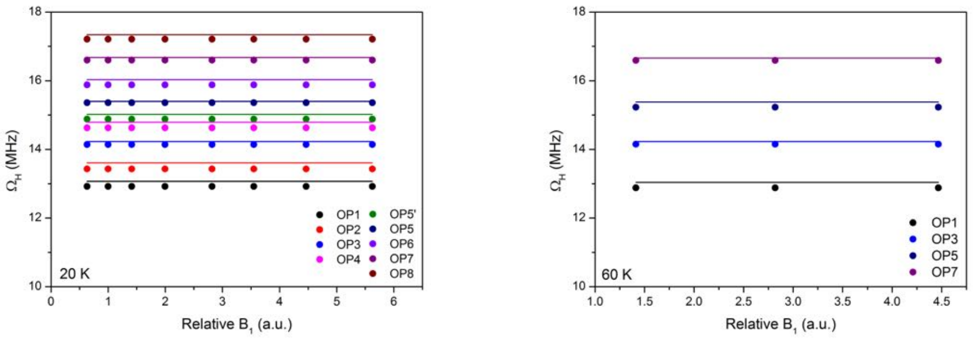

Figure S53. B_1 dependence of the ^{1}H nuclear frequency (Ω_H) of **2** at different observable positions (OP) and at (left) 20 K and (right) 60 K. The solid line shows the theoretical ^{1}H nuclear frequency (Ω_H) for each OP.

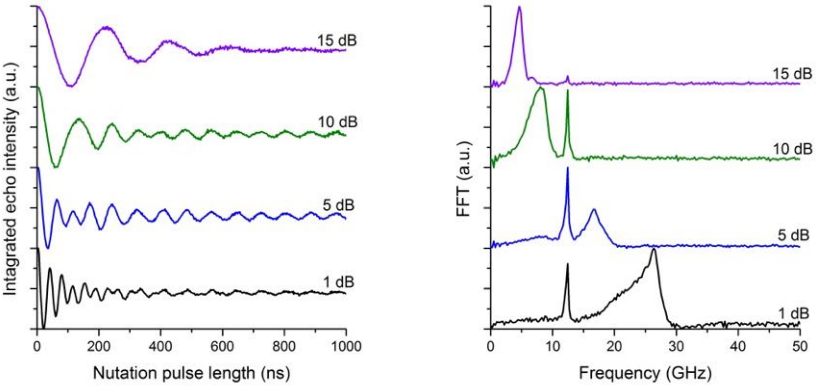

Figure S54. (left) Rabi oscillations for **3** at OP1 and at 20 K, acquired at different microwave attenuations, and (right) the corresponding Fourier transforms.

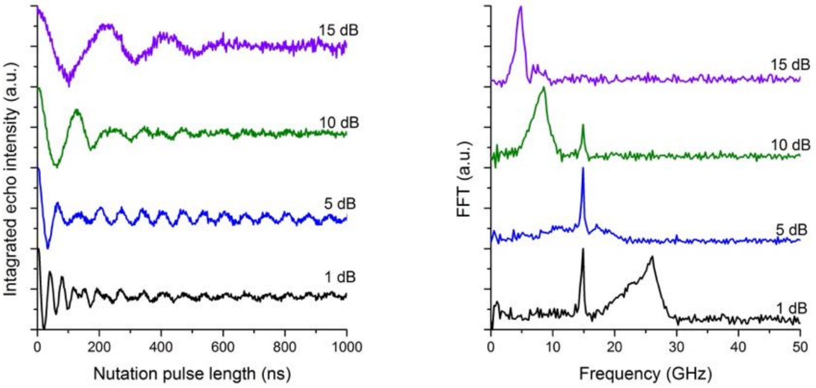

Figure S55. (left) Rabi oscillations for **3** at OP2 and at 20 K, acquired at different microwave attenuations, and (right) the corresponding Fourier transforms.

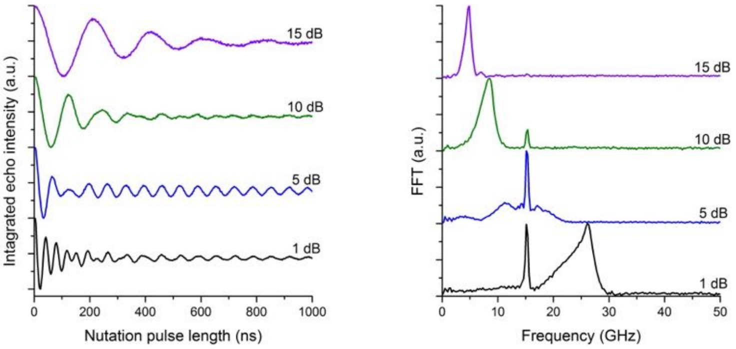

Figure S56. (left) Rabi oscillations for **3** at OP3 and at 20 K, acquired at different microwave attenuations, and (right) the corresponding Fourier transforms.

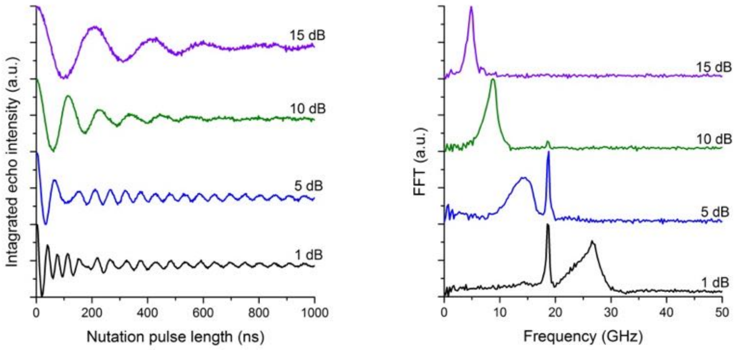

Figure S57. (left) Rabi oscillations for **3** at OP4 and at 20 K, acquired at different microwave attenuations, and (right) the corresponding Fourier transforms.

Table S11. Rabi frequencies for **3** in a 10 mM THF at 80 K.

Attenuation (dB)	Relative B1 (a.u.)	OP1	OP3	OP5	OP7
1	5.62341	26.19	26.37	26.01	26.74
5	3.54813	17.06	16.56	17.06	14.65
10	1.99526	8.46	8.01	8.45	8.79
15	1.12202	4.77	4.64	4.77	4.87

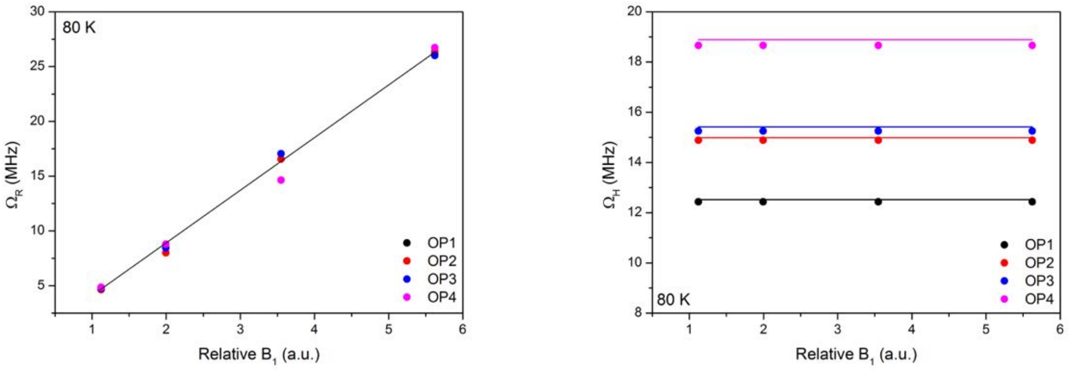

Figure S58. (left) B_1 dependence of the Rabi frequency (Ω_R) of **3** at different observable positions (OP) at 80 K. The solid line is a guide for the eye emphasizing on the linear behaviour. (right) B_1 dependence of the ^{1}H nuclear frequency (Ω_H) of **3** at different applied field positions (OP) and at 80 K. The solid line shows the theoretical ^{1}H nuclear frequency (Ω_H) for each OP.

3.5 HYSCORE Spectra

HYSCORE experiments used a four-pulse electron spin-echo sequence, *π/2 - τ - π/2 - t1 - π - t2 - π/2 - τ – echo*, with π/2 and π pulse lengths of 16 and 32ns, respectively, and fixed τ time of 136 and 200 ns. The initial t_1 and t_2 times are 100 ns increasing during the experiment with 20 ns steps up to 5200 ns; 256 points are collected in both dimensions. The absolute values were obtained after fast Fourier transformation of the obtained data in both directions, yielding to nuclear cross-peaks on a 2D (ν_1,

ν_2) spectra. On the frequency domain spectra the (+,+) quadrant is described as the weak coupling regime ($2|\nu_n|>|A|$) and displays cross-peaks centred at the Larmor frequency of each nucleu, separated by the hyperfine coupling strength. Isotropic hyperfine couplings lead to ridges on the anti-diagonal of the HYSCORE spectra, while anisotropic contribution causes deviation from the anti-diagonal analogues to the magnitude of the anisotropy of the hyperfine coupling constants.

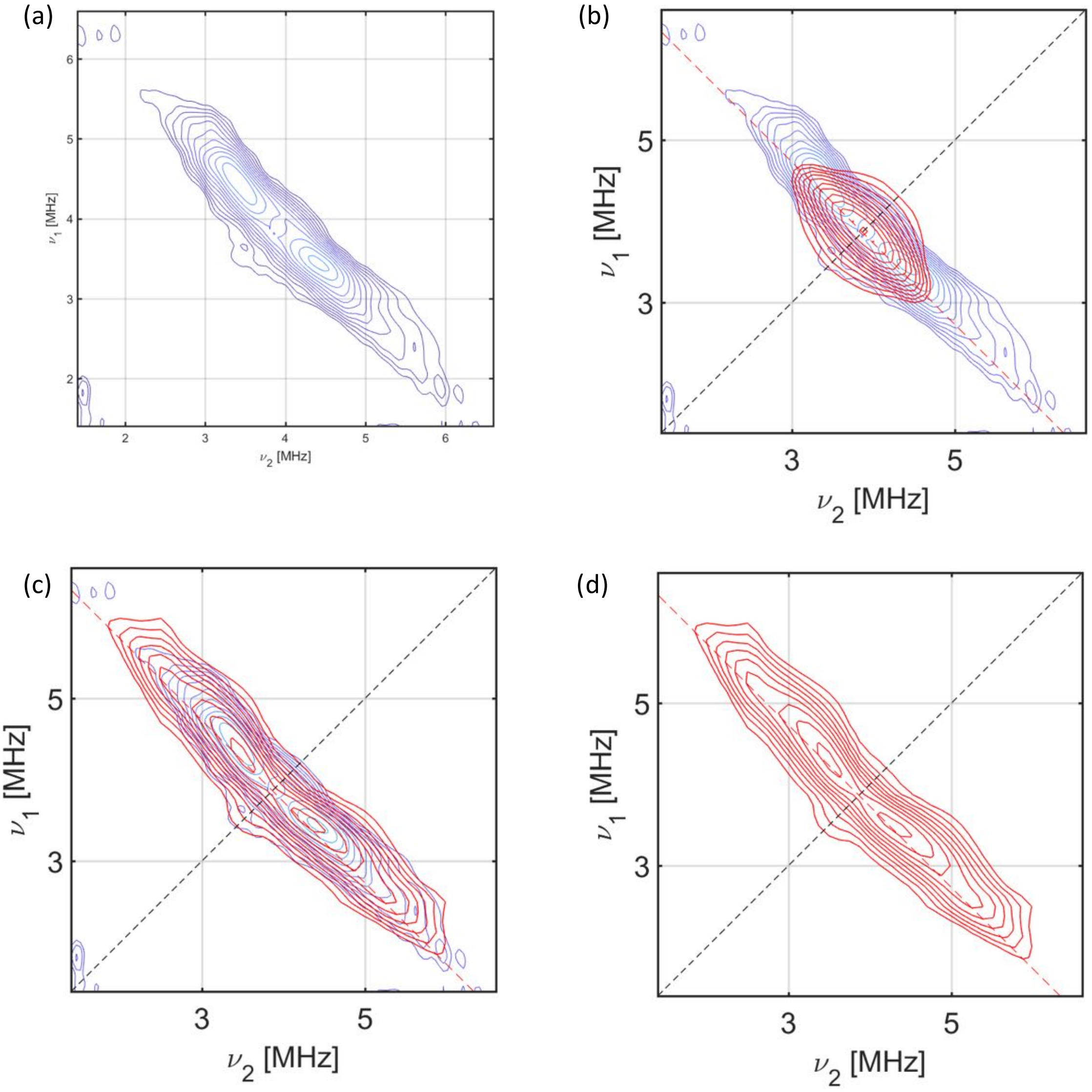

Figure S59. (a) ^{13}C HYSCORE spectrum for **1** (THF) at B_0 = 360.8 mT (**OP10**; Figure S2), T = 5 K and X-band (9.734 GHz); (b) Calculation of the ^{13}C HYSCORE spectrum of **1** based on the dipole model only (see main text); (c) Calculation taking into account the point-dipole interactions and the associated spin densities at C^{2,5} and C^{3,4}, yielding: $A_{\parallel}^{C2,5}$ = 13.4 MHz, $A_{\perp}^{C2,5}$ = 3.4 MHz, and $A_{\parallel}^{C3,4}$ = 5.3 MHz and $A_{\perp}^{C3,4}$= 0.4 MHz; and (d) Calculated ^{13}C HYSCORE spectra of **1** for the g_{xy}. The dashed-red antidiagonal line marks the ^{13}C Larmor frequency.

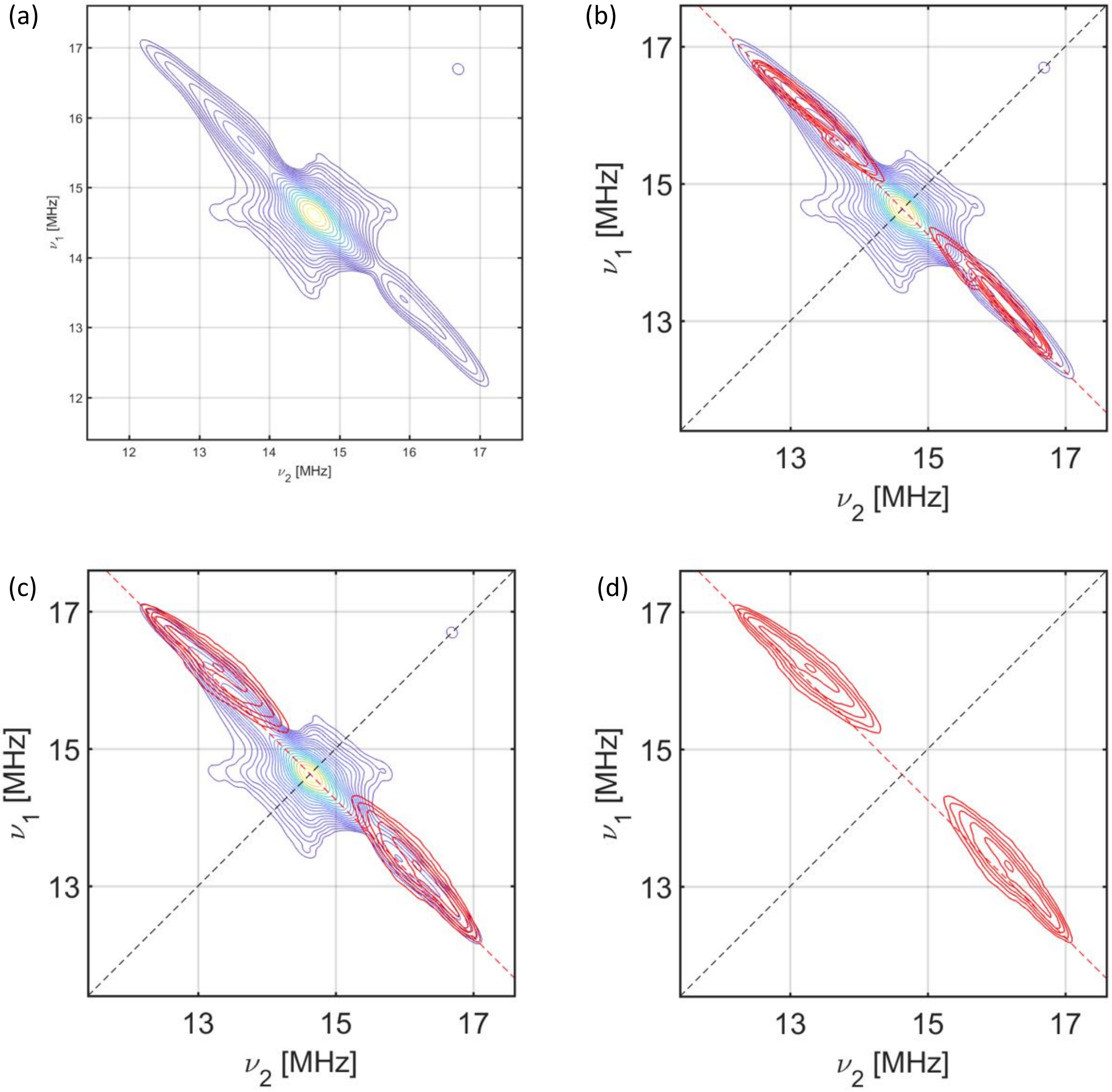

Figure S60. (a) ^{1}H HYSCORE spectrum for **1** (THF) at B_0 = 345.3 mT (**OP7**; Figure S2), T = 15 K and X-band (9.734 GHz); (b) Calculation of the ^{1}H HYSCORE spectrum of **1** based on the dipole model only (see main text); (c) Calculation based on the model described in the main text using $\alpha_{isoH2,5}$ = - 2.616 and $\alpha_{isoH3,4}$ = - 1.149 occurring from the $A^{C2,5}$ and $A^{C3,4}$ using the McConnell model (see main text); and (d) Calculated ^{1}H HYSCORE spectra of **1** for the g_{xy}. The dashed-red antidiagonal line marks the ^{1}H Larmor frequency.

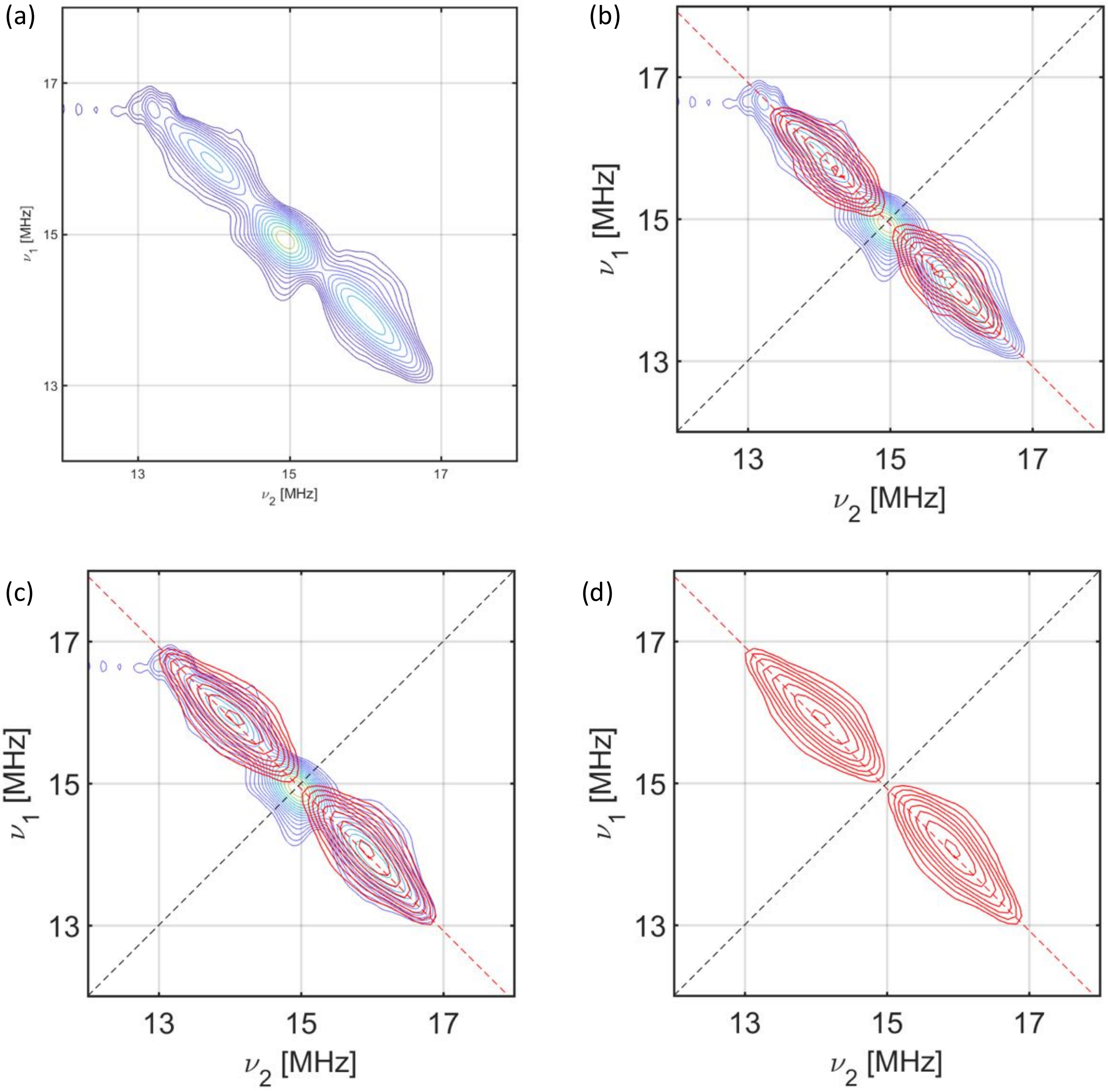

Figure S61. (a) ^{1}H HYSCORE spectrum for **1** (THF) at B_0 = 353.8 mT (**OP9**; Figure S2), T = 10 K and X-band (9.734 GHz); (b) Calculation of the ^{1}H HYSCORE spectrum of **1** based on the dipole model only (see main text); (c) Calculation based on the model described in the main text using $\alpha_{isoH2,5}$ = - 2.612 and $\alpha_{isoH3,4}$ = - 1.149, which are in good agreement with the corresponding α_{iso} values of the *xy*-orientation; and (d) Calculated ^{1}H HYSCORE spectra of **1** for the g_z. The dashed-red antidiagonal line marks the ^{1}H Larmor frequency.

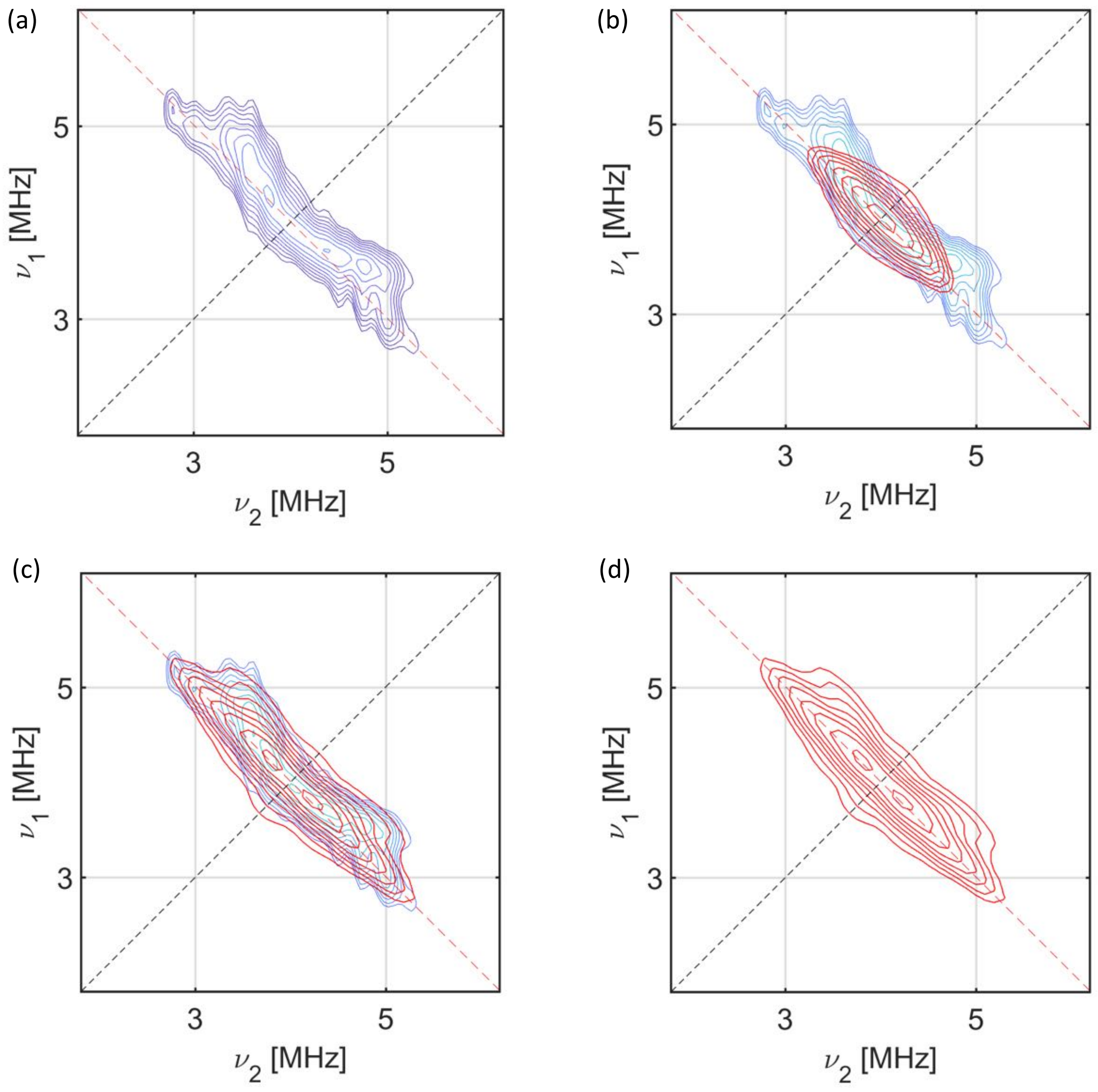

Figure S62. (a) ^{13}C HYSCORE spectrum for **2** (THF) at B_0 = 373.8 mT (**OP6**; Figure S3), T = 20 K and X-band (9.718 GHz); (b) Calculation of the ^{13}C HYSCORE spectrum of **2** based on the dipole model only (see main text); (c) Calculation taking into account the point-dipole interactions and the associated spin densities at C^2 and C^{1,3}, yielding: $A_{\parallel}^{\mathrm{C2}}$ = 7.3 MHz, $A_{\perp}^{\mathrm{C2}}$ = 0.8 MHz, and $A_{\parallel}^{\mathrm{C1,3}}$ = 2.0 MHz and $A_{\perp}^{\mathrm{C1,3}}$= 0.8 MHz; (d) Calculated ^{13}C HYSCORE spectra of **2** for the g_{xy}. The dashed-red antidiagonal line marks the ^{13}C Larmor frequency.

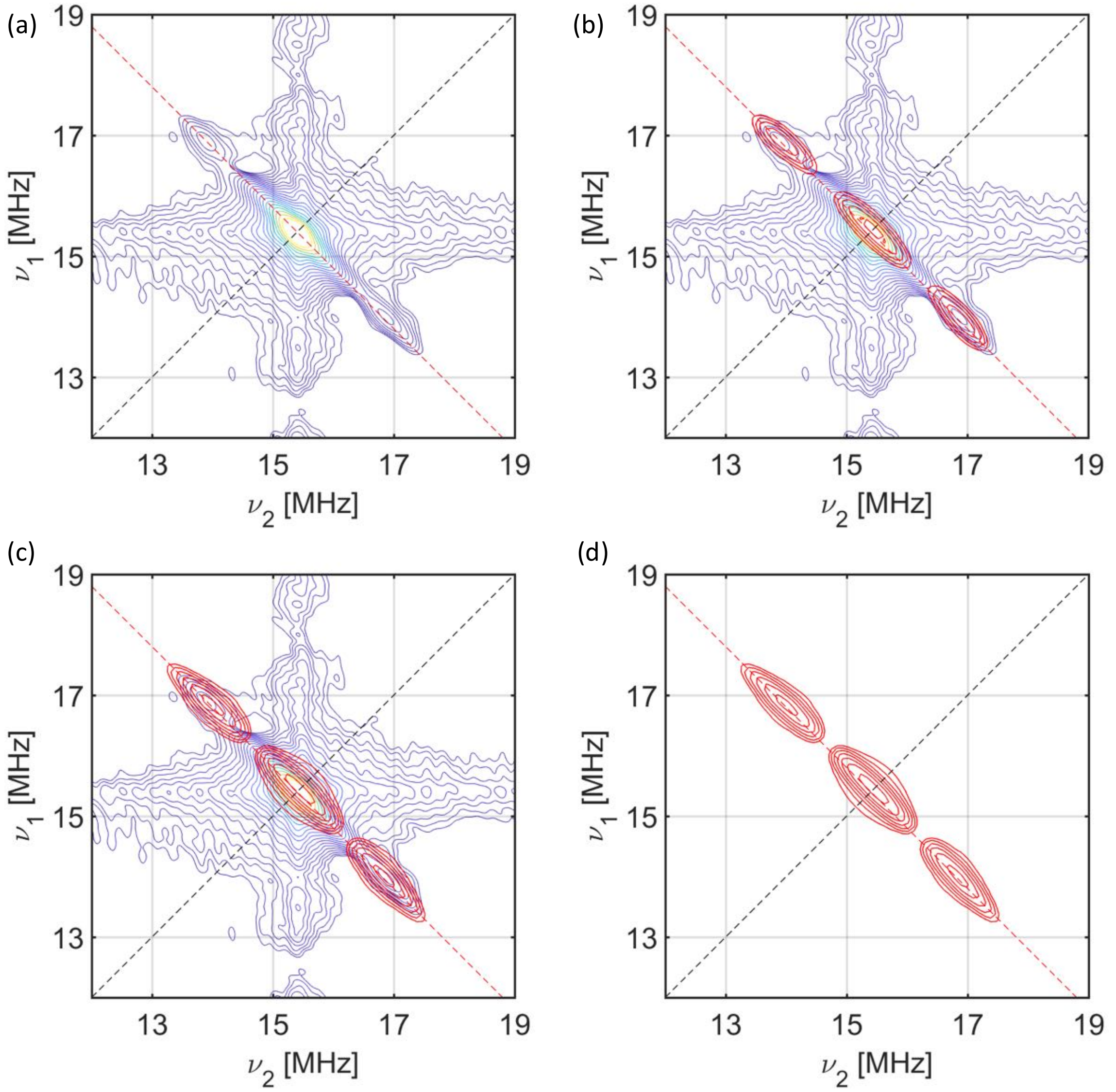

Figure S63. (a) ^{1}H HYSCORE spectrum for **2** (THF) at B_0 = 361.7 mT (**OP5**; Figure S3), T = 20 K and X-band (9.718 GHz); (b) Calculation of the ^{1}H HYSCORE spectrum of **2** based on the dipole model only (see main text); (c) Calculation based on the model described in the main text using α_{isoH2} = - 1.698 and $\alpha_{isoH1,3}$ = 0, being in excellent agreement with the calculated α_{iso} values occurring from the A^{C2} and $A^{C1,3}$ using the McConnell model (see main text - Table 2); and (d) Calculated ^{1}H HYSCORE spectra of **2** for the g_{xy}. The dashed-red antidiagonal line marks the ^{1}H Larmor frequency.

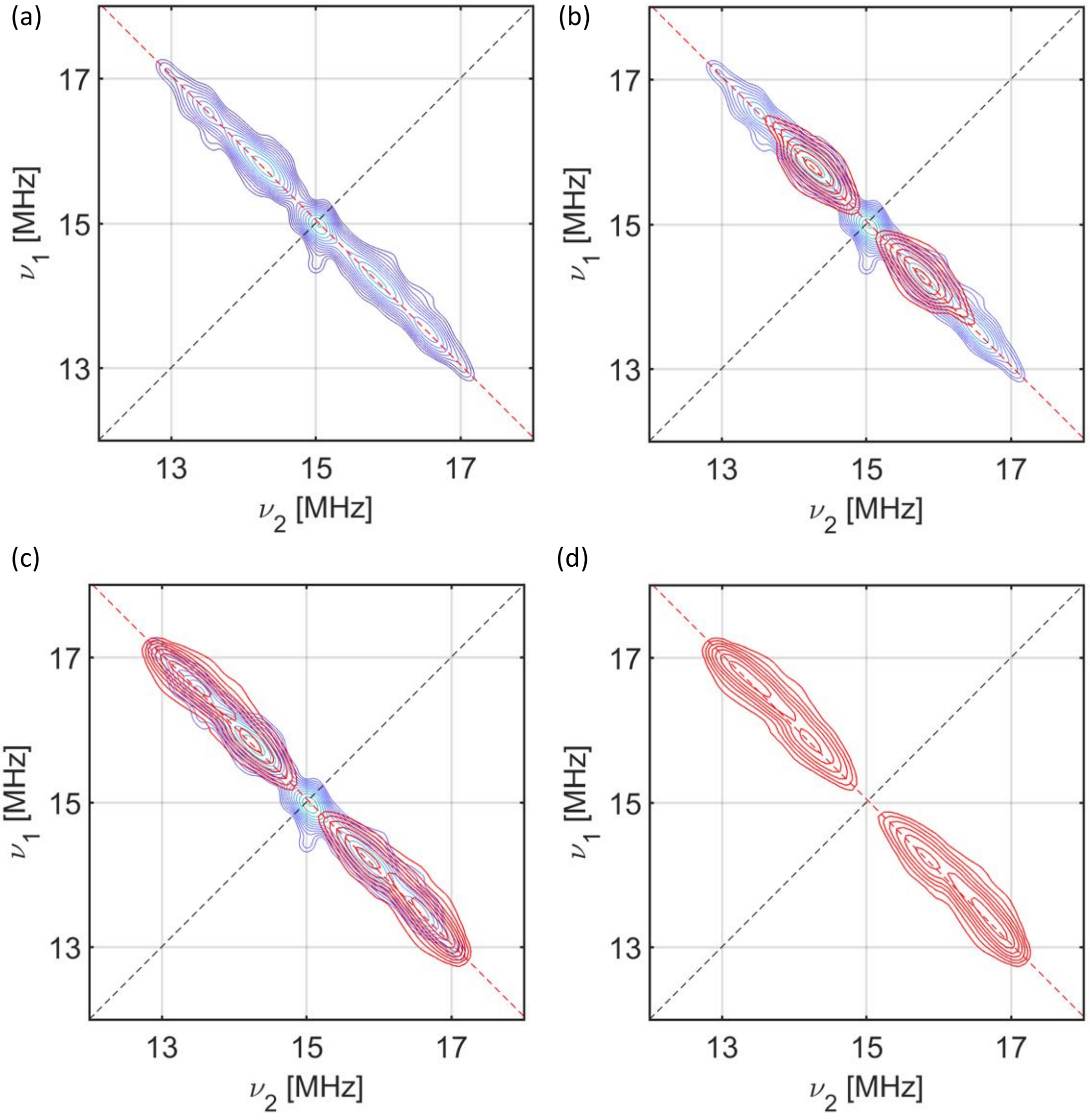

Figure S64. (a) ^{1}H HYSCORE spectrum for **2** (THF) at B_0 = 352.8 mT (**OP5'**; Figure S3), T = 20 K and X-band (9.718 GHz); (b) Calculation of the ^{1}H HYSCORE spectrum of **2** based on the dipole model only (see main text); (c) Calculation based on the model described in the main text using α_{isoH2} = - 1.645 and $\alpha_{isoH1,3}$ = 0, which are in good agreement with the corresponding α_{iso} values of the *xy*-orientation; and (d) Calculated ^{1}H HYSCORE spectra of **2** for the g_z. The dashed-red antidiagonal line marks the ^{1}H Larmor frequency.

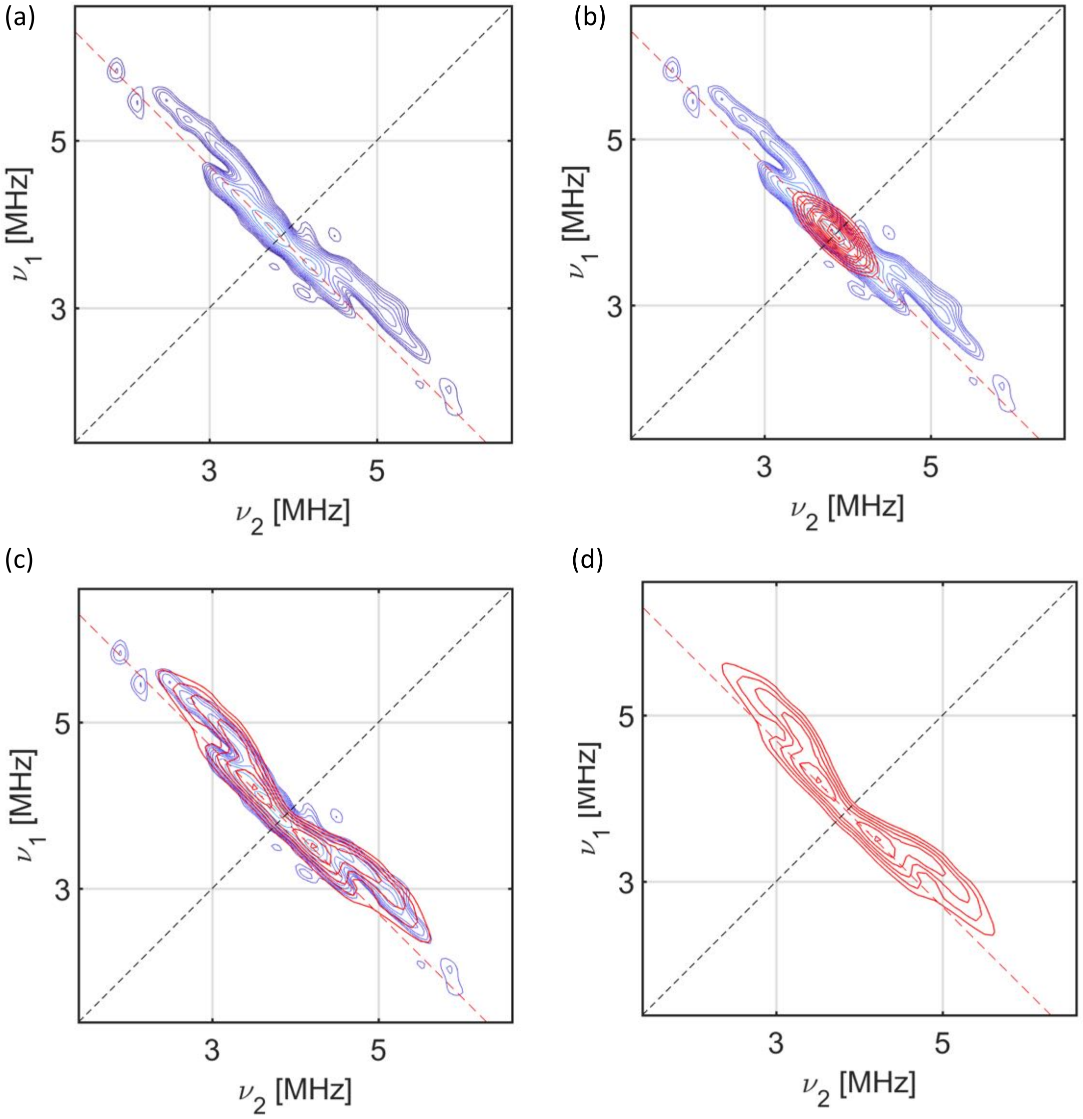

Figure S65. (a) ^{13}C HYSCORE spectrum for **3** (THF) at B_0 = 362.2 mT (**OP3**; Figure S4), T = 10 K and X-band (9.761 GHz); (b) Calculation of the ^{13}C HYSCORE spectrum of **3** based on the dipole model only (see main text); (c) Calculation taking into account the point-dipole interactions and the associated spin densities on all the carbon atoms on the Cp^{tt} ring, yielding the following 3 sets of hyperfine values: $A_{\parallel,\perp}^{C2}$ = 13.4, 1.8 MHz, $A_{\parallel,\perp}^{C1,3}$ = 5.6, 0.6 MHz and $A_{\parallel,\perp}^{C4,5}$ = 0.8, 0.6 MHz; and (d) Calculated ^{13}C HYSCORE spectra of **3** for the g_{xy}. The dashed-red antidiagonal line marks the ^{13}C Larmor frequency.

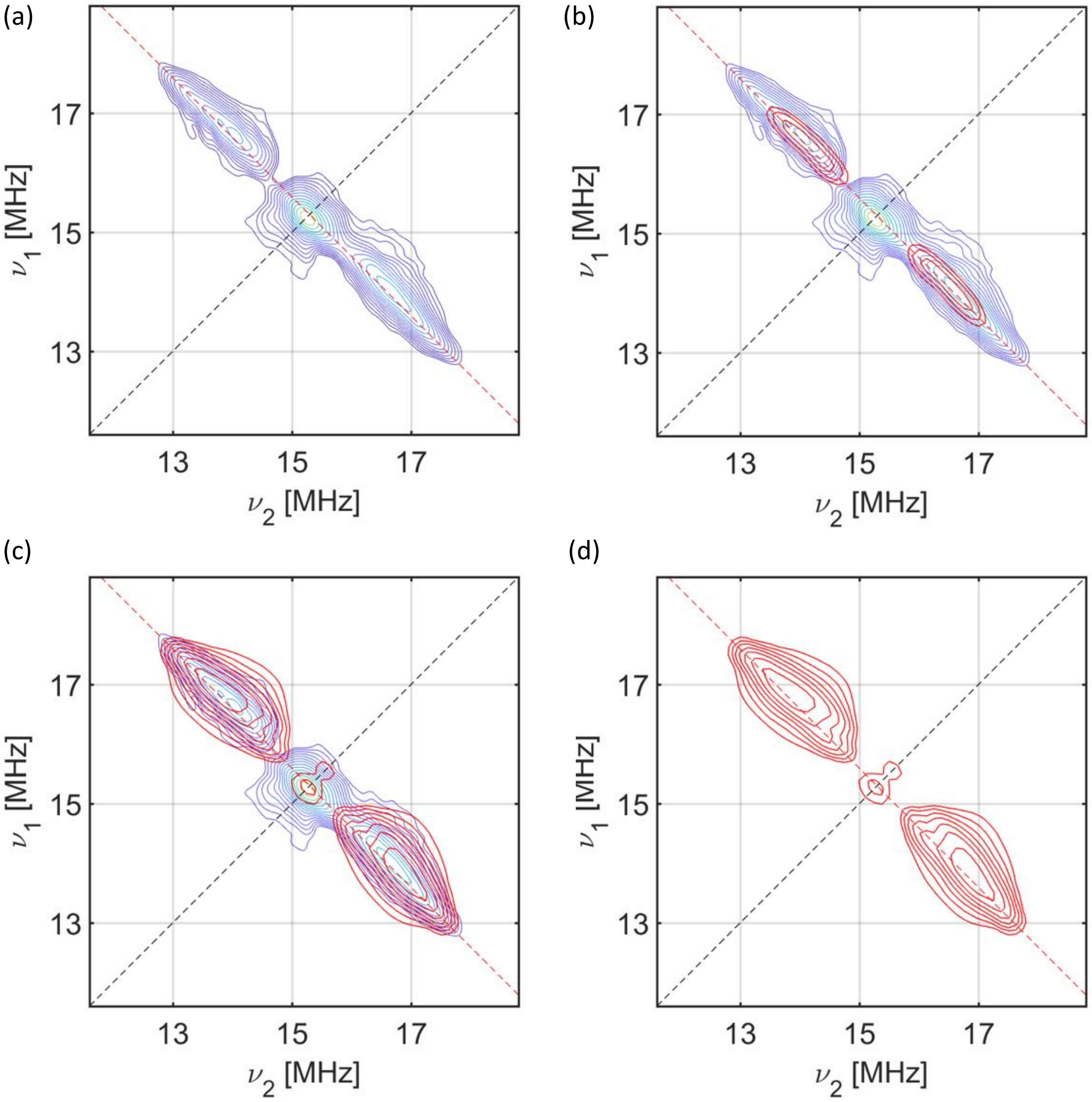

Figure S66. (a) ^{1}H HYSCORE spectrum for **3** (THF) at B_0 = 362.2 mT (**OP3**; Figure S4), T = 20 K and X-band (9.761 GHz); (b) Calculation of the ^{1}H HYSCORE spectrum of **3** based on the dipole model only (see main text); (c) Calculation based on the model described in the main text using α_{isoH2} = - 3.00 and $\alpha_{isoH4,5}$ = - 0.056 which are in excellent agreement with the calculated ones occurring from the A^{C2} and $A^{C4,5}$ using the McConnell model (see main text - Table 2); and (d) Calculated ^{1}H HYSCORE spectra of **3** for the g_{xy}. The dashed-red antidiagonal line marks the ^{1}H Larmor frequency.

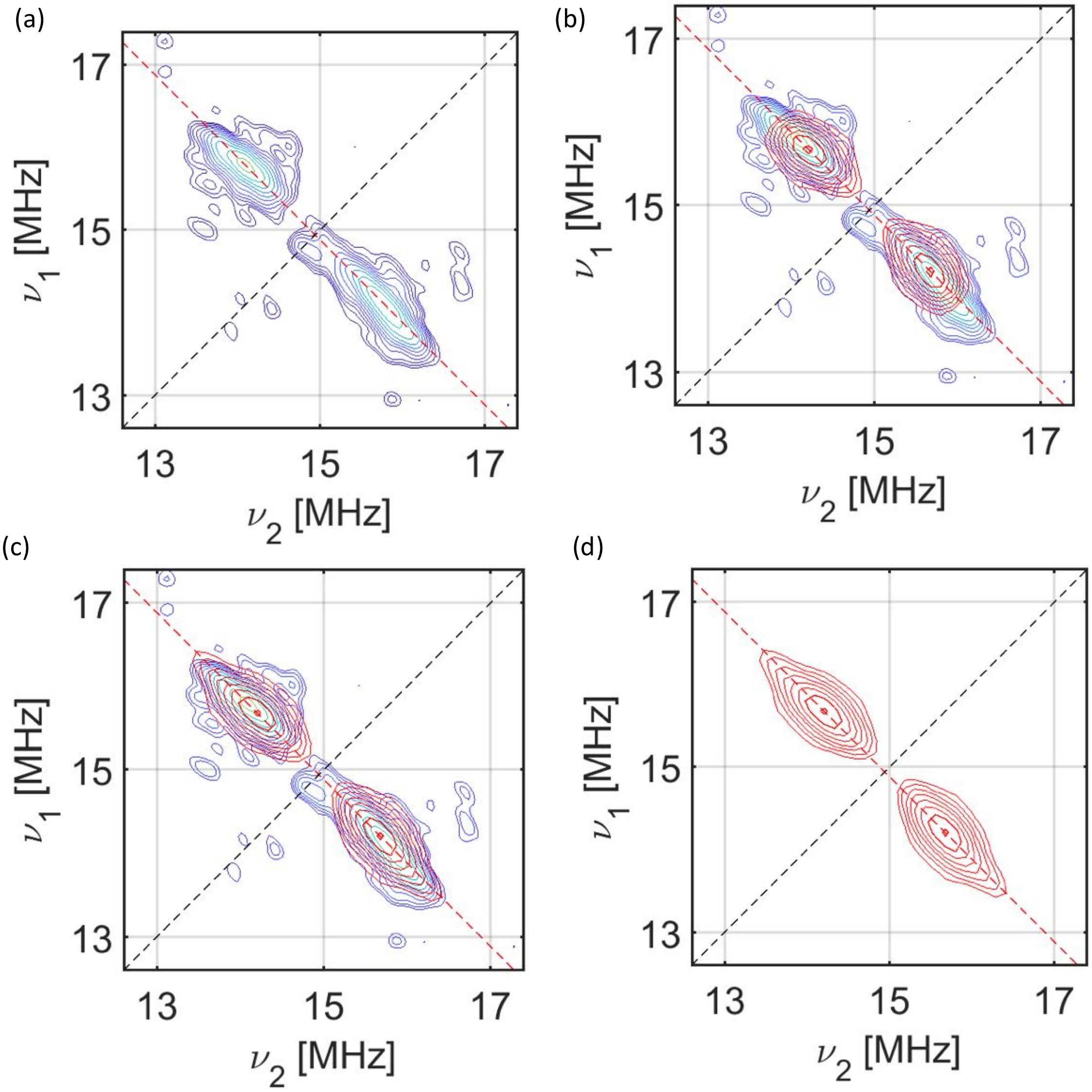

Figure S67. (a) ^{1}H HYSCORE spectrum for **3** (THF) at B_0 = 352.4 mT (**OP2**; Figure S4), T = 10 K and X-band (9.761 GHz); (b) Calculation of the ^{1}H HYSCORE spectrum of **3** based on the dipole model only (see main text); (c) Calculation based on the model described in the main text using α_{isoH2} = - 3.00 and $\alpha_{isoH4,5}$ = - 0.056, which are in good agreement with the corresponding α_{iso} values of the *xy*-orientation; and (d) Calculated ^{1}H HYSCORE spectra of **3** for the g_z. The dashed-red antidiagonal line marks the ^{1}H Larmor frequency.

References

1. M. R. MacDonald, J. E. Bates, J. W. Ziller, F. Furche and W. J. Evans. Completing the series of 2+ ions for the lanthanide elements: Synthesis of molecular complexes of Pr2+, Gd2+, Tb2+ and Lu2+. *J. Am. Chem. Soc.*, **2013**, 135, 9857-9868.

2. S. Stoll and A. Schweiger. Easyspin, a comprehensive software package for spectral simulation and analysis in EPR. *J. Magn. Reson.*, **2006**, 178, 42-55.

3. S. Stoll and R. D. Britt. General and efficient simulation of pulse EPR spectra. *Phys. Chem. Chem. Phys.*, **2009**, 11, 6614-6625.

4. M. E. Fieser, M. R. MacDonald, B. T. Krull, J. E. Bates, J. W. Ziller, F. Furche and W. J. Evans. Structural, Spectroscopic, and Theoretical Comparison of Traditional vs Recently Discovered Ln^{2+} Ions in the $[K(2.2.2\text{-cryptand})][(C_5H_4SiMe_3)_3Ln]$ Complexes: The Variable Nature of Dy^{2+} and Nd^{2+}. *J. Am. Chem. Soc.*, **2015**, 137, 369-382.

5. P. B. Hitchcock, M. F. Lappert, L. Maron and A. V. Protchenko. Lanthanum Does Form Stable Molecular Compounds in the +2 Oxidation State. *Angew. Chem. Int. Ed.*, **2008**, 47, 1488-1491.

6. J. Liu, PhD thesis, University of Manchester, 2019.

7. A. Schweiger and J. Jeschke. Principles of Pulse Electron Paramagnetic Resonance. *Oxford University Press*, Oxford, **2001**.

Chapter VII. Manuscript draft 3

An Organometallic Yttrium(II) Spin Qubit Based on a Rigid Aryloxide Ligand Displaying Enhanced Coherence Properties

Lydia E. Nodaraki,[1,2] Daniel N. Huh,[3] Fabrizio Ortu,[1] William J. Evans[3] and Floriana Tuna[1,2]

[1]Department of Chemistry, The University of Manchester, Oxford Road, Manchester M13 9PL, UK
[2]Photon Science Institute, The University of Manchester, Oxford Road, Manchester M13 9PL, UK
[3]Department of Chemistry, University of California, Irvine, CA 92697-2025

Abstract: Paramagnetic molecular systems can exhibit long quantum coherence times enabling their potential use as the elementary unit for quantum information science (QIS) applications. In the race for longer coherence times, understanding the mechanisms of decoherence as well as eliminating the influence of the thermal vibrations and magnetic noise constitute a great challenge. Here, we present the electronic, spin dynamics and coherence studies of an yttrium(II) aryloxide complex, [K(2.2.2-cryptand)][Y(OAr^{Ad,Ad,Me})$_3$] (Ad = $(CH)_4(CH_2)_6$; Me = CH_3) (**1**). Engineering the electronic structure to an *S*-like ground state resulted in elongated T_1 and T_m times, despite the very rich ^{1}H nuclear spin environment. Carr-Purcel-Meiboom-Gill (CPMG) pulse sequences were applied to decouple the nuclear and electron spins thus leading to significantly expanded phase memory times of up to 600 μs. ENDOR and HYSCORE spectroscopies were applied to probe the weak interactions between the unpaired electron and ^{1}H and ^{13}C atoms of the ligands, thus providing some insights into decoherence mechanisms. The ability of **1** to cycle between its superposition states was confirmed by the observation of Rabi oscillations, nominating its potential as molecular spin qubit.

INTRODUCTION

In recent years, significant efforts have been invested in the quantum information research with the aim of identifying systems that would allow to revolutionize data processing and storing.[1-6] The strength of quantum computing lies in the possibility of using a coherent superposition of states as quantum registry, and the interference between them, which enables to build more elaborated and complex computation algorithms that are not possible in classical computing. The first step in building a quantum computer is to realize a viable two-level quantum state (the *qubit*).[7] Several types of systems have been proposed as qubit platforms, including defects[8] and impurities[9,10] in solids, superconducting circuits,[11,12] quantum dots,[13] polarized photons,[14,15] trapped ions,[16,17] non-magnetic[18] and magnetic[1-7,19,20] molecules amongst others. Each has advantages and disadvantages, making difficult to predict which of these approaches will prove successful. Among them, electronic[1-4] and nuclear[9] spins, as well as hybrid architectures of electron-nuclear systems[5,6] have been proposed as potential spin qubits harnessing their intrinsic two-level structures. The latter presents the advantage of expanding the number of states available for computation within a quantum object, through electron spin-nuclear spin hyperfine interactions, without requiring inter-objects interactions. The larger number of states in a single quantum object opens opportunity for quantum parallelism,[21] and thus faster data processing as more operations can be done in a single computation step. Additionally, a larger volume of information can be processed with the same number of quantum objects. Another advantage is the intrinsic shielding nature of nuclear spins that protects them from environmental noise, affording extremely long coherence times and very low error rates.[22] Experimentally, the electronic doublet of the qubit can be accessed *via* EPR transitions,[23-25] while the nuclear states can be easily manipulated with EPR and NMR pulse sequences.[26]

Compared to the nuclear spins, electronic qubits interact more strongly with their environments, and are subject to quantum decoherence.[27-29] In molecular systems, this phenomenon is primarily induced through electron–electron and electron–nuclei interactions, which ultimately relate to paramagnetic species concentration, dynamics of nuclear spin bath, and presence of nuclear spins embedded in the ligand shells.[30,31] Understanding these effects has launched several successful strategies that enable enhancement of the coherence times of molecular qubits. These imply the use of nuclear spin-free ligands,[32] ligand deuteration,[33] and magnetic dilutions,[34] alongside other strategies that aim at working at atomic clock to cancel out the effect of magnetic noise,[35] or with rigid ligands aimed to correct for vibrational effects.[36,37]

In a recent study our group has demonstrated that it is possible to promote robust quantum properties even in the presence of rich nuclear-spin environments and in relatively concentrated samples, through the engineering of the electronic configuration instead, i.e. making compounds with a ^{2}S ground state.[38] This essentially means designing systems with quenched orbital angular momentum to disfavor magnetization transfer between electron spin and lattice. The validity of this approach was demonstrated for a family of divalent tris-cyclopentadienyl complexes of C_3 symmetry, [K(2.2.2-cryptand)][Ln(Cp′)$_3$] (Ln = Y, La, Lu; Cp′ = $C_5H_4SiMe_3$).[38] The Cp′ ligand is the opposite of what has been established so far to accomplish long coherence times in molecular qubits: it has many magnetic nuclei and the methyl substituents rotate freely and hence does not provide rigidity. However, the C_3 symmetry of the complex lowers the energy of the d_{z2} orbital, enabling *s*/*d* orbital mixing (*i.e.* SOMO has a pronounced *s*-character), and this appears to provide the qubit with some immunity against environmental magnetic noise. Despite a very rich nuclear spin environment, the compound shows robust quantum coherence (T_m ~ 2 μs below 30 K), including at room temperature (T_m ~ 0.4 μs) where coherent Rabi oscillations in a single crystal of 2% Y@YbCp′$_3$ could also be observed. Remarkably, T_1 and T_m were found to be largely unaffected by the nature of the sample (single crystal versus THF solution) or which electronuclear transition is monitored, while g and A are essentially isotropic due to significant *s*-character of the SOMO orbital and quenched orbital magnetic moment.

We anticipated that combining this strategy with the engineering of the vibrational modes of ligands would enable to prolong the lifetime of the qubit. Herein, we report the electronic and coherence properties of a new divalent yttrium complex [K(2.2.2-cryptand)][Y(OArAd,Ad,Me)3] (**1**) (2,6-Ad2-4-Me-C6H2O-; Ad = 1-adamantyl). In 1 the +2 oxidation state and the local pseudo-C3 symmetry were maintained as in the previous studies, while we aimed to remove the nuclear spin from the direct environment of the unpaired electron, as a means of eliminating the magnetic decoherence through the hyperfine interaction. In addition the use of a bulkier ligand allowed probing the effect of the rigidity on the relaxation and quantum coherence properties.

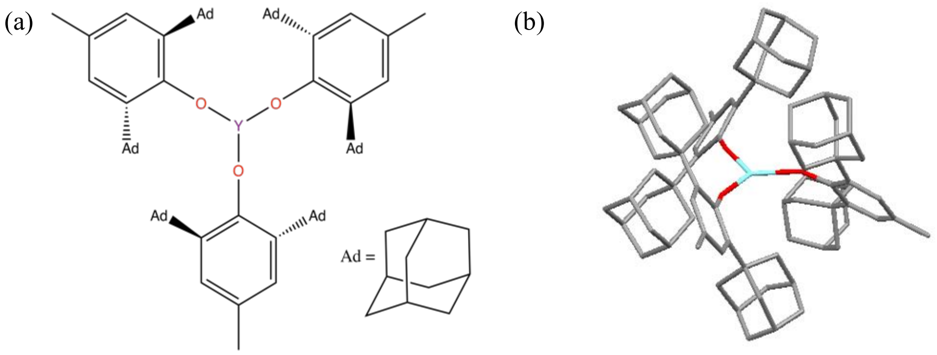

Figure 1. (a) Schematic representation of the molecular structure of **1**, (b) Molecular structure of the precursor **2**.

RESULTS AND DISCUSSION

Synthesis and characterization of the complex

The synthetic procedure of using a bulky aryloxide ligand, $^{-}$OAr^{Ad,Ad,Me}, to stabilize the Y^{II} ion has been previously reported and involves the reduction of the crystallographically characterized yttrium(III) precursor [Y(OAr^{Ad,Ad,Me})$_3$] (2,6-Ad$_2$-4-Me-C$_6$H$_2$O$^-$; Ad = 1-adamantyl) (**2**) with potassium graphite, KC$_8$ in the presence of 2.2.2-cryptand.[39] The reduced complex [K(2.2.2-cryptand)][Y(OAr^{Ad,Ad,Me})$_3$] (**1**) was fully characterized in solution, but unfortunately good X-ray quality crystals were not isolated and its solid state structure was not resolved. However, the crystal structure of a related complex, [K(2.2.2-cryptand)][Y(OAr$^{Ad,Ad,t\text{-}Bu}$)$_3$] (**3**), which only differs by a ^{t}Bu instead of Me substituent in the *para* position of the OAr group, provided confidence that the proposed structure is correct. Both **1** and **3** display a *pseudo*-C$_3$ symmetry around the Y(II) ion, with an average Y-O distance of 2.111 Å in **3** (Y-O1 2.106 Å Y-O2 2.108 Å Y-O3 2.118 Å) that is 0.06 Å longer than in **2**. We assume that **1** has a similar metal environment as **3**.

CW Electron Paramagnetic Resonance Spectroscopy

Frozen solution continuous wave (CW) EPR spectra for complex **1** exhibit an axial double resonance signal because of the interaction of the unpaired electron with the nuclear spin of ^{89}Y ion, *I*

= 1/2 (100% natural abundance). Modelling of the spectra was performed in the basis of a simple axial Hamiltonian $\widehat{H} = g\mu_B BS + IAS$, where g is the g-tensor, μ_B is the Bohr magneton, B is the applied magnetic field, S is the electronic spin, I is the nuclear spin of the ^{89}Y ion and A is the hyperfine coupling tensor, yielding the following parameters: $g_{\parallel}$= 1.965 and $g_{\perp}$= 1.934; and $A_{\parallel}$= 414 MHz and $A_{\perp}$= 430 MHz. The limited anisotropy in both g- and A- tensors is uncommon for an electron based on the 4d orbital. However, this highly isotropy would be compatible with our initial assumption that a significant electronic spin density of the Y^{II} ion resides in a more spherical orbital, such as the 5s-orbital. A useful comparison of the CW data of **1** with the previous reported [Y(Cp′)$_3$] complex shows a more anisotropic character for both g- and A- tensors in the case of **1**. Simulation parameter of [Y(Cp′)$_3$] complex; $g_{\parallel}$= 2.001 and $g_{\perp}$= 1.986; and $A_{\parallel}$= 98.6 MHz and $A_{\perp}$= 100.8 MHz, confirmed the limited anisotropy, while the significant difference of the isotropic hyperfine coupling between these complexes (A_{iso} = 425 MHz of **1** and A_{iso} = 100 MHz of [Y(Cp')$_3$]) suggests increased s-orbital character of the SOMO orbital which is predominantly the $4d_z^{2}$.[40]

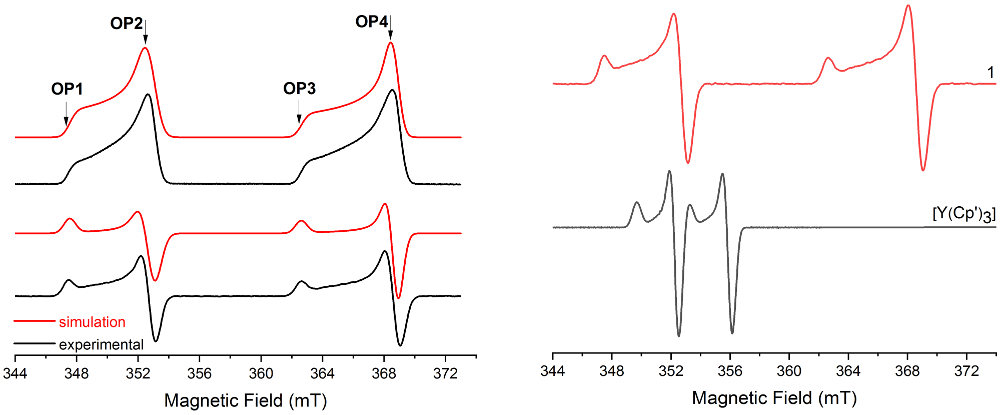

Figure 2. (a) Experimental (black) and simulated (red) X-band CW (lower) and EDFS (upper) spectra for **1** recorded in THF (10 mM) at 20 K; simulation parameters are given in the text. Observer positions **OP1-OP4** mark the magnetic fields at which time-dependent pulsed EPR data were recorded. (b) Compasion of the X-band CW EPR spectrum of [Y(Cp′)$_3$] (black) and **1** (red) recorded from frozen THF solutions (10 mM).

Pulse Electron Paramagnetic Resonance Spectroscopy

The echo-detected field swept (EDFS) spectra (Figure 2 and Figure S1) were recorded using a standard Hahn echo sequence, π/2 – π – τ – *echo*,[41] and detecting the fluctuation of the Hahn echo intensity with the variation of the applied magnetic field. The EDFS spectra is fully reproduced by a spin Hamiltonian that takes into account the same magnetic parameters as obtained from CW EPR simulation, suggesting that both EPR transitions associated to the $|M_S, M_I\rangle$ manifold; $|-1/2,-1/2\rangle \rightarrow |+1/2,-1/2\rangle$ and $|-1/2,+1/2\rangle \rightarrow |+1/2,+1/2\rangle$ are accessible via microwave pulses for relaxation measurements and quantum coherence studies.

To probe the viability of the qubit, the spin-lattice, T_1, and spin-spin (phase memory), T_m, relaxation times were measured from 5 K up to 120 K at the **OP1-OP4** field positions shown in Fig. 2. T_1 relaxation studies were performed via inversion recovery experiments, with the pulse sequence $(\pi - t - \pi/2 - \pi - \tau - echo)$[41]; during the experiment a $\pi = 32$ ns microwave pulse is applied to inverse the spin resonance that corresponds to the $M_S = -1/2 \rightarrow M_S = +1/2$ transition, so the intensity of the echo is recorded via a detection-Hahn echo sequence until saturation is achieved. The magnitude of the echo intensity is plotted as a function of the delay time t on a logarithmic scale leading to sigmoidal curves, which are then fitted by a bi-exponential equation (see the supporting information) to obtain the T_1 relaxation times varying from *ca*. 0.3 ms at 100 K to 313 ms at 5 K (**OP1**; Table S2). The temperature dependence of the spin-lattice relaxation times was analyzed by fitting the T_1 data with the Raman equation,[42] $T_1^{-1} = CT^n$, yielding $C = 1.58(1) \times 10^{-6}$ $\mu s^{-1}K^{-n}$ and $n = 2.08(2)$. As a long phase memory time is fundamental for a qubit candidate, we measured the T_m times using the Hahn echo sequence $(\pi/2 - \pi - \tau - echo)$[41] and incrementing the inter-pulse delay τ, while the decay of the echo intensity was recorded. Fitting of the echo traces with a stretch mono-exponential equation (see supporting information eqn. 1) provided the phase memory time, which varies from *ca*. 0.8 μs at 100 K to 3.6 μs at 5 K (**OP1**; Table S4). Both T_1 and T_m (up to 80 K) relaxation times (Fig. 3) are essentially independent of the molecular orientation (**OP1-OP4**), and additionally T_m is almost temperature independent between 5 and 80 K.

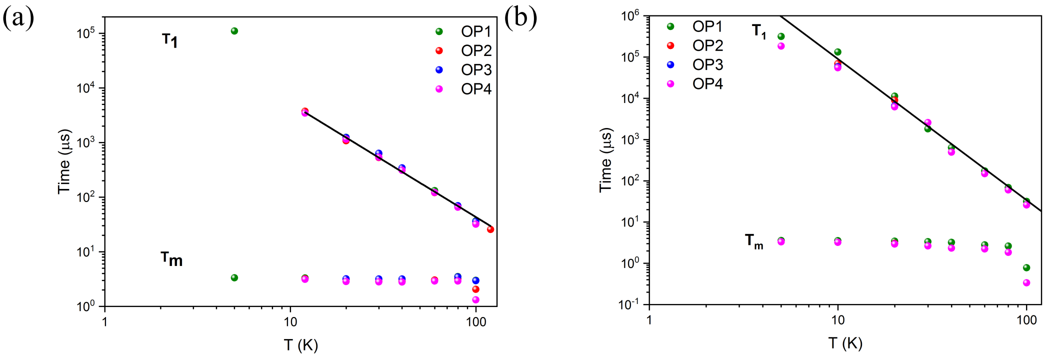

Figure 3. Temperature dependence of T_1 and T_m for **1** (10 mM THF) measured at (a) X-band and (b) Q-band and at different observer positions, as indicated in Fig. 2 and Fig. S1b. The black line in both graphs shows the fitting of the T_1 data with the Raman equation, $T_1^{-1} = CT^{-n}$.

Application of a dynamical decoupling Carr-Purcell-Meiboom-Gill (CPMG) sequence[43] has significantly elongated the T_m relaxation times. CPMG train sequences are used to improve the sensitivity by suppressing the low frequency noise originating from the nuclear spin flip-flops.[44] Application of this sequence in spin-based quantum bits results on lengthening of the phase memory time,[45] as the induced spectral diffusion is the main decoherence source in non-nuclear free magnetic systems. CPMG consists of a π pulse train applied after a Hahn-echo sequence; $\pi/2 - (\tau - \pi - \tau - echo)_n$. Recorded CPMG echo traces were then fitted by a mono-exponential equation, like in the case of the standard Hahn-echo decay, while the observed T_{CPMG} times were remarkably longer with respect to the ones measured via the Hahn-echo sequence. The T_{CPMG} are reaching 20 μs at 80 K and 598 μs at 5 K, which is to the best of our knowledge the longest relaxation time observed for a molecular system of such high concentration, including for any Y(II) organometallic system.

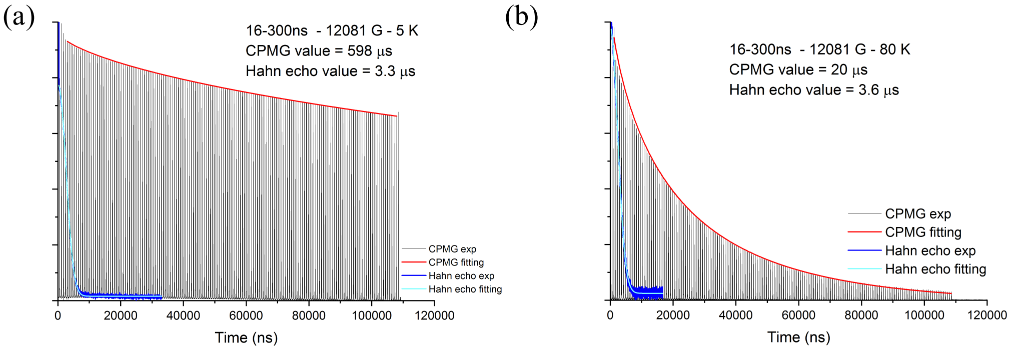

Figure 4. CPMG echoes (black) and the fitting of the decay (red) measured at B_0 = 1208.1 mT (**OP1**; Fig. S1) giving (a) T_{CPMG} = 598 μs at 5 K and (b) T_{CPMG} = 20 μs at 80 K. Corresponding Hahn echo decay traces (blue) and mono-exponential fitting (cyan) yields ~ 3 μs T_{m} times.

Given the remarkable coherence properties of **1**, we performed transient nutation experiments to probe the coherence manipulation of spins via microwave pulses. In this experiment a variable microwave tipping pulse is applied followed by a standard Hahn echo sequence detecting the smooth oscillation of the echo signal. This allows coherent back-and-forth quantum transitions between the $|0\rangle$ and $|1\rangle$ states, termed as Rabi oscillations.[46] The tipping angle controls the composition of the superposition of its two $|\pm \mathrm{M_S}\rangle$ states, which also depends on the applied B_1 power and on the length of the nutation pulse. The observed Rabi oscillations (Fig. 5) establish the ability of **1** to cycle through any arbitrary superposition of its states, showing the coherent spin manipulation of this potential molecular qubit. The angular frequency of these oscillations known as Rabi frequency, Ω_{R}, is expected to display a linear dependence with the power of the microwave field B_1. This linear dependence is more obvious after the Fourier transform analysis of the Rabi oscillations (Fig. S7b-S12b), which also reveals a B_1-independent frequency, approximately at 15 MHz corresponding to the Larmor frequency of ^{1}H nuclei in **1**.

In addition, the nutation data enables to determine the time of a single-qubit NOT computational operation[47], as the time length between adjacent minima and maxima of the Rabi oscillations (Fig. 5a), here found to be *ca.* 25 ns at 1 dB. A key qubit figure of merit, $\mathrm{Q_M}$, is described by the ratio of the quantum coherence time and the quantum gate operation time; $2\Omega_{\mathrm{R}}T_{\mathrm{m}}$[48] and illustrates the number of operations that could be performed during the coherence time T_{m}. The single qubit figure of merit for **1** is ~ 25200. This number of coherent oscillations, $\mathrm{Q_M}$, should be in the order of 10,000 for the successful operation of a quantum computation.[49]

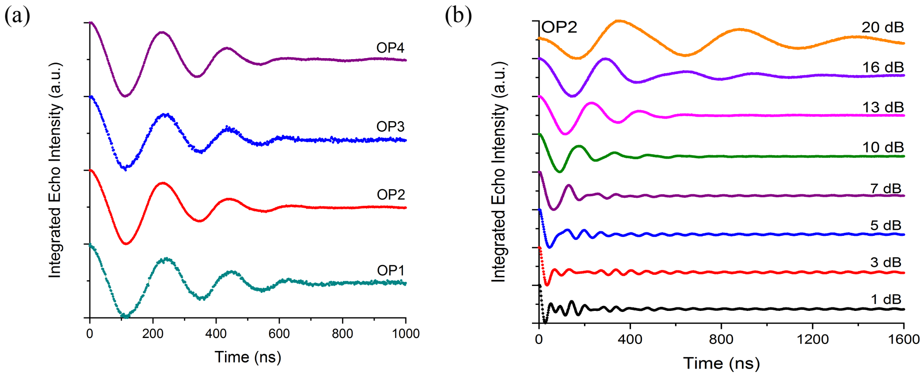

Figure 5. (a) Rabi oscillations for **1** (THF) at 20 K and different field positions (**OP1**–**OP4**; Figure 2), acquired at 13 dB; (b) Rabi oscillations for **1** (THF) at 20 K measured at B_0 = 352.6 mT (**OP2**; Fig. 2), acquired at various power from 1–20 dB.

As there is only a small anisotropy in the *g*-tensor, and negligible *A*-tensor anisotropy, one can assign the long relaxation times and robust qubit properties to possible admixing between $4d_{z2}$ and 5s orbitals, and thus pronounced *s*-character of the single occupied molecular orbital. Next step was to characterize the environment of the metal ions in greater detail; therefore more advanced pulse EPR techniques such as electron nuclear double resonance (ENDOR) and two-dimensional hyperfine sublevel correlation (HYSCORE) spectroscopy were performed. ENDOR and HYSCORE methods provide a useful tool for extracting information about the hyperfine coupling of the unpaired electron with the nuclear spin active nuclei (^{1}H and ^{13}C) in the vicinity.

Electron nuclear double resonance spectroscopy

Standard ENDOR pulse sequences such as Mims ($\pi/2 - \tau - \pi/2 - \pi_{RF} - \pi/2 - \tau -$ *stimulated echo*) and Davies ($\pi - \pi_{RF} - \pi/2 - \tau - \pi - \tau -$ *inverted echo*),[41] operating under non-selective and selective microwave pulses, respectively, were used to investigate **1**. During both methods nuclear polarization is generated and then inverted by the radiofrequency pulses enabling spin polarization transfer. For the simulation of the ENDOR (and also HYSCORE) spectra the hyperfine dipolar constants were calculated by the equation (1):

$$A^{\mathrm{dip}} = \frac{\mu_0}{4\pi h}\beta_e\beta_n\sum_k \rho_k \frac{3(\mathbf{g}{\cdot}\mathbf{n}_\mathbf{k})(\tilde{\mathbf{n}}_\mathbf{k}{\cdot}g_n\mathbf{1})-\mathbf{g}{\cdot}g_n\mathbf{1}}{r_k^3} \qquad \text{(Equation 1)}$$

where **g** and g_n**1** are the electron and nuclear **g** (3x3) matrices (g_n is a scalar; **1** is the unit matrix), β_e and β_n are the electron and nuclear magnetons ($\beta_e = 9.27 \cdot 10^{-24}$ J·T^{-1}; $\beta_n = 5.05 \cdot 10^{-27}$ J·T^{-1}), ρ_k is the electron spin population at atom *k* ($0 \leq \rho_k \leq 1$), r_k is *n*…*k* distance (in m), $\mathbf{n}_k$ and $\tilde{\mathbf{n}}_k$ are the *n*…*k* unit vector expressed in the molecular frame (a column vector) and its transpose, h is the Plank's constant ($6.63 \cdot 10^{-34}$ J·s) and μ_0 is the vacuum permittivity ($1.26 \cdot 10^{-6}$ T^2·J^{-1}·m^3). The nuclear *g*-values for ^{1}H and ^{13}C are: $g_H = 5.586$ and $g_C = 1.405$.

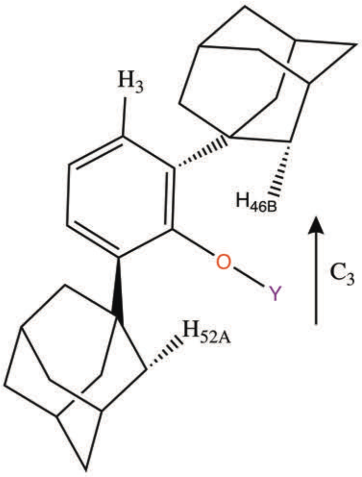

Figure 6. Schematic representation of **1** emphasizing on the H atoms used for the ENDOR and HYSCORE simulations, the vector shows the direction of the molecular C_3 axis, which coincides with the g_z axis.

Modelling of both Mims and Davies data involved three different H atoms; H46B and H52A, which are the closest H atoms to the ^{89}Y ion and the H_3 one of the H atoms of the aromatic ring (Fig. 6). The dipolar constants were not significant for reproducing the larger ^1H splitting of ~10 MHz that was observed, so additional contributions to the spin density was necessary. Best simulation yields a set of anisotropic A parameters for H46B; A_{H46B} = [-1, 4, -1] and an isotropic set for H52A; A_{H52A} = [1, 1, 1] (Fig. 7). Same parameters were used for the simulation of the ^1H Mims **OP3** (at g_z) and ^1H Davies at **OP2** (at g_{xy}) spectra presented in supporting information (Fig. S14-S15).

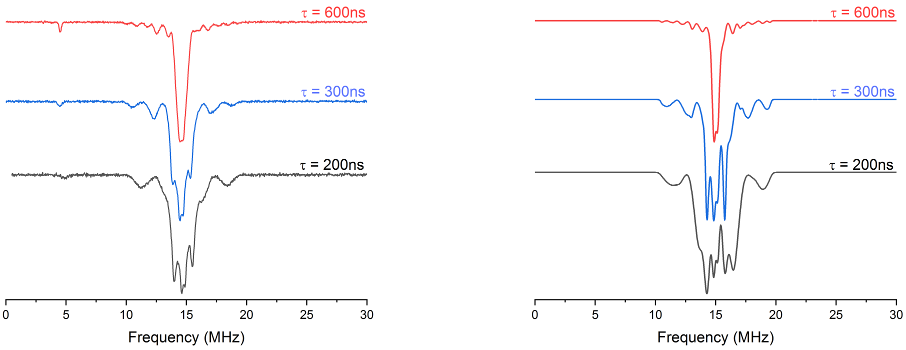

Figure 6. (a) ^1H Mims ENDOR spectra at B_0 = 352.6 mT (**OP2**; Fig. 2) and 20 K with τ of 200 ns (black), 300 ns (blue) and 600 ns (red) (b) simulation of the spectra of (a) using the parameters described in the text.

Hyperfine sublevel correlation spectroscopy

HYSCORE spectroscopy was also involved in order to detect and quantify in greater detail the weak hyperfine interactions of the primarily metal-based unpaired electron with the ^{13}C and ^1H nuclei of the aryloxide ligand, due to the assumption that electron spin density can be transferred from the metal ion towards the ligands. HYSCORE technique uses a four-pulse electron spin-echo sequence, $\pi/2 - \tau - \pi/2 - t1 - \pi - t2 - \pi/2 - \tau - echo$, which generates correlations between the nuclear frequencies in the α and β electron spin manifolds.[50]

The HYSCORE data of **1** (Fig. 7-9) were modelled using a similar approach[51] with the ENDOR spectra simulations. Initially only the dipolar hyperfine constants, which were calculated via the crystal structure, were taken into account while the experimental spectra were not fully reproduced. Hence, based on the assumption that the total hyperfine coupling matrix ($\mathbf{A}$) for a given ^{13}C nucleus is defined by the sum of the spin density ($\mathbf{A}^{Cn}$) and point dipole ($\mathbf{A}^{dip}$)~~,~~ contributions according to: $\mathbf{A} = \mathbf{A}^{Cn} + \mathbf{A}^{dip}$ (Equation 2). Therefore for all HYSCORE simulations we added covalent spin density contribution to the hyperfine interaction summing up with the point dipole model.

For complex **1** the large detected coupling in ^{13}C HYSCORE spectra cannot be reproduced using a dipole-only model (Fig. 7a), thus dipolar and spin density contribution of C1 (the C atom of the ring bonded to the O atoms; equivalent with C31 and C61 of the other ligands) was entailed. Excellent simulation of the experimental ^{13}C HYSCORE spectra was achieved with $A^{C1}_{z,xy}$ = 8.2, 4.8 MHz hyperfine coupling constants, while negligible contribution was considered for all the other C atoms of the structure as they are found in a greater distance from the metal ion.

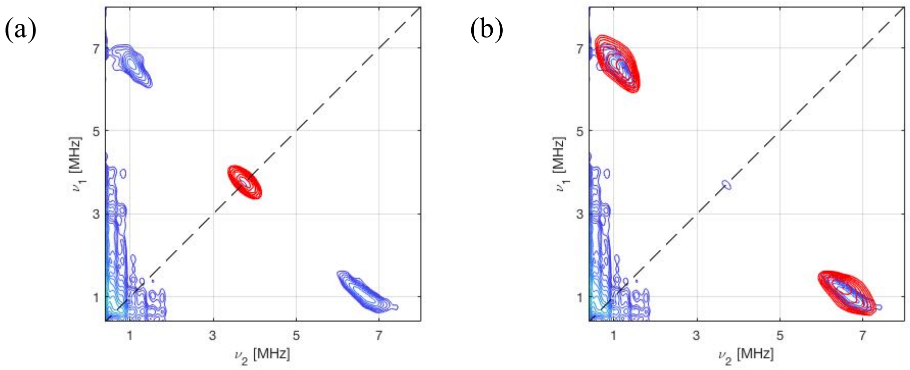

Figure 7. X-band HYSCORE spectra for **1** (a) ^{13}C region at a static field of B_0 = 352.6 mT (at g_{xy}) with calculation in red based on the point dipole model C1 contribution, (b) same as for (a) but the simulation (red) also includes spin density contribution on C1, described by the following values; $A^{C1}_{z,xy}$ = 8.2, 4.8 MHz.

Simulation of the ^{1}H HYSCORE for the g_{xy} orientation (Fig. 8) was performed using the dipolar interaction constants of three different H atoms~~,~~ mentioned above for the ENDOR simulation. Best simulation yields the following hyperfine parameters additionally to the dipolar constants for H46B and H52A; A_{H46B} = [-1.8, 4, -1.8] and A_{H52A} = [1, 1, 1], while for H3 spin density contribution was not required. Moving to the g_z orientation, modelling of the ^{1}H region involved the dipolar interaction of the H46B, H52A, and H3, with additional spin density contribution only for H46B described by the following A parameters A_{H46B} = [-1, 4, -1].

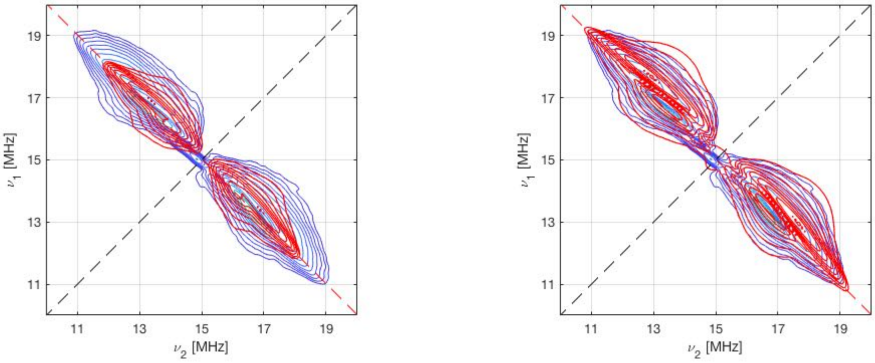

Figure 8. X-band HYSCORE spectra for **1** (a) ^{1}H region at a static field of B_0 = 352.6 mT (at g_{xy}) with calculation in red based only on the point dipole model including H46B, H52A and H3 (b) same as for (a) but the simulation (red) includes spin density contribution on H46B and H52A as a hyperfine interactions matrix described in the text.

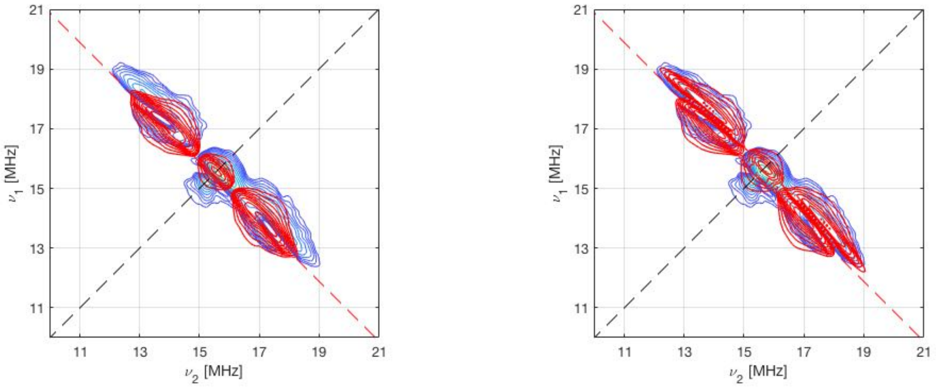

Figure 9. X-band HYSCORE spectra for **1** (a) ^{1}H region at a static field of B_0 = 362.7 mT (at g_z) with calculation in red based only on the point dipole model including H46B, H52A and H3 (b) same as for (a) but the simulation (red) includes spin density contribution only on H46B as a hyperfine interactions matrix described in the text.

CONCLUSIONS

In summary, we report the first coherence studies undertaken on a Y^{II} complex with aryloxide ligands, [K(2.2.2-cryptand)][Y(OAr^{Ad,Ad,Me})$_3$] **1**. The complex contains a yttrium ion in the unusual +2 oxidation state adopting a C_3 symmetric environment allowing the *s*- and d_{z2} atomic orbital admixture. Compared to [K(2.2.2-cryptand)][Y(Cp')$_3$], the only other yttrium(II) complex reported to display quantum coherence, complex **1** was engineered to have negligible magnetic anisotropy and increased rigidity of the ligands, yielding to higher energies for the low frequency vibrational modes. Hence, the enhanced structural rigidity facilitates the observation of longer T_1 and T_m relaxation times, reaching 313 ms and 3.6 μs at 5 K, respectively. More importantly, use of multi-pulse CPMG microwave sequences has revealed remarkable prolongation of the phase memory time to 600 μs at 5 K, due to the dynamical decoupling of the spins and low-frequency noise suppression. Additional information about the interaction of the unpaired electron with the surrounding spin active nuclei was extracted via ENDOR and HYSCORE methods. Analysis of the spectra points out that significant electron spin density contribution is delocalized onto the ligands, represented by the following sets of hyperfine matrices for C; A^{C1} = [4.8, 4.8, 8.2] MHz and for H atoms; A_{H46B} = [-1.8, 4, -1.8] and A_{H52A} = [1, 1, 1].

References

1. A. Gaita-Ariño, F. Luis, S. Hill and E. Coronado. Molecular spins for quantum computation. *Nat. Chem.*, **2019**, *11*, 301-309.

2. S. G. McAdams, A.-M. Ariciu, A. K. Kostopoulos, J. P. S. Walsh and F. Tuna. Molecular single-ion magnets based on lanthanides and actinides: Design considerations and new advances in the context of quantum technologies. *Coord. Chem. Rev.,* **2017**, *346*, 216-239.

3. F. Tuna. Molecular spins as qubits. *Chem.*, **2020**, *6*, 799-800.

4. M. Atzori and R. Sessoli. The second quantum revolution: Role and challenges of molecular chemistry. *J. Am. Chem. Soc.*, **2019**, *141*, 11339-11352.

5. K. S. Pedersen, A.-M. Ariciu, S. McAdams, H. Weihe, J. Bendix, F. Tuna and S. Piligkos. Toward molecular 4f single-ion magnet qubit. *J. Am. Chem. Soc.*, **2016**, *138*, 18, 5801-5804.

6. E. Moreno-Pineda, C. Godfrin, F. Balestro, W. Wernsdorfer and M. Ruben. Molecular spin qudits for quantum alghoritms. *Chem. Soc. Rev.*, **2018**, *47*, 501-513.

7. M. Leuenberger and D. Loss. Quantum computing in molecular magnets. *Nature*, **2001**, *410*, 789-793.

8. P. Neumann, J. Beck, M. Steiner, F. Rempp, H. Fedder, P. R. Hemmer, J. Wrachtrup and F. Jelezko. Single-shot readout of a single nuclear spin. *Science*, **2010**, *329*, 542-544.

9. J. J. Pla, K. Y. Tan, J. P. Dehollain, W. H. Lim, J. J. L. Morton, F. A. Zwanenburg, D. N. Jamieson, A. S. Dzurak and A. Morello. High-fidelity readout and control of a nuclear spin qubit in silicon. *Nature*, **2013**, *496*, 334-338.

10. J. J. Pla, K. Y. Tan, J. P. Dehollain, W. H. Lim, J. J. L. Morton, D. N. Jamieson, A. S. Dzurak and A. Morello. A single-atom electron spin qubit in silicon. *Nature*, **2012**, *489*, 541-545.

11. J. Clarke and F. K. Wilhelm, Superconducting quantum bits. *Nature*, **2008**, *453*, 1031-1042.

12. I. Chiorescu, Y. Nakamura, C. J. P. M. Harmans and J. E. Mooij Coherent Quantum dynamics of a superconducting flux qubit. *Science*, **2003**, *299*, 1869-1871.

13. B. Trauzettel, D. V. Bulaev, D. Loss and G. Burkard. Spin qubits in graphene quantum dots. *Nat. Phys.*, **2007**, *3*, 192-196.

14. Y. Wang, J. Li, S. Zhang, K. Su, Y. Zhou, K. Liao, S. Du, H. Yan and S.-L. Zhu. Efficient quantum memory for single-photon polarization qubits. *Nat. Photonics*, **2019**, *13*, 346-351.

15. A. C. Dada, J. Leach, G. S. Buller, M. J. Padgett and E. Andersson. Experimental high-dimensional two-photon entanglement and violations of generalized Bell inequalities. *Nat. Phys.*, **2011**, *7*, 677-680.

16. I. Bloch, Quantum coherence and entanglement with ultracold atoms in optical lattices. *Nature*, **2008**, *453*, 1016-1022.

17. J. Benhelm, G. Kirchmair, C. F. Roos and R. Blatt. Towards fault-tolerant quantum computing with trapped ions. *Nature Phys.*, **2008**, *4*, 463-466.

18. I. L. Chuang, L. M. K. Vandersypen, X. Zhou, D. W. Leung and S. Lloyd. Experimental realization of a quantum algorithm. *Nature*, **1998**, *393*, 143-146.

19. F. Troiani and M. Affronte, Molecular spins for quantum information technologies, *Chem. Soc. Rev.*, **2011**, *40*, 3119-3129.

20. G. Aromí, D. Aguilà, P. Gamez, F. Luis and O. Roubeau. Design of magnetic coordination complexes for quantum computing. *Chem. Soc. Rev.*, **2012**, *41*, 537-546.

21. P. W. Shor. Polynomial-time algorithms for prime factorization and discrete logarithms on a quantum computer. *SIAM J. Comput.*, **1997**, *26*, 1484-1509.

22. P. C. Maurer, G. Kucsko, C. Latta, L. Jiang, N. Y. Yao, S. D. Bennett, F. Pastawski, D. Hunger, N. Chisholm, M. Markham, D. J. Twitchen, J. I. Cirac and M. D. Lukin. Room temperature quantum bit memory exceeding one second. *Science*, **2012**, *336*, 1283-1286.

23. A. Ardavan, O. Rival, J. J. L. Morton, S. J. Blundell, A. M. Tyryshkin, G. A. Timco and R. E. P. Winpenny. Will Spin-Relaxation Times in Molecular Magnets Permit Quantum Information Processing?. *Phys. Rev. Lett.*, **2007**, *98*, 057201.

24. F. Moro, D. Kaminski, F. Tuna, G. F. S. Whitehead, G. A. Timco, D. Collison, R. E. P. Winpenny, A. Ardavan and E. J. L. McInnes. Coherent electron spin manipulation in dilute oriented

ensemble of molecular nanomagnets: pulsed EPR on doped single crystal. *Chem. Commun.*, **2014**, *50*, 91-93.
25. A. Ardavan, A. M. Bowen, A. Fernandez, A. J. Fielding, D. Kaminski, F. Moro, C. A. Muryn, M. D. Wise, A. Ruggi, E. J. L. McInnes, K. Severin, G. A. Timco, C. R. Timmel, F. Tuna, G. F. Whitehead and R. E. P. Winpenny, Engineering coherent interactions in molecular nanomagnet dimers. *npj Quantum Inf.*, **2015**, *1*, 15012.
26. H.-J. Lim, S. Welinski, A. Ferrier, P. Goldner and J. J. L. Morton. Coherent spin dynamics of ytterbium ions in yttrium orthosilicate. *Phys. Rev. B.*, **2018**, *97*, 064409.
27. J. Chen, C. Hu, J. F. Stanton, S. Hill, H.-P. Cheng and X.-G. Zhang. Decoherence in molecular electron spin qubits: Insights from quantum many-body simulations. *J. Phys. Chem. Lett.*, **2020**, *11*, 2074-2078.
28. R. Myrzoyan and R. G. Hadt. The dynamic ligand field of a molecular qubit: decoherence through spin-phonon coupling. *Phys. Chem. Chem. Phys.*, **2020**, *22*, 11249-11265.
29. M. J. Graham, J. M. Zadrozny, M. Shiddig, J. S. Anderson, M. Fataftah, S. Hill and D. E. Freedman. Influence of electronic spin and spin-orbit coupling on decoherence in mononuclear transition metal complexes. *J. Am. Chem. Soc.*, **2014**, *136*, 7623-7626.
30. V. V. Dobrovitski, M. I. Katsnelson, and B. N. Harmon. Mechanisms of decoherence in weakly anisotropic molecular magnets. *Phys. Rev. Lett.*, **2000**, *84*, 3458.
31. S. Ballmann, R. Härtle, P. B. Coto, M. Elbing, M. Mayor, M. R. Bryce, M. Thoss and H. B. Weber. Experimental evidence for quantum interference and vibrationally induced decoherence in single-molecule junctions. *Phys. Rev. Lett.*, **2012**, *109*, 056801.
32. J. M. Zadrozny, J. Niklas, O. G. Poluektov and D. Freedman. Millisecond coherence time in a tunable molecular electronic spin qubit. *ACS Cent. Sci.*, **2015**, *1*, 488-492.
33. C. J. Wedge, G. A. Timco, E. T. Spielberg, R. E. George, F. Tuna, S. Rigby, E. J. L. McInnes, R. E. P. Winpenny, S. J. Blundell and A. Ardavan. Chemical engineering of molecular qubits. *Phys. Rev. Lett.*, **2012**, *108*, 107204.
34. K. Bader, D. Dengler, S. Lenz, B. Endeward, S.-D. Jiang, P. Neugebauer and J. van Slageren. Room temperature quantum coherence in a potential molecular qubit. *Nat. Commun.*, **2014**, *5*, 5304.
35. M. Shiddiq, D. Komijani, Y. Duan, A. Gaita-Ariño, E. Coronado and S. Hill. Enhancing coherence in molecular spin qubits via atomic clock transitions. *Nature*, **2016**, *531*, 348-351.
36. K. Bader, M. Winkler and J. van Slageren. Tuning of molecular qubits: very long coherence and spin-lattice relaxation times. *Chem. Comm.*, **2016**, *52*, 3623-3626.
37. M. Atzori, L. Tesi, E. Morra, M. Chiesa, L. Sorace and R. Sessoli, Room-temperature quantum coherence and Rabi oscillations in vanadyl phthalocyanine: Toward multifunctional molecular spin qubits. *J. Am. Chem. Soc.*, **2016**, *138*, 2154-2157.
38. A.-M. Ariciu, D. H. Woen, D. N. Huh, L. E. Nodaraki, A. K. Kostopoulos, C. A. P. Goodwin, N. F. Chilton, E. J. L. McInnes, R. E. P. Winpenny, W. J. Evans and F. Tuna. Engineering electronic structure to prolong relaxation times in molecular qubits by minimising orbital angular momentum. *Nat. Commun.*, **2019**, *10*, 3330.
39. S. A. Moehring, M. Michlich, C. J. Hoerger, K. Meyer, J. W. Ziller and W. J. Evans. A room-temperature stable Y(II) aryloxide: Using steric saturation to kinetically stabilize Y(II) complexes. *Inorg. Chem.*, **2020**, *59*, 3207-3214.
40. T. F. Hunter and M. C. R. Symons, Spin polarization in atoms and π-radicals, *Nature*, **1967**, *213*, 1121-1122.
41. A. Schweiger and G. Jeschke, Principles of pulse electron paramagnetic resonance. Oxford University press, **2001**.

42. L. J. Berliner, S. S. Eaton and G. R. Eaton, Distance measurements in biological systems by EPR. Kluwer Academic/ Plenum Publishers, New York, **2000**.
43. H. Y. Carr and E. M. Purcell, Effects of diffusion on free precession in nuclear magnetic resonance experiments. *Phys. Rev.*, **1954**, *94*, 630-638.
44. F. Mentink-Vigier, A. Collauto, A. Feintuch, I. Kaminker, V. Tarle and D. Goldfarb. Increasing sensitivity of pulse EPR experiments using echo train detection schemes. *J. Magn. Reson.*, **2013**, *236*, 117-125.
45. G. Mitrikas, E. K. Efthimiadou and G. Kordas. Extending the electron spin coherence time of atomic hydrogen by dynamical decoupling. *Phys. Chem. Chem. Phys.*, **2014**, *16*, 2378-2383.
46. I. I. Rabi. Space quantisation in a gyrating magnetic field. *Phys. Rev.*, **1937**, *51*, 652-654.
47. G. Aromi and O. Roubeau. Handbook on the physics and chemistry of rare earths, Vol. 56, Chapter 3: Lanthanide molecules for spin-based quantum technologies, *Elsevier*, **2019**.
48. M. J. Martínez-Pérez, S. Cardona-Serra, C. Schlegel, F. Moro, P. J. Alonso, H. Prima-García, J. M. Clemente-Juan, M. Evangelisti, A. Gaita-Ariño, J. Sesé, J. van Slageren, E. Coronado and F. Luis. Gd-based single-ion magnets with tunable magnetic anisotropy: Molecular design of spin qubits. *Phys. Rev. Lett.*, **2012**, *108*, 247213.
49. D. P. DiVincenzo, *Fortschr. Phys*., **2000**, *48*, 771-783.
50. S. Van Doorslaer, Hyperfine Spectroscopy: ESSEM, *eMagRes*, **2017**, Vol 6: 51-70.
51. A. Formanuik, A.-M. Ariciu, F. Ortu, R. Beekmeyer, A. Kerridge, F. Tuna, E. J. L. McInnes and D. Mills. Actinide covalency measured by pulsed electron paramagnetic resonance spectroscopy. *Nat. Chem.*, **2017**, *9*, 578-583.

Electronic Supporting Information

An Organometallic Yttrium(II) Spin Qubit Based on a Rigid Aryloxide Ligand Displaying Enhanced Coherence Properties

Lydia E. Nodaraki,[1,2] Daniel N. Huh,[3] Fabrizio Ortu,[1] William J. Evans[3] and Floriana Tuna[1,2]

[1]Department of Chemistry, The University of Manchester, Oxford Road, Manchester M13 9PL, UK
[2]Photon Science Institute, The University of Manchester, Oxford Road, Manchester M13 9PL, UK
[3]Department of Chemistry, University of California, Irvine, CA 92697-2025

Contents

1. EPR measurements and general procedures
2. Additional echo-detected field-swept (EDFS) EPR spectra
3. Spin-lattice relaxation measurement
4. Phase memory time measurements
5. Carr-Purcell-Meiboom-Gill (CPMG) spin-spin relaxation time measurements
6. Transient nutation experiments
7. ENDOR spectra
8. HYSCORE spectra

1. EPR measurements and general procedures

Continuous wave EPR experiments were performed with Bruker EMX 300 spectrometers operating at X-band (ca. 9.3-9.4 GHz). Pulse EPR data were collected with a Bruker ElexSys E580X spectrometer equipped with either an MD4 or an MD5 resonator and operating at ca. 9.7 GHz. Simulation of the data was performed using the EasySpin software.[1] All manipulation and sample preparation were carried out using Schlenk and glove box techniques under argon or dinitrogen atmosphere with strict exclusion of oxygen and water. Solvents were purged with UHP grade argon, passed through columns containing alumina and molecular sieves and degased before use.

2. Additional echo-detected field-swept (EDFS) EPR spectra

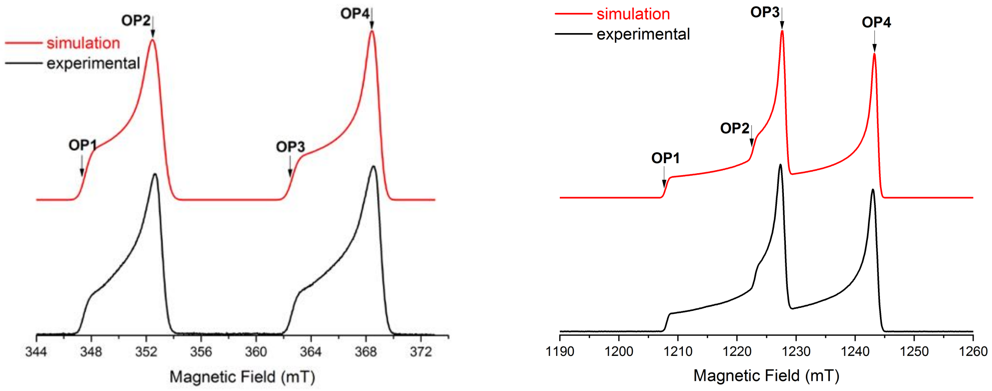

Figure S1. Echo-detected field-swept (EDFS) spectra measured at (a) X-band (9.71 GHz) and (b) Q-band (33.5 GHz) at 20 K, simulated with the following parameters; $g_{\|}$= 1.965 and $g_{\perp}$= 1.934; and $A_{\|}$= 414 MHz and $A_{\perp}$= 430 MHz.

Table S1. Summary of observer field positions OP1-OP4 at X- and Q-band.

Magnetic Field (X-band)	
347.2 mT	OP1
352.6 mT	OP2
362.6 mT	OP3
368.5 mT	OP4

Magnetic Field (Q-band)	
1208.1 mT	OP1
1223.2 mT	OP2
1227.5 mT	OP3
1243.1 mT	OP4

3. Spin-lattice relaxation measurements

For the spin–lattice relaxation time, T_1, measurements were carried out by using a standard magnetization inversion recovery pulse sequence ($\pi - t - \pi/2 - \tau - \pi - \tau - echo$)[2] with 16 and 32 ns π/2 and π pulse lengths, respectively, a fixed τ and variable t. The T_1 constant was calculated by fitting the experimental data according to the following equation:

$$Y(t) = Y_1 e^{(-t/T_1)} + Y_{SD}^{(-t/T_{SD})} \quad \text{(eqn S1)}$$

where Y_1 and Y_{SD} are the amplitudes, and T_{SD} is the spectral diffusion time constant.

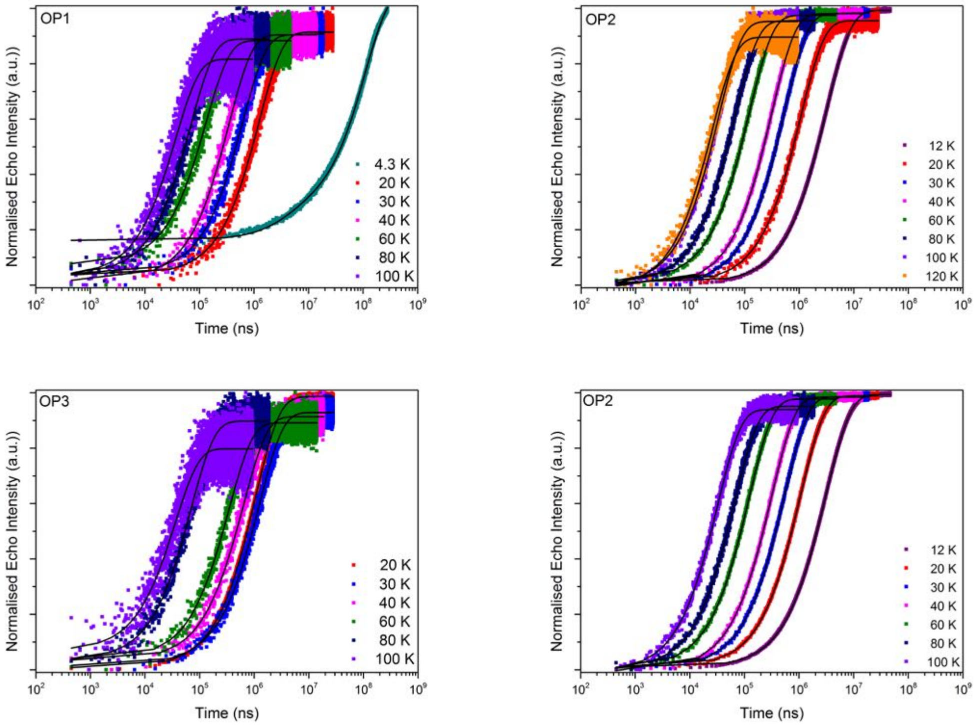

Figure S2. X-band inversion recovery data for **1** (10 mM; THF) at selected temperatures from 4.3 to 120 K, and at (a) B_0 = 347.2 mT (**OP1**), B_0 = 352.6 mT (**OP2**), B_0 = 362.6 mT (**OP3**) and B_0 = 368.5 mT (**OP4**). The black lines correspond to the best fits to the biexponential model (Equation S1), giving the parameters in Table S2.

Table S2. Extracted T_1 time constants for **1** (10 mM THF) at X-band

T (K)	OP1 T_m (μs)	OP2 T_m (μs)	OP3 T_m (μs)	OP4 T_m (μs)
5	313354	-	-	183824
10	132015	68554.5	58042.8	54797.8
20	11258.4	8915.43	6581.62	6181.78
30	1814.8	-	-	2582.86
40	637.489	-	-	495.14
60	174.054	-	-	148.513
80	68.083	-	-	59.766
100	31.665	-	-	25.994

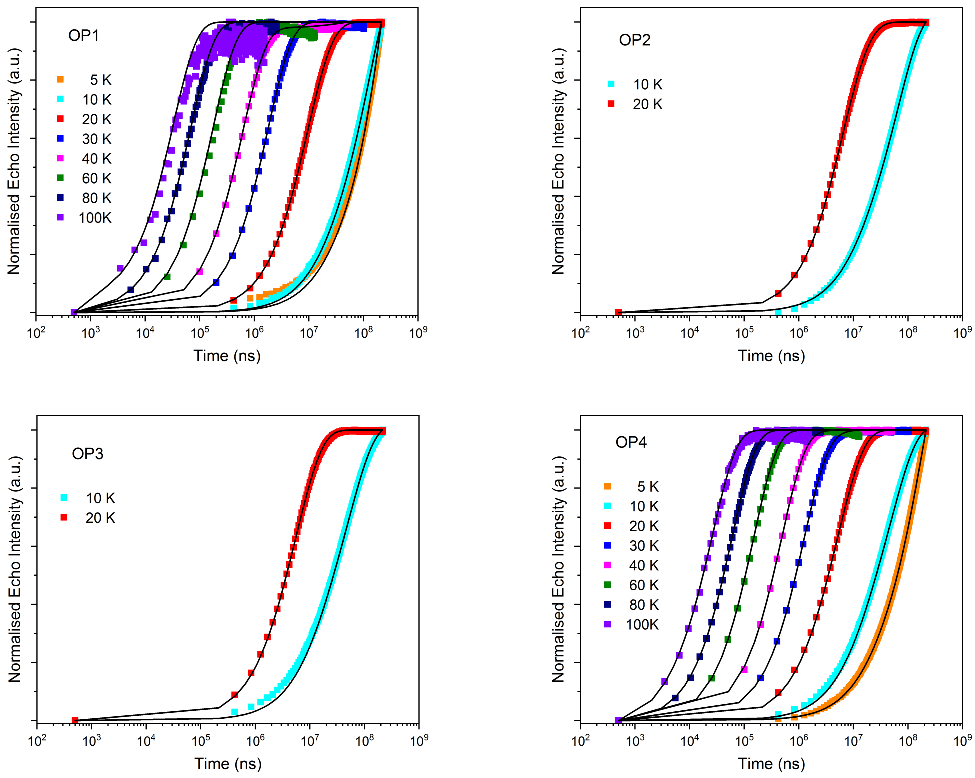

Figure S3. Q-band inversion recovery data for **1** (10 mM; THF) at selected temperatures from 5 to 100 K, and at (a) B_0 = 1208.1 mT (**OP1**), B_0 = 1223.2 mT (**OP2**), B_0 = 1227.5 mT (**OP3**) and B_0 = 1243.1 mT (**OP4**). The black lines correspond to the best fits to the biexponential model (Equation S1), giving the parameters in Table S3.

Table S3. Extracted T_1 time constants for **1** (10 mM THF) at Q-band

T (K)	OP1 T_m (μs)	OP2 T_m (μs)	OP3 T_m (μs)	OP4 T_m (μs)
5	109540	-	-	-
12	-	3740.89	-	3452.28
20	1246.35	1076.16	1239.21	1147.11
30	621.486	532.874	634.369	538.813
40	343.904	312.315	343.728	312.138
60	131.314	121.054	-	121.196
80	69.043	65.464	69.442	65.442
100	36.59	32.701	35.741	32.033
120	-	25.657	-	-

4. Phase memory time measurements

The phase memory time, T_m, measurements were carried out using a Hahn echo sequence ($\pi/2 - \tau - \pi - \tau - echo$)[2] with gradually increasing the inter-pulse delay, τ. Using microwave pulse length of 32 ns or 128 ns for π pulse, strong proton-electron spin modulation was observed. In order to suppress the

^{1}H modulation in the echo decays, longer microwave pulses of length $\pi = 256$ ns or $\pi = 1000$ ns were used. The fitting functions used for the echo decays were: $Y(2\tau) = Y_0 e^{(-2\tau/T_\mathrm{m})^\mathrm{k}} + \mathrm{c}$

where Y_0 is the amplitude and k is the stretch factor.

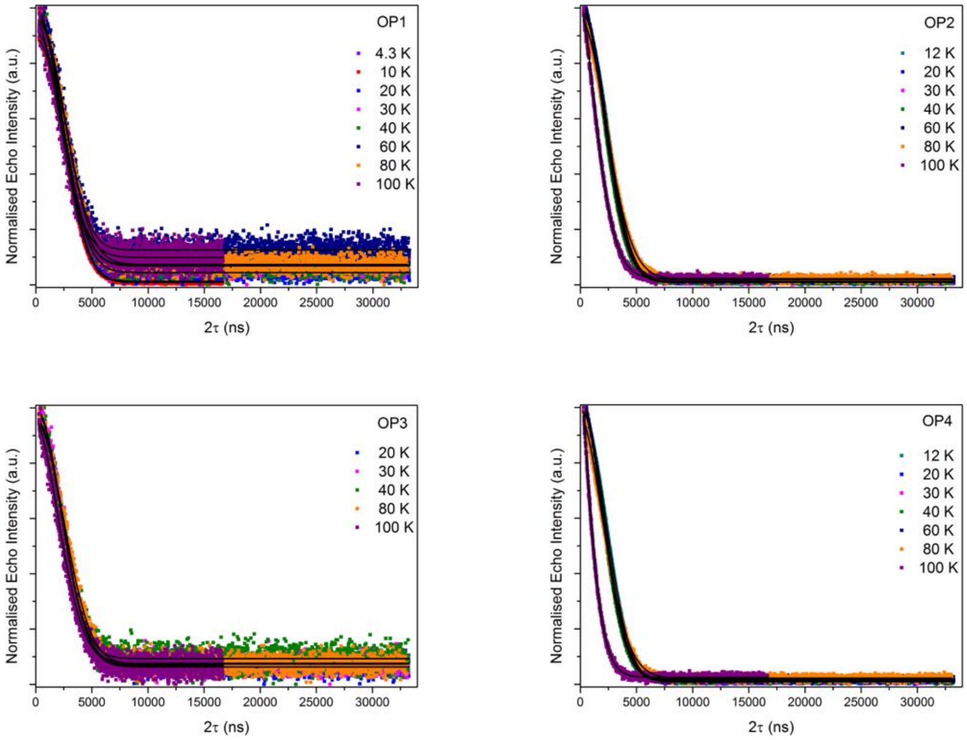

Figure S4. Normalized Hahn-echo signal intensities as a function of the inter-pulse delay 2τ, for **1** (a) B_0 = 347.2 mT (**OP1**), B_0 = 352.6 mT (**OP2**), B_0 = 362.6 mT (**OP3**) and B_0 = 368.5 mT (**OP4**), at selected temperatures (4.3–100 K);

Table S4. Extracted T_m time constants for **1** (10 mM THF) at X-band

T (K)	OP1 T_m (μs)	OP2 T_m (μs)	OP3 T_m (μs)	OP4 T_m (μs)
5	3.561			3.303
10	3.536			3.215
20	3.445	3.043	2.948	2.931
30	3.327			2.64
40	3.225			2.335
60	2.78			2.224
80	2.6			1.851
100	0.782			0.336

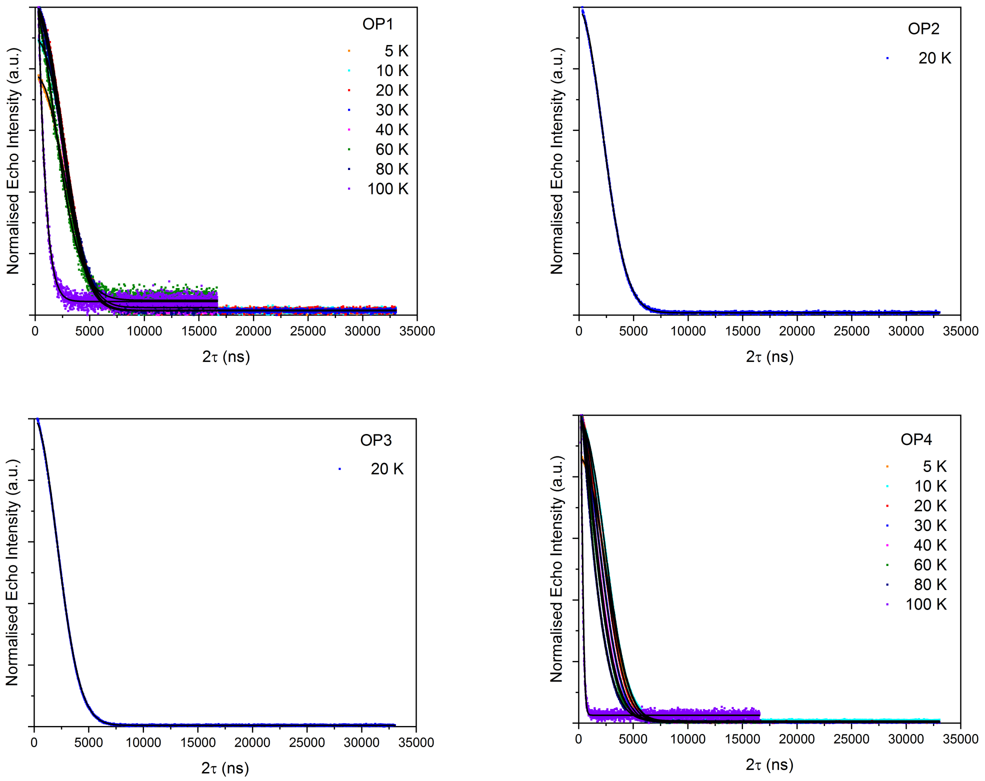

Figure S5. Normalized Hahn-echo signal intensities as a function of the inter-pulse delay 2τ, for **1** (a) B_0 = 1208.1 mT (**OP1**), B_0 = 1223.2 mT (**OP2**), B_0 = 1227.5 mT (**OP3**) and B_0 = 1243.1 mT (**OP4**), at selected temperatures (5–100 K);

Table S5. Extracted T_m time constants for **1** (10 mM THF) at Q-band

T (K)	OP1 T_m (μs)	OP2 T_m (μs)	OP3 T_m (μs)	OP4 T_m (μs)
5	3.338	-	-	-
12	3.313	3.19	-	3.125
20	3.195	3.113	3.203	2.859
30	3.174	2.898	3.181	2.805
40	3.186	2.894	3.183	2.784
60	-	3.043	-	2.912
80	3.503	3.205	3.458	2.918
100	3.003	2.054	2.956	1.316

5. Carr-Purcell-Meiboom-Gill (CPMG) spin-spin relaxation time measurements

The spin-spin relaxation time measurements based on the CPMG sequence were carried out using a train of π pulses to refocus the echo and significantly suppress the nuclear spin flip-flops. CPMG sequence, $\pi/2 - (\tau - \pi - \tau - echo)_n$,[3] was applied with π = 32 ns and different τ values at several temperatures. Analysis of the CPMG echo traces with the following mono-exponential equation; $Y(2\tau) = Y_0 e^{(-2\tau/T_{\mathrm{CPMG}})} + c$ resulted the T_{CPMG} relaxation times.

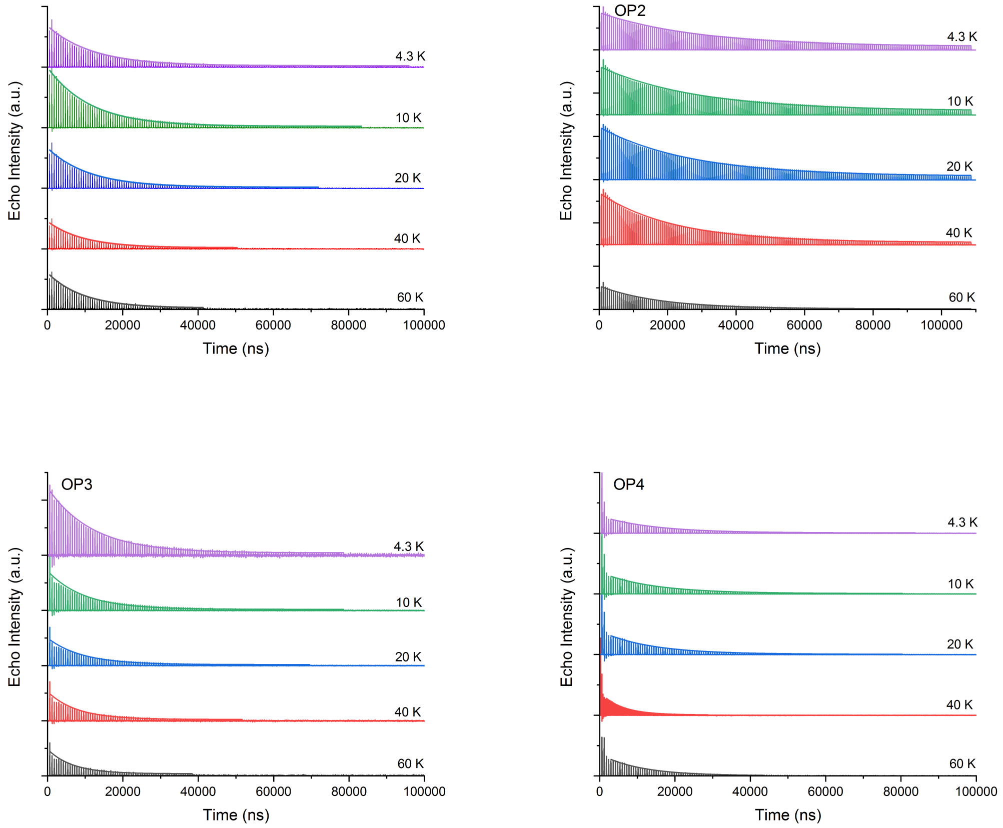

Figure S6. CPMG echo signal intensities as a function of the inter-pulse delay 2τ, for **1** (a) B_0 = 347.2 mT (**OP1**), B_0 = 352.6 mT (**OP2**), B_0 = 362.6 mT (**OP3**) and B_0 = 368.5 mT (**OP4**), at selected temperatures (4.3–60 K); solid line represents the mono-exponential fitting of the traces.

Table S6. Extracted T_{CPMG} time constants for **1** (10 mM THF) at X-band

T (K)	OP1 T_{CPMG} (μs)	OP2 T_{CPMG} (μs)			OP3 T_{CPMG} (μs)	OP4 T_{CPMG} (μs)	
	300 ns	300 ns	400 ns	500 ns	300 ns	300 ns	400 ns
4.3	11647	28684	19954	-	11789	15011	10951
10	11060	28107	19313	-	9542	14699	10921
20	10546	26317	18303	11438	9137	13969	10893
40	8950	21619	-	9770	7632	6193	11137
60	9455	17396	-	8781	8979	10573	-

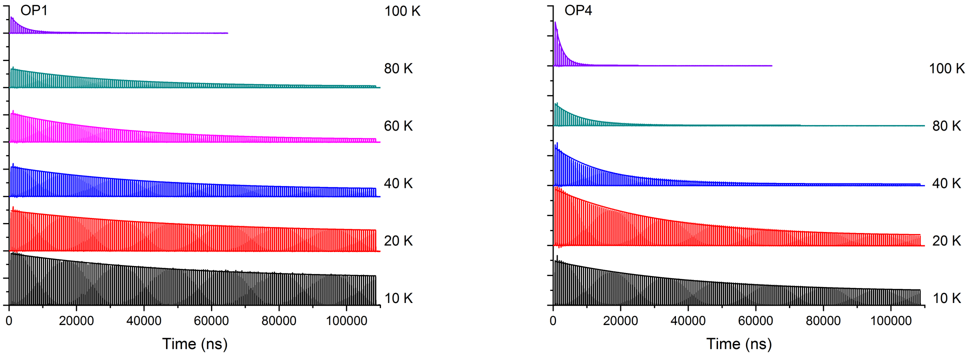

Figure S7. CPMG echo signal intensities as a function of the inter-pulse delay 2τ, for **1** (a) B_0 = 1208.1 mT (**OP1**) and B_0 = 1243.1 mT (**OP4**), at selected temperatures (10–100 K); solid line represents the mono-exponential fitting of the traces.

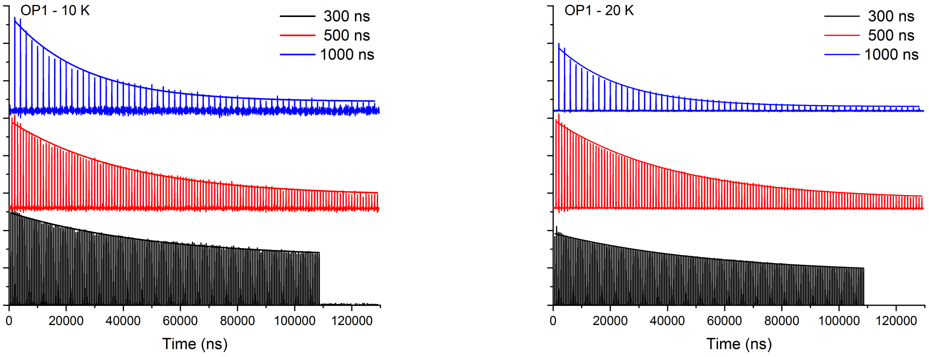

Figure S8. CPMG echo signal intensities as a function of the inter-pulse delay 2τ, for **1** B_0 = 1208.1 mT at (a) 10 K and (b) 20 K measured with τ values of 300 ns (black), 500 ns (red) and 1000 ns (blue); solid line represents the mono-exponential fitting of the traces.

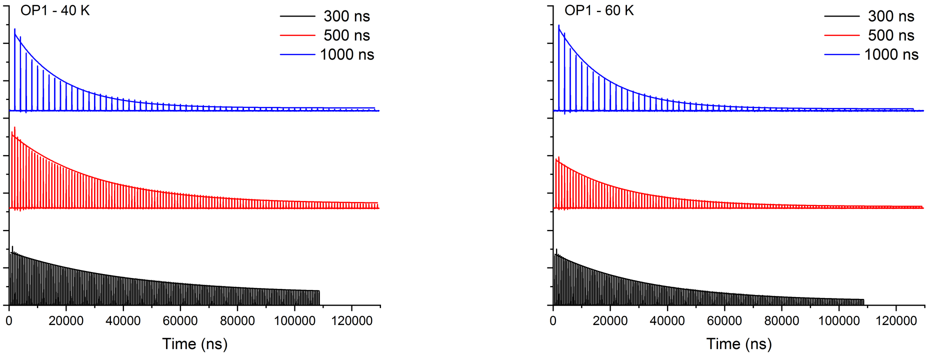

Figure S9. CPMG echo signal intensities as a function of the inter-pulse delay 2τ, for **1** B_0 = 1208.1 mT at (a) 40 K and (b) 60 K measured with τ values of 300 ns (black), 500 ns (red) and 1000 ns (blue); solid line represents the mono-exponential fitting of the traces.

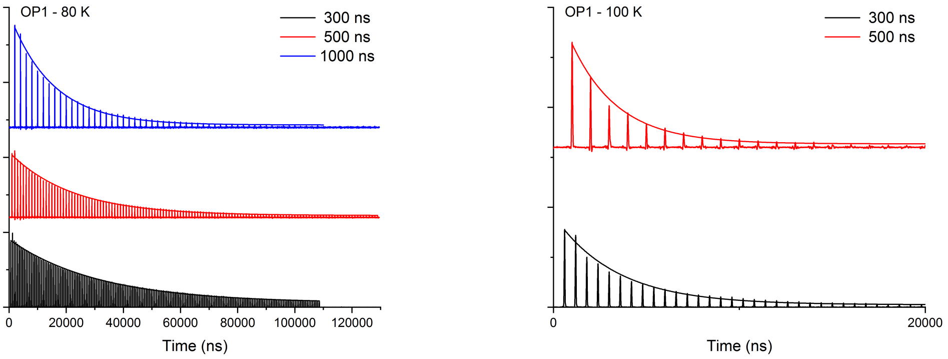

Figure S10. CPMG echo signal intensities as a function of the inter-pulse delay 2τ, for **1** B_0 = 1208.1 mT at (a) 80 K and (b) 100 K measured with τ values of 300 ns (black), 500 ns (red) and 1000 ns (blue); solid line represents the mono-exponential fitting of the traces.

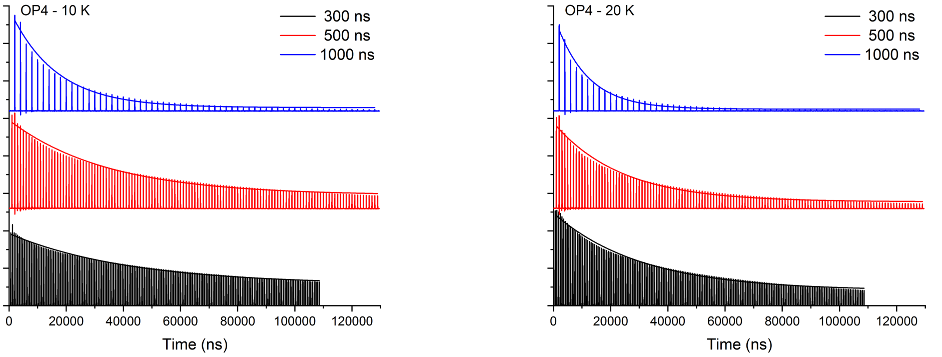

Figure S11. CPMG echo signal intensities as a function of the inter-pulse delay 2τ, for **1** B_0 = 1243.1 mT at (a) 10 K and (b) 20 K measured with τ values of 300 ns (black), 500 ns (red) and 1000 ns (blue); solid line represents the mono-exponential fitting of the traces.

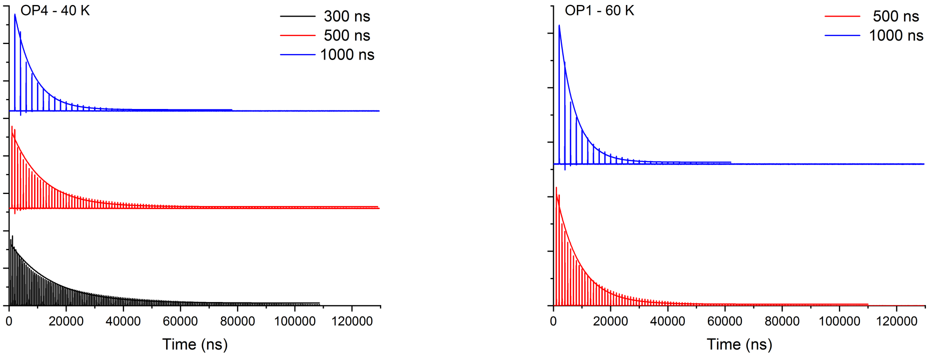

Figure S12. CPMG echo signal intensities as a function of the inter-pulse delay 2τ, for **1** B_0 = 1243.1 mT at (a) 40 K and (b) 60 K measured with τ values of 300 ns (black), 500 ns (red) and 1000 ns (blue); solid line represents the mono-exponential fitting of the traces.

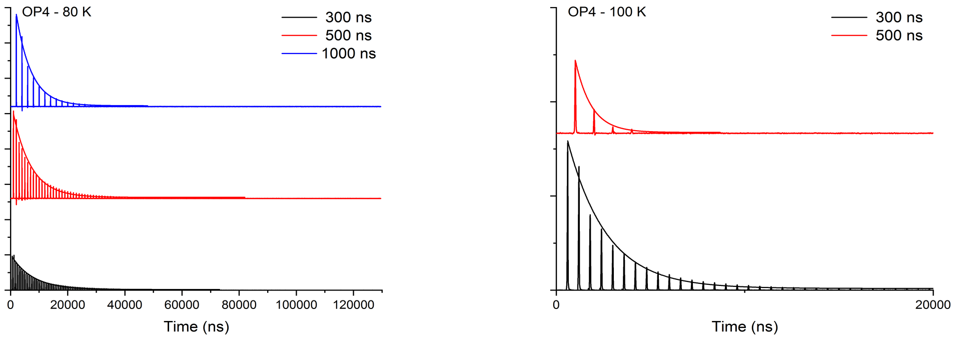

Figure S13. CPMG echo signal intensities as a function of the inter-pulse delay 2τ, for **1** B_0 = 1243.1 mT at (a) 80 K and (b) 100 K measured with τ values of 300 ns (black), 500 ns (red) and 1000 ns (blue); solid line represents the mono-exponential fitting of the traces.

Table S7. Extracted T_{CPMG} time constants for **1** (10 mM THF) at Q-band

T (K)	OP1 T_{CPMG} (μs)			OP4 T_{CPMG} (μs)		
	300 ns	500 ns	1000 ns	300 ns	500 ns	1000 ns
10	99658	50499	20544	84333	35827	10149
20	55224	46800	15875	32977	16988	5526
40	56151	27010	10720	10138	6186	5727
60	35342	21319	12930	-	5165	4388
80	32216	19480	12274	5628	4232	5635
100	2394	1425	-	1784	1027	-

6. Transient nutation experiments

The transient nutation experiments involve a microwave nutation pulse, t_{p}, applied with an angle $\theta = \mu_{\mathrm{B}} B_1 t_{\mathrm{p}}/\hbar$ that rotates the magnetization. Data are recorded with a microwave pulse sequence of the form $t_p - t_w - \pi/2 - \tau - \pi - \tau - echo$, with fixed τ = 200 ns and t_{w} = 6000 ns, chosen to be much longer than T_{m}. The Rabi frequency (Ω_{R}) was defined by zero-filling the Rabi oscillation curves followed by Fourier transformation.

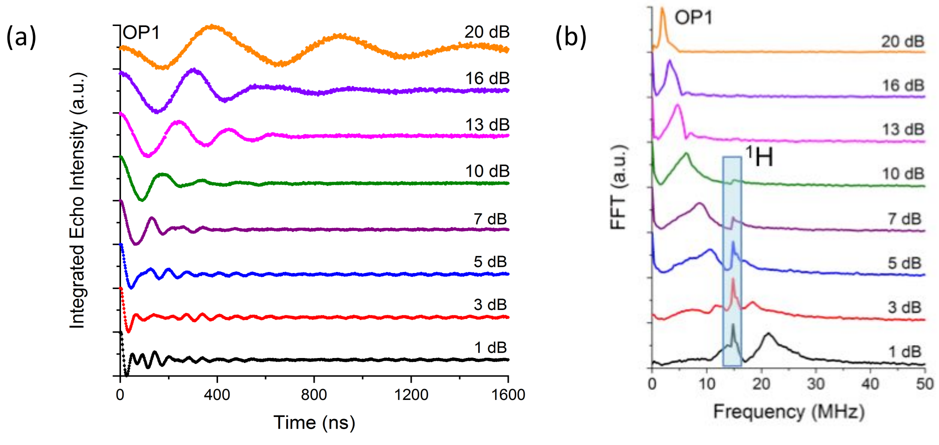

Figure S14. (a) Rabi oscillation for **1** (THF) at 20 K and B_0 = 347.2 mT (**OP1**), acquired with different microwave attenuations; and (b) the corresponding Fourier transforms.

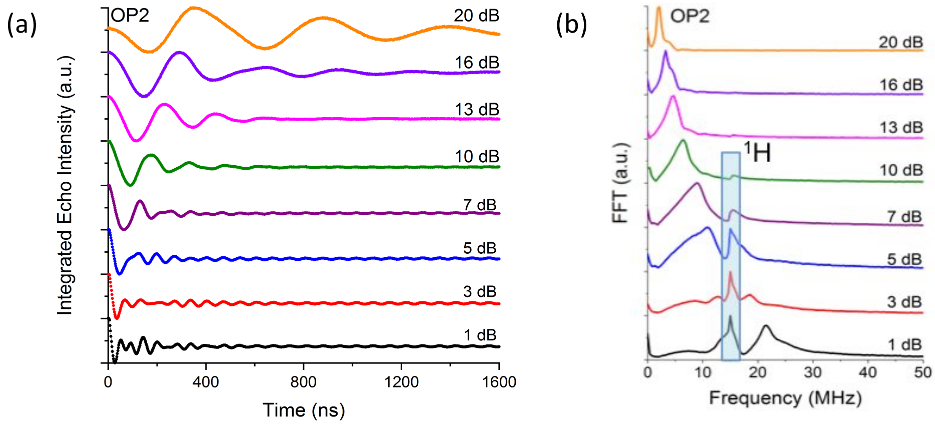

Figure S15. (a) Rabi oscillation for **1** (THF) at 20 K and B_0 = 352.6 mT (**OP2**), acquired with different microwave attenuations; and (b) the corresponding Fourier transforms.

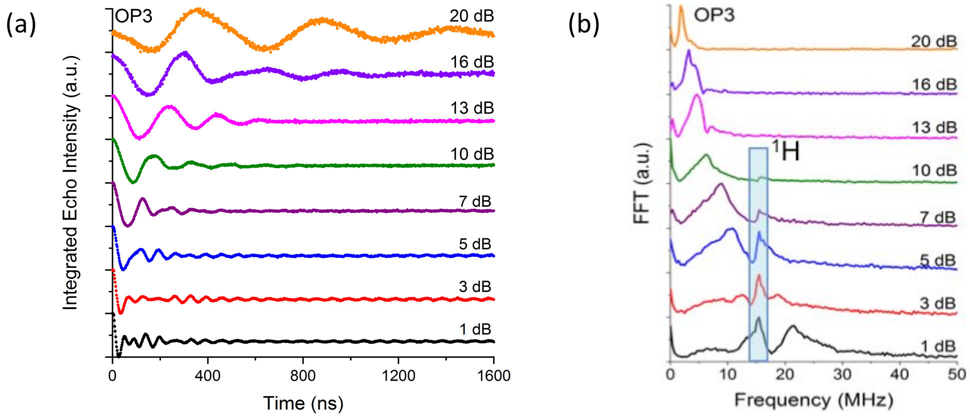

Figure S16. (a) Rabi oscillation for **1** (THF) at 20 K and B_0 = 362.6 mT (**OP3**), acquired with different microwave attenuations; and (b) the corresponding Fourier transforms.

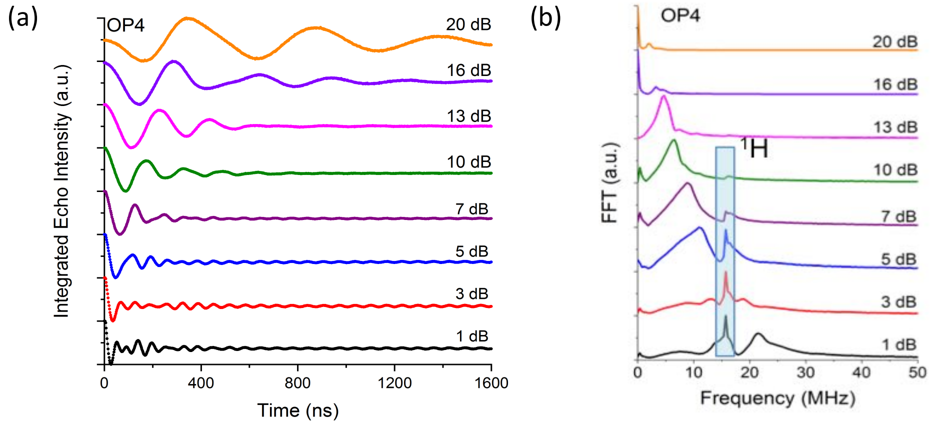

Figure S17. (a) Rabi oscillation for **1** (THF) at 20 K and B_0 = 368.5 mT (**OP4**), acquired with different microwave attenuations; and (b) the corresponding Fourier transforms.

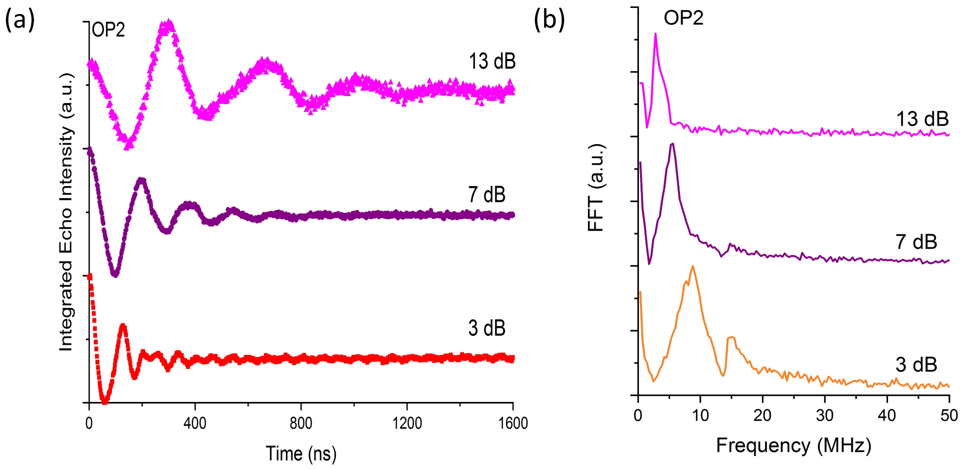

Figure S18. (a) Rabi oscillation for **1** (THF) at 80 K and B_0 = 352.6 mT (**OP2**), acquired with different microwave attenuations; and (b) the corresponding Fourier transforms.

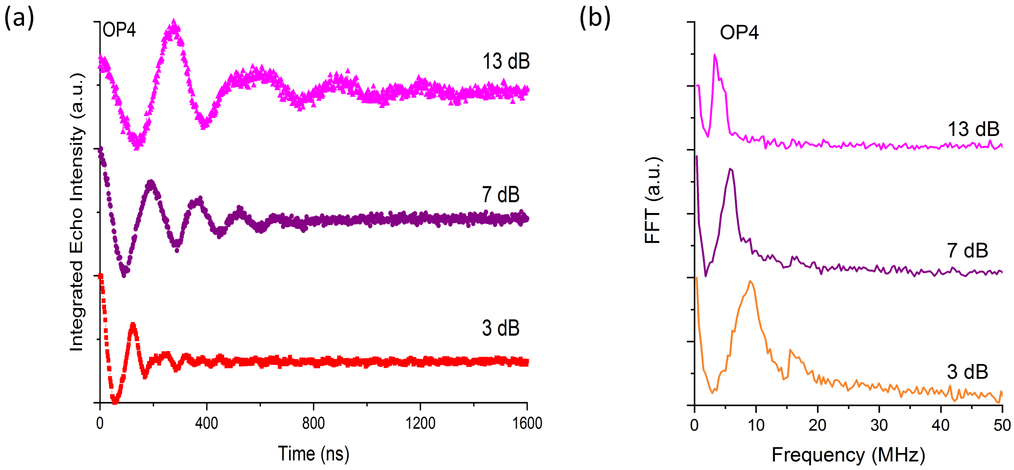

Figure S19. (a) Rabi oscillation for **1** (THF) at 80 K and B_0 = 368.5 mT (**OP4**), acquired with different microwave attenuations; and (b) the corresponding Fourier transforms.

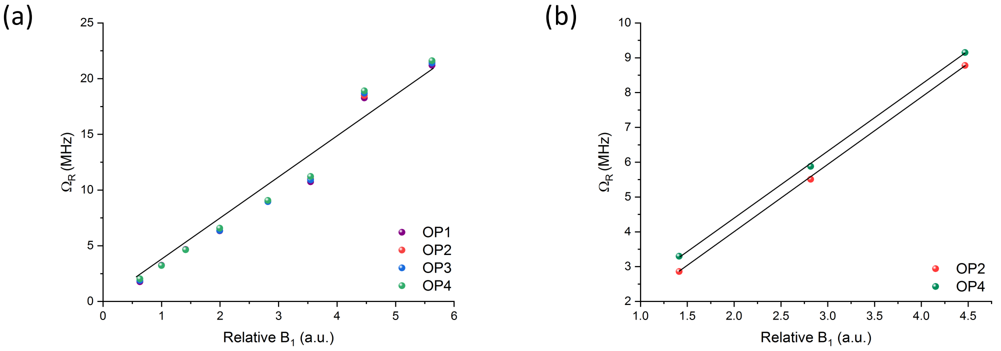

Figure S20. B_1 dependence of Rabi frequency for **1** (THF) (a) at 20 K and (b**)** at 80 K and different observable positions (**OP1-OP4**), the solid line emphasizes on the linear behavior.

7. ENDOR spectra

The ENDOR spectroscopy was carried out using the Mims ($\pi/2 - \tau - \pi/2 - \pi_{RF} - \pi/2 - \tau -$ *stimulated echo*) and Davies ($\pi - \pi_{RF} - \pi/2 - \tau - \pi - \tau -$ *inverted echo*), pulse sequences. Mims ENDOR data were recorded by a stimulated echo with non-selective π/2 and π pulses of 16 and 32 ns, and with various τ values (from 136 up to 600 ns) as a means of correcting the effect of potential blind spots. Davies ENDOR experiments use long τ times of 500 ns and selective microwave π/2 and π pulses of 64-128 ns and 128-256 ns.

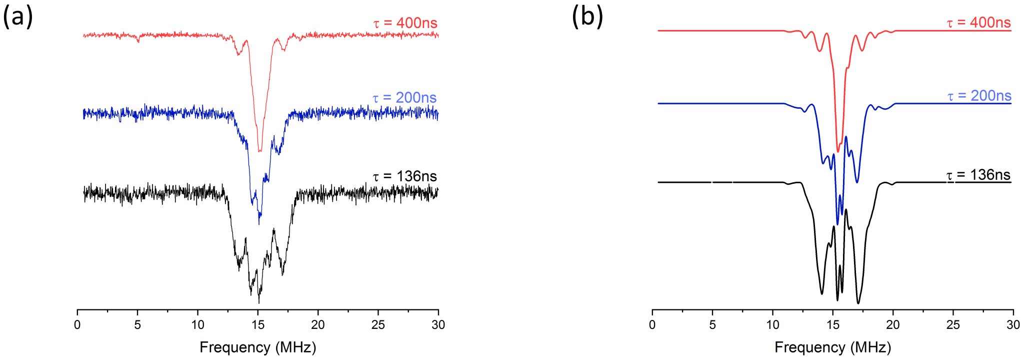

Figure S21. (a) ^{1}H Mims ENDOR spectra at B_0 = 362.6 mT (**OP3**; Fig.2) and 20 K with τ of 136 ns (black), 200 ns (blue) and 400 ns (red) (b) simulation of the spectra using the parameters described in the text.

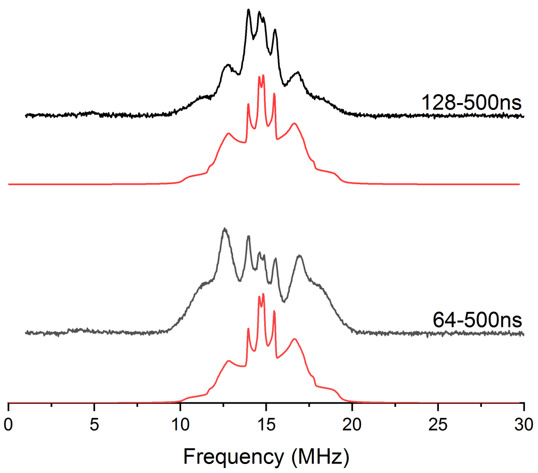

Figure S22. (a) ^{1}H Davies ENDOR spectra at B_0 = 352.6 mT (**OP2**; Fig. 2) and 40 K with microwave pulses of 64 – 500 ns and 128 – 500ns for π/2 – τ; the red line represents the corresponding simulation of the spectra using the parameters described in the text.

8. HYSCORE spectra

HYSCORE experiments operated with a four-pulse sequence, $\pi/2 - \tau - \pi/2 - t_1 - \pi - t_2 - \pi/2 - \tau -$ *echo*, with $\pi/2$ and π pulse lengths of 16 and 32 ns, respectively, and fixed τ time of 136, 200 and 400 ns. In both dimensions 256 points were collected, with initial t_1 and t_2 times of 100 ns incremented by 20 ns steps during the experiment. Fast Fourier transformation of the absolute values lead to nuclear cross-peaks on a 2D (ν_1,ν_2) spectra. In the frequency domain spectra the (+,+) quadrant, which is described as the weak coupling regime ($2|\nu_n|>|A|$), shows cross-peaks centred on the Larmor frequency of each nuclei and separated by the hyperfine coupling strength. Ridges on the anti-diagonal of the HYSCORE spectra can be described by isotropic hyperfine couplings, while deviation from it displays anisotropic contributions related to the magnitude and anisotropy of the hyperfine coupling constants.

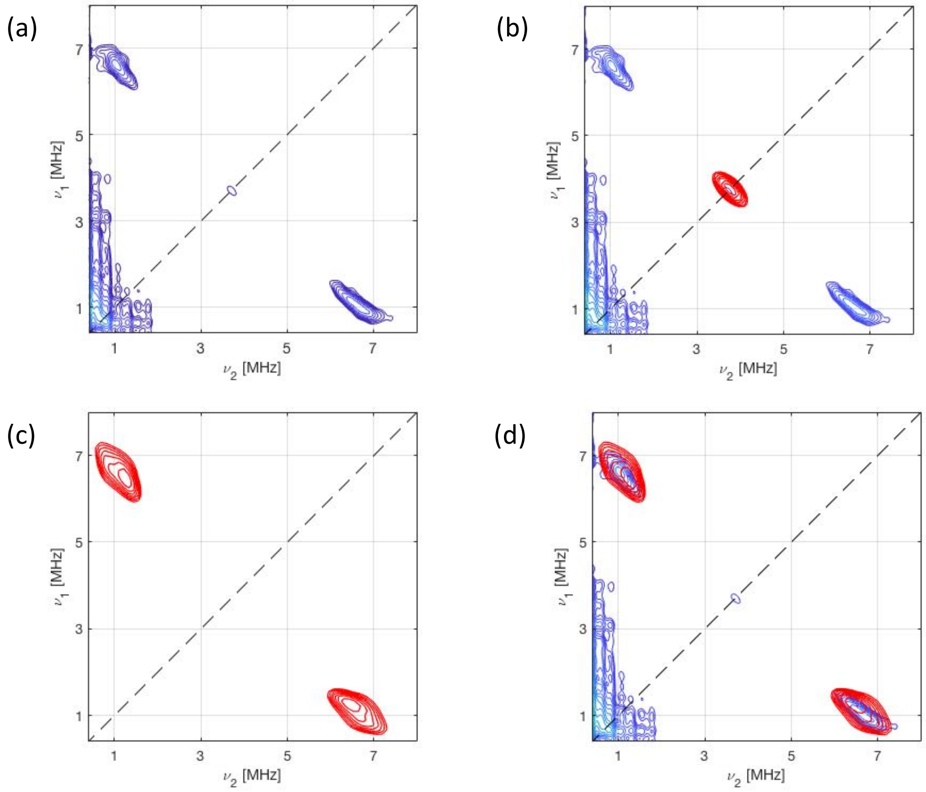

Figure S23. X-band ^{13}C HYSCORE spectra for **1** (a) experimental data at a static field of B_0 = 352.6 mT (at g_{xy}); (b) calculation in red based on the point dipole model only for C1 contribution; (c-d) same as for (b) but the simulation (red) also includes spin density contribution on C1, described by the following values; $A^{C1}_{z,xy}$ = 8.2, 4.8 MHz.

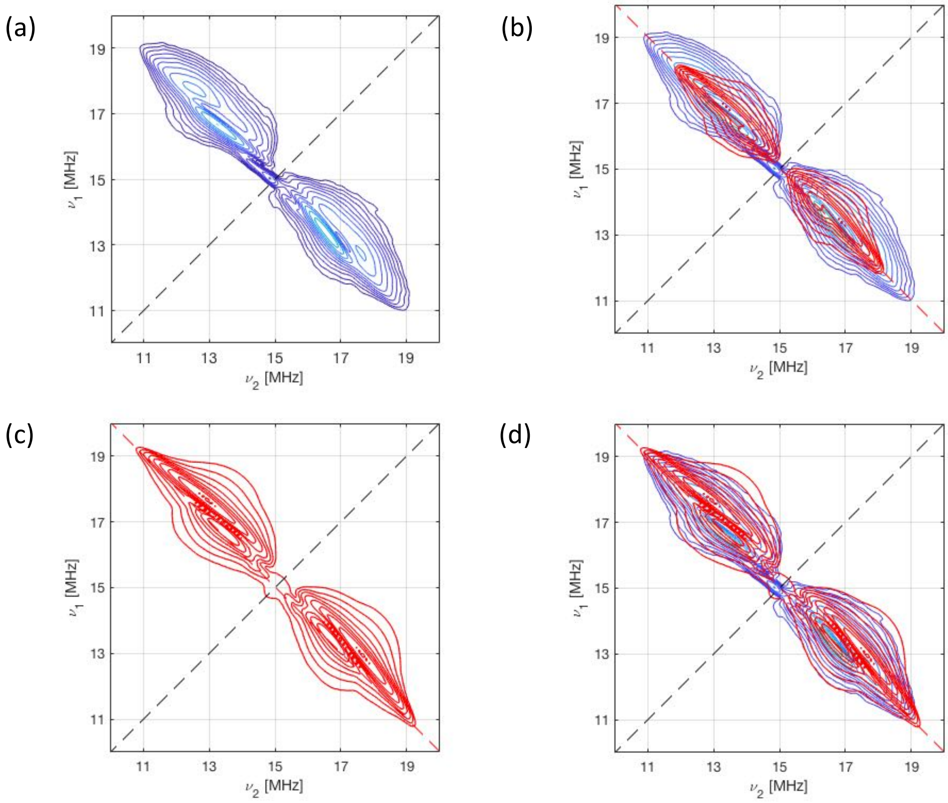

Figure S24. X-band ^{1}H HYSCORE spectra for **1** (a) experimental data at a static field of B_0 = 352.6 mT (at g_{xy}); (b) with calculation in red based only on the point dipole model including H46B, H52A and H3; (c-d) same as for (b) but the simulation (red) includes spin density contribution on H46B and H52A as a hyperfine interactions matrix described in the text.

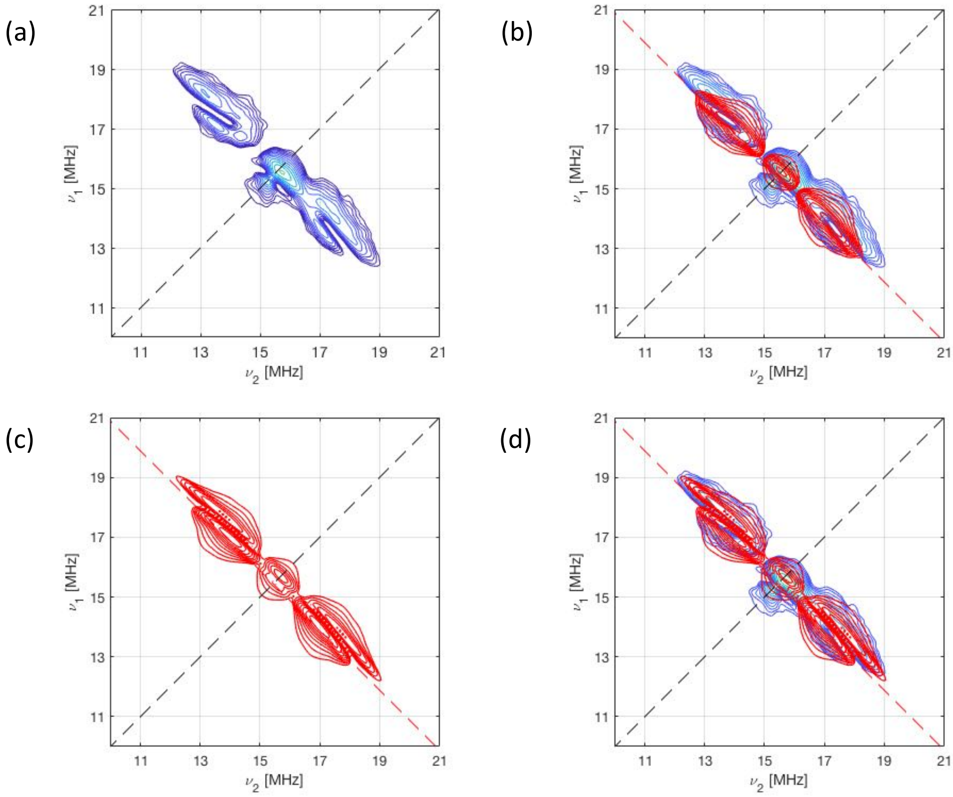

Figure S25. X-band ^{1}H HYSCORE spectra for **1** (a) experimental data at a static field of B_0 = 362.7 mT (at g_z); (b) calculations in red based only on the point dipole model including H46B, H52A and H3; (c-d) same as for (b) but the simulation (red) includes spin density contribution only on H46B as a hyperfine interactions matrix described in the text.

References

1. S. Stoll and A. Schweiger. Easyspin, a comprehensive software package for spectral simulation and analysis in EPR. *J. Magn. Reson.*, **2006**, 178, 42-55.

2. A. Schweiger and J. Jeschke. Principles of Pulse Electron Paramagnetic Resonance. *Oxford University Press*, Oxford, **2001**.

3. H. Y. Carr and E. M. Purcell, Effects of diffusion on free precession in nuclear magnetic resonance experiments. *Phys. Rev.*, **1954**, *94*, 630-638.

Chapter VIII. Manuscript draft 4:

Covalency in LnCp$^{tt}_3$ (Ln = Ce, Nd, Sm) evaluated via HYSCORE spectroscopy

Lydia E. Nodaraki,[†,‡,§] Jingjing Liu,[†,§] Ana-Maria Ariciu,[†,‡] Fabrizio Ortu,[†] Letitia Birnoschi,[†] Nicholas Chilton,[†] David P. Mills,[†,*] Eric J. L. McInnes,[†, ‡,*] Floriana Tuna,[†,‡,]*

[†] Department of Chemistry, University of Manchester, Oxford Road, Manchester, M13 9PL, UK

[‡]Photon Science Institute, University of Manchester, Oxford Road, Manchester, M13 9PL, UK

[§] These authors contributed equally.

Supporting Information Placeholder

ABSTRACT: Presence of covalency in predominantly electrostatic lanthanide (Ln) chemical bonds has been a source of intense research and controversy, while experimental methods to measure such weak covalency are essentially underdeveloped. Here we examine Ln bonding in a family of early Ln^{3+} complexes [Ln(Cp^{tt})$_3$] (**1-Ln**, Ln = La, Ce, Nd, Sm; Cp^{tt} = C$_5$H$_3{}^t$Bu$_2$-1,3) by advanced pulsed electron paramagnetic resonance (EPR) methods, and provide the first characterization of **1-La** and **1-Nd** by single crystal XRD, multinuclear NMR, IR and UV/Vis/NIR spectroscopy. We measure T_1 and T_m relaxation times of 12 and 0.2 μs (**1-Nd**), 89 and 1 μs (**1-Ce**) and 150 and 1.7 μs (**1-Sm**) respectively. Application of hyperfine sublevel correlation (HYSCORE) spectroscopy allowed determining the electron spin densities at magnetically active nuclei on the ligands, via hyperfine couplings. Analysis of such ^{13}C and ^{1}H HYSCORE data indicated that the extent of covalency is negligible in these compounds, confirming the large electrostatic nature of the 4f element.

INTRODUCTION

Lanthanides (Lns) have numerous applications due to their unique physicochemical properties.[1] However, their chemical similitude to late actinides makes their separation from actinides rather difficult causing serious problems to the nuclear waste recycling.[2] Central to these problems is understanding the differences in chemical bonding and covalency (i.e. the extent of mixing between ligand and metal orbitals), which directly impact the electronic properties and chemical behavior of the compounds. Ln organometallic chemistry has been dominated by cyclopentadienyl (Cp) ligands and their derivatives (Cp^R).[3] Due to the poor shielding of 4f orbitals, they become "core-like" and as a result the bonding in Ln is predominantly ionic. However, the employment of relatively soft ligands like Cp can introduce interesting bonding regimes. However, the amount of covalency, the extent of electron sharing between Ln and coordinated ligands, is often vanishingly small.[4] To date, investigations into Ln covalency lag behind the d-block metals, which have often been investigated by X-ray absorption near-edge spectroscopy (XANES).[5] Nuclear magnetic resonance (NMR) spectroscopy has been shown to be effective for the measurement of covalency in diamagnetic f-block systems,[6] but most Ln ions are paramagnetic. For paramagnetic systems electron paramagnetic resonance (EPR) spectroscopy can be employed to measure f-block covalency *via* the "superhyperfine' interaction of primarily metal-based unpaired electrons with ligand nuclei that have a non-zero nuclear spin.[7] In 2011 Denning and co-workers reported significant covalency in [Yb(Cp)$_3$] from pulse EPR measurements enabling to quantify the accumulation of spin density at the ^{13}C atoms of the Cp rings.[8] Most recently, pulsed EPR studies of two actinide (An) complexes, [An(Cp^{tt})$_3$] (An = Th, U; Cp^{tt} = C$_5$H$_3{}^t$Bu$_2$-1,3), have revealed that the U^{3+} complex has a greater total spin density on the ligands than Th^{3+},[7] while the covalency of the Th complex is comparable with that of [Yb(Cp)$_3$].[8]

To continue this work and allow a comparison of early Ln *vs.* An covalency in the same ligand environment by pulsed EPR methods, we synthesized a series of Ln^{3+} analogues [Ln(Cp^{tt})$_3$] (**1-Ln**, Ln = La, Ce, Nd, Sm) by reacting the parent LnCl$_3$ with three equivalents of KCp^{tt}. Complexes **1-Ce**[9] and **1-Sm**[10] have been prepared previously by alternative synthetic routes, whilst **1-La** and **1-Nd** were structurally characterized for the first time. We report the CW and pulsed EPR data for **1-Ce**, **1-Nd** and **1-Sm**, along with the NMR data of diamagnetic **1-La**. The spin density at paramagnetic Ln^{3+} centers was measured and compared with the data previously obtained for analogous An complexes for a quantitative assessment of 4f *vs.* 5f covalency by pulsed EPR methods.

RESULTS AND DISCUSSION

Synthesis and spectroscopic characterization. Complexes **1-Ln** (Ln = La, Ce, Nd, Sm) were prepared from the parent LnCl$_3$ and three equivalents of KCp^{tt} (Scheme 1) by modification of the reported syntheses of **1-Sm** using SmI$_3$ and KCp^{tt},[10] and **1-Ce** from Ce(OTf)$_3$ and LiCp^{tt}.[9] The crystalline yields for **1-La**, **1-Ce**, **1-Nd** and **1-Sm** were 41%, 54%, 34% and 52%, respectively.

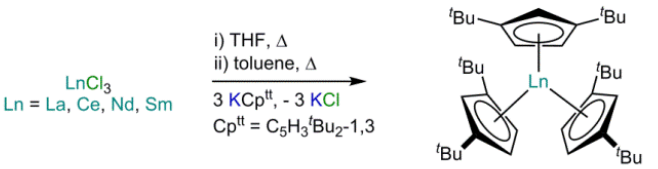

Scheme 1. Synthesis of the Ln complexes **1-Ln** (Ln = La, Ce, Nd, Sm).

^{1}H NMR spectra support the formulation of the compounds. The spectra were measured from 0 to +10 ppm for the diamagnetic **1-La** and from –200 to +200 ppm for paramagnetic **1-Ce**, **1-Nd** and **1-Sm** (see Supporting Information Figures S4, S6-S10). Three signals were observed in all spectra in a ratio of 54:6:3; these correspond to the magnetically equivalent ^{t}Bu groups and the two unique environments of the Cp^{tt} ring protons, respectively. The paramagnetism of **1-Ce**, **1-Nd** and **1-Sm** precluded assignment of their ^{13}C{^{1}H} NMR spectra, however, for diamagnetic **1-La** this could be interpreted, with the two ^{t}Bu group resonances at 32.77 and 33.75 ppm and the three Cp^{tt} ring carbon environments located at 110.57 (*C*H-Cp), 110.69 (*C*H-Cp) and 143.45 (*C*-Cp) ppm (see Supporting Information Figure S5).

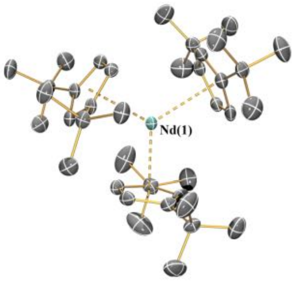

Figure 1. Crystal structrure of **1-Nd**. Displacement ellipsoids are at the 30% propability level. Hydrogens are omitted for clarity.

Crystallography. The solid-state structures of compounds **1-Ln** were determined by single crystal XRD. The structural data of **1-La** and **1-Nd** are reported here, while those of **1-Ce**[9] and **1-Sm**[10] have been reported previously (see Supporting Information). The crystal structure of **1-Nd** is depicted in Figure 1. As expected the structures of **1-Ln** are trigonal planar with respect to the η^5-Cp^{tt} centroids, with the three C2 atoms in the plane defined by the Ln^{3+} ion and the three Cp^{tt} centroids. The three Cp^{tt} ligands adopt the same orientation to form a “picket-fence” motif with three ^{t}Bu groups above and three below the trigonal plane. The structures of **1-Ln** are also consistent with those found for [M(Cp^{tt})$_3$] (M = Th,[7] U,[7] Yb[11]). The mean Ln···Cp$_{centroid}$ distances decrease regularly across the lanthanide series [mean La···Cp$_{centroid}$ = 2.635(2) Å; Ce···Cp$_{centroid}$ = 2.587(8) Å; Nd···Cp$_{centroid}$ = 2.56(3) Å; Sm···Cp$_{centroid}$ = 2.531(3) Å;[10] Yb···Cp$_{centroid}$ = 2.47(1) Å[11]]. Additionally, the mean M···Cp$_{centroid}$ distances in **1-Nd** are shorter than those seen in [U(Cp^{tt})$_3$] [2.570(4) Å],[7] which has an analogous electronic configuration (Nd^{3+}: [Xe]4f^3; U^{3+}: [Rn]5f^3). Conversely, in **1-Ce**, the mean M···Cp$_{centroid}$ distances are longer than those seen in [Th(Cp^{tt})$_3$] [2.566(3) Å],[7] which has an different valence electronic configuration (Ce^{3+}: [Xe]4f^1; Th^{3+}: [Rn]6d^1) due to the stabilization of the Th 6d$_{z2}$ orbital in trigonal ligand environments.[12]

Solution phase optical properties. The electronic spectra of complexes **1-Ln** (Figures 2, S16-S20) further confirm the trivalent oxidation state of the Ln ion in all these complexes. These were obtained at room temperature from 0.5 mM toluene solutions of each complex. **1-La** is essentially colorless, as expected for a closed shell La^{3+} ion, with charge-transfer (CT) bands restricted to the UV region. Dilute toluene solutions of **1-Ce** and **1-Nd** are pale purple and pale green, respectively, whilst **1-Sm** is pale orange in toluene. Due to their Laporte-forbidden nature, even spin-allowed f-f transitions are relatively weak (ε < 200 M^{-1} cm^{-1}),[1] so CT bands tailing in from the UV region dominate the spectrum. The f-f transitions in **1-Nd** were clearly observed, with the most intense absorption at $\tilde{\upsilon}_{max}$ = 16,750 cm^{-1} (ε = 390 mol^{-1} dm^3 cm^{-1}) likely arising from the $^4I_{9/2} \rightarrow {}^4G_{5/2}$ transition.[13] In contrast, **1-Ce** shows a strong broad absorption at $\tilde{\upsilon}_{max}$ = 17,400 cm^{-1} (ε = 230 mol^{-1} dm^3 cm^{-1}) due to [Xe]4f^1 → [Xe]4f^{0}5d^1 transitions, which are formally allowed by electric dipole selection rules.[14] The spectrum of **1-Sm** shows a weak set of f-f transitions in the near-IR region around 7,000 cm^{-1} (ε < 50 mol^{-1} dm^3 cm^{-1}), likely arising from the $^6H_{5/2} \rightarrow {}^6F_J$ transitions.[13]

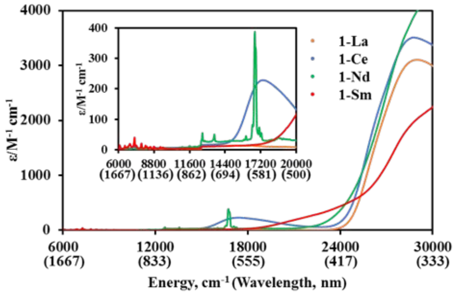

Figure 2. UV-vis-NIR spectrum of **1-La**, **1-Ce**, **1-Nd**, **1-Sm**, in the region 6000–30000 cm^{-1} (inset 6000–20000 cm^{-1}) recorded as 0.5 mM solutions in toluene at room temperature.

EPR Spectroscopy. Continuous wave (CW) EPR spectra of **1-Nd, 1-Ce** and **1-Sm** are observed at temperatures below ~30 K (Figures 3 and S21-S23). Complex **1-Nd** displays rhombic EPR spectra at all temperatures. One such spectrum is presented in Figure 3a. The ground Kramers doublet of the J = 9/2 ground term of Nd^{3+} ($^4I_{9/2}$) can be approximated as an effective spin-1/2 system, and the EPR spectra modeled with the spin Hamiltonian eqn. (1).

$$\hat{\mathcal{H}} = g \cdot \mu_B \cdot B \cdot \hat{S} + \hat{I} \cdot A \cdot \hat{S} \qquad (1)$$

Best simulation of the spectra was achieved with g_z = 3.332, g_y = 1.22 and g_x = 0.56, and hyperfine coupling constants of A_z = 1280 MHz, A_y = 700 MHz and A_x = 200 MHz, measuring the interaction of the unpaired electron with the I = 7/2 nuclear spin of Nd^{III} ion (the natural composition of neodymium encompasses the ^{143}Nd - 12.2% and ^{145}Nd - 8.3% isotopes). Similarly, spectra of **1-Ce** and **1-Sm** can be simulated with the same spin Hamiltonian eqn. (1), with $g_z = 3.15$, $g_y = 1.88$ and $g_x = 0.636$ for **1-Ce** (Figure 3b)**,** and $g_x = g_y = 0.905$ for **1-Sm** (Figure S23; the g_z component of **1-Sm** is not observed).

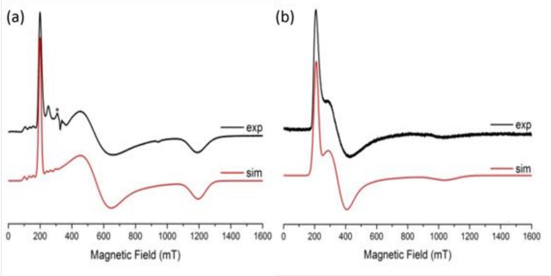

Figure 3. X-band CW EPR spectra of (a) **1-Nd** and (b) **1-Ce**, measured from frozen toluene:hexane (9:1) solutions at the indicated temperatures.

Pulse EPR spectroscopy. The echo-detected field-swept spectra (EDFS) of **1-Nd, 1-Ce** and **1-Sm** (in toluene-hexane) are observed up to 10 K. These were recorded by integration of the Hahn echo generated with the standard pulse sequence $\pi/2 - \tau - \pi - echo$, where $\pi/2$ and π are microwave pulses and τ is the inter-pulse delay.[15] The EDFS spectrum at 5 K for **1-Nd** is presented in Figure 4a. This agrees with the CW spectrum of the compound in the *x/y* region, but the g_z component is not observed. A possible explanation for the absent transition in the experimental EDFS spectra is that the phase memory time of the *z*-orientated molecules, aligned parallel to the magnetic field, is significantly shorter than for the *x*- and *y*- orientations. The obtained EDFS spectra are well reproduced with the set of parameters deducted from the simulation of CW data, respectively $g_y = 1.28$, $g_x = 0.57$, $A_y = 700$ MHz and $A_x = 200$ MHz (Figure 4a). In addition, small hyperfine components due to the interaction with magnetically active nuclear isotopes of Nd are observed in both the EDFS and CW spectra of **1-Nd** (Figure 3a and 4a). Complex **1-Ce** exhibits a similar behaviour to **1-Nd**, with the g_z component being undetectable in the EDFS spectra due to a faster spin-spin relaxation for this orientation (Figure 4b). The spectra are well reproduced with the parameters deducted from the simulation of CW data. Complex **1-Sm** displays a strongly axial spectrum with $g_{xy} = 0.905$ and $g_z = 0.55$ (Figure S29).

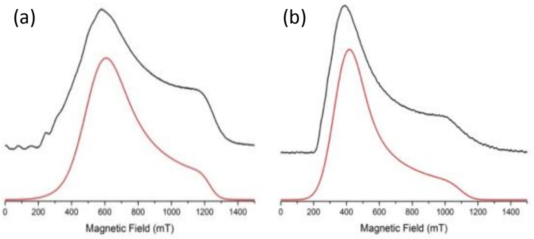

Figure 4. X-band (9.7 GHz) EDFS spectra of (a) **1-Nd** and (b) **1-Ce**, measured at 5 K from toluene: hexane (9:1) solution.

Measurements of the spin-lattice (T_1) and phase-memory (T_m) relaxation times were performed on 10 mM frozen solution samples of **1-Nd**, **1-Ce** and **1-Sm** at low temperatures (5 K). T_1 data were recorded with an inversion recovery pulse sequence followed by the fitting of the obtained echo trace with a bi-exponential function (see Supporting Information eqn. 3), where the fastest process is assigned to the spectral diffusion and the slow process is attributed to the spin-lattice relaxation.[16] T_1 for **1-Nd** displays strong field dependence and reaches a maximum value of 12 μs (g_x). Much longer relaxation times of 89 μs (g_x) and 150 μs (g_y) were obtained for **1-Ce** and **1-Sm**, respectively. In addition, the spin-lattice relaxation times for the **1-Ce** and **1-Sm** complexes exhibit a less field dependent trend. T_m was determined by the fitting the Hahn echo decays recorded with a Hahn echo sequence upon variation of the inter-pulse delay τ to a stretched mono-exponential function (see Supportiing Information eqn. 1).[17] The obtained T_m relaxation time follows an analogue trend as T_1 for all complexes, reaching 0.7, 1.0 and 1.7 μs for **1-Nd, 1-Ce** and **1-Sm**, respectively. Furthermore, all three complexes exhibit slower relaxation of the *xy*-magnetisation at higher magnetic fields corresponding to the *x*-orientation of the molecular frame. These relaxation times are long enough to allow further investigation of the complexes by multi-pulse microwave sequences.

In order to do a more detailed characterization of the system, as well as quantifying the narrower interactions between the unpaired electrons and their surrounding ^{1}H and ^{13}C nuclei, a two-dimensional hyperfine sub-level correlation (HYSCORE) technique was performed. HYSCORE is a 2D technique which uses a four-pulse spin echo envelope modulation sequence; $\pi/2 - \tau - \pi/2 - t_1 - \pi - t_2 - \pi/2 - echo$, with t_1 and t_2 independently varied.[18] In the HYSCORE experiment the first two $\pi/2$ pulses generate a nuclear coherence, which is then transferred by the mixing π pulse from one electron spin manifold to another. Fourier transformation leading to a frequency domain spectrum, in which for weakly-coupled nuclei ($2|\nu_n|>|A|$) cross-peaks will appear about at the Larmor frequencies (ν_n). The ridges of the spectra are due to the anisotropic hyperfine couplings; moreover, their length and the shift from the anti-diagonal about the nuclear Larmor frequency, ν_n, depend on the anisotropy and the magnitude of the hyperfine couplings.[19]

Focusing on the ^{13}C region of the HYSCORE spectra (Figure 5a) measured at $B_0 = 353.0$ mT, cross-peak ridges were observed in the (+,+) quadrant (i.e. the weakly coupling region); these are centered at the ^{13}C Larmor frequency with the ridges being spread at $\nu_n \pm 1.4$ MHz. For modeling the HYSCORE data, a previously reported theoretical approach[7] was used. This model is based on the assumption that the hyperfine matrix (A) at each carbon nucleus (n) includes a contribution from the point dipole (through space) interactions (A^{dip}) and from the C $2p_\pi$-spin density (A^{Cn}). The point dipole contribution (A^{dip}) for each atom was calculated by the following equation, using the crystal structure:

$$\mathrm{A^{dip}} = \frac{\mu_0}{4\pi h}\beta_e\beta_n\sum_k \rho_k \frac{3(g.\mathrm{n_k})(\tilde{\mathrm{n}}_k.g_n1) - g.g_n1}{\mathrm{r}_k^3}$$

where g and g_n1 are the electron and nuclear g (3×3) matrices (g_n is a scalar; 1 is the unit matrix), ρ_k is the electron spin population at atom k ($0 \leq \rho_k \leq 1$ and dimensionless), r_k is the n…k distance (in m), n_k and $\tilde{n}_k$ are the n…k unit vector expressed in the molecular frame (a column vector) and its transpose (i.e. a row vector), β_e and β_n are the electron and nuclear magnetons, h is the Plank's constant, and μ_0 is the vacuum permittivity.

Figure 5 shows the calculated spectra (red ridges) matching the experimental one (blue ridges) using only the calculated values of the point dipolar interactions of each unique carbon atom of a Cp^{tt} ring (A^{dip}; Supporting Information Table S8-S9). Hence, no additional contribution from the spin density on the Cp^{tt} ligand was needed in order to model the experimental data. Similarly, ^{1}H HYSCORE data could be successfully reproduced by a dipole-only model, which is also supported by the higher magnetic moment of ^{1}H than ^{13}C, leading to ^{1}H HYSCORE dominated by dipolar interactions. A^{dip} was calculated for all hydrogen atoms in the molecule by using the crystallographic data. Excellent simulation (Figure 5b) was achieved with a model that included the different H atoms on the Cp^{tt} rings (H^2, H^4, H^5) (Figure 6). Thus, HYSCORE data for both carbon and hydrogen regions can be nicely reproduced with only a dipolar interaction model without any additional contribution from spin density on the Cp^{tt} ligands.

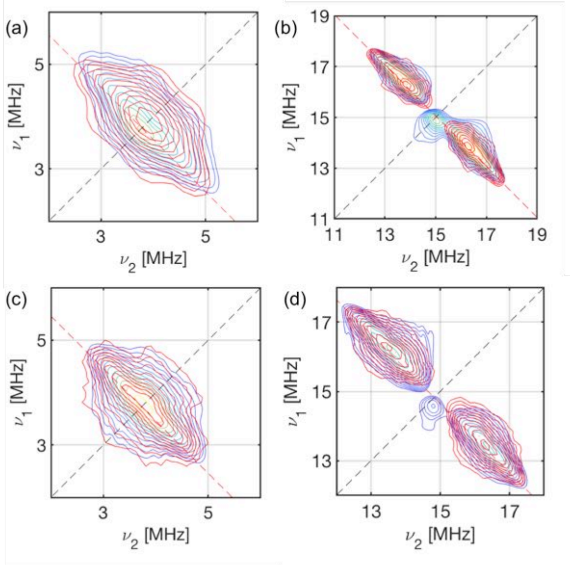

Figure 5. X-Band HYSCORE spectra at a static field of (a), (b) B$_0$ = 353.0 mT and (c), (d) B$_0$ = 348.2 mT at 5 K. (a) ^{13}C region with the Larmor frequency of ν_n = 3.78 MHz and the calculated spectrum (red ridges) based on the C – Nd dipole model including C1-C5; (b) ^{1}H region (Larmor frequency ν_n = 15.03 MHz) with the simulation based only on dipolar interactions of Nd^{III} ion with the H2, H4 and H5 protons (Table S8); (c) ^{13}C region with the Larmor frequency of ν_n = 3.73 MHz and the calculated spectrum (red ridges) based on the C – Ce dipole model including C1-C5; (d) ^{1}H region (Larmor frequency ν_n = 14.82 MHz) with the simulation based on dipolar interactions of Ce^{III} ion with the three protons on the Cp^{tt} ring (Table S9).

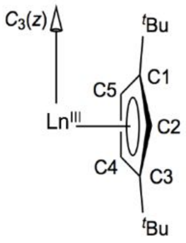

Figure 6. Schematic representation of C$_3$ axis and numbering of the C atoms on the Cp^{tt} ligands used for the simulation of HYCORE data.

A similar procedure was followed to model the HYSCORE data of the **1-Ce** analogue; no significant differences were observed compared to **1-Nd**. Calculated spectra based on the assumption of Ce…H (H^2, H^4, H^5 of the Cp^{tt} rings) dipolar interactions only give well defined ^{1}H ridges that are in good agreement with the experimental features (Figure 5b). In a similar way, the ^{13}C region could be nicely simulated by including all five carbons of the Cp^{tt} ligands in a dipole-only model. This calculation gives us a match between the experimental and the simulated ridges, supporting the results of the ^{1}H HYSCORE, which is more accurate due to the larger magnetic moment of the ^{1}H (compared to ^{13}C). Unfortunately for complex **1-Sm** we detected a very week signal on both ^{1}H and ^{13}C regions presumably due to the lower magnetic moment of the Sm ion, which limits the strength of the interaction with the ^{1}H and ^{13}C nuclei on the ligands.

EXPERIMENTAL SECTION

Material and Methods. All manipulations were carried out using standard Schlenk line and glove box techniques under dry argon. Solvents were passed through columns containing alumina or were dried by refluxing over K, and were stored over K mirrors or 4 Å molecular sieves (THF) and degassed before use. NMR solvents (C_6D_6) were dried by refluxing over K, degassed by three freeze-pump-thaw cycles, and vacuum-transferred before use. Anhydrous LnCl$_3$ were purchased from Alfa Aesar and were used as received. KCp^{tt} was prepared according to literature methods,[20] whilst **1-Ln** were made by modification of literature procedures.[9,10] ^{1}H (400 and 500 MHz) and ^{13}C{^{1}H} (100 and 125 MHz) NMR spectra were obtained on Avance III 400 or 500 MHz spectrometers at 298 K. UV-vis-NIR spectroscopy was performed on samples in Youngs tap-appended 10 mm path length quartz cuvettes on an Agilent Technologies Cary Series UV-vis-NIR spectrophotometer at 175-3300 nm. ATR-Fourier transform infrared (ATR-FTIR) spectra were recorded as microcrystalline powders using a Bruker Tensor 27 spectrometer. Elemental analyses were performed by Mrs Anne Davies and Mr Martin Jennings at The University of Manchester School of Chemistry Microanalysis Service, Manchester, UK. General synthetic procedures for **1-Ln** are given below; full details can be found in the Supporting Information. Continuous wave EPR measurements were carried out on a Bruker EMX300 spectrometer; pulsed EPR X-band studies were made on a Bruker ElexSys E580 spectrometer. The primary Hahn-echo sequence ($\pi/2$ - τ - π - τ - *echo*) was used for the two-pulse electron spin echo measurements, with initial π/2 and π pulse of 16 and 32 ns, respectively. For the relaxation time measurements, T_m studies were made by incrementing the τ time in the Hahn-echo sequence (longer pulses were used to suppress the ^{1}H modularion), T_1 was measured by the inversion recovery sequence (π-t - $\pi/2$ - τ - π - τ - *echo*), with π/2 and π pulse of 16 and 32 ns, respectively, and fixed τ = 300 ns. HYSCORE measurements were performed using the four-pulse sequence ($\pi/2$ - τ - $\pi/2$ - t_1 - π - t_2 - $\pi/2$ - *echo*), π/2 and π pulse of 16 and 32 ns, respectively, initial times t1,2 = 0.1 μs and τ values of 136 and 200 ns.

General Synthesis of 1-Ln. THF (30 mL) was added to a pre-cooled (−78 °C) ampoule containing LnCl$_3$ (2 mmol) and KCp^{tt} (6 mmol). The reaction mixture was allowed to reflux for 16 hours. The solvent was removed *in vacuo* and toluene (30 mL) was added. The reaction mixture was allowed to reflux for 40 hours. The resultant suspension was allowed to settle for 3 hours and filtered. The solution was concentrated to 2 mL and stored at 8 °C to afford crystals of **1-Ln**.

1-La: colorless crystals (0.550 g, 41 %). Anal calcd (%) for C$_{39}$H$_{63}$La: C, 69.81; H, 9.47. Found (%): C, 67.03; H, 9.50. ^{1}H NMR (C$_6$D$_6$, 400 MHz, 298 K): δ = 1.35 (s, 54H, C(C*H*$_3$)$_3$), 6.21 (s, 3H, Cp-*H*), 6.28 (s, 6H, Cp-*H*) ppm. ^{13}C{^{1}H} NMR (C$_6$D$_6$, 100 MHz, 298 K): δ = 32.77 (C(*C*H$_3$)$_3$), 33.75 (*C*(CH$_3$)$_3$), 110.57 (*C*H-Cp ring), 110.69 (*C*H-Cp ring), 143.45 (*C*-Cp ring) ppm. FTIR (ATR, microcrystalline): $\tilde{\nu}$ = 2960 (s), 2899 (w), 2862 (w), 1459 (m), 1388 (w), 1356 (m), 1252 (s), 1198 (w), 1163 (w), 1088 (br, s), 1018 (s), 927 (w), 803 (s), 736 (s), 660 (w), 605 (w) cm^{-1}.

1-Ce: blue crystals (0.726 g, 54%). Anal calcd (%) for C$_{39}$H$_{63}$Ce: C, 69.68; H, 9.45. Found (%): C, 67.49; H, 9.43. ^{1}H NMR (C$_6$D$_6$, 500 MHz, 298 K): δ = −5.01 (s, 54H, C(C*H*$_3$)$_3$), 17.14 (s, 6H, Cp-*H*), 26.30 (s, 3H, Cp-*H*) ppm. The paramagnetism of **1-Ce** precluded assignment of its ^{13}C{^{1}H} NMR spectrum. μ_{eff} (Evans method, 298 K, C$_6$D$_6$): 2.42 μ_B. FTIR (ATR, microcrystalline): $\tilde{\nu}$ = 2951 (br, s), 2899 (w), 2863 (w), 1459 (s), 1388 (m), 1356 (s), 1298 (w), 1251 (s), 1198 (m), 1164 (s), 1051 (m), 1021 (m), 927 (s), 806 (s), 738 (s), 674 (s), 659 (s), 604 (w), 556 (br, w), 480 (w), 422 (m) cm^{-1}.

1-Nd: green crystals (0.460 g, 34%). Anal calcd (%) for C$_{39}$H$_{63}$Nd: C, 69.26; H, 9.40. Found (%): C, 65.81; H, 9.30. ^{1}H NMR (C$_6$D$_6$, 400 MHz, 298 K): δ = –9.06 (s, 54H, C(C*H*$_3$)$_3$), 12.68 (s, 6H, Cp-*H*), 34.47 (s, 3H, Cp-*H*). The paramagnetism of **1-Nd** precluded assignment of its ^{13}C{^{1}H} NMR spectrum. μ_{eff} (Evans method, 298 K, C$_6$D$_6$): 3.69 μ_B. FTIR (ATR, microcrystalline): $\tilde{\nu}$ = 2950 (s), 2899 (w), 2863 (w), 1459 (s), 1388 (w), 1356 (s), 1251 (s), 1164 (m), 1060 (br, w), 1021 (w), 927 (s), 806 (s), 737 (s), 659 (s), 605 (w), 423 (w) cm^{-1}.

1-Sm: orange crystals (0.716 g, 52%). ^{1}H NMR (C$_6$D$_6$, 400 MHz, 298 K): δ = –1.58 (s, 54H, C(C*H*$_3$)$_3$), 18.66 (s, 6H, Cp-*H*), 21.19 (s, 3H, Cp-*H*). The paramagnetism of **1-Sm** precluded assignment of its ^{13}C{^{1}H} NMR spectrum. FTIR (ATR, microcrystalline): $\tilde{\nu}$ = 2952 (s), 2901 (m), 2864 (w), 1460 (s), 1390 (s), 1366 (s), 1298 (s), 1250 (s), 1199 (s), 1164 (s), 1085 (w), 1060 (w), 1022 (m), 927 (s), 807 (s), 741 (s), 700 (s), 661 (s), 606 (m), 560 (m), 519 (w), 483 (w), 426 (s) cm^{-1}.

CONCLUSION

We have synthesized a family of trivalent Ln complexes [Ln(Cp^{tt})$_3$] (**1-Ln**; Ln = La, Ce, Nd, Sm) using a salt metathesis synthetic route. The solid state structures of **1-Ln** reveal that the distances between the Ln^{3+} centers and the Cp^{tt} centroids decrease regularly from La^{3+} to Sm^{3+} due to the ionic radii of Ln^{3+} ions decreasing across the series. Complexes **1-La** and **1-Nd** exhibit *pseudo*-trigonal planar geometries, which is consistent with the previously reported structures of **1-Ce**,[8] **1-Sm**[9] and **1-Yb**.[10] Continuous wave and pulse EPR studies were performed on **1-Nd**, **1-Ce**, and **1-Sm**. The CW spectra show a rhombic system with anisotropic *g*-values for both frozen solution and powder samples for **1-Nd** and **1-Ce**. T_1 relaxation time is approaching ~10 μs for **1-Nd** and ~100 μs for **1-Ce** and **1-Sm**, respectively, while the phase memory time reaches 0.7 μs (**1-Nd**), 1 μs (**1-Ce**) and 1.7 (**1-Sm**). The $4f^n$ electronic configuration of all complexes gives rise to fast electron-spin relaxation. We have performed 2D HYSCORE spectroscopy in order to characterize in more details the interactions of the Nd^{III} and Ce^{III} ions with the Cp^{tt} ligands. The simulation of the HYSCORE spectra for both ^{13}C and ^{1}H regions were performed with a dipole-only model. These results are not surprising as the lanthanide interactions with the organic ligands are considered as being mostly ionic, due to the strongly localized and unavailable for bonding 4*f*-orbitals. The previously reported studies of the two actinide complexes [An(Cp^{tt})$_3$] (An = Th and U), show greater total spin density on the ligands of U^{III} than Th^{III} complex. In addition, comparison of the HYSCORE spectra of the Yb^{III} and Th^{III} complexes displaying apparent similarities, which indicates covalency akin to late lanthanides and the light actinides. Finally, comparison of the HYSCORE results of Nd^{III} and U^{III} analogues did not emphasize many similarities between these two ions. HYSCORE simulation showed negligible spin density on the ligands of **1-Nd** and **1-Ce** complexes, highlighting the more significant contribution of the 5*f*-orbitals than the 4*f*-orbitals in bonding to the cyclopentadienyl ligands.

ACKNOWLEDGMENTS

We thank the Engineering and Physical Sciences Research Council (studentship to L.N. and EP/P002560/1), the China Scholarship Council (studentship to J.L.), The European Commission Marie Curie Initial Training Network ‘Magic’ (studentship to A.M.A), The University of Manchester Single Crystal X-ray Diffraction Service and the EPSRC UK National Electron Paramagnetic Resonance Service for generously supporting this work. Research data files supporting this publication are available from Mendeley Data at X.

REFERENCES

(1) Atwood, D. A. *The Rare Earth Elements: Fundamentals and Applications*; John Wiley and Sons Ltd., 2012.

(2) (a) Dam, H. H.; Reinhoudt, D. N.; Verboom, W. Chem. Soc. Rev., 2007, 36, 367-377. (b) Nash, K. L. *Solvent Extr. Ion Exch.* **1993**, *11*, 729-768.

(3) (a) Schumann, H.; Meese-Marktscheffel, J. A.; Esser, L. *Chem. Rev.* **1995**, *95*, 865-986. (b) Walter, O. *Chem. Eur. J.* **2019**, *25*, 2927-2934. (c) Ephritikhine, M. *Organometallics* **2013**, *32*, 2464-2488.

(4) Neidig, M. L.; Clark, D. L.; Martin, R. L. *Coord. Chem. Rev.* **2013**, *257*, 394-406.

(5) *Inorganic Structure and Spectroscopy*; Solomon, E. I.; Lever, A. B. P. Eds; Wiley, 1999.

(6) (a) Smiles, D. E.; Wu, G.; Hrobárik, P.; Hayton, T. W. *J. Am. Chem. Soc.* **2016**, *138*, 814–825. (b) Staun, S. L.; Sergentu, D.-C.; Wu, G.; Autschbach, J.; Hayton, T. W. *Chem. Sci.* **2019**, *10*, 6431-6436. (c) Smiles, D. E.; Wu, Guang, Hrobárik, P.; Hayton, T. W. *Organometallics*, **2017**, *36*, 4519-4524.

(7) Formanuik, A.; Ariciu, A.-M.; Ortu, F.; Beekmeyer, R.; Kerridge, A.; Tuna, F.; McInnes, E. J. L.; Mills, D. P. *Nature Chemistry* **2017**, *9*, 578-583.

(8) Denning, R. G.; Harmer, J.; Green, J. C.; Irwin, M. *J. Am. Chem. Soc.* **2011**, *133*, 20644-20660.

(9) Sofield, C. D.; Andersen, R. A. *J. Organomet. Chem*. **1995**, *501*, 271-276.
(10) Pushkarevsky, N. A.; Ilyin, I. Y.; Petrov, P. A.; Samsonenko, D. G.; Ryzhikov, M. R.; Roesky, P. W.; Konchenko, S. N. *Organometallics* **2017**, *36*, 1287-1295.
(11) Khvostov, A. V.; Bulychev, B. M.; Belsky, V. K.; Sizov, A. I.; *J. Organomet. Chem*. **1998**, *568*, 113-119.
(12) Ortu, F.; Formanuik, A.; Innes, J. R.; Mills, D. P. *Dalton Trans.* **2016**, *45*, 7537-7549
(13) Volkovich, V. A.; Ivanov, A. B.; Yakimov, S. M.; Tsarevskii, D. V.; Golovanova, O. A.; Sukhikh, V. V.; Griffiths, T. R. *Electronic absorption spectra of rare earth(III) species in NaCl-2CsCl eutectic based melts*, AIP Publ. New York, 2016
(14) (a) Kaltsoyannis, N.; Scott, P. *The f elements*; Oxford University Press: New York, 1999; pp 26-27. (b) Cotton, S. *Lanthanide and actinide chemistry*, John Wiley and Sons Ltd., 2006.
(15) Schweiger, A.; Jeschke, J. *Principles of Pulse Electron Paramanetic Resonance*, Oxford University Press, 2001**.**
(16) Eaton, S. S.; Eaton, G. R. in *Distance Measurements in Biological Systems by EPR*; Berliner L. J.; Eaton, G. R.; Eaton, S. S.; Eds.; Springer US Boston, MA, 2002; Vol 19, pp 29-154.
(17) Bader, K; Winkler, M.; van Slageren, J. *Chem. Commun.* **2016**, *52*, 3623-3626.
(18) Van Doorslear, S. Hyperfine Spectroscopy: ESSEM. *eMagRes* **2017**, *6*, 51-70.
(19) Harmer, J.; Mitrikas, G.; Schweiger, A. *Advanced Pulse EPR Methods for the Characterization of Metalloproteins*, In *High Resolution EPR*; Hanson, G.; Berliner, L.; Eds.; Springer Science: New York, 2009; Vol 28, pp 13-61.
(20) Jaroschik, F.; Nief, F.; Le Goff, X. F.; Ricard, L. *Organometallic* **2007**, *26*, 3552-3558.

Electronic Supplementary Information

Covalency in LnCp$^{tt}_3$ (Ln = Ce, Nd, Sm) evaluated by HYSCORE spectroscopy

Lydia E. Nodaraki,[†,‡,§] Jingjing Liu,[†,§] Ana-Maria Ariciu,[†,‡] Fabrizio Ortu,[†] David P. Mills,[†,*] Eric J. L. McInnes,[†, ‡,*] Floriana Tuna,[†,‡,*]

[†] School of Chemistry and [‡]Photon Science Institute, University of Manchester, Oxford Road, Manchester, M13 9PL, UK;

[§] These authors contributed equally.

Contents

1. **Synthetic procedures of 1-Ln complexes**
2. **Crystallography**
    2.1 Molecular structures of 1-La, 1-Ce and 1-Nd
3. **NMR Spectroscopy**
4. **ATR IR Spectroscopy**
5. **UV-VIS NIR Spectroscopy**
6. **EPR spectroscopy**
    6.1. Continuous wave EPR measurements
    6.2. Pulsed EPR measurements
        6.2.1 Echo-detected EPR
        6.2.2 Phase memory time (T_m)
        6.2.3 Spin-lattice relaxation time (T_1)
        6.2.4 HYSCORE (Hyperfine sub-level correlation) measurements
7. **Magnetic studies**
8. **Computational studies**
    8.1. Methods
        8.1.1. Calculated Properties of 1-Nd, 1-Ce and 1-Sm
        8.1.2. Optimized Geometries

1. Synthetic procedures of **1-Ln** complexes

[La(Cp^{tt})$_3$] (1-La). THF (30 mL) was added to a pre-cooled (−78 °C) ampoule containing $LaCl_3$ (0.491 g, 2 mmol) and KCp^{tt} (1.298 g, 6 mmol). The reaction mixture was allowed to reflux for 16 hours. The solvent was removed *in vacuo* and toluene (30 mL) was added. The reaction mixture was allowed to reflux for 40 hours. The resultant pale yellow suspension was allowed to settle for 3 hours and filtered. The pale yellow solution was concentrated to 2 mL and stored at 8 °C to afford **1-La** as colorless crystals (0.550 g, 41 %). Anal calcd (%) for $C_{39}H_{63}La$: C, 69.81; H, 9.47. Found (%): C, 67.03; H, 9.50. ^{1}H NMR (C_6D_6, 400 MHz, 298 K): δ = 1.35 (s, 54H, C(C*H*$_3$)$_3$), 6.21 (s, 3H, Cp-*H*), 6.28 (s, 6H, Cp-*H*) ppm. ^{13}C{^{1}H} NMR (C_6D_6, 100 MHz, 298 K): δ = 32.77 (C(*C*H$_3$)$_3$), 33.75 (*C*(CH$_3$)$_3$), 110.57 (*C*H-Cp ring), 110.69 (*C*H-Cp ring), 143.45 (*C*-Cp ring) ppm. FTIR (ATR, microcrystalline): $\tilde{\upsilon}$ = 2960 (s), 2899 (w), 2862 (w), 1459 (m), 1388 (w), 1356 (m), 1252 (s), 1198 (w), 1163 (w), 1088 (br, s), 1018 (s), 927 (w), 803 (s), 736 (s), 660 (w), 605 (w) cm^{-1}.

[Ce(Cp^{tt})$_3$] (1-Ce). THF (30 mL) was added to a pre-cooled (−78 °C) ampoule containing $CeCl_3$ (0.493 g, 2 mmol) and KCp^{tt} (1.298 g, 6 mmol). The reaction mixture was allowed to reflux for 16 hours. The solvent was removed *in vacuo* and toluene (30 mL) was added. The dark green reaction mixture was allowed to reflux for 40 hours. The resultant suspension was allowed to settle for 3 hours and filtered. The dark purple solution was concentrated to 2 mL and stored at 8 °C to afford **1-Ce** as blue crystals (0.721 g, 54 %). Anal calcd (%) for $C_{39}H_{63}Ce$: C, 69.68; H, 9.45. Found (%): C, 67.49; H, 9.43. ^{1}H NMR (C_6D_6, 500 MHz, 298 K): δ = −5.01 (s, 54H, C(C*H*$_3$)$_3$), 17.14 (s, 6H, Cp-*H*), 26.30 (s, 3H, Cp-*H*) ppm. The paramagnetism of **1-Ce** precluded assignment of its ^{13}C{^{1}H} NMR spectrum. μ_{eff} (Evans method, 298 K, C_6D_6): 2.42 μ_B. FTIR (ATR, microcrystalline): $\tilde{\upsilon}$ = 2951 (br, s), 2899 (w), 2863 (w), 1459 (s), 1388 (m), 1356 (s), 1298 (w), 1251 (s), 1198 (m), 1164 (s), 1051 (m), 1021 (m), 927 (s), 806 (s), 738 (s), 674 (s), 659 (s), 604 (w), 556 (br, w), 480 (w), 422 (m) cm^{-1}.

[Nd(Cp^{tt})$_3$] (1-Nd). THF (30 mL) was added to a pre-cooled (–78 °C) ampoule containing $NdCl_3$ (0.501 g, 2 mmol) and KCp^{tt} (1.298 g, 6 mmol). The light blue mixture was allowed to reflux for 16 hours. The solvent was removed in *vacuo* and toluene (30 mL) was added. The reaction mixture was allowed to reflux for 40 hours. The resultant suspension was allowed to settle for 3 hours and filtered. The green solution was concentrated to 2 mL and stored at 8 °C to give **1-Nd** as green crystals (0.460 g, 34%). Anal calcd (%) for $C_{39}H_{63}Nd$: C, 69.26; H, 9.40. Found (%): C, 65.81; H, 9.30. ^{1}H NMR (C_6D_6, 400 MHz, 298 K): δ = –9.06 (s, 54H, C(C*H*$_3$)$_3$), 12.68 (s, 6H, Cp-*H*), 34.47 (s, 3H, Cp-*H*). The paramagnetism of **1-Nd** precluded assignment of its ^{13}C{^{1}H} NMR spectrum. μ_{eff} (Evans method, 298 K, C_6D_6): 3.69 μ_B. FTIR (ATR, microcrystalline): $\tilde{\upsilon}$ = 2950 (s), 2899 (w), 2863 (w), 1459 (s), 1388 (w), 1356 (s), 1251 (s), 1164 (m), 1060 (br, w), 1021 (w), 927 (s), 806 (s), 737 (s), 659 (s), 605 (w), 423 (w) cm^{-1}.

[Sm(Cp^{tt})$_3$] (1-Sm) and [Sm(Cp^{tt})$_2$(μ-Cl)]$_2$·(C$_7$H$_8$) (2). THF (30 mL) was added to a pre-cooled (−78 °C) ampoule containing $SmCl_3$ (0.513 g, 2 mmol) and KCp^{tt} (1.298 g, 6 mmol). The reaction mixture was allowed to reflux for 16 hours. The bright yellow solvent was removed *in vacuo* and toluene (30 mL) was added. The reaction mixture was allowed to reflux for 40 hours. The resultant suspension was allowed to settle for 3 hours and filtered. The orange solution was concentrated to 2 mL and stored at 8 °C to afford **1-Sm** as orange crystals (0.716 g, 52%). ^{1}H NMR (C_6D_6, 400 MHz, 298 K): δ = –1.58 (s, 54H, C(C*H*$_3$)$_3$), 18.66 (s, 6H, Cp-*H*), 21.19 (s, 3H, Cp-*H*). The paramagnetism of **1-Sm** precluded assignment of its ^{13}C{^{1}H} NMR spectrum. FTIR (ATR, microcrystalline): $\tilde{\upsilon}$ = 2952 (s), 2901 (m), 2864 (w), 1460 (s), 1390 (s), 1366 (s), 1298 (s), 1250 (s), 1199 (s), 1164 (s), 1085 (w), 1060 (w), 1022 (m), 927 (s), 807 (s), 741 (s), 700 (s), 661 (s), 606 (m), 560 (m), 519 (w), 483 (w), 426 (s) cm^{-1}.

2. Crystallography

The crystal data for complexes **1-La**, **1-Ce** and **1-Nd** are compiled in **Table S1**. Crystals of **1-La**, **1-Ce**, and **1-Nd** were examined using an Oxford Diffraction Supernova diffractometer with a CCD area detector and a mirror-monochromated Mo Kα radiation (λ = 0.71073 Å). Intensities were integrated from data recorded on 1° (**1-La**, **1-Ce**, and **1-Nd**) frames by ω rotation. Cell parameters were refined from the observed positions of all strong reflections in each data set. A Gaussian grid face-indexed (**1-Ce** and **1-Nd**) or multi-scan (**1-La**) absorption correction with a beam profile was applied.[1] The structures were solved using SHELXS;[2] the datasets were refined by full-matrix least-squares on all unique F^2 values,[3] with anisotropic displacement parameters for all non-hydrogen atoms, and with constrained riding hydrogen geometries; U_{iso}(H) was set at 1.2 (1.5 for methyl groups) times U_{eq} of the parent atom. The largest features in final difference syntheses were close to heavy atoms and were of no chemical significance. CrysAlisPro[1] was used for control and integration, and SHELX[2,3] was employed through OLEX2[4] for structure solution and refinement. ORTEP-3[5] and POV-Ray[6] were employed for molecular graphics. CCDC XXXXXXX–XXXXXXX contain the supplementary crystal data for this article. These data can be obtained free of charge from the Cambridge Crystallographic Data Centre via www.ccdc.cam.ac.uk/data_request/cif.

Table S1. Crystallographic data for **1-Ln**.

[a]Conventional $R = \Sigma||Fo| - |Fc||/\Sigma|Fo|$; $Rw = [\Sigma w(Fo^2 - Fc^2)^2/\Sigma w(Fo^2)^2]^{1/2}$; $S = [\Sigma w(Fo^2 - Fc^2)^2/\text{no. data} - \text{no. params})]^{1/2}$ for all data.

	1-La	**1-Ce**	**1-Nd**
Formula	$C_{39}H_{63}La$	$C_{39}H_{63}Ce$	$C_{39}H_{63}Nd$
Formula weight	670.80	672.01	676.13
Crystal size, mm	0.0678 × 0.0646 × 0.047	0.146 × 0.117 × 0.069	0.442 × 0.309 × 0.243
Crystal system	triclinic	triclinic	Monoclinic
Space group	P-1	P-1	$P2_1/n$
a, Å	10.7001(8)	10.7185(10)	10.7938(3)
b, Å	18.4935(9)	17.980(2)	19.4422(5)
c, Å	19.7113(13)	20.0687(17)	17.8596(5)
α, °	83.299(5)	82.851(8)	90
β, °	77.365(6)	78.793(8)	104.394(3)
γ, °	74.640(5)	74.326(9)	90
V, Å^3	3663.0(4)	3642.1(7)	3630.25(18)
Z	4	2	4
ρ_{calc}, g cm^3	1.216	1.226	1.237
μ, mm^{-1}	1.189	1.273	1.453
F(*000*)	1416	1420	1428
No. of reflections (unique)	21453(13284)	30825(12875)	15912 (6631)
S^a	1.005	1.013	1.044
$R_1(wR_2)$ ($F^2 > 2\sigma(F^2)$)	0.0564 (0.0852)	0.1008 (0.2021)	0.0402 (0.0811)
R_{int}	0.050	0.155	0.040
Min./max. diff map, Å^{-3}	−0.97, 1.07	−1.75, 2.64	−0.39, 1.75

2.1 Molecular structures of complexes **1-La**, **1-Ce** and**1-Nd**

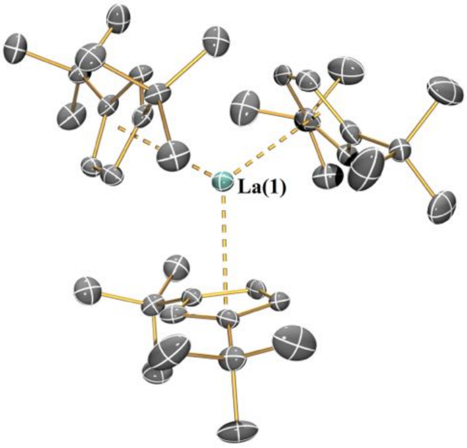

Figure S1. Molecular structure of [La(Cp^{tt})$_3$] (**1-La**) with selected labelling. Displacement ellipsoids set at 30 % probability level and hydrogen atoms are omitted for clarity. Selected distances and angles: La1···Cp$_{centroid1}$, 2.657(2) Å; La1···Cp$_{centroid2}$, 2.623(2) Å; La1···Cp$_{centroid3}$, 2.625(3) Å; Cp$_{centroid1}$···La1···Cp$_{centroid2}$, 120.38(7)°; Cp$_{centroid1}$···La1···Cp$_{centroid3}$, 118.74(8)°; Cp$_{centroid2}$···La1···Cp$_{centroid3}$, 120.88(8)°.

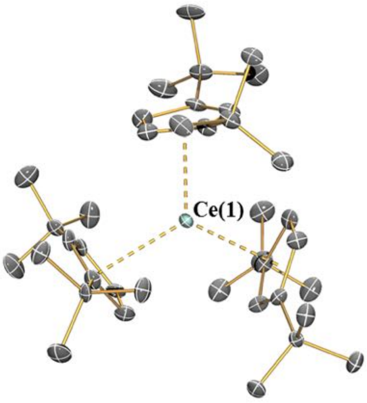

Figure S2. Molecular structure of [Ce(Cp^{tt})$_3$] (**1-Ce**) with selected labelling. Displacement ellipsoids set at 30 % probability level and hydrogen atoms are omitted for clarity. Selected distances and angles: Ce1···Cp$_{centroid1}$, 2.581(6) Å; Ce1···Cp$_{centroid2}$, 2.592(6) Å; Ce1···Cp$_{centroid3}$, 2.600(6) Å; Cp$_{centroid1}$···Ce1···Cp$_{centroid2}$, 119.5(2)°; Cp$_{centroid1}$···Ce1···Cp$_{centroid3}$, 119.8(2)°; Cp$_{centroid2}$···Ce1···Cp$_{centroid3}$, 120.65(19)°.

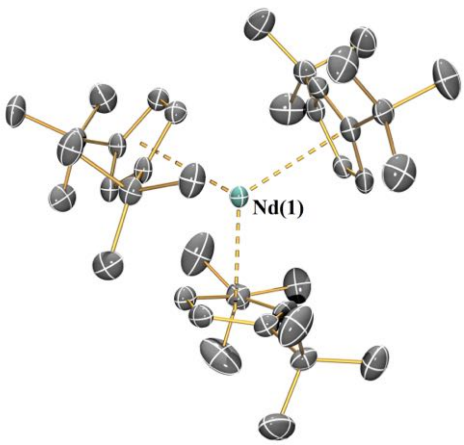

Figure S3. Molecular structure of [Nd(Cp^{tt})$_3$] (**1-Nd**) with selected labelling. Displacement ellipsoids set at 30 % probability level and hydrogen atoms are omitted for clarity. Selected distances and angles: Nd1···Cp$_{centroid1}$, 2.558(18) Å; Nd1···Cp$_{centroid2}$, 2.558(16) Å; Nd1···Cp$_{centroid3}$, 2.567(15) Å; Cp$_{centroid1}$···Nd1···Cp$_{centroid2}$, 119.68(5)°; Cp$_{centroid1}$···Nd1···Cp$_{centroid3}$, 120.60(6)°; Cp$_{centroid2}$···Nd1···Cp$_{centroid3}$, 119.71(6)°.

3. NMR spectroscopy

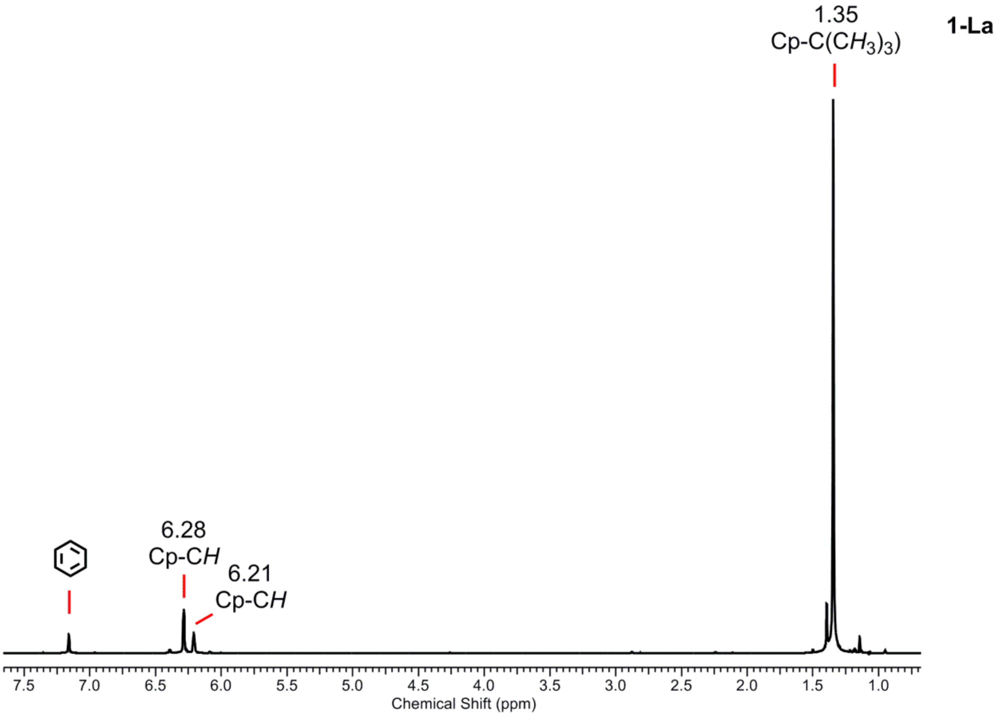

Figure S4. ^{1}H NMR spectrum of complex **1-La** in C_6D_6 zoomed in the region 1 and 7.5 ppm. Solvent residual marked.

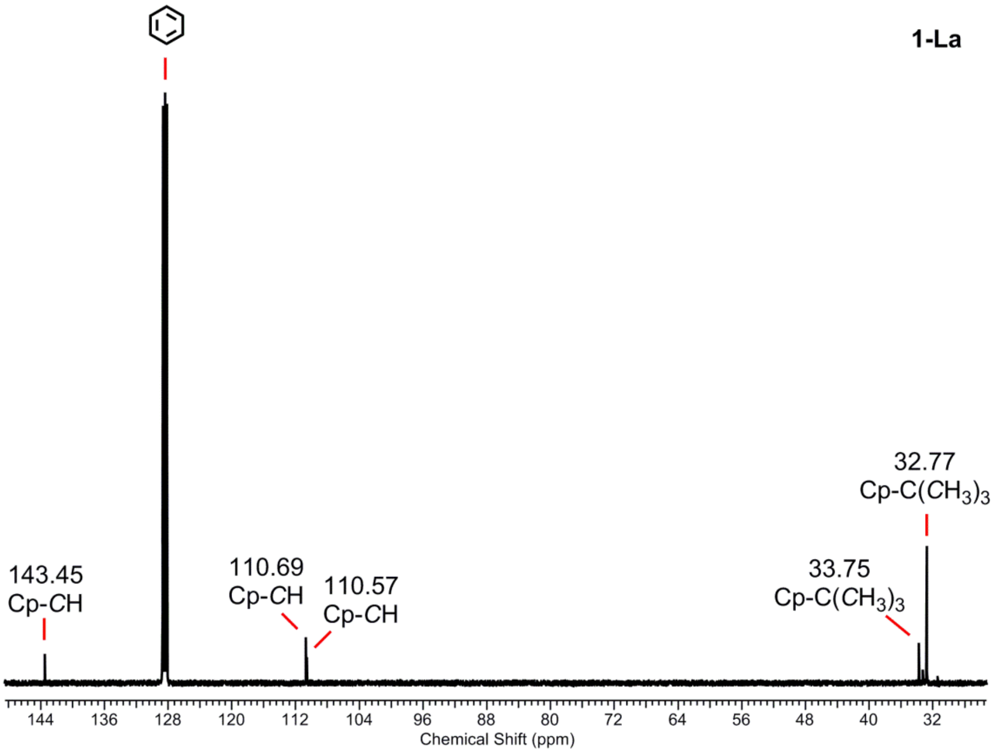

Figure S5. $^{13}C\{^1H\}$ NMR spectrum of complex **1-La** in C_6D_6. Solvent residual marked.

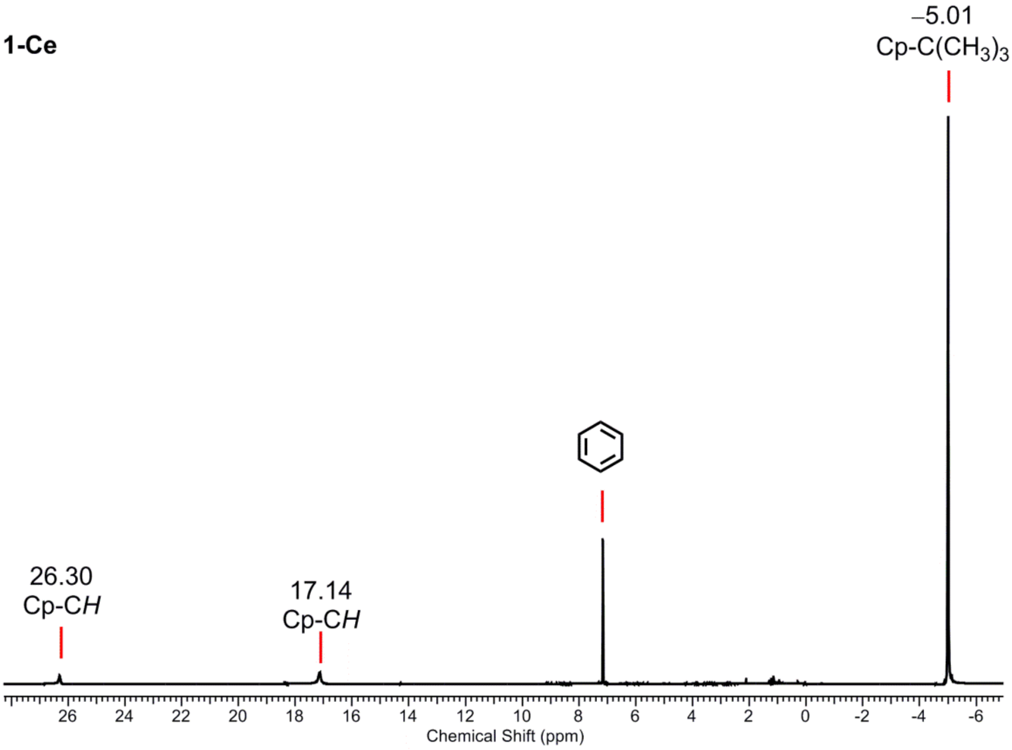

Figure S6. ^1H NMR spectrum of complex **1-Ce** in C_6D_6 zoomed in the region –7 and 28 ppm. Solvent residual marked; minor diamagnetic impurities can be seen between 0 and 4 ppm.

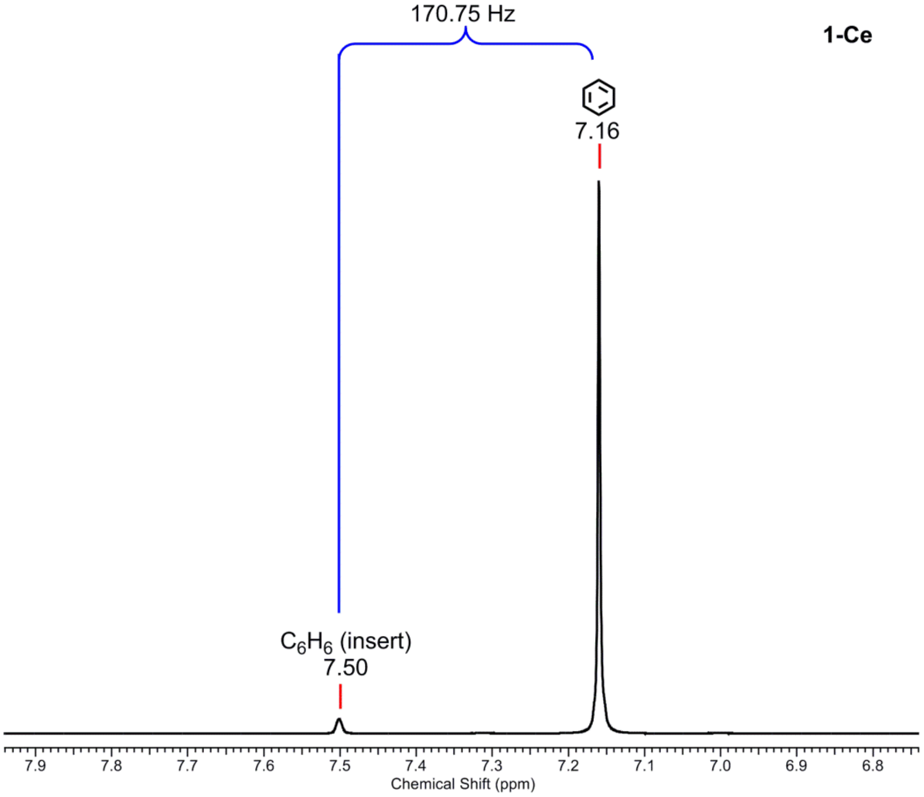

Figure S7. ^{1}H NMR spectrum of complex **1-Ce** in C_6D_6 with a C_6H_6/C_6D_6 insert. Solvent residual marked.

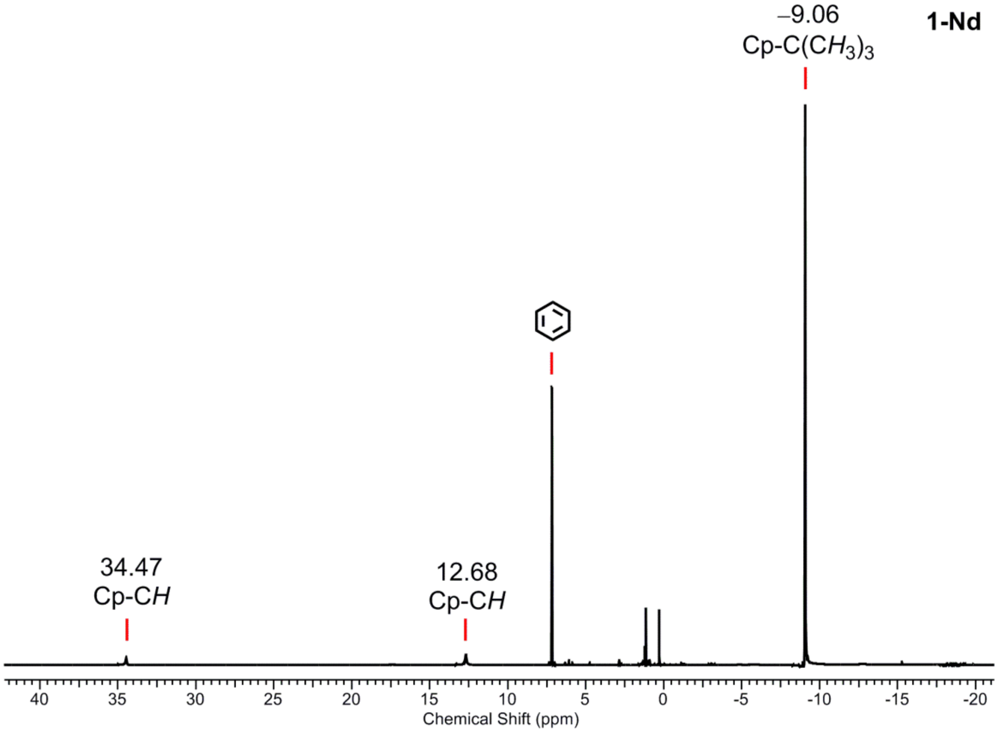

Figure S8. ^{1}H NMR spectrum of complex **1-Nd** in C_6D_6 zoomed in the region –20 and 40 ppm. Solvent residual marked; minor diamagnetic impurities can be seen between 0 and 7 ppm.

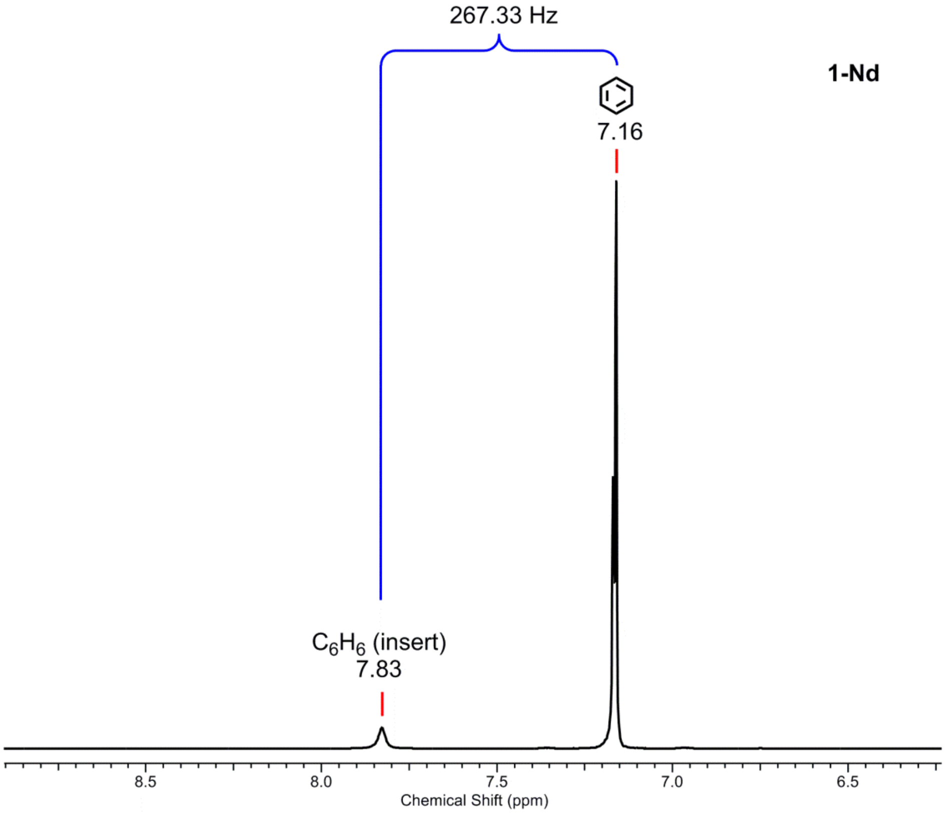

Figure S9. ^{1}H NMR spectrum of complex **1-Nd** in C_6D_6 with a C_6H_6/C_6D_6 insert. Solvent residual marked.

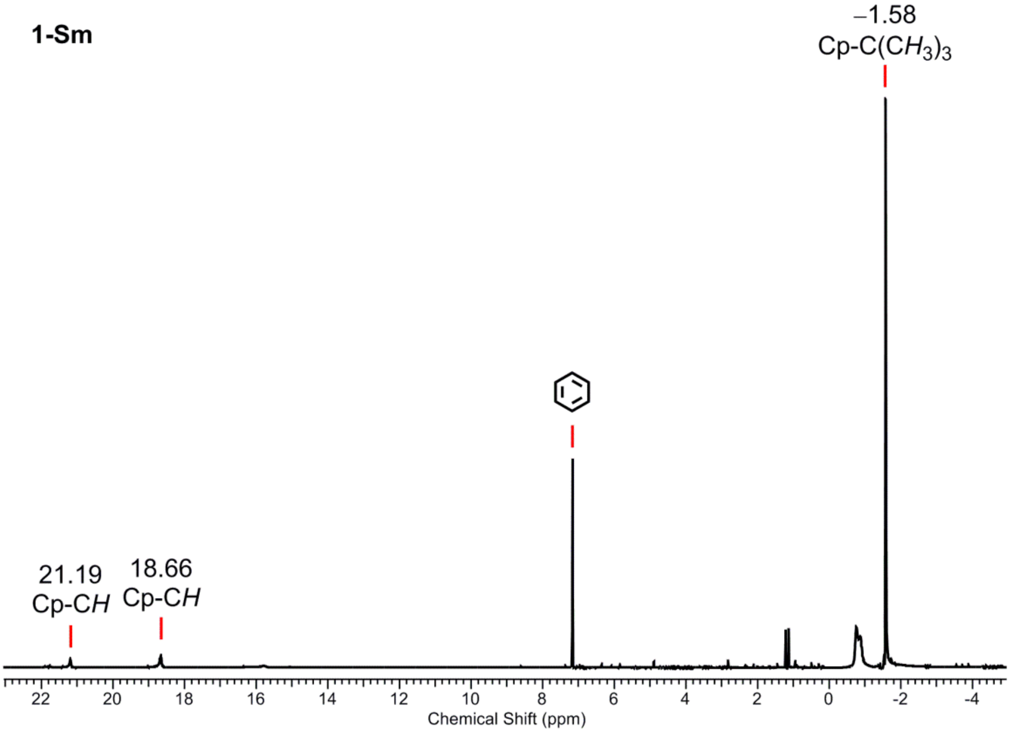

Figure S10. ^{1}H NMR spectrum of complex **1-Sm** in C_6D_6 zoomed in the region –4 and 22. Solvent residual marked; minor diamagnetic impurities can be seen between –1 and 7 ppm.

4. ATR-IR spectroscopy

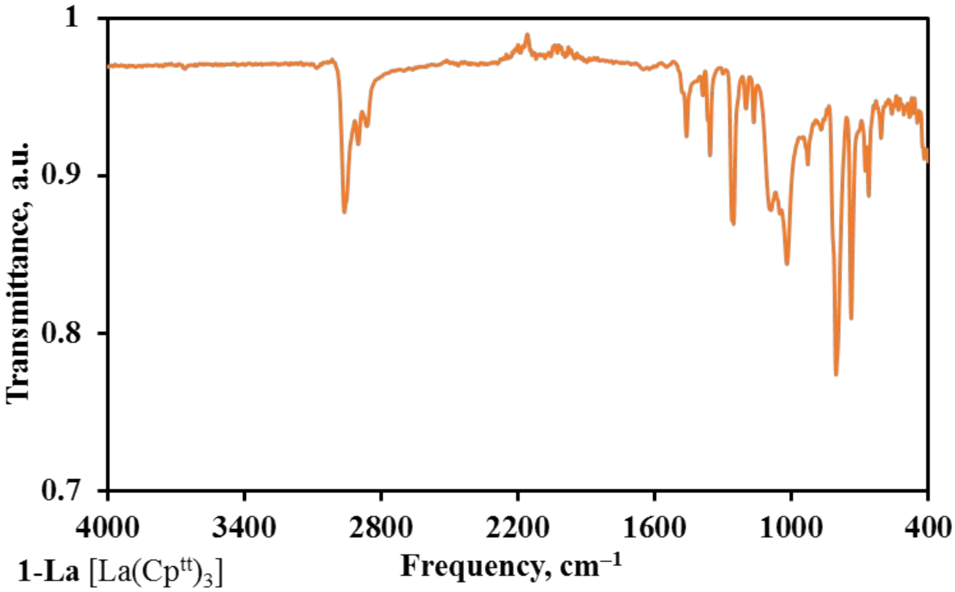

Figure S11. ATR-IR spectrum of **1-La** recorded as a microcrystalline powder.

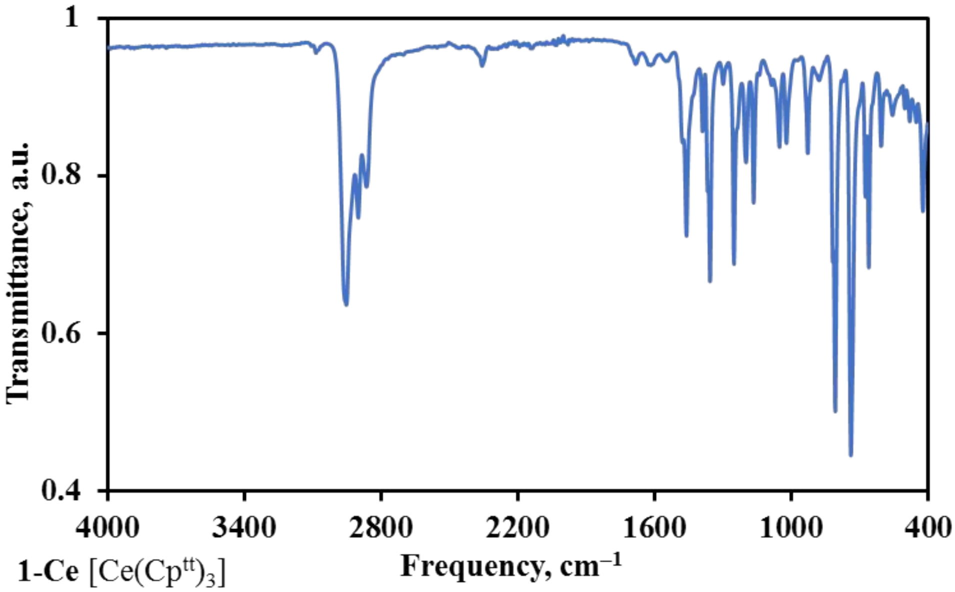

Figure S12. ATR-IR spectrum of **1-Ce** recorded as a microcrystalline powder.

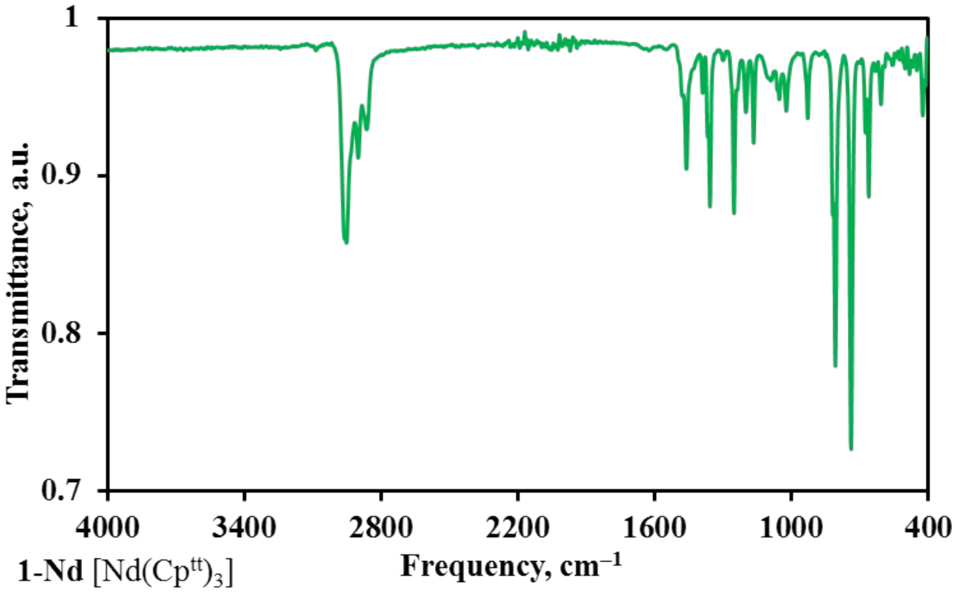

Figure S13. ATR-IR spectrum of **1-Nd** recorded as a microcrystalline powder.

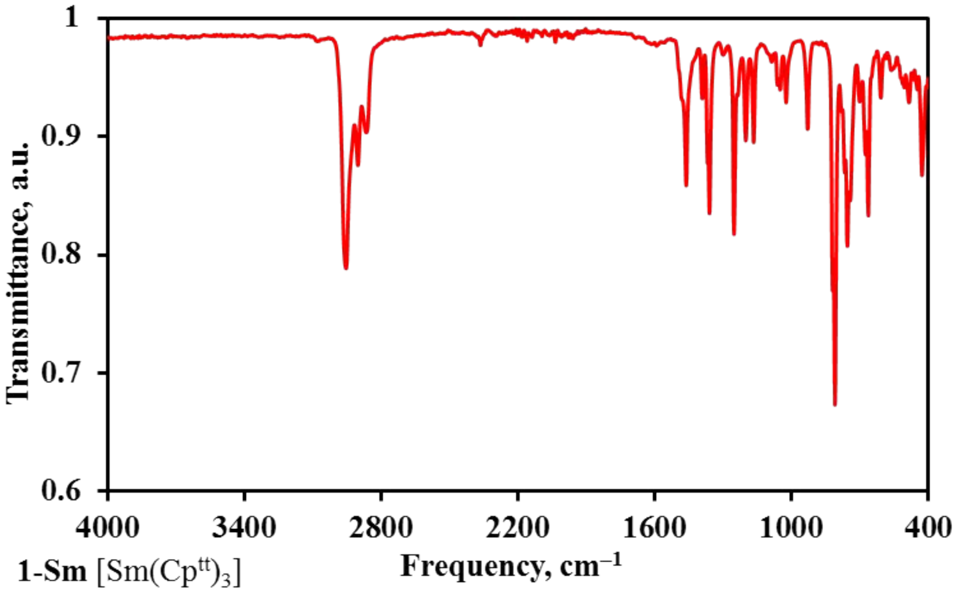

Figure S14. ATR-IR spectrum of **1-Sm** recorded as a microcrystalline powder.

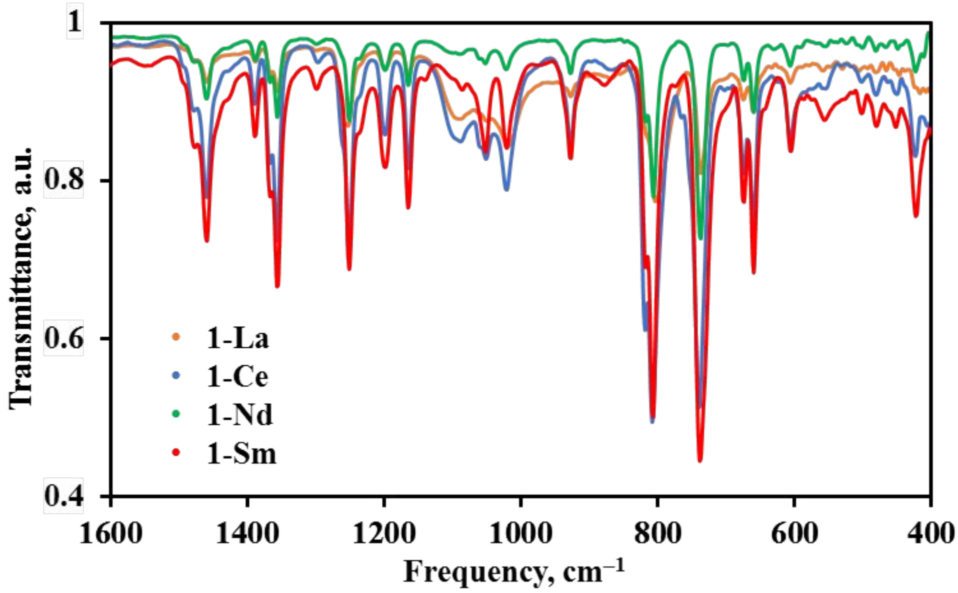

Figure S15. ATR-IR spectra of **1-La**, **1-Ce**, **1-Nd**, **1-Sm** in the region 1600–400 cm^{-1} intended to show the similarities between both spectra.

5. UV-vis NIR spectroscopy

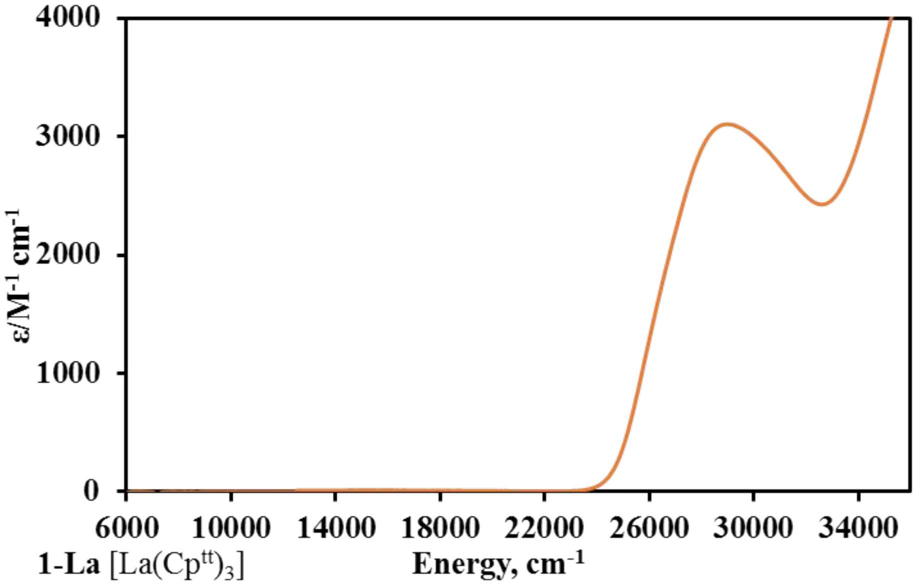

Figure S16. UV-vis-NIR spectrum of **1-La** between 36000–6000 cm^{-1} (278–1650 nm) recorded as a 0.5 mM solution in toluene.

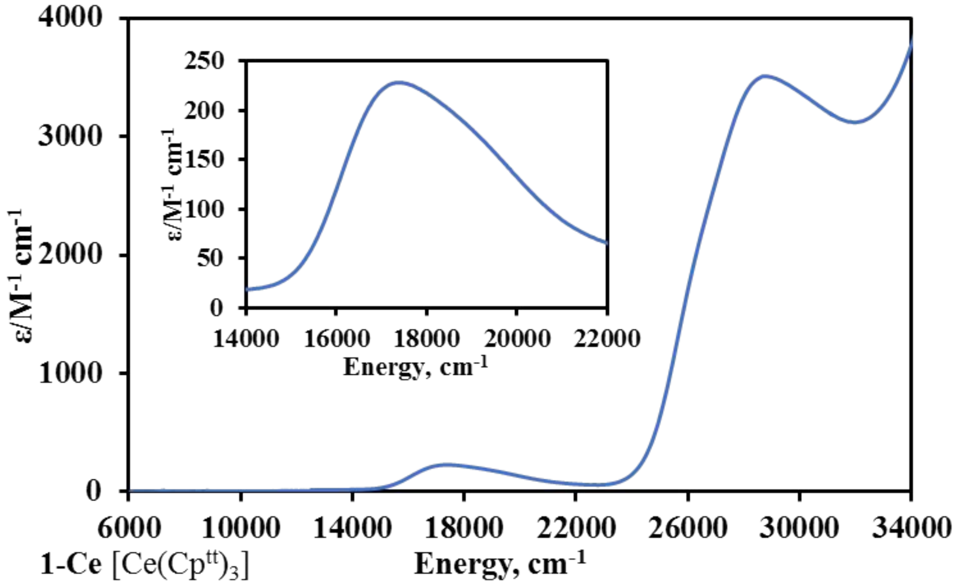

Figure S17. UV-vis-NIR spectrum of **1-Ce** between 34000–6000 cm^{-1} (295–1650 nm) recorded as a 0.5 mM solution in toluene. Inset shows the region 22000–14000 cm^{-1} (455–714 nm).

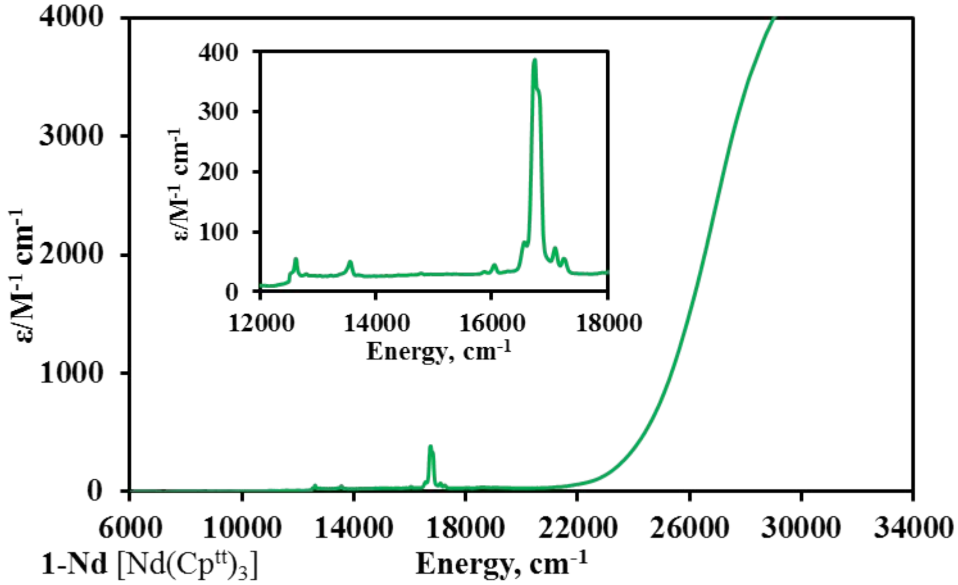

Figure S18. UV-vis-NIR spectrum of **1-Nd** between 34000–6000 cm^{-1} (295–1650 nm) recorded as a 0.5 mM solution in toluene. Inset shows the region 18000–12000 cm^{-1} (555–833 nm).

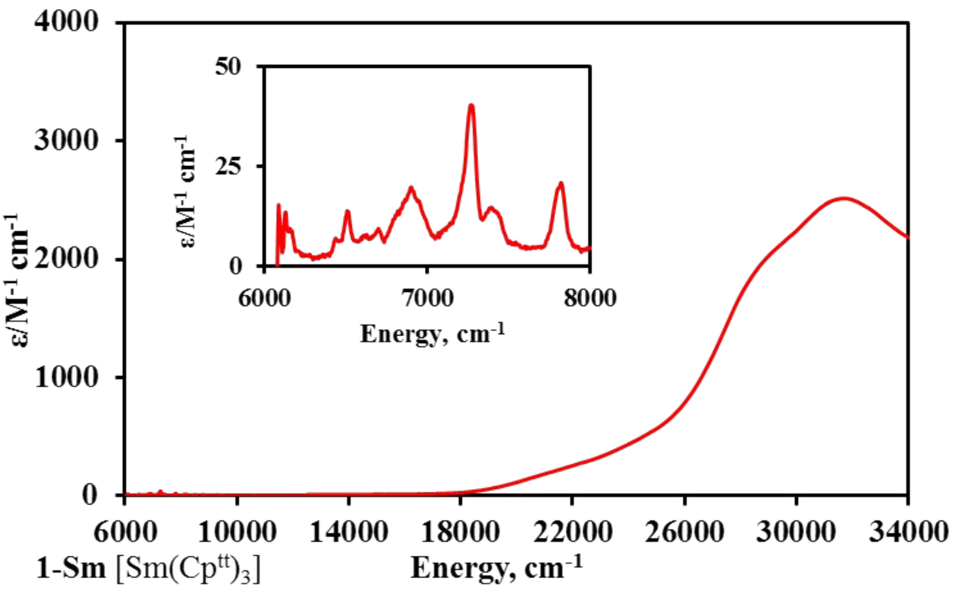

Figure S19. UV-vis-NIR spectrum of **1-Sm** between 34000–6000 cm^{-1} (295–1650 nm) recorded as a 0.5 mM solution in toluene. Inset shows the region 8000–6000 cm^{-1} (1250–1667 nm).

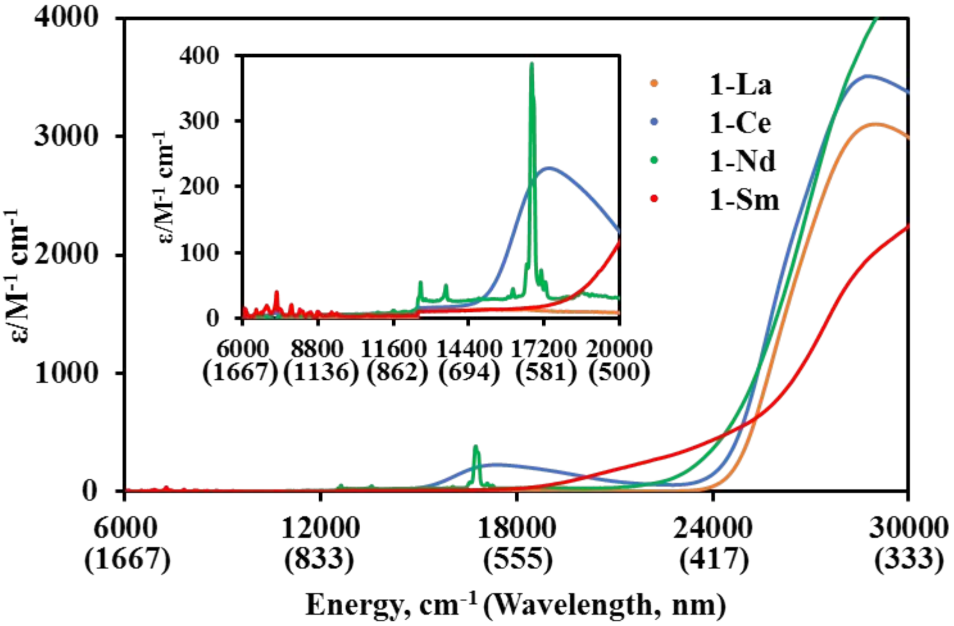

Figure S20. UV-vis-NIR spectrum of **1-La**, **1-Ce**, **1-Nd**, **1-Sm**, in the region 6000–30000 cm^{-1} (inset 6000–20000 cm^{-1}) recorded as 0.5 mM solutions in toluene at room temperature.

6. EPR spectroscopy

6.1 Continuous-wave EPR Measurements

Continuous-wave (CW) electron paramagnetic resonance (EPR) spectra of **1-Ln** (Figs. S21-S23) were recorded on Bruker EMX 300 and Bruker ElexSys E580 EPR spectrometers operating at either X-band (*ca.* 9.4-9.8 GHz) or Q-band (*ca.* 34 GHz) mw frequencies and variable temperatures. Spectra were simulated using the EasySpin software.[7]

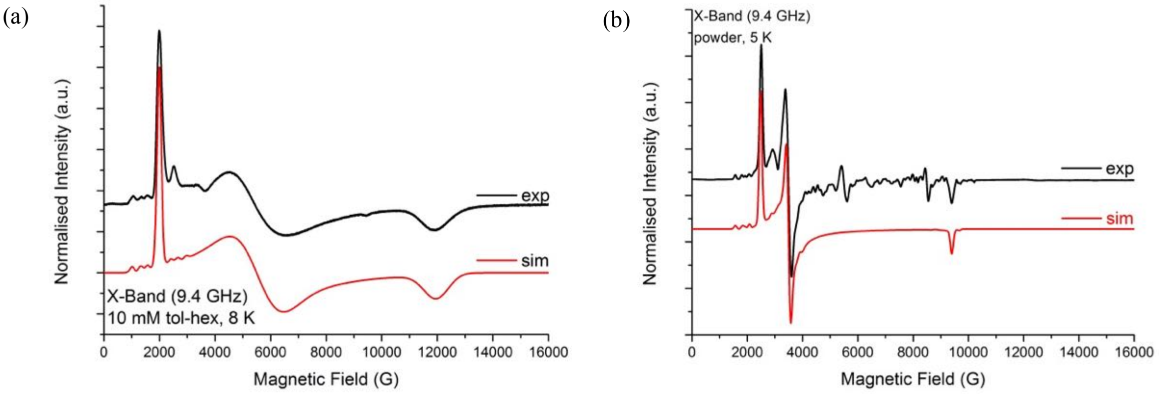

Figure S21. Experimental (black) and simulated (red) CW X-band EPR spectra of **1-Nd** (a) 10 mM toluene-hexane (9:1) solution at 8 K; (b) powder at 5 K. We observe polycrystallinity effects, previously reported for similar complexes.[8] Simulation parameters are given in Table S2.

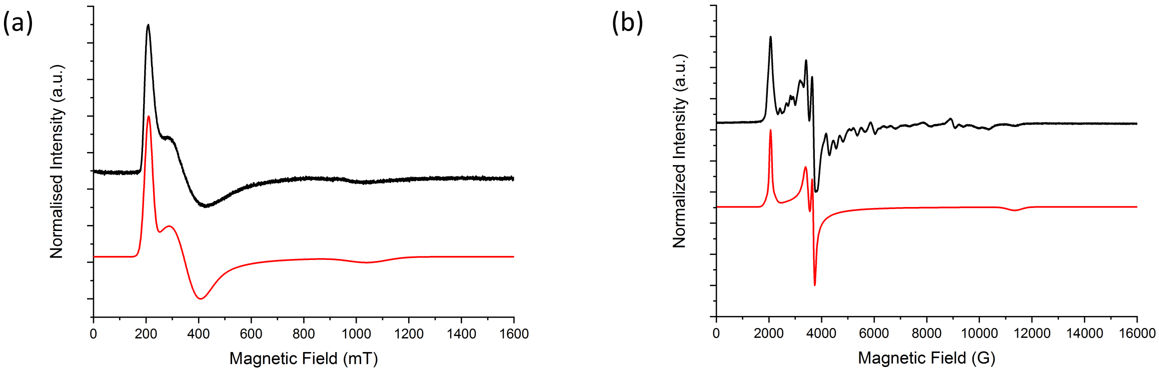

Figure S22. Experimental (black) and simulated (red) CW X-band EPR spectra of **1-Ce** (a) 20 mM toluene-hexane (9:1) solution at 10 K; (b) powder at 10 K. We observe polycrystallinity effects, previously reported for similar complexes.[8] Simulation parameters are given in Table S2.

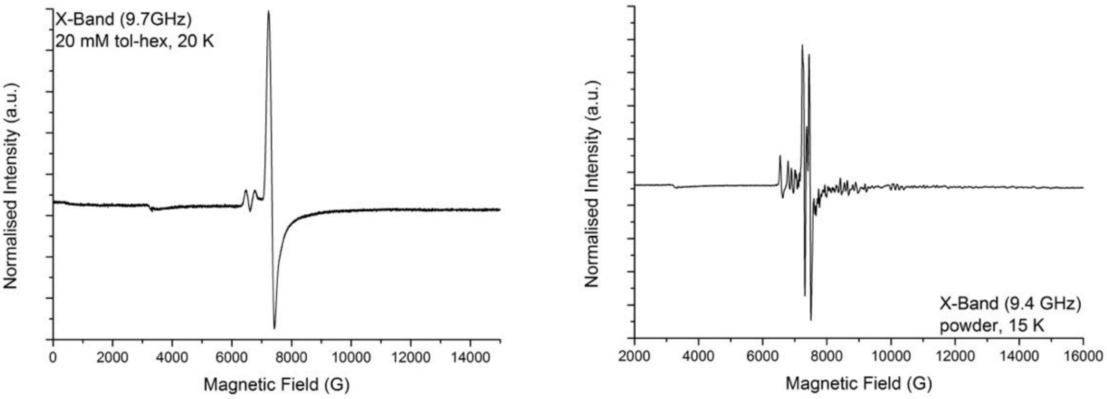

Figure S23. Experimental (black) and simulated (red) CW X-band EPR spectra of **1-Sm** (a) 20 mM toluene-hexane (9:1) solution at 20 K; (b) powder at 15 K. We observe polycrystallinity effects, previously reported for similar complexes.[8] Simulation parameters are given in Table S2.

Table S2. Hamiltonian parameters obtained from the CW simulation of **1-Ce**, **1-Nd** and **1-Sm**.

Compound	*T* (K)	*g*	|*A*| (MHz)
1-Nd (10 mM, Tol/Hex)	8	$g_{x/y/z}$ = 3.332/1.22/0.56	$\|A_{x/y/z}^{Nd}\|$ = 1280/700/200
1-Nd (powder)	5	$g_{x/y/z}$ = 2.70/1.92/0.714	$\|A_{x/y/z}^{Nd}\|$ = 980/350/100
1-Ce (10 mM, Tol/Hex)	10	$g_{x/y/z}$ = 3.15/1.88/0.636	$\|A_{x/y/z}^{Ce}\|$ = 0
1-Ce (powder)	10	$g_{x/y/z}$ = 3.24/ 1.92-1.81/ 0.588	$\|A_{x/y/z}^{Ce}\|$ = 0
1-Sm (10 mM, Tol/Hex)	20	$g_{x/y/z}$ = 0.905/0.905/0.55	$\|A_{x/y/z}^{Sm}\|$ = 0
1-Sm (powder)	15	$g_{x/y/z}$ = 0.905/0.905/0.55	$\|A_{x/y/z}^{Sm}\|$ = 0

6.2 Pulsed EPR Measurements

Pulsed EPR spectra were recorded with a Bruker ElexSys E580 instrument equipped with either a MD5 or a MD4 resonator, and operating at *ca*. 9.7 GHz and various temperatures. Solution samples of different concentrations (2, 5 and 10 mM in toluene/hexane) were investigated to check reproducibility and to achieve an acceptable signal-to-noise response in HYSCORE experiments. Data were simulated with the Easy Spin software package.[7]

6.2.1. Echo-detected EPR

The echo-detected field-swept (EDFS) spectra recorded at 9.7 GHz (X-band) (Figs. 4 and S24a-c) were recorded with a two-pulse primary Hahn-echo sequence ($\pi/2$ - τ - π - τ - *echo*),[9] with microwave π pulses of 32 or 64 ns, a fixed delay time τ = 300 ns, and with the variation of the static B_0 magnetic field. Those measurements at 34GHz (Q-band; Fig. S25) were recorded with microwave π pulses of 40 ns, and a fixed delay time $\tau = 300$ ns.

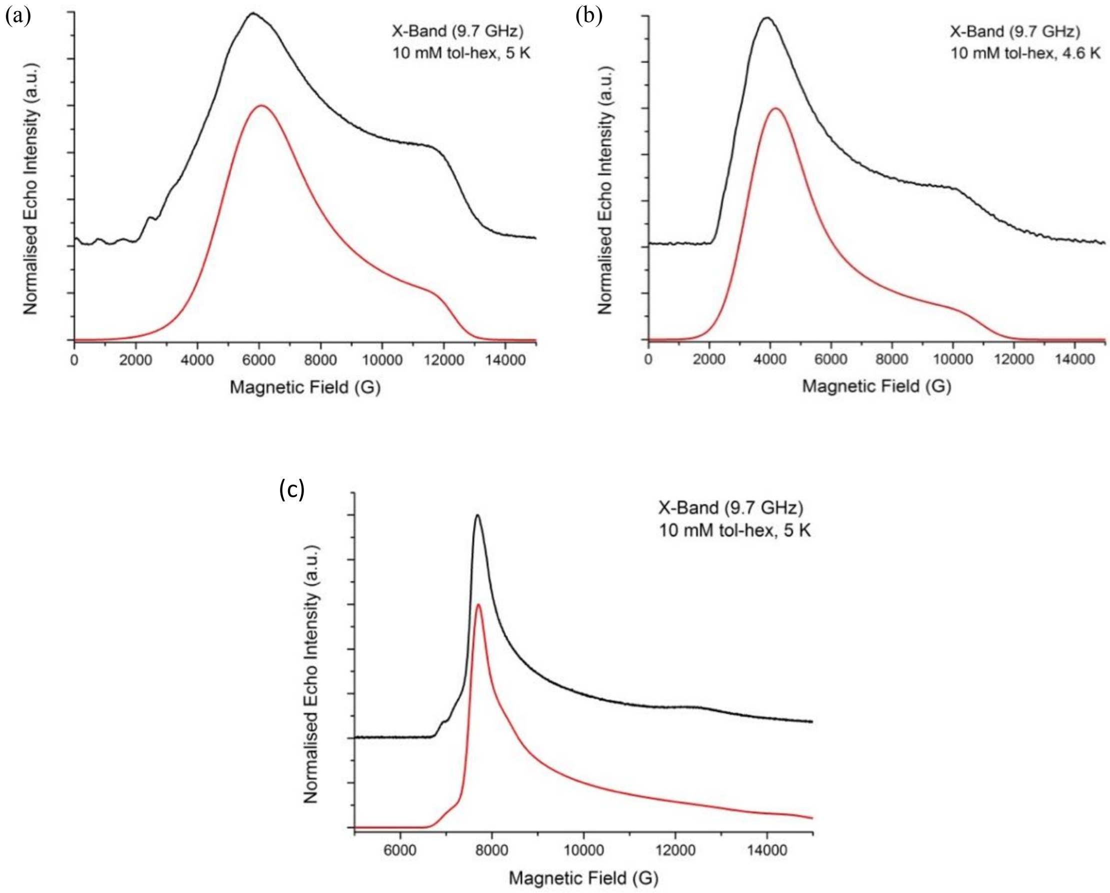

Figure S24. X-band (9.7 GHz) EDFS spectrum of a frozen solution **(**10 mM in 9:1 toluene-hexane) of (a) **1-Nd**, (b) **1-Ce** and (c) **1-Sm** simulated with the *g*- and *A*-parameters in Table S2.

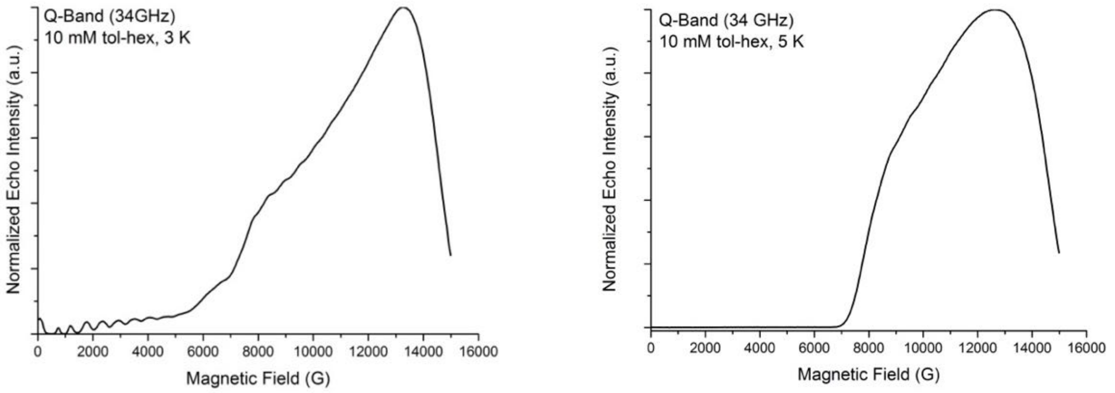

Figure S25. Q-band (34 GHz) EDFS spectrum of a frozen solution **(**10 mM in 9:1 toluene-hexane) of (a) **1-Nd** at 3 K and (b) **1-Ce** at 5 K.

6.2.2. Phase Memory Time (T_{m})

Electron spin echo envelope modulation (ESEEM) measurements involved monitoring the echo intensity generated with a primary Hahn-echo sequence as a function of τ. A similar pulse sequence was used to measure the phase memory time, T_{m}, with the difference that longer pulse durations (up to 128 ns) were necessary to suppress possible ^{1}H nuclear modulation effects in the echo decays (Figs. S26-S28). T_{m} was determined by least squares fitting of the experimental echo decay data using a stretched exponential function with a solver based on the Levenberg-Marquardt algorithm.

The fitting function used was:

$$Y(2\tau) = Y(0)e^{(-2\tau/T_m)X} \quad \text{(Equation 1)}$$

or, for strongly modulated data,

$$Y(2\tau) = Y(0)e^{(-2\tau/T_m)X}(1 + k\sin(\omega t + \Phi)) \quad \text{(Equation 2)}$$

where k is the modulation depth, ω is the Larmor angular frequency of a nucleus I coupled to the electron spin, ϕ is the phase correction, X is the stretching parameter, $Y(2\tau)$ is the echo integral for a pulse separation τ, and $Y(0)$ is the echo intensity extrapolated to $\tau = 0$.[10-13]

The extracted T_{m} times are given in Tables S3-S7.

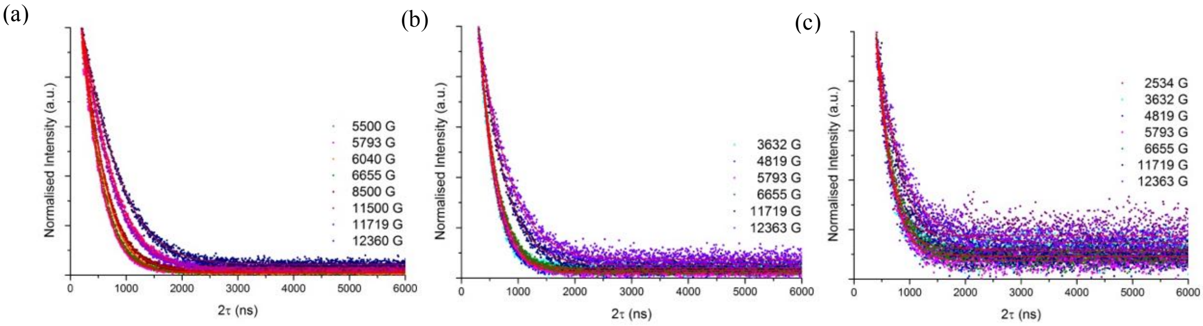

Figure S26. Normalised Hahn echo signal intensities of **1-Nd** as a function of the inter-pulse delay 2τ at different magnetic fields at 5 K, measured with π/τ (ns) of (a) 32/200; (b) 64/300, and (c) 128/400.

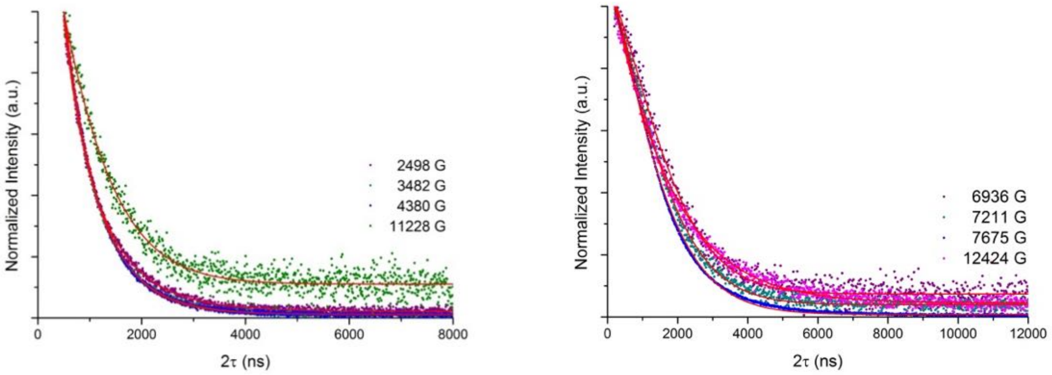

Figure S27. Normalised Hahn echo signal intensities of **1-Ce** and **1-Sm** as a function of the inter-pulse delay 2τ at different magnetic fields at 5 K, measured with π/τ (ns) of (a) 128/500 and (b) 32/200.

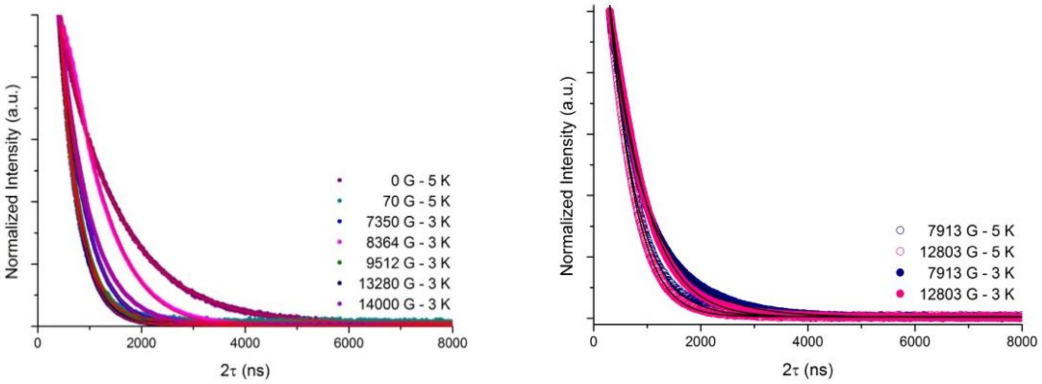

Figure S28. Normalised Hahn echo signal intensities at Q-band of (a) **1-Nd** and (b) **1-Ce** as a function of the inter-pulse delay 2τ at different magnetic fields at 5 K, measured with π/τ (ns) of 40/400.

6.2.3. Spin–lattice Relaxation Time (T_1)

Spin-lattice relaxation time data (Figs S29-S30) were acquired with a standard magnetisation inversion recovery sequence, *π - t - $\pi/2$ - τ - π - τ - echo*,[9] with t_π = 32 ns and τ = 300 ns for X-band and with t_π = 40 ns and τ = 400 ns for Q-band, and variable *t.* The spin-lattice relaxation time constant, T_1, was determined by fitting the experimental data to the following biexponential decay function:

$$Y(t) = Y(0) + Y_1 e^{(-t/T_1)} + Y_{SD} e^{(-t/T_{SD})} \quad \text{(Equation 3)}$$

where Y_1 and Y_{SD} are the amplitudes, and T_{SD} is the spectral diffusion time constant,[12] giving the results presented in Tables S3-S7. The presence of two decays is commonly attributed to the occurrence of both spectral diffusion (SD) and spin-lattice relaxation (T_1) of which the latter is usually assigned as being the slower process.[13] We notice that the magnetization recovery curves do not reach full saturation below 15 K, indicating that the T_1 spin-lattice relaxation time is very long. Fitting such curves to an exponential model is likely to introduce some inaccuracy in the determination of the T_1 values at these temperatures.

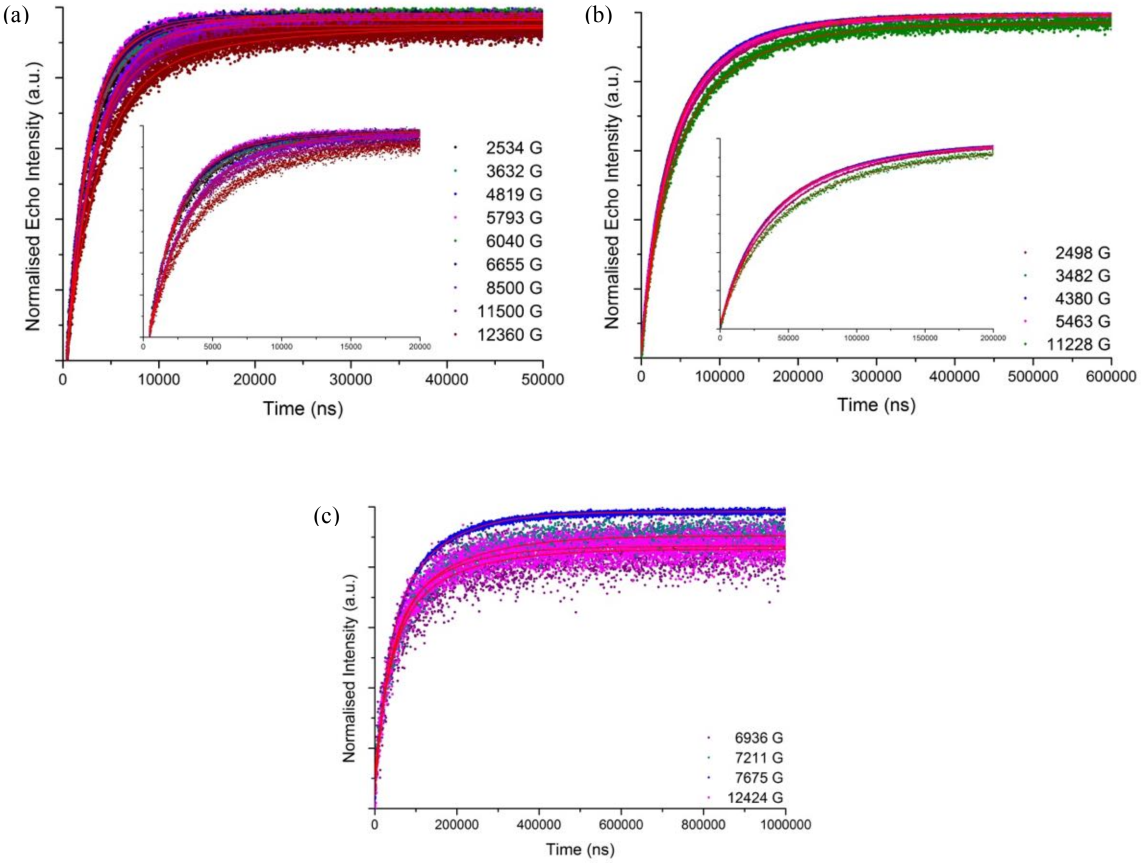

Figure S29. Inversion recovery data for (a) **1-Nd**, (b) **1-Ce** and (c) **1-Sm** measured at 5 K.

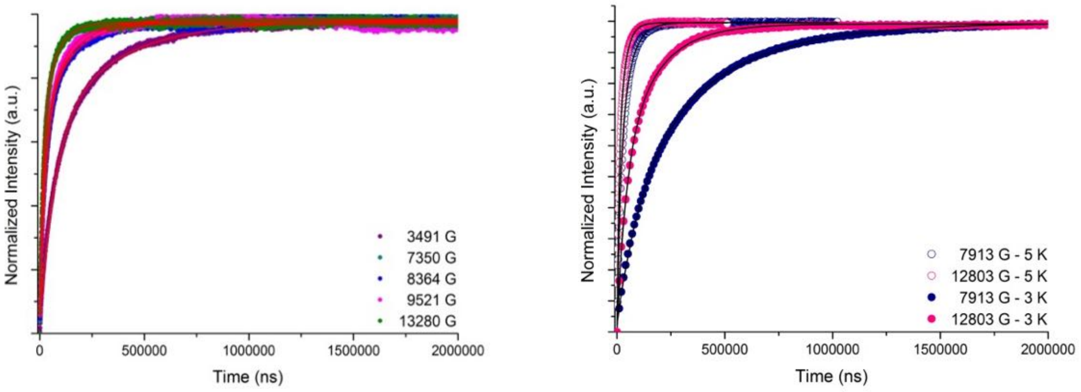

Figure S30. Inversion recovery data at Q-band of (a) **1-Nd** and (b) **1-Ce** measured at 3 and 5 K with π/τ (ns) of 40/400.

Table S3. Extracted spin lattice (T_1) and phase memory (T_m) times and the stretching parameter X for **1-Nd** at 5 K (10 mM tol-hex). T_m studies were performed with pulses of valuable lengths indicated in the following table in the format of π-τ (ns).

Field (G)	T_1 (ns)	T_{SD} (ns)	T_m (ns) 32-200ns	X (eqn1)	T_m (ns) 64-300ns	X (eqn1)	T_m (ns) 128-400ns	X (eqn1)
2534	4084±126	1715±65					254±75	1.031 ±0.167
3632	3660±62	1501±47			313±9	1.139 ±0.024	246±42	1.002 ±0.090
4819	4052±84	1706±28			362±6	1.201 ±0.015	316±29	1.113 ±0.065
5793	3501±54	1579±30	454±2	1.315 ±0.007	410±4	1.232 ±0.011	379±21	1.219 ±0.050
6040	4964±46	2181±31	535±1	1.367 ±0.005				
6655	4060±79	1756±28	463±2	1.295 ±0.005	419±5	1.225 ±0.013	373±24	1.138 ±0.051
8500	5771±107	2270±33	520±2	1.281 ±0.005				
11500	9864±245	2648±24	670±3	1.303 ±0.006				
11719			619±3	1.283 ±0.008	567±9	1.248 ±0.021	537±31	1.207 ±0.059
12360	12097±332	3215±40	678±5	1.239 ±0.010	643±13	1.223 ±0.025	581±40	1.166 ±0.068

Table S4. Extracted spin lattice (T_1) and phase memory (T_m) times and the stretching parameter X for **1-Ce** at 5 K (10 mM tol-hex). T_m studies were performed with pulses of valuable lengths indicated in the following table in the format of π-τ (ns).

Field (G)	T_1 (ns)	T_{SD} (ns)	T_m (ns) 128-500ns	X (eqn1)
2498	85458±287	28041±146	494±14	0.796±0.011
3482	78130±160	24613±74	538±6	0.863±0.005
4380	77178±159	23574±80	664±6	0.988±0.006
5463	81614±236	25262±110	-	
11228	89414±838	27081±469	1077±35	1.195±0.040

Table S5. Extracted spin lattice (T_1) and phase memory (T_m) times and the stretching parameter X for **1-Sm** at 5 K (10 mM tol-hex), T_m studies were performed with pulses of valuable lengths indicated in the following table in the format of π-τ (ns).

Field (G)	T_1 (ns)	T_{SD} (ns)	T_m (ns) 32-200ns	X (eqn1)
6936	149245±9106	38586±2934	1882±18	1.457±0.026
7211	155023±4426	38261±1436	1732±9	1.394±0.012
7675	117638±518	29498±224	1597±4	1.304±0.005
12424	125845±4849	30153±1518	1745±16	1.066±0.011

Table S6. Extracted spin lattice (T_1) and phase memory (T_m) times for **1-Nd** at 3 and 5 K (10 mM tol-hex) measured at Q-band.

Field (G)	T_1 (ns)	T_{SD} (ns)	T_m (ns)	X (eqn1)
0	-	-	1155±2	1.016±0.002
70	-	-	235±4	0.8±0.006
3491	341755±1634	76010±405	-	-
7350	135475±689	28923±163	618±1	1.193±0.001
8364	135575±1113	26677±264	1153±3	1.457±0.005
9521	87113±831	19079±351	481±1	1.125±0.002
13280	65100±733	15655±216	482±1	1.210±0.002
14000	-	-	657±1	1.114±0.002

Table S7. Extracted spin lattice (T_1) and phase memory (T_m) times for **1-Ce** at 3 and 5 K (10 mM tol-hex) measured at Q-band.

Field (G)	T_1 (ns)		T_{SD} (ns)		T_m (ns)		X (eqn1)	
	3 K	**5 K**	**3 K**	**5 K**	**3 K**	**5K**	**3 K**	**5K**
7913	406922 ±3494	49273 ±373	116122 ±2114	15191 ±208	582±3	527±2	0.860 ±0.003	1.021 ±0.003
12803	165852 ±2720	28959 ±232	42824 ±1175	8322 ±124	761±2	579±1	1.153 ±0.003	1.205 ±0.002

6.2.4 HYSCORE (Hyperfine sub–level correlation) Measurements

The HYSCORE spectra were recorded at X-band with a four–pulse sequence, $\pi/2$ - τ - $\pi/2$ - t_1 - π - t_2 - $\pi/2$ - *echo*,[9] with pulses $\pi/2$ and π of 16 and 32 ns, respectively, and fixed τ (136, 200 or 400 ns). Times t_1 and t_2 were varied from 100 to 5200 ns in increments of 20 ns. 256 data points were collected in both dimensions. A four-step phase-cycle procedure was used to eliminate unwanted echo contributions. Fourier transformation of the data in both directions yielded 2D (ν_1,ν_2) spectra in which the nuclear cross-peaks (i.e. peaks that correlate nuclear frequencies from opposite spin-manifolds) of the ^{1}H and ^{13}C nuclei appeared in the (+,+) quadrant of the (ν_1,ν_2) map, at separations equivalent with the corresponding hyperfine coupling frequencies (weak coupling regime: $2|\nu_n|>|A|$).[9] The contour lineshape of the cross peaks, and their displacement from the anti-diagonal about the nuclear Larmor frequency (ν_n), relate to the magnitude and anisotropy of the hyperfine couplings, and thus analysis of the HYSCORE spectra allows to determine such parameters. Spectra modelling with EasySpin[7] has assumed that the total hyperfine coupling matrix (A) for a given ^{13}C nucleus n is determined by the spin density at nucleus n (A^{Cn}), and the point dipole (through space) interactions with spin density at other atoms k (A^{dip}), according to the equation: $A = A^{Cn} + A^{\mathrm{dip}}$.[10] A^{Cn} relates directly to the covalency. A^{dip} is given by Equation (4):

$$A^{\mathrm{dip}} = \frac{\mu_0}{4\pi h}\beta_e\beta_n \sum_k \rho_k \frac{3(\mathbf{g}.\mathbf{n_k})(\tilde{\mathbf{n}}_\mathbf{k}.g_n\mathbf{1})-\mathbf{g}.g_n\mathbf{1}}{r_k^3} \qquad \text{(Equation 4)}$$

where g and $g_n\mathbf{1}$ are the electron and nuclear g (3x3) matrices (g_n is a scalar; **1** is the unit matrix), β_e and β_n are the electron and nuclear magnetons, ρ_k is the electron spin population at atom k ($0 \leq \rho_k \leq 1$),

r_k is $n \ldots k$ distance, n_k and $\tilde{n}_k$ are the $n \ldots k$ unit vector expressed in the molecular frame (a column vector) and its transpose, h is the Plank's constant, and μ_0 is the vacuum permittivity. It is also assumed that g_z lies along the C_3 unique axis (Fig. 6), and the dominant spin density is located at the lanthanide ion (ρ_{Ln} = 1). A^{dip} is then calculated for each unique carbon position in the Cp^{tt} ligands, using the crystallographic coordinates of the atoms. Simulations considering only A^{dip} appear to reproduce satisfactory the experimental data of **1-Nd** and **1-Ce** (Figs. 5). Addition of A^{Cn} to A^{dip} was not necessary to satisfactory model the data (Figs S31-S32).

Table S8. Calculated dipolar interactions of **1-Nd** used for HYSCORE simulations.

1-Nd	A_{xx}	A_{xy}	A_{xz}	A_{yx}	A_{yy}	A_{yz}	A_{zx}	A_{zy}	A_{zz}
C1	2.05	0.52	-1.49	0.19	-0.47	-0.08	-0.25	-0.04	-0.12
C2	2.02	1.45	0.025	-0.53	-0.25	0.004	0.004	0.002	-0.22
C3	2.03	0.47	1.52	-0.17	-0.48	0.08	0.255	0.03	-0.12
C4	2.34	-1.58	1.10	-0.58	-0.37	-0.16	0.19	-0.07	-0.22
C5	2.30	-1.52	-1.16	-0.555	-0.38	-0.165	-0.2	0.08	-0.21
H2	2.87	-4.59	0.08	-1.68	0.11	0.02	0.01	0.01	-0.53
H4	2.75	-1.04	0.73	-1.85	-0.03	-0.195	0.12	-0.09	-0.08
H5	2.71	-2.30	-1.76	-1.78	-0.11	0.46	-0.295	0.21	-0.17

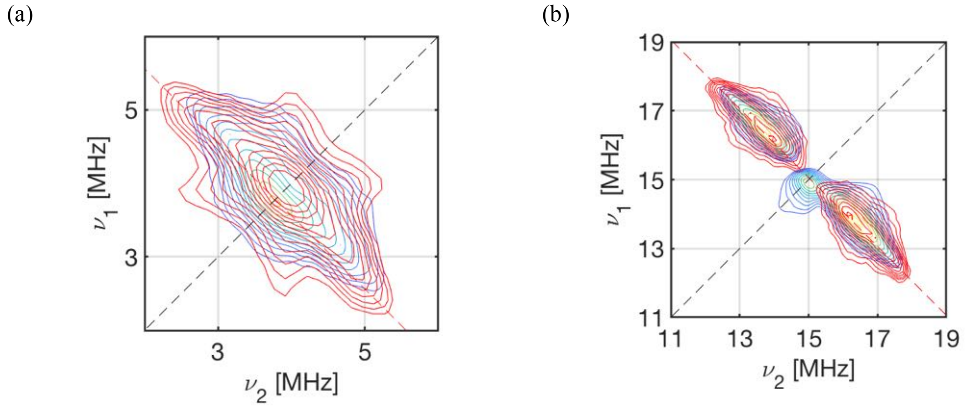

Figure S31. X-band HYSCORE spectra of **1-Nd** at B_0 = 353.0 mT and at 4.3 K (a) ^{13}C region with the Larmor frequency of ν_n = 3.78 MHz and the calculated spectrum (red ridges) based on the C – Nd dipole model with additional spin desity of 0.5 MHz on C1-C5 atoms; (b) ^{1}H region (Larmor frequency ν_n = 15.03 MHz) with the simulation based on A^{dip} and additional A^{Cn} of 0.5 MHz on the three protons of the Cp^{tt} ring.

Modelling of ^{1}H HYSCORE region for **1-Ce** involved a similar approach. We initially calculated the point dipolar ^{1}H hyperfine constants (A^{dip}) for all protons of the cyclopentadienyl rings, and all protons of the methyl groups supposed to be close to the Ln(III) ion. This calculation gave the simulation spectrum presented in Figure S38. We calculated the A^{dip} for all the hydrogen atoms of the molecule by using the crystal structure coordinates; the simulated spectra took into account the H atoms on the Cp^{tt} ring (H^2, H^4, H^5) and the three closest H atoms of the ^{t}Bu groups. Thus, our experimental HYSCORE data, for both carbon and hydrogen regions, can be nicely reproduced with only a dipolar interaction model without any additional contribution from spin density on the Cp^{tt} ligands. Additional spin density was introduced in Fig. S34 to highlight the difference of the extend of the ridges by considering small amount of spin density in the simulation.

Table S9. Calculated dipolar interactions of **1-Ce** used for HYSCORE simulations.

1-Ce	A_{xx}	A_{xy}	A_{xz}	A_{yx}	A_{yy}	A_{yz}	A_{zx}	A_{zy}	A_{zz}
C1	-0.05	0.86	1.57	0.51	-0.40	0.66	0.32	0.22	0.15
C2	1.10	0.04	1.81	0.02	-0.75	0.02	0.37	0.006	0.03
C3	-0.02	-0.825	1.49	-0.49	-0.38	-0.62	0.30	-0.21	0.13
C4	-1.39	-0.17	0.64	-0.10	-0.71	-0.655	-0.13	-0.22	0.52
C5	-1.38	0.13	0.50	0.08	-0.69	0.63	0.10	0.21	0.51
H2	4.67	0.16	3.37	0.09	-1.83	0.04	0.68	0.01	-0.32
H4	-3.77	0.40	-0.90	0.24	-1.19	-2.53	-0.18	-0.85	1.17
H5	-3.47	-0.45	-1.09	-0.27	-1.21	2.26	-0.22	0.76	1.11

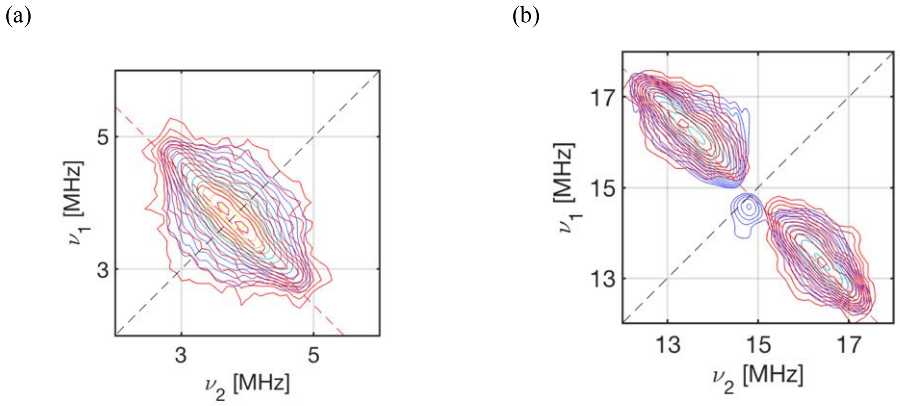

Figure S32. X-band HYSCORE spectra of **1-Ce** at $B_0 = 348.2$ mT and at 5 K (a) ^{13}C region with the Larmor frequency of $\nu_n = 3.73$ MHz and the calculated spectrum (red ridges) based on the C dipole model and additional spin desity of 0.5 MHz on C1-C5 atoms; (b) ^{1}H region (Larmor frequency $\nu_n = 14.82$ MHz) with the simulation based on dipolar interactions of Ce^{III} ion with three protons on the Cp^{tt} ring and additional A^{Cn} on the same H atoms.

7. Magnetic studies

Magnetic measurements were performed on solid-state polycrystalline samples restrained in a known amount of eicosane (to prevent orientation of the crystallites with the applied magnetic field) and flame-sealed under vacuum in an NMR-type tube. Data were collected with a Quantum Design MPMS-XL7 SQUID magnetometer under the dc magnetic field of 0.1 T by varying the temperature from 2 to 300 K. Experimental data were corrected for the diamagnetism of the sample, using Pascals constants, and for the contribution of the sample holder and eicosane. For **1-Nd**, the measured χT value of 1.46 cm^{3}mol^{-1}K at 300 K (Fig. S35a), is very close to the expected value of 1.63 cm^{3}mol^{-1}K (Nd^{III}, S = 3/2, L = 6, $^4I_{9/2}$). The χT product decreases gradually upon cooling up to 50 K, while below this temperature it drops to reach 0.45 cm^{3}mol^{-1}K at 2 K, in a field of 0.5 T. The decrease of χT at low temperatures can be attributed to the depopulation of the Zeeman split crystal field levels, also termed as Stark sub-levels. Isothermal magnetisation measurements of 1 at a field range of 0 – 7 T and at temperatures of 2, 4 and 7 K are depicted in Fig. S35b. The lack of magnetisation for both temperatures can be ascribed to the large magnetic anisotropy of the system and/or to the presence of low-lying excited states, which is also indicated by the non-overlapping curves in the reduced magnetisation plot (Fig. S36).

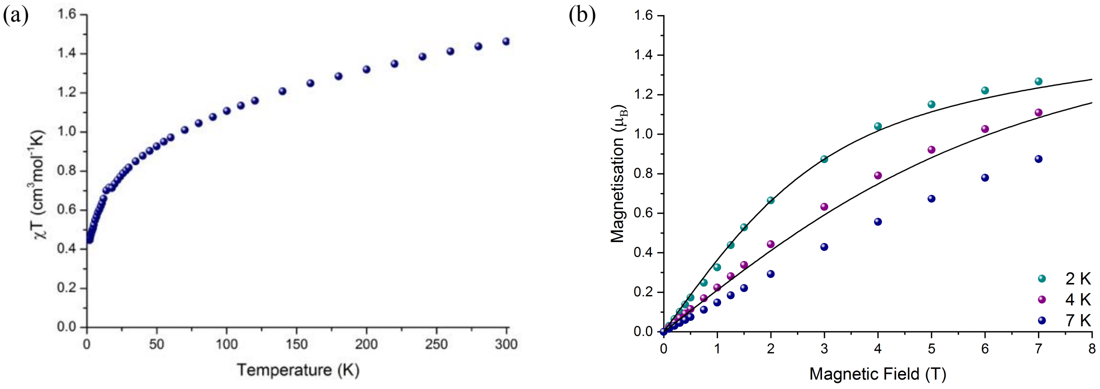

Figure S35. (a) Variable-temperature magnetic susceptibility of **1-Nd** in a 0.1 T static magnetic field; (b) Experimental (dots) and calculated (line) field dependence of the magnetisation curve.

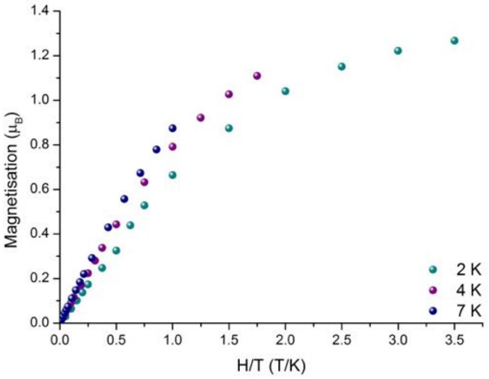

Figure S36. Reduced magnetisation of **1-Nd** at 2, 4 and 7 K.

DC magnetic measurements were performed for **1-Ce** at variable temperatures and with 0.5 T applied magnetic field (Fig. S37a). The χT product at 300 K is 0.70 cm^{3}mol^{-1}K, which is very close to the expected value of 0.80 cm^{3}mol^{-1}K (Ce^{III}, S = 1/2, L = 3, $^2F_{5/2}$). It remains stable down to 75 K, when it starts decreasing uniformly upon cooling to 15 K, and then appears to increase with further cooling, suggesting some field orientation effects. Field-dependent magnetisation measurements were carried out at 2 and 4 K, under 0 – 7 T field (Fig. S37b). The magnetisation curve at 2 K does not reach saturation at 7 T, while the reduced magnetisation plots at 2 and 4 K do not superpose over a common master curve, which is evidence of anisotropic effects.

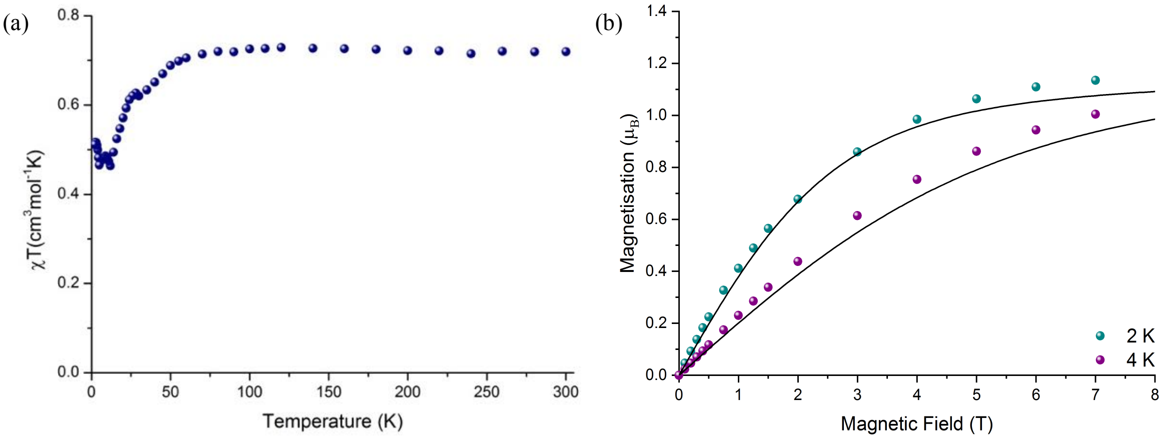

Figure S37. (a) Variable-temperature magnetic susceptibility of **1-Ce** in a 0.5 T static magnetic field; (b) Experimental (dots) and calculated (line) field dependence of the magnetisation curve.

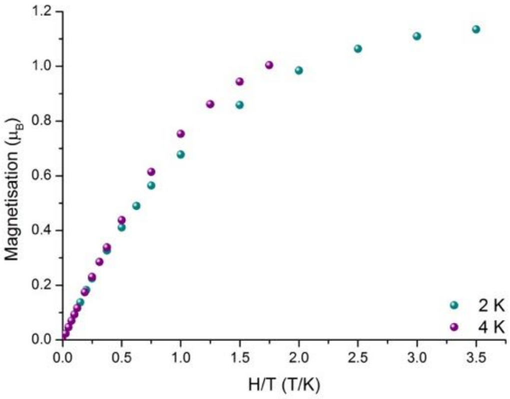

Figure S38. Reduced magnetisation of **1-Ce** at 2 and 4 K.

For **1-Sm,** DC magnetic susceptibility measurements were recorded at 0.5 T applied magnetic field. The magnetic susceptibility-temperature (χT) product is 0.20 cm^{3}mol^{-1}K at 300 K, close to the expected value of 0.09 cm^{3}mol^{-1}K (Sm^{III}, S = 5/2, L = 5, $^6H_{5/2}$). It decreases gradually with the decrease of the temperature (Fig. S39a), while beneath 50 K additional undulation features were observed suggesting the presence of further interactions. Field-dependent magnetisation measurements were performed at low temperatures (2 and 4 K) with variation od the field from 0 to 7 T (Fig. S39b). The isothermal magnetisation curves do not reach saturation in the range of field measured; this is indicative of anisotropic effects. In agreement with this, the magnetisation values at 2 K and 7 T are significantly lower than the theoritical saturation values.

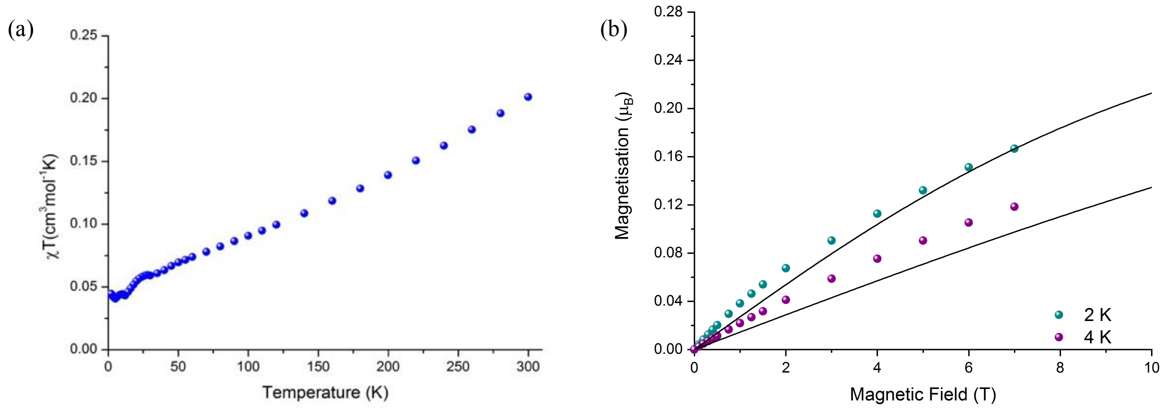

Figure S39. (a) Variable-temperature magnetic susceptibility of **1-Sm** in a 0.5 T static magnetic field; (b) Field dependence of the magnetisation at 2 and 4 K

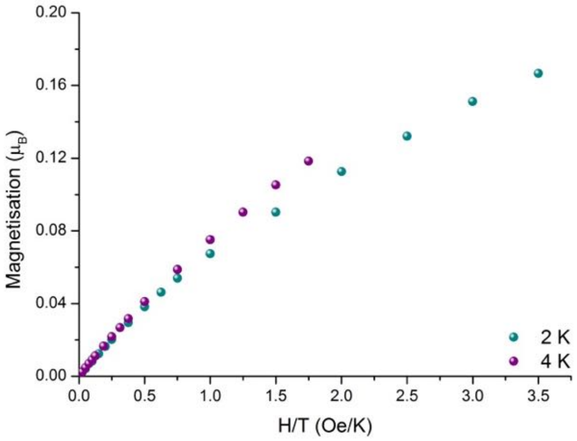

Figure S40. Reduced magnetisation of **1-Sm** at 2 and 4 K.

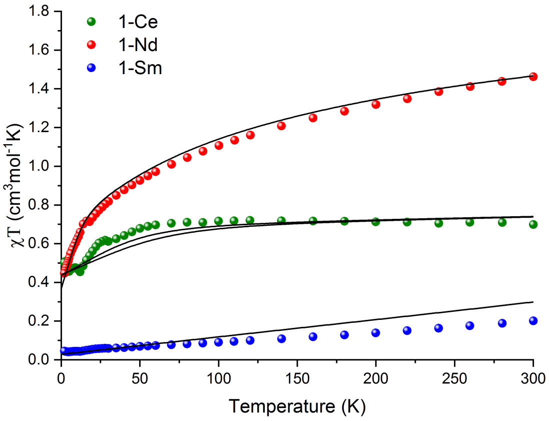

Figure 41. Experimental (dots) and calculated (line) magnetic susceptibility curves of **1-Nd, 1-Ce** and **1-Sm**.

8. Computational studies

8.1 Methods

The following crystal field Hamiltonian was used:

$$H_{cf} = \sum_{k,q} B(k,q)O(k,q)$$

where *O(k, q)* are extended Stevens operators, *k* is the rank of the irreducible tensor operator (ITO) and q is the component of the ITO.

8.1.1 Calculated properties of **1-Nd, 1-Ce** and **1-Sm**

Table S10. Crystal field parameters for **1-Nd**

k	*q*	*B*(*k*, *q*)
2	-2	0.08487
2	-1	0.02020
2	0	6.68254
2	1	0.15109
2	2	0.06585
4	-4	0.00249
4	-3	-0.00468
4	-2	0.00214
4	-1	-0.00063
4	0	-0.01480
4	1	0.00345
4	2	-0.00132
4	3	0.01239
4	4	0.00122
6	-6	0.02087
6	-5	-0.00029
6	-4	-0.00013
6	-3	0.00012
6	-2	-0.00032
6	-1	0.00002
6	0	-0.00140
6	1	-0.00019
6	2	0.00022
6	3	-0.00026
6	4	-0.00012
6	5	0.00073
6	6	-0.04738

Table S11. Energies (in cm^{-1}) and g-values for **1-Nd**

Energy	g_x	g_y	g_z	Angle (°)
0	1.06	2.23	2.38	0
28.20	0.03	0.21	0.90	86.69
132.07	0.55	3.50	3.73	37.80
507.21	0.02	0.04	5.42	88.96
608.92	2.50	2.58	2.70	80.53

Table S12. Crystal field states of **1-Nd**

Energy (cm^{-1})	**$\lvert m_j\rangle$ wavefunction contributions (%)**									
	$\lvert -4.5\rangle$	$\lvert -3.5\rangle$	$\lvert -2.5\rangle$	$\lvert -1.5\rangle$	$\lvert -0.5\rangle$	$\lvert 0.5\rangle$	$\lvert 1.5\rangle$	$\lvert 2.5\rangle$	$\lvert 3.5\rangle$	$\lvert 4.5\rangle$
0.00	0.00	15.87	31.08	0.06	0.00	0.01	0.01	40.97	11.98	0.01
28.20	2.46	0.01	0.06	69.34	0.00	0.05	19.11	0.02	0.01	8.95
132.07	0.01	0.00	0.00	0.00	77.84	22.10	0.04	0.00	0.00	0.00
507.21	44.28	0.00	0.00	5.71	0.00	0.00	5.72	0.00	0.01	44.28
608.92	0.00	61.38	4.04	0.00	0.00	0.00	0.00	23.82	10.74	0.01

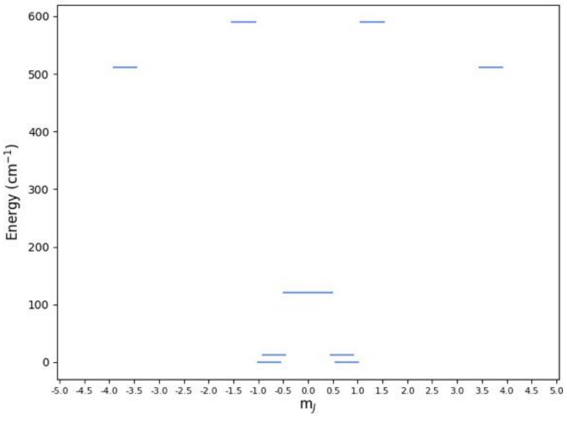

Figure 42. Crystal field eigenstates of **1-Nd**.

Table S13. Crystal field parameters for **1-Ce**

Molecule 1			**Molecule 2**		
k	q	$B\ (k,q)$	k	q	$B\ (k, q)$
2	-2	-2.7510	2	-2	3.5746
2	-1	0.5796	2	-1	-27.5754
2	0	48.7695	2	0	42.9627
2	1	29.0233	2	1	-52.8239
2	2	-1.4390	2	2	2.8387
4	-4	0.1221	4	-4	-0.2439
4	-3	-0.1821	4	-3	0.0300
4	-2	-0.0237	4	-2	0.1739
4	-1	0.2581	4	-1	-1.1819
4	0	0.5216	4	0	0.4514
4	1	1.1359	4	1	-2.0242
4	2	0.0485	4	2	0.0911
4	3	0.2029	4	3	0.2065
4	4	-0.0966	4	4	-0.1112

Table S14. Energies, g-values and crystal field states of **1-Ce**, molecule 1 and molecule 2.

Energies and g-values for CeCp^{tt}_3, molecule 1

Energy					$\lvert m_J\rangle$ wavefunction contributions (%)					
(cm^{-1})	g_x	g_y	g_z	Angle (°)	$\lvert -2.5\rangle$	$\lvert -1.5\rangle$	$\lvert -0.5\rangle$	$\lvert 0.5\rangle$	$\lvert 1.5\rangle$	$\lvert 2.5\rangle$
0	0.71	2.09	3.03	0	0.03	2.63	59.46	37.80	0.07	0.01
134.63	0.44	0.47	2.65	89.68	0.77	55.67	1.76	0.96	40.40	0.43
859.46	0.16	0.19	3.94	89.35	95.22	1.17	0.01	0.00	0.07	3.54

Energies and g-values for CeCp^{tt}_3, molecule 2

Energy					$\lvert m_J\rangle$ wavefunction contributions (%)					
(cm^{-1})	gx	g_y	g_z	Angle (°)	$\lvert -2.5\rangle$	$\lvert -1.5\rangle$	$\lvert -0.5\rangle$	$\lvert 0.5\rangle$	$\lvert 1.5\rangle$	$\lvert 2.5\rangle$
0	0.73	2.22	2.92	0	0.25	8.95	42.80	46.30	1.68	0.01
105.15	0.31	0.36	2.67	88.25	2.98	45.26	5.52	5.25	38.25	2.73
800.42	0.15	0.21	3.95	88.66	84.63	5.17	0.11	0.01	0.69	9.39

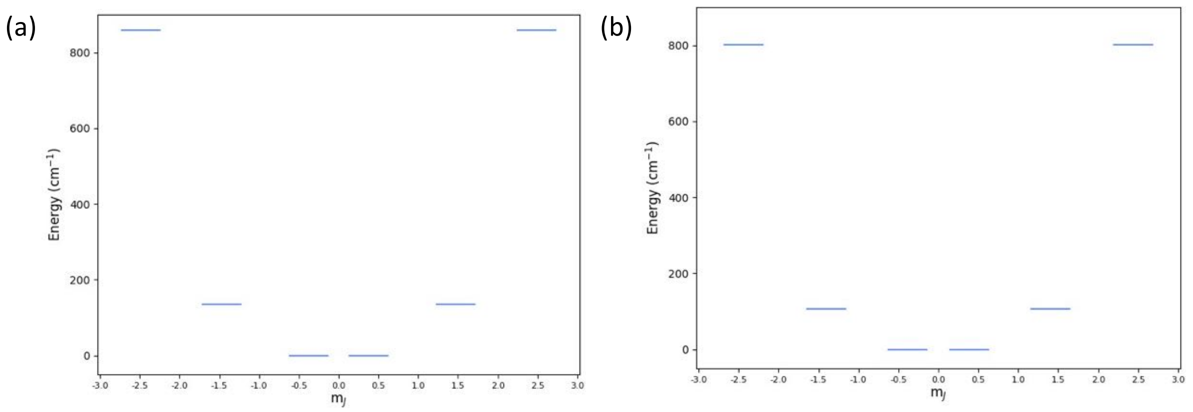

Figure 43. Crystal field eigenstates of **1-Ce** (a) molecule 1 and (b) molecule 2

Table S15. Crystal field parameters for **1-Sm**

k	*q*	*B* (*k*, *q*)
2	-2	-0.1011
2	-1	-1.3342
2	0	-27.2901
2	1	2.7270
2	2	0.3286
4	-4	0.0463
4	-3	0.1179
4	-2	0.0073
4	-1	-0.0589
4	0	-1.5096
4	1	0.1090
4	2	-0.0296
4	3	0.1349
4	4	0.1078

Table S16. Crystal field parameters for **1-Sm**

Energy					$|m_J\rangle$ wavefunction contributions (%)					
(cm^{-1})	g_x	g_y	g_z	Angle (°)	$|-2.5\rangle$	$|-1.5\rangle$	$|-0.5\rangle$	$|0.5\rangle$	$|1.5\rangle$	$|2.5\rangle$
0	0.41	0.41	0.76	0	84.8764	0.0169	0.0001	0.0017	0.0002	15.1047
400.75	0.01	0.01	0.11	0.95	0.0001	0.0019	87.689	12.3008	0.0067	0.0017
690.06	0.59	1.13	1.16	89.97	0.0152	99.6902	0.0037	0.0049	0.2841	0.0019

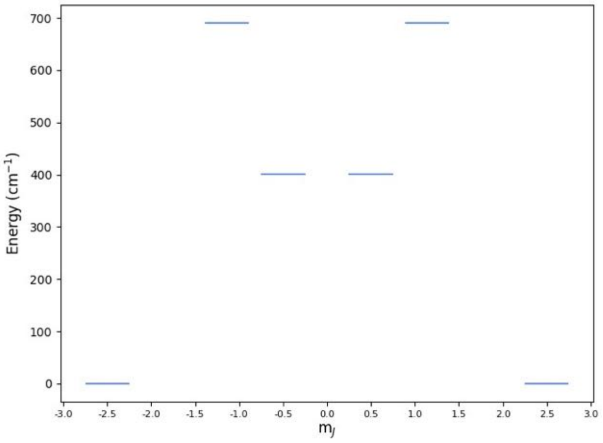

Figure 44. Crystal field eigenstates of **1-Sm**.

8.1.2 Optimized Geometries

Atomic coordinates from X-ray diffraction experiments were used as provided. The unit cell of $\mathrm{CeCp}^{tt}{}_3$ contains two molecules (labelled molecule 1 and molecule 2, respectively), therefore we computed the electronic structure for both.

Table S17. Atomic coordinates of **1-Nd**.

Atom	x (˚A)	y (˚A)	z (˚A)
Nd	4.79355	4.156354	16.07213
C	3.028344	2.996043	14.08655
C	4.190482	2.231965	13.95335
H	4.249628	1.327027	14.15781
C	5.251442	3.001876	13.47417
C	4.744545	4.327834	13.35481
H	5.229562	5.07002	13.07211
C	3.3866	4.327834	13.73366
H	2.824046	5.068445	13.75049
C	1.609481	2.428331	14.13499
C	0.593052	3.433493	14.69721
H	0.767377	3.578201	15.62943
H	-0.29548	3.086935	14.58701
H	0.671451	4.266338	14.22413
C	1.500823	1.164588	14.97053
H	2.115083	0.506703	14.63728
H	0.605594	0.822852	14.91851
H	1.713681	1.367467	15.88451
C	1.228441	2.103646	12.70091
H	1.281139	2.901379	12.16773

H	0.332521	1.761677	12.67648
H	1.832752	1.445275	12.34965
C	6.508663	2.459438	12.77702
C	7.021357	1.185974	13.42054
H	7.334195	1.379346	14.30706
H	7.742975	0.831698	12.89618
H	6.311159	0.541679	13.46486
C	6.100508	2.125032	11.33083
H	5.380202	1.490284	11.34052
H	6.851122	1.751334	10.86524
H	5.814056	2.92677	10.88673
C	7.624794	3.489875	12.73896
H	7.325215	4.269254	12.26547
H	8.388504	3.117557	12.29078
H	7.86756	3.733116	13.63515
C	3.767658	6.769774	16.60182
C	4.655953	7.014746	15.56735
H	4.394756	7.300838	14.72156
C	5.983628	6.787272	15.92889
C	5.917718	6.338157	17.2834
H	6.643669	6.088772	17.80819
C	4.574257	6.334269	17.68993
H	4.263567	6.0885	18.53142
C	2.303285	7.17806	16.70562
C	2.234544	8.334871	17.69685
H	2.601854	8.056964	18.53919
H	1.319551	8.598371	17.81794
H	2.739311	9.077388	17.35705
C	1.446788	6.04458	17.24189
H	1.544961	5.274747	16.67654
H	0.526954	6.317607	17.25424
H	1.728271	5.825233	18.1329
C	1.738776	7.636896	15.35976
H	2.284047	8.343659	15.00816
H	0.84094	7.955146	15.48154
H	1.73539	6.898812	14.74554
C	7.239202	7.300546	15.25077
C	7.025068	7.508578	13.75095
H	6.858214	6.660723	13.3317
H	7.810708	7.905354	13.3675
H	6.273091	8.087741	13.61256
C	8.440288	6.382874	15.44106
H	8.677828	6.353808	16.37019
H	9.182935	6.716016	14.93099

H	8.218255	5.49804	15.1397
C	7.563755	8.671221	15.84932
H	6.806629	9.251804	15.74739
H	8.32077	9.047758	15.39622
H	7.766666	8.571152	16.78308
C	4.22603	2.688856	18.48741
C	5.509034	3.227405	18.72441
H	5.699513	3.874811	19.36532
C	6.462203	2.649972	17.85773
C	5.743864	1.765352	17.01873
H	6.108957	1.248773	16.33663
C	4.383186	1.792571	17.3872
H	3.701168	1.308402	16.98055
C	3.051169	2.671358	19.44405
C	3.310299	1.495105	20.41106
H	3.345702	0.674294	19.91344
H	2.600949	1.447569	21.05581
H	4.146021	1.630462	20.86363
C	1.716101	2.453606	18.75382
H	1.566185	3.157122	18.11817
H	1.013256	2.459574	19.40863
H	1.724676	1.608239	18.30105
C	2.9989	3.948711	20.3038
H	3.84731	4.079732	20.73377
H	2.313492	3.85811	20.97013
H	2.803554	4.703651	19.74436
C	7.968126	2.636362	18.0757
C	8.709385	2.1192	16.86131
H	8.36827	1.253497	16.62267
H	9.645326	2.049616	17.06193
H	8.583619	2.725058	16.12693
C	8.218931	1.65842	19.24338
H	7.760025	1.971828	20.02597
H	9.160847	1.609795	19.42247
H	7.892175	0.788051	19.00675
C	8.526976	3.987595	18.48049
H	8.46544	4.594367	17.7397
H	9.446432	3.889198	18.7387
H	8.022252	4.33318	19.22056

Table S18. Atomic coordinates of **1-Ce**.

Molecule 1				**Molecule 2**			
Atom	x (˚A)	y (˚A)	z (˚A)	Atom	x (˚A)	y (˚A)	z (˚A)
Ce	4.8059	4.8528	5.8561	Ce	6.9087	5.2606	15.6379
C	6.3706	3.0435	7.5021	C	6.3465	2.5611	16.7336
C	5.4906	2.2188	6.927	C	7.4168	3.07	17.4795
H	5.7492	1.5805	6.3007	H	7.3142	3.3011	18.3742
C	4.1524	2.37	7.3196	C	8.5815	3.2098	16.8631
C	4.2366	3.5177	8.2029	C	8.335	2.9112	15.4008
H	3.5001	3.9195	8.6045	H	8.9328	2.9792	14.691
C	5.5813	3.9572	8.3815	C	6.9653	2.5037	15.3694
H	5.8936	4.6486	8.9187	H	6.5156	2.2348	14.6008
C	7.869	2.9717	7.6278	C	5.1265	1.8161	17.0653
C	3.0208	1.4072	7.2489	C	10.0004	3.2682	17.4461
C	3.2565	0.369	8.4325	C	10.985	3.8563	16.4647
H	2.5495	-0.2806	8.433	H	10.9363	3.3747	15.6361
H	4.0983	-0.0742	8.3056	H	10.771	4.7793	16.3124
H	3.2629	0.8361	9.2705	H	11.8727	3.788	16.8235
C	1.6743	2.0469	7.4864	C	10.072	4.0167	18.7455
H	0.9872	1.3785	7.4269	H	9.444	3.6397	19.3663
H	1.6583	2.4452	8.3593	H	10.9586	3.9485	19.1049
H	1.5192	2.7238	6.8229	H	9.8569	4.9398	18.5938
C	3.0127	0.6103	5.9495	C	10.3721	1.8048	17.6875
H	2.267	0.0049	5.9497	H	10.3275	1.3229	16.858
H	2.9365	1.2109	5.2047	H	11.2644	1.7554	18.0382
H	3.8293	0.1105	5.8753	H	9.759	1.4176	18.3159
C	6.1544	5.019	3.2466	C	5.1895	7.1336	17.0574
C	4.8645	5.368	2.9875	C	6.2267	7.9123	16.6452
H	4.6048	6.2147	2.7051	H	6.0983	8.5938	16.025
C	3.9837	4.3221	3.1877	C	7.4278	7.671	17.1576
C	4.7712	3.2111	3.6686	C	7.2289	6.5233	18.088
H	4.4705	2.3646	3.9067	H	7.8758	6.1192	18.6201
C	6.0993	3.6944	3.6961	C	5.831	6.1633	17.9977
H	6.8362	3.1996	3.975	H	5.4115	5.4617	18.442
C	7.4284	5.6429	2.8246	C	3.669	7.3579	17.1163
C	8.5601	5.6145	3.8119	C	2.9112	6.1338	17.4755
H	9.3282	6.0447	3.4308	H	3.2495	5.7782	18.2993
H	8.2984	6.0756	4.6123	H	1.9816	6.3523	17.5779
H	8.7761	4.703	4.0246	H	3.0108	5.4807	16.7788

Atom	x (˚A)	y (˚A)	z (˚A)	Atom	x (˚A)	y (˚A)	z (˚A)
C	7.2153	7.1382	2.5694	C	3.1795	7.9686	15.8189
H	8.0447	7.5379	2.2968	H	3.6932	8.7561	15.6229
H	6.5606	7.2558	1.8781	H	3.2822	7.3338	15.1072
H	6.908	7.5603	3.3761	H	2.253	8.2054	15.9064
C	7.8336	5.049	1.4859	C	3.4882	8.4346	18.2254
H	8.6595	5.4436	1.1969	H	3.9814	9.2241	17.9889
H	7.9476	4.0998	1.5774	H	2.5579	8.6528	18.3129
H	7.1495	5.227	0.8358	H	3.8164	8.0923	19.061
C	2.4651	4.2054	2.8835	C	8.6668	8.5421	17.3205
C	1.9678	5.4663	2.2122	C	5.8766	5.2162	12.9884
H	2.4887	5.6365	1.4233	C	7.1063	4.871	12.7744
H	1.0453	5.3575	1.9678	H	7.3084	4.0229	12.4505
H	2.0529	6.2066	2.8171	C	8.087	5.7576	13.0276
C	2.3178	3.0885	1.8373	C	7.348	7.0178	13.4791
H	2.8187	3.3182	1.0517	H	7.7081	7.8439	13.7081
H	2.6518	2.2645	2.2004	C	5.9386	6.6154	13.4693
H	1.3916	2.9848	1.6082	H	5.2153	7.1437	13.7187
C	1.6926	3.8762	4.126	C	4.5399	4.6046	12.6861
H	2.0423	3.0723	4.5164	C	3.7121	4.4545	13.962
H	1.7756	4.5988	4.7535	H	4.1951	3.9167	14.5946
H	0.768	3.7497	3.9041	H	3.546	5.3207	14.3394
C	5.1858	7.4416	7.0625	H	2.8768	4.0295	13.7539
C	4.0576	7.0408	7.6631	C	4.6688	3.1551	12.0678
H	4.0381	6.871	8.5764	H	5.1308	2.5838	12.6857
C	2.9324	6.8887	6.8956	H	3.7927	2.8002	11.8982
C	3.4455	7.2371	5.5864	H	5.1603	3.2006	11.2448
H	2.9458	7.2394	4.8021	C	3.8145	5.4365	11.6791
C	4.7819	7.5639	5.6727	H	2.961	5.0393	11.4905
H	5.3291	7.8184	4.964	H	3.6861	6.3211	12.028
C	6.4449	8.1715	7.5983	H	4.331	5.4828	10.8709
C	7.6399	8.099	6.6483	C	9.5402	5.9475	12.6351
H	7.386	8.4412	5.7878	C	4.1456	1.5648	15.9504
H	8.3621	8.6232	7.0009	H	3.392	1.0661	16.2935
H	7.9222	7.1852	6.5577	H	3.8378	2.395	15.5913
C	6.8131	7.64	8.9566	H	4.5688	1.0488	15.2579
H	6.0518	7.6931	9.539	C	4.4488	2.6204	18.1665
H	7.0917	6.7242	8.8775	H	3.6402	2.1833	18.4314
H	7.5316	8.1622	9.3207	H	5.0418	2.6861	18.9216
C	6.0287	9.6635	7.7985	H	4.2503	3.5016	17.8419
H	5.7841	10.0439	6.9521	C	5.6235	0.4755	17.6679
H	5.2805	9.7096	8.3985	H	4.8651	-0.0652	17.9082
H	6.7661	10.1543	8.1691	H	6.1529	0.0101	17.0174
C	1.5395	6.9001	7.3157	H	6.1508	0.6512	18.448
C	8.1241	1.8082	8.6229	C	9.9624	7.7818	17.3852

Atom	x (˚A)	y (˚A)	z (˚A)	Atom	x (˚A)	y (˚A)	z (˚A)
H	7.6674	1.021	8.3203	H	10.6907	8.3998	17.4875
H	9.0672	1.6317	8.6741	H	9.9451	7.1823	18.1351
H	7.7985	2.0535	9.4927	H	10.0806	7.2794	16.5764
C	8.6019	4.1526	8.1518	C	8.7295	9.4652	16.0799
H	8.183	4.4527	8.9629	H	7.9128	9.9647	16.01
H	9.5115	3.9115	8.3305	H	9.4689	10.0709	16.1684
H	8.5767	4.8575	7.5004	H	8.8464	8.932	15.2892
C	8.5703	2.5644	6.3754	C	8.5235	9.4607	18.5591
H	8.1294	1.7976	5.9976	H	7.6933	9.9408	18.5086
H	8.5466	3.2876	5.7453	H	8.5355	8.9272	19.3577
H	9.4814	2.3416	6.5754	H	9.2527	10.085	18.5813
C	1.1443	5.6218	8.0773	C	10.0433	4.5451	12.2935
H	0.2234	5.6729	8.3335	H	9.4783	4.1566	11.6216
H	1.2806	4.8584	7.5111	H	10.943	4.5998	11.9621
H	1.6928	5.5371	8.8627	H	10.0258	3.9977	13.0819
C	1.3769	8.1	8.248	C	9.6311	6.8216	11.3651
H	0.4621	8.1449	8.551	H	9.0685	6.452	10.6813
H	1.9558	8.0007	9.0045	H	9.3417	7.7138	11.5707
H	1.5933	8.9054	7.7766	H	10.5396	6.8431	11.0564
C	0.5879	7.1671	6.1203	C	10.4269	6.5469	13.6833
H	-0.3161	7.176	6.4271	H	11.3202	6.6255	13.3412
H	0.8034	8.029	5.7367	H	10.0979	7.4175	13.9212
H	0.7077	6.4892	5.4588	H	10.4302	5.9836	14.4608

Table S19. Atomic coordinates of **1-Sm**.

Atom	x (˚A)	y (˚A)	z (˚A)
Sm	4.723463	4.136775	9.822412
C	5.747163	6.726381	9.303253
C	4.858197	6.976031	10.36581
H	5.11912	7.266416	11.23239
C	3.527542	6.735692	9.968704
C	3.592557	6.287215	8.624393
H	2.849698	6.036595	8.088216
C	4.947257	6.27577	8.21577
H	5.267773	6.011378	7.36105
C	7.200354	7.16225	9.190654
C	7.250494	8.343964	8.210098
H	8.179054	8.635901	8.09853
H	6.714123	9.08399	8.564397
H	6.889062	8.063665	7.34214
C	7.764905	7.621396	10.53737
H	7.738768	6.87652	11.17394
H	7.226793	8.364331	10.8817
H	8.691916	7.916242	10.41927
C	8.078812	6.054441	8.625424
H	8.034185	5.270382	9.212486
H	9.00487	6.368298	8.569555
H	7.76093	5.811581	7.730649
C	2.28043	7.274175	10.66063
C	2.002515	8.664609	10.05397
H	2.78437	9.241112	10.18548
H	1.224615	9.064592	10.49663
H	1.820642	8.571888	9.09559
C	2.486088	7.456902	12.16224
H	2.634847	6.583613	12.58014
H	1.689329	7.873567	12.55264
H	3.264707	8.030689	12.31884
C	1.05572	6.391963	10.42443
H	0.820128	6.407093	9.473784
H	0.302859	6.729097	10.9539
H	1.258349	5.472119	10.69604
C	4.264138	3.01112	12.41563
C	5.325122	2.213677	11.92741
H	5.261108	1.286074	11.73092
C	6.492128	2.991723	11.77373
C	6.128351	4.317174	12.12442
H	6.702709	5.072525	12.10396

Atom	x (˚A)	y (˚A)	z (˚A)
C	4.772716	4.326679	12.50949
H	4.282146	5.091923	12.78643
C	3.017418	2.466818	13.10686
C	3.428582	2.138995	14.55535
H	4.15343	1.480052	14.54847
H	2.658589	1.771019	15.03841
H	3.734093	2.956225	15.00059
C	2.496351	1.182878	12.46943
H	2.203228	1.369485	11.55386
H	1.741218	0.841865	12.991
H	3.211828	0.512102	12.45293
C	1.888979	3.500721	13.1452
H	2.193673	4.298552	13.62705
H	1.112124	3.119166	13.60471
H	1.640081	3.745715	12.22945
C	7.910394	2.426471	11.7335
C	8.928728	3.425651	11.18959
H	8.794787	3.536219	10.22502
H	9.835168	3.092009	11.35616
H	8.810974	4.288854	11.63809
C	8.282994	2.106795	13.18904
H	8.254567	2.929068	13.7216
H	9.187843	1.730284	13.21963
H	7.646669	1.458715	13.55485
C	8.009059	1.133607	10.92382
H	7.377872	0.475246	11.28224
H	8.920074	0.779792	10.98485
H	7.790618	1.317111	9.986067
C	5.28957	2.682716	7.439955
C	4.009969	3.219453	7.178829
H	3.812681	3.867921	6.513549
C	3.065274	2.640235	8.062086
C	3.784613	1.76617	8.913196
H	3.414876	1.245339	9.616467
C	5.14536	1.799922	8.53672
H	5.847172	1.311291	8.951188
C	6.460752	2.674181	6.452694
C	6.201948	1.488199	5.505144
H	6.168534	0.657585	6.023615
H	6.925715	1.433497	4.846053
H	5.348231	1.619716	5.042027
C	6.515416	3.944931	5.601755
H	5.654819	4.071598	5.148609
H	7.226401	3.860162	4.933726
H	6.697635	4.715605	6.178331

Atom	x (˚A)	y (˚A)	z (˚A)
C	7.809059	2.462357	7.148401
H	7.963543	3.187059	7.789098
H	8.525311	2.459641	6.479168
H	7.801141	1.604198	7.620629
C	1.555511	2.610168	7.826401
C	1.320166	1.63698	6.655716
H	0.357793	1.549884	6.49292
H	1.695632	0.760394	6.879711
H	1.758445	1.982455	5.849989
C	0.991837	3.975385	7.432047
H	1.058623	4.589519	8.193079
H	0.052386	3.87762	7.171952
H	1.504375	4.335408	6.676861
C	0.805185	2.087785	9.046768
H	0.944556	2.696294	9.802127
H	1.141753	1.196844	9.27953
H	-0.15091	2.032889	8.842886

References

1. *CrysAlisPRO*, version 39.27b; Oxford Diffraction /Agilent Technologies UK Ltd: Yarnton, U.K., 2017.
2. Sheldrick, G. M. *Acta Crystallogr., Sect. A*., 2008, **64**, 112.
3. Sheldrick, G. M. *Acta Crystallogr., Sect. C*, 2015, **71**, 3.
4. Dolomanov, O. V.; Bourhis, L. J.; Gildea, R. J.; Howard, J. A. K.; Puschmann, H. *J. Appl. Crystallogr*., 2009, **42**, 339.
5. L. J. Farrugia, *J. Appl. Crystallogr*., 2012, **45**, 849.
6. *POV-Ray. Persistence of Vision Raytracer*; Persistence of Vision Pty. Ltd.: Williamstown, Victoria, Australia, 2013.
7. S. Stoll, R. D. Britt, *Phys. Chem. Chem. Phys.*, **2009**, *11*, 6614.
8. C. A. P. Goodwin, N. F. Chilton, G. F. Vettese, E. Moreno Pineda, I. F. Crowe, J. W. Ziller, R. E. P. Winpenny, W. J. Evans, D. P. Mills, *Inorg. Chem.* **2016**, *55*, 10057.
9. A. Schweiger and J. Jeschke. *Principles of Pulse Electron Paramagnetic Resonance*, 2001, Oxford University Press.
10. C. J. Wedge, G. A. Timco, E. T. Spielberg, R. E. George, F. Tuna, S. Rigby, E. J. L. McInnes, R. E. P. Winpenny, S. J. Blundell, and A. Ardavan, *Phys. Rev. Lett.* **2012**, *108*, 107204/1-107204/5.
11. A. Formanuik, A.-M. Ariciu, F. Ortu, R. Beekmeyer, A. Kerridge, F. Tuna, E. J. L. McInnes, D. Mills, *Nature Chem.* **2017**, *9*, 578-583.
12. K. S. Pedersen, A.-M. Ariciu, A. McAdams, H. Weihe, J. Bendix, F. Tuna, S. Piligkos, *J. Am. Chem. Soc*. **2016**, *138*, 5801-5804.
13. K. Bader, M. Winkler, J. van Slageren, *Chem. Commun.* **2016**, *52*, 3623-3626.

Chapter IX. Conclusions and future work

Electron paramagnetic resonance spectroscopy was applied on various rare earth organometallic complexes investigating their electronic structures, relaxation times and coherence manipulation. The oxidation state as well as the ligand environment and geometry of these complexes proved to be of utmost importance for their magnetic relaxation mechanisms and quantum coherence properties.

Initial EPR studies on these types of divalent complexes was performed on an yttrium (II) complex, $[K(2.2.2\text{-cryptand})][Y(Cp')_3]$. This compound exhibits remarkably long coherence time and accessible quantum Rabi oscillations at room temperature in a magnetically diluted Y/Yb single crystal sample. A useful comparison of the observed g- and A-tensors, as well as the relaxation times between the three isostructural complexes, $[K(2.2.2\text{-cryptand})][Ln(Cp')_3]$; Ln = Y^{II}, La^{II} and Lu^{II}, shows lower anisotropy and longer relaxation times for the Y^{II} compound. In addition, analysis of the HYSCORE and ENDOR data yielded 6 % of the total electron spin density on the cyclopentadienyl ligands, which is significantly reduced compared to the other complexes i.e. 21% of $[Lu(Cp')_3]^-$.

Continuous wave and pulse EPR spectroscopic studies were conducted on a lutetium (II) complex $[K(2.2.2\text{-cryptand})][Lu(Cp')_3]$ (**1**) and a scandium (II) complex $[K(2.2.2\text{-cryptand})][Sc(N(SiMe_3)_2)_3]$ (**2**). The highly isotropic g and A tensors for both ^{175}Lu and ^{45}Sc ions, obtain by the 1st derivative and absorption measurements, support the assumption of an S-like ground state despite the fact that the unpaired electron was expected to reside on a d-orbital. A two-dimensional pulse EPR method, HYSCORE, has been involved for a more detailed characterization of the compounds spin state, molecular environment and coherence properties. Both compounds display long-lived quantum coherence, as well as nuclear Rabi modulations, notwithstanding their very rich nuclear spin environment (^{1}H, ^{13}C, ^{14}N, ^{29}Si). We also proved that all electronuclear transitions in **1** and **2**, occurring from the interaction of the unpaired electron of ^{175}Lu and ^{45}Sc with the nuclear spin (I = 7/2), are accessible for quantum information processing, probing their potential as molecular spin qu*d*its.

The effect of the structural modification of a family of organometallic La^{II} complexes on the spin dynamics and coherence properties was studied via advanced pulse EPR techniques. Comparison of the relaxation times and the HYSCORE data, displaying information of the metal-ligand covalency, suggested that the spin-lattice relaxation time is influenced by the spin-delocalization onto the ligands. Longer coherence times obtained for the complex showing greater spin density delocalization and higher rigidity of the ligand. Nutation experiments recorded Rabi oscillations at each electronuclear transitions, exploring their abilities as spin qudits.

Further research on the effect of the rigidity of the ligand on the quantum bits properties was performed via pulse EPR methods on a new Y^{II} complex; [K(2.2.2-cryptand)][$Y(OAr^{Ad,Ad,Me})_3$] based on a bulky aryloxide ligand. In this complex, the combination of the negligible magnetic anisotropy and the greater rigidity of the ligand prolonged the coherence times, which were further enhanced by dynamical decoupled measurements. Pulse hyperfine EPR studies, were performed to capture and analyse the weak interactions of the unpaired electron with the surrounding spin active nuclei on the ligands, resulting on significant electron spin density delocalized on the ligands.

These results suggested a new approach to design robust spin qubits of molecular systems with highly isotropic nature, such as molecules with unpaired electron predominantly residing in an *s*-like orbital. Hence, the minor orbital angular momentum of the ground state establishes systems insignificantly sensitive to the magnetic noise that cause the quantum decoherence.

Finally, we have applied both continuous wave and pulse EPR techniques to probe the degree of covalency in a family of [$Ln(Cp')_3$] (Ln = Ce, Nd and Sm) complexes. Analysis of the EPR data enabled a good understanding of their electronic structures and relaxation mechanisms. However, the electronic configuration of these complexes, with the unpaired electron residing in 4f-orbitals, did not allow as long coherence times as observed in the divalent lanthanide analogues, due to faster decay of the magnetization. Hyperfine sublevel correlation (HYSCORE) spectroscopy enables the direct measurements of the lanthanide covalency via the weak superhyperfine interactions. To quantify the covalency of the complexes the interactions of the unpaired electron with the ^1H and ^{13}C on the ligands was measured. More importantly, analysis and simulation of the HYSCORE data shows negligible covalency on Ce^{III} and Nd^{III} cyclopentadienyl complexes, which can be explained by the shielding of 4f electrons (ie lanthanide contraction effects) and their spatially inner character that allows negligible mixing of the metal and ligand orbitals.

Breakthroughs in the fundamental physics and chemistry of quantum materials are essential for emerging technologies in information processing, computation and communication. In future work, investigating both the nature of the quantum states and materials, and also issues of engineering and scalability might prove important. Our studies provide a great starting point for understanding the importance of studying and engineering the electronic structures in order to prolong the coherence times. It will be important that future research investgate in more detail the influence of the spin active nuclei atoms on the coherence properties of these systems, as well as more advanced studies about the scalability of the molecules, their ability to initialize the qubit state and to devise universal quantum gates.

References

1. A. Abragam and B. Bleaney. Electron paramagnetic resonance of transition ions. Oxford, England: Oxford University Press, Oxford **1970**.
2. 1. M. Brustolon and E. Giamello. Electron Paramagnetic Resonance, A practitioner's Toolkit, John Wiley and Sons Inc., New Jersey **2009**.
3. N. M. Atherton. Principles of Electron Spin Resonance. Ellis Horwood Ltd., Chichester **1993**.
4. F. E. Mabbs and D. Collison. Electron Paramagnetic Resonance of d Transition Metal Compounds. Elsevier, London **1992**.
5. M. Symons. Chemical and Biochemical Aspects of Electron Spin Resonance Spectroscopy, van Nostrand Reinhold, New York **1978**.
6. D. M. Murphy. EPR Spectroscopy of Polycrystalline Oxide Systems, John Wiley and Sons Inc., New Jersey **2009**.
7. A. Lund, M. Shiotani and S. Shimida. Principles and Applications of ESR spectroscopy, Springer, New York **2011**.
8. J. A. Weil and J. R. Bolton. Electron Paramagnetic Resonance: Elementary Theory and Practical Application, John Wiley and Sons Inc., New Jersey **2007**.
9. M. Bennati. EPR Interactions-Hyperfine couplings, *eMagRes*, **2018**, 6, 81.
10. C. Karunakaran and M. Balamurugan, Electron Paramagnetic Resonance Spectroscopy in Spin Resonance Spectroscopy: Principles and applications, Elsevier, **2018**.
11. M. M. Roessler and E. Salvadori. Principles and application of EPR spectroscopy in the chemical sciences. *Chem. Soc. Rev.*, **2018**, 47, 2534.
12. S. Richert, C. E. Tait, C. R. Timmel, *J. Magn. Reson.*, **2017**, 280, 103.
13. N. J. Stone. Table of nuclear magnetic dipole and electric quadrupole moments. At. Data. Nucl. Data Tables, **2005**, 90, 75.
14. C. P. Slichter, Principles of Magnetic Resonance, Springer, New York **1963**.
15. E. L. Hahn, *Physical Review*, 1950, 80, 580 and E. L. Hahn, *Physical Review B*, **1946**, 80, 460.
16. S. S. Eaton and G. R. Eaton. Relaxation Times of Organic Radicals and Transition Metal Ions. In L. J. Berliner, S. S. Eaton, and G. R. Eaton, editors, Distance Measurements in Biological Systems by EPR, chapter 2, Kluwer Academic/Plenum Publishers, New York **2000**.
17. A. Schweiger and G. Jeschke. Principles of Pulse Electron Paramagnetic Resonance. Oxford University Press, New York **2001**.
18. S. Stoll, Pulse EPR. *eMagRes*, **2018**, 6, 215.
19. L. G. Rowan, E. L. Hahn and W. B. Mims, *Physical Review*, **1965**, 137, A61.
20. P. Höfer, A. Grupp, H. Nebenführ, and M. Mehring, *Chem. Phys. Lett.*, **1986**, 132, 279.
21. S. Van Doorslaer. Hyperfine Spectroscopy: ESSEM EPR, EPR Spectroscopy: Fundamentals and methods, *eMagRes*, **2018**, 377.
22. J. Harmer, G. Mitrikas and A. Schweiger. Advanced pulse EPR methods for the characterization of metalloproteins. High Resolution EPR, Springer-Verlag, New York **2009**.
23. N. Ploutarch-Benetis, D. C. Paresh and D. Goldfarb. Characteristics of ESSEM and HYSCORE spectra of S>1/2 centers in orientationally disordered systems. J. Magn. Reson., **2002**, 158, 126.
24. G. Mitrikas, C. Calle, A. Schweiger, Asymmetric spin density distribution in the copper (II) complex of N-confused tetraphenylporphyrin: a multifrequency continuous-wave and pulse EPR study. *Angew. Chem. Int. Ed.*, **2005**, 44, 3301.
25. J. R. Harmer. Hyperfine spectroscopy – ENDOR, EPR Spectroscopy: Fundamentals and methods, **2018**, 331.

26. J. P. Dowling and G. J. Milburn, Quantum technology: The second quantum revolution. *Philos. Trans. R. Soc. London Ser. A Math. Phys. Eng. Sci.*, **2003**, 361, 1655.
27. A. Ghirri, A. Candini and M. Affronte. Molecular spins in the context of quantum technologies. *Magnetochemistry*, **2017**, 3, 12.
28. M. A. Nielsen and I. L. Chuang, Quantum computation and quantum information. Cambridge University press, Cambridge **2010**.
29. D. J. Christle, A. L. Falk, P. Andrich, P. V. Klimov, J. U. Hassan, N. T. Son, E. Janzen, T. Ohshima and D. D. Awschalom. Isolated electronic spins in silicon carbide with millisecond coherence times. *Nat. Mater.*, **2014**, 14, 160.
30. R. Harson and D. D. Awschalom, Coherent manipulation of single spins in semiconductors, *Nature*, **2008**, 453, 1043.
31. M. H. Devoret, R. J. Schoelkopf, *Science*, **2013**, *339*, 1169.
32. C. Monroe and J. Kim. Scaling the ion trap quantum processor. *Science*, **2013**, 339, 1164.
33. E. Knill, R. Laflamme and G. J. Millburn. A scheme for efficient quantum computation with linear optics. *Nature*, **2001**, 409, 46.
34. D. P. DiVincenzo, *Fortschr. Phys*., **2000**, *48*, 771.
35. S. Ballmann, R. Härtle, P. B. Coto, M. Elbing, M. Mayor, M. R. Bryce, M. Thoss and H. B. Weber. Experimental evidence for quantum interference and vibrationally induced decoherence in single-molecule junctions. *Phys. Rev. Lett.*, **2012**, 109, 056801.
36. V. V. Dobrovitski, M. I. Katsnelson, and B. N. Harmon. Mechanisms of decoherence in weakly anisotropic molecular magnets. *Phys. Rev. Lett.*, **2000**, 84, 3458.
37. . I. I. Rabi. Space quantisation in a gyrating magnetic field. *Phys. Rev.*, **1937**, *51*, 652.
38. M. J. Martínez-Pérez, S. Cardona-Serra, C. Schlegel, F. Moro, P. J. Alonso, H. Prima-García, J. M. Clemente-Juan, M. Evangelisti, A. Gaita-Ariño, J. Sesé, J. van Slageren, E. Coronado and F. Luis. Gd-based single-ion magnets with tunable magnetic anisotropy: Molecular design of spin qubits. *Phys. Rev. Lett.*, **2012**, *108*, 247213.
39. J. J. Pla, K. Y. Tan, J. P. Dehollain, W. H. Lim, J. J. L. Morton, F. A. Zwanenburg, D. N. Jamieson, A. S. Dzurak and A. Morello. High-fidelity readout and control of a nuclear spin qubit in silicon. *Nature*, **2013**, 496, 334.
40. K. S. Pedersen, A. M. Ariciu, S. McAdams, H. Weihe, J. Benedix. F. Tuna and S. Piligkos. Towards molecular 4f single-ion magnet qubits. *J. Am. Chem. Soc*., **2016**, *138*, 5801.
41. K. R. Brown, J. Kim and C. Monroe. Co-designing a scalable quantum computer with trapped atomic ions. *npj Quantum Inf 2*, **2016**, 16034.
42. K. Saeedi, S. Simmons, J. Z. Salvail, P. Dluhy, H. Riemann and N. V. Abrosimov. Room-temperature quantum bit storage exceeding 39 minutes using ionized donors in silicon-28. *Science*, **2013**, 342, 830.
43. A. Ardavan, O. Rival, J. J. L. Morton, S. J. Blundell, A. M. Tyryshkin, G. A. Timco and R. E. P. Winpenny. Will spin-relaxation times in molecular magnets permit quantum information processing? *Phys. Rev. Lett.*, **2007**, 98, 057201.
44. J. Ferrando-Soria, E. Moreno Pineda, A. Chiesa, A. Fernandez, S. A. Magee, S. Carretta, P. Santini, I. J. Vitorica-Yrezabal, F. Tuna, G. A. Timco, E. J. L. McInnes and R. E. P. Winpenny. A modular design of molecular qubits to implement universal quantum gates. *Nat. Commun.*, **2016**, 7, 11377.
45. J. M. Zadrozny, J. Niklas, O. G. Poluektov and D. Freedman. Millisecond coherence time in a tunable molecular electronic spin qubit. *ACS Cent. Sci.*, **2015**, 1, 488.
46. M. Atzori, L. Tesi, E. Morra, M. Chiesa, L. Sorace and R. Sessoli. Romm-temperature quantum coherence and Rabi oscillations in vanadyl phthalocyanine: Toward multifunctional moleculaer spin qubits. *J. Am. Chem. Soc.*, **2016**, 138, 2154.
47. K. Bader, D. Dengler, S. Lenz. B. Endeward, S.-D. Jiang, P. Neugebauer and J. van Slageren. Room temperature quantum coherence in a potential molecular qubit. *Nat. Commun.*, **2014**, 5, 5304.

48. M. Shiddiq, D. Komijani, Y. Duan, A. Gaita-Ariño, E. Coronado and S. Hill. Enhancing coherence in molecular spin qubits via atomic clock transitions. *Nature*, **2016**, 531, 348.
49. R. M. Brown, Y. Ito, J. H. Warner, A. Ardavan, H. Shinohara, G. A. D. Briggs and J. J. L. Morton. Electron spin coherence in metallofullerenes: Y, Sc, La@C82. *Phys Rev. B: Condens. Matter Mater. Phys.*, **2010**, 82, 033410.
50. S. Thiele, F. Balestro, R. Ballou, S. Klyatskaya, M. Ruben and W. Wernsdorfer. Electrically driven nuclear spin resonance in single-molecule magnets. *Science*, **2014**, 344, 1135.
51. G. Godfrin, A. Ferhat, R. Ballou, S. Klyatskaya, M. Ruben, W. Wernsdorfer and F. Balestro. Operating quantum states in single magnetic molecules: Impementation of Grover's quantum algorithm. *Phys. Rev. Lett.*, **2017**, 119, 187702.
52. N. Kaltsoyannis and P. Scott. The f elements, Oxford chemistry primers, Oxford University Press, Oxford **1999**.
53. R. C. Mehrotra, P. N. Kapoor and J. M. Batwara. Coordination chemistry of lanthanides with emphasis on derivatives with Ln-O-C bonds. *Coord. Chem. Rev.*, **1980**, 31, 67.
54. (a) M. P. Jensen and A. H. Bond. Comparison of covalency in the complexes of trivalent actinide and lanthanide cations. *J. Am. Chem. Soc.*, **2002**, 124, 9870; (b) I. D. Prodan, G. E. Scuseria and R. L. Martin. Covalency in the actinide dioxides: Systematic study of the electronic properties using screened hydrid density functional theory. *Phys. Rev. B*, **2007**, 76, 033101.
55. (a) M. L. Neidig, D. L. Clark and L. R. Martin. Covalency in f-element complexes. *Coord. Chem. Rev.*, **2013**, 257, 394; (b) G. R. Choppin. Covalency in f-element bonds. *J. Alloys Compd.*, **2002**, 344, 55.
56. W. Kolbe and N. Edelstein. Electron-nuclear double resonance of Pu^{3+} in CaF_2. *Phys. Rev. B*, **1971**, 4, 2869.
57. M. A. Denecke. Synchrotron applications to f-element research in the nuclear fuel cycle. *Dalton Trans.*, **2015**, 44, 2606.
58. G. Concas, C. Muntoni, G. Spano, M. Bettinelli and A. Speghini. Mossbauer investigation of Eu^{3+} site occupancy and Eu-O covalency in Y_2O_3 and Gd_2O_3 nanocrystals. *Z. Naturforsch*, **2001**, 56a, 267.
59. A. F. Povey and P. M. A. Sherwood. Covalent character of lithium compounds studied by X-ray photoelectron spectroscopy. *J. Chem. Soc., Faraday Trans. 2*, **1974**, 70, 1240.
60. S. L. Staun, D.-C. Sergentu, G. Wu, J. Autschbach and T. W. Hayton. Use of 15N NMR spectroscopy to probe covalency in a thorium nitride. *Chem. Sci.*, **2019**, 10, 6431.
61. B. Bleaney, P. M. Llewellyn and D. A. Jones. Paramagnetic resonance of uranium ions. *Proc. Phys. Soc. B*, **1956**, 69, 858.
62. A. Formanuik, A. –M. Ariciu, F. Ortu, R. Beekmeyer, A. Kerridge, F. Tuna, E. J. L. McInnes and D. P. Mills. Actinide covalency measured by pulsed electron paramagnetic resonance spectroscopy. *Nat. Chem.*, **2017**, 9, 578.
63. R. G. Denning, J. Harmer, J. C. Green and M. Irwin. Covalency in the 4f shell of tris-cyclopentadienyl ytterbium ($YbCp_3$) - A spectroscopic evaluation. *J. Am. Chem. Soc.*, **2001**, 133, 20644-20660.